RUHR-UNIVERSITÄT BOCHUM

SFB 837
Interaction Modeling in Mechanized Tunneling

Thomas Barciaga

Constitutive modeling of natural clay
with application to mechanized tunneling

Bochum 2024 Heft 81

Schriftenreihe des Lehrstuhls für
Bodenmechanik, Grundbau und Umweltgeotechnik

Herausgeber: Torsten Wichtmann

ISSN 2699-1020

Thomas Barciaga Constitutive modeling of natural clay

81

ISSN 2699-1020

Ruhr-Universität Bochum
Schriftenreihe Bodenmechanik, Grundbau und Umweltgeotechnik
Heft 81

Herausgeber:
Prof. Dr.-Ing. habil. Torsten Wichtmann
Ruhr-Universität Bochum
Fakultät für Bau- und Umweltingenieurwissenschaften
Lehrstuhl für Bodenmechanik, Grundbau und Umweltgeotechnik
44801 Bochum
Telefon: 0234/ 3226135
Telefax: 0234/ 3214236
Internet: www.bgu.ruhr-uni-bochum.de

ISSN 2699-1020

© 2024 der Herausgeber

Constitutive modeling of natural clay with application to mechanized tunneling

Dissertation

as a requirement for the degree of

Doktor-Ingenieur (Dr.-Ing.)

at the

Department of Civil and Environmental Engineering

Ruhr-Universität Bochum

by

Thomas Barciaga

Reviewers

Prof. Torsten Wichtmann

Prof. Maria Datcheva

Prof. Mahdi Taiebat

Bochum, November 2024

Preface of the editor

Mechanized tunneling is a well-established construction method for underground infrastructure. In urban areas the effects of tunnel construction, in particular the resulting settlements at the ground surface and their impacts on existing buildings or aboveground infrastructure must be carefully assessed. Natural structured clays are especially prone to tunneling-induced settlements because of a possible destructuration caused by mechanical loading. Generally, mechanized tunneling in structured clay is a 3D problem with complex hydro-mechanical interactions. Realistic and reliable predictions need numerical methods like finite element simulations with sophisticated constitutive models.

The doctoral thesis of Thomas Barciaga follows the question if and how detailed the various features of natural clay, like inherent and induced anisotropy, structure and destructuration, and the response to non-monotonic or cyclic loading paths should be considered in an adequate numerical model for mechanized tunneling. For his investigations Thomas Barciaga has developed a smart hierarchical constitutive modeling approach based on bounding surface plasticity (BSP) which allows to separately activate or deactivate the different features of natural clay behavior. The robust implementation of the complex constitutive equations into a commercial finite element code (Plaxis) undertaken by Thomas Barciaga enabled him to investigate not only geotechnical laboratory tests but also a tunnel construction process using a detailed 3D model considering several subsystems.

For an effective calibration of the BSP model parameters based on experimental data Thomas Barciaga applied a global sensitivity analysis, identifying the most suitable types and phases of element tests for the calibration of a certain parameter. While some of the parameters can be directly derived from the experiments or calculated from analytical equations, the remaining ones are determined from an inverse analysis applying particle swarm optimization. Thomas Barciaga demonstrates the calibration for Onsoy clay as a typical representative of natural structured clay, using laboratory tests performed at RUB as well as additional data from the literature.

The calibrated set of parameters is used in a finite element parametric study simulating the staged mechanized construction of a shallow tunnel under greenfield conditions.

Thomas Barciaga meticulously investigates the impact of the various clay features on the tunneling-induced settlements, excess pore-water pressures and effective stress paths, considering different initial overconsolidation degrees and drainage conditions. Based on the numerical results he derives practical recommendations regarding the necessary level of complexity of the applied constitutive model when simulating mechanized tunneling in natural structured clay. Among others he emphasizes the need to consider the degradation of structure for clays with low overconsolidation degrees in order to prevent an underestimation of surface settlements and inclination of the settlement trough.
The doctoral thesis of Thomas Barciaga represents a valuable contribution towards more realistic and reliable numerical predictions of the effects of mechanized tunneling in natural structured clay. The derived recommendations with respect to the necessary complexity of the constitutive model for different boundary conditions are of high interest for future researchers and practitioners.
This research has been done in the framework of the project A5 of Collaborative Research Center (SFB) 837 "Interaction Modeling in Mechanized Tunneling" at Ruhr-Universität Bochum. The funding of German Research Council (DFG) is gratefully acknowledged.

Bochum, November 2024,
Torsten Wichtmann

Abstract

Mechanized tunneling is a very common method to conduct subsurface infrastructural projects particularly in urban areas due to the limited surface space. Especially mechanized tunneling in natural clay deposits is challenging due to the complex constitutive soil behavior governed by current state, stress-strain history and structure composed of fabric and interparticle bonding. The aim of the present study is to propose a concept for an adequate numerical analysis of mechanized tunneling in natural clay based on the required complexity of the constitutive modeling to ensure realistic and reliable predictions of the system behavior such as surface settlements. Therefore, the spatial and construction stage dependent evolution of the influence of the particular soil mechanical properties of natural clay (e.g. inherent and stress-induced anisotropy, initial structure and progressive destructuration, behavior under non-monotonic or cyclic loading incorporating stress-strain hysteresis and elastoplastic transition, stiffness degradation and accumulative effects) on the response of a numerical model simulating mechanized tunneling is evaluated employing the concept of the hierarchical bounding surface plasticity (BSP) model family.

To achieve realistic and reliable predictions of the system behavior resulting from mechanized tunneling an appropriate numerical 3D simulation model considering a homogeneous, water-saturated natural Onsøy clay deposit under greenfield conditions is developed in a state-of-the-art finite element model code. Furthermore, a sophisticated constitutive BSP model accounting for the complex constitutive behavior of natural clay is employed and implemented to the model code by numerical integration of the constitutive equations incorporating the modified Euler approach with automatic error control and sub-stepping approach. The demanding calibration of the constitutive BSP model parameters with respect to natural Onsøy clay is conducted via direct experimental and analytical determination and automated inverse analysis using particle swarm optimization. Beforehand, global sensitivity analysis is applied to provide additional information on the geotechnical laboratory test and even loading stage to be selected to most properly identify a particular constitutive BSP model parameter. Moreover, the influence of the hierarchical complexity of the BSP model on the model response regarding numerical simulations of geotechnical

laboratory tests on natural Onsøy clay is investigated to better interpret the results from the mechanized tunneling simulation afterwards.
The study concludes with the development of practical recommendations if typical mechanical properties of natural clay have to be considered in the numerical analysis of mechanized tunneling with respect to realistic and reliable predictions of surface settlements in design and construction phases. Since initial structure and destructuration have significant impact on the settlement behavior, because of the striking stiffness and strength degradation governed by plastic straining, consideration is always required in regard to safety issues and damage assessment. To be more precise, due to destructuration the maximum surface settlements will significantly increase and the transverse settlement trough and the longitudinal settlement trough hurrying ahead of the shield machine become more steep. However, the influence of anisotropy and soil behavior under non-monotonic or cyclic loading on the settlement behavior is less pronounced and strongly dependent on the initial stress conditions and drainage conditions, so that the necessity of consideration has to be decided from case to case with respect to risk management of aboveground edifices and infrastructure.

Contents

Preface of the editor i

Abstract iii

Table of contents v

List of symbols xi

1 Introduction 1

1.1 Motivation 1
1.2 Objectives and methodology 4
1.3 Structure of the present study 6

2 State of the art 9

2.1 Natural clay 10
2.1.1 Clay and clay minerals 10
2.1.2 Clay system 11
2.1.3 Structure of natural clay 13
2.1.3.1 Fabric and interparticle bonding 13
2.1.3.2 Structured and reconstituted clay 14
2.1.3.3 Strength sensitivity 15
2.1.3.4 Destructuration 17
2.1.4 In situ stress conditions 17
2.1.4.1 Normally consolidated and overconsolidated clay 17
2.1.4.2 Coefficient of earth pressure at rest 18
2.1.4.3 Yield stress 19
2.1.5 Geological characteristics of selected natural clays 21
2.1.6 Summary 23

2.2 Mechanical behavior of natural clay . . . 23
2.2.1 Volumetric behavior . . . 23
2.2.1.1 Influence of structure and destructuration . . . 23
2.2.1.2 Quantification of structure . . . 28
2.2.1.3 Classification of natural clay by intrinsic void index . . . 29
2.2.1.4 Influence of overconsolidation . . . 31
2.2.2 Shear strength and associated stress-strain behavior . . . 32
2.2.2.1 General triaxial stress-strain behavior . . . 32
2.2.2.2 Inherent and stress-induced anisotropy . . . 36
2.2.2.3 Anisotropic yielding characteristics . . . 38
2.2.2.4 Influence of structure and destructuration . . . 43
2.2.3 Cyclic behavior . . . 50
2.2.3.1 Generation of excess pore-water pressure and evolution of effective stress path . . . 51
2.2.3.2 Degradation of stiffness and accumulation of plastic strain 54
2.2.3.3 Influence of structure and destructuration . . . 54
2.2.4 Summary . . . 55
2.3 Constitutive modeling of natural clay . . . 56
2.3.1 Critical state models . . . 57
2.3.2 Modeling of anisotropy . . . 59
2.3.2.1 Rotational hardening . . . 59
2.3.2.2 Rotational hardening rules . . . 60
2.3.2.3 Further approaches . . . 62
2.3.3 Modeling of structure and destructuration . . . 63
2.3.3.1 Intrinsic reference yield surface and structure variable . . . 63
2.3.4 Modeling of cyclic behavior . . . 69
2.3.4.1 Bounding surface plasticity . . . 69
2.3.4.2 Radial projection rule . . . 70
2.3.4.3 Plasticity modulus and distance function . . . 71
2.3.4.4 Stiffness degradation . . . 72
2.3.4.5 Updated projection center . . . 74
2.3.4.6 Further approaches . . . 75
2.3.5 Summary . . . 75
2.4 Numerical modeling of mechanized tunneling . . . 77
2.4.1 Mechanized tunneling with EPB shield machine . . . 78
2.4.2 Shield tunneling induced settlements . . . 81

2.4.3 Numerical modeling of subsystems 84
2.4.3.1 3D tunnel simulation model 85
2.4.3.2 Tunnel face support 86
2.4.3.3 Tail void grouting 88
2.4.3.4 Volume loss 90
2.4.3.5 Soil-structure interaction 91
2.4.3.6 Machine steering and jack thrust forces 92
2.4.4 Constitutive modeling 93
2.4.5 Summary 96

3 Formulation of BSP model for natural clay 99
3.1 Model structure 99
3.2 Elasticity 101
3.3 Bounding surface plasticity 101
3.3.1 BSP concept 101
3.3.2 Critical state soil mechanics 106
3.3.3 Anisotropy and rotational hardening 106
3.3.4 Uniqueness of critical state 110
3.3.5 Restriction of excessive rotation 110
3.3.6 Non-associated flow rule and Lode angle dependence 111
3.3.7 Isotropic hardening/softening and destructuration 112
3.3.8 Shape hardening function and damage variable 116
3.3.9 Projection center 116
3.4 Summary 118

4 Implementation of BSP model for natural clay 121
4.1 Concept 121
4.2 Global iterative procedure 123
4.3 Coupling between FE-code and constitutive BSP model 125
4.4 Integration of constitutive equations 127
4.4.1 General formulations 127
4.4.2 Explicit integration scheme with automatic error control and sub-stepping approach 129
4.4.3 Modified Euler approach 142
4.4.4 Drift correction 154
4.4.5 Tangent and secant elastic stiffness matrix 162
4.4.6 Elastic nucleus 164

4.4.7 Intersection stress and intersection factor . . . 166
4.4.8 Similarity ratio . . . 171
4.4.9 Lode angle dependence . . . 176
4.4.10 Gradients . . . 185
4.5 Summary . . . 188

5 Sensitivity analysis regarding BSP model parameters 191
5.1 Concept . . . 191
5.2 Global sensitivity analysis . . . 193
5.2.1 Variance-based GSA . . . 193
5.2.2 Constitutive BSP model parameters . . . 195
5.2.3 Numerical testing program . . . 198
5.2.4 Settings of GSA . . . 201
5.3 General ability of the BSP model . . . 202
5.3.1 Oedometer test . . . 202
5.3.2 Isotropic compression test . . . 203
5.3.3 Monotonic undrained triaxial tests . . . 204
5.3.4 Cyclic undrained triaxial tests . . . 210
5.4 Results of GSA . . . 214
5.4.1 Oedometer test . . . 215
5.4.2 Monotonic undrained triaxial tests . . . 220
5.4.3 Cyclic undrained triaxial test . . . 235
5.5 Recommendations . . . 241
5.6 Summary . . . 248

6 Calibration of BSP model parameters 249
6.1 Experimental data on Onsøy clay . . . 250
6.2 Experimental determination . . . 255
6.2.1 BSP model parameters . . . 255
6.2.2 Initial conditions . . . 261
6.3 Analytical determination . . . 263
6.4 Inverse analysis . . . 267
6.4.1 Concept . . . 267
6.4.2 Particle swarm optimization . . . 269
6.4.3 Constitutive BSP model parameters . . . 271
6.4.4 Numerical testing program . . . 271
6.4.5 Objective function . . . 272

6.4.6 Settings of PSO . . . 275
6.5 Results of calibration . . . 276
6.5.1 BSP model parameter set for natural Onsøy clay . . . 276
6.5.2 BSP model performance regarding monotonic tests . . . 276
6.5.3 BSP model performance regarding cyclic test . . . 280
6.6 Summary . . . 283

7 Hierarchical BSP model family 285
7.1 Concept . . . 285
7.2 Influence of hierarchical BSP model complexity . . . 288
7.2.1 Numerical testing program . . . 288
7.2.2 Oedometer test . . . 288
7.2.3 Monotonic undrained triaxial compression test . . . 293
7.2.4 Monotonic undrained triaxial extension test . . . 297
7.2.5 Cyclic undrained triaxial test . . . 300
7.3 Summary . . . 303

8 Numerical model for mechanized tunneling 307
8.1 Numerical 3D tunnel simulation model . . . 308
8.1.1 Geometry, discretization, initial and boundary conditions . . . 308
8.1.2 Numerical subsystems . . . 310
8.1.3 Staged construction . . . 313
8.2 Summary . . . 315

9 Natural clay behavior with application to mechanized tunneling 317
9.1 Numerical analysis . . . 319
9.1.1 Setup . . . 319
9.1.2 Scenarios . . . 319
9.1.3 Synthetic measurement section . . . 320
9.1.4 Construction stages . . . 320
9.1.5 Model responses . . . 321
9.2 Results and evaluation . . . 322
9.2.1 Surface settlements, vertical soil displacements and void ratio . . . 322
9.2.1.1 Transverse settlement trough . . . 323
9.2.1.2 Longitudinal settlement trough . . . 331
9.2.1.3 Evolution of surface settlements s . . . 333
9.2.1.4 Evolution of vertical soil displacements u_v . . . 337

9.2.1.5 Evolution of void ratio e . . . 344
9.2.2 Effective stress path and excess pore-water pressure . . . 347
9.2.2.1 Above the tunnel . . . 348
9.2.2.2 Between the tunnel and the ground surface . . . 357
9.2.2.3 Beside the tunnel . . . 362
9.2.2.4 Below the tunnel . . . 369
9.2.3 State variables of the BSP model and plastic strain . . . 378
9.2.3.1 Evolution of plastic strain $|\boldsymbol{\varepsilon}^{\mathrm{p}}|$ . . . 378
9.2.3.2 Evolution of structure variable S_{i} . . . 385
9.2.3.3 Evolution of rotational hardening variable $|\boldsymbol{\alpha}|$ . . . 391
9.2.3.4 Evolution of damage variable d . . . 394
9.3 Practical recommendations regarding surface settlements . . . 400
9.3.1 Initial structure and destructuration . . . 401
9.3.2 Inherent and stress-induced anisotropy . . . 405
9.3.3 Non-monotonic or cyclic behavior . . . 407

10 Conclusions and outlook **411**

Bibliography **421**

List of symbols

$\boldsymbol{A}_{\mathrm{s}}$	auxiliary matrix for sensitivity analysis
A	parameter controlling fraction of plastic strain for destructuration
A_{b}	auxiliary variable for calculation of similarity ratio
A_{f}	area of tunnel face
A_{int}	auxiliary variable for calculation of intersection stress
a_{bs}	auxiliary variable for determination of X_{pc}
a_{dam}	parameter controlling the rate of stiffness degradation
$\boldsymbol{B}$	strain interpolation matrix
$\boldsymbol{B}_{\mathrm{s}}$	auxiliary matrix for sensitivity analysis
B	auxiliary variable for calculation of α_{K_0}
B_{b}	auxiliary variable for calculation of similarity ratio
B_{int}	auxiliary variable for calculation of intersection stress
b	similarity ratio
b_{eln}	similarity ratio for elastic nucleus
b_{max}	maximum similarity ratio
b_{min}	minimum similarity ratio
$\boldsymbol{C}_{n_{\mathrm{cp}}}$	auxiliary matrices for sensitivity analysis
C_{b}	auxiliary variable for calculation of similarity ratio
C_{c}	elastoplastic compression index
C_{c}^{*}	intrinsic compression index
C_{int}	auxiliary variable for calculation of intersection stress
C_{s}	elastic swelling index
c_1	constant learning factor for inverse analysis

c_2	constant learning factor for inverse analysis
c_α	parameter controlling the rate of rotation
convergence	logical variable
$\boldsymbol{D}^{\mathrm{e}}$	elastic stiffness matrix
$\boldsymbol{D}^{\mathrm{e}}_{\mathrm{sec}}$	secant elastic stiffness matrix
$\boldsymbol{D}^{\mathrm{ep}}$	elastoplastic stiffness matrix
D	diameter of the excavated area of the tunnel
D_{f}	diameter of tunnel face
d	damage variable
$\tilde{d}$	auxiliary damage variable
d_{drift}	damage variable for drift correction
$\tilde{d}_{\mathrm{drift}}$	auxiliary damage variable for drift correction
d_{lining}	thickness of lining
d_{shield}	thickness of shield machine
$\boldsymbol{e}$	deviatoric strain tensor
$\boldsymbol{e}^{\mathrm{p}}$	plastic deviatoric strain tensor
E	global error for iterative procedure
$E_{\Delta \mathrm{F,lim}}$	limit value for inverse analysis
$E_{\mathrm{F,tol}}$	tolerated error for inverse analysis
E_{lining}	Young's modulus of lining
$E_{\mathrm{max,ci}}$	maximum resulting support force due to effective earth pressure
E_{shield}	Young's modulus of shield machine
E_{tol}	tolerance for global error for iterative procedure
EA	axial rigidity
EI	flexural rigidity
e	void ratio
e_0	initial void ratio
$e_{0,\mathrm{cs}}$	void ratio at critical state for unit pressure
e^*_{100}	intrinsic void ratio at effective stress of 100 kPa
e^*_{1000}	intrinsic void ratio at effective stress of 1,000 kPa
$e_{\mathrm{consol.}}$	void ratio after consolidation

e_{cs}	void ratio at critical state
e^{e}	elastic void ratio
e_{L}	void ratio at liquid limit
e_{n}	natural void ratio
e_{reset}	storage void ratio at beginning of sub-step
$\boldsymbol{F}$	tensor of forces
$\Delta\boldsymbol{F}$	tensor of unbalanced forces
$\boldsymbol{F}_{\mathrm{ext}}$	tensor of external nodal forces
$\boldsymbol{F}_{\mathrm{int}}$	tensor of internal nodal forces
F	bounding surface
F_{i}	intrinsic reference surface
$F(\boldsymbol{P})$	objective function for inverse analysis
$F'(\boldsymbol{P})$	sum of the error measures for inverse analysis
f	yield surface
$\hat{f}$	distance function
f_{eln}	elastic nucleus
G	plastic potential surface for bounding surface plasticity
G^{e}	elastic shear modulus
$G^{\mathrm{e}}_{\mathrm{sec}}$	secant elastic shear modulus
g	plastic potential surface
H	overburden depth
$\hat{h}$	shape hardening function
h_0	parameter defining initial shape hardening stiffness
$\boldsymbol{I}$	identity tensor
I_{C}	consistency index
I_{L}	liquidity index
I_{P}	plasticity index
I_{v}	intrinsic void index
i	number of iteration
$i_{\max}$	maximal number of iterations
i_{TBM}	counting variable for position of shield machine

int	scalar stress multiplier
$inter$	scalar strain intersection factor
J_{lt}	number of sets of measurements for inverse analysis
j	number of iteration for drift correction
j_{lt}	specific measurement set (laboratory test) for inverse analysis
$j_{\max}$	maximal number of iterations for drift correction
$\boldsymbol{K}$	global stiffness matrix
K_0	coefficient of earth pressure at rest
$K_{0,\mathrm{el}}$	elastic coefficient of earth pressure at rest
$K_{0,\mathrm{ur}}$	coefficient of earth pressure at rest in unloading/reloading
K^{e}	elastic bulk modulus
$K^{\mathrm{e}}_{\mathrm{sec}}$	secant elastic bulk modulus
$K_{j_{\mathrm{lt}}}$	number of measurement points for inverse analysis
K_{p}	plasticity modulus
$\bar{K}_{\mathrm{p}}$	plasticity modulus for image stress
k	interpolation variable
k_{f}	coefficient of permeability
k_{i}	parameter controlling the rate of destructuration
k_{mp}	specific measurement point for inverse analysis
L	plastic loading index
L_{drift}	plastic loading index for drift correction
l	iteration number
$l_{\max}$	maximum iteration number
$M(\theta)$	Lode angle dependent critical state stress ratio
M_{c}	critical state stress ratio in triaxial compression
M_{e}	critical state stress ratio in triaxial extension
M_{lining}	internal bending moment for lining
$M_{\mathrm{r}}(\theta_{\mathrm{r}})$	Lode angle dependent critical state stress ratio for bounding attractor
M_{sw}	number of swarm particles for inverse analysis
m	sub-step number for time integration
m_{cs}	ratio of M_{e} and M_{c}

$m_{\max}$	maximal number of sub-steps for time integration
m_{sw}	specific swarm particle for inverse analysis
m_{α}	parameter controlling bounding attractor
$\boldsymbol{n}_{\mathrm{pc}}$	unit norm tensor for projection center
$\boldsymbol{n}_{\mathrm{r}}$	unit norm deviatoric stress tensor
$\bar{\boldsymbol{n}}_{\mathrm{r}}$	unit norm deviatoric image stress tensor
$N(\theta)$	Lode angle dependent variable defining shape of bounding surface
N_{c}	parameter defining shape of bounding surface in compression
N_{calc}	auxiliary variable for iterative solution for similarity ratio
N_{cp}	number of constitutive model parameters for inverse analysis
N_{e}	parameter defining shape of bounding surface in extension
N_{inter}	auxiliary variable for iterative solution of intersection stress
N_{lining}	internal normal force for lining
n	calculation step number for time integration
n_{cp}	specific constitutive model parameter for inverse analysis
n_{cs}	ratio of N_{e} and N_{c}
n_{fail}	number of cycles at failure
n_{α}	parameter controlling bounding attractor
OCR	overconsolidation ratio
$\boldsymbol{P}$	tensor of constitutive model parameters
p	total mean stress
p_0	consolidation stress / isotropic hardening variable for bounding surface
$p_{0,\mathrm{i}}$	isotropic hardening variable defining size of intrinsic reference surface
$\tilde{p}_{0,\mathrm{i}}$	auxiliary isotropic hardening variable
$p_{0,\mathrm{s}}$	isotropic hardening variable defining size of bounding surface
$\tilde{p}_{0,\mathrm{s}}$	auxiliary isotropic hardening variable
$p_{0,\mathrm{s,eln}}$	hardening variable defining size of elastic nucleus
$p_{0,\mathrm{s,eln,mod}}$	modified hardening variable defining size of elastic nucleus
$p_{0,\mathrm{s,init}}$	parameter defining initial size of bounding surface
p_{atm}	atmospheric pressure
p_{w}	pore-water pressure

Δp_{w}	excess pore-water pressure
p_{α}	hardening variable defining size of plastic potential surface
$p_{\alpha,\mathrm{lim}}$	limiting value for p_{α}
p'	effective mean stress
$\bar{p}'$	effective mean image stress
$p'_{\mathrm{BS,init}}$	effective mean stress on the initial bounding surface for YSR
p'_{cs}	effective mean stress at critical state
$p'_{\mathrm{cur\text{-}pc}}$	effective mean stress for $\boldsymbol{\sigma}'_{\mathrm{cur\text{-}pc}}$
p'_{eln}	effective mean stress for elastic nucleus
$p'_{\mathrm{eln,mod}}$	modified effective mean stress for elastic nucleus
$p'_{\mathrm{eln,origin}}$	effective mean stress for origin of elastic nucleus
p'_{pc}	effective mean stress for projection center
p'_{peak}	effective mean stress corresponding to q_{peak}
p'_{trial}	effective trial mean stress
$\boldsymbol{q}$	tensor of state variables
$\tilde{\boldsymbol{q}}$	auxiliary tensor of state variables
$\boldsymbol{q}_{\mathrm{drift}}$	tensor of state variables for drift correction
$\tilde{\boldsymbol{q}}_{\mathrm{drift}}$	auxiliary tensor of state variables for drift correction
q	deviatoric stress
$q_{0,\mathrm{cyc}}$	initial cyclic shear stress
q_{cs}	deviatoric stress at critical state
q_{peak}	peak deviatoric stress
Δq_{cyc}	cyclic shear stress amplitude
r	scalar distance between image stress and projection center
R_{inter}	interaction factor
$\boldsymbol{r}$	deviatoric stress ratio tensor
$\bar{\boldsymbol{r}}$	deviatoric image stress ratio tensor
$\boldsymbol{r}_{\mathrm{pc}}$	deviatoric stress ratio tensor for projection center
R	relative error for time integration
R_{s}	number of sample sets for sensitivity analysis
R_{Tol}	error tolerance for time integration

r_1	independent random weighting factor for inverse analysis
r_2	independent random weighting factor for inverse analysis
$\boldsymbol{s}$	deviatoric stress tensor
$\bar{\boldsymbol{s}}$	deviatoric image stress tensor
$\boldsymbol{s}_{\mathrm{bs}}$	auxiliary stress tensor for X_{pc}
$\boldsymbol{s}_{\mathrm{BS,init}}$	deviatoric stress tensor for initial bounding surface via YSR
$\boldsymbol{s}_{\text{cur-pc}}$	deviatoric stress tensor for $\boldsymbol{\sigma}'_{\text{cur-pc}}$
$\boldsymbol{s}_{\mathrm{eln}}$	deviatoric stress tensor for elastic nucleus
$\boldsymbol{s}_{\mathrm{eln,mod}}$	modified deviatoric stress tensor for elastic nucleus
$\boldsymbol{s}_{\mathrm{pc}}$	deviatoric stress tensor for projection center
$\boldsymbol{s}_{\mathrm{trial}}$	trial deviatoric stress tensor
$\boldsymbol{s}_{\alpha}$	auxiliary stress tensor for X_{pc}
S_{ci}	face support force
S_{i}	structure variable
$\tilde{S}_{\mathrm{i}}$	auxiliary structure variable
$S_{\mathrm{i,0}}$	parameter defining initial structure
$S_{\mathrm{i,drift}}$	structure variable for drift correction
$\tilde{S}_{\mathrm{i,drift}}$	auxiliary structure variable for drift correction
$S_{n_{\mathrm{cp}}}$	first order sensitivity index
$S_{\mathrm{T}_{n_{\mathrm{cp}}}}$	total effect sensitivity index
$S_{\mathrm{T}_{n_{\mathrm{cp}}},\mathrm{norm}}$	normalized total effect sensitivity index
S_{t}	strength sensitivity
S_{λ}	stiffness sensitivity
S_{σ}	stress sensitivity
s	settlement
s_{eln}	parameter defining size of elastic nucleus
$s_{\text{face, crown}}$	face pressure at tunnel crown
$s_{\text{face, invert}}$	face pressure at tunnel invert
$s_{\text{grout, crown}}$	grouting pressure at tunnel crown
s_{u}	undrained shear strength
s_{α}	parameter controlling bounding attractor

T	pseudo time for time integration
$T_{\min}$	minimum pseudo time for time integration
$\boldsymbol{u}$	tensor of displacements
u_{lining}	radial lining displacements
u_{v}	vertical soil displacements
u_{VL}	radial deformation for volume loss
$\boldsymbol{V}_{m_{\text{sw}}}$	current velocity of m_{sw}-th swarm particle
V	volume
V_{g}	soil volume change
V_{s}	surface volume loss
V_{t}	tunnel volume loss
v	specific volume
v_{cs}	specific volume at critical state
W_{ci}	resulting support force due to hydrostatic water pressure
$w_{j_{\text{lt}}}$	weighting factor for inverse analysis
$w_{k_{\text{mp}}}$	weighting factor for inverse analysis
w_{L}	liquid limit
w_{n}	natural water content
w_{P}	plastic limit
$\boldsymbol{X}_{m_{\text{sw}}}$	current position of m_{sw}-th swarm particle
$\boldsymbol{X}^{\text{Global}}$	previous global best position among all swarm particles
$\boldsymbol{X}^{\text{Local}}_{m_{\text{sw}}}$	previous own local best position of m_{sw}-th swarm particle
X	coordinate in transverse tunnel direction
X_{pc}	auxiliary variable for position of projection center
x_{α}	parameter controlling bounding attractor
$\boldsymbol{y}_{\text{A}}$	model output tensor for sensitivity analysis
$\boldsymbol{y}_{\text{B}}$	model output tensor for sensitivity analysis
$\boldsymbol{y}_{\text{C}_{\boldsymbol{n}_{\text{cp}}}}$	model output tensor for sensitivity analysis
$\boldsymbol{y}^{\text{meas}}_{\text{CAUC}}$	measurement data tensor for CAUC-2 test
$\boldsymbol{y}^{\text{meas}}_{\text{CAUcyc}}$	measurement data tensor for CAUcyc-40 test
$\boldsymbol{y}^{\text{meas}}_{\text{CAUE}}$	measurement data tensor for CAUE-8 test

$\boldsymbol{y}_{\mathrm{oed}}^{\mathrm{meas}}$	measurement data tensor for CSR-Oed-B1-35
Y	coordinate in longitudinal tunnel direction
YSR	yield stress ratio
y	model output for GSA
$\bar{y}_{\mathrm{A}}$	mean value estimate for $\boldsymbol{y}_{\mathrm{A}}$
$\bar{y}_{\mathrm{B}}$	mean value estimate for $\boldsymbol{y}_{\mathrm{B}}$
$y_{j_{\mathrm{lt}},k_{\mathrm{mp}}}^{\mathrm{calc}}(\boldsymbol{P})$	numerically calculated model responses for inverse analysis
$y_{j_{\mathrm{lt}},k_{\mathrm{mp}}}^{\mathrm{meas}}$	experimental measurement data for inverse analysis
Z	coordinate in vertical direction
z_α	parameter controlling bounding attractor
$\boldsymbol{\alpha}$	fabric stress tensor
$\tilde{\boldsymbol{\alpha}}$	auxiliary fabric stress tensor
$\boldsymbol{\alpha}_{\mathrm{b}}$	bounding attractor for fabric stress tensor
$\boldsymbol{\alpha}_{\mathrm{cs}}$	fabric stress tensor at critical state
α	rotational hardening variable
α_0	parameter defining initial rotation
α_{b}	bounding attractor
α_{cs}	parameter defining rotation at critical state
$\alpha_{\mathrm{K_0}}$	rotation of plastic potential surface under K_0 loading
α_{VL}	factor for core support method
β	variable for rotation of yield surface
β_{VL}	factor for stress reduction method
γ	unit weight
γ'	unit weight under buoyancy
γ_{lining}	unit weight of lining
γ_{s}	unit weight of support medium
γ_{shield}	unit weight of shield machine
Δ	increment
δ	scalar distance between image stress and current stress
δ_{VL}	factor for lining reduction method
$\boldsymbol{\varepsilon}$	strain tensor

$\boldsymbol{\varepsilon}^{\mathrm{e}}$	elastic strain tensor
$\boldsymbol{\varepsilon}^{\mathrm{p}}$	plastic strain tensor
$\boldsymbol{\varepsilon}^{\mathrm{p}}_{\mathrm{drift}}$	plastic strain tensor for drift correction
ε_{a}	axial strain
$\varepsilon_{\mathrm{a,compr}}$	axial strain in triaxial compression
$\varepsilon_{\mathrm{a,ext}}$	axial strain in triaxial extension
ε_{d}	triaxial deviatoric strain
$\varepsilon^{\mathrm{p}}_{\mathrm{d}}$	plastic deviatoric strain
$\varepsilon^{\mathrm{p}}_{\mathrm{destr}}$	plastic destructuration strain
$\tilde{\varepsilon}^{\mathrm{p}}_{\mathrm{destr}}$	auxiliary plastic destructuration
ε_{r}	radial strain
ε_{v}	volumetric strain
$\varepsilon^{\mathrm{p}}_{\mathrm{v}}$	plastic volumetric strain
ζ	strain extrapolation factor
η	stress ratio
$\bar{\eta}$	image stress ratio
η_{E}	safety factor for earth pressure
η_{init}	initial stress ratio
$\eta_{\mathrm{in\,situ}}$	in situ stress ratio
η_{iso}	isotropic stress ratio
$\eta_{\mathrm{K_0}}$	stress ratio for K_0
$\eta_{\mathrm{K_{0,el}}}$	elastic stress ratio for $K_{0,\mathrm{el}}$
$\eta_{\mathrm{K_{0,pl}}}$	plastic stress ratio for K_0
η_{W}	safety factor for water pressure
θ	Lode angle
θ_{r}	Lode angle for bounding attractor
κ	elastic swelling parameter
λ	elastoplastic compression parameter
λ_0	compression index for yielding state
λ_{cs}	compression index at critical state
λ_∞	compression index for fully destructured state

μ_α	parameter controlling the exponential decay of $\boldsymbol{\alpha}/M_\mathrm{r}$ over $\bar{\boldsymbol{r}}/M_\mathrm{r}$
ν	Poisson's ratio
ν_lining	Poisson's ratio of lining
ν_shield	Poisson's ratio of shield machine
ξ	variable restricting excessive rotation
ρ_s	grain density
$\boldsymbol{\sigma}$	total stress tensor
$\boldsymbol{\sigma}'$	effective stress tensor
$\bar{\boldsymbol{\sigma}}'$	effective image stress tensor
$\boldsymbol{\sigma}'_\mathrm{BS,init}$	effective stress tensor on the initial bounding surface for YSR
$\boldsymbol{\sigma}'_\mathrm{corr}$	effective plastic stress corrector tensor
$\boldsymbol{\sigma}'_\mathrm{cur\text{-}pc}$	stress tensor for distance between current stress and projection center
$\boldsymbol{\sigma}'_\mathrm{drift}$	effective stress tensor for drift correction
$\boldsymbol{\sigma}'_\mathrm{eln}$	effective stress tensor for elastic nucleus
$\boldsymbol{\sigma}'_\mathrm{eln,origin}$	effective stress tensor for origin of elastic nucleus
$\boldsymbol{\sigma}'_\mathrm{inter}$	effective intersection stress tensor
$\boldsymbol{\sigma}'_\mathrm{int\text{-}pc}$	stress tensor for distance between intersection and projection center
$\boldsymbol{\sigma}'_\mathrm{pc}$	effective stress tensor for projection center
$\boldsymbol{\sigma}'_\mathrm{pred}$	effective elastic stress predictor tensor
$\boldsymbol{\sigma}'_\mathrm{reset}$	effective storage stress tensor at beginning of sub-step
$\boldsymbol{\sigma}'_\mathrm{trial}$	effective elastic trial stress tensor
σ	total stress
σ_a	total axial stress
σ_r	total radial stress
σ'	effective stress
σ'_a	effective axial stress
$\sigma'_\mathrm{a,yield}$	effective axial yield stress
$\sigma'_\mathrm{a,yield,rec}$	effective axial yield stress for reconstituted state
σ'_hor	effective horizontal stress
σ'_r	effective radial stress
σ'_vert	effective vertical stress

$\sigma'_{\text{vertical,in situ}}$	effective vertical in situ stress
φ'	effective friction angle
φ'_{cs}	effective friction angle at critical state
φ'_{inter}	effective friction angle for soil-structure interface
ψ	difference between e and e_{cs} at same p'
$\Omega(i)$	inertia weight coefficient for inverse analysis

1 Introduction

1.1 Motivation

Geotechnical applications in natural clay deposits are challenging due to the complex constitutive soil behavior governed by current state, stress-strain history and structure. Consequently, realistic and reliable predictions of the system behavior with respect to serviceability and ultimate state in the design phase and the construction period require sophisticated understanding of the constitutive behavior of natural clay under various mechanical and hydraulic initial, boundary and loading conditions.
The structure of natural clay is characterized by fabric referring to the arrangement and orientation of particles, aggregates and particle contacts and by interparticle bonding. Anisotropic fabric which is formed during deposition results in inherent anisotropy of the constitutive behavior. Interparticle bonding imparts additional strength and stiffness to clay compared to its intrinsic properties. Accordingly, natural clay can sustain higher stresses without yielding. Furthermore, plastic straining initiated after exceeding the yield stress induces anisotropy of the constitutive behavior with respect to the loading direction. In addition, plastic straining mobilizes the process of destructuration which is defined as progressive damage of interparticle bonding causing certain loss of strength and stiffness. Both, inherent and stress-induced anisotropy as well as interparticle bonding and its destructuration have significant impact on the stress-strain behavior of natural clay. Besides, non-monotonic or cyclic stress paths are quite typical for advanced geotechnical applications in natural clay deposits. Due to the non-monotonic construction processes mechanized tunneling is a very prominent example for the occurrence of non-monotonic or cyclic stress path. The stress-strain behavior of natural clay under non-monotonic or cyclic loading is strongly dependent on the stress/strain history and loading direction and magnitude. Natural clay under non-monotonic or cyclic loading shows smooth elasto-plastic transition and hysteresis of the stress-strain behavior during unloading/reloading cycles and underlies certain stiffness degradation and accumulation of plastic strain with increasing number of cycles.

The superposition of the complex constitutive behavior of natural clay and sophisticated stress paths related to advanced geotechnical applications makes the analysis of the system behavior demanding. To conclude, in order to ensure realistic and reliable predictions of the system behavior of geotechnical applications in natural clay deposits under complex stress paths numerical analyses are mandatory. Therefore, it is essential to employ an adequate constitutive model which accounts for the complex constitutive behavior of natural clay such as inherent and stress-induced anisotropy as well as initial structure and destructuration and the behavior under non-monotonic or cyclic loading.

The present research is embedded in the Collaborative Research Center (SFB 837) on "Interaction modeling in mechanized tunneling" funded by the German Research Foundation (DFG). Consequently, mechanized tunneling is the chosen application in the present work. Mechanized tunneling is a largely applied method to conduct subsurface infrastructural projects especially in urban areas due to the limited surface space. However, mechanized tunneling is a very complex process requiring the interaction of many disciplines such as geotechnical engineering and tunneling, construction management and logistics, infrastructure engineering, design and construction of concrete and steel structures and material science. The various processes and disciplines can be connected and compiled in a building information model applied to mechanized tunneling (see e.g. Schindler et al., 2014; Hegemann et al., 2014). The subproject A5 deals with adequate numerical modeling of excavation processes and realistic and reliable predictions of the system behavior induced by mechanized tunneling. In this framework the system to be investigated is composed of natural clay deposit and tunnel.

Important engineering aims for tunnel projects are the safe and economical design as well as the adaptive construction of the tunnel. On that account, mechanized tunneling is a suitable technique because it minimizes the soil displacements and surface settlements and causes just small disturbance of the aboveground edifices and infrastructure. However, realistic and reliable predictions of surface settlements, ground movements, stress distribution and generation of excess pore-water pressure in the vicinity of the lining are essential. Adequate predictions require deep and precise understanding of the constitutive soil behavior of natural clay. Moreover, sophisticated knowledge on the complex mechanical and hydraulic interactions induced by mechanized tunneling resulting in non-monotonic stress paths is needed.

The proposed concept of an appropriate numerical analysis of the system behavior caused by mechanized tunneling is schematically visualized by the flowchart in Figure 1.1. In the current study the concept is formulated with respect to the mechanized tunneling application case but it can be generally adopted to any geotechnical application.

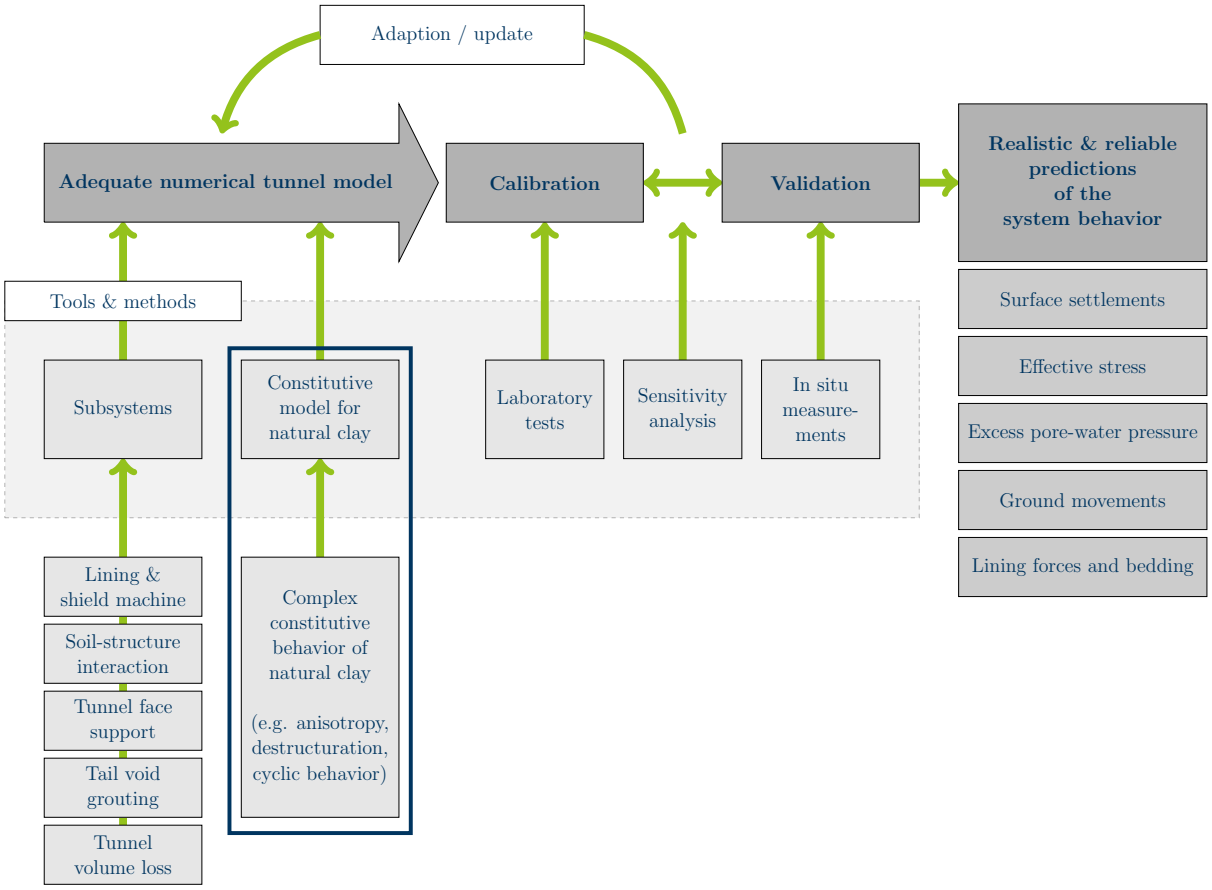

Figure 1.1: Concept of an appropriate numerical analysis of the system behavior induced by mechanized tunneling

To achieve realistic and reliable predictions of the system behavior resulting from mechanized tunneling the development of an adequate numerical simulation model is an essential issue. The adequate numerical simulation model has to account for the most decisive subsystems involved in mechanized tunneling and utilizes an adequate constitutive model for natural clay. The subsystems such as lining and shield machine, soil-structure interaction, tunnel face support, tail void grouting and volume loss around the tunnel have to properly simulate the physical reality of mechanized tunneling. Furthermore, the employed constitutive model for natural clay has to adequately reproduce the complex constitutive behavior of natural clay.

The numerical model has to be calibrated against laboratory tests and validated against in situ measurements. However, model calibration and validation can be enhanced by employing global sensitivity analysis. In case of deviations of the numerical model response from experimental test results or in situ measurements the numerical simulation model

can be adapted or updated to optimize the model quality and to ensure the most appropriate predictions of the system behavior caused by the mechanized tunneling in natural clay deposits.
The present study is mainly focused on the constitutive part of the numerical analysis composed of formulation, numerical integration, calibration and application of an adequate constitutive model for natural clay which is highlighted in the flowchart in Figure 1.1.

1.2 Objectives and methodology

In the framework of this work the overall engineering problem is to provide realistic and reliable predictions of the system behavior resulting from mechanized tunneling in natural clay. The large number of advanced mechanical and hydraulic processes involved in mechanized tunneling and the interaction with the complex constitutive behavior of natural clay demand for sophisticated analysis based on numerical simulations. Therefore, the aim of the present study is to propose a concept for an adequate numerical analysis of mechanized tunneling in natural clay.
The current study is focusing on the constitutive modeling part of the numerical analysis. That is, the constitutive modeling should be performed as simple as possible, but not simpler to still guarantee realistic and reliable predictions of the system behavior caused by mechanized tunneling. Consequently, the required complexity of constitutive modeling has to be evaluated. Hence, an adequate analysis concept is developed based on the assessment of the influence of the soil mechanical properties of natural clay on the system behavior resulting from mechanized tunneling. To be more specific, this defines the main objectives of the present study:

- Evaluation of the influence of the soil mechanical properties of natural clay on the numerical model response in mechanized tunneling considering construction stages.
- Assessment of the necessity of a certain level of complexity of the constitutive model for natural clay employed in the numerical analysis of mechanized tunneling and development of practical recommendations.

The influence of the following typical soil mechanical properties of natural clay on the numerical model response in mechanized tunneling is investigated: inherent and stress-induced anisotropy, initial structure and its progressive destructuration and the behavior under non-monotonic or cyclic loading incorporating stress-strain hysteresis and elasto-

plastic transition, stiffness degradation and accumulative effects. The following model responses in mechanized tunneling are chosen for evaluation: transverse and longitudinal surface settlements, the distribution of ground movements and the evolution of effective stresses and excess pore-water pressure in the soil domain.
The methodology of the investigation performed in this study is described in the following section. In general, elaborated numerical simulations are the main basis for achieving the objectives in this research work. Hence, in order to obtain realistic and reliable predictions of the system behavior caused by mechanized tunneling numerical simulations using finite element method (FEM) are utilized. For an appropriate approximation of the system behavior with respect to the complex mechanized tunneling process an adequate three-dimensional simulation model is developed in the framework of the present work.
The evaluation of the influence of the constitutive properties of natural clay on the system behavior resulting from mechanized tunneling is conducted by employing the concept of the hierarchical BSP model family. The hierarchical structure of the constitutive BSP model allows for the elaboration of the importance of the soil mechanical properties of natural clay by activation or deactivation of the corresponding features by proper setting of the constitutive BSP model parameters. That is, the complexity of the constitutive BSP model is of hierarchical structure and varies for different numerical simulation runs within the same hierarchical model family. Afterwards, numerical model responses of different simulation runs of each hierarchical BSP model extension are compared to each other. The differences are evaluated with respect to the relative importance of particular soil mechanical properties of natural clay related to specific model responses regarding mechanized tunneling. The hierarchical structure of the adequate constitutive BSP model for natural clay used in the present study is listed below.

- Extended Modified Cam-Clay (**MCC**) → basic model, elastoplasticity, isotropic hardening and softening, non-associated flow
- **Saniclay** → additional inherent and stress-induced anisotropy
- **Saniclay D** → additional destructuration
- **Saniclay D + BSP** → additional bounding surface plasticity incorporating stress-strain hysteresis and elastoplastic transition, stiffness degradation and accumulative effects under non-monotonic or cyclic loading

In conclusion, using the hierarchical BSP model family concept offers the opportunity to understand the influence of the complexity level of the constitutive BSP model on the numerical model responses caused by mechanized tunneling. Moreover, it enables to evaluate the necessity of a certain degree of complexity of the constitutive BSP model. To be

more specific, the proposed approach allows to define rational recommendations if typical mechanical properties of natural clay have to be considered in the numerical analysis of specific numerical model responses in design and construction phases of mechanized tunneling.
To conduct numerical simulations of mechanized tunneling the developed constitutive BSP model is efficiently and robustly implemented in a three-dimensional state-of-the-art finite element code in the present work. Moreover, the constitutive BSP model is numerically calibrated against a number of geotechnical laboratory tests on natural clay samples.

1.3 Structure of the present study

In this section the structure of the present study composed of ten chapters is outlined.

Chapter 2 – State of the art
This chapter is divided into four parts. At first, an introduction to the mineralogy and structure of natural clay is provided, followed by an analysis of the fundamentals of its mechanical behavior. Afterwards, special focus is set on the understanding of volume change behavior, shear strength and associated stress-strain relationship as well as response under cyclic loading. Moreover, the constitutive modeling of natural clay is reviewed and evaluated with respect to advantages and limitations of existing modeling approaches. The basics of constitutive modeling in the framework of critical state soil mechanics are provided. Furthermore, various existing constitutive modeling concepts to account for inherent and stress-induced anisotropy, initial structure and destructuration as well as cyclic behavior of natural clay are emphasized. Finally, with respect to the investigated application case decisive aspects of the numerical simulation of mechanized tunneling are surveyed.

Chapter 3 – Formulation of BSP model for natural clay
In this chapter the formulation of an adequate BSP model for natural clay is presented. To be more specific, the formulations of non-linear elasticity, bounding surface plasticity with respect to non-associated flow rule and Lode angle dependence as well as hardening plasticity rules such as rotational hardening, isotropic hardening, isotropic softening and destructuration in the framework of critical state soil mechanics are discussed. Regarding the BSP concept the chapter is especially focusing on formulations regarding shape hardening function, damage parameter and moving projection center.

Chapter 4 – Implementation of BSP model for natural clay
This chapter covers the numerical implementation of the BSP model. Special attention is given to the numerical integration of the constitutive equations. The incorporated modified Euler approach with automatic error control and sub-stepping scheme is highlighted.

Chapter 5 - Sensitivity analysis regarding BSP model parameters
The global sensitivity analysis (GSA) is introduced as a valuable approach to enhance the subsequent calibration of the constitutive BSP model parameters. At first, the general capabilities of the BSP model are discussed in relation to stress-strain model responses obtained from numerical simulations of various geotechnical laboratory tests to facilitate the interpretation of the GSA results. Subsequently, the sensitivity of the numerical model responses to the constitutive BSP model parameters, based on the geotechnical laboratory tests, is investigated employing the GSA. The chapter concludes with recommendations regarding the adequate choice of geotechnical laboratory tests and even loading stages to be preferentially considered to achieve a most adequate calibration of a particular constitutive parameter of the BSP model.

Chapter 6 – Calibration of BSP model parameters
The calibration of the BSP model parameters is treated in this chapter based on recommendations proposed in the former chapter. The constitutive model parameters are calibrated against experimental data from RUB and further literature on natural Onsøy clay which is chosen as representative for typical natural clay behavior. The parameter calibration is conducted via direct determination and inverse analysis using a particle swarm optimization algorithm. Special consideration is given to experimental data from oedometer and triaxial tests under monotonic and cyclic loading, various initial conditions and varying mechanical and hydraulic boundary conditions.

Chapter 7 – Hierarchical BSP model family
This chapter deals with the concept of the hierarchical BSP model family employed for the investigation of the influence of the properties of natural clay on the system behavior resulting from geotechnical applications. To evaluate the concept of the hierarchical BSP model family, the influence of the level of complexity of a particular hierarchical BSP model extension on the model response is illustrated with respect to the numerical simulations of specific geotechnical laboratory tests.

Chapter 8 – Numerical model for mechanized tunneling
In this chapter the developed numerical simulation model and the associated subsystems are introduced. The geometry and the boundary conditions of the synthetic numerical simulation model are chosen with respect to an imaginary mechanized tunnel excavation in a water-saturated natural Onsøy clay deposit. The description highlights the geometry of the system, the initial and boundary conditions, the discretization of the system and the numerical simulation of the staged construction of mechanized tunneling.

Chapter 9 – Natural clay behavior with application to mechanized tunneling
This chapter handles the numerical analysis regarding the influence of the properties of natural clay on the system behavior caused by mechanized tunneling. The study focuses on the spatial and construction stage dependent influence of inherent and stress-induced anisotropy, initial structure and its progressive destructuration and behavior under non-monotonic or cyclic loading on the numerical model responses such as ground movements and the stress and excess pore-water pressure distribution in the soil domain. Concluding, practical recommendations are elaborated regarding the question if particular soil mechanical properties of natural clay need to be considered in the numerical analysis of mechanized tunneling with respect to design and construction of tunnel projects.

Chapter 10 – Conclusions and outlook
The last chapter summarizes the conclusions drawn based on the numerical results obtained in the foregoing chapters. Moreover, in the outlook part of this chapter, recommendations for subsequent further studies in this research field are suggested.

2 State of the art

As described in the former chapter on the motivation and objectives of the current work natural clay manifests a complex constitutive behavior which depends on current state, monotonic or cyclic stress-strain history and structure. Hence, for the adequate analysis of the system behavior of any geotechnical application deep understanding of the mechanical behavior of natural clay based on the microstructural properties is required.
Consequently, the state-of-the-art review comprises a brief introduction to the structure of natural clay and clay minerals. Exemplarily, the properties of four specific natural clays are presented. Furthermore, special attention is given to basic knowledge about the mechanical stress-strain behavior of natural clay with special focus on volumetric and strength behavior. In particular, inherent and stress-induced anisotropy as well as destructuration are elaborated. Beyond that, the behavior of natural clay under cyclic loading is discussed. Realistic and reliable predictions of the system behavior of complex boundary value problems in natural clay deposits require numerical modeling. To properly approximate the mechanical behavior of natural clay by numerical simulations adequate constitutive models are needed. The state-of-the-art review is focusing on existing concepts regarding constitutive modeling of natural clay. Beside covering the theoretical background of critical state soil mechanics and its constitutive modeling, several approaches for the constitutive modeling of anisotropy and destructuration in the framework of plasticity concepts are introduced, reviewed and evaluated. Additionally, different constitutive models considering clay behavior induced by cyclic loading paths are presented and analyzed. To accurately predict the system behavior regarding mechanized tunneling as the selected application case a proper numerical simulation model considering the decisive subsystems involved in the construction process has to be created. Therefore, at the end of the state-of-the-art review recent developments and important features of numerical modeling of mechanized tunneling are discussed.

2.1 Natural clay

This section provides a general introduction with respect to natural clay. At first, the terms clay and clay minerals are defined. This is followed by the description of the clay system incorporating arrangement of sheets, layers, particles and aggregates, pore space, acting forces, induced interactions and occurring water. Afterwards, the structure of natural clay composed of fabric and bonding as well as the strength sensitivity and the process of destructuration are described in detail. Furthermore, the in situ stress conditions and the stress-strain history of natural clay (consolidation state, stress distribution, yield stress) are discussed as key factors for the analysis of geotechnical boundary value problems.

2.1.1 Clay and clay minerals

In accordance with the recommendations of the Joint Nomenclature Committee (JNC) of the Clay Minerals Society (CMS) and the Association Internationale Pour l'Etude des Argiles (AIPEA, International Association for the Study of Clays) the term clay is referred to natural materials mainly consisting of fine-grained minerals (see e.g. Guggenheim and Martin, 1995, 1996; Guggenheim et al., 2006). Whereat, the upper threshold value for the maximum clay particle size is not explicitly given. In the community of geotechnical engineering a limiting range of 2-4 μm is widely accepted for the maximum clay particle size. However, clay possesses small particle size and large specific surface area. Additionally, by definition of the JNC, clay generally shows plasticity at appropriate water content and hardening behavior when dried or burned. However, a quantification of plasticity is not specified. The origin of clay is manifold. Clay could for example originate from altering/weathering of rocks, sedimentary (marine) deposition after sediment erosion and transportation and postdepositional processes (physical, chemical and biological). Hence, clay is not restricted to a particular genesis but specific engineering properties and the mechanical behavior of clay are highly influenced by environmental conditions such as confining pressure, temperature, water content, water occurrence and composition (see e.g. Mitchell and Soga, 2005; Bergaya and Lagaly, 2013).
As mentioned above, clay is mainly composed of fine-grained clay minerals. The term clay mineral, as defined by the JNC, is used with respect to phyllosilicate minerals (e.g. Kaolinite, Montmorillonite, Illite or Smectite) which are usually the principal constituents of clay. However, it is also used with respect to all various minerals which induce plasticity to clay and show hardening behavior when dried and burned. Therefore, by definition, clay minerals in contrast to clay may have synthetic origin. On the other hand, in compliance

with the JNC, minerals which do not impart plasticity to clay are called associated minerals (e.g. carbonate, feldspar, quartz, (hydr)oxides of iron and aluminum). Furthermore, non-crystalline or amorphous materials (so-called gels) including organics are defined as associated phases in clay.

2.1.2 Clay system

Phyllosilicate minerals, formed by geological processes, exhibit crystalline structure composed of planes of atoms and silica tetrahedral or aluminum, iron or magnesium octahedral sheets. The assembly of one or more tetrahedral sheets and one octahedral sheet is called layer having a dimension in the nanometer range (see e.g. Guggenheim et al., 2006; Bergaya and Lagaly, 2013). Two types of layers have to be distinguished: the 1:1 layer (two sheet layer containing one tetrahedral and one octahedral sheet) and the 2:1 layer (three sheet layer containing one octahedral sheet between two opposing tetrahedral sheets). Layers may be separated by interlayer materials (e.g. (hydrated) cations, organics, hydroxide octahedral groups and sheets). The entity of sheets forming layer and interlayer material is defined as unit structure. In addition, an assembly of layers including interlayer materials is specified as particle usually in platy shape. An assembly of particles is defined as aggregate (see e.g. Mitchell and Soga, 2005; Bergaya and Lagaly, 2013). The arrangement of layers and number of layers stacked to a particle (ranges from one up to several hundreds) depend on the clay mineral type and environmental conditions (confining pressure, temperature, pore-water content and availability, pH value, ionic strength/concentration, salinity) and will be discussed in the following sections. The system of sheets, layers and particles is schematically shown in Figure 2.1.The definition of layers, particles and aggregates in compliance with the JNC is given in Figure 2.2.
Besides, the arrangement of layers and particles results in different types of pores such as interlayer and interparticle pore space filled with water and/or air. Several types of water may occur in the pore system such as e.g. free water (no strong attraction to the clay minerals), bonded water in the crystalline structure and water in the diffuse double layer considering adsorbed water and diffusion of water molecules. As a result, clay and clay minerals are known as complex multiphase system containing solid, liquid and gas phases. Within the present study the material is assumed as two-phase system of solid and pore-water. This means the pore system is fully water-saturated. The solid-liquid-gas interaction (unsaturated material having capillary stress and suction) is not taken into consideration.

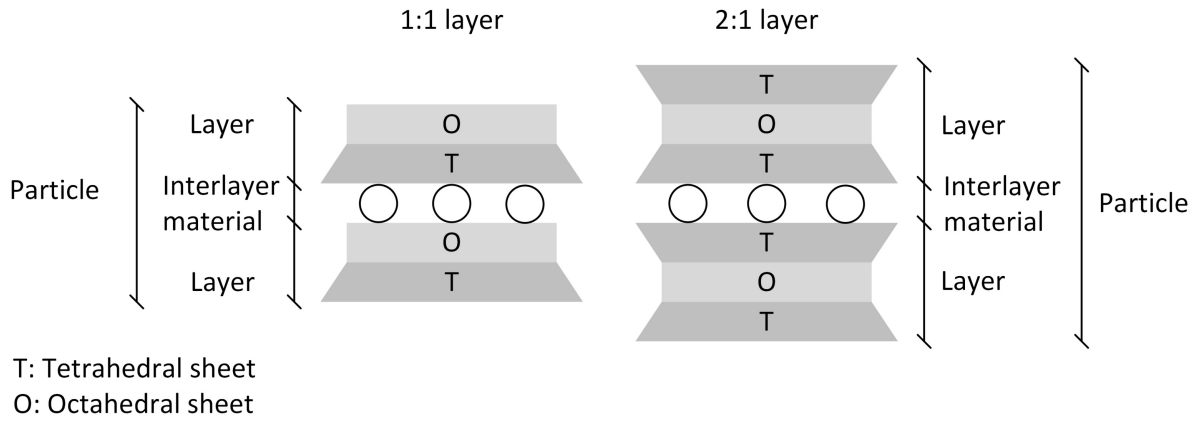

Figure 2.1: Schematic system of sheets, layers and particles modified after Mitchell and Soga (2005) and Bergaya and Lagaly (2013)

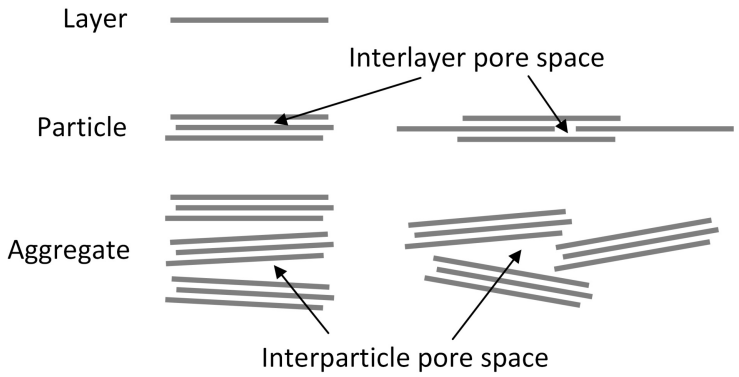

Figure 2.2: Definitions of layers, particles and aggregates according to JNC modified after Bergaya and Lagaly (2013)

By reasons of small particle size and large specific surface area the behavior of clay particles is primarily controlled by surface-induced contact forces rather than gravity-induced forces. Due to physico-chemical forces at the phase boundaries significant solid-liquid interactions occur. The clay surface may exhibit negative charge equalized by positively charged interlayer material (primarily exchangeable cations). This is, water is attracted to the clay surface by mechanisms like hydrogen bonding, cation hydration, surface dipole attraction, or osmosis affecting the swelling behavior (see e.g. Mitchell and Soga, 2005). However, the interplay between attraction and repulsion of electronegative clay surface, cations and anions (appearing as salt precipitates solved in occurrence of water) results in a certain distribution of ion concentration in the adjacent liquid. When there is a high

concentration of cations near the clay surface due to electrostatic attraction, the system of solid and liquid undergoes charge or concentration equalization through the diffusion of water molecules. The region of attracted positive ions in solution and the negatively charged surface of the clay is termed diffuse double layer. The diffuse double layer is electrically neutral and spatially bounded by the distance where cations and anions have same concentration.
Recapitulating, after Mitchell and Soga (2005), the assembly of clay layers and particles is evoked by various attraction and repulsion forces depending on clay mineralogy and environmental conditions. It is distinguished between short-range interaction forces on nanometer level (e.g. repulsive surface and ion hydration forces, repulsive electrostatic forces (Born repulsion), attractive electrostatic forces induced by potential difference, ionic or covalent bonding forces due to chemical interactions such as cementation) and long-range interaction forces (e.g. repulsive forces caused by interacting double layers and attractive electromagnetic van der Waals forces). The interaction between attraction and repulsion forces, which is called the net energy of interaction, significantly controls the arrangement of particles associated to fabric of natural clay.

2.1.3 Structure of natural clay

2.1.3.1 Fabric and interparticle bonding

Originally, structure of natural clay is formed during geological processes such as deposition, (marine) sedimentation and postdepositional processes. The structure of natural clay is highly affected by mineralogy and environmental conditions as described above and time of deposition (Lambe and Whitman, 1969). Time-dependent postdepositional processes could have physical (e.g. oedometric consolidation, shearing, swelling, drying and wetting, hydraulics) and/or chemical (e.g. weathering, precipitation, cementation, leaching, thixotropy, aging) origin. The structure of natural clay consists of two parts namely fabric and interparticle bonding (Lambe and Whitman, 1969; Burland, 1990; Mitchell and Soga, 2005).
The fabric of soils refers to the spatial arrangement of particles and aggregates and orientation of interparticle and interaggregate contacts. Hence, it governs the orientation of the associated forces. Due to preferred orientation of particles the spatial arrangement of clay particles and contacts may show distinct anisotropy. Inherent anisotropy is developed during deposition whereas further changes in loading conditions will cause stress-induced anisotropy depending on the loading direction. The anisotropic fabric results in certain

anisotropy with respect to the mechanical behavior of natural clay. Generally, it is differentiated between modes of particle association as illustrated in Figure 2.3 (see e.g. van Olphen, 1977; Collins and McGown, 1974; Mitchell and Soga, 2005) depending on mineralogy and depositional conditions. A clay particle association can either be dispersed (no face-to-face association) or aggregated (face-to-face association). Beyond this distinction, clay particle association can be either flocculated (edge-to-edge (E-E) or edge-to-face (E-F) association) or deflocculated (no association).
The interparticle forces and interparticle bonding are related to several time-dependent physicochemical processes. For example, precipitation of calcite, silica, alumina, iron oxides and other organic or inorganic compounds may cause bonding due to interparticle cementation. Hence, bonding is related to interparticle forces which are not of pure frictional kind. Among others, Kavvadas et al. (1994) stated that cementation bonds tend to develop isotropically.

2.1.3.2 Structured and reconstituted clay

Following the definitions by Burland (1990) and Leroueil and Vaughan (1990) it is distinguished between clay in its natural structured and in its reconstituted or destructured state. The former term *structured* is related to natural undisturbed clay. The latter terms *reconstituted* and *destructured* are referred to the same clay but having no structure due to either reconstitution or destructuration of clay as described in the following. Thereby,

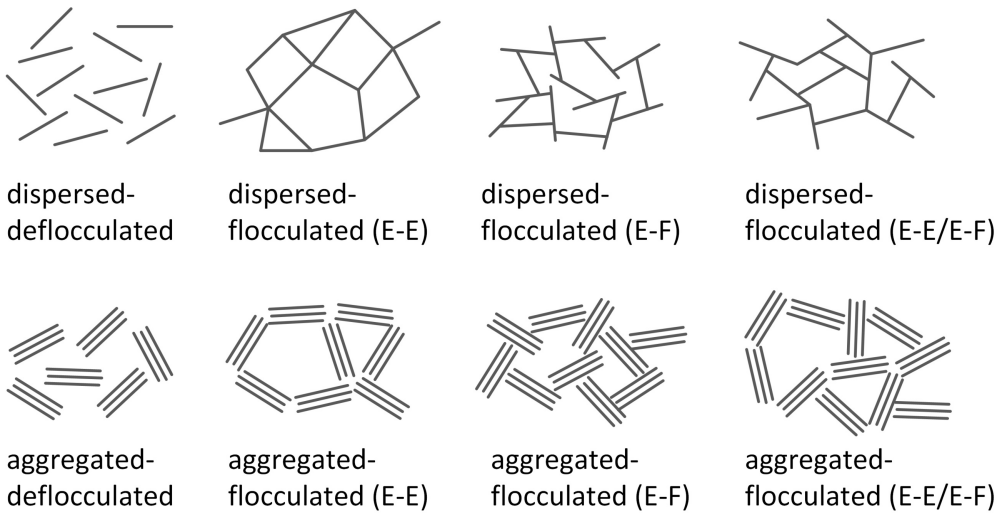

Figure 2.3: Clay particle association modified after van Olphen (1977) and Mitchell and Soga (2005)

reconstitution means that the structure of natural clay (fabric and bonding) is destroyed by accurate mixing of the sample at a water content equal or higher than the liquid limit w_{L}. The properties of clay in the reconstituted state are specified as intrinsic properties by reasons of inherence to the soil and independence of the natural state. The stress/strain history and environmental boundary conditions are cleared.
To assess the role of structure of natural clay on the mechanical behavior main focus is usually set on the comparison of clay in its natural and reconstituted state manifesting intrinsic properties. The observed differences of the mechanical behavior are attributed to the structure of the clay, which includes its fabric and bonding. Therefore, the reconstituted clay with its intrinsic properties serves as a reference for further analysis of how structure influences the mechanical behavior (Burland, 1990). This is discussed in detail in the following sections. Natural clay can sustain higher effective stress compared to the same clay in reconstituted state having the same void ratio. Or in other words, natural clay can exist at a higher void ratio compared to the reconstituted state at the same stress level.

2.1.3.3 Strength sensitivity

Among others, the approach of strength sensitivity of clay introduced by Terzaghi (1944) and further investigated by Skempton and Northey (1952) can be employed to quantify the structure of natural clay. The strength sensitivity S_{t} of clay is defined as the ratio of shear strength in natural, undisturbed state to shear strength in reconstituted state at same water content as given by Equation 2.1.

$$S_{\mathrm{t}} = \frac{\text{undisturbed strength}}{\text{reconstituted strength}} \tag{2.1}$$

According to Mitchell and Soga (2005), various phenomena such as metastable fabric, cementation, weathering, thixotropic hardening, leaching, ion exchange, changes in the monovalent/divalent cation ratio, and the formation or addition of dispersing agents can affect the sensitivity of clay and lead to variations in its volumetric and strength behavior. However, the sensitivity of natural clay and consequently its shear strength are closely correlated to the geological characteristics of the clay (see e.g. Skempton and Northey, 1952; Bjerrum, 1954; Wroth and Wood, 1978; Kulhawy and Mayne, 1990). Exemplarily, the classification of the degree of sensitivity after Skempton and Northey (1952) is shown in Table 2.1.

Table 2.1: Classification of clay based on strength sensitivity by Skempton and Northey (1952)

Classification	**Sensitivity S_t**
Insensitive clay	≈ 1.0
Clays of low sensitivity	1-2
Clays of medium sensitivity	2-4
Sensitive clay	4-8
Extra-sensitive quick clay	8-16
Quick clay	> 16

The distributions of undrained shear strength s_u with respect to overburden depth for natural clays from different sites (Bothkennar, Murro, Onsøy, Pisa) are displayed in Figure 2.4. For comparison and as indicator for the magnitude of strength sensitivity the distributions of the undrained shear strength of the corresponding reconstituted samples of Bothkennar clay, Murro clay and Onsøy clay are additionally given in Figure 2.4a. All results show a linear increase of the undrained shear strength with increasing depth.

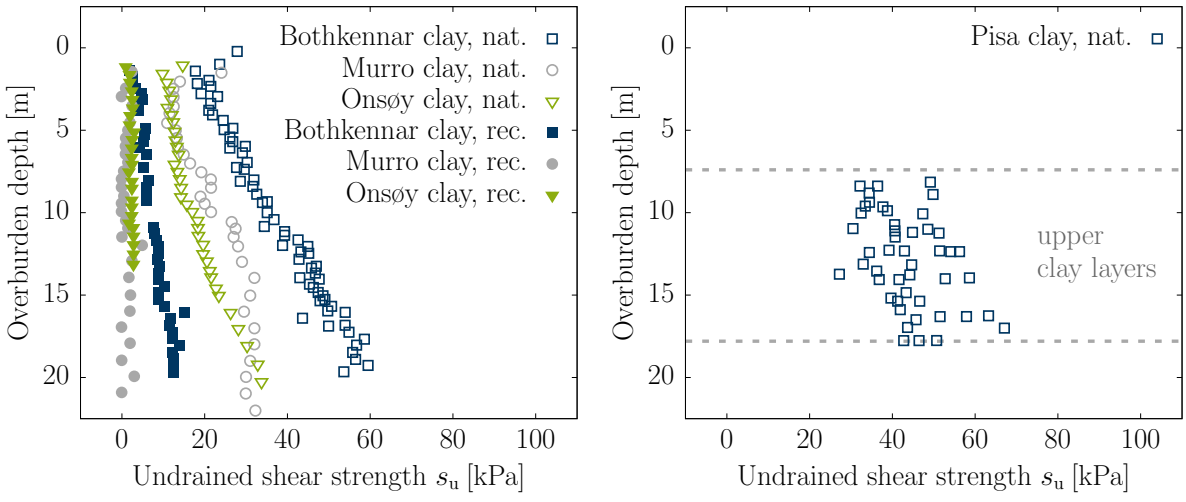

Figure 2.4: Distribution of undrained shear strength s_u with respect to the overburden depth a) for natural and reconstituted Bothkennar clay (Nash et al., 1992b), Murro clay (Karstunen and Yin, 2010) and Onsøy clay (Lunne et al., 2003) and b) for natural Pisa clay (Calabresi et al., 1993; Rampello et al., 1996)

2.1.3.4 Destructuration

Destructuration is defined as progressive degradation of the structure of natural clay (fabric and bonding) caused by different external loading conditions (mechanical, hydraulic, chemical and/or thermal forces) exceeding the strength of the bonds. Destructuration involves the rearrangement and reorientation of particles and associated contacts as well as the progressive damage of interparticle bonding. Within this study the term destructuration is used in matters of damage due to mechanically induced effective stress or strain only.

2.1.4 In situ stress conditions

2.1.4.1 Normally consolidated and overconsolidated clay

When investigating geotechnical boundary value problems in natural clay deposits the initial in situ stress conditions and the stress-strain history are most relevant. For natural clay deposits it is distinguished between normally consolidated and overconsolidated states. Overconsolidated clay has been subjected to stress conditions larger than the current overburden stress. The overconsolidation ratio (OCR) is defined as the ratio of the maximum effective vertical stress (preconsolidation stress) the clay has ever experienced to the current in situ effective vertical stress as given in Equation 2.2.

$$OCR = \frac{\text{maximum effective vertical stress}}{\text{in situ effective vertical stress}} \tag{2.2}$$

Hence, OCR is a measure of stress history. The most common occurrence of overconsolidation in natural clay deposits is due to removal of soil close to the ground surface (e.g. by weathering or erosion). This causes a reduction of the effective vertical stress. However, higher OCR values are directly correlated to higher undrained shear strength obtained for example from in situ shear vane tests (see e.g. Kulhawy and Mayne, 1990). The OCR value of natural clay deposits strongly depends on the overburden depth and the environmental conditions at the investigation site. Exemplarily, the distributions of OCR with respect to the overburden depth as investigated for Bothkennar clay by Hight et al. (1992b, 2003a) and for Onsøy clay by Lunne et al. (2003) are visualized in Figure 2.5a.

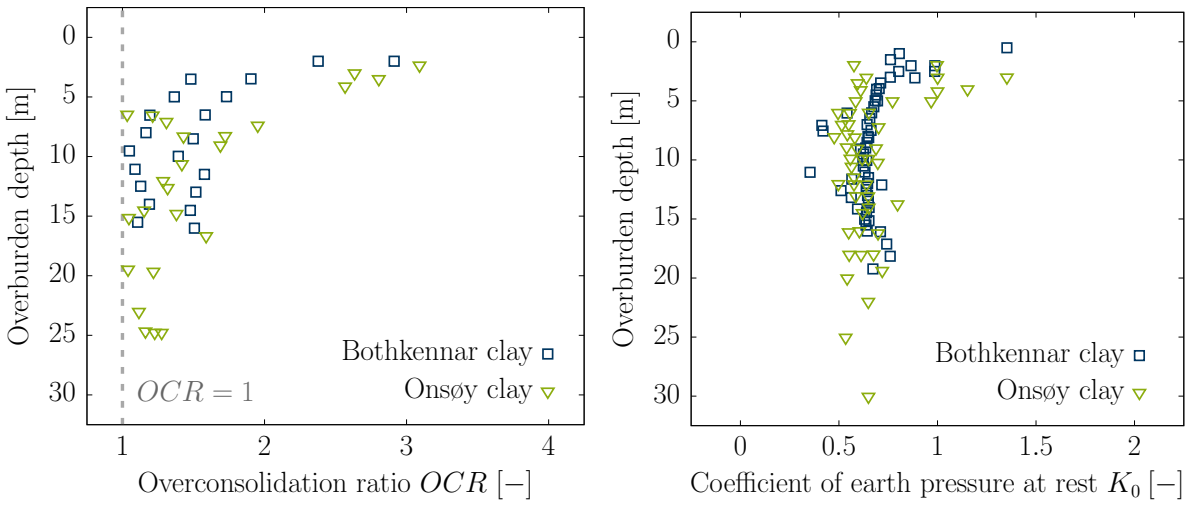

Figure 2.5: Distribution of a) overconsolidation ratio and b) coefficient of earth pressure at rest K_0 with respect to the overburden depth for natural Bothkennar clay after Hight et al. (1992b, 2003a) and for natural Onsøy clay after Lunne et al. (2003)

2.1.4.2 Coefficient of earth pressure at rest

In natural clay deposits the effective horizontal stress σ'_{hor} generally develops with respect to the effective vertical stress σ'_{vert} and the lateral deformation. If the lateral deformation is confined as it is the case for sedimentary deposition of natural clay the stress state is defined as earth pressure at rest. Whereat, the correlation between effective horizontal and vertical stresses is described by the coefficient of earth pressure at rest K_0 as given in Equation 2.3.

$$K_0 = \frac{\sigma'_{\mathrm{hor}}}{\sigma'_{\mathrm{vert}}} \tag{2.3}$$

The K_0 value of natural clay is strongly affected by structure and stress history. Kulhawy and Mayne (1990) depict a correlation between the degree of overconsolidation and K_0. When normally consolidated natural clay experiences a release of effective vertical stress due to unloading the effective horizontal stress does not decrease in the same order due to interlocking effects and anisotropic fabric (particle arrangement and orientation). Anisotropic fabric is induced by stress-strain history and especially controlled by loading direction. Hence, the higher the OCR value the higher the K_0 value.

The correlation can be estimated by Equation 2.4 including the effective internal friction angle φ'.

$$K_0 = \{1 - \sin\varphi'\} \{OCR\}^{\sin\varphi'} \tag{2.4}$$

Add to this, the value of K_0 is strongly dependent on the overburden depth as investigated for Bothkennar clay by Hight et al. (1992b, 2003a) and for Onsøy clay by Lunne et al. (2003). The distribution of K_0 with respect to the overburden depth is displayed in Figure 2.5b. The upper zone close to the ground surface manifests overconsolidated state due to depositional and postdepositional effective vertical stress release (e.g. weathering, erosion and water level fluctuation). The analogous distribution of K_0 with respect to overburden depth reveals strong correlation between OCR and K_0. In the upper zone effective horizontal stress is predominant according to the reasons mentioned above. However, with increasing overburden depth the K_0 value decreases and becomes almost constant. Any K_0 other than one introduces fabric anisotropy in natural clay.

2.1.4.3 Yield stress

The yield stress of natural clay is defined as the stress state at which a distinct discontinuity in the stress-strain behavior under monotonic stress paths occurs (Leroueil and Vaughan, 1990). The yield stress was introduced to describe the effects of stress history in sedimentary clay on the mechanical behavior (Roscoe et al., 1958; Schofield and Wroth, 1968). The mechanical properties of natural clay such as stiffness and strength are highly effected by the pre-yield and the post-yield process. Consequently, the mechanical behavior significantly differs when comparing the stress states before and after exceeding the effective yield stress since the material behavior is changing from predominantly elastic to elastoplastic. The term *predominantly elastic* is used because clay responses are almost always slightly elastoplastic represented by induced plastic strain and degradation of small-strain stiffness dependent on the stress history. The transition zone between purely elastic and elastoplastic behavior is material dependent.
The effective axial yield stress $\sigma'_{\mathrm{a,yield}}$ of natural clay obtained from one-dimensional compression tests is highly affected by the overburden depth and the corresponding effective vertical in situ stress $\sigma'_{\mathrm{vertical,in\,situ}}$ as shown in Figures 2.6a and 2.7a. The Bothkennar clay, the Murro clay, the Onsøy clay and the Pisa clay are analyzed with respect to their effective axial yield stress. As reference the effective vertical in situ stress distribution with respect to the overburden depth is also plotted. As observed in Figure 2.6a the effective

axial yield stress exceeds the effective vertical in situ stress. For reasons of classification of the yield stress of different natural clays Burland (1990) introduced the term yield stress ratio (YSR) which relates the effective axial yield stress to the effective vertical in situ stress as given in Equation 2.5.

$$YSR = \frac{\sigma'_{\mathrm{a,yield}}}{\sigma'_{\mathrm{vertical,in\,situ}}} \tag{2.5}$$

The use of the yield stress ratio in the framework of natural clay is more convenient than the use of the overconsolidation ratio since the latter one is restricted to the effective stress history (mechanical unloading paths) the clay has experienced only. The several causes of having $YSR > 1$ can not clearly be distinguished but the effect on the mechanical behavior is similar. It can be originated from either depositional or postdepositional stress history resulting in overconsolidated state or from structural effects such as interparticle bonding due to cementation, aging of natural clay under constant effective stress or changes in physical or chemical composition (diagenesis). The structural effects and their influence on the volumetric and strength behavior will be discussed in the following sections.
The qualitative distribution of the yield stress ratio with respect to the overburden depth in Figure 2.6b is similar for all investigated clays showing a convergence to almost constant

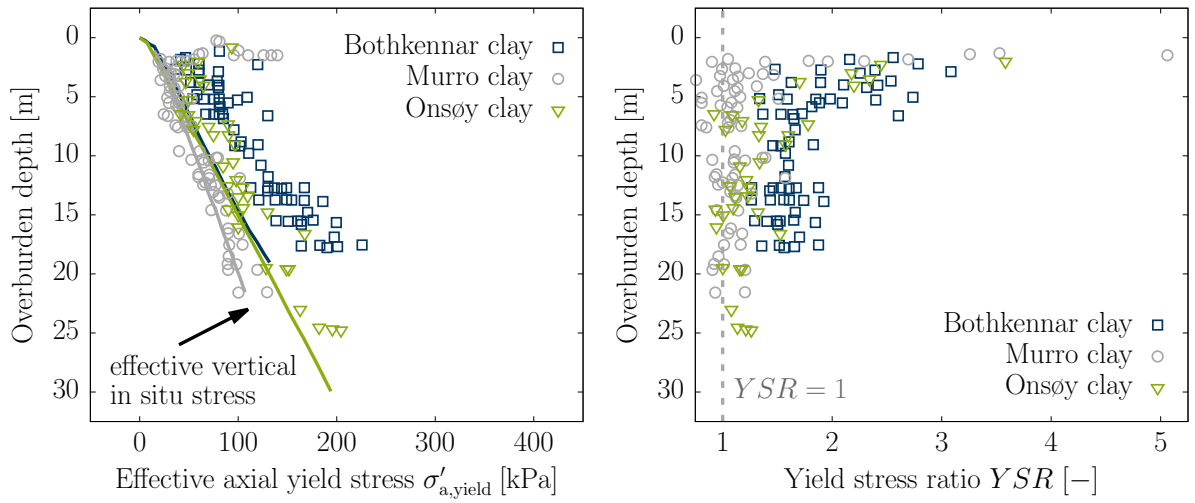

Figure 2.6: Distribution of a) the effective axial yield stress and b) the yield stress ratio with respect to the overburden depth obtained from oedometer tests on natural Bothkennar clay (Nash et al., 1992b), natural Murro clay (Karstunen and Yin, 2010) and natural Onsøy clay (Lunne et al., 2003)

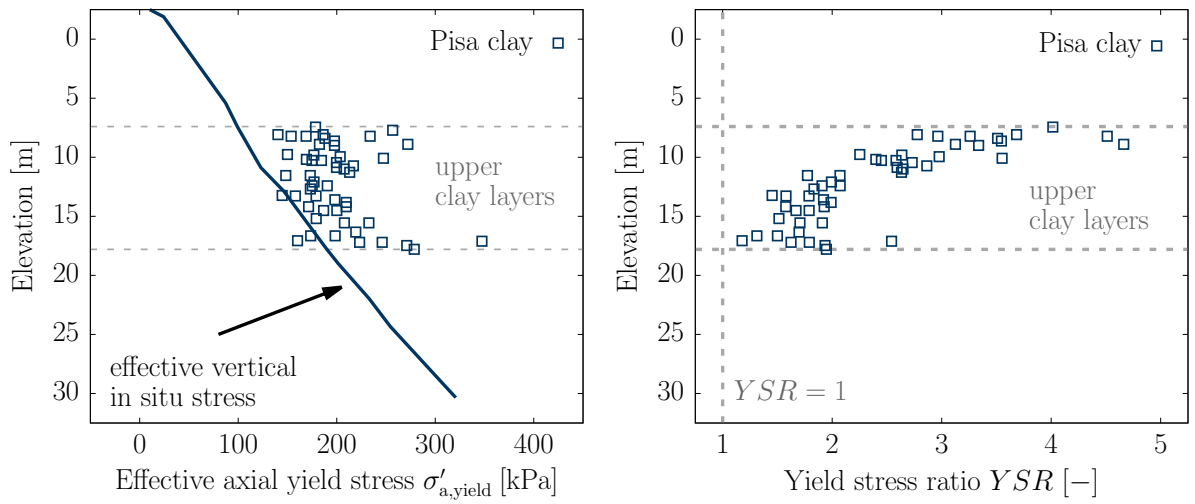

a) b)

Figure 2.7: Distribution of a) the effective axial yield stress and b) the yield stress ratio with respect to the elevation obtained from oedometer tests on natural Pisa clay (Calabresi et al., 1993; Rampello et al., 1996)

values with increasing depth beside the general scatter in the measurements. However, the Bothkennar clay exhibits higher values of the yield stress ratio compared to the Onsøy clay and the Murro clay. This differences suggest larger structural effects of the Bothkennar clay. The Murro clay exhibits much smaller values of the yield stress ratio close to one. That is, the effective axial yield stress almost equals the effective vertical in situ stress indicating much smaller influence of structure especially with increasing depth. Add to this, the distribution of the effective axial yield stress and the yield stress ratio of the Pisa clay is shown in Figure 2.7b (Calabresi et al., 1993; Rampello et al., 1996). The upper Pisa clay layers (elevation of 7.4-17.8 m) are analyzed because of the special geological situation of having an overlay of different filling, silt and sand layers of approximately 10 m thickness. The Pisa clay is showing a qualitatively similar yielding behavior compared to the natural clays investigated above.

2.1.5 Geological characteristics of selected natural clays

To illustrate the properties of natural clay, a geological characterization of four specific clay samples, namely Bothkennar clay, Murro clay, Onsøy clay and Pisa clay, is presented in this section.

- Bothkennar clay at depth of 5-7 m (investigated by e.g. Hight et al., 1992b, 2003a; Nash et al., 1992a,b; Smith, 1992a; Smith et al., 1992b)
- Murro clay at depth of 6-8 m (investigated by e.g. Koskinen and Karstunen, 2004; Karstunen and Koskinen, 2004; Karstunen et al., 2005; Karstunen and Koskinen, 2008; Karstunen and Yin, 2010; Koskinen, 2014)
- Onsøy clay at depth of 10-12 m (investigated by e.g. RUB, Lacasse et al., 1985; Lunne et al., 2003, 2006; Bamberg, 2009; Wichtmann et al., 2013; Lieske, 2015; Wichtmann, 2016; Müthing et al., 2017a; Müthing, 2017b)
- Pisa clay at depth of 11-13 m (investigated by e.g. Jamiolkowski et al., 1993; Calabresi et al., 1993; Rampello et al., 1996; Rampello and Callisto, 1998; Callisto and Calabresi, 1998; Presti et al., 2003; Callisto and Rampello, 2004)

The four specific natural clays have been chosen as typical representatives of natural clay and are used to generally describe volumetric and shear stress-strain behavior of natural clay. The variability in composition and structure strongly affects the mechanical behavior. The corresponding material characteristics of the investigated four specific natural clays are summarized in Table 2.2. Furthermore, Hight et al. (1992a) and Lunne et al. (2006) studied disturbance of clay structure before testing due to sampling and sample preparation. Sample disturbance yields to a decrease of peak strength, stiffness, yield stress and post-yield compressibility. Lunne et al. (2006) found out that the higher the degree of sample disturbance the higher the degree of destructuration (damage of interparticle bonding) and the lower the shear strength.

Table 2.2: Geological characteristics of selected natural clays

Parameter	**Unit**	**Bothkennar**	**Murro**	**Onsøy**	**Pisa**
w_n	[%]	67-73	67-83	62-68	51-63
e_n	[−]	1.8-2.2	1.9-2.2	1.7-2.1	1.4-1.8
w_L	[%]	74-86	88	62-68	61-87
I_P	[%]	39-59	55	32-38	33-56
ρ_s	$[\mathrm{g/cm^3}]$	2.68-2.71	2.66	2.77-2.79	2.75-2.81
S_t	[−]	4-8	7-10.5	4-8	4-6
OCR / YSR	[−]	1.4-1.6	1-1.2	1.2-1.6	1.5-2.0
K_0	[−]	0.5-0.6	0.35-0.5	0.5-0.6	0.55-0.75
Clay content	[%]	29-41	25-30	35-45	56-69
Organic content	[%]	2.5-5	2-3.5	< 1	< 1

2.1.6 Summary

In conclusion, the mechanical behavior of natural clay on the macroscale (e.g. compressibility, swelling, shear strength) is strongly related to the structural characteristics on the microscale. Whereat, the structure of natural clay is composed of fabric and interparticle bonding. After Mitchell and Soga (2005), the engineering properties of clay are influenced by the type and quantity of clay minerals and associated minerals and phases, by shape and size of correspondingly formed clay particles, by arrangement of particles and aggregates, by attractive and repulsive interparticle forces and by interparticle bonding due to cementation. Moreover, the structure and consequently the mechanical behavior of natural clay are dependent on and most sensitive to current state (e.g. void ratio), stress/strain history and environmental conditions.

2.2 Mechanical behavior of natural clay

2.2.1 Volumetric behavior

The volumetric behavior of natural clay is a key issue for the design of geotechnical applications with respect to serviceability. Hence, the volumetric behavior of natural clay (compression and swelling) induced by changes of effective stress is analyzed in this section. The caused rearrangement of the particles/aggregates results in volumetric deformations of the clay. At first, the general influence of structure and destructuration on the volumetric behavior of natural clay is described. It is followed by a more specific example of natural Bothkennar clay. Afterwards, concepts for the quantification of structure by use of the stress and stiffness sensitivity and the classification of natural clay by use of the intrinsic void ratio are introduced. The volumetric behavior of natural structured clay is analyzed with regard to the microstructural changes. Moreover, the yielding characteristics of natural clay are emphasized. Finally, the influence of overconsolidation on the volumetric behavior of natural clay is discussed. However, the effects of time-dependent consolidation and creep as well as rate-dependence on the volumetric behavior of natural clay are not addressed in this study.

2.2.1.1 Influence of structure and destructuration

The influence of the structure of natural clay on the compressibility was examined by various researchers (see e.g. Burland, 1990; Burland et al., 1996; Liu and Carter, 1999;

Chai et al., 2004; Low et al., 2008; Hong et al., 2012). They confirmed differences in the compression behavior of structured and reconstituted clay owing to differences in the structure and the void ratio/water content at the yield stress state. The structure imparts additional strength and resistance against compression. The void ratio at a certain effective stress state is additionally sustained by the clay structure. Whereat, the void ratio change depends on index properties, degree of strength and stress sensitivity, current effective stress state and yield stress state. Consequently, for natural clay exhibiting fabric and bonding, the elastoplastic compression index C_c after Terzaghi (1943) or the compression parameter λ after Schofield and Wroth (1968) are strongly varying with respect to the amount of structure and destructuration.

The schematic logarithmic effective stress versus void ratio diagram shown in Figure 2.8 indicates the typical compression behavior of natural clay exhibiting a certain structure composed of fabric and bonding. There are several superposed processes affecting the volumetric behavior of natural clay such as sedimentary deposition, postdepositional processes like bonding and aging as well as destructuration of fabric and bonding.

Starting from an initial equilibrium state having a metastable fabric at point A, the void ratio decreases as a result of increasing effective stress induced by sedimentary deposition (e.g. increase of overburden height and weight, dissipation of excess pore-water pressure). Assuming that the clay is normally consolidated at point A the development of the void ratio with respect to the increasing effective stress following path A-B is called virgin compression. The virgin compression line is unique for a given type of clay. Further loading would induce a decrease of the void ratio following the virgin compression line between the points B-E. The clay compacts from a metastable to a more stable and denser state by dissipation of pore-water, increase of effective stress, changes in fabric such as rearrangement of particles/aggregates and reorientation of particle contacts and volumetric deformations.

For reasons of comparison, the compression behavior of clay in the reconstituted state is displayed as well. The reconstituted state is achieved in a way that the structure of the clay composed of fabric and bonding is initially fully destroyed. Afterwards, the clay is consolidated to the in situ effective stress state of natural clay. For each effective stress state an associated void ratio can be determined for the reconstituted state exemplarily shown in point C. The quantity of the structure at any effective stress state is referred to the difference in void ratio of the structured state to the reconstituted state. By way of example, the difference in void ratio Δe can be seen between points B-C. It can be observed that natural clay due to fabric exhibits a higher void ratio and consequently a lower density than reconstituted clay at the same effective stress state.

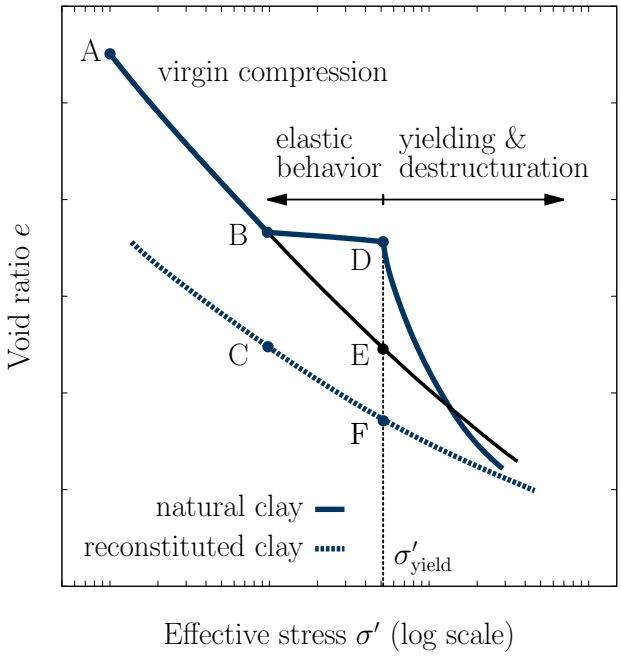

Figure 2.8: Volumetric behavior of natural clay modified after Mitchell and Soga (2005)

Due to the postdepositional processes, bonding may develop at constant stress state and void ratio (at point B). Bonding imparts additional stiffness and strength to the soil due to the physicochemical interparticle forces. Generally, a higher effective stress can be applied to bonded clay without causing yielding. This corresponds to an increasing effective yield stress (shifting the yield point from B to D) higher than the current preconsolidation stress.

While loading until the yield stress is reached the clay behavior is predominantly elastic. A comparison of the void ratio of natural clay exhibiting fabric and bonding at the effective yield stress (point D) and the void ratio of the same clay in the reconstituted state (point F) without structure at the same effective stress state indicates the influence of structure on the volumetric behavior of clay (Δe between points D-F). In addition to this, point E on the virgin compression line represents the same effective stress state and the corresponding void ratio of natural clay, which possesses a certain fabric but no bonding. Therefore, the difference in the void ratio can be theoretically divided into the influence of bonding (Δe between points D-E) and fabric (Δe between points E-F).

Further plastic loading after yielding (point D) will progressively degrade the structure of natural clay resulting in macroscale effects on the mechanical behavior such as reduction of stiffness (increasing compressibility) and strength. The destructuration as an irreversible post-yield phenomenon abruptly occurs and induces a discontinuity in the

stress-volumetric strain behavior of clay after reaching the yield stress. Thereafter, the strength of the bonding is exceeded. Moreover, the changes of the stress-volumetric strain behavior depend on void ratio, effective stress state and quantity of interparticle bonding forces when yielding starts. The destructuration is controlled by the plastic volumetric and deviatoric strain accumulation. The particle arrangement after the destructuration is also affected by the direction of the plastic straining.
Depending on the amount of structure and the applied stress/strain, the effective stress-void ratio curve of natural clay approaches towards the compression curve for the reconstituted state until the structure is fully destroyed. The compression behavior of natural clay assimilates towards the compression behavior of the reconstituted state and is not following the virgin compression line due to superposition of several processes such as coupled destructuration of bonding and fabric, change of environmental conditions during postdeposition or engineering time scale of loading contrary to geological time scale during sedimentary deposition.

Experimental evidence on Bothkennar clay

To be more specific, the results of an oedometer test on Bothkennar clay from a depth of 6.2 m are exemplarily shown in an effective axial stress versus void ratio diagram in Figure 2.9 (Smith, 1992a; Smith et al., 1992b). For reasons of comparison, the test results for a reconstituted sample of Bothkennar clay are also plotted. The natural clay sample is successively loaded exceeding the yield stress, followed by an unloading phase and reloaded exceeding the former effective stress state afterwards.
The yield stress of this particular Bothkennar clay sample has an approximate value in the range of 75-90 kPa. The determination of the yield stress from the logarithmic effective stress-void ratio behavior is indistinct. The yield stress is determined after Casagrande by the intersection of the tangents of the pre-yield and the post-yield behavior. This leads to a bandwidth of values. The reconstituted clay sample is exposed to a loading phase followed by an unloading phase only. It can be clearly observed that due to bonding of the natural clay the yield stress is increased compared to the reconstituted state at the same void ratio. This allows for loading paths with a higher effective mean stress without causing yielding. The yielding characteristics of natural clay were investigated by many researchers (see e.g. Graham and Li, 1985; Burland, 1990; Leroueil and Vaughan, 1990; Diaz-Rodriguez et al., 1992; Kavvadas et al., 1994; Cotecchia and Chandler, 2000). Cotecchia and Chandler (2000) found out that the shape of the yield surface of natural clay in the effective mean stress vs. deviatoric stress space is similar and almost homologous

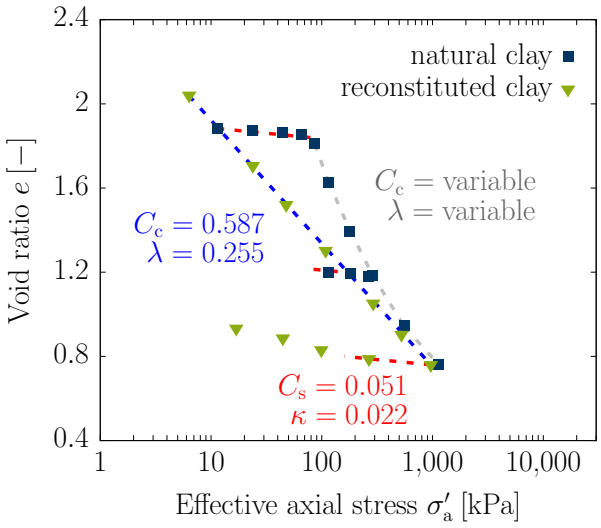

Figure 2.9: Compression and swelling behavior of clay in its natural and reconstituted state obtained from oedometer tests on Bothkennar clay from a depth of 6.2 m (Smith, 1992a; Smith et al., 1992b)

to that of the associated reconstituted state. Whereat, the size of the yield surface of the natural clay depends on the structure indicated by the undrained strength sensitivity.
The stress-volumetric strain behavior until the yield stress is reached seems to be predominantly elastic. The slope of the loading path before reaching the yield stress and the slope of the unloading-reloading paths are similar to the slope of the elastic unloading path of the reconstituted clay (indicated by the almost parallel red lines). Therefore, the same elastic swelling index C_s after Terzaghi (1943) or swelling parameter κ after Schofield and Wroth (1968) can be assessed. To be more detailed, the initial part of the unloading shows a very stiff and almost purely elastic material behavior corresponding to a constant Poisson's ratio ν controlling the value of $K_{0,\mathrm{ur}} = \nu / \{1 - \nu\}$ in the oedometric unloading. With further unloading the behavior becomes strongly nonlinear due to the induced elastoplasticity. A subsequent reloading would cause hysteresis due to elastoplastic transition.
After exceeding the yield stress destructuration abruptly occurs. Destructuration causes a reduction of stiffness and strength of the natural clay resulting in large compression. Consequently, the compression index C_c or the compression parameter λ are large. Due to the progressive nature of the destructuration C_c and λ are gradually decreasing (indicated by the gray lines). Cotecchia and Chandler (2000) observed that the strength sensitivity significantly decreases after exceeding the yield stress due to the progressive damage of the interparticle bonding with increasing plastic straining. Furthermore, they

detected changes of the size of the yield surface, which are dependent on both volumetric hardening and destructuration. Both phenomena are governed by the development of plastic straining. The destructuration continuous until the stress-void ratio curve of the natural clay converges to the corresponding curve of the reconstituted state (indicated by the blue line). The destructuration process is then completed and almost no structure remains. Generally, the structure can be damaged by both compression and swelling.
Among others, Martin and Ladd (1975) and Delage and Lefebvre (1984) investigated the change of the microstruture during one-dimensional consolidation. Natural clay exhibits an aggregate structure including interaggregate and intraaggregate pores. The change of the structure during consolidation is progressive. Firstly, the larger interaggregate pores are affected before the smaller intraaggregate pores are involved. Hence, the volumetric compression is mostly associated with the compression of the interaggregate pores.

2.2.1.2 Quantification of structure

To quantify the structure of natural clay with respect to the reconstituted state, Cotecchia (1996), Cotecchia and Chandler (1997) and Cotecchia and Chandler (2000) introduced the stress sensitivity in addition to the strength sensitivity concept introduced by Terzaghi (1944). In brief, the stress sensitivity S_σ is defined as the ratio of the effective axial yield stress $\sigma'_{\mathrm{a,yield}}$ associated to the structured state and the effective axial yield stress $\sigma'_{\mathrm{a,yield,rec}}$ related to the reconstituted state at the same intrinsic void index. The stress sensitivity is given by Equation 2.6.

$$S_\sigma = \frac{\sigma'_{\mathrm{a,yield}}}{\sigma'_{\mathrm{a,yield,rec}}} \tag{2.6}$$

Exemplarily, the stress sensitivity of natural Bothkennar clay obtained from oedometer tests on natural and reconstituted samples is visualized in Figure 2.10. However, the determination of the stress sensitivity strongly depends on the accuracy of the identification of the yield stress. Whereat, the yield stress is identified with respect to the more or less distinct change in the stress-void ratio behavior. As an additional method for the quantification of structure of natural clay with respect to the reconstituted state, Yang et al. (2014) proposed the stiffness sensitivity S_λ according to Equation 2.7.

$$S_\lambda = \frac{\lambda_0}{\lambda_\infty} \tag{2.7}$$

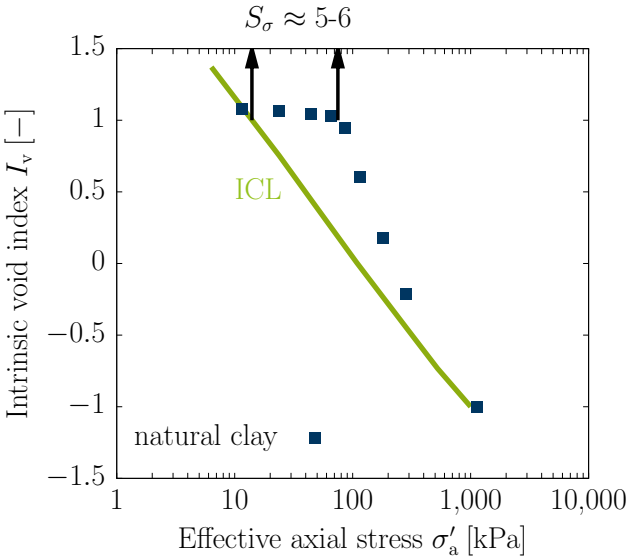

Figure 2.10: Stress sensitivity of natural clay obtained from an oedometer test on Bothkennar clay from a depth of 6.2 m (Smith, 1992a; Smith et al., 1992b)

The stiffness sensitivity defines the ratio between the compressibility initially after yielding expressed by the compression parameter λ_0 and the compressibility at the state when no more destructuration occurs given by the compression parameter λ_∞. It is to be noted that λ_∞ does not necessarily coincide with the compression parameter of the reconstituted clay having intrinsic properties.

2.2.1.3 Classification of natural clay by intrinsic void index

Skempton (1970) investigated the consolidation of natural clay by gravitational compaction. Therefore, the in situ void ratio in different depths is plotted against the corresponding vertical effective consolidation stress due to overburden pressure. The linear relationship between the void ratio and the logarithmic consolidation stress of a particular natural clay is called sedimentation compression curve. To compare different sedimentation compression curves of various clays with the intrinsic compression line (ICL) related to the reconstituted state, Burland (1990) applied the concept of normalization of the void ratio to determine the intrinsic void index I_v as given by Equation 2.8.

$$I_v = \frac{e - e^*_{100}}{e^*_{100} - e^*_{1000}} = \frac{e - e^*_{100}}{C^*_c} \tag{2.8}$$

Whereat, e is the current or in situ void ratio with respect to the structured state and e^*_{100} and e^*_{1000} are the intrinsic void ratios with respect to the reconstituted state at the effective stresses of 100 kPa and 1,000 kPa, respectively. Moreover, the intrinsic compression index C^*_c is defined as the difference of e^*_{100} and e^*_{1000}. Based on the normalization by applying the intrinsic void index I_v the intrinsic compression curves of many different clays converge. The resulting curve is called the intrinsic compression line (ICL). Burland (1990) figured out that the sedimentation compression curves for various clays lie in a continuous band. They also converge to a so-called sedimentation compression line (SCL) when plotting them in a void index-logarithmic vertical effective stress space.
The classification of natural clay with respect to ICL and SCL modified after Chandler (2010) is visualized in Figure 2.11a. Accordingly, the SCL and the range of the sedimentation compression (SC) are marked. The difference between ICL and SCL (lies always above ICL) indicates the influence of structure (fabric and bonding) of natural clay compared to the intrinsic properties in the reconstituted state. Natural clay can exist at a higher void ratio at the same effective stress or can sustain a higher effective stress at the same void ratio compared to the reconstituted state.
Exemplarily, the natural Bothkennar clay and Murro clay are classified in Figure 2.11b. It can be observed that the reconstituted Bothkennar clay as well as the reconstituted Murro clay fit well the ICL. That is, due to the reconstitution the structure composed of bonding and fabric is completely destroyed. Moreover, the natural Bothkennar clay lies

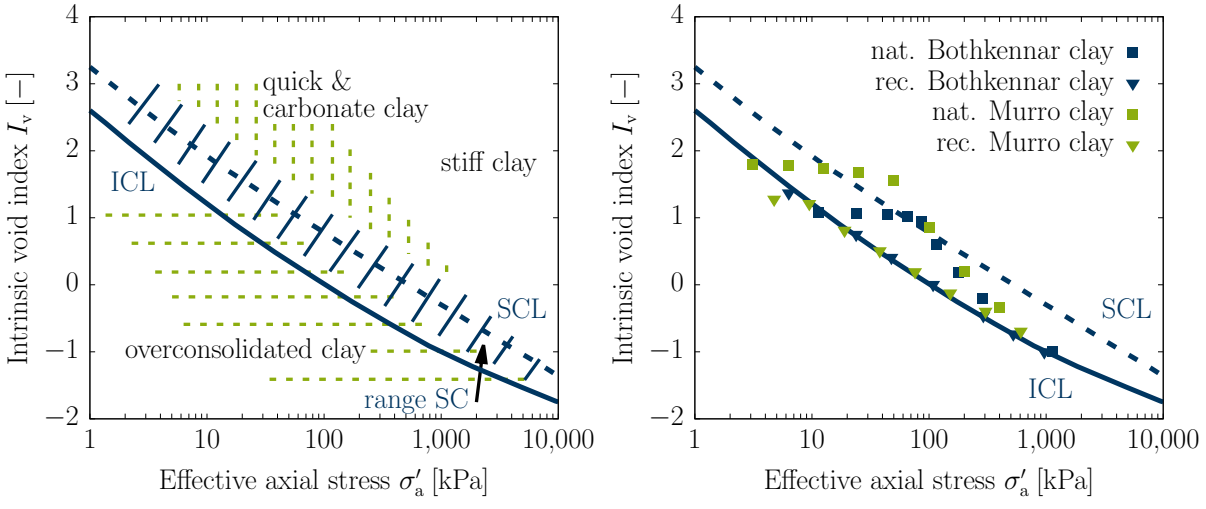

Figure 2.11: a) Classification of natural clay with respect to the intrinsic compression line (ICL) and the sedimentation compression line (SCL) modified after Chandler (2010) and b) Classification of Bothkennar and Murro clay

just slightly above the SCL. Hence, according to the approach of Mitchell and Soga (2005) given in Figure 2.8 the natural Bothkennar clay is just weakly bonded but strongly influenced by the natural clay fabric. However, the bonding of the natural Murro clay is more pronounced indicated by the compression curve existing at higher stress at the same void ratio. The compression curves of both materials converge towards the ICL with increasing plastic straining and destructuration. Consequently, the induced plastic straining during the one-dimensional compression progressively destroys the structure composed of fabric and bonding.
Cotecchia (1996), Cotecchia and Chandler (1997), Cotecchia and Chandler (2000) and Chandler (2010) investigated the properties of a stiff sedimentary clay with respect to the geological history. They stated that for a sedimentary clay the yield stress and mechanical strength behavior are additionally (beside the sedimentation process) controlled by the interparticle bonding due to the diagenetic changes in situ. That is, the yield stress of structured clay is larger than the expected maximum preconsolidation stress developed during geological history induced by sedimentation. Consequently, the yield stress ratio is higher than the expected geological overconsolidation ratio. Therefore, the natural clay lies to the right of the SCL of natural clay. Especially bonded clay such as quick and carbonate clays usually lie above the SCL due to additionally imparted strength and stiffness, which allow for states with a higher void ratio at same effective stress. Similarly, stiff clays lie above the SCL as they can sustain much higher load at the same void ratio due to their compacted and dense state. Geological unloading due to erosion may bring the clay to an overconsolidated state afterwards. Generally, overconsolidation of clay leads to states left to the SCL due to the release of vertical effective stress less than the geological preconsolidation stress. Therefore, the overconsolidated but not altered natural clay manifests a yield stress, which is close to the geological preconsolidation stress.

2.2.1.4 Influence of overconsolidation

In the following, the volumetric behavior of overconsolidated clay is shorty discussed. Overconsolidated clay exists at relatively higher density and lower void ratio compared to a normally consolidated clay in a metastable state at the same effective stress state. That is, the fabric of clay particles and aggregates exists in a more stable state than needed for the equilibrium of the system at the corresponding effective stress state. Consequently, the stress-void ratio behavior of overconsolidated clay is very stiff and predominantly elastic until the reloading stress path approaches to the maximum preconsolidation stress again. Subsequently, at further loading larger than the preconsolidation stress the compression

behavior follows the virgin compression line manifesting the same normally consolidated compression behavior as before. Due to slightly induced elastoplastic material behavior, hysteretic effects can be observed during unloading-reloading cycles depending on over-consolidation ratio, number of cycles and amount of plasticity induced by compression prior to the unloading-reloading cycles.

2.2.2 Shear strength and associated stress-strain behavior

Indeed, the shear strength of natural clay plays an important role for the design of geotechnical applications with respect to the bearing capacity and the ultimate limit state. Therefore, the shear strength and the associated stress-strain behavior of natural clay are presented in this section.
According to Mitchell and Soga (2005), the shear strength of natural clay is among others mainly controlled by the structure composed of fabric and bonding. That is, the shear strength of natural clay is influenced by interparticle frictional resistance and interparticle bonding forces. Therefore, the associated stress-strain behavior is governed by the kinematics between the clay particles/aggregates. Plastic shear strain will change the structure of natural clay by rearrangement of particles/aggregates, reorientation of the particle and aggregate contacts and progressive damage of the bonding.
Firstly, this section provides a general discussion on the triaxial shear strength and the associated stress-strain behavior of natural clay. Special emphasis is given to the influence of drainage conditions and consolidation state. Inherent and stress-induced anisotropy with respect to fabric and material properties as well as anisotropic yielding characteristics are highlighted. Finally, the influence of structure on the shear strength is analyzed. However, rate effects on the shear strength are not discussed in the present study. Moreover, the issue of the tensile strength is also not addressed.

2.2.2.1 General triaxial stress-strain behavior

The general stress-strain behavior of clay under triaxial loading with a certain preconsolidation stress can be divided in four phases (Smith et al., 1992b). Initially, at very small strain, the behavior is linear elastic but maybe anisotropic. The elastic strains are fully recoverable. In the next phase, clay shows a non-linear and hysteretic elastic stress-strain behavior and manifests a stress-dependent stiffness with respect to the stress-strain history. Within the following phase, further loading results in an elastoplastic soil response and irrecoverable plastic straining since relative movements of the particles/aggregates

occur even before reaching the yield surface. In the last phase, after reaching the initial yield surface, significant changes in volume and stiffness arise.

Two consecutive processes of natural clay behavior under shearing have been observed. On the one hand, natural clay exhibits an elastoplastic stress-strain behavior after yielding (hardening, softening, destructuration). And on the other hand, natural clay behavior reaches a critical state after a certain amount of plastic shearing. The critical state of natural clay is defined as the state, where clay under sustained loading deforms at a constant volume (see e.g. Roscoe et al., 1958, 1963; Schofield and Wroth, 1968). The void ratio and the water content of clay are not changing at the critical state. It is observed that densification and rearrangement of the metastable structure of normally consolidated clay, or strain softening of overconsolidated clay after reaching the peak strength, or destructuration, which is defined as the progressive damage of the interparticle bonding of natural clay are completed at the critical state. In conclusion, the critical state defines a unique but material-dependent relationship between the volumetric stress specified by effective mean stress p'_{cs}, deviatoric stress q_{cs} at failure and void ratio e_{cs} or specific volume v_{cs} at the critical state independently of the initial state.

The general triaxial shear behavior and the associated stress-strain behavior of clay dependent on the drainage conditions is schematically illustrated by the effective stress paths in Figure 2.12 and the effective mean stress-void ratio relationships in Figure 2.13. In addition to this, the Figures are divided into a) normally consolidated clay and b) heavily

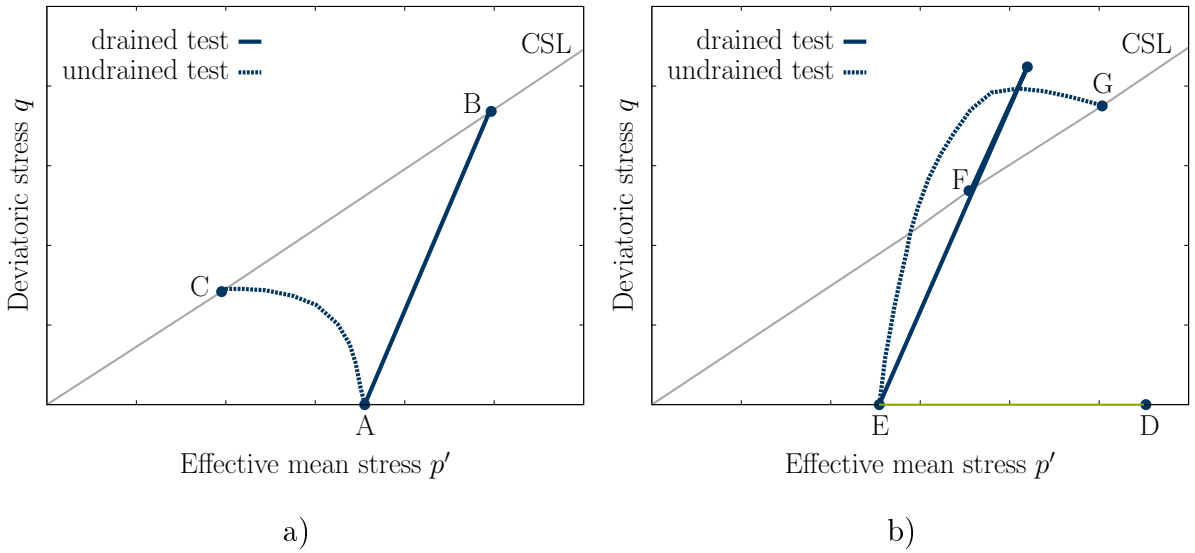

Figure 2.12: General effective stress paths of clay in drained and undrained triaxial tests in a) normally consolidated state and b) overconsolidated state modified after Mitchell and Soga (2005)

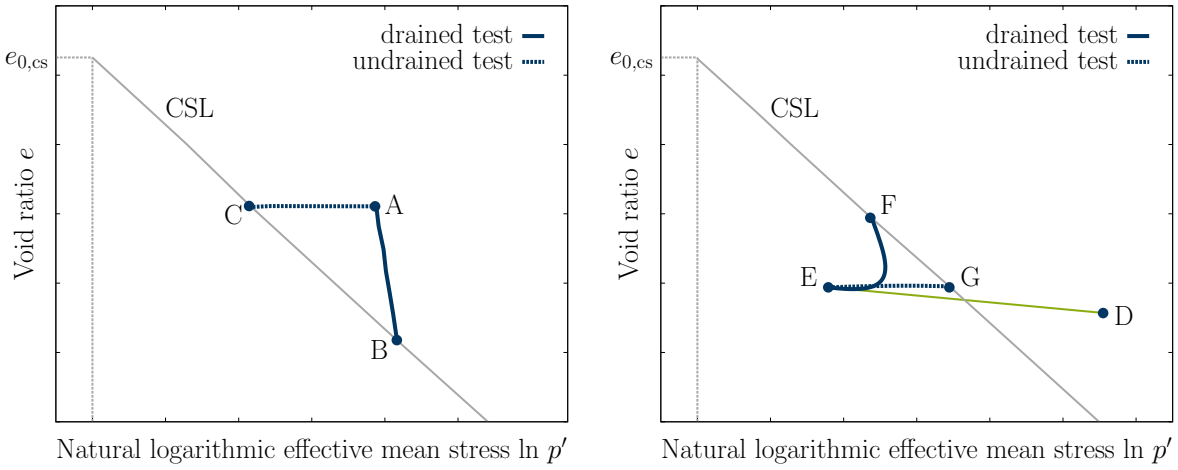

Figure 2.13: General effective mean stress vs. void ratio behavior of natural clay in drained and undrained triaxial tests in a) normally consolidated state and b) overconsolidated state modified after Mitchell and Soga (2005)

overconsolidated clay to show the effect of stress history. The normally consolidated clay is isotropically consolidated to point A. Whereas, the overconsolidated clay is isotropically preconsolidated to point D and isotropically unloaded to point E afterward. The drained triaxial effective stress paths to the critical state line are denoted by A-B for the normally consolidated clay and E-F for the overconsolidated clay. Similarly, the undrained triaxial effective stress paths are denoted by A-C for the normally consolidated clay and E-G for the overconsolidated clay.

The effective mean stress-void ratio state of normally consolidated clay initially lies above the critical state line. The metastable state of normally consolidated soil leads to a contractive behavior due to the elastoplastic hardening response. That is, the metastable structure has a higher potential for rearrangement of particles/aggregates and reorientation of the particle and aggregate contacts induced by shearing.

On the contrary, the effective mean stress-void ratio state of heavily overconsolidated clay lies below the critical state line. This is, the clay exists in a more stable state due to the stress history and its effects on the fabric of clay. The formerly applied stress resulted in rearrangement of the particles/aggregates and reorientation of the interparticle contacts. Accordingly, the fabric changes cause a denser state and a lower void ratio. The unloading leads to an effective stress reduction. Hence, the clay exists in a more stable state with respect to the current effective stress state after unloading. Overconsolidated clay is expected to initially have a predominantly elastic contractive behavior due to the

more stable fabric state followed by an elastoplastic dilative behavior after reaching the peak strength. The strain-softening behavior results in a reduction of the deviatoric stress returning the stress path to the critical state line. Consequently, the peak deviatoric stress q_{peak} exceeds the deviatoric stress at the critical state q_{cs}. This indicates the difference between the peak strength and the strength at the critical state due to strain softening. Mitchell and Soga (2005) listed the following possible triggers for the appearance of the strain-softening during shearing of clay.

- Strength loss due to changes in the fabric higher than the strength gain due to the consolidation
- Re-orientation and alignment of the platy particles along a shear plane associated with a reduction in peak shear strength towards the strength at the critical state
- Destructuration and progressive damage of the interparticle bonding
- Dilative material behavior and associated increase in water content during drained shearing of heavily overconsolidated clay after reaching the peak strength (Skempton, 1985)
- Undrained shearing at high confining pressure associated with the contractive behavior and generation of high excess pore-water pressure

Under drained conditions normally consolidated clay shows a contractive behavior during shearing until reaching the critical state at point B. This causes a decrease of the void ratio under an increasing effective mean stress. The normally consolidated clay exhibits elastoplastic material behavior from the beginning of shearing.
Conversely, under undrained conditions normally consolidated clay is not allowed to show volume change which means that it remains at a constant void ratio. However, due to the general contractive internal behavior of normally consolidated clay under shearing the sample wants to deform by means of decreasing volume. To compensate the restriction of a constant volume during undrained shearing energy is transferred to plasticity. Undrained conditions require a resulting zero total volumetric strain increment as the sum of the elastic and the plastic strain components. Accordingly, balancing this contractive internal behavior results in a counteracting decrease of the effective mean stress and associated simultaneous increase of the excess pore-water pressure until reaching the critical state line at point C. Under undrained conditions no dissipation of pore-water is allowed. The evolution of the excess pore-water pressure in undrained conditions is directly correlated to the structural changes (Lambe and Whitman, 1969).

Heavily overconsolidated clay changes from a contractive to a dilative behavior during the drained triaxial test from point E to point F. At the beginning of the drained shearing the heavily overconsolidated clay predominantly behaves elastically and exhibits a contractive behavior. The effective mean stress and the deviatoric stress are increasing until reaching the yield stress even crossing the critical state line. Afterwards, the clay shows an elastoplastic dilative behavior since the current state does not allow for further densification, which requires a high compaction energy. The brittle and strain softening behavior is indicated by a stress reversal after reaching the peak strength. The clay is then showing a decreasing deviatoric and effective mean stress returning back to the critical state line.
Under undrained triaxial conditions claiming constant volume and void ratio, the heavily overconsolidated clay due to the contractive internal behavior responses predominantly elastically until the critical state line is crossed and the yield stress is approached. The purely elastic response will not result in any change in the effective mean stress due to the restriction of a constant volume under undrained conditions and the linear elastic relationship via the Hooke‘s law between strain and stress. Afterward, the clay behavior is elastoplastic due to the change from contractive to dilative internal behavior. The clay tends to deform by means of an increase of the volume. The associated and counteracting plasticity of the overconsolidated clay causes an increase of the effective mean stress until reaching the critical state line at point G. The excess pore-water pressure is initially increased due to the contractive behavior followed by a decrease of the excess pore-water pressure even up to negative values by reasons of the dilative behavior.

2.2.2.2 Inherent and stress-induced anisotropy

Experimental investigations on natural clay by various researchers showed the dependence of the mechanical properties such as stiffness and shear strength on the sample orientation with respect to the deposition plane, initial isotropic or anisotropic consolidation conditions and loading direction. The associated anisotropy with respect to the mechanical clay properties can be divided into inherent and stress-induced anisotropy.
The inherent anisotropy with respect to the mechanical clay properties is directly related to the clay fabric anisotropy, which is developed during sedimentary deposition or one-dimensional consolidation depending on the clay mineralogy and the environmental conditions as discussed before (Graham et al., 1983). Whereat, the fabric tensor describes the arrangement of the clay particles/aggregates and the orientation of the interparticle/interaggregate contacts.

Generally, a non-isotropic plastic loading induces anisotropy with respect to the mechanical clay properties due to the fabric rearrangement of the particles/aggregates and reorientation of interparticle/interaggregate contacts depending on the loading direction. This phenomenon is called stress-induced anisotropy. Whereat, the evolution of the fabric is strongly related to the evolution of the volumetric and deviatoric plastic strains.
Many researchers investigated the inherent fabric anisotropy and its evolution during consolidation and shearing and discussed the consequences on the mechanical behavior of clay (see e.g. Lo, 1965; Duncan and Seed, 1966; Pusch, 1970; Mitchell, 1970, 1972; Barden, 1972; Martin and Ladd, 1975; Stipho, 1978; Smith et al., 1992b; Adachi et al., 1995; Anandarajah and Kuganenthira, 1995; Anandarajah et al., 1996; Callisto and Calabresi, 1998; Anandarajah, 2000; Hicher et al., 2000; Wheeler et al., 2003; Amorosi and Rampello, 2007; Gasparre et al., 2007a; Hattab and Fleureau, 2010; Wichtmann, 2016). The most important findings are presented in the following.

- During sedimentary deposition the platy clay particles tend to preferentially align in the direction perpendicular to the gravitational loading. Consequently, this results in an anisotropic distribution of the contact normals, a preferred orientation of the void space and hence a predominantly dispersed fabric. Gasparre et al. (2007a) showed that the degree of compaction and the preferential orientation of clay particles generally increase with an increasing overburden depth due to the higher maximum consolidation stress.

- Among many others, Martin and Ladd (1975) investigated the influence of the direction of one-dimensional loading in relation to the direction of the initial consolidation of the sample on the evolution of the fabric. They experimentally confirmed that changing the loading direction from parallel to normal to the initial consolidation direction causes a rotation of the preferred orientation of the particles towards the normal of the applied stress increment. During induced stress paths different from the initial stress ratio the inherent fabric anisotropy will be changed by a continuous plastic straining process. However, a large stress increment may be required to change the direction of the preferred orientation dependent on the initial conditions. A higher initial consolidation stress state and a higher initial degree of anisotropy slow down the stress-induced fabric changes.

- Hattab and Fleureau (2010) evaluated the evolution of fabric at different stages during anisotropic consolidation, isotropic loading and triaxial shearing. The preferential orientation of clay particles and aggregates develops normal to the loading direction during deposition or one-dimensional compression resulting in an anisotropic

fabric. Under isotropic loading the sample is solely densified and due to the rearrangement the particle orientation becomes more random showing a tendency to have a predominantly isotropic and flocculated fabric. Applying triaxial shearing afterwards leads to rotation and preferential orientation of clay particles and aggregates due to changes in the deviatoric stress tensor. They stated that the microstructure and the mechanical behavior after shearing is dominated by the orientation of aggregates and load carrying aggregate contacts rather than the single particles. This results are confirmed by Pusch (1970), Martin and Ladd (1975), Anandarajah (2000) and Hicher et al. (2000). Furthermore, Hattab and Fleureau (2010) discovered that the initiation of the rotation and reorientation requires a certain accumulation of the plastic deviatoric strain.

- Among many others, Lo (1965), Duncan and Seed (1966), Mitchell (1972), Callisto and Calabresi (1998) and Hicher et al. (2000) detected anisotropy of natural clay with respect to the shear strength. The shear strength of normally or slightly overconsolidated clay is largest when the load is applied normal to the deposition plane and reduces when the loading direction rotates. That is, the peak shear strength of clay is significantly dependent on the loading direction (see also Stipho, 1978; Adachi et al., 1995; Amorosi and Rampello, 2007; Wichtmann, 2016). For example, the shear strength is usually lower in extension than in compression.

2.2.2.3 Anisotropic yielding characteristics

The inherent anisotropy with respect to the mechanical properties results in a rotation of the initial yield surface. The yield surface of a particular clay geometrically describes the yield stress points for any loading direction within the entire stress space. Consequently, the yield surface approximately represents the anisotropic yielding characteristics of the clay.

The initial yield surfaces for Murro clay from a depth of 6.9-7.6 m (Karstunen and Koskinen, 2004, 2008; Karstunen and Yin, 2010), Bothkennar clay from a depth of 5.9-6.3 m (Smith, 1992a; Smith et al., 1992b), Onsøy clay from a depth of 11.4-11.5 m (Lunne et al., 2003) and Pisa clay from a depth of 12.3-12.8 m (Callisto and Calabresi, 1998) are exemplarily determined by an optimal fit of a rotated and distorted ellipse with respect to the yield stress points as displayed in Figure 2.14a-d. The inherent anisotropy with respect to the mechanical properties of clay can be proven by means of a rotated initial yield surface for all four natural clays.

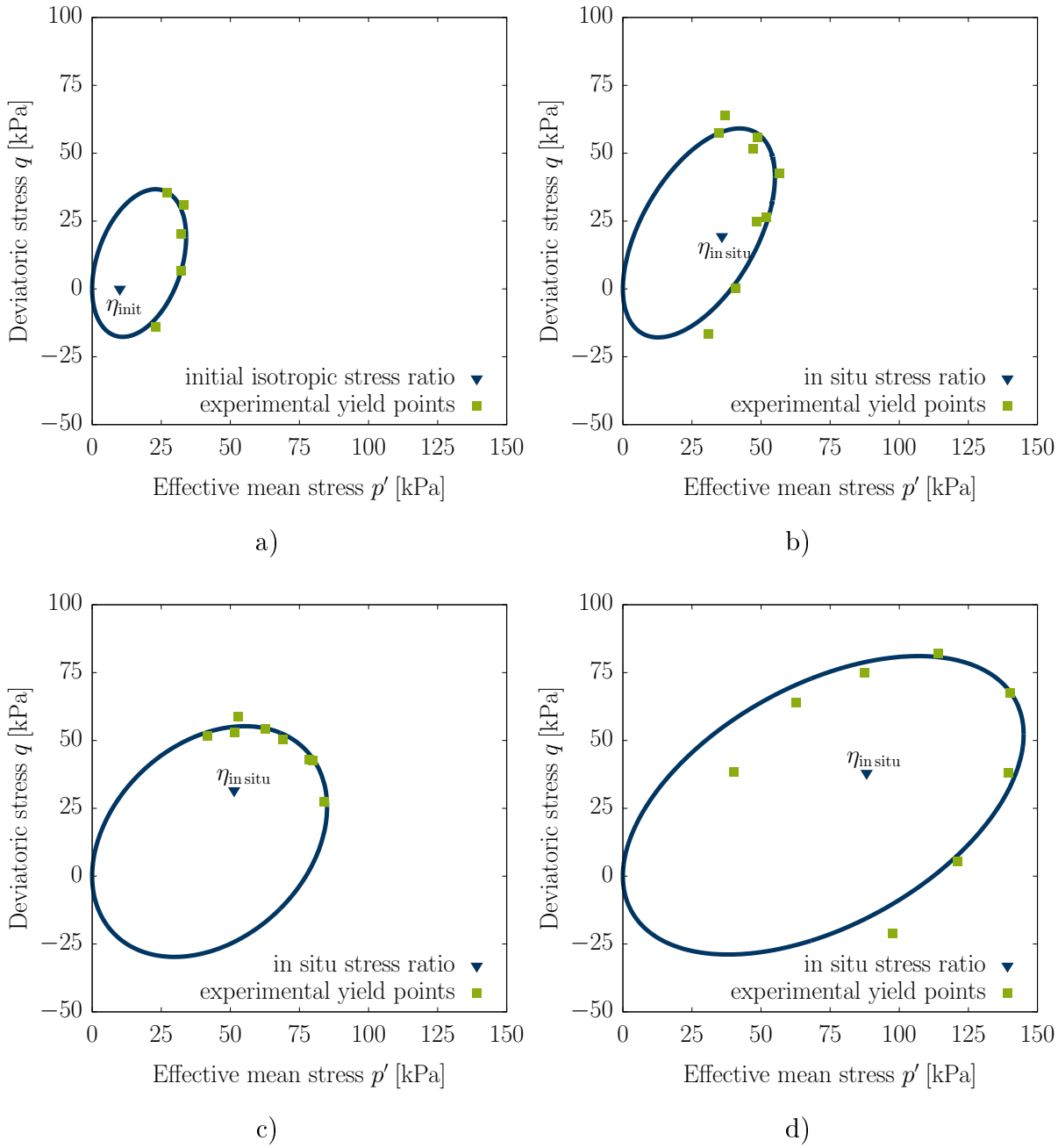

Figure 2.14: Rotated yield surfaces in p', q stress space of different natural clays obtained from triaxial tests with different loading directions in compression and extension on a) Murro clay from a depth of 6.9-7.6 m (Karstunen and Koskinen, 2004; Karstunen and Yin, 2010) b) Bothkennar clay from a depth of 5.9-6.3 m (Smith, 1992a; Smith et al., 1992b) c) Onsøy clay from a depth of 11.4-11.5 m (Lunne et al., 2003) d) Pisa clay from a depth of 12.3-12.8 m (Callisto and Calabresi, 1998)

Furthermore, due to the differences between the four clays, it can be stated that size, shape and rotation of the initial yield surface strongly depend on clay type, structure, current void ratio, current stress state and stress/strain history. Moreover, Diaz-Rodriguez et al. (1992) and Jiang and Ling (2010) presented a compilation of rotated yield surfaces for various clays.

Among others, Wong and Mitchell (1975), Graham et al. (1983) and Graham et al. (1988) investigated the yielding behavior of natural clay and they observed a unique but rotated yield surface for a given clay. Their experiments have shown that the yield surface of anisotropically consolidated clay tends to align in the stress space according to the K_0 value. Furthermore, they explored that clay shows homologous yield surfaces even for different overconsolidation states. The homologous yield surfaces can be merged to a unique yield surface, when applying a stress normalization by the vertical preconsolidation pressure. The direction of the plastic strain is not necessarily normal to the yield surface. That is, the plastic potential surface may be different from the yield surface.

The size of the yield surface is stress-dependent and the yield surface will develop in size, shape and rotation when plastic volumetric and deviatoric strains are evolving. The expansion of the yield surface is related to contraction of clay in a normally consolidated state and controlled by the plastic volumetric strain hardening. The shrinkage is related to dilatancy and governed by the plastic volumetric strain softening. Moreover, destructuration induced by plastic straining results in a reduction of the size of the yield surface as well. Applying further loading after exceeding the yield stress will continuously induce plastic anisotropy. Accordingly, rotation of the yield surface is activated corresponding to the direction of the induced stress and associated plastic straining.

Exemplarily, the stress-induced anisotropy is analyzed based on the test data on Murro clay from a depth of 6.9-7.6 m (Karstunen and Koskinen, 2004, 2008; Karstunen and Yin, 2010). The experimental results are visualized in Figure 2.15a-b and 2.16c-d. A special test procedure according to Wheeler et al. (2003) was applied to determine the stress-induced anisotropy. The clay sample is loaded in a first phase following a constant stress ratio η_1 up to a maximum stress, which is 2-3 times higher than the yield stress detected during this first loading phase. Hence, the first loading phase has two objectives: Identify the size, shape and rotation of the initial yield surface and completely erase the interparticle bonding and induce anisotropy and rotation with respect to the applied stress ratio η_1. Afterwards, the clay sample is unloaded by applying the same stress ratio η_1 but just having a different sign convention. It follows a second loading phase under a different stress ratio η_2 up to a stress level, which is again 2-3 times higher than the yield stress newly observed in this second loading phase.

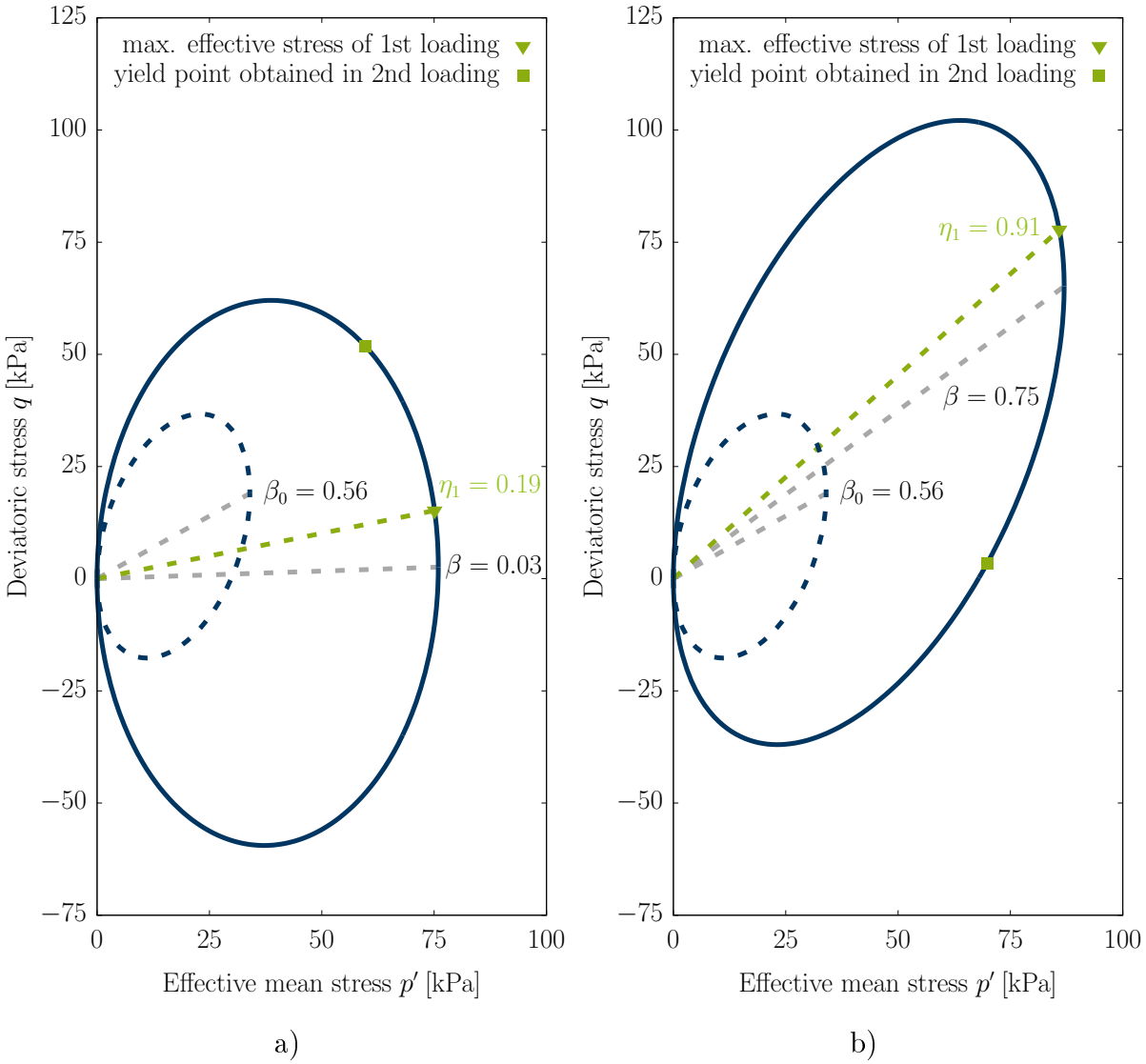

Figure 2.15: Rotation of yield surface in p', q stress space due to stress-induced anisotropy obtained from triaxial tests in compression and extension on natural Murro clay from a depth of 6.9-7.6 m. a) $\eta_1 = 0.19$, $\eta_2 = 0.87$ b) $\eta_1 = 0.91$, $\eta_2 = 0.05$

The new yield stress can be again identified as the stress state, where a significant change in the stress-strain behavior occurs. Accordingly, the anisotropy, which is induced by the stress path η_1 can be identified by means of incremental expansion and rotation of the yield surface. The initial yield surface obtained from the first loading phase is displayed as the reference surface using dashed lines. The maximum effective stress reached in the first loading phase which exceeds the initial yield stress is indicated by a triangle. The yield stress determined within the second loading phase is indicated by a rectangle.

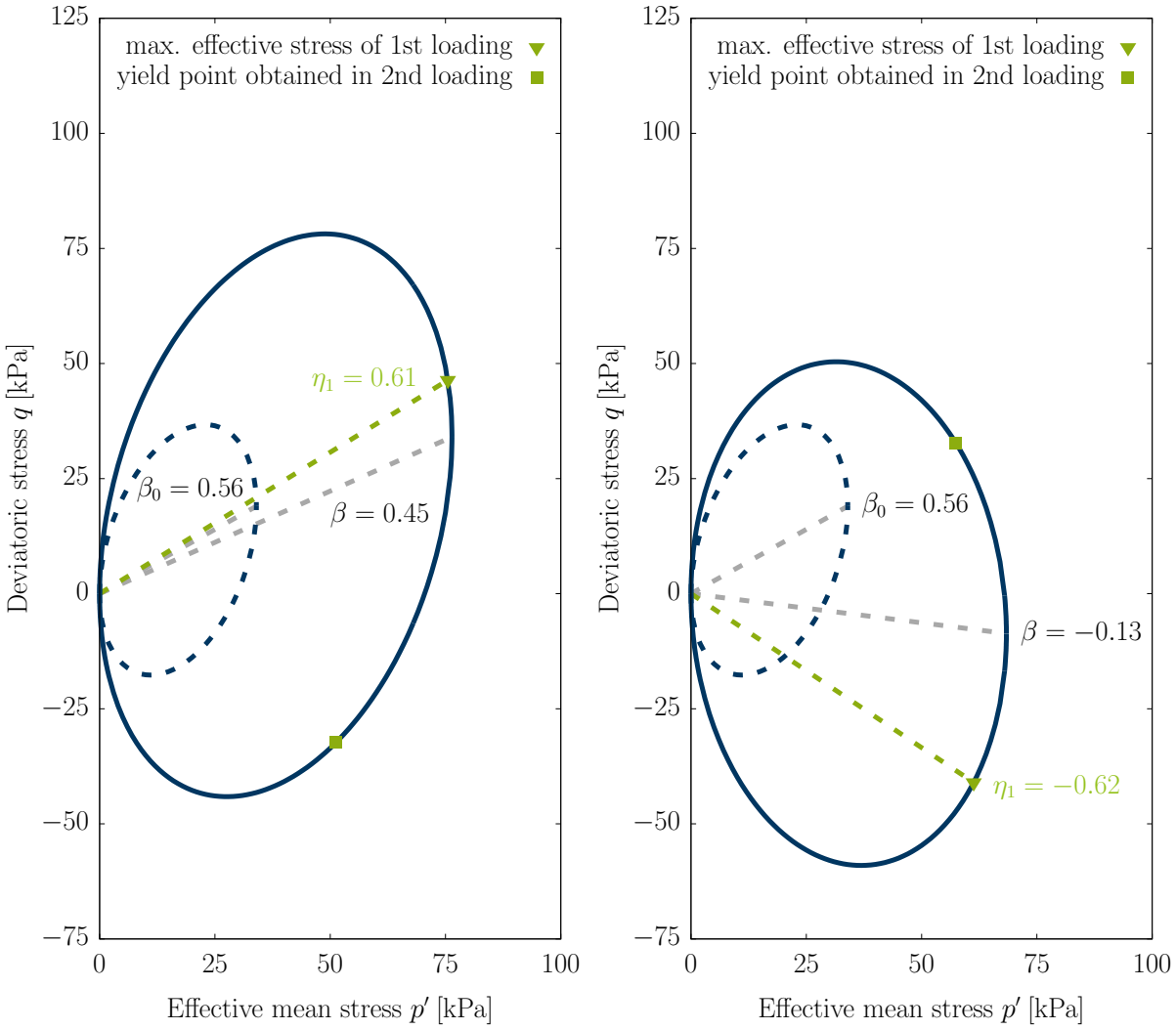

Figure 2.16: Rotation of yield surface in p', q stress space due to stress-induced anisotropy obtained from triaxial tests in compression and extension on natural Murro clay from a depth of 6.9-7.6 m. c) $\eta_1 = 0.61$, $\eta_2 = -0.63$ d) $\eta_1 = -0.62$, $\eta_2 = 0.57$

The evolution of the yield surface from the initial state to the stress-induced state due to loading under η_1 can be clearly identified by the fitted ellipses with respect to these both stress states. For reason of simplicity, it is assumed that the shape of the yield surface will not change. The yield surface expands and hardens due to the applied loading and increasing effective stress. Moreover, the yield surface tends to rotate from the initial state towards the direction of the loading applied in the first phase indicated by η_1. The changes in the rotation are indicated by the difference between β_0 and β. The stress-induced anisotropy with respect to the applied loading path η_1 can be clearly detected.

2.2.2.4 Influence of structure and destructuration

Many researchers investigated the influence of structure on the shear strength and the corresponding stress-strain behavior of natural clay by comparison to the reconstituted state (see e.g. Mitchell, 1970; Sangrey, 1972; Leroueil et al., 1979; Leroueil and Vaughan, 1990; Burland, 1990; Smith, 1992a; Smith et al., 1992b; Burland et al., 1996; Cotecchia and Chandler, 1997; Saihi et al., 2002; Callisto and Rampello, 2004; Karstunen and Koskinen, 2004, 2008; Karstunen and Yin, 2010). The most important findings are presented in the following.

- Sangrey (1972) analyzed naturally bonded sensitive clay in drained and undrained triaxial tests. He observed yield surfaces which are controlled by the interparticle bonding of natural clay. Therefore, the concept of yield surfaces can be used to describe the strength of naturally bonded clay. At stress states below the yield stress bonding imparts additional shear strength and resistance to associated deformations. Hence, the volumetric and deviatoric strains are small. After reaching the yield surface the structure and especially the bonding abruptly collapses.
- Leroueil et al. (1979) stated that any clay behavior at a given depth is governed by the so-called limit state surface in the stress-void ratio space. The limit state surface reflects and incorporates the shear strength, void ratio, stress/strain history and structure (distribution and strength of interparticle contacts). The limit state surface of intact natural clay corresponding to the peak strength is always larger than the limit state surface of the destructured clay. The effects of structure on the shear strength and the stress-strain behavior of natural clay was investigated by Leroueil et al. (1979) and Leroueil and Vaughan (1990) utilizing undrained triaxial tests on natural and associated reconstituted clay. The structure of natural clay and primarily the interparticle bonding impart additional shear strength and resistance in comparison to the reconstituted state. The post-yield behavior with respect to the increasing plastic straining is indicated by the progressive loss of structure and a brittle stress-strain behavior after reaching the peak strength. The destructuration during shearing leads to a reduction of the shear strength. Consequently, the yield surface is shrinking with the evolving destructuration. The destructured clay is less stiff due to significant reduction of bulk and shear modulus during destructuration and reaches a smaller peak strength at a larger failure strain. Hence, the magnitude of shear strain to reach failure increases with increasing degree of destructuration. The difference between the peak deviatoric stress and the deviatoric stress at the critical state is more pronounced for structured clay than for reconstituted clay.

However, the deviatoric stress at the critical state at large strain converges to a common value for both the natural and the reconstituted clay. That is, the interparticle bonding of natural clay is progressively destroyed during shearing up to large strain and the particles/aggregates and contacts rearrange and reorientate similarly for both states.

- Burland (1990) and Burland et al. (1996) also examined the influence of structure of natural clay on the peak strength and the associated stress-strain behavior based on undrained triaxial tests on reconstituted and natural samples. For natural clay they observed brittle behavior, formation of shear surfaces and rapid loss of strength after reaching the peak strength. For a small confining stress the post-rupture shear resistance of natural clay converges to the critical state shear resistance of the reconstituted clay. This is primarily due to the damage of the interparticle bonding. Conversely, for a large confining stress the post-rupture shear resistance is somewhat lower than the critical state shear resistance because of an additional stress-induced change of the fabric due to particle/aggregate and contact rearrangement and reorientation.
- Cotecchia and Chandler (1997) and Callisto and Rampello (2004) performed drained triaxial tests with different constant stress paths. They figured out that the degradation of structure due to increasing plastic straining leads to two simultaneous but counteracting effects on the yield stress such as strain hardening and destructuration. The changes of volume and structure lead to an isotropic increase or decrease of the yield stress, respectively. They introduced a normalization stress to define a unique normalized state boundary surface for a given natural clay. The normalization stress additionally accounts for the current degree of structure rather than just considering the stress history and void ratio. Whereat, the evolution of the normalization stress controls the size of the state boundary surface.
- Callisto and Rampello (2004) investigated the degradation of structure for three natural clays by performing drained triaxial tests having different constant stress paths. However, they figured out that for the analyzed clays the volumetric plastic strain has a stronger influence on the progressive damage of the structure (fabric and bonding) than the deviatoric plastic strain (ratio of 2-3.5). Whereat, the proportion between volumetric and deviatoric plastic strains influencing the destructuration process is material dependent.

Experimental evidence on Bothkennar clay

The undrained triaxial behavior of natural clay was experimentally analyzed by Smith (1992a) and Smith et al. (1992b) conducting isotropically and anisotropically consolidated undrained triaxial tests in compression and extension on Bothkennar clay from a depth of 5.9-6.3 m. The associated effective stress paths and the axial strain-deviatoric stress behavior are illustrated in Figures 2.17 and 2.18. The undrained triaxial tests in compression and extension were conducted after following different drained consolidation paths before shearing:

- Drained reconsolidation to the effective in situ stress state $\eta_{\text{in situ}}$ following the effective stress path A-B-C-$\eta_{\text{in situ}}$
- Drained isotropic consolidation applying large strain to η_{iso} following the effective stress path A-η_{iso}
- Drained anisotropic consolidation applying large strain to η_{K_0} following the effective stress path A-B-C-η_{K_0}

The reconsolidation to the effective in situ stress state represents the real field conditions. At this stress state the microstructure of the Bothkennar clay is still intact because the yield stress is not exceeded yet and predominantly elastic behavior occurs. For reasons of reference the initial yield surface of natural Bothkennar clay from a depth of 5.9-6.3 m is also shown in Figure 2.17. The influence of the isotropic and the anisotropic large strain consolidation on the shearing behavior of natural clay can be analyzed using the two other consolidation paths, where each stress state lies outside the initial yield surface. The large strain consolidation paths result in certain stress-induced anisotropy and destructuration. The main findings are summarized in the following.
The slope of the critical state line at large shearing is nearly independent of the stress history and the original structure (fabric and bonding). This fact is pointed out by the comparison of the three undrained triaxial compression tests each having a different drained consolidation history, which induces changes of the effective stress and structure. Despite the different stress history all three stress paths induced by undrained shearing in compression approach to a unique critical state line specified by the parameter M_{c}. Whereas, the strength behavior in extension significantly differs from the strength behavior in compression due to the different fabric evolution of the clay. This results in a different slope of the critical state line in the extension regime denoted by the parameter M_{e}.
Indeed, the differences of the undrained shearing behavior of isotropically and anisotropically consolidated samples can be obviously seen in Figure 2.17. The development of

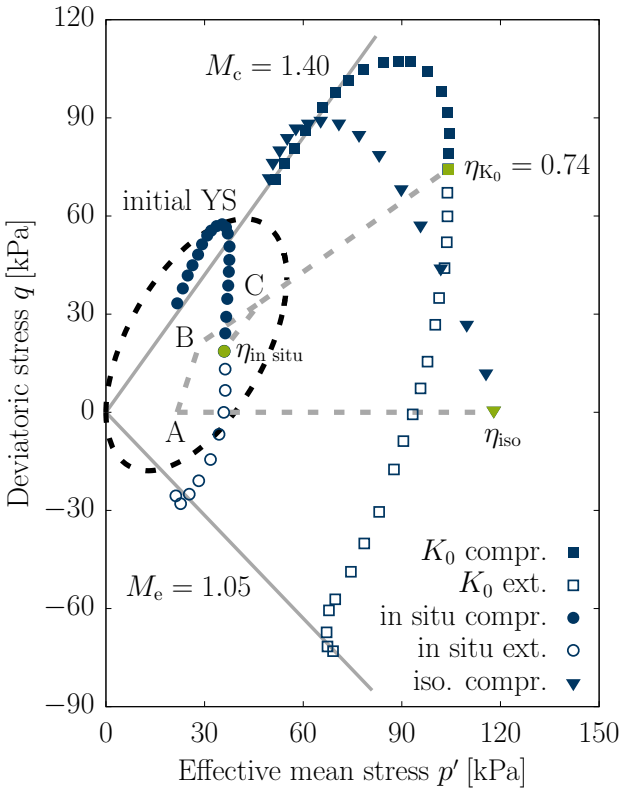

Figure 2.17: Effective stress paths in the p', q stress space obtained from undrained triaxial tests in compression and extension (reconsolidated to the effective in situ stress, isotropically consolidated at large strain and K_0 consolidated at large strain) on natural Bothkennar clay from a depth of 5.9-6.3 m (Smith, 1992a; Smith et al., 1992b)

the excess pore-water pressure and the reduction of the effective mean stress are deviating. This is because the consolidation before shearing results in stress-induced changes of the void ratio and the fabric. The particles/aggregates are rearranged and the particle contacts are reorientated with respect to the different consolidation stress tensors. Consequently, the stress-induced anisotropy results in a rotation of the yield surface towards the loading direction. The changes of the void ratio and the structural effects directly affect the shear behavior and the internal volumetric behavior such as the tendency of showing contraction or dilation. The subsequent undrained shearing of the normally consolidated samples immediately results in elastoplastic behavior. The effective stress paths are following the evolving yield surface until reaching the critical state line. The yield surface of the anisotropically consolidated sample is much more rotated and hence the effective stress paths deviate. Moreover, the isotropically consolidated sample shows a more contractive internal behavior causing larger excess pore-water pressure and a more pronounced re-

duction of the effective mean stress. Whereas, the undrained shearing behavior of the reconsolidated and fully structured clay starting from the in situ stress is very stiff and predominantly elastic. This behavior is observed while moving within the yield surface and crossing the critical state line until reaching the yield stress. Afterwards, plasticity and destructuration are induced resulting in generation of excess pore-water pressure. The sample is showing strain-softening and destructuration and accordingly the stress path is returning back to the critical state line following the updated yield surface.
The deviatoric stress-axial strain behavior of the Bothkennar clay under undrained loading is visualized in Figure 2.18a for the reconsolidated in situ state and Figure 2.18b for the K_0-consolidated state. The natural clay sample in the fully structured state shows a brittle stress-strain behavior under triaxial compression. Whereas, the K_0-consolidated sample manifests a less brittle stress-strain behavior during shearing. This is due to the already induced destructuration process during the large strain anisotropic consolidation. Whereat, an isotropic consolidation at large strain before shearing causes a more ductile response than the anisotropic consolidation. Besides, natural clay generally show a ductile stress-strain behavior in undrained triaxial extension tests independently of the degree of structure and the consolidation state. The required amount of strain to reach the critical state is lower in the extension regime than in the compression regime.

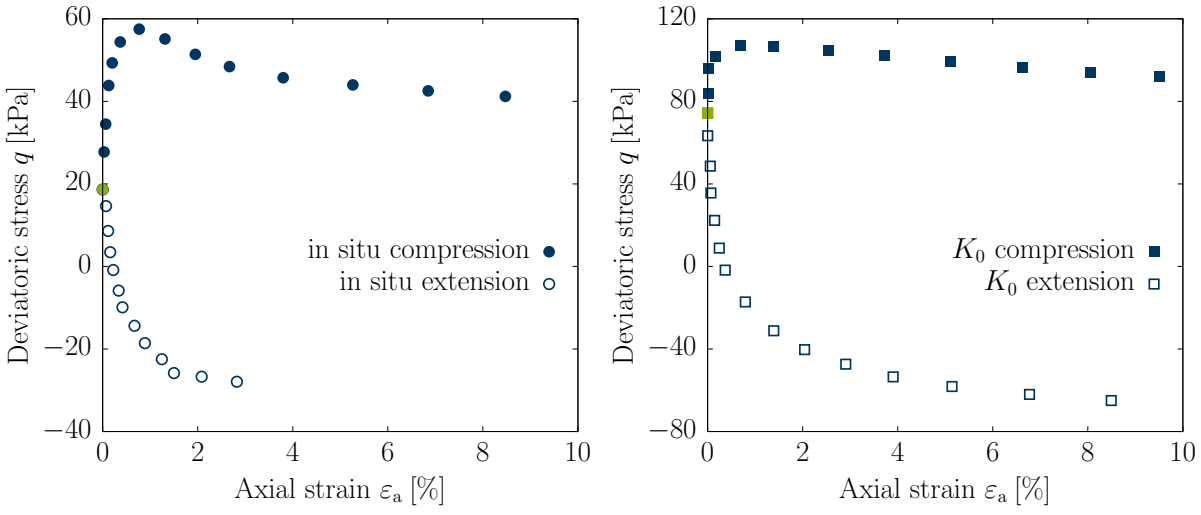

Figure 2.18: Axial strain vs. deviatoric stress behavior of natural clay obtained from undrained triaxial tests in compression and extension on Bothkennar clay from a depth of 5.9-6.3 m a) reconsolidated to the in situ stress and b) K_0-consolidated (Smith, 1992a; Smith et al., 1992b)

Experimental evidence on Murro clay

Furthermore, the drained stress-strain behavior of Murro clay was analyzed by Karstunen and Koskinen (2004, 2008) and Karstunen and Yin (2010) based on the investigation of drained triaxial tests on natural and reconstituted Murro clay from a depth of 6.9-7.6 m. These tests allow for comparison of the behavior in its natural and reconstituted state to evaluate the influence of structure. The effective stress paths, effective mean stress-volumetric strain behavior and deviatoric strain-deviatoric stress behavior are visualized in Figures 2.19 - 2.21.

The reconstituted clay is firstly reconsolidated to the in situ stress state and unloaded afterwards to the overconsolidated state. This testing procedure ensures similar yield stresses for the natural and reconstituted state. For reasons of reference the yield surfaces for the natural and reconstituted state are given in Figure 2.19. The yield surfaces are alike in size and shape and just slightly different in rotation. The following testing procedure of the drained triaxial shearing is applied for both clay samples: The initial loading with the

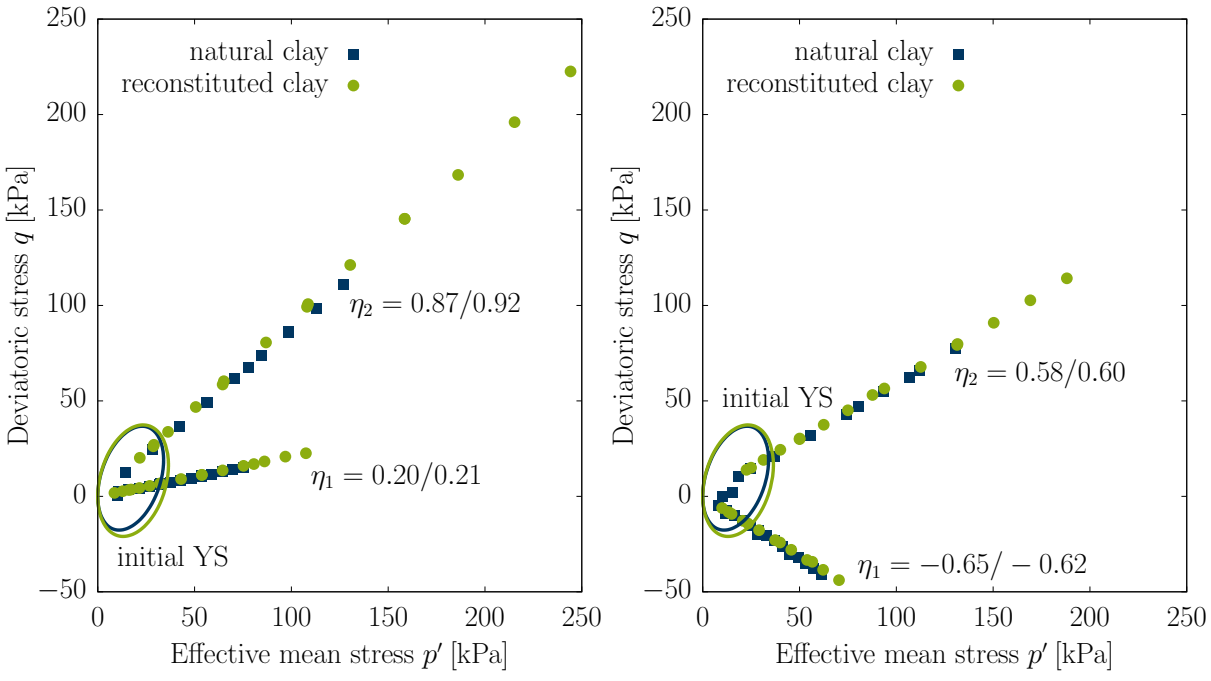

Figure 2.19: Effective stress paths in p', q stress space obtained from drained triaxial tests in a) compression and b) extension and compression on natural and reconstituted Murro clay from a depth of 6.9-7.6 m (Karstunen and Koskinen, 2004, 2008; Karstunen and Yin, 2010)

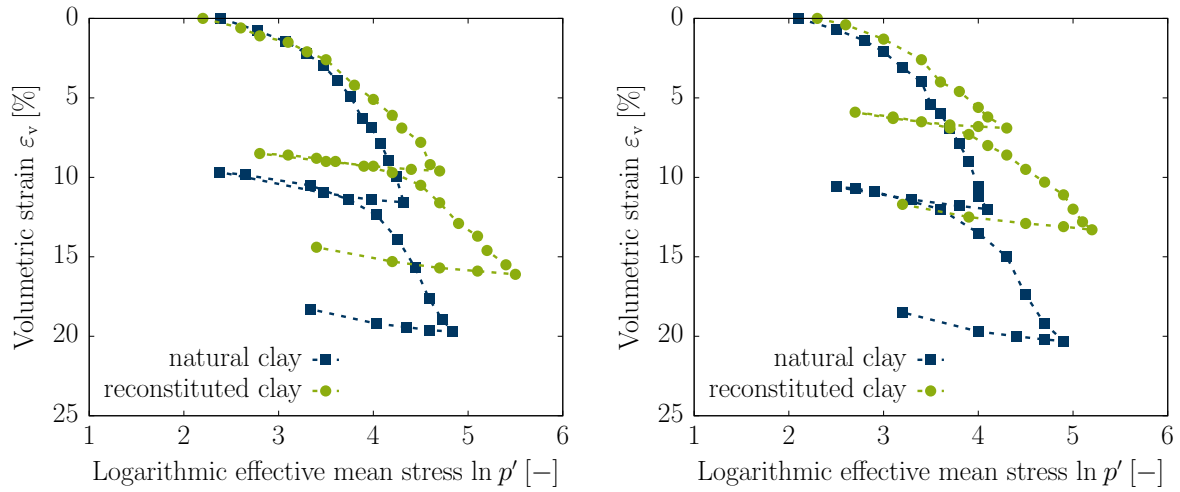

Figure 2.20: Mean stress vs. volumetric strain behavior of clay in its natural and reconstituted state obtained from drained triaxial tests in a) compression and b) extension and compression on Murro clay from a depth of 6.9-7.6 m (Karstunen and Koskinen, 2004, 2008; Karstunen and Yin, 2010)

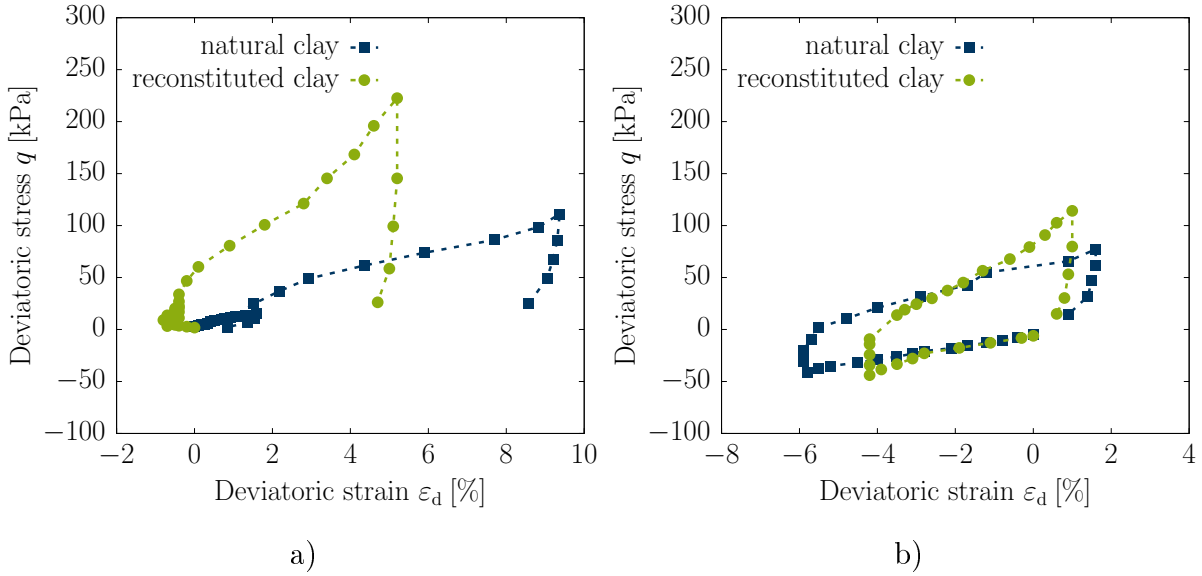

Figure 2.21: Deviatoric strain vs. deviatoric stress behavior of clay in its natural and reconstituted state obtained from drained triaxial tests in a) compression and b) extension and compression on natural and reconstituted Murro clay from a depth of 6.9-7.6 m (Karstunen and Koskinen, 2004, 2008; Karstunen and Yin, 2010)

constant stress ratio η_1 is followed by an unloading with the same stress ratio. Afterwards, the samples are loaded and unloaded with another constant stress ratio η_2. In the Figures 2.19 - 2.21 two different tests are evaluated such as $\eta_1 = 0.20/0.21$, $\eta_2 = 0.87/0.92$ and $\eta_1 = -0.65/-0.62$, $\eta_2 = 0.58/0.60$. It is to be mentioned that there is a slight deviation in the stress ratio and a more pronounced deviation in the maximum effective stress of each loading phase between the tests for natural and reconstituted state.
Initially, both the natural and the reconstituted clay manifest a similar predominantly elastic volumetric behavior until reaching the yield surface. The yield stress, which is alike for both the natural and reconstituted clay, is imparted by interparticle bonding of the natural clay and induced overconsolidation of the reconstituted clay. After exceeding the yield stress, the samples in the natural and the reconstituted state show elastoplastic material behavior. The plastic straining causes plastic volumetric hardening and rotational hardening. In addition to this, destructuration is induced to the natural clay. The progressive damage of the interparticle bonding results in significantly larger compressibility of the natural clay and larger volumetric straining is generated compared to the much stiffer behavior of the reconstituted clay. During unloading and reloading the stress-strain behavior is again predominantly elastic. Therefore, the volumetric stress-strain behavior of the natural clay is similar to that of the reconstituted clay. Due to the progressive destructuration of interparticle bonding during second loading, the volumetric behavior of the natural clay tends to adapt the behavior of the reconstituted clay. This is indicated by almost parallel effective mean stress-volumetric strain paths during loading at higher stress states as shown in Figure 2.20. Regarding the deviatoric stress-strain behavior it is to be noted that most of the quantitative differences of the deviatoric stress between natural and reconstituted state arise from the different applied loading paths. Despite the issue of different maximum stress states, it is clearly pointed out that the destructuration of the natural clay induces an extensive increase of deviatoric strain, when comparing same stress states.

2.2.3 Cyclic behavior

Cyclic loading occurs in various geotechnical applications related to natural clay deposits (e.g. earthquake shaking, wind and wave loads regarding onshore and offshore foundations, locks or dams, traffic loads, and recurring processes in mechanized tunneling). Hence, for realistic and reliable predictions of the system behavior induced by any geotechnical application it is necessary to understand the stress-strain behavior of natural clay under cyclic loading. For the short-term analysis of geotechnical applications in natural clay

under cyclic loading undrained conditions become most relevant since the material properties such as low hydraulic conductivity and low stiffness strongly retard the dissipation of excess pore-water pressure. The behavior of natural clay under undrained conditions and cyclic loading will be discussed in this section founded on experimental evidence. The literature review incorporates the most important findings on the generation of excess pore-water pressure, evolution of the effective stress path, degradation of stiffness and accumulation of plastic strain. However, cyclic failure modes as well as viscous effects and frequency and rate dependence during cyclic loading are not considered in this work.

2.2.3.1 Generation of excess pore-water pressure and evolution of effective stress path

The generation of excess pore-water pressure and the corresponding evolution of the effective stress path with respect to the cyclic triaxial loading under undrained conditions was investigated by various researchers (see e.g. Seed and Chan, 1966; Sangrey et al., 1969; Brown et al., 1975; Andersen et al., 1980; Matsui et al., 1980; Takahashi, 1981; Yasuhara et al., 1982; Lefebvre and LeBoeuf, 1987; Vucetic and Dobry, 1988a; Diaz-Rodriguez, 1989; Vucetic and Dobry, 1991; Yasuhara et al., 1992; Matsui et al., 1992; Zergoun and Vaid, 1994; Hyodo et al., 1994; Vucetic, 1994; Adachi et al., 1995; Hyodo et al., 1999; Zhou and Gong, 2001; Moses et al., 2003; Hsu and Vucetic, 2006; Lee and Sheo, 2007; Okur and Ansal, 2007; Li et al., 2011; Wichtmann et al., 2013; Hanna and Javed, 2014; Wichtmann, 2016).

Undrained cyclic triaxial tests on normally or slightly overconsolidated clay generally show an increase of the mean value of the excess pore-water pressure and an associated reduction of the effective mean stress. Consequently, the excess pore-water pressure generated during loading is larger than the counteracting one during unloading, so that the average value is increasing. The effective stress path migrates towards zero effective mean stress. The reduction of the effective mean stress is strongly influenced by the shear stress amplitude. The larger the shear stress amplitude the larger the accumulation of the average excess pore-water pressure at the same number of cycles. Consequently, the more pronounced is the effective stress reduction. However, the excess pore-water pressure increase slows down with an increasing number of cycles. The same holds true for the associated decrease of the effective mean stress. Moreover, inherent and stress-induced anisotropy result in an inclination of the effective stress path during cyclic loading.

A stress state with zero effective mean stress (liquefaction), as it can be seen for more granular materials, is not reached for clay manifesting a certain plasticity. In fact, the effective stress path will significantly change in shape and stabilize in the vicinity of the critical state stress ratio. Whereat, the effective stress path might stabilize in butterfly shape, lense shape or constant effective mean stress shape, mainly dependent on the isotropic or anisotropic consolidation stress state, which corresponds to the average cyclic shear stress level and the cyclic shear stress amplitude.
The findings are confirmed by the experimental results on natural Onsøy clay conducted by Wichtmann et al. (2013) and Wichtmann (2016). The evolution of the excess pore-water pressure and the effective stress path is visualized in Figures 2.23b and 2.22. However, continuous migration of the effective stress path to the stress origin during loading and unloading as seen in Zergoun and Vaid (1994) and Hyodo et al. (1994) is expected rather than observing a temporary increase of the effective mean stress during unloading. Due to the measurements at the bottom of the sample just an approximate average of the

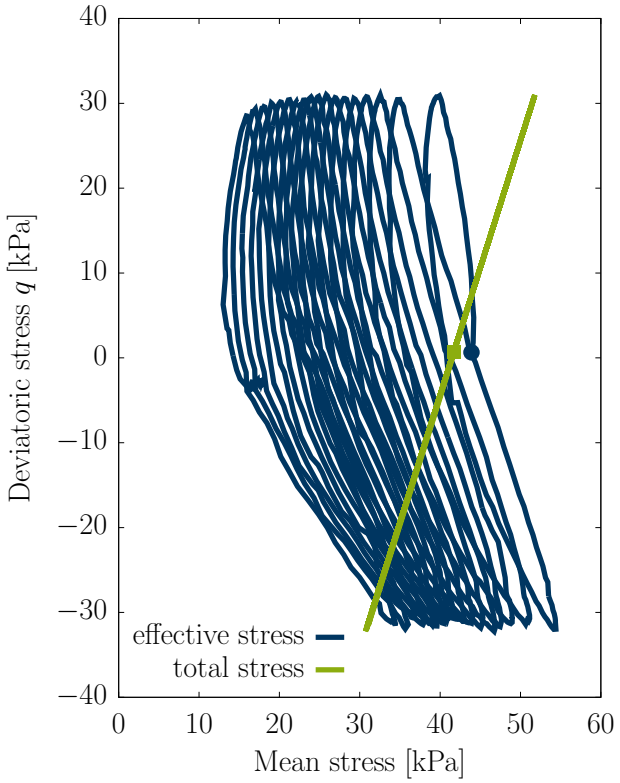

Figure 2.22: Total and effective cyclic stress paths obtained from an anisotropically consolidated undrained cyclic triaxial test on natural Onsøy clay from a depth of 10.5-10.9 m (Wichtmann et al., 2013; Wichtmann, 2016)

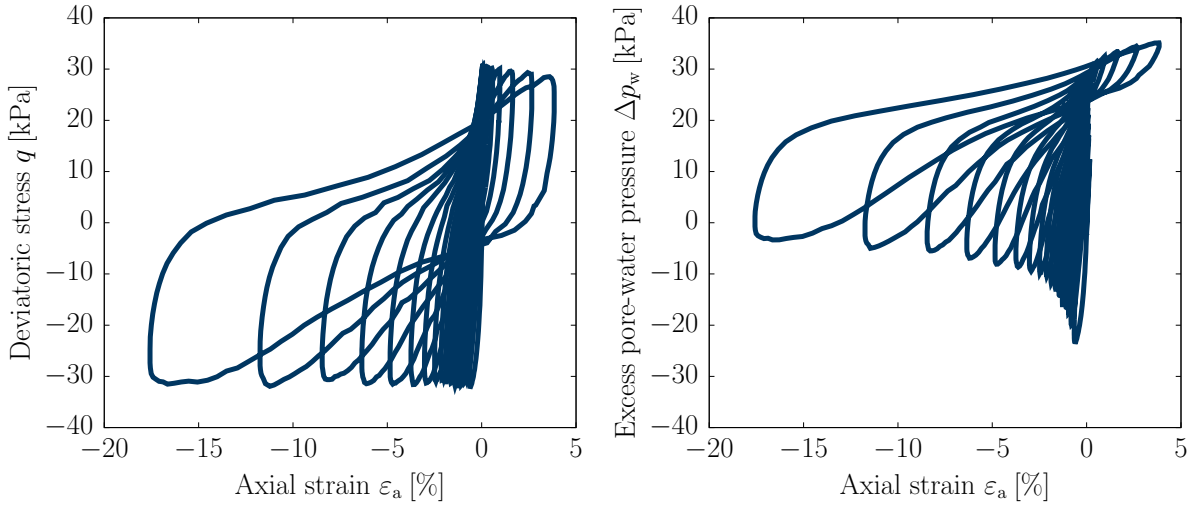

Figure 2.23: a) Axial strain vs. deviatoric stress and b) axial strain vs. excess pore-water pressure behavior obtained from an anisotropically consolidated undrained cyclic triaxial test on natural Onsøy clay from a depth of 10.5-10.9 m (Wichtmann et al., 2013; Wichtmann, 2016)

inhomogeneous distribution of the excess pore-water pressure over the sample volume is considered for the calculation of the effective stress path which may be not fully representative. An inhomogeneous excess pore-water pressure field may arise from the discrepancy between the relatively high loading frequency and the low permeability of the clay.
Furthermore, many researchers analyzed the influence of overconsolidation on the undrained cyclic triaxial behavior of clay (see e.g. Brown et al., 1975; Andersen et al., 1980; Matsui et al., 1980; Vucetic and Dobry, 1988a; Matsui et al., 1992; Hyodo et al., 1999; Zhou and Gong, 2001; Hanna and Javed, 2014). They identified that cyclic loading of overconsolidated clay samples initially generates negative excess pore-water pressure due to the internal dilative behavior and the associated demand for volume increase. The dilative internal behavior initially causes an increase of the effective mean stress. The larger the overconsolidation ratio the larger the dilative part. After a certain number of cycles, however the reduction of the effective mean stress starts to develop since the internal behavior switches from dilation to contraction. To sum up, normally consolidated clay shows a larger reduction of the effective mean stress than overconsolidated clay due to the more contractive internal behavior.

2.2.3.2 Degradation of stiffness and accumulation of plastic strain

The stiffness degradation and the associated accumulation of plastic strain during cyclic loading was investigated by various researchers (see e.g. Brown et al., 1975; Vucetic and Dobry, 1988a; Diaz-Rodriguez, 1989; Matsui et al., 1992; Zergoun and Vaid, 1994; Vucetic, 1994; Zhou and Gong, 2001; Moses et al., 2003; Lee and Sheo, 2007; Okur and Ansal, 2007). During cyclic loading plastic strain start to accumulate with an increasing number of cycles. This indicates a progressive degradation of the stiffness strongly dependent on the accumulated cyclic plastic strain level. That means, the increment of stiffness degradation increases with respect to the accumulation of plastic strain. A high material damping and dissipation of energy is involved. The degradation of stiffness and hence the accumulation of plastic strain is correlated to the cyclic stress amplitude. The larger the cyclic shear stress amplitude the larger the increments of stiffness degradation and plastic strain accumulation. Moreover, the stiffness degradation is more pronounced for normally consolidated clay than for overconsolidated clay because of the less stable fabric state.
The accumulation of plastic strain either in the compression or the extension regime is strongly dependent on the average cyclic shear stress level and the cyclic shear stress amplitude. To be more specific, samples, which are cyclically loaded at a small average cyclic shear stress level and with a cyclic shear stress amplitude above the threshold value show accumulation of plastic strain in compression and extension. Exemplarily, the stress-strain behavior of a natural Onsøy clay sample, as investigated by Wichtmann et al. (2013) and Wichtmann (2016), is shown in Figure 2.23a. The stress-strain hysteresis is growing with an increasing number of cycles and an accelerated migration of the axial strain towards the extension regime can be observed. However, samples cyclically loaded at a large average cyclic shear stress level and with a cyclic shear stress amplitude above the threshold value show an accumulation of strain in compression only. On the contrary, samples which are cyclically loaded below the threshold value show stress-strain hysteresis, which remains constant in size after a few cycles.
clearpage

2.2.3.3 Influence of structure and destructuration

Several research on the cyclic behavior of undisturbed and reconstituted clay can be found in literature (see e.g. Andersen et al., 1980; Yasuhara et al., 1982; Lefebvre and LeBoeuf, 1987; Diaz-Rodriguez, 1989; Matsui et al., 1992; Adachi et al., 1995; Hyodo et al., 1999; Moses et al., 2003; Li et al., 2011; Hanna and Javed, 2014; Wichtmann et al., 2013). The

main findings are summarized in the following. The cyclic response of structured clay before exceeding the yield stress is predominantly elastic and the development of excess pore-water pressure and accumulation of plastic strain are relatively small. Therefore, the structured clay manifests less reduction of the effective mean stress within the very first cycles compared to the reconstituted state. The structure and especially the bonding imparts additional strength and resistance against cyclic loading. For structured clay a larger shear stress amplitude is needed to exceed the expanded yield surface. The higher the yield stress ratio the stronger the resistance against undrained cyclic shearing. That is, structured clay resists more shear cycles until failure occurs. If once the yield stress is exceeded during cyclic loading the undrained cyclic shear behavior will be affected by the destructuration process, so that significant generation of excess pore-water pressure and excessive plastic strain accumulation occur.

2.2.4 Summary

The influence of structure of natural clay on the mechanical behavior was analyzed in this section. In particular, the volumetric and shearing behavior and the behavior under cyclic loading were reviewed. The most important findings are summarized in the following.
The mechanical behavior of natural clay strongly depends on the amount of structure. The structure of natural clay composed of fabric and interparticle bonding initially imparts additional stiffness, strength and resistance against compression and shearing compared to the reconstituted state. Whereat, the quantity of the structure may be indicated by the stress and stiffness sensitivity concepts. The structure results in an increase of the yield stress. Due to the anisotropic fabric developed during deposition natural clay shows an inherent anisotropy with respect to the mechanical behavior. Inherent anisotropy leads to an initial rotation of the yield surface. Effective stress paths (compression, extension, shearing) below the yield stress cause predominantly elastic material behavior. After reaching the yield stress the induced plastic straining evoke an evolution (expansion, shrinkage, rotation) of the yield surface with respect to the loading direction. Induced plastic straining will significantly change the structure of natural clay composed of fabric and interparticle bonding by rearrangement of particles/aggregates, reorientation of contacts and progressive damage of bonding. Dependent on plastic straining isotropic hardening or softening, stress-induced anisotropy indicated by rotational hardening and destructuration occur.
Regarding the volumetric behavior of natural clay progressive destructuration after yielding causes an abrupt reduction of the stiffness and generation of large compression. The shear strength and the associated stress-strain behavior of natural clay are also strongly

influenced by structure composed of fabric and interparticle bonding. Natural clay exhibits a higher peak shear strength and a more brittle stress-strain behavior in compression as compared to the more ductile behavior of reconstituted clay. After exceeding the yield stress destructuration of natural clay results in a significant decrease of shear strength and associated development of large volumetric and deviatoric strains. In general, the strength behavior in compression may differ from the strength behavior in extension, where the latter manifests a smaller triaxial shear strength and a more ductile stress-strain behavior. Furthermore, the structure and especially the bonding of natural clay initially impart additional strength and resistance against cyclic loading. If the yield stress is exceeded during cyclic loading the destructuration process will affect the undrained cyclic shear behavior causing a significant generation of excess pore-water pressure and corresponding migration of the effective mean stress towards the effective stress origin as well as an excessive strain accumulation due to the progressive degradation of stiffness.
Consequently, an adequate constitutive model for natural clay has to be able to properly approximate the mechanical stress-strain behavior including all characteristics, which were discussed in the former sections. The various concepts of the constitutive modeling of the mechanical behavior of natural clay with special consideration of anisotropy, structure and destructuration and behavior under cyclic loading are evaluated in the following sections.

2.3 Constitutive modeling of natural clay

According to the discussion on the mechanical behavior of natural clay in the former sections an adequate constitutive modeling of natural clay behavior should incorporate the following decisive mechanical aspects with respect to the complex stress-strain behavior.

- Critical state soil mechanics concept
- Non-linear elasticity
- Elastoplastic transition behavior within the yield surface dependent on the distance between current stress state and a bounding surface
- Elastoplastic hardening behavior after exceeding the yield stress
- Elastoplastic softening behavior after reaching the peak strength
- Dilative behavior of overconsolidated clay
- Elastoplastic unloading and hysteresis effects after stress reversal
- Differences of the behavior in compression and extension

- Inherent and stress-induced anisotropy
- Initial structure and stress-induced destructuration
- Cyclic behavior incorporating accumulation of plastic strain and degradation of stiffness
- Viscoplastic and strain-rate dependent behavior

A state-of-the-art review on the different concepts for constitutive modeling of natural clay is provided in the following sections. After a short introduction on critical state models, special emphasize is put on the modeling of inherent and stress-induced anisotropy, structure and destructuration and cyclic behavior. Whereat, the concepts of rotational hardening, intrinsic reference yield surface and bounding surface plasticity are highlighted. It is to be noted that the state-of-the-art review is not all-embracing, but it considers the most important concepts and theories. Besides, the existing modeling approaches accounting for viscoplasticity and strain-rate dependence of natural clay are not considered within the present study.

2.3.1 Critical state models

The concept of critical state soil mechanics offers a framework for the development of constitutive models describing the mechanical stress-strain behavior of natural clay. The constitutive BSP model employed in the present study is also based on the critical state soil mechanics theory. Gens and Potts (1988) and Potts and Zdravkovic (1999) gave an overview of the critical state models developed and used in computational geomechanics. The most common critical state models are the Cam-Clay models initially proposed in the framework of general elastoplasticity. Within the original Cam-Clay model Roscoe et al. (1958), Roscoe et al. (1963) and Schofield and Wroth (1968) derived the plastic potential surface from a dilatancy expression based on the plastic work rate. The dilatancy is generally defined as the stress-induced volumetric plastic strain per deviatoric plastic strain. Whereat, the volumetric and deviatoric plastic strains are controlled by the plastic flow rule. Hence, they are expressed in terms of the derivative of the plastic potential with respect to volumetric or deviatoric stress, respectively. The resulting bullet-shape plastic potential surface caused problems for loading along the effective mean stress axis due to discontinuities at the intersection of the plastic potential surface with the effective mean stress axis. That is, the corresponding normality rule induces deviatoric strains even for isotropic loading conditions along the effective mean stress axis. Besides, the

original Cam-Clay formulation showed a discontinuity at the stress origin. To overcome these problems, Burland (1965) and Roscoe and Burland (1968) modified the Cam-Clay model by using an enhanced expression for the plastic work rate. Incorporating dilatancy to the enhanced plastic work rate equation led to a single ellipse formulation for the plastic potential surface. The ellipse intersects the effective mean stress axis having horizontal normals to the plastic potential surface. This condition ensures to avoid any plastic deviatoric strain during isotropic loading along the effective mean stress axis. The Modified Cam-Clay model originally obeys an associated flow rule, where the yield surface and plastic potential surface coincide.

The non-linear and stress-dependent elastic stress-strain behavior inside the yield surface is governed by an isotropic hypoelastic form of the incremental stress-strain relation. For the sake of simplicity this formulation neglects the elastic potentials. Since the elastic deformation is small compared to the plastic deformation, the elastic energy dissipation is also small compared to the plastic dissipation.

Isotropic hardening and softening is considered by an isotropic hardening variable controlling the size of the yield surface. The isotropic hardening variable represents the stress history in terms of the maximum volumetric consolidation stress. The evolution of the hardening variable is defined by an isotropic hardening rule as a function of the volumetric plastic strain increment. Moreover, the definition of the isotropic hardening variable as a function of the specific volume, the elastic swelling parameter κ and the elastoplastic compression parameter λ ensure that the compression and swelling behavior of clay is incorporated accurately.

At the critical state the evolution of the isotropic hardening variable is restricted due to the constant volume condition. That is, the normal to the plastic potential surface at the intersection point of the ellipse and the critical state line has to be always vertical to the effective mean stress axis to ensure a constant volume at the critical state. Consequently, the volumetric plastic strain increment is zero. For plastic loading paths below the critical state boundary surface (subcritical or wet side) clay exhibits a stable strain hardening behavior showing an expansion of the yield surface. The associated plasticity modulus becomes positive. The volumetric part of the normal to the plastic potential is positive. Therefore, contractive volumetric plastic strain is generated. On the contrary, for plastic loading paths above the critical state boundary surface (supercritical or dry side) clay shows an unstable plastic strain softening behavior due to the violation of Drucker's stability condition and shear band localization. Consequently, the plasticity modulus becomes negative. The volumetric part of the normal to the plastic potential is negative. Therefore, dilative volumetric plastic strain is generated.

The Cam-Clay models generally allow for modeling the constitutive behavior of clay. Nevertheless, advanced soil mechanical properties of natural clay such as inherent and stress-induced anisotropy, destructuration and the material behavior under cyclic loading have to be additionally incorporated. To remedy these drawbacks various researchers further modified the Cam-Clay critical state models.

2.3.2 Modeling of anisotropy

In this section the constitutive modeling of anisotropy with respect to the material properties of natural clay is discussed. An appropriate constitutive model should account for the inherent and stress-induced anisotropy. The current literature review is focusing on the concept of rotational hardening of an anisotropic fabric stress tensor with respect to the development of plastic straining and the induced stress ratio since this approach is applied in the constitutive BSP model of the current study. The evaluation of further approaches is beyond the scope of this work.

2.3.2.1 Rotational hardening

The rotation of the yield surface represents the anisotropic material behavior of clay with respect to the arrangement and orientation of the clay particles and aggregates and the associated contacts. Ohta et al. (1975) and Sekiguchi and Ohta (1977) accounted for the inherent anisotropic material behavior by incorporating a constant anisotropic fabric stress tensor in the yield surface formulations of their models. However, plastic straining causes stress-induced anisotropy with respect to the material behavior represented by an evolving rotation of the yield surface.
Therefore, Hashiguchi (1977b) and Hashiguchi (1979) introduced an evolving anisotropic fabric stress tensor to additionally take into consideration the stress-induced anisotropic material behavior due to changes in the anisotropic fabric during plastic straining. However, the inherent anisotropy is specified by the initialization of the fabric stress tensor. Hashiguchi (1977b) and Hashiguchi (1979) originally proposed the concept of rotational hardening, where the evolution of the anisotropic fabric stress tensor is governed by an appropriate rotational hardening rule as a function of the plastic strain increment and the deviatoric stress ratio tensor. Any induced stress increment with deviating stress ratio results in a certain rotation. Hence, the yield surface rotates towards the current deviatoric stress ratio and the magnitude of rotation is governed by the strain increment. Whereat, the stress origin is the center of rotation. If the anisotropic fabric stress tensor and the

current deviatoric stress ratio tensor coincide the rotation is in a saturated state and the increment of rotation converges to zero.

2.3.2.2 Rotational hardening rules

In the subsequent paragraphs several different rotational hardening rules following the same approach as proposed by Hashiguchi (1977b) and Hashiguchi (1979) are presented.

- Kavvadas (1982) and Kavvadas (1983) used an anisotropic fabric stress tensor to account for the rotation of the yield surface within the framework of the MIT-E1 model. The evolution of the anisotropic fabric stress tensor is governed by a rotational hardening rule defined as a function of the volumetric plastic strain increment controlling the magnitude of rotation. The direction of the rotation is defined by the relative difference between the deviatoric stress tensor and the product of the effective mean stress and the anisotropic fabric stress tensor. The evolution of the anisotropic fabric stress tensor describes the erasure of the history memory of the former stress state and the update with respect to the induced stress ratio. Furthermore, the rotation is slowed down when the anisotropic fabric stress tensor converges to the induced stress ratio. When the induced stress ratio does not deviate from the current degree of anisotropy no rotation of the yield surface is activated. Furthermore, the rotation is related to the reciprocal of the current isotropic hardening variable defining the actual size of the surface.

- Whittle and Kavvadas (1993) and Whittle and Kavvadas (1994) employed the rotational hardening rule proposed by Kavvadas (1982) and Kavvadas (1983) in the MIT-E3 model. They extended the rotational hardening rule by including a scalar variable, which describes the relative orientation of the rotated surface with respect to the critical state. That is, the scalar variable slows down the rotation when approaching to the critical state.

- Pestana and Whittle (1999) in their unified model for clays and sands slightly modified the rotational hardening rule proposed by Whittle and Kavvadas (1993) by making the rotation dependent on both the volumetric and deviatoric plastic strain increments.

- Anandarajah and Dafalias (1986) modified the work of Dafalias and Herrmann (1986b) by introducing an anisotropic fabric stress tensor in the bounding surface plasticity framework. The evolution of the rotation towards the induced stress ratio

is controlled by both the volumetric and deviatoric plastic strain increments. Furthermore, the rotational hardening rule was formulated in a way to decelerate the rotation with an increasing degree of anisotropy, to accelerate the rotation for stress states on the bounding surface compared to overconsolidated stress states inside and to prevent the excessive rotation in case of large normalized stress ratio.

- Several other researchers such as Ling et al. (2002), Jiang et al. (2012) and Nieto-Leal et al. (2017) followed the same concepts as discussed above and slightly modified the rotational hardening rule in the framework of the bounding surface plasticity.

- Dafalias (1986c) proposed an anisotropic critical state soil plasticity model, where the anisotropy was considered by incorporating an anisotropic fabric stress tensor and a rotational hardening rule related to the isotropic hardening rule of the Cam-Clay models as a function of the (initial) void ratio and the compression and the swelling parameters. The magnitude of rotation is predominantly governed by the plastic strain increment proportionally rendered via the plastic multiplier. Again, the yield surface rotates towards the induced stress ratio tensor with respect to the current degree of anisotropy. Whereat, a constitutive model parameter defines the rotation, which can develop under a certain constant stress ratio to adequately model the K_0 consolidation path. Further rotation at the critical state is prohibited by adding a term including the volumetric plastic strain increment, which becomes zero at the critical state. Additionally, the absolute value of the volumetric plastic strain increment is used to allow for downward rotation for stress states above the critical state showing dilatancy. Moreover, the rotation is decelerated for highly overconsolidated stress states.

- Dafalias et al. (2002) and Dafalias et al. (2006) extended the model proposed by Dafalias (1986c) to consider non-associated plastic flow. Consequently, the rotation of the plastic potential surface and the yield surface are governed by different fabric stress tensors.

- Dafalias et al. (2006) and Dafalias and Taiebat (2013) introduced a tensorial bounding attractor to avoid excessive rotation beyond the critical stress ratio. That is, the anisotropic fabric stress tensor converges towards the bounding attractor for loading under any constant stress ratio up to the critical stress ratio. Furthermore, Dafalias and Taiebat (2014) proposed a new formulation of the bounding attractor with respect to the open discussion whether there exist anisotropic or isotropic fabric at the critical state.

- Hashiguchi and Chen (1998) presented a rotational hardening rule in the framework of the subloading surface modeling concept. The rotational hardening rule is mainly governed by the deviatoric plastic strain increment and the difference between the current stress ratio and the anisotropic fabric stress tensor. Furthermore, Hashiguchi and Chen (1998) introduced a limit surface for the rotational hardening to restrict the excessive rotation due to continuous plastic straining.

- Koskinen et al. (2002) and Wheeler et al. (2003) proposed an elastoplastic model for soft clays (SCLAY1) which accounts for the inherent and the stress-induced anisotropy. The rotational hardening rule is defined with respect to the volumetric and deviatoric plastic strain increments. Moreover, the rotation of the yield surface under constant stress ratio loading is forced to asymptotically approach the empirical equilibrium values for the volumetric and the deviatoric cases, respectively. The incorporation of the deviatoric component of the plastic strain increment avoids the freezing of the rotation when reaching the critical state. As a drawback an extensive rotation may occur. Moreover, the absolute value of the deviatoric plastic strain increment ensures a rotation towards the deviatoric target ratio independently of the direction of strain. The Macauley brackets for the volumetric plastic strain increment make sure that the deviatoric model response is noticeable even when the volumetric strain increment is negative (e.g. yielding on the dry side of the critical state).

- Huang et al. (2011) in the framework of the bounding surface plasticity slightly modified the rotational hardening rule proposed by Koskinen et al. (2002) and Wheeler et al. (2003) in order to explicitly control the rotation when the induced stress ratio converges to the critical stress ratio.

2.3.2.3 Further approaches

A detailed evaluation of further approaches is beyond the scope of this work. Some approaches are mentioned in the following.

- Concept of kinematic hardening (see e.g. Prager, 1956; Ziegler, 1959; Mroz, 1967; Mroz et al., 1978; Prevost, 1978; Mroz et al., 1979; Pietruszczak and Mroz, 1983; Dafalias and Popov, 1975; Hashiguchi, 1980, 1981; Al-Tabbaa and Wood, 1989; Kavvadas and Amorosi, 2000; Belokas and Kavvadas, 2010).

- Contact mechanics in the multi-laminate framework (see e.g. Pande and Sharma, 1983; Pietruszczak and Pande, 1988, 2001; Cudny and Vermeer, 2004; Schweiger et al., 2009; Galavi and Schweiger, 2009).

2.3.3 Modeling of structure and destructuration

This section deals with the constitutive modeling of structure and destructuration. Natural clay exhibits a different mechanical behavior in the structured state compared to the reconstituted state with respect to the intrinsic properties. An appropriate constitutive model should account for the initial degree of structure of natural clay as well as for the destructuration process caused by plastic straining. The current literature review is focusing on the concept of an intrinsic reference yield surface and an evolving structure variable governed by plastic straining since this approach is applied in the constitutive BSP model of the current study. The evaluation of further approaches is beyond the scope of this work.

2.3.3.1 Intrinsic reference yield surface and structure variable

Most of the constitutive models taking into account the initial structure of natural clay and the plastic straining induced destructuration are based on the concept of an intrinsic reference yield surface by Gens and Nova (1993). The concept is governed by the assumption that the yield stress of natural clay and therefore the size of the yield surface depend on the current amount of structure and the associated degree of destructuration. Therefore, an imaginary intrinsic reference yield surface, which is homologous to the classical yield surface is introduced. The intrinsic yield surface describes the yield stress with respect to the reconstituted, fully destructured state in reference to the natural structured state at the same void ratio. The difference in size between the yield surface regarding the natural state and the intrinsic yield surface indicates the current amount of structural effects and the degree of interparticle bonding at each effective stress state.
The size of both yield surfaces is specified by two different isotropic hardening variables p_{c0} and p_c representing the structured and intrinsic state, respectively. Consequently, the current degree of structure and bonding is always given by the current ratio between the isotropic hardening variable of the structured and the associated intrinsic state.

Both isotropic hardening variables are linked via a structure variable b according to Equation 2.9. In the fully destructured state the ratio between both surfaces is equal to one, so that the structure variable b equals to zero.

$$\frac{p_{c0}}{p_c} = 1 + b \tag{2.9}$$

To sum up, the additional strength and resistance against deformation added by structure is modeled by an increasing size of the yield surface of the natural clay with respect to an intrinsic reference yield surface. This concept allows for effective stress paths to a higher effective mean stress without causing plastic yielding. Hence, additional structure enlarges the regime, where the material behavior is predominantly elastic and more stiff. This is equivalent to the observation that structured clay at a certain effective mean stress can exist at higher void ratio as compared to the reconstituted state.
To consider structure and destructuration in the constitutive equations, Gens and Nova (1993) introduced the isotropic hardening variable p_{c0} representing the structured state to the general yield surface formulation. Whereat, the initial size of the yield surface regarding the structured state is specified by a proper initialization of the associated isotropic hardening variable p_{c0} according to the experimentally obtained yield stress of natural clay in the undisturbed state. Moreover, the ratio of the experimentally obtained yield stresses of the structured and the corresponding reconstituted state defines the initial value of the structure variable b_0 representing the initial degree of bonding.
Furthermore, the structure may even impart additional strength in the tensile regime. Consequently, the isotropic expansion of the initial size of the yield surface in the tensile regime is defined via the hardening variable p_t as given in Equation 2.10. That is, the structural effects in the tensile regime are a function of the effects in the compression regime indicated by a function of the same governing structure variable b, where α_t is a constitutive model parameter.

$$\frac{p_t}{p_c} = \alpha_t \, b \tag{2.10}$$

According to Gens and Nova (1993) the evolution of the size of the yield surface with respect to plastic straining is governed by two superimposed phenomena such as conventional isotropic hardening/softening and progressive degradation of the structure. Any isotropic hardening/softening rule can be applied for the evolution of the hardening variable p_c of the intrinsic state. However, in the model by Gens and Nova (1993) the isotropic

hardening/softening rule is dependent on the volumetric and deviatoric plastic strain increments $\Delta\varepsilon_{\mathrm{v}}^{\mathrm{p}}$ and $\Delta\varepsilon_{\mathrm{d}}^{\mathrm{p}}$. Moreover, the evolution of the hardening variable p_{c0} of the structured state with respect to the isotropic hardening/softening is controlled by the increment of the intrinsic hardening variable Δp_{c}.
To account for the effects of destructuration the hardening variable p_{c0} is additionally defined as a function of the evolving structure variable b. The structure variable b evolves according to Equation 2.11 by Gens and Nova (1993) with respect to the plastic straining, which induces the progressive degradation of structure. Hence, the destructuration process affects the size of the yield surface with respect to the structured state via the evolution of the structure variable b. Consequently, the hardening variable p_{c0} will be updated according to Equation 2.9 using the updated value of b.
Whereat, the evolution of the structure variable b is defined as the product of the initial value of the structure variable b_0 and a decreasing exponential function of an internal damage variable h and its initial value h_0. The damage parameter h is again an increasing function of the proportion of the volumetric and deviatoric plastic strain increments $\Delta\varepsilon_{\mathrm{v}}^{\mathrm{p}}$ and $\Delta\varepsilon_{\mathrm{d}}^{\mathrm{p}}$ as given in Equation 2.12. Therein h_1 and h_2 are constitutive model parameters. The absolute values of the plastic strain increments are used to ensure that the destructuration increases monotonically. In case of having volumetric strain increments it implies that both plastic compression and dilation contribute to destructuration. In conclusion, with increasing plastic straining the effects of destructuration increase and the yield surface with respect to the structured state shrinks. The size of the intrinsic reference yield surface is not affected by the destructuration process.

$$b = b_0 \exp^{-\{h-h_0\}} \tag{2.11}$$

$$\Delta h = h_1 \ |\Delta\varepsilon_{\mathrm{d}}^{\mathrm{p}}| + h_2 \ |\Delta\varepsilon_{\mathrm{v}}^{\mathrm{p}}| \tag{2.12}$$

To sum up, the hardening variable p_{c0} is simultaneously influenced by the counteracting phenomena of either isotropic hardening or softening and destructuration. If the destructuration process is completed both surfaces coincide because the structure variable equals to zero and the size ratio equals to one. That is, changes in the size of the yield surface will occur just due to isotropic hardening or softening afterwards.

The concept of intrinsic reference yield surface and structure variable was applied, modified and enhanced by many researchers as listed in the following.

- Lagioia and Nova (1995) applied the concept of Gens and Nova (1993) within an elastoplastic strain hardening model based on experimental results on cemented soil. The progressive damage of the structure is directly governed by an exponential evolution of the isotropic hardening variables with respect to volumetric plastic staining rather than via the evolution of a structure variable.

- Tamagnini and D'Elia (1999) employed the concepts of Gens and Nova (1993) and Lagioia and Nova (1995) in the framework of the bounding surface plasticity. As an extension the evolution of the isotropic hardening variables due to destructuration depends on the current value of the particular hardening variable and a proportion of both volumetric and deviatoric plastic strain increments.

- Rouainia and Wood (2000) proposed a model accounting for the loss of structure during plastic loading within the framework of the kinematic hardening bubble model as proposed by Al-Tabbaa and Wood (1989). They introduced three surfaces having the same elliptical shape. The reference surface, which represents the material behavior related to the reconstituted state, the kinematically hardening bubble, which is acting as the yield surface separating the elastic and the elastoplastic domain and the bounding or structure surface, which specifies the current state of structure and anisotropy of the material. To account for structural effects the size of the structure surface is related to the size of the reference surface via an evolving size ratio as a decaying function of the volumetric and the deviatoric plastic strain increments and the current value of the size ratio itself representing the current amount of structure. Furthermore, they introduced a dimensionless deviatoric structure tensor as a function of the size ratio to control the position of the structure surface. Consequently, both size and position of the structure surface are affected by the destructuration process.

- Huang et al. (2011) applied the same approach as proposed by Rouainia and Wood (2000) in the framework of their bounding surface plasticity model.

- Gajo and Wood (2001) also employed the same concept as Rouainia and Wood (2000) for their two surface kinematic hardening/bounding surface plasticity model. They just modified the evolution equation for the size ratio by use of a power function.

- Asaoka et al. (2000) introduced a similarity ratio between the classical Cam-Clay yield surface and a so-called enlarged superloading yield surface to describe the effects of structure with respect to the destructured state in the framework of the subyield concept of Hashiguchi and Ueno (1977a) and Hashiguchi (1980). The concept is in accordance with the concept of the intrinsic reference yield surface. The evolution of the similarity ratio is a function of the deviatoric plastic strain increment and scalar functions considering a slowdown of the destructuration process with decreasing value of the similarity ratio itself and the specific volume.

- Koskinen et al. (2002) and Karstunen et al. (2005) followed the concept of an intrinsic reference surface and structure variable introduced by Gens and Nova (1993) for their elastoplastic S-CLAY1S model for soft clays, which accounts for structure and destructuration as an extension of the S-CLAY1 model by Wheeler et al. (2003). The evolution of the structure variable is defined as a function of the volumetric and the deviatoric plastic strain increments and the current value of the structure ratio itself.

- Taiebat et al. (2010) also employed the concept of an intrinsic reference surface by Gens and Nova (1993) in their proposed Saniclay D model as an extension of the simple anisotropic clay (Saniclay) model by Dafalias et al. (2006) to account for structure and the so-called isotropic and frictional destructuration processes. The isotropic destructuration is related to the evolution of the size of the yield surface due to destructuration with respect to the intrinsic reference surface. The frictional destructuration considers the reduction of the critical stress ratio related to the influence of the progressive damage of structure on the critical friction angle. The changes in the critical stress ratio due to structural changes are treated by incorporating the critical stress ratio with respect to the structured state in the plastic potential Equation. The ratio of the critical stress ratio related to the structured and intrinsic state is defined by an additional scalar structure variable as a measure of the frictional structure effects. The evolution equations of both destructuration mechanisms are defined in similar manner as functions of the volumetric and deviatoric strain increments and the current values of the void ratio and the structure variables.

- Seidalinov and Taiebat (2014) and Park and Kutter (2016) used the same or similar isotropic destructuration rule as proposed by Taiebat et al. (2010) in the framework of the bounding surface plasticity concept to account for the mechanical behavior of sensitive structured clay.

- Belokas and Kavvadas (2010) extended the two-surface model for structured soils (MSS) proposed by Kavvadas and Amorosi (2000) to the MSS-2 model. Beside the so-called bond strength envelope and the plastic yield envelope, they included an additional intrinsic strength envelope to relate the material behavior of the structured state to the intrinsic reference state. The novelty in the evolution equation of the hardening variable governing the size of the bond strength envelope is the dependence of the destructuration on the accumulation of the volumetric and deviatoric plastic strains. That is, the increment of decay of structure decreases with increasing accumulated plastic strain. Moreover, the exponential evolution equation is again dependent on the increments of the volumetric and deviatoric plastic strains and the current values of the void ratio and the hardening variable itself.

- Baudet and Stallebrass (2004) proposed the sensitivity three-surface kinematic hardening model (S3-SKH) for structured clay as an extension of the 3-SKH model by Stallebrass (1990) for reconstituted clay. The model is based on the concept of stress sensitivity as introduced by Cotecchia (1996). They introduced a so-called sensitivity surface to account for structural effects. Whereat, the size of the sensitivity surface is given as a multiple of the size of the intrinsic bounding surface dependent on the current stress sensitivity. The destructuration is described by the evolution of the stress sensitivity as a function of the volumetric and deviatoric plastic strain increments and the current stress sensitivity. The novelty of the concept is to allow for an ultimate sensitivity greater than unity. Hence, this allows for the coexistence of stable components and degradation of metastable components of the structure. The theory of having stable components of the structure is based on some experimental results, where the compression curve of natural clay does not converge to the curve of a corresponding reconstituted state even at large stress level. The stable components of the structure, which do not degenerate may arise from fabric effects rather than from bonding.

- Liu et al. (2013) and Xiao et al. (2017) also employed the general concept of stress sensitivity in their constitutive models. Furthermore, Galavi and Schweiger (2009) also used the concept of convergence towards a stable component of the structure in their model.

- Liu and Carter (2002) incorporated the concept of additional and decaying void ratio arising from structural effects as proposed by Liu and Carter (1999) and Liu and Carter (2000a) in a so-called structured Cam Clay model (SCC). Liu and Carter (2003b) extended the model to a three surface model. That is, they introduced an

equivalent yield surface with respect to the reconstituted state, a structural yield surface with respect to the structured state and a subloading surface through the current stress state to allow for plastic deformation and therefore induced destructuration for stress paths within the structural yield surface. During virgin yielding the structural yield surface evolves with respect to an evolution equation incorporating the theory of a decaying additional increment of the void ratio and the volumetric plastic strain increment.

2.3.4 Modeling of cyclic behavior

This section handles the constitutive modeling of the material behavior under complex non-monotonic and cyclic loading. An appropriate constitutive model should account for the smooth transition from elastic to elastoplastic material behavior, hysteretic material behavior, degradation of stiffness, accumulation of plastic strain, generation of excess pore-water pressure and migration of the effective mean stress during non-monotonic and cyclic loading. The current literature review is focusing on the bounding surface plasticity concept since this approach is applied in the constitutive BSP model of the current study. The evaluation of further approaches is beyond the scope of this work.

2.3.4.1 Bounding surface plasticity

Dafalias and Popov (1975) originally proposed the bounding surface plasticity (BSP) concept for metals. At the same time, Krieg (1975) independently developed a similar two surface plasticity theory. The BSP concept as introduced by Dafalias and Popov (1975) is based on the assumption that a loading surface through the current stress state is always enclosed by a geometrically similar bounding surface F, which represents the stress history of the material. The BSP concept enables the modeling of the material behavior under cyclic loading by allowing the development of elastoplastic strain even for stress paths within the bounding surface. This is in contrast to the classical concept of elastoplasticity, where the model response for stress paths within the yield surface is limited to elasticity only.

To be more specific, the elastoplastic BSP model response for stress states within the bounding surface is governed by relating the plasticity modulus with respect to the current stress to the plasticity modulus associated to a corresponding so-called image stress on the bounding surface by a convenient distance function between current and image

stress and a shape hardening function. That is, the more the current stress state approaches to the bounding surface during loading the smaller becomes the value of the corresponding plasticity modulus and the higher the degree of induced plasticity. This ensures a smooth elastoplastic model response. The BSP concept can be applied to any classical elastoplastic model by just incorporating the modified distance dependent plasticity modulus as explained above. The unique image stress state on the bounding surface related to the current stress is calculated via a proper mapping or projection rule.
Dafalias (1986a) additionally introduced a homologous elastic nucleus f_{eln} in order to simulate purely elastic material behavior for stress paths inside. Whereat, the size of the elastic nucleus relative to the size of the bounding surface is indirectly defined by a constitutive model parameter s_{eln}. The current stress is allowed to cross the elastic nucleus and move outside with a smooth elastoplastic transition according to the distance function governing the plasticity modulus.
In the 1980's the BSP concept was applied to soil plasticity (Dafalias et al., 1981; Dafalias and Herrmann, 1982) and further developed to consider the critical state soil mechanics concept, anisotropic soil behavior and non-associated flow (see e.g. Dafalias, 1986a; Dafalias and Herrmann, 1986b; Anandarajah and Dafalias, 1986; Kaliakin and Dafalias, 1989; Ling et al., 2002; Jiang et al., 2012). The BSP concept was frequently applied in former works with various versions of the formulation of the plasticity modulus incorporating different distance functions and so-called shape hardening functions controlling the response curves during plastic hardening and softening. The most important improvements of the BSP concept will be presented in the following sections.

2.3.4.2 Radial projection rule

As an alternative to the original mapping rule, Dafalias (1986a) employed a radial projection rule 2.13, which was originally proposed by Hashiguchi and Ueno (1977a) and Hashiguchi (1981).

$$\bar{\boldsymbol{\sigma}}' = b\left\{\boldsymbol{\sigma}' - \boldsymbol{\sigma}'_{\mathrm{pc}}\right\} + \boldsymbol{\sigma}'_{\mathrm{pc}} \tag{2.13}$$

The current stress $\boldsymbol{\sigma}'$ is radially mapped from the projection center $\boldsymbol{\sigma}'_{\mathrm{pc}}$ towards the image stress $\bar{\boldsymbol{\sigma}}'$ on the bounding surface. The projection of the current stress to the image stress on the bounding surface is governed by a newly introduced back stress tensor $\boldsymbol{\sigma}'_{\mathrm{pc}}$ and the similarity ratio variable b. The back stress tensor is simultaneously used as projection

center and center of homology between loading surface and bounding surface to ensure the same direction of the gradient vector. The similarity ratio variable defines the evolving ratio between image and current stress with respect to the same projection center. The value of b is derived from inserting the radial projection rule in the bounding surface formulation. The approach of radial projection in the framework of the BSP concept is displayed in Figure 2.24.

2.3.4.3 Plasticity modulus and distance function

Dafalias (1986a) proposed a formulation of the plasticity modulus K_p related to the current stress on the loading surface as the sum of the plasticity modulus $\bar{K}_\mathrm{p}$ with respect to the projected stress on the bounding surface and the product of a shape hardening function $\hat{h}$ and a distance function $\hat{d}$ as given in Equation 2.14.

$$K_\mathrm{p} = \bar{K}_\mathrm{p} + \hat{h}\,\frac{\delta}{\langle r - s_\mathrm{eln}\,\delta\rangle} = \bar{K}_\mathrm{p} + \hat{h}\,\left\langle \frac{b}{b-1} - s_\mathrm{eln} \right\rangle^{-1} \tag{2.14}$$

Whereat, the plasticity modulus $\bar{K}_\mathrm{p}$ associated to the image stress on the bounding surface is calculated from the consistency condition as in the classical theory of elastoplasticity. However, the consistency condition is related to the bounding surface since the image

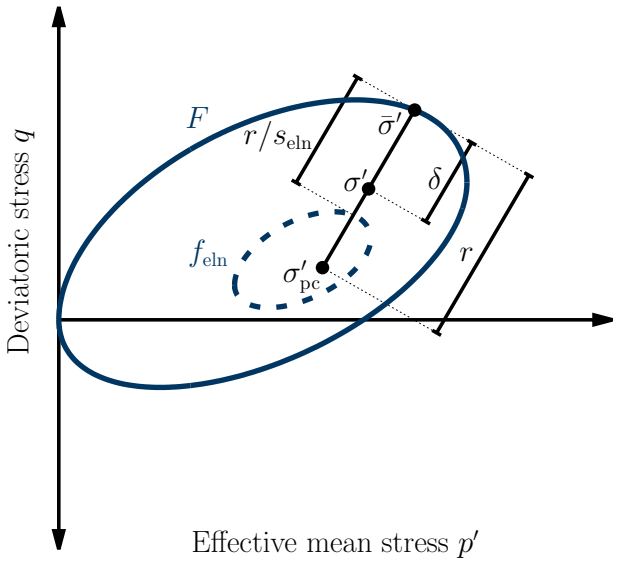

Figure 2.24: Schematic illustration of the radial mapping and the Euclidian distances in the framework of the BSP concept

stress must always remain on the bounding surface even in case of changing stress state and hardening variables. The various versions of BSP models from literature mainly differ in the formulation of the distance and shape hardening functions.
Dafalias (1986a) introduced a distance function 2.14, where all distances according to Figure 2.24 are related to the projection center. Whereat, δ is the Euclidian distance between the current and image stress and r is the distance between the freely moving projection center and the image stress. The distance function leads to infinite values of the plasticity modulus K_p associated to the current stress in case of detecting a stress state within the elastic nucleus, so that $r - s_\mathrm{eln}\,\delta < 0$. After crossing the elastic nucleus the plasticity modulus K_p is calculated dependent on the distance to the bounding surface. Whereas, in case of having a stress state on the bounding surface ($\delta = 0$) the distance function ensures that the plasticity moduli K_p and $\bar{K}_\mathrm{p}$ corresponding to the current and image stress coincide. The model response is then identical to conventional elastoplasticity. That is, the model response becomes most soft and the largest amount of plasticity is induced. To sum up, the value of the plasticity modulus K_p varies between the values of $K_\mathrm{p} = \bar{K}_\mathrm{p}$, when the current stress state is on the bounding surface and $K_\mathrm{p} \to \infty$, when the current stress state is on or inside the elastic nucleus.
As already mentioned, many researchers employed the BSP concept to model the material behavior under cyclic loading. Whereat, the formulations mainly differ in the definition of the plasticity modulus, the shape hardening function and the distance function (see e.g. Mroz et al., 1978; Banerjee and Yousif, 1986; Whittle and Kavvadas, 1993, 1994; Ganendra and Potts, 1995; Pestana and Whittle, 1999; Kavvadas and Amorosi, 2000; Belokas and Kavvadas, 2010; Suebsuk et al., 2011; Jung and Yune, 2011; Park and Kutter, 2016). However, some researchers explicitly incorporated different stress paths dependent plasticity moduli for different loading conditions such as loading, unloading and reloading mainly governed by different distance functions (see e.g. Zienkiewicz et al., 1985; Wathugala and Desai, 1993; Yu et al., 2007b; Rezania et al., 2014). It has to noted that different treatment of the plasticity moduli for loading, unloading and reloading results in a large number of constitutive model parameters to be calibrated.

2.3.4.4 Stiffness degradation

In the BSP framework some concepts for considering stiffness degradation during cyclic loading based on a damage variable were proposed by various researchers as briefly discussed in the following.

- Zienkiewicz et al. (1985) accounted for the progressive stiffness degradation during cyclic loading by introducing a damage variable as an exponent of the distance function. Whereat, the damage variable is defined as an exponential function of the accumulated plastic deviatoric strain increments. The evolution of the damage variable with respect to the accumulated deviatoric plastic strain ensures a progressive reduction of the plasticity modulus during cyclic loading. Hence, the model response becomes softer and more plasticity is induced. Li and Meissner (2002) also applied this approach in a just slightly modified manner to take into consideration the cyclic degradation of stiffness.

- Liang and Ma (1992) incorporated the damage variable as proposed by Zienkiewicz et al. (1985) to their shape hardening function instead of using it as an exponent of the distance function. However, Huang et al. (2011) employed exactly the same concept.

- Yu et al. (2007b) accounted for the stiffness degradation by directly considering the accumulated deviatoric plastic strain in their formulation of the plasticity modulus.

- Hu et al. (2012) proposed a damage-dependent bounding surface model to capture the effects of cyclic shakedown and stiffness degradation depending on the threshold value of the cyclic stress amplitude. Cyclic loading below the threshold value results in a stable cyclic shakedown state. On the contrary, cyclic loading above the threshold value leads to failure due to significant stiffness degradation and large deformations. Therefore, a damage variable was incorporated into the isotropic hardening and softening formulation of the model. That is, the exponential evolution of the damage variable with respect to the accumulation of the deviatoric plastic strain induces an isotropic shrinkage of the bounding surface representing a progressive degradation of stiffness and a reduction of the strength. Another term allows for the evolution of the damage variable for cyclic stress above the threshold cyclic stress only.

- Seidalinov and Taiebat (2014) introduced an evolving damage variable in the shape hardening function to consider the stiffness degradation during cyclic loading with respect to the deviatoric plastic strain increment. The generated plastic deviatoric strain developed during cyclic loading result in an increase of the damage variable and a decrease of the shape hardening function. Hence, plastic straining under cyclic loading causes degradation of plasticity modulus and stiffness resulting in a more soft and more plastic model response.

- Palmieri and Taiebat (2024) enhanced the model of Seidalinov and Taiebat (2014) by proposing an activation mechanism for cyclic stiffness degradation of clays when subjected to cyclic stress ratios exceeding a degradation threshold. A memory state variable defined as the similarity ratio updated at each stress reversal was introduced and serves as a proxy for the applied cyclic stress ratio. Furthermore, a corresponding cyclic stress threshold parameter was incorporated. However, isotropic destructuration according to Taiebat et al. (2010) is used as the degradation mechanism when the degradation threshold is exceeded instead of damage.

2.3.4.5 Updated projection center

When the projection center is allowed to freely translate in the stress space as proposed by Dafalias (1986a) the image stress is always projected with respect to the current loading direction. That is, the image stress after stress reversal is projected onto the opposite bounding surface compared to the image stress before stress reversal. Hence, the plastic loading index becomes positive again because the normal to the bounding surface associated to the new image stress and the direction of the stress increment result in an angle below ninety degree. The concept ensures a very stiff, almost elastic material behavior initially after stress reversal due to the large distance δ from the stress reversal state to the image stress on the opposite bounding surface. According to Equation 2.14, the plasticity modulus K_p becomes infinity. With continued stress path after stress reversal a smooth elastoplastic transition occurs because of the again decreasing distance to the bounding surface.
On the contrary, if the projection center is either fixed to the stress origin (see e.g. Dafalias et al., 1981; Dafalias and Herrmann, 1982; Zienkiewicz et al., 1985; Banerjee and Yousif, 1986; Wathugala and Desai, 1993; Whittle and Kavvadas, 1993, 1994; Crouch and Wolf, 1994a; Crouch et al., 1994b; Pestana and Whittle, 1999; Kavvadas and Amorosi, 2000; Yu et al., 2007b; Belokas and Kavvadas, 2010; Huang et al., 2011; Suebsuk et al., 2011; Rezania et al., 2014; Park and Kutter, 2016), or just moving on the mean stress axis as a certain ratio of the maximum volumetric consolidation stress (see e.g. Dafalias and Herrmann, 1986b; Kaliakin and Dafalias, 1989) or just moving on the anisotropic rotated stress axis as a certain ratio of the maximum anisotropic consolidation stress (see e.g. Anandarajah and Dafalias, 1986; Ling et al., 2002; Liang and Ma, 1992; Jiang et al., 2012) the BSP model shows limitations such as overdamping.
However, there are some more advanced approaches in literature to account for an updated projection center in the BSP framework as briefly described in the following. Among

others, Borja and Amies (1994), Li and Meissner (2002), Jung and Yune (2011) and Hu et al. (2012) also followed the approach of an update of the projection center with respect to the last stress reversal state, but incorporating slightly different distance functions. Seidalinov and Taiebat (2014) also proposed a concept for the update of the projection center with respect to the last stress reversal state but simultaneously conditioning an update of the elastic nucleus as well. Hence, the material behavior immediately after stress reversal is purely elastic because the stress is located within the updated elastic nucleus. Controlled by a distance function the model response becomes elastoplastic whenever the stress path is again crossing the elastic nucleus afterwards. Moreover, the projection center also translates in the stress space with respect to the evolution of the internal hardening variables to ensure the relative position of the projection center within the evolving bounding surface.

2.3.4.6 Further approaches

A detailed evaluation of further approaches of constitutive modeling of cyclic behavior is beyond the scope of this work. Some approaches are mentioned in the following.

- Concept of multi-surface plasticity (see e.g. Mroz, 1967; Prevost, 1978; Mroz et al., 1978; Pietruszczak and Mroz, 1983)
- Concept of subyielding and subloading modeling (see e.g. Hashiguchi and Ueno, 1977a; Hashiguchi, 1980, 1989)
- Concept of kinematic hardening bubble surface (see e.g. Al-Tabbaa and Wood, 1989; Stallebrass and Taylor, 1997; Rouainia and Wood, 2000; Grammatikopoulou et al., 2006)
- Concept of intergranular strain (see e.g. Niemunis and Herle, 1997; Masin, 2005; Fuentes et al., 2017) in the framework of the hypoplasticity concept as proposed by Kolymbas (1991), Gudehus (1996) and von Wolffersrdorf (1996)
- Concept of shear stress reversal technique (see e.g. Yin and Chang, 2009a; Yin et al., 2013)

2.3.5 Summary

The state-of-the-art review on the constitutive modeling of natural clay gave an overview on different concepts used for adequate approximation of the complex mechanical behavior. After a short introduction on critical state models, the focus was set on constitutive

modeling of inherent and stress-induced anisotropy, structure and the stress-induced destructuration and the behavior of natural clays under non-monotonic and cyclic loading. However, viscoplasticity as well as frequency and rate effects were not taken into consideration.

In the literature review it was figured out that inherent and stress-induced anisotropy can be adequately captured by introducing an anisotropic fabric stress tensor whose evolution is controlled by a sophisticated rotational hardening rule as a function of the plastic strain increment. A proper rotational hardening rule has to account for the dependence of the rotation on the induced stress ratio and the current degree of anisotropy. In addition, the rotational hardening rule should be able to limit the excessive rotation at high stress ratios at the critical state and to guarantee the uniqueness of the critical state line. This can be treated by a proper definition of a so-called bounding attractor. If there is fabric anisotropy left when reaching the critical state is still an open and debatable question. Nevertheless, both cases can optionally be considered in sophisticated rotational hardening rules.

Furthermore, it was shown that the current amount of structure and the destructuration process can be adequately taken into consideration by introducing a structure variable and an intrinsic reference surface. Whereat, the structure variable generally relates the size of the yield surface of natural clay to the size of the intrinsic reference surface of the corresponding reconstituted clay having intrinsic properties. The destructuration process associated with a progressive damage of the interparticle bonding can be directly linked to the evolution of the structure variable governed by the evolution of the volumetric and deviatoric plastic strains. Further approaches suggest to consider the influence of structure and destructuration on the critical friction angle as well by introducing another structure variable. Moreover, other researchers follow the concept of a remaining stable structure even after large plastic straining.

Moreover, it was revealed that the BSP concept offers a platform to capture the fundamental aspects of the mechanical behavior of natural clay under non-monotonic or cyclic stress paths. The constitutive modeling of the behavior of natural clay under cyclic loading has to consider a smooth elastoplastic transition especially after stress reversal as well as the gradual stiffness degradation and accumulation of plastic strain. Furthermore, for cycling loading under undrained conditions the generation of excess pore-water pressure and the associated migration of the effective stress path towards the stress origin have to be treated properly. The BSP concept is suitable by introducing appropriate formulations for the radial projection rule, distance function and shape hardening function relating the plasticity modulus associated to the current and image stress. Moreover, the incorporation

of elastic nucleus, damage variable and moving projection center with respect to the last stress reversal state and evolving internal hardening variables is required.
An adequate hierarchical constitutive soil model is fundamental to accurately approximate the complex and highly non-linear mechanical behavior of natural clay. As presented in the former sections there exist various sophisticated constitutive models for natural clay. Based on the conclusions from the literature review an adequate hierarchical constitutive soil model in the frameworks of the critical state soil mechanics and the bounding surface plasticity (BSP) with respect to the Saniclay model family is modified and employed within the present study (Dafalias et al., 2006; Taiebat et al., 2010; Seidalinov and Taiebat, 2014; Dafalias and Taiebat, 2013, 2014; Barciaga et al., 2017). The hierarchical structure and the formulation of the adequate constitutive BSP model for natural clay are presented and intensively discussed in the next chapter 3.

2.4 Numerical modeling of mechanized tunneling

The numerical analysis of real case mechanized tunneling projects became a popular method in geotechnical engineering due to the complex boundary conditions of the problem (see e.g. Finno and Clough, 1985; Addenbrooke et al., 1997; Komiya et al., 1999; Vermeer et al., 2003; Bakker, 2003; Xu et al., 2003; Kasper and Meschke, 2006b; Wongsaroj et al., 2007; Möller and Vermeer, 2008; Dang and Meguid, 2008; Grammatikopoulou et al., 2008a; Lambrughi et al., 2012; Gonzalez et al., 2012; Wongsaroj et al., 2013; Dias and Kastner, 2013; Do et al., 2014; Zhao et al., 2015a; Fargnoli et al., 2015; Avgerinos et al., 2016; Bian et al., 2016; Vu et al., 2017; Ieronymaki et al., 2017).
Numerical simulations provide a helpful tool for gaining deep understanding of the mechanical and hydraulic processes in the soil domain induced by mechanized tunneling. Moreover, numerical tunnel simulations allow to analyze elastoplastic ground movements, stress redistribution and generation of excess pore-water pressure and corresponding evolution of effective stress. In brief, due to adequate numerical simulations of the construction processes involved in mechanized tunneling and modeling of the elastoplastic soil behavior the numerical approach is more beneficial and powerful compared to the empirical and analytical approaches, which are limited to more simplifications and constraints. Moreover, the system geometry and the mechanical and hydraulic boundary conditions can be clearly defined and easily varied in a numerical parameter study which is not possible for the empirical solutions. Hence, the numerical modeling approach is convenient to obtain reliable predictions of the physical reality of mechanized tunneling.

The basis of the numerical modeling approach is the development of an adequate numerical simulation model in a state-of-the-art model code. This research is focusing on the numerical modeling of mechanized tunneling employing the finite element method (FEM) as the most relevant numerical method for tunneling applications. The advanced simulation model has to consider the most decisive complex interactions of the manifold components (e.g. ground, tunnel boring machine, lining, support media and environment) and construction processes (subsystems) involved in mechanized tunneling.
This section deals with the introduction of mechanized tunneling in natural clay deposits using shield machines with earth pressure balance support (EPB shield machine). Moreover, shield tunneling induced settlements are discussed. The main focus is set on a literature review on techniques for numerical modeling of subsystems and processes involved in mechanized tunneling. The section closes with an overview of numerical simulations of mechanized tunneling conducted in previous studies and the corresponding constitutive models.

2.4.1 Mechanized tunneling with EPB shield machine

The current study is focusing on mechanized tunneling in natural clay deposits. In particular the construction of shallow tunnels in urban areas is investigated. According to the recommendation by DAUB (2010), shield machines are mainly utilized in soft ground conditions. Moreover, especially for natural clay deposits and fine-grained soils shield machines with earth pressure balance support (EPB shield machine) are preferentially used rather than machines with hydraulic support using slurry suspension (hydro-shield machine), which are more appropriate for sandy and gravely ground conditions. The EPB shield machine directly uses excavated material as support medium at the tunnel face, whereas the hydro-shield machine uses bentonite slurry. The generated earth pressure has to balance active earth pressure and water pressure acting at the tunnel face.
The EPB shield application demands for fine-grained soil with high clay and silt content and low hydraulic conductivity to guarantee the requested support pressure and to avoid water inflow into the excavation chamber. The typical range of application of EPB shield tunneling (with optional water, polymer, foam conditioning) with respect to the grain size distribution of the soil deposit is given in Figure 2.25 modified after Galli (2016). The range is divided into four groups with respect to the conditioning: (1) Water for the required consistency + foam for stickiness, (2) Foam, (3) Foam + Polymers, water pressure $<$ 2 bar, (4) Foam + Polymers + Slurries of fines, no water pressure.

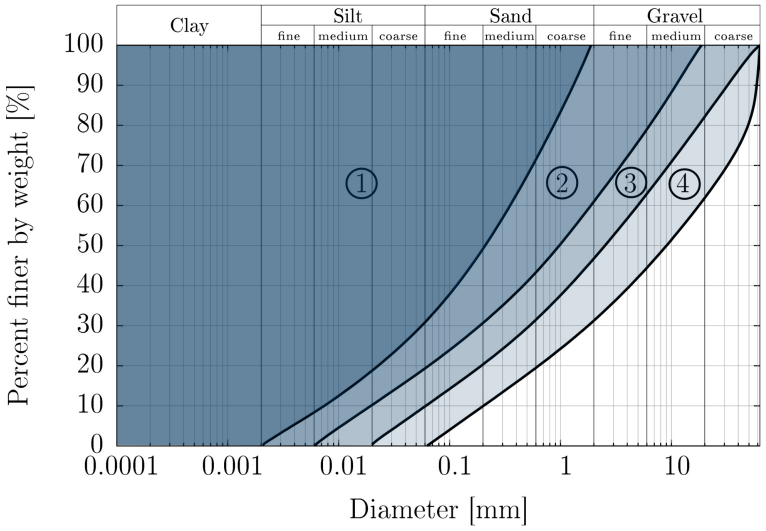

Figure 2.25: Typical range of application of EPB shield tunneling (with optional water, polymer, foam conditioning) with respect to the grain size distribution of the soil deposit modified after Galli (2016); (1) Water for the required consistency + foam for stickiness, (2) Foam, (3) Foam + Polymers, water pressure $<$ 2 bar, (4) Foam + Polymers + Slurries of fines, no water pressure

According to Table 2.2 the clay content of natural clays from the sites in Bothkennar, Murro, Onsøy and Pisa is larger than the required value of 30 %. Consequently, mechanized tunneling with EPB shield machine is considered for the analysis of the tunnel excavation in natural clay deposits in the current study.
The general setup of the EPB shield machine which is visualized in Figure 2.26 consists of the following components: (1) Cutting wheel assembled with cutting tools, (2) Excavation chamber, (3) Bulkhead, (4) Screw conveyor, (5) Thrust jacks, (6) Shield, (7) Annular gap, (8) Lining segment erector, (9) Installed lining.
The mode of operation of the EPB shield machine is composed of a phase of excavation and a subsequent phase of ring building. In the phase of excavation the adjacent soil is removed by the rotating cutting wheel which is assembled with cutting tools such as cutting knives and disc cutters. The excavated soil enters the excavation chamber through openings and is mixed to a plastic earth muck of required consistency. The plastic soil paste in the excavation chamber generates the tunnel face support pressure. During the excavation process the machine head is pushed forward toward the adjacent soil by the thrust jacks and the machine continuously advances. The bulkhead transfers the pressure of the thrust jacks to the soil paste in the excavation chamber. Accordingly, the tunnel face support pressure can be adjusted by the advance rate. The spoil is extracted from the

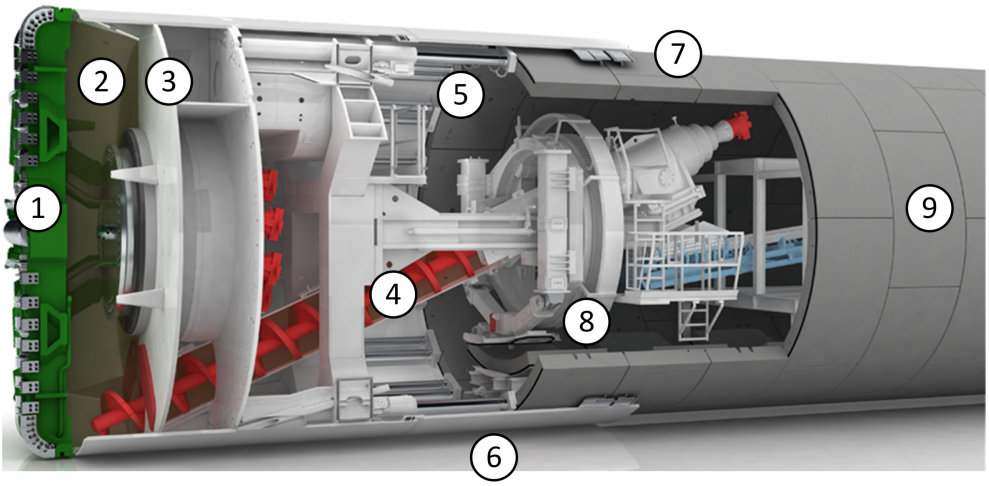

Figure 2.26: Longitudinal section of an EPB shield machine modified after Herrenknecht AG (2018); (1) Cutting wheel assembled with cutting tools, (2) Excavation chamber, (3) Bulkhead, (4) Screw conveyor, (5) Thrust jacks, (6) Shield, (7) Annular gap, (8) Lining segment erector, (9) Installed lining

excavation chamber by a screw conveyor. Whereat, the velocity of the rotation controls the quantity of the extracted material and hence the support pressure can be adjusted. The required face support pressure can be calculated according to the recommendation by DAUB (2016) assuming a certain failure mechanism at the tunnel face such as sliding wedge and prism. The equilibrium of the pressure inside the chamber and the acting pressure at the tunnel face is monitored by earth pressure sensors. In case of maintenance the excavation chamber is often air-pressurized whereat the bulkhead separates the areas of different pressure.

After the phase of excavation the ring building is conducted. The thrust jack forces are released within this phase. The prefabricated lining segments often made of reinforced concrete are positioned by use of a vacuum erector and installed under the protection of the shield of the machine made of steel. Whereat, the outer diameter of the lining ring is smaller than the inner diameter of the shield tail. Hence, due to the lining installation inside the shield an annular gap of 5-20 cm thickness between the lining segments and the adjacent soil develops at the tail when the machine advances. The tail void is continuously backfilled with grouting material during the phase of excavation with respect to the sequential advance of the machine. The sealing to the inner of the machine is ensured by use of steel brushes. Moreover, the shield has a conical shape to better control the steering and advance of the machine. For the same reason, the diameter of the cutting

wheel is slightly larger than the outer diameter of the shield causing overcutting at the tunnel face. Consequently, due to the conicity of the shield and the overcutting an annular steering gap between the shield and adjacent soil develops.

2.4.2 Shield tunneling induced settlements

Surface settlements induced by mechanized tunneling using a shield machine may occur due to various reasons. The surface settlements are strongly dependent on in situ soil conditions (material properties such as stiffness and strength, structure, inhomogeneity), stress conditions (anisotropy, K_0, OCR/YSR), hydraulic conditions, geometrical conditions (tunnel diameter, overburden depth), soil-structure interactions in the nearfield of the tunnel (soil vs. shield and soil vs. lining), boundary conditions from existing surface and subsurface structures (magnitude, direction and eccentricity of the loading, soil-structure interaction) and employed tunneling method and support techniques. A schematic illustration of the settlements induced by mechanized tunneling is given in Figure 2.27 modified after Mair and Taylor (1997) and Möller (2006).

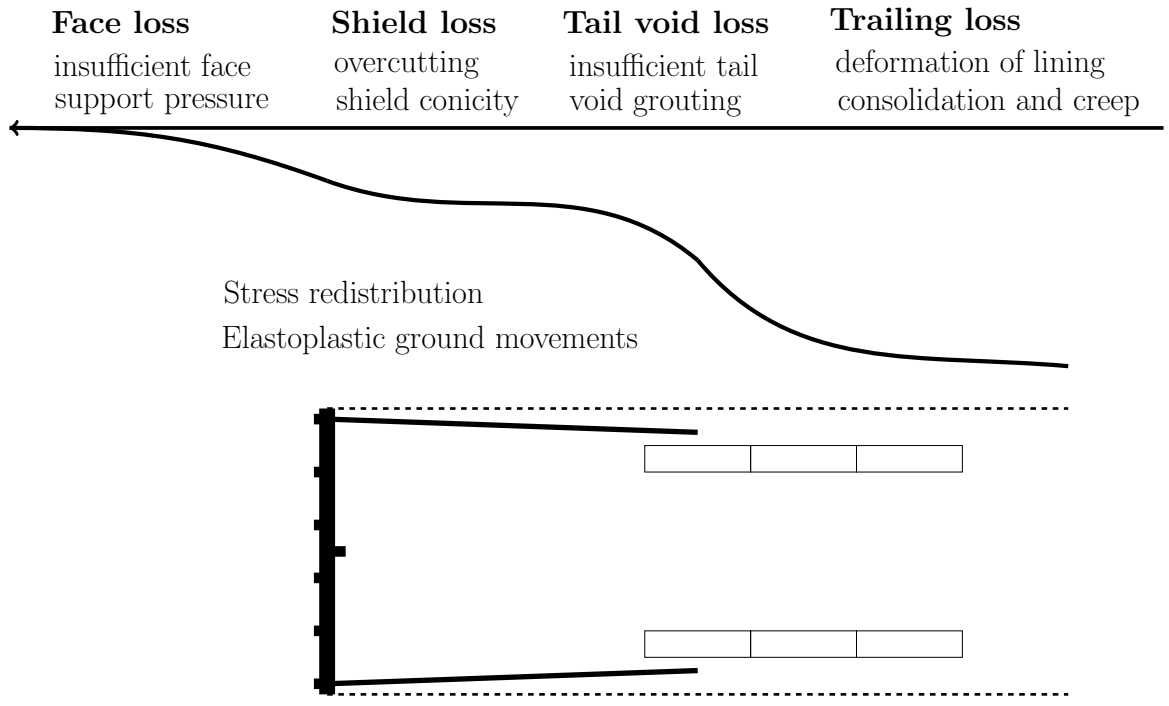

Figure 2.27: Schematic illustration of the settlements induced by mechanized tunneling modified after Mair and Taylor (1997) and Möller (2006)

- Face loss: The earth pressure of the excavated and pressurized soil paste in the excavation chamber always has to be in an equilibrium with active earth pressure and water pressure acting on the tunnel face. Stress conditions out of balance will yield in further ground movements. Too small tunnel face support pressure will result in uncontrolled inflow of soil into the excavation chamber and a corresponding deformation mechanism composed of a sliding wedge and a prism (chimney) on top will develop (Horn, 1961). Dependent on the overburden depth the mechanism will form up to the ground surface. Too large tunnel face support pressure will push the adjacent soil upwards.
- Shield loss: The annular steering gap between shield and adjacent soil due to overcutting and conicity of the shield induces radial deformation toward the shield. The stress release due to soil excavation induces upward ground movements and elastic deformation at the tunnel invert.
- Tail void loss: The mechanized tunneling technique and the mode of operation as described above enforce an annular gap at the shield tail between the lining segments and the adjacent soil. To avoid large ground movements in the nearfield around the machine it is needed to continuously backfill the tail void with injected grout. Accordingly, an insufficient adjustment of the required grouting pressure leads to further radial ground movement into the tail void.
- Trailing loss: Deformation of the lining due to compressibility may cause further downward ground movements. However, the material behavior of prefabricated reinforced concrete lining is usually very stiff and just small deformations occur. Besides, the unit weight of the lining may induce soil deformation during the ring built, when comparing to the unit weight of the excavated soil. For mechanized tunneling in water-saturated soil uplift effects may occur dependent on the overburden depth. Moreover, long-term settlements might be induced due to consolidation and creep processes during tunneling in water-saturated natural clay deposits.

The EPB shield tunneling induced deformations in the nearfield around the tunnel cause a certain stress redistribution around the machine which is propagated through the entire overlaying soil domain up to the ground surface. The associated elastoplastic deformations result in a settlement profile at the ground surface. Mair and Taylor (1997) summarized several studies on the prediction of ground movements induced by mechanized tunneling based on empirical methods, closed form analytical solutions, finite element analysis and physical modeling.

Various researchers empirically determined the allowable differential settlements, deflection ratios (sagging or hogging zones) and horizontal tensile strain of structures to avoid damage and ensure the serviceability of the structure (see e.g. Skempton and MacDonald, 1956; Bjerrum, 1963b; Burland and Wroth, 1974, 1995; Rankin, 1988; Potts and Addenbrooke, 1997; Franzius et al., 2004; Zhao et al., 2019b). The mechanized tunneling induced settlements were empirically analyzed and several empirical methods for the prediction of maximum surface settlements and the shape of the transverse and longitudinal settlement trough were developed (see e.g. Peck, 1969; Attewell and Farmer, 1974, 1975; O'Reilly and New, 1982; Mair et al., 1993; Fillibeck, 2012). Among other aspects, the shape of the settlement trough is given by the position of the inflection point defining the sagging and hogging zones. The most prominent methods which are common practice are modified from the Gaussian distribution of the transverse settlement trough as introduced by Peck (1969). He incorporated the maximum settlements and the position of the inflection point with respect to the tunnel centerline only. To estimate the longitudinal settlement trough the cumulative probability curve of the Gaussian error function is often used. A schematic view of the transverse settlement trough induced by mechanized tunneling can be seen in Figure 2.28. The drawbacks of most of the empirical methods are that the prediction of the settlements is strongly governed by the initial guess of the tunnel volume loss V_t which is based on experience and that the elastoplastic volume change V_g of the soil domain is not considered for the estimation of the surface volume loss V_s.

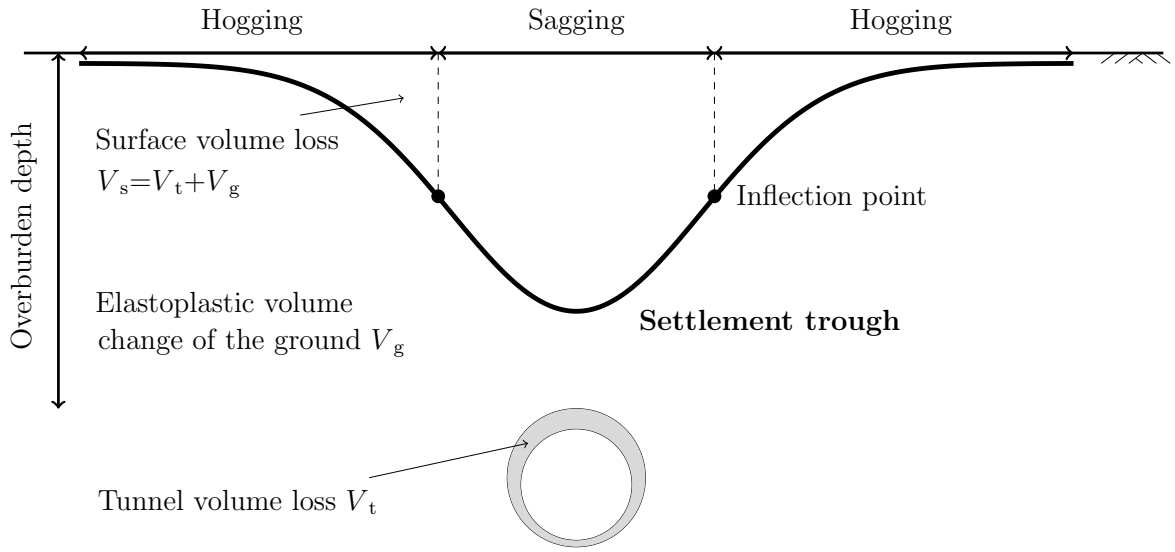

Figure 2.28: Schematic illustration of the transverse settlement trough and the volume loss induced by mechanized tunneling modified after Möller (2006)

Hence, the settlement behavior was also numerically investigated by various researchers (see e.g. Mair et al., 1982; Finno and Clough, 1985; Lee and Rowe, 1990a,b; Addenbrooke et al., 1997; Potts and Addenbrooke, 1997; Komiya et al., 1999; Vermeer et al., 2003; Kasper and Meschke, 2004; Franzius et al., 2004; Kasper and Meschke, 2006a,b; Wongsaroj et al., 2007; Möller and Vermeer, 2008; Nagel and Meschke, 2011; Fillibeck, 2012; Lambrughi et al., 2012; Wongsaroj et al., 2013; Dias and Kastner, 2013; Do et al., 2014; Zhao et al., 2015a; Fargnoli et al., 2015; Ieronymaki et al., 2017; Do and Dias, 2017; Kavvadas et al., 2017; Zhao et al., 2019a,b). The numerical analyses of the settlement behavior accounting for the elastoplastic soil behavior as well as the complex boundary conditions of mechanized tunneling discovered significant deviations from the Gaussian settlement profiles. It was found that beside the soil properties such as stiffness and strength, overconsolidation ratio and associated coefficient of earth pressure at rest have significant influence on the settlement profile. The larger the values of OCR and K_0, the smaller the maximum vertical surface settlements and the wider the settlement trough (see e.g. Zhao et al., 2019a). Regarding the settlement profile it has to be distinguished between mechanized tunneling excavation of shallow and deep tunnels. The influence of the overburden depth on the tunneling induced settlements was investigated in several studies (see e.g. Kasper and Meschke, 2006b; Schanz et al., 2012; Wongsaroj et al., 2013).

2.4.3 Numerical modeling of subsystems

There are many construction processes and so-called subsystems involved in mechanized tunneling such as shield machine and lining, tunnel face support, tail void grouting, volume loss, lining installation, soil-structure interaction, sequential advance, machine steering and jack thrust forces. An overview of the subsystems involved in mechanized tunneling and its consequences on the system behavior can be found in Schanz et al. (2012).
The complexity of the numerical simulation model for mechanized tunneling should be as simple as possible to limit the computational costs and the uncertainty but not simpler to still adequately simulate the physical reality and obtain realistic and reliable predictions of the system behavior induced by mechanized tunneling. Further recommendations on the appropriate development of numerical models for geotechnical applications can be found in the EANG recommendations by DGGT (2014) (e.g. dimension of the mesh, displacement boundary conditions).

However, since the present study is focusing on the investigation of the influence of the soil mechanical properties of natural clay on the system behavior induced by mechanized tunneling a most complex and most detailed modeling of the subprocesses involved in mechanized tunneling is not intended. Hence, just the most decisive subsystems are intensively reviewed in the following.

2.4.3.1 3D tunnel simulation model

A sophisticated 3D tunnel simulation model is needed to adequately predict the physical reality because mechanized tunneling represents a three-dimensional engineering problem. In the 3D simulation model the soil domain is discretized into and represented by a multitude of soil volume elements. The advantages of a 3D model compared to a 2D plain strain model are listed below.

- The entire time- and space-dependent sequential advance can be simulated in a unique 3D model, while a 2D model is restricted to a particular cross section in the space at a given time. That is, using a 3D model allows to simultaneously analyze longitudinal and transverse directions. This enables to evaluate the development of the longitudinal settlement profile with respect to the sequential advance. Whereas, numerous cross sections are needed in a 2D model.
- Utilizing a 3D model offers the possibility to consider the influence of the tunnel face support on the system behavior. On the contrary, a 2D model using a particular cross section can not account for effects of the face support. However, the face stability can be analyzed in a 2D model but using a different particular longitudinal section.
- Spatial soil mechanical effects such as spatial earth pressure considering additional shear stresses acting in the flanks and combined spatial arching effects in longitudinal and transverse directions around the shield and at the tunnel face can be taken into account in a 3D model.
- Spatial mechanical and hydraulic processes in the nearfield of the shield machine and the tunnel such as hydraulic flow and infiltration of support media can be captured.
- Geometrical aspects with respect to the direction of the tunnel advance such as non-homogeneous and layered ground profiles, aboveground edifices or geotechnical structures such as damns and dikes which are spatially bounded in the longitudinal direction and inclined tunnels with varying overburden depth can be considered in a unique 3D model.

- Steering processes of the machine following curved tunnel tracks and sophisticated tunnel advance processes such as jack thrust forces acting on the lining segments can be simulated in a 3D model.
- Further processes such as the grouting of the annular gap, the tunneling induced volume loss, the installation of the lining and the soil-structure interaction can be captured in both the 2D and the 3D model.

To sum up, a 3D model is more suitable to adequately simulate the multiaxial stress distribution and the corresponding strain behavior resulting from the various construction processes involved in mechanized tunneling and its complex interaction at the expense of higher efforts in model development and calculation time. The influence of 2D modeling versus 3D modeling on the model response in mechanized tunneling was compared by various researchers (see e.g. Franzius et al., 2005; Möller and Vermeer, 2008; Dias and Kastner, 2013; Zhao et al., 2015a; Do and Dias, 2017; Zhao et al., 2017).

2.4.3.2 Tunnel face support

During the entire phases of excavation and ring build the acting resulting forces (from earth pressure and water pressure) and the resulting support force have to be in equilibrium state. In case of EPB shield tunneling the required support pressure is provided by the earth pressure of the pressurized soil paste in the excavation chamber which is generated and mobilized by the jack thrust forces pushing the bulkhead. For the design of the face support pressure with respect to the face stability, magnitude and direction of the acting forces especially of the earth pressure have to be approximated based on adequate theories and models (analytical, empirical, experimental or numerical solutions). There exist plenty of literature on the various design methods for the face stability and the corresponding required face support pressures.
The analytical methods which are usually based on different approaches of failure mechanism and equilibrium of forces are widely used for the assessment of the face stability (see e.g. Horn, 1961; Davis et al., 1980; Leca and Dormieux, 1990; Chambon and Corte, 1994; Anagnostou and Kovari, 1994, 1996; Broere, 2001; Li et al., 2009; Mollon et al., 2010; Perazzelli et al., 2014; Vu et al., 2015). The most common mechanism is the sliding wedge with a prism on top as originally introduced by Horn (1961). Many variations of this mechanism are elaborated with modified geometries, varying complexity of the considered acting stresses and forces (reduced vertical stress due to arching and silo effects, shear forces acting in the flanks of the wedge, interaction forces between the rigid soil bodies,

hydrostatic water pressure, seepage flow forces) and different theories for the kinematics of the mechanism. The mechanism in clay deposits is usually wider than in more coarse grained soil.

The required value of the resulting face support force S_{ci} for a circular tunnel face acting at the tunnel axis is given by Equation 2.15. Whereat, $E_{\mathrm{max,ci}}$ is the maximum resulting support force due to effective earth pressure obtained from the chosen analytical solution and W_{ci} is the resulting support force due to hydrostatic water pressure. Moreover, $\eta_{\mathrm{E}} = 1.50$ and $\eta_{\mathrm{W}} = 1.05$ are the safety factors for the earth pressure and the water pressure, respectively. The resulting support force due to earth pressure can be calculated according to the recommendation by DAUB (2016) related to the German recommendations ZTV-ING by BAST (2012) assuming a certain failure mechanism at the tunnel face such as sliding wedge and prism after Horn (1961) and Anagnostou and Kovari (1996).

Generally, the resulting support force due to effective earth pressure (composed of self weight of the sliding wedge, vertical force on the wedge including surface load, friction force on the triangular vertical plane of the sliding wedge) is a function of the soil properties in front of the tunnel face (internal friction angle, cohesion, unit weight and lateral earth pressure coefficient) and the geometrical parameters such as diameter of the excavated area and overburden depth. Thereby, the sliding angle is varied in a way that the resulting support force due to effective earth pressure becomes maximal. For larger overburden depth silo effects have to be considered for the calculation of the effective stresses.

The resulting support force due to hydrostatic water pressure is a function of the unit weight of water, groundwater level above the tunnel axis and diameter of the excavated area. The corresponding values of the face pressure at the tunnel invert $s_{\mathrm{face,invert}}$ and the tunnel crown $s_{\mathrm{face,crown}}$ can be derived from Equation 2.16 with respect to the tunnel area A_{f}, the tunnel diameter D_{f} and the unit weight of the support medium γ_{s}. Hence, a linear distribution of the face support pressure over the height of the tunnel face is assumed which is an idealization of the reality due to inhomogeneity of the soil paste.

$$S_{\mathrm{ci}} = \eta_{\mathrm{E}}\, E_{\mathrm{max,ci}} + \eta_{\mathrm{W}}\, W_{\mathrm{ci}} \tag{2.15}$$

$$s_{\mathrm{face,invert/crown}} = \frac{S_{\mathrm{ci}}}{A_{\mathrm{f}}} \pm \gamma_{\mathrm{s}}\, D_{\mathrm{f}}/2 \tag{2.16}$$

Moreover, an upper limit of the face support pressure is defined to avoid a break up of the overburden. A blow out of the support medium can be excluded due to the choice of an earth pressure balance shield. According to DAUB (2016), the maximal support pressure has to be smaller than 90% of the total vertical stress at the tunnel crown.

Furthermore, the tunnel face stability was numerically investigated by several researchers (see e.g. Broere, 2001; Vermeer et al., 2002, 2003; Kirsch, 2009; Li et al., 2009; Lambrughi et al., 2012). The studies resulted in design charts for the minimum required face pressure with respect to soil type (unit weight, shear strength), geometrical boundary conditions (overburden depth and tunnel diameter and its ratio), hydraulic conditions (water pressure, water flow forces, drainage conditions) and eventual surface loading. Moreover, they figured out that the face stability is strongly governed by the shear strength of the adjacent soil, development of arching effects and drainage conditions. The larger the shear strength the smaller the required face support pressure. If the soil manifests a certain shear strength the face stability is independent of the overburden depth. A certain amount of cohesion may even allow for open face tunneling without face support. The overburden depth generally influences the shape of the failure mechanism and its spatial propagation in the ground domain even up to the ground surface.
In most of the numerical models the face support pressure boundary is applied as distributed surface load (total pressure) mechanically acting on the adjacent soil elements at the tunnel face (see e.g. Schanz et al., 2012; Lambrughi et al., 2012; Do et al., 2014; Zhao et al., 2015a; Fargnoli et al., 2015; Lavasan et al., 2017a; Do and Dias, 2017; Kavvadas et al., 2017). Whereat, the mechanical load linearly increases with depth from crown to invert with respect to the unit weight of the support medium.

2.4.3.3 Tail void grouting

To avoid large radial ground movements due to the annular gap between the installed lining and the adjacent soil the tail void has to be continuously filled with grouting material. The grouting material such as cement mortar is injected in a pressurized liquid condition to support the annular gap and to compensate ground movements. The support pressure at each position of the annular gap should be larger than the sum of the effective radial stress of the adjacent soil and the water pressure. Too large grouting pressure will induce local radial outwards displacements in the soil domain around the tunnel. The grouting material will harden and consolidate by time afterwards showing an increase of stiffness and a decrease of hydraulic conductivity. Measurements of the grout pressures during mechanized tunneling and the analysis of the consolidation of the grout material can exemplarily be found in Bezuijen et al. (2004) and Talmon and Bezuijen (2009).
The influence of tail void grouting on the ground surface settlements and the lining was numerically studied by various researchers (see e.g. Kasper and Meschke, 2004, 2006a,b; Nagel and Meschke, 2011; Schanz et al., 2012; Do et al., 2014; Lavasan et al., 2017a;

Kavvadas et al., 2017). They stated that the numerical method to simulate the tail void grouting and the hydro-mechanical interactions can significantly affect the surface settlements and the structural forces and deformations of the lining. There exist several methods to numerically account for the tail void grouting in tunnel simulations. Two of the methods are introduced in the following. Lavasan et al. (2017a) provided a comparison of both methods to simulate the annular gap grouting.

- The grouting pressure can be considered by the application of a distributed mechanical surface load (total pressure) directly acting on the adjacent soil elements at the tail void (see e.g. Komiya et al., 1999; Schanz et al., 2012; Do et al., 2014; Zhao et al., 2015a; Fargnoli et al., 2015; Lavasan et al., 2017a). The surface load is applied over the length of one or two excavation steps in the sections directly behind the shell elements which represent the shield. For the subsequent lining rings the grout is assumed to be hardened and no grouting pressure is acting. Similar to the face support pressure, the mechanical surface load linearly increases with depth from tunnel crown to tunnel invert with respect to the unit weight of the support medium. The surface load specifying the grouting pressure is just acting on the soil volume elements and not in the opposite direction on the deactivated lining elements. Consequently, this approach is limited with respect to the realistic prediction of the lining behavior.
- Another approach to consider the tail void grouting is to explicitly introduce a thin layer (5-20 cm) of volume elements around the lining behind the shield representing the tail void filled with grouting material. Some approaches even explicitly considered the conical steering gap around the shield as filled with grouting material represented by a thin layer of volume elements or with gap interface elements. A constitutive model describing the mechanical behavior of the grouting material and in particular even including the time-dependent evolution of the stiffness and hydraulic conductivity can be employed (see e.g. Kasper and Meschke, 2004, 2006a,b; Nagel and Meschke, 2011; Lambrughi et al., 2012; Dias and Kastner, 2013; Do et al., 2014; Lavasan et al., 2017a; Lavasan and Schanz, 2017b; Kavvadas et al., 2017). Whereat, the grouting pressure in the thin layer is applied as predefined hydrostatic total pore-water pressure. Accordingly, the grouting pressure will be isotropically transferred to the adjacent soil volume elements and the shell or volume elements representing the lining. For the subsequent lining rings the grout is assumed to be hardened and consolidated and the grouting pressure continuously decreases.

Beyond that, Lavasan et al. (2017a) investigated the development of a so-called filter cake by infiltration of fine grouting particles into the pore space of the adjacent soil under a certain grouting pressure and Nagel and Meschke (2011) numerically considered the viscous flow of the liquid grouting material in the annular gap around the shield. The effects of infiltration processes affecting the consolidation behavior and viscous flow will be neglected in the current study.

2.4.3.4 Volume loss

Mechanized tunneling induces a certain tunnel volume loss V_t in the nearfield around the tunnel. The corresponding stress redistribution in the entire overlaying ground domain causes an elastoplastic soil volume change V_g. Hence, the resulting surface volume loss V_s is the sum of $V_t + V_g$. In this study the surface volume loss V_s is defined as the volume of the settlement trough and the tunnel volume loss V_t as the difference of the excavated volume and the final tunnel volume specified by the outer diameter of the lining ring. The tunnel volume loss ratio is given as the tunnel volume loss divided by the excavated volume. Due to optimized techniques the mechanized tunneling induced tunnel volume loss ratio nowadays varies within 0.5-2% (see e.g. Möller and Vermeer, 2008). A schematic view of the volume loss induced by mechanized tunneling is displayed in Figure 2.28.
The influence of the tunnel volume loss in the nearfield of the tunnel on the surface volume loss was numerically examined by various researchers (see e.g. Vermeer et al., 2003; Möller, 2006; Möller and Vermeer, 2008; Dang and Meguid, 2008; Wongsaroj et al., 2013; Zhao et al., 2015b; Do and Dias, 2017; Kavvadas et al., 2017). Generally it can be stated that the larger the tunnel volume loss the larger the maximum surface settlements and the wider the transverse settlement trough.
The tunnel volume loss is numerically considered by applying extra stress or strain boundary conditions around the tunnel. A detailed overview on various approaches such as core support method (α-method), lining reduction method (δ-method), stress reduction method (β-method) combined with the volume loss control method according to Addenbrooke et al. (1997), gap method as introduced by Rowe et al. (1983), or non-uniform gap closure employed by Cattoni et al. (2016) can be found in the works by Möller (2006); Möller and Vermeer (2008); Lavasan and Schanz (2017b). The most relevant methods of considering tunnel volume loss for 3D tunnel models such as the grout pressure method by Möller and Vermeer (2008) and the contraction method by Brinkgreve et al. (2016) are described in the following.

- Möller and Vermeer (2008) proposed the grout pressure method which combines parts of the stress reduction method and the gap method. The lining is surrounded by a thin layer of grouting material considered as a gap where a certain grouting pressure is acting. In the study of Möller and Vermeer (2008) the gap due to overcutting, shield conicity and tail void is represented by a prescribed grouting pressure. The grouting pressure may increase from the tunnel face toward the tail of the shield machine. As stated by Möller and Vermeer (2008) and Kavvadas et al. (2017) this method allows for realistic simulation of vertical and horizontal soil displacements and lining behavior (structural forces/moments and deformation).
- The contraction method accounts for the volume loss by a certain contraction of the tunnel (Brinkgreve et al., 2016). The method is originally composed of two computational phases. In a first phase the tunnel core material is removed and the lining is installed which causes surface settlements and generate lining forces/moments and deformations due to the stress release and the stress redistribution. In a subsequent phase, a certain uniform and radial contraction toward the center of the tunnel is applied to the elements representing the shield (annular steering gap due to overcutting and conicity of the shield leads to volume loss) and the lining (annular gap due to tail void leads to volume loss). The contraction is generated by applying a strain boundary to the elements defined as volumetric strain which does not result from an additional force. However, this strain is added to the strain caused by the stress redistribution during the tunnel excavation. The disadvantage of this method are the possibly non-realistic manually predefined uniform radial deformations around the tunnel. Hence, the pressure model along the shield machine leads to more realistic results especially when evaluating the influence of mechanized tunneling on the lining. However, the contraction method was used in various numerical studies (see e.g. Bakker, 2003; Zhao et al., 2015a,b; Fargnoli et al., 2015).

2.4.3.5 Soil-structure interaction

The soil-structure interaction during mechanized tunneling can be divided into different groups with respect to the spatial position. There are interactions between soil and shield machine (steel structure) and between soil and lining (reinforced concrete structure) in the nearfield around the tunnel. The soil-structure interaction will cause shearing of the soil due to frictional forces. Both interactions will predominantly influence the corresponding structural forces/moments and deformations, but also the surface settlements due to stress redistribution in the soil domain.

The influence of the soil-structure interaction on the model response caused by mechanized tunneling was studied by e.g. Kasper and Meschke (2004); Nagel and Meschke (2011); Schanz et al. (2012); Kämper et al. (2016); Zhao et al. (2017). The smaller the shear strength of the interface with respect to the shear strength of the adjacent soil the larger the relative ground movements around the tunnel and the larger the surface settlements. The influence of the interface properties decreases with increasing overburden depth.
The soil-structure interaction is numerically captured by interface or contact modeling between soil and adjacent structure. In this study, so-called interface elements are used as described by van Langen and Vermeer (1991) and Brinkgreve et al. (2016). The interface elements manifest pairs of nodes instead of single nodes, whereat the distance between the nodes of each node pair is zero. The node pairs are compatible with the nodes of volume and shell elements. Hence, the concept of interface elements allows for relative/differential displacements between two volume elements (soil vs. soil or soil vs. lining) or one volume element and one shell element (soil vs. steel structure). At the end of an interface element the node pair is degenerated to a single node to ensure the connection between both adjacent elements. The relative/differential displacements between the node pair can occur due to slipping (this is, relative movement parallel to the interface governed by shear stress and interface shear stiffness) and gapping (this is, relative movement perpendicular to the interface governed by normal stress and interface normal stiffness). Whereat, the material properties of an interface element such as stiffness and shear strength can be manually defined by assigning an own constitutive soil model. Consequently, the soil-structure interaction can be controlled by applying a certain reduction of the interface properties (stiffness and shear strength parameters) with respect to the properties of the adjacent soil to induce a weaker and more flexible interface behavior.

2.4.3.6 Machine steering and jack thrust forces

The most accurate simulation of the shield machine advance and steering is not considered in the present study. For more information, it is referred to Komiya et al. (1999), who employed the numerical technique of remeshing of the soil domain at each time step, utilizing so-called excavating elements representing the disturbed area at the tunnel face and applying external jack thrust forces between the shield machine and the lining. Further researchers explicitly modeled the hydraulic jacks by truss elements connected to the lining segments and the bulkhead of the machine (see e.g. Kasper and Meschke, 2004, 2006a,b; Nagel and Meschke, 2011; Alsahly et al., 2016).

2.4.4 Constitutive modeling

The well-considered choice of a proper constitutive model is a key issue for the realistic and reliable prediction of the system behavior induced by mechanized tunneling because it strongly governs the simulated stress-strain behavior of the soil and hence impacts the model responses such as surface settlements. The constitutive behavior of natural clay has to be simulated by employing an adequate constitutive model incorporating the relevant material properties such as inherent and stress-induced anisotropy, structure and destructuration and the behavior under cyclic loading such as stiffness degradation and accumulation of plastic strain. The constitutive behavior can be considered applying the theories as described in section 2.3. Several FE analyses of mechanized tunneling processes in fine-grained soil were conducted by employing less complex elastoplastic models such as:

- The Modified Cam-Clay model with isotropic hardening employed by e.g. Mair et al. (1982); Finno and Clough (1985); Lambrughi et al. (2012); Cattoni et al. (2016)
- The hierarchical model family of isotropic/anisotropic and linear/nonlinear elastic perfect plastic models by Jardine et al. (1986) and Franzius et al. (2005) employed by e.g. Addenbrooke et al. (1997); Franzius et al. (2005)
- The hierarchical model family of the Mohr-Coulomb model including the hardening soil model by Schanz (1998) and Schanz et al. (1999) with stress path and stress state dependent stiffness and the hardening soil model with consideration of small-strain stiffness by Benz (2006) and Benz et al. (2009) employed by e.g. Möller and Vermeer (2008); Lambrughi et al. (2012); Dias and Kastner (2013); Zhao et al. (2015a); Fargnoli et al. (2015); Ieronymaki et al. (2017)
- The Sekiguchi/Ohta model by Sekiguchi and Ohta (1977) employed by e.g. Komiya et al. (1999)

The applied constitutive models were not fully suitable to properly simulate the surface settlements induced by mechanized tunneling in fine-grained soil deposits. For example, the transverse settlement trough was numerically predicted too wide and shallow compared to the more steep and deep in situ measurements. This might be explained by non-consideration of specific material properties of fine-grained soils such as inherent and stress-induced anisotropy, structure and destructuration and behavior under non-monotonic stress paths as induced by the mechanized tunneling process. However, Addenbrooke et al. (1997) stated that the elastic anisotropy does not play a significant role in mechanized tunneling problems.

Numerical studies on mechanized tunneling, where more sophisticated constitutive soil models were employed are mostly based on tunneling projects in heavily overconsolidated London clay deposits. It has to be stated that the stress paths induced by mechanized tunneling will induce very stiff and predominantly elastic behavior of overconsolidated clay and the plasticity governed phenomena such as stress-induced anisotropy and destructuration are only slightly mobilized. Therefore, the effects are more related to stress history and consolidation state rather than to clay structure.

- Grammatikopoulou et al. (2008a) used the M3-SKH three-surface kinematic hardening model (bubble model) by Grammatikopoulou et al. (2006). Gonzalez et al. (2012) applied a kinematic hardening soil model incorporating structure and stiffness degradation based on the models by Rouainia and Wood (2000) and Grammatikopoulou et al. (2006).
- Wongsaroj et al. (2013) applied the subloading surface concept by Hashiguchi and Ueno (1977a); Hashiguchi and Chen (1998).
- Avgerinos et al. (2016) utilzed the M2-SKH two-surface kinematic hardening model by Grammatikopoulou et al. (2006).
- Ieronymaki et al. (2017) employed the MIT-S1 model by Pestana and Whittle (1999).

Some rare examples on the application of more sophisticated constitutive soil models to investigate the influence of clay structure on the system behavior caused by mechanized tunneling can be found in literature. The studies are limited to plane strain simulation models. In general it can be stated that utilizing advanced constitutive models improves the prediction of surface settlements caused by mechanized tunneling compared to the in situ measurements.

- Dang and Meguid (2008) applied the multilaminate model by Cudny and Vermeer (2004) to simulate the undrained response of structured Canadian clay to shield tunneling in a plane strain model. The Canadian clay is slightly to highly overconsolidated (OCR in the range 2-9) with a shear strength sensitivity between 2.5 and 7. The constitutive model incorporates anisotropy, interparticle bonding and destructuration of natural clay but is limited to non-linear elastic behavior during unloading and reloading. The predicted maximum surface settlements still deviated from the larger field measurements. However, they figured out that the initial interparticle bonding decreases the maximum settlements since bonding imparts additional strength and stiffness to the soil. The destructuration is just slightly influencing ground surface settlements and lining stresses because plasticity is not

strongly mobilized around the tunnel due to stiff and predominantly elastic behavior of overconsolidated clay and overburden depth of five times the tunnel diameter. The anisotropy does not have a distinct impact on the surface settlement. However, they again highlighted the effect of the initial consolidation state on the surface settlements. That is, the larger the OCR the smaller the maximum surface settlements and the wider the settlement trough.

- Xu et al. (2003) investigated the soil disturbance of Shanghai silty clay during EPB tunneling by field measurements. They evaluated the so-called effective stress disturbance degree defined as 1 minus the ratio of the effective stress measured after and before tunneling. The stress disturbance degree was about 20-27 % in a distance of 0.25-1.25 times the tunnel diameter from the tunnel side. The closer the distance to the excavated area the larger the disturbance. Moreover, they defined a teardrop-shaped area of disturbance around and above the tunnel. The evolution of effective stress and excess pore-water pressure at the depth of the tunnel center were also recorded. The effective stress and excess pore-water pressure started to increase when the shield machine approached to a distance of 2.5 times the tunnel diameter to the measurement section. The maximum values were reached when the shield machine crossed the measurement section. Afterwards the effective stress and excess pore-water pressure decreased until the shield machine departed to a distance of 6-10 times the tunnel diameter to the measurement section. The evolution of the stress disturbance during mechanized tunneling directly affects the stiffness and undrained strength of natural clay. The larger the stress disturbance degree the smaller the stiffness and the undrained strength.

- Bian et al. (2016) numerically examined the effects of soil structure on the ground response during EPB shield tunneling with respect to the in situ measurements on tunneling in Shanghai soft clay as given by Xu et al. (2003). The constitutive model in the numerical study of Bian et al. (2016) was based on the models by Wheeler et al. (2003) and the subloading concept by Hashiguchi and Ueno (1977a) and Hashiguchi and Chen (1998). The inherent anisotropy was taken into consideration by a fixed rotation of the yield surface while the stress-induced anisotropy was neglected. The undrained numerical simulations were performed using a plane strain model employing the stress reduction method. It was clearly observed that clay structure and tunneling induced destructuration have a distinct effect on magnitude and shape of the surface settlements, horizontal deformations of the ground domain and development of excess pore-water pressure. The degradation of stiffness

due to destructuration causes larger deformations around the tunnel and leads to larger maximum surface settlements and a more narrow settlement trough which is close to the in situ measurements. Due to strain softening the soil experiences much more stress redistribution when incorporating destructuration. This results in larger mobilized shear stress and plastic strain and a narrower plastic shear band mechanism above the tunnel. Consequently, the surface settlement trough is deeper and narrower.

Avgerinos et al. (2016) demonstrated the importance of the proper choice of the constitutive parameters to obtain realistic and reliable model responses. Especially the type of laboratory test the constitutive parameters are calibrated against is most relevant.

2.4.5 Summary

After a short introduction on EPB shield tunneling and corresponding settlements, numerical modeling was discussed as a powerful tool for providing realistic and reliable predictions of the system behavior induced by mechanized tunneling such as surface settlements and elastoplastic ground movements. Techniques for numerical modeling of the most important subsystems involved in mechanized tunneling were reviewed to provide an adequate 3D tunnel simulation model to be used in this study for the investigation of the influence of the soil mechanical properties of natural clay on the system behavior induced by mechanized tunneling. Since mechanized tunneling is a three-dimensional geotechnical problem, as intensively analyzed in the former sections, an adequate 3D tunnel simulation model has to be employed.

As a conclusion, the following components of an adequate 3D simulation model for mechanized tunneling will be considered in the present study: ground domain represented by soil volume elements; sequential advance; shield machine by elastic shell elements rather than using most complex pressure model; lining segments by elastic volume elements without consideration of joints; soil-structure interaction/contact modeling between soil, shield machine and lining by interface elements; tunnel face support by distributed surface load; tail void grouting pressure by distributed surface load without consideration of thin grouting layer and time-dependent behavior of the grouting material; tunnel volume loss due to overcutting and conicity of the shield machine by contraction of the shield and lining elements; tunnel volume loss at the tail void by contraction of the lining elements. Beside of an adequate numerical 3D tunnel simulation model, the most important factor for providing realistic and reliable predictions of the system behavior caused by mechanized tunneling in natural clay deposits is the utilization of an adequate constitutive

model. It was shown in the literature review that the use of more complex constitutive models for natural clay, as employed in some rare numerical plane strain studies, significantly enhanced the model response of tunnel simulations such as the shape of the transverse ground settlement trough with respect to the in situ measurements. Consequently, an adequate constitutive model for natural clay has to consider the stress-strain history, stress path direction and decisive soil mechanical properties such as inherent and stress-induced anisotropy, structure and destructuration and cyclic behavior incorporating stiffness degradation and accumulation of plastic straining.

To sum up, this study provides coupling of an adequate 3D simulation model for mechanized tunneling with an appropriate constitutive BSP model for natural clay, which was not considered in the already existing numerical studies. The adequate 3D tunnel simulation model allows for a sophisticated analysis of the influence of the soil mechanical properties of natural clay on the system behavior induced by mechanized tunneling considering the spatial stress-strain behavior and excess pore-water pressure distribution in the entire ground domain. The application of the sophisticated constitutive BSP model enhances the analysis compared to the existing research. The model development and formulation based on the bounding surface plasticity concept is described in the following chapter.

3 Formulation of BSP model for natural clay

3.1 Model structure

Among various sophisticated constitutive models for natural clay an adequate constitutive soil model based on the bounding surface plasticity (BSP) concept is employed within this study (Dafalias et al., 2006; Taiebat et al., 2010; Seidalinov and Taiebat, 2014; Dafalias and Taiebat, 2013, 2014; Barciaga et al., 2017). The hierarchical structure of the adequate constitutive BSP model for natural clay is shown in Figure 3.1. In accordance with the conventional sign convention in geomechanics both stress and strain quantities are defined positive in compression and negative in extension.

The constitutive BSP model in its simplest form is based on the elastoplastic critical state soil mechanics concept using the Modified Cam-Clay (MCC) approach for normally and overconsolidated clay. Hence, the employed constitutive model incorporates non-linear stress-dependent elasticity and classical isotropic hardening and softening governed by the development of plastic volumetric strain. In addition to this, the model employs a non-associated plastic flow rule.

Moreover, the enhanced hierarchical BSP model family captures the more sophisticated soil mechanical features of natural clay. The inherent and stress-induced anisotropy is considered by an anisotropic fabric stress tensor whose evolution is controlled by a sophisticated rotational hardening rule as a function of plastic strain increment and stress ratio. A structure variable is introduced to account for the current amount of structure. The structure variable relates the size of the bounding surface with respect to the natural structured state to the size of an intrinsic reference surface associated to the corresponding reconstituted state. The destructuration process is directly linked to the evolution of the structure variable which is governed by the evolution of volumetric and deviatoric plastic strains. The BSP concept including appropriate projection rule, elastic nucleus, shape hardening function, damage variable as well as moving projection center with re-

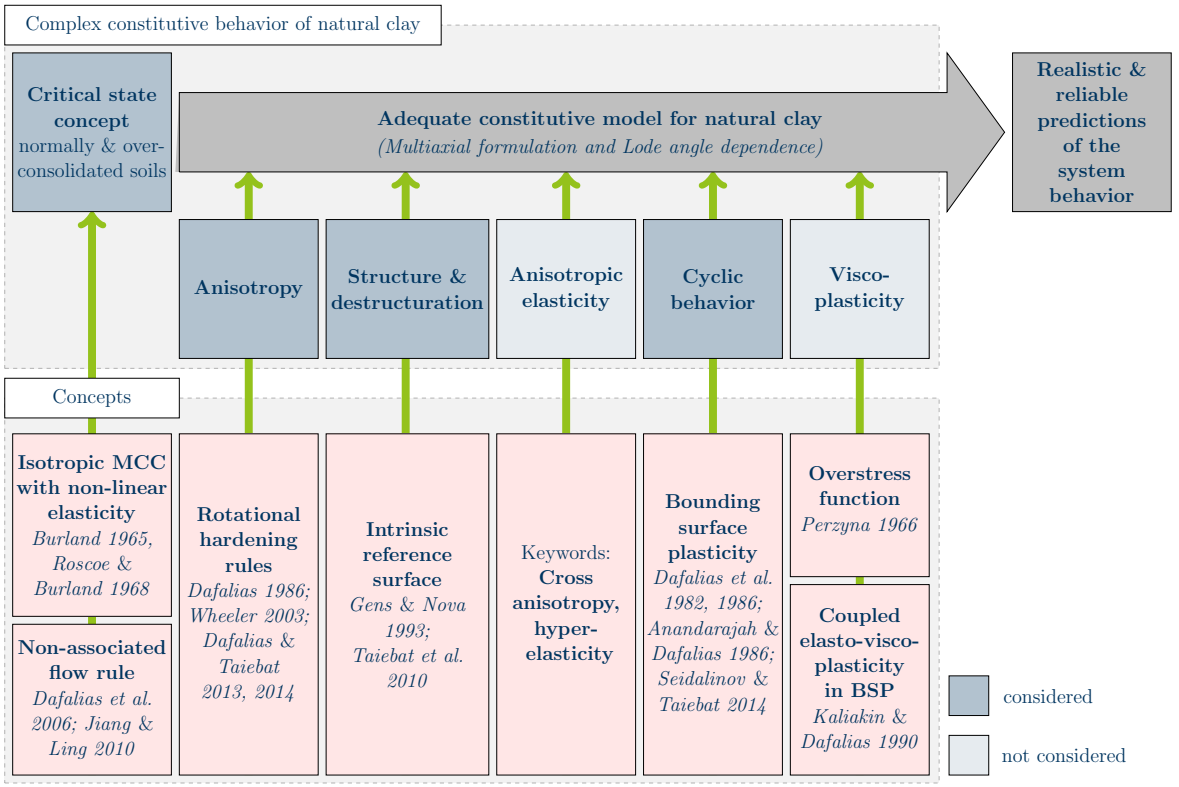

Figure 3.1: Concept of an appropriate numerical analysis of the system behavior induced by mechanized tunneling in order to provide realistic and reliable predictions

spect to the stress reversal state allows for a smooth elastoplastic transition, degradation of stiffness and accumulation of plastic strain with respect to cyclic loading.
In conclusion, the presented constitutive BSP model is capable to adequately simulate the mechanical behavior of natural clay under complex stress paths as described in the former chapter. Within the current work, the constitutive equations are modified in order to be applicable for the bounding surface plasticity concept. Due to the fact that mechanized tunneling is a three-dimensional geotechnical problem the constitutive model equations are formulated with respect to the multiaxial stress space additionally accounting for Lode angle dependence. It is to be noted that viscoplastic and strain-rate dependent material behavior as well as anisotropic elasticity are not considered within the present study.
The hierarchical structure of the adequate constitutive BSP model is described in the following sections. Firstly, the non-linear elastic model response is introduced followed by the general description of the bounding surface plasticity concept. Afterwards, the model extensions to capture the more sophisticated soil mechanical features of natural clay such as anisotropy and destructuration are introduced. To finalize, some special features of

the constitutive BSP model concerning a more appropriate cyclic model response such as shape hardening function, damage parameter and moving projection center are presented.

3.2 Elasticity

The elastic stress-strain behavior is described by a non-linear stress-dependent isotropic hypo-elastic relation as already used in the Modified Cam-Clay models by Burland (1965) and Roscoe and Burland (1968). The stress and strain tensors can be presented as the sum of the deviatoric and volumetric components. The elastic stress-strain relationship in the multiaxial stress and strain space is given in Equation 3.1.

$$\Delta\boldsymbol{\varepsilon}^{\mathrm{e}} = \frac{1}{3}\,\Delta\varepsilon_{\mathrm{v}}\,\boldsymbol{I} + \Delta\boldsymbol{e} = \frac{\Delta p'}{3\,K^{\mathrm{e}}}\,\boldsymbol{I} + \frac{\Delta\boldsymbol{s}}{2\,G^{\mathrm{e}}} \tag{3.1}$$

The elastic strain tensor $\boldsymbol{\varepsilon}^{\mathrm{e}}$ is composed of the volumetric strain ε_{v} as a function of the effective mean stress p' and the elastic bulk modulus K^{e} multiplied by the identity tensor $\boldsymbol{I}$ and the deviatoric strain tensor $\boldsymbol{e}$ as a function of the deviatoric stress tensor $\boldsymbol{s}$ and the elastic shear modulus G^{e}. The elastic bulk modulus K^{e} as given in Equation 3.2 is assumed to be dependent on the stress state expressed by the effective mean stress p'. Furthermore, the elastic bulk modulus K^{e} is defined by the specific volume $v = 1 + e$ and the elastic swelling parameter κ. In this study the definition of the specific volume $v = 1 + e$ is related to the current void ratio e. The elastic shear modulus G^{e} is expressed in terms of the elastic bulk modulus K^{e} and a constant Poisson's ratio ν as specified by Equation 3.3.

$$K^{\mathrm{e}} = \frac{1+e}{\kappa}\,p' \tag{3.2}$$

$$G^{\mathrm{e}} = \frac{3\,(1-2\,\nu)}{2\,(1+\nu)}\,K^{\mathrm{e}} \tag{3.3}$$

3.3 Bounding surface plasticity

3.3.1 BSP concept

The BSP concept as intensively described in section 2.3.4 was originally developed by Dafalias and Popov (1975) for metals and further modified to be applicable for clay type materials by Dafalias and Herrmann (1982), Dafalias (1986a), Dafalias and Herrmann

(1986b) and Anandarajah and Dafalias (1986). It allows for a more sophisticated modeling of the behavior of complex reversal stress paths during cyclic loading. Seidalinov and Taiebat (2014) adopted the BSP concept to the Saniclay models introduced by Dafalias et al. (2006) and Taiebat et al. (2010), which account for inherent and stress-induced anisotropy as well as structure and destructuration.
The multiaxial formulations of the plastic potential surface G and the bounding surface F are given by Equations 3.4 and 3.5, respectively. The constitutive features incorporated in the plastic potential surface and the bounding surface such as critical state soil mechanics, isotropic hardening and softening, anisotropy and destructuration, non-associated flow rule and Lode angle dependence and the corresponding constitutive parameters will be explained in the following sections.

$$G = \frac{3}{2}\,\{\bar{\boldsymbol{s}} - \bar{p}'\,\boldsymbol{\alpha}\} : \{\bar{\boldsymbol{s}} - \bar{p}'\,\boldsymbol{\alpha}\} - \left\{M^2 - \frac{3}{2}\,\boldsymbol{\alpha} : \boldsymbol{\alpha}\right\}\,\bar{p}'\,\{p_\alpha - \bar{p}'\} = 0 \tag{3.4}$$

$$F = \frac{3}{2}\,\{\bar{\boldsymbol{s}} - \bar{p}'\,\boldsymbol{\alpha}\} : \{\bar{\boldsymbol{s}} - \bar{p}'\,\boldsymbol{\alpha}\} - \left\{N^2 - \frac{3}{2}\,\boldsymbol{\alpha} : \boldsymbol{\alpha}\right\}\,\bar{p}'\,\{p_{0,\mathrm{s}} - \bar{p}'\} = 0 \tag{3.5}$$

The bounding surface F represents the stress-strain history of natural clay. Whereat, the bounding surface is governed by the hardening variable $p_{0,\mathrm{s}}$ specifying the size related to the maximum mean stress state, the Lode angle dependent variable N specifying the shape and the fabric stress tensor $\boldsymbol{\alpha}$ specifying the rotation. However, the hardening variable $p_{0,\mathrm{s}}$ is explicitly introduced to define the enlarged size of the bounding surface with respect to the natural structured state compared to the reconstituted intrinsic state. An additional elastic nucleus f_{eln} homologous to the bounding surface with respect to the projection center $\boldsymbol{\sigma}'_{\mathrm{pc}}$ defines the purely elastic range. The size of the elastic nucleus is indirectly defined via the constitutive parameter s_{eln}. For visualization the bounding surface F, the plastic potential surface G and the elastic nucleus f_{eln} in the triaxial p', q effective mean vs. deviatoric stress space are schematically illustrated in Figure 3.2. Moreover, the anisotropic bounding surface (BS), the associated Lode angle dependent N-cone, the anisotropic plastic potential surface (PPS) and the associated Lode angle dependent critical state surface (CSS) in the principle stress space are shown in Figure 3.3. The N-cone and the critical state surface are governed by the Lode angle dependent variables $N(\theta)$ and $M(\theta)$, respectively.
The main feature of the BSP concept is the relation between the plasticity modulus K_{p} with respect to the current stress state $\boldsymbol{\sigma}'$ and the plasticity modulus $\bar{K}_{\mathrm{p}}$ with respect to the corresponding image stress state $\bar{\boldsymbol{\sigma}}'$ on the bounding surface indicated with a bar via a distance function $\hat{f}$ and a shape hardening function $\hat{h}$ as defined in Equation 3.6.

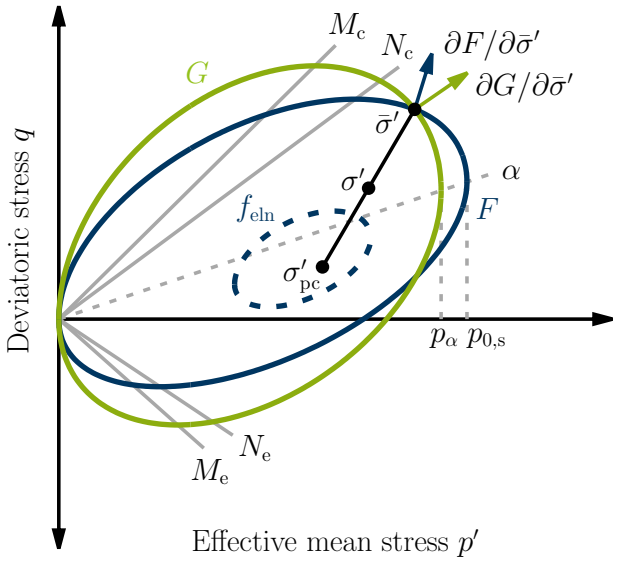

Figure 3.2: Schematic illustration of the bounding surface, the plastic potential surface and the elastic nucleus in the p', q effective stress space

The more the current stress point approaches to the bounding surface during loading the lower the value of the plasticity modulus K_p and the higher the degree of plasticity. This approach ensures a smooth elastoplastic transition and enables the occurrence of elastoplastic deformations for stress paths within the bounding surface outside of the elastic nucleus.

$$K_p = \bar{K}_p + \hat{f}\,\hat{h} \tag{3.6}$$

$$\hat{f} = \frac{\delta}{\langle r - s_{eln}\,\delta\rangle} = \left\langle \frac{b-1}{b-\{b-1\}\;s_{eln}} \right\rangle \tag{3.7}$$

The plasticity modulus $\bar{K}_p$ with respect to the image stress state is determined from the consistency condition of the bounding surface $\dot{F} = 0$. This results in Equation 3.8, where $\boldsymbol{q}$ is the vector of the hardening variables derived from the hardening rules with respect to the image stress state on the bounding surface.

$$\bar{K}_p = -\frac{\partial F}{\partial \boldsymbol{q}} : \tilde{\boldsymbol{q}} = -\left\{ \frac{\partial F}{\partial p_{0,s}}\,\tilde{p}_{0,s} + \frac{\partial F}{\partial \boldsymbol{\alpha}} : \tilde{\boldsymbol{\alpha}} \right\} \tag{3.8}$$

The image stress state is obtained by a radial projection rule as specified by Equation 3.9 as a function of the similarity ratio ($1 \le b < \infty$) between an imaginary loading surface through the current stress state and the bounding surface through the image stress state

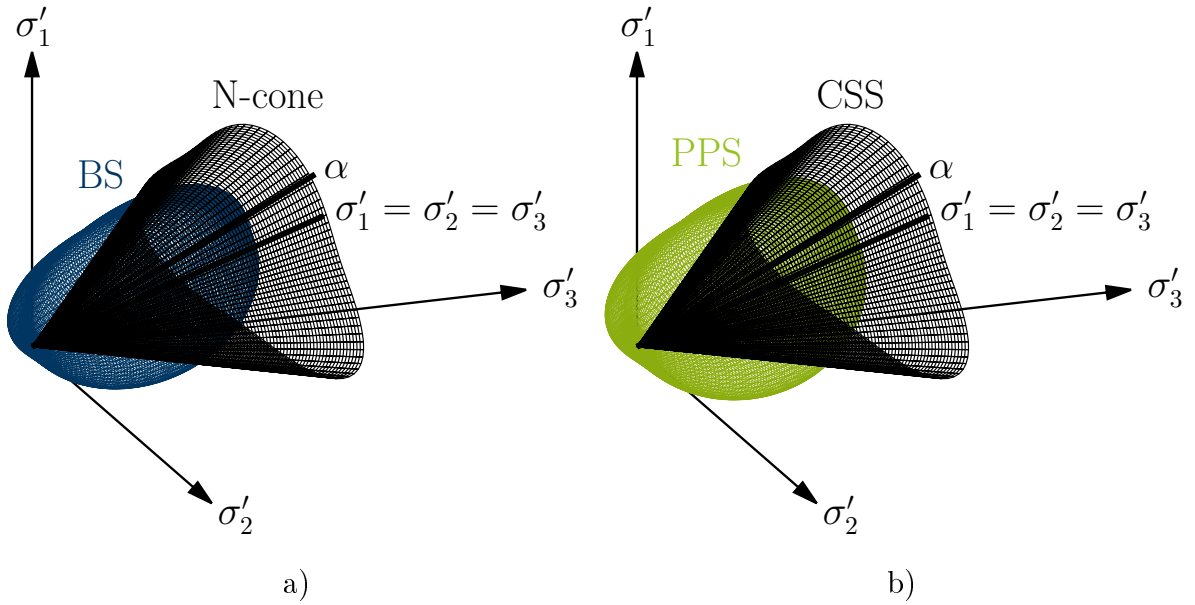

Figure 3.3: Schematic illustration of the surfaces in the principle stress space a) anisotropic bounding surface (BS) and Lode angle dependent N-cone b) anisotropic plastic potential surface (PPS) and Lode angle dependent critical state surface (CSS)

as well as the projection center $\boldsymbol{\sigma}'_{\mathrm{pc}}\left(p'_{\mathrm{pc}}, \boldsymbol{s}_{\mathrm{pc}}\right)$. The projection center $\boldsymbol{\sigma}'_{\mathrm{pc}}$ serves as the center of homology for the loading surface and the elastic nucleus. The similarity ratio b can be obtained from inserting the projection rule in the bounding surface formulation as shown in chapter 4 on the numerical implementation.

$$\bar{\boldsymbol{\sigma}}' \;=\; b\left\{\boldsymbol{\sigma}' - \boldsymbol{\sigma}'_{\mathrm{pc}}\right\} + \boldsymbol{\sigma}'_{\mathrm{pc}} \tag{3.9}$$

The constitutive parameter s_{eln} is an indirect measure of the size of the elastic nucleus. For a stress point inside the elastic nucleus with $r/s_{\mathrm{eln}} < \delta$ the latter term in Equation 3.6 and the plastic modulus converge to infinity indicating a purely elastic behavior. The generalized scalar distances $\delta = |\bar{\boldsymbol{\sigma}}' - \boldsymbol{\sigma}'|$ and $r = \left|\bar{\boldsymbol{\sigma}}' - \boldsymbol{\sigma}'_{\mathrm{pc}}\right|$ are schematically illustrated in the p', q effective stress space in Figure 3.4. By setting a huge value for s_{eln} the model response reduces from bounding surface plasticity to conventional elastoplasticity. On the contrary, by setting $s_{\mathrm{eln}} = 1$ the elastic nucleus shrinks to a point in the stress space and just elastoplastic model response without having a purely elastic range occurs.
When the current stress point reaches the bounding surface the model response is identical to conventional elastoplasticity because the plasticity moduli with respect to the current stress state and the image stress state coincide. That is, for a stress point on the bounding

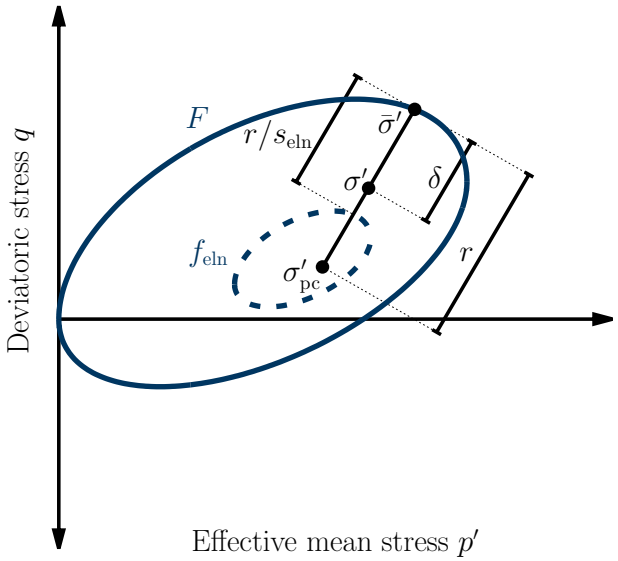

Figure 3.4: Schematic illustration of the BSP concept

surface with $\delta = 0$ or $b = 1$ the latter term in Equation 3.6 converges to zero and $K_{\mathrm{p}} = \bar{K}_{\mathrm{p}}$. Hence, the bounding surface acts like a yield surface in conventional elastoplasticity. For all other loading paths having a positive scalar plastic loading index L elastoplastic straining will be induced in accordance with Equations 3.10 and 3.11 as a function of the plasticity index K_{p} related to the current stress state. Whereat, the scalar plastic loading index L, which defines the magnitude of the plastic strain increment $\Delta\boldsymbol{\varepsilon}^{\mathrm{p}}$ is derived from combining flow rule and consistency condition on the bounding surface by use of the image stress state.

$$L = \frac{1}{K_{\mathrm{p}}} \frac{\partial F}{\partial \bar{\boldsymbol{\sigma}}'} : \Delta\boldsymbol{\sigma}' \tag{3.10}$$

$$L = \frac{\left\{\dfrac{\partial F}{\partial \bar{\boldsymbol{\sigma}}'}\right\} : \boldsymbol{D}^{\mathrm{e}} : \Delta\boldsymbol{\varepsilon}}{\left\{\dfrac{\partial F}{\partial \bar{\boldsymbol{\sigma}}'}\right\} : \boldsymbol{D}^{\mathrm{e}} : \left\{\dfrac{\partial G}{\partial \bar{\boldsymbol{\sigma}}'}\right\} + K_{\mathrm{p}}} \tag{3.11}$$

Concluding, the plastic strain increment $\Delta\boldsymbol{\varepsilon}^{\mathrm{p}}$ is given by the flow rule as defined by Equation 3.12. The induced plastic straining results in an updated bounding surface since expansion, shrinkage or rotation due to isotropic hardening or softening, anisotropy or destructuration occur.

$$\Delta\boldsymbol{\varepsilon}^{\mathrm{p}} = \langle L \rangle \frac{\partial G}{\partial \bar{\boldsymbol{\sigma}}'} \tag{3.12}$$

3.3.2 Critical state soil mechanics

To describe the mechanical stress-strain behavior of natural clays the BSP model is generally formulated in the framework of critical state soil mechanics. The constitutive model employed in the current study is based on the concept of critical state soil mechanics by use of the Modified Cam-Clay (MCC) formulation (Roscoe et al., 1958, 1963; Burland, 1965; Roscoe and Burland, 1968; Schofield and Wroth, 1968).
The elastoplastic compression parameter λ and the elastic swelling parameter κ define the natural logarithmic effective mean stress-void ratio behavior in loading and unloading-reloading respectively. In addition to this, the Poisson's ratio ν is utilized. The Lode angle dependent critical state stress ratio $M(\theta)$ is governed by the constitutive model parameters M_c and M_e defining the critical stress ratio in triaxial compression and extension, respectively. Moreover, the isotropic hardening variable $p_{0,\mathrm{s}}$, which defines the size of the bounding surface is initialized by the constitutive parameter $p_{0,\mathrm{s,init}}$. Furthermore, the current void ratio e is initialized by the constitutive parameter e_0 representing the initial void ratio.

3.3.3 Anisotropy and rotational hardening

The anisotropic fabric of natural clay imparts anisotropy with respect to the mechanical properties. The inherent anisotropy leads to an initial rotation of the bounding surface representing the anisotropy of the mechanical properties and induced plastic straining results in an evolution (expansion, shrinkage, rotation) of the bounding surface with respect to the loading direction.
To capture inherent and stress-induced anisotropy, Dafalias (1986c) extended the isotropic formulation of the plastic potential surface to an anisotropic formulation by proposing a new rate expression of plastic work. This formulation results in a rotated and distorted elliptical plastic potential surface. The anisotropy is introduced to Equation 3.4 by a fabric stress tensor $\boldsymbol{\alpha}$ and a model variable p_α specifying the size of the plastic potential surface as visualized in Figure 3.2. In the present study, the rotation of the bounding surface and the plastic potential surface are governed by the same fabric stress tensor $\boldsymbol{\alpha}$. The value of p_α for a given image stress state can be obtained by solving the plastic potential surface formulation as given in Equation 3.13.

$$p_\alpha = \frac{3/2\ \{\bar{\boldsymbol{s}} - \bar{p}'\,\boldsymbol{\alpha}\} : \{\bar{\boldsymbol{s}} - \bar{p}'\,\boldsymbol{\alpha}\}}{\{M^2 - 3/2\ \{\boldsymbol{\alpha} : \boldsymbol{\alpha}\}\}\ \bar{p}'} + \bar{p}' \tag{3.13}$$

However, this equation fails when the mean stress component of the image stress state equals zero. To remedy this problem, a minimum limit value $p_{\alpha,\mathrm{lim}}$ as given in Equation 3.14 is derived for stress ratios and effective mean stress states converging to zero. Moreover, the maximum value of p_α is implicitly limited by the value of the hardening variable $p_{0,\mathrm{s}}$ since both surfaces are governed by the same fabric stress tensor $\boldsymbol{\alpha}$ and $N \leq M$. Consequently, $p_{\alpha,\mathrm{lim}} \leq p_\alpha \leq p_{0,\mathrm{s}}$.

$$p_{\alpha,\mathrm{lim}} = \frac{N^2 - 3/2\ \{\boldsymbol{\alpha} : \boldsymbol{\alpha}\}}{M^2 - 3/2\ \{\boldsymbol{\alpha} : \boldsymbol{\alpha}\}} \tag{3.14}$$

The inherent anisotropy is controlled by an initial rotation of the bounding surface and the plastic potential surface. The initial rotation of the surfaces is governed by an appropriate initial setting of the fabric stress tensor $\boldsymbol{\alpha}$ governed by the constitutive model parameter α_0. Thereby, the principal components of $\boldsymbol{\alpha}$ are defined as $\alpha_{11} = 2/3\,\alpha_0$ and $\alpha_{22} = \alpha_{33} = -1/3\,\alpha_0$. The other components of the symmetric tensor $\alpha_{12} = \alpha_{21} = 0$, $\alpha_{23} = \alpha_{32} = 0$ and $\alpha_{31} = \alpha_{13} = 0$ are initially assumed to be zero independently of the value of α_0.

The stress-induced evolution of the fabric stress tensor $\boldsymbol{\alpha}$ is controlled employing a sophisticated rotational hardening rule as function of the volumetric and deviatoric plastic strain increments and the stress path history. The concept of rotational hardening of the bounding surface in the p', q effective stress space is schematically illustrated in Figure 3.5. In the present study the bounding surface and the plastic potential surface have the same fabric stress tensor $\boldsymbol{\alpha}$ governed by the same rotational hardening rule.

The chosen evolution of the fabric stress tensor $\boldsymbol{\alpha}$ is given by Equation 3.15 modified according to Dafalias and Taiebat (2013) in order to be applicable for the bounding surface plasticity concept. It has to be mentioned that the plasticity modulus $\bar{K}_\mathrm{p}$ is derived at the image stress state on the bounding surface. Consequently, all equations corresponding to the evolution of the fabric stress tensor are formulated with respect to the image stress state indicated with a bar. The rate of anisotropy and rotation is controlled by the constitutive parameter c_α as a proportional factor. The ratio $\bar{p}'/p_{0,\mathrm{s}}$ slows down the evolution for heavily overconsolidated clays and the atmospheric pressure p_atm is used for reasons of dimensional consistency.

Furthermore, all evolution equations include a proper target value for the fabric stress tensor specified by the bounding attractor $\boldsymbol{\alpha}_\mathrm{b}$. The bounding attractor $\boldsymbol{\alpha}_\mathrm{b}$ is defined with respect to the applied stress paths indicated by the stress ratio tensor $\bar{\boldsymbol{r}} = \bar{\boldsymbol{s}}/\bar{p}'$ or the scalar $|\bar{\eta}| = \sqrt{3/2\,\bar{\boldsymbol{r}} : \bar{\boldsymbol{r}}}$ associated to the image stress state. Consequently, the bounding

surface and the plastic potential surface rotate towards the bounding attractor, which is for each loading case defined with respect to a certain fixed stress ratio. If the target value is reached and the stress ratio does not change no further rotation will appear. Any consecutive change in the stress ratio will again influence the bounding attractor and induce rotation of the surfaces. The bounding attractor $\boldsymbol{\alpha}_\mathrm{b}$ is given either by Equation 3.16 modified according to Dafalias and Taiebat (2013), or Equation 3.17 modified according to Dafalias and Taiebat (2013), or Equations 3.18-3.19 modified according to Dafalias and Taiebat (2014).

$$\Delta\boldsymbol{\alpha} = \langle L \rangle \; c_\alpha \, p_\mathrm{atm} \, \frac{\bar{p}'}{p_{0,\mathrm{s}}} \, \{\boldsymbol{\alpha}_\mathrm{b} - \boldsymbol{\alpha}\} = \langle L \rangle \; \tilde{\boldsymbol{\alpha}} \tag{3.15}$$

$$\boldsymbol{\alpha}_\mathrm{b} = \frac{\bar{\boldsymbol{r}}}{x_\alpha} \tag{3.16}$$

$$\boldsymbol{\alpha}_\mathrm{b} = \sqrt{\frac{2}{3}} \, \frac{M_\mathrm{r}}{z_\alpha} \left\{ 1 - \exp\left(-s_\alpha \, \frac{|\bar{\eta}|}{M_\mathrm{r}} \right) \right\} \bar{\boldsymbol{n}}_\mathrm{r} \tag{3.17}$$

$$|\bar{\eta}| \leq M_\mathrm{r}: \quad \boldsymbol{\alpha}_\mathrm{b} = \left\{ \frac{\alpha_\mathrm{cs}}{M_\mathrm{r}} + m_\alpha \left\{ 1 - \left\{ \frac{|\bar{\eta}|}{M_\mathrm{r}} \right\}^{n_\alpha} \right\} \right\} \bar{\boldsymbol{r}} \tag{3.18}$$

$$|\bar{\eta}| \geq M_\mathrm{r}: \quad \boldsymbol{\alpha}_\mathrm{b} = \frac{\alpha_\mathrm{cs}}{M_\mathrm{r}} \exp\left(-\mu_\alpha \left\{ \frac{|\bar{\eta}|}{M_\mathrm{r}} - 1 \right\} \right) \bar{\boldsymbol{r}} \tag{3.19}$$

That is, three different formulations of the bounding attractor $\boldsymbol{\alpha}_\mathrm{b}$ are considered in the constitutive BSP model which will be explained in the following and might be individually chosen by the user. However, within this study, the focus is set on employing the rotational hardening rule given by Equation 3.15 and Equation 3.17.

In Equation 3.16 the constitutive parameter x_α controls the target value of the fabric stress tensor. Hence, the rotation is limited to a constant proportion of the stress ratio $\bar{\boldsymbol{r}}$. In Equation 3.17 the bounding attractor is modified by substituting the constant constitutive parameter x_α by an exponential function of the stress ratio $|\bar{\eta}|$ with respect to the Lode angle dependent critical state stress ratio $M_\mathrm{r}(\theta_\mathrm{r})$, which will be explained in section 3.3.6. The constitutive parameters s_α and z_α define the target value and the unit norm deviatoric image stress tensor $\bar{\boldsymbol{n}}_\mathrm{r} = \bar{\boldsymbol{r}} / |\bar{\boldsymbol{r}}|$ is used to define the direction of the rotation. Equation 3.17 by adding the ratio M_r/z_α in combination with the exponential function has the advantage of restricting the fabric stress tensor to a value which is always smaller than the critical state stress ratio for any stress ratio, which becomes particularly important when the stress ratio approaches the critical state stress ratio. On the contrary, Equation 3.16 in its simplest form results in an unlimited rotation when the stress ratio

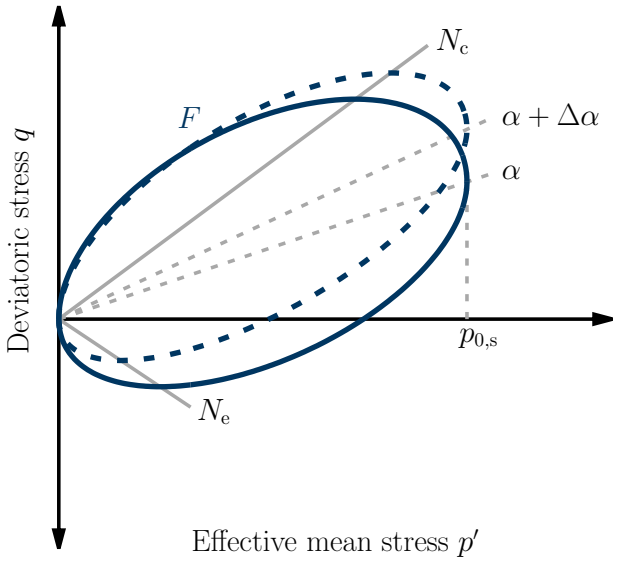

Figure 3.5: Schematic illustration of rotational hardening of the bounding surface in the p', q effective stress space

is larger than the critical state stress ratio. Both given definitions of the bounding attractor guarantee correct modeling of K_0 loading paths by a proper setting of the model constants x_α or s_α and z_α, respectively. Moreover, the rotation of the plastic potential surface specified by $\boldsymbol{\alpha}$ is not allowed to stabilize at $\bar{\boldsymbol{r}}$ because loading under a constant stress ratio has to produce not only volumetric plastic strain but also deviatoric plastic strain.

With respect to the open discussion whether there exist anisotropic fabric at the critical state ($\boldsymbol{\alpha}_{cs} \neq 0$) or isotropic fabric ($\boldsymbol{\alpha}_{cs} = 0$), Dafalias and Taiebat (2014) proposed a new formulation of the bounding attractor as defined by Equations 3.18-3.19. It is differentiated between two independent formulations of the bounding attractor dependent on the relative position of the stress ratio with respect to the critical state stress ratio. Equation 3.18, which is valid for the condition $|\bar{\eta}| \leq M_r$ defines the bounding attractor with respect to the stress ratio in similar manner as described before governed by the constitutive parameters m_α and n_α. Additionally, the formulation guarantees that the bounding attractor equals the residual fabric at the critical state ($\boldsymbol{\alpha}_b = \boldsymbol{\alpha}_{cs}$), when the stress ratio reaches the critical state stress ratio $|\bar{\eta}| = M_r$. The approach allows for a direct control of the residual fabric at the critical state $\boldsymbol{\alpha}_{cs}$ via a constitutive parameter α_{cs}. A possible zero value implies the existence of isotropic fabric at critical state.

Furthermore, due to Equation 3.19 the bounding attractor and therefore the rotational hardening parameter exponentially decay from the value at the critical state to zero when

$|\bar{\eta}| \geq M_\mathrm{r}$ and $|\bar{\eta}| \to \infty$. The constitutive parameter μ_α is needed to control the exponential decay of $\boldsymbol{\alpha}/M_\mathrm{r}$ over $\bar{\boldsymbol{r}}/M_\mathrm{r}$. The ratio $\boldsymbol{\alpha}_\mathrm{cs}/M_\mathrm{r}$ must be independent of the Lode angle θ for reasons of uniqueness of the critical state.

3.3.4 Uniqueness of critical state

The rotational hardening rule proposed by Dafalias (1986c) incorporated a term $|\partial G/\partial p'|$, which proportionally relates the increment of the rotational hardening variable to the plastic volumetric strain increment. As a consequence that term will freeze the evolution of the rotational hardening variable at the critical state, where $\partial G/\partial p' = 0$. That means the rotation is stopped before reaching its critical state value $\boldsymbol{\alpha}_\mathrm{cs}$. This results in a non-uniqueness of the critical state in compression (M_c) and extension (M_e) due to the lack of rotation on the extension side. To overcome this non-uniqueness, Dafalias and Taiebat (2013) modified the rotational hardening rule proposed by Dafalias (1986c) to Equation 3.15 by neglecting the term $|\partial G/\partial p'|$. By simply removing the term from the rotational hardening rule the surfaces will continuously rotate even at the critical state up to converging to the bounding attractor $\boldsymbol{\alpha}_\mathrm{b}$. Employing that approach leads to a unique critical state. $\boldsymbol{\alpha}_\mathrm{cs}$ and p'_cs at the critical state have to be unique and therefore Lode angle independent. The drawback of removing this term is a "hook-type" shape when the undrained stress path crosses the critical state, especially in extension. This "hook-type" shape was experimentally not observed.

3.3.5 Restriction of excessive rotation

To avoid an excessive rotation of the bounding surface and the plastic potential surface the formulation of the bounding attractor is modified by applying a certain restrictive condition governed by a model variable ξ. Whereat, the model variable ξ is defined based on the requirement that the maximum rotation has to be bounded for stress ratios exceeding a multiple of the critical state stress ratio and the restriction that the maximum rotation must not exceed the values of $M_\mathrm{c}, M_\mathrm{e}, N_\mathrm{c}$ and N_e. The latter restriction accounts for the minimum values of both variables M and N because the plastic potential surface and the bounding surface incorporate the same fabric stress tensor. If the stress ratio exceeds a multiple of the critical state stress ratio $|\bar{\eta}| > \xi\, M_\mathrm{r}$ the following restrictions as given in Equations 3.16 and 3.17 are applied to the bounding attractor. The stress ratio tensor $\boldsymbol{r}$ in Equation 3.16 has to be replaced by the limiting term $\sqrt{2/3}\, \xi\, M_\mathrm{r}\, \boldsymbol{n}_\mathrm{r}$. The scalar stress ratio $|\bar{\eta}|$ has to be replaced by the limiting term $\xi\, M_\mathrm{r}$ in Equation 3.17. The

constitutive parameter ξ is defined in Equation 3.20 with respect to Equation 3.16 and in Equation 3.21 with respect to Equation 3.17, respectively.

$$\xi \leq x_\alpha \frac{\min\left(M_\mathrm{c}, M_\mathrm{e}, N_\mathrm{c}, N_\mathrm{e}\right)}{M_\mathrm{c}} \tag{3.20}$$

$$\xi \leq -\frac{1}{s_\alpha} \ln\left\{1 - z_\alpha \frac{\min\left(M_\mathrm{c}, M_\mathrm{e}, N_\mathrm{c}, N_\mathrm{e}\right)}{M_\mathrm{c}}\right\} \tag{3.21}$$

The approach using the residual fabric at the critical state as a defined input constitutive parameter smaller than the critical state stress ratio and having a subsequent exponential decay of the bounding attractor towards zero as given by Equations 3.18 and 3.19 makes it unnecessary to explicitly restrict the excessive rotation in terms of ξ.

3.3.6 Non-associated flow rule and Lode angle dependence

To account for a more accurate modeling of softening behavior of clay under shearing a non-associated flow rule is introduced (Dafalias et al., 2006; Jiang and Ling, 2010; Jiang et al., 2012). The non-associativity is established by adopting a bounding surface F similar to the plastic potential surface G. The formulation of the bounding surface in terms of a non-associated flow rule is achieved by replacing the variables M and p_α in the formulation of the plastic potential surface by the variables N and $p_{0,\mathrm{s}}$ controlling the shape and the size of the yield surface. Dafalias et al. (2006) showed that $N \leq M$. If $N = M$ the model formulation results in an associated flow rule form.
The most important feature of the non-associated flow rule with $N \neq M$ is the fact that the deviatoric peak stress on $F = 0$ is not at the critical state stress ratio M but at N. That allows for a further evolution of the plastic volumetric strain inducing strain softening until reaching the critical state.
Furthermore, the Lode angle dependence of the plastic potential surface and the bounding surface is taken into account to capture the different constitutive behavior in compression and extension (Dafalias et al., 2006; Jiang and Ling, 2010; Jiang et al., 2012). To ensure this phenomenon, the critical state stress ratio $M(\theta)$ for the plastic potential surface and the variable $N(\theta)$ for the bounding surface are functions of the Lode angle θ, which is defined as the third stress invariant given by Equations 3.22-3.25 (Zienkiewicz and Pande, 1977; Sheng et al., 2000). The constitutive parameters $M_\mathrm{c}, M_\mathrm{e}$ and $N_\mathrm{c}, N_\mathrm{e}$ which are specifying the values of M and N in triaxial compression and triaxial extension are used for the interpolation dependent on the current stress state. Besides, their ratios are defined

as $m_{\mathrm{cs}} = M_{\mathrm{e}}/M_{\mathrm{c}}$ and $n_{\mathrm{cs}} = N_{\mathrm{e}}/N_{\mathrm{c}}$. Furthermore, $\boldsymbol{r} - \boldsymbol{\alpha}$ denotes the effective stress ratio.

$$M(\theta) = \frac{2\, m_{\mathrm{cs}}}{\{1 + m_{\mathrm{cs}}\} - \{1 - m_{\mathrm{cs}}\}\, \cos(3\,\theta)}\, M_{\mathrm{c}} \tag{3.22}$$

$$N(\theta) = \frac{2\, n_{\mathrm{cs}}}{\{1 + n_{\mathrm{cs}}\} - \{1 - n_{\mathrm{cs}}\}\, \cos(3\,\theta)}\, N_{\mathrm{c}} \tag{3.23}$$

$$\cos(3\,\theta) = \sqrt{6}\, \mathrm{tr}(\boldsymbol{n}_{\mathrm{r}\alpha}^3) \tag{3.24}$$

$$\boldsymbol{n}_{\mathrm{r}\alpha} = \frac{\boldsymbol{r} - \boldsymbol{\alpha}}{|\boldsymbol{r} - \boldsymbol{\alpha}|} = \frac{\boldsymbol{r} - \boldsymbol{\alpha}}{\sqrt{\{\boldsymbol{r} - \boldsymbol{\alpha}\} : \{\boldsymbol{r} - \boldsymbol{\alpha}\}}} \tag{3.25}$$

Whereas, when determining the Lode angle with respect to the image stress state the following Equations 3.26-3.27 hold true. $\bar{\boldsymbol{r}} - \boldsymbol{\alpha}$ denotes the effective image stress ratio.

$$\cos(3\,\theta) = \sqrt{6}\, \mathrm{tr}(\bar{\boldsymbol{n}}_{\mathrm{r}\alpha}^3) \tag{3.26}$$

$$\bar{\boldsymbol{n}}_{\mathrm{r}\alpha} = \frac{\bar{\boldsymbol{r}} - \boldsymbol{\alpha}}{|\bar{\boldsymbol{r}} - \boldsymbol{\alpha}|} = \frac{\bar{\boldsymbol{r}} - \boldsymbol{\alpha}}{\sqrt{\{\bar{\boldsymbol{r}} - \boldsymbol{\alpha}\} : \{\bar{\boldsymbol{r}} - \boldsymbol{\alpha}\}}} \tag{3.27}$$

When calculating the bounding attractor of the fabric stress tensor the Lode angle dependent critical state stress ratio $M_{\mathrm{r}}(\theta_{\mathrm{r}})$ is defined according to Equations 3.28-3.30 using the stress ratio $\bar{\boldsymbol{r}}$ with respect to the image stress state.

$$M_{\mathrm{r}}(\theta_{\mathrm{r}}) = \frac{2\, m_{\mathrm{cs}}}{\{1 + m_{\mathrm{cs}}\} - \{1 - m_{\mathrm{cs}}\}\, \cos(3\,\theta_{\mathrm{r}})}\, M_{\mathrm{c}} \tag{3.28}$$

$$\cos(3\,\theta_{\mathrm{r}}) = \sqrt{6}\, \mathrm{tr}(\boldsymbol{n}_{\mathrm{r}}^3) \tag{3.29}$$

$$\bar{\boldsymbol{n}}_{\mathrm{r}} = \frac{\bar{\boldsymbol{r}}}{|\bar{\boldsymbol{r}}|} = \frac{\bar{\boldsymbol{r}}}{\sqrt{\bar{\boldsymbol{r}} : \bar{\boldsymbol{r}}}} \tag{3.30}$$

3.3.7 Isotropic hardening/softening and destructuration

The initial structure due to bonding of natural clay imparts additional stiffness and strength. Furthermore, structural phenomena increase the yield stress associated to the natural structured state compared to the reconstituted state at the same void ratio allowing for loading paths with higher effective mean stress without causing yielding. The stress-volumetric strain behavior of a natural clay until the yield stress is reached seems to be predominantly elastic having nearly the same slope and therefore the same swelling index as the reconstituted clay during unloading-reloading paths. After exceeding the yield stress destructuration abruptly occurs causing reduction of stiffness and strength

resulting in large compression. Due to the progressive nature of destructuration the volumetric behavior of natural clay at higher stress states converges to the corresponding behavior with respect to the reconstituted state. The destructuration is completed and no structure remains.

In the present study, initial structure and the destructuration are considered by applying the general approach of Gens and Nova (1993) as described in section 2.3.3. The bounding surface defines the stress history of the natural structured state. Whereat, the size of the bounding surface related to the structured state is defined by the hardening variable $p_{0,\mathrm{s}}$. However, the initial size of the bounding surface is specified by the constitutive parameter $p_{0,\mathrm{s,init}}$. A homologous intrinsic reference surface F_i is introduced to describe the size of the yield surface related to the reconstituted state having intrinsic properties independent of the natural state as visualized in Figure 3.6. The size of the intrinsic reference surface is governed by an additional isotropic hardening variable $p_{0,\mathrm{i}}$.

Taiebat et al. (2010) incorporated the concept of an intrinsic reference surface in the Saniclay model introduced by Dafalias et al. (2006). The concept is based on the assumption that the size of the bounding surface of natural clay depends on the current amount of structure. The difference in size of the surfaces related to the natural and intrinsic state indicates the amount of structural effects and interparticle bonding forces. Consequently, the degree of structure is specified by the structure variable $S_\mathrm{i} = p_{0,\mathrm{s}}/p_{0,\mathrm{i}}$ defined as the

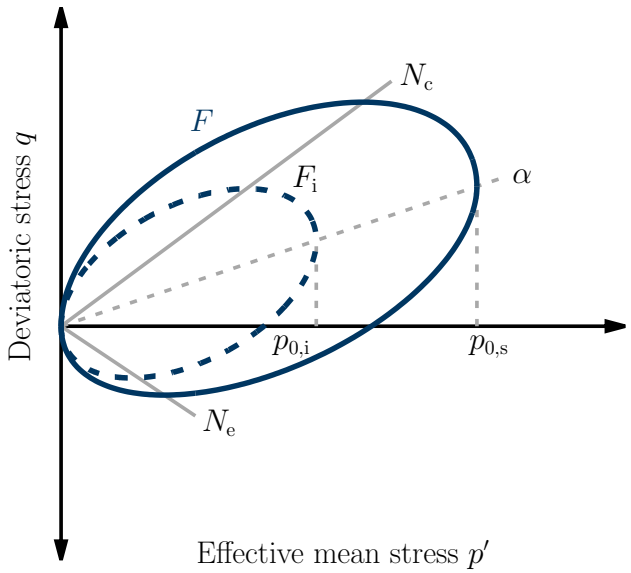

Figure 3.6: Schematic illustration of the bounding surface regarding natural state and the intrinsic reference surface regarding reconstituted state in the p', q effective stress space

ratio of the hardening variable $p_{0,\mathrm{s}}$ related to the natural structured state and $p_{0,\mathrm{i}}$ with respect to the reconstituted state having intrinsic properties. The initial structure is specified by the constitutive parameter $S_{\mathrm{i},0} \geq 1$. In case of having no initial structure, the structure variable $S_{\mathrm{i},0} = 1$ indicates that the bounding surface and the intrinsic reference surface coincide. However, the stress sensitivity introduced by Cotecchia and Chandler (2000) can be directly related to the structure variable S_{i}.

$$\Delta p_{0,\mathrm{s}} = S_{\mathrm{i}}\, \Delta p_{0,\mathrm{i}} + \Delta S_{\mathrm{i}}\, p_{0,\mathrm{i}} = \langle L \rangle \left\{ S_{\mathrm{i}}\, \tilde{p}_{0,\mathrm{i}} + \tilde{S}_{\mathrm{i}}\, p_{0,\mathrm{i}} \right\} = \langle L \rangle\ \tilde{p}_{0,\mathrm{s}} \tag{3.31}$$

$$\Delta p_{0,\mathrm{i}} = \left\{ \frac{1+e}{\lambda - \kappa} \right\} p_{0,i}\, \Delta \varepsilon_{\mathrm{v}}^{\mathrm{p}} = \langle L \rangle \left\{ \frac{1+e}{\lambda - \kappa} \right\} p_{0,i}\, \mathrm{tr} \left(\frac{\partial G}{\partial \bar{\boldsymbol{\sigma}}'} \right) = \langle L \rangle\ \tilde{p}_{0,\mathrm{i}} \tag{3.32}$$

$$\Delta S_{\mathrm{i}} = -k_{\mathrm{i}} \left\{ \frac{1+e}{\lambda - \kappa} \right\} \{ S_{\mathrm{i}} - 1 \}\ \Delta \varepsilon_{\mathrm{dest\,r}}^{\mathrm{p}} = \langle L \rangle\ \tilde{S}_{\mathrm{i}} \tag{3.33}$$

$$\Delta \varepsilon_{\mathrm{dest\,r}}^{\mathrm{p}} = \sqrt{ \{1 - A\}\ \{ \Delta \varepsilon_{\mathrm{v}}^{\mathrm{p}} \}^2 + A \left\{ \frac{2}{3}\, \Delta \boldsymbol{e}^{\mathrm{p}} : \Delta \boldsymbol{e}^{\mathrm{p}} \right\} } \tag{3.34}$$

$$\tilde{S}_{\mathrm{i}} = -k_{\mathrm{i}} \left\{ \frac{1+e}{\lambda - \kappa} \right\} \{ S_{\mathrm{i}} - 1 \}\ \tilde{\varepsilon}_{\mathrm{dest\,r}}^{\mathrm{p}} \tag{3.35}$$

$$\tilde{\varepsilon}_{\mathrm{dest\,r}}^{\mathrm{p}} = \sqrt{ \{1 - A\} \left\{ \mathrm{tr} \left(\frac{\partial G}{\partial \bar{\boldsymbol{\sigma}}'} \right) \right\}^2 + A\, \frac{2}{3} \left\{ \frac{\partial G}{\partial \bar{\boldsymbol{\sigma}}'} - \frac{1}{3}\, \mathrm{tr} \left(\frac{\partial G}{\partial \bar{\boldsymbol{\sigma}}'} \right) \boldsymbol{I} \right\} : \left\{ \frac{\partial G}{\partial \bar{\boldsymbol{\sigma}}'} - \frac{1}{3}\, \mathrm{tr} \left(\frac{\partial G}{\partial \bar{\boldsymbol{\sigma}}'} \right) \boldsymbol{I} \right\} } \tag{3.36}$$

The hardening variable $p_{0,\mathrm{s}}$ is explicitly introduced to the formulation of the bounding surface in Equation 3.5. The evolution of the hardening variable $p_{0,\mathrm{s}}$ given by Equation 3.31 is governed by the superposition of two competing phenomena: On the one hand, the classical isotropic hardening of the hardening variable $p_{0,\mathrm{i}}$ related to the intrinsic reference yield surface in accordance with Equation 3.32. On the other hand, the counteracting evolution of the structure variable S_{i} as a decaying function of the plastic volumetric and deviatoric strain increments $\Delta \varepsilon_{\mathrm{v}}^{\mathrm{p}}$ and $\Delta \boldsymbol{e}^{\mathrm{p}}$ as given by Equation 3.33. Hence, plastic strain hardening tends to increase the size of the bounding surface. On the contrary, plastic strain softening results in a decrease of the size of the bounding surface. Both effects are expressed by the former part of Equation 3.31. Moreover, the destructuration process leads to a decreasing size of the structured yield surface represented by the latter part of Equation 3.31. The total evolution of the size of the bounding surface is superposed.

The constitutive BSP model incorporates classical isotropic hardening for the evolution of the hardening variable $p_{0,\mathrm{i}}$ as used in the Cam-Clay models according to Equation 3.32.

The hardening variable $p_{0,\mathrm{i}}$ is controlling the evolution of the size of the intrinsic reference surface as a function of the plastic volumetric strain increment $\Delta\varepsilon_{\mathrm{v}}^{\mathrm{p}}$. Therefore, the BSP model is suitable to simulate the softening behavior of heavily overconsolidated clays on the dry side of the critical state even when employing an associated flow rule. The concept of isotropic hardening of the intrinsic reference surface in the p', q effective stress space is schematically illustrated in Figure 3.7.

The evolution of the structure variable S_{i} is given by Equations 3.33 and 3.34. Whereat, the constitutive parameter k_{i} specifies the rate of destructuration as a proportional factor and the constitutive parameter A describes the fraction of volumetric and deviatoric plastic strain increments $\Delta\varepsilon_{\mathrm{v}}^{\mathrm{p}}$ and $\Delta\boldsymbol{e}^{\mathrm{p}}$ influencing the destructuration. The void ratio e, the elastoplastic compression parameter λ and the elastic swelling parameter κ are introduced to ensure consistency with the classical isotropic hardening. During the destructuration process induced by volumetric and deviatoric plastic straining the structure variable evolves towards unity specifying the fully destructured state, where both surfaces coincide, so that $p_{0,\mathrm{s}} = p_{0,\mathrm{i}}$. It is to be noted that the frictional destructuration process as proposed by Taiebat et al. (2010) considering the reduction of the critical state stress ratio as a result of the influence of the progressive damage of the structure on the shear strength and the friction angle is not incorporated in the current study.

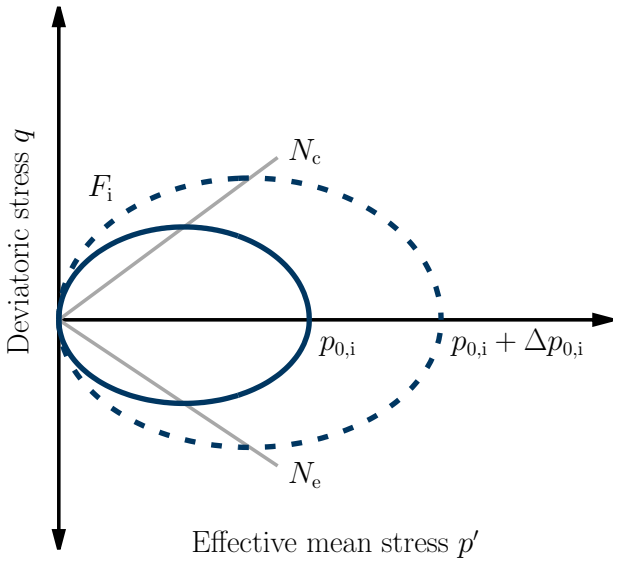

Figure 3.7: Schematic illustration of isotropic hardening of the intrinsic reference surface in the p', q effective stress space

3.3.8 Shape hardening function and damage variable

For stress paths inside the bounding surface the plasticity modulus K_p with respect to the current stress as given in Equation 3.6 is governed by the plasticity modulus $\bar{K}_\mathrm{p}$ with respect to the image stress state and the distance function $\hat{f}$ between the current stress and the image stress state on the bounding surface and the shape hardening function $\hat{h}$ given by Equation 3.37.
The shape hardening function $\hat{h}$ controls the degradation of stiffness, the accumulation of plastic strain and accordingly the evolution of the elastoplastic stress-strain response loops during cyclic loading as evaluated in section 2.3.4. Whereat, h_0 is a constitutive parameter defining the initial value of the shape hardening function. The higher the initial value h_0 the stiffer the initial model response. The accumulation of plastic strain is captured by the damage variable d. Whereat, the evolution of the damage variable d is given by Equation 3.38 as a function of the deviatoric plastic strain increment $\Delta \boldsymbol{e}^\mathrm{p}$ and the constitutive parameter a_dam as a proportional factor controlling the rate of stiffness degradation. The term $\{p_{0,\mathrm{s}}\}^3$ is added for reasons of stress-dependence and dimensional consistency of the shape hardening function. With increasing accumulated plastic deviatoric strain during cyclic loading the damage variable d increases and the shape hardening function $\hat{h}$ decreases. Consequently, the plasticity modulus K_p and the stiffness degrade and the model response becomes more soft and more plasticity is induced.

$$\hat{h} = \{p_{0,\mathrm{s}}\}^3 \, \frac{h_0}{1+d} \tag{3.37}$$

$$\Delta d = a_\mathrm{dam} \sqrt{\frac{2}{3} \, \Delta \boldsymbol{e}^\mathrm{p} : \Delta \boldsymbol{e}^\mathrm{p}} \tag{3.38}$$

3.3.9 Projection center

The projection center $\boldsymbol{\sigma}'_\mathrm{pc}(p'_\mathrm{pc}, \boldsymbol{s}_\mathrm{pc})$ is always updated to the last point of stress reversal to allow for a more accurate simulation of the evolution of plastic strain during unloading and reloading paths. A stress reversal is revealed by the condition related to the plastic loading index $L \leq 0$. That means the next stress increment is pointing inside the imaginary loading surface. After updating the projection center a new image stress state is determined by use of the radial projection of the current stress onto the bounding surface from the updated position of the projection center in direction of the stress increment. Consequently, the plastic loading index L will become positive again.

Because the projection center serves as the center of homology for the elastic nucleus the position of the elastic nucleus is updated in an analogous manner. Accordingly, the initial part of the next stress increment yields to purely elastic behavior depending on the size of the elastic nucleus. After crossing the elastic nucleus during further loading the plasticity modulus will again be calculated dependent on the distance between the current stress state and the updated image stress state on the bounding surface. This initially results in a stiff and predominantly elastic model response due to the large distance of the current stress state to the image stress state on the bounding surface. The model response is continuously getting more elastoplastic as the stress state approaches to the bounding surface. Hence, the update of the projection center allows for a more realistic modeling of the cyclic material behavior after stress reversal.
Moreover, the projection center underlies a certain translation and repositioning in the stress space with respect to the evolution of the hardening variables. The evolution of the projection center $\Delta\boldsymbol{\sigma}'_{\mathrm{pc}}(\Delta p'_{\mathrm{pc}}, \Delta\boldsymbol{s}_{\mathrm{pc}})$ as a function of the evolution of the hardening variables $\Delta\boldsymbol{q}$ is given by Equations 3.39 - 3.42.

$$\Delta p'_{\mathrm{pc}} = \frac{p'_{\mathrm{pc}}}{p_{0,\mathrm{s}}}\,\Delta p_{0,\mathrm{s}} \tag{3.39}$$

$$\begin{aligned}\Delta\boldsymbol{s}_{\mathrm{pc}} &= \frac{\boldsymbol{s}_{\mathrm{pc}}}{p_{0,\mathrm{s}}}\,\Delta p_{0,\mathrm{s}} \\ &\quad + \left\{ p'_{\mathrm{pc}}\,\boldsymbol{\Delta\alpha} - X_{\mathrm{pc}}\sqrt{\frac{2}{3}}\,\frac{p'_{\mathrm{pc}}\,\left\{p_{0,\mathrm{s}} - p'_{\mathrm{pc}}\right\}\,\frac{3}{2}\,\{\boldsymbol{\alpha}:\boldsymbol{\Delta\alpha}\}}{\sqrt{\left\{N^2 - \frac{3}{2}\,\{\boldsymbol{\alpha}:\boldsymbol{\alpha}\}\right\}\,p'_{\mathrm{pc}}\,\left\{p_{0,\mathrm{s}} - p'_{\mathrm{pc}}\right\}}}\,\boldsymbol{n}_{\mathrm{pc}} \right\}\end{aligned} \tag{3.40}$$

$$X_{\mathrm{pc}} = \frac{\sqrt{\frac{3}{2}\,\{\boldsymbol{s}_{\mathrm{pc}} - \boldsymbol{s}_\alpha\} : \{\boldsymbol{s}_{\mathrm{pc}} - \boldsymbol{s}_\alpha\}}}{\sqrt{\frac{3}{2}\,\{\boldsymbol{s}_{\mathrm{bs}} - \boldsymbol{s}_\alpha\} : \{\boldsymbol{s}_{\mathrm{bs}} - \boldsymbol{s}_\alpha\}}} \tag{3.41}$$

$$\boldsymbol{n}_{\mathrm{pc}} = \frac{\{\boldsymbol{s}_{\mathrm{pc}} - \boldsymbol{s}_\alpha\}}{|\boldsymbol{s}_{\mathrm{pc}} - \boldsymbol{s}_\alpha|} = \frac{\{\boldsymbol{s}_{\mathrm{pc}} - \boldsymbol{s}_\alpha\}}{\sqrt{\{\boldsymbol{s}_{\mathrm{pc}} - \boldsymbol{s}_\alpha\} : \{\boldsymbol{s}_{\mathrm{pc}} - \boldsymbol{s}_\alpha\}}} \tag{3.42}$$

$$a_{\mathrm{bs}} = \sqrt{\frac{\left\{N^2 - \frac{3}{2}\,\{\boldsymbol{\alpha}:\boldsymbol{\alpha}\}\right\}\,p'_{\mathrm{pc}}\,\left\{p_{0,\mathrm{s}} - p'_{\mathrm{pc}}\right\}}{\frac{3}{2}\,\{\boldsymbol{n}_{\mathrm{pc}}:\boldsymbol{n}_{\mathrm{pc}}\}}} \tag{3.43}$$

The update of the projection center with respect to the evolution of the hardening variables ensures the relative position within the evolving bounding surface due to isotropic or rotational hardening, destructuration or softening. This requirement arises from the condition of uniqueness of the image stress state for a given projection center and stress

state. To ensure the proper position of the projection center the ratio X_{pc} in Equation 3.41 should be kept constant. Whereat, $\boldsymbol{s}_{\alpha} = p'_{\mathrm{pc}}\,\boldsymbol{\alpha}$ and $\boldsymbol{s}_{\mathrm{bs}} = \boldsymbol{s}_{\alpha} + \boldsymbol{n}_{\mathrm{pc}}\,a_{\mathrm{bs}}$ is the stress state on the bounding surface, which is closest to the projection center.

3.4 Summary

A sophisticated constitutive BSP model of hierarchical structure was presented in this chapter. The hierarchical structure of the constitutive model generally allows for an adequate analysis of the influence of the mechanical behavior on the model response induced by mechanized tunneling. The constitutive BSP model accounts for the mechanical behavior of natural clay under complex stress paths by incorporating the following hierarchical features of the constitutive behavior.

- Extended MCC model
  - Critical state concept (Roscoe et al., 1958, 1963; Schofield and Wroth, 1968)
  - Classical theory of elastoplasticity
  - Modified Cam-Clay model (Burland, 1965; Roscoe and Burland, 1968)
  - Non-linear and stress-dependent elasticity
  - Isotropic hardening and softening with respect to volumetric plastic strain
  - Non-associated flow rule (Dafalias et al., 2006; Jiang and Ling, 2010; Jiang et al., 2012)
  - Lode angle dependence of the critical state surface and the N-cone (Dafalias et al., 2006; Jiang and Ling, 2010; Jiang et al., 2012)
- Saniclay model (Dafalias et al., 2006)
  - Additional consideration of inherent and stress-induced anisotropy by use of an anisotropic fabric stress tensor (Dafalias, 1986c) to account for the rotation of the bounding surface and the plastic potential surface
  - Rotational hardening rule with respect to plastic strain increment and loading direction (Dafalias, 1986c; Dafalias et al., 2006; Dafalias and Taiebat, 2013, 2014)

- Saniclay D model (Taiebat et al., 2010)
  - Additional consideration of initial structure and stress-induced destructuration by applying the concept of intrinsic reference surface and structure variable indicating the current degree of structure (Gens and Nova, 1993)
  - Evolution law for the structure variable considering destructuration with respect to volumetric and deviatoric plastic strain increments (Taiebat et al., 2010)
- Saniclay D + BSP model (Seidalinov and Taiebat, 2014; Barciaga et al., 2017)
  - Additional consideration of the bounding surface plasticity concept (Dafalias and Herrmann, 1982; Dafalias, 1986a; Dafalias and Herrmann, 1986b; Anandarajah and Dafalias, 1986; Seidalinov and Taiebat, 2014)
  - Smooth and more realistic elastoplastic model response in unloading-reloading cycles by means of BSP concept and update of projection center in case of stress reversal
  - Stiffness degradation and accumulation of plastic strain during cyclic loading by use of cyclic damage variable evolving with respect to deviatoric plastic strain increment

Furthermore, an overview of the constitutive parameters of the BSP model is given in Table 3.1. For employing the constitutive BSP model in a finite element code to analyze geotechnical problems such as mechanized tunneling the constitutive equations have to be numerically integrated. The appropriate numerical integration scheme applied in the present study will be presented in the next chapter.

Table 3.1: Overview of the constitutive parameters of the BSP model

Type	Parameter	Description
Critical state soil mechanics MCC	κ	Elastic swelling parameter
	ν	Poisson's ratio
	λ	Elastoplastic compression parameter
	M_{c}	Critical state stress ratio in triaxial compression
	M_{e}	Critical state stress ratio in triaxial extension
Non-associated flow rule	N_{c}	Parameter defining shape of BS in compression
	N_{e}	Parameter defining shape of BS in extension
Anisotropy and rotational hardening	α_0	Parameter defining initial rotation
	c_α	Parameter controlling the rate of rotation
	$s_\alpha = z_\alpha$	Parameters controlling bounding attractor
Structure and destructuration	$S_{\mathrm{i},0}$	Parameter defining initial structure
	k_{i}	Parameter controlling the rate of destructuration
	A	Parameter controlling fraction of plastic strain components
Bounding surface plasticity	s_{eln}	Parameter defining size of elastic nucleus
	h_0	Parameter defining initial shape hardening stiffness
	a_{dam}	Parameter controlling the rate of stiffness degradation
Initial conditions	e_0	Initial void ratio
	K_0	Coefficient of earth pressure at rest
	YSR	Yield stress ratio

4 Implementation of BSP model for natural clay

4.1 Concept

The finite element method is a powerful tool to analyze geotechnical boundary value problems such as mechanized tunneling. The entire domain is discretized by finite elements. Interpolation functions such as the strain interpolation matrix $\boldsymbol{B}$ are used to get from nodal values to the corresponding interpolated values at the Gauss integration points within an element and vice versa. Whereat, displacements $\boldsymbol{u}$ and forces $\boldsymbol{F}$ are acting at the nodes and strain $\boldsymbol{\varepsilon}$ and stress $\boldsymbol{\sigma}'$ are evaluated on the Gauss integration point level. This allows for the integration over the volume of all elements.
The finite element analysis requires the fulfillment of the global static equilibrium condition as given by Equation 4.1. That is, the increment of the nodal displacement tensor $\Delta\boldsymbol{u}$ multiplied by the global stiffness matrix $\boldsymbol{K}$ has to be in equilibrium with the unbalance force tensor $\Delta\boldsymbol{F} = \boldsymbol{F}_{\text{ext}} - \boldsymbol{F}_{\text{int}}$ composed of the external nodal forces and the internal nodal reaction forces.

$$\boldsymbol{K}\,\Delta\boldsymbol{u} = \boldsymbol{F}_{\text{ext}} - \boldsymbol{F}_{\text{int}} \tag{4.1}$$

When accounting for the constitutive behavior of soil, the unbalance force tensor $\Delta\boldsymbol{F}$ caused by the difference between external and internal forces has to be balanced by a stress increment tensor $\Delta\boldsymbol{\sigma}'$. Consequently, an admissible strain increment tensor $\Delta\boldsymbol{\varepsilon}$ has to be found to ensure equilibrium between external force, internal reaction and stress increment. Global iterative procedures incorporating all integration points have to be applied to find the appropriate strain field to satisfy the equilibrium condition. Iterative procedures to determine the strain field are needed because the global stiffness matrix is usually a function of the strain itself and the stress-strain relations are highly nonlinear. The current study is focusing on constitutive modeling. Therefore, a robust and efficient

integration procedure for the constitutive equations is emphasized in this chapter to get the final stress state related to a given strain increment. In the present work the integration is conducted along the incremental strain path at each Gauss point. The finite total strain increment is provided by the finite element code in each numerical integration step. The constitutive equations are solved for getting the final stress state via an algorithm for the plastic stress correction of an elastic trial stress state.

Various researchers investigated different explicit and implicit integration methods especially for critical state and bounding surface plasticity models and even sub-stepping approach (see e.g. Potts and Gens, 1985; Herrmann et al., 1987; Sloan, 1987; Borja and Lee, 1990; Potts and Zdravkovic, 1999; Jeremic and Sture, 1997; Manzari and Nour, 1997; Borja et al., 2001; Sloan et al., 2001; Rouainia and Wood, 2001; Tamagnini et al., 2002; Zhao et al., 2005; Kaliakin, 2005; Wang et al., 2006; Amorosi et al., 2008; Manzari and Yonten, 2014; Kan and Taiebat, 2014a; Kan et al., 2014b; Hu and Liu, 2014). Explicit methods are based on the initial stress state and state variables, whereas implicit methods are based on the unknown final stress state and state variables. Since the final stress state is unknown the implicit integration requires iterations until the solution converges. However, in this study an explicit integration method is employed as it is more straightforward and more robust with respect to the convergence of the solution with varying strain increment size.

This chapter starts with a short introduction on a global iterative procedure based on a Modified Newton-Raphson approach employed by the finite element code Plaxis. Moreover, the coupling between global iterative procedure and integration procedure of the constitutive equations is discussed. Hence, the communication between the finite element code Plaxis and the constitutive model is introduced.

Afterwards the numerical integration of the constitutive equations is emphasized. Special focus is set on the description of an explicit integration scheme with automatic error control and sub-stepping approach and a second order accurate Forward Euler solution (Modified Euler approach) which is adapted and further modified in this study to be applicable to the BSP model. Furthermore, a drift correction algorithm is presented. The drift correction may become relevant when due to numerical inaccuracy and tolerances the stress state slightly lies outside the bounding surface after a successful Modified Euler calculation step. In addition to the integration schemes some specific subroutines are highlighted such as determination and calculation of tangent and secant elastic stiffness matrix, elastic nucleus, similarity ratio, intersection stress and intersection factor and Lode angle dependence of the bounding surface. Finally, some particular incremental formulations are provided such as gradients of the bounding surface and plastic potential

with respect to stress and Lode angle, gradient of the Lode angle with respect to stress and gradients of the bounding surface with respect to hardening variables.

4.2 Global iterative procedure

The aim of the global iterative procedure is to fulfill the global static equilibrium between incremental displacement tensor $\Delta \boldsymbol{u}$ and unbalance force tensor $\Delta \boldsymbol{F}$ according to Equation 4.1. The concept of the global iterative procedure by means of the Modified Newton-Raphson approach is visualized in Figure 4.1. At the beginning of each calculation step the global stiffness matrix $\boldsymbol{K}$ has to be formed. Within the Modified Newton-Raphson approach employed by the finite element code Plaxis the global stiffness matrix is kept constant for all iterations within one calculation step. Whereat, a full Newton-Raphson approach would update the global stiffness matrix for each iteration. The more accurate the global stiffness matrix the less iterations are needed to achieve convergence. However, in the global iterative procedure used in the finite element code Plaxis the calculation of the global stiffness matrix $\boldsymbol{K}$ is based on the elastic stiffness matrix $\boldsymbol{D}^{\mathrm{e}}$ rather than the tangent stiffness matrix $\boldsymbol{D}^{\mathrm{ep}}$ as shown in Equation 4.2. Moreover, the unbalance force tensor $\Delta \boldsymbol{F} = \boldsymbol{F}_{\mathrm{ext}} - \boldsymbol{F}_{\mathrm{int}}$ is initialized as the difference between the external force tensor $\boldsymbol{F}_{\mathrm{ext}}$ acting in the current step and the internal reaction tensor $\boldsymbol{F}_{\mathrm{int}}$ from the previous step. The reaction tensor from the previous step is derived as a function of the constitutive stress tensor $\boldsymbol{\sigma}'$ from the previous step and the transposed strain interpolation matrix $\boldsymbol{B}^{\mathrm{T}}$ integrated over the volume V.

$$\boldsymbol{K} = \int \boldsymbol{B}^{\mathrm{T}}\, \boldsymbol{D}^{\mathrm{e}}\, \boldsymbol{B}\, \mathrm{dV} \tag{4.2}$$

For each iteration within one calculation step the following procedure is applied. The displacement increment tensor $\Delta \boldsymbol{u}$ is updated by adding a term from the equilibrium condition as the product of the inverted global stiffness matrix $\boldsymbol{K}^{-1}$ and the current unbalance force tensor $\Delta \boldsymbol{F}$ as given by Equation 4.3. The strain increment tensor $\Delta \boldsymbol{\varepsilon}$ with respect to the integration point level is derived from the current displacement increment tensor $\Delta \boldsymbol{u}$ multiplied by the strain interpolation matrix $\boldsymbol{B}$ as specified by Equation 4.4.

$$\Delta \boldsymbol{u} = \Delta \boldsymbol{u} + \boldsymbol{K}^{-1}\, \Delta \boldsymbol{F} \tag{4.3}$$

$$\Delta \boldsymbol{\varepsilon} = \boldsymbol{B}\, \Delta \boldsymbol{u} \tag{4.4}$$

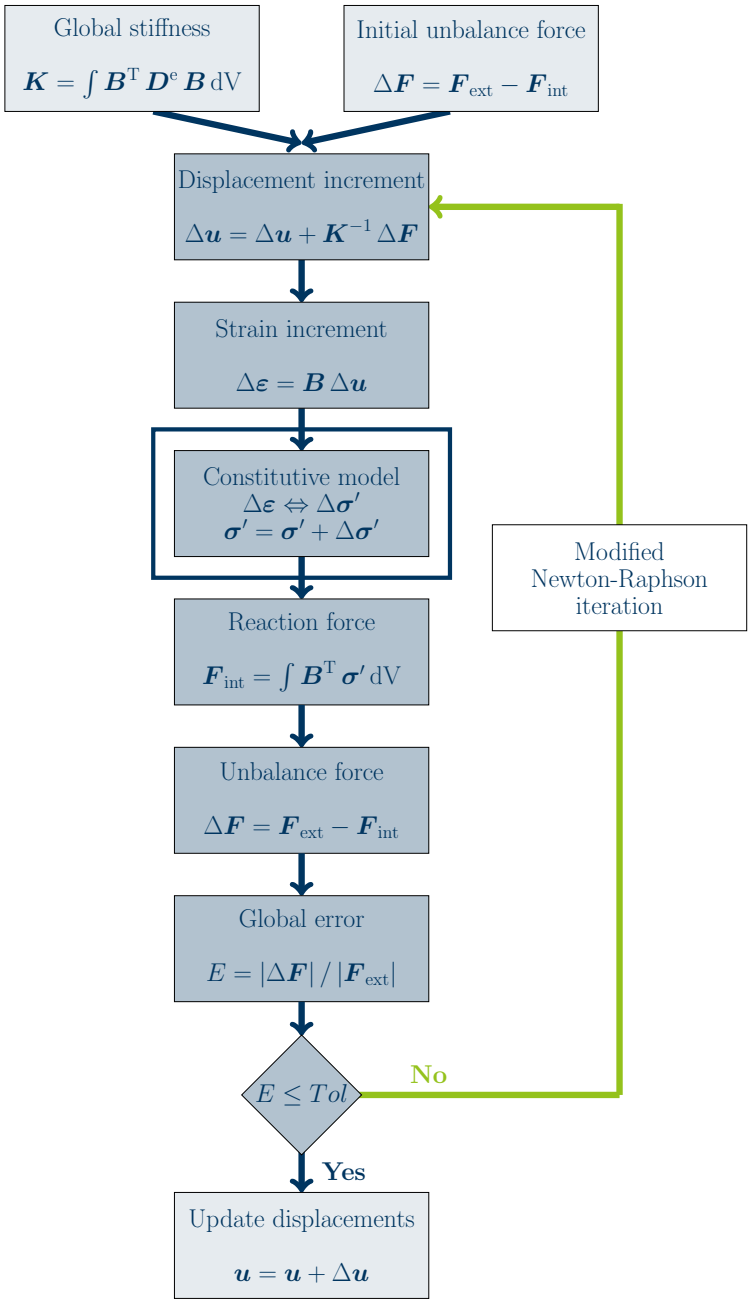

Figure 4.1: The concept of the global iterative procedure by means of Modified Newton-Raphson approach

For each Gauss integration point in each global iteration the admissible constitutive stress $\boldsymbol{\sigma}'$ corresponding to the given strain increment $\Delta\boldsymbol{\varepsilon}$ has to be calculated by applying a proper integration procedure. The integration procedure incorporates an adequate constitutive model with incremental stress-strain relations acting on the integration point

level. Afterwards, the resulting reaction force tensor $\boldsymbol{F}_{\text{int}}$ is formed and updated as a function of the constitutive stress tensor $\boldsymbol{\sigma}'$ obtained based on the stress-strain relations on the integration point level multiplied by the transposed strain interpolation matrix $\boldsymbol{B}^{\text{T}}$ integrated over the volume to account for all Gauss integration points as given by Equation 4.5. Accordingly, the unbalance force tensor $\Delta\boldsymbol{F}$ has to be updated. The global error E, which is defined by Equation 4.6 as a function of the ratio between the norm of the unbalance force tensor $|\Delta\boldsymbol{F}|$ and the norm of the external force tensor $|\boldsymbol{F}_{\text{ext}}|$, will be subsequently calculated. If the calculated global error is larger than a predefined tolerance value so that $E > E_{\text{Tol}}$ a further iteration is required. The new iteration will consider the updated unbalance force tensor $\Delta\boldsymbol{F}$ for the new calculation of the displacement increment tensor $\Delta\boldsymbol{u}$ and the strain increment tensor $\Delta\boldsymbol{\varepsilon}$.

$$\boldsymbol{F}_{\text{int}} = \int \boldsymbol{B}^{\text{T}}\,\boldsymbol{\sigma}'\,\text{dV} \tag{4.5}$$

$$E = \frac{|\Delta\boldsymbol{F}|}{|\boldsymbol{F}_{\text{ext}}|} \tag{4.6}$$

In case of getting a global error smaller than the tolerance value so that $E \leq E_{\text{Tol}}$ the iterative procedure of the current calculation step is successful and the system is in a global equilibrium state. The displacements from the former calculation step can be finally updated by the derived displacement increment according to Equation 4.7. Special techniques and algorithms such as arc-length control, over-relaxation and extrapolation may improve the global iterative procedure (Brinkgreve et al., 2016).

$$\boldsymbol{u} = \boldsymbol{u} + \Delta\boldsymbol{u} \tag{4.7}$$

4.3 Coupling between FE-code and constitutive BSP model

The current study emphasizes the constitutive part of the global iterative procedure as highlighted in Figure 4.1. The constitutive part covers the stress-strain behavior by means of an adequate constitutive model. Therefore, the finite element code has to be coupled with the constitutive BSP model and the constitutive equations have to be numerically integrated as described in the following sections. To properly perform the global iterative

procedure including the integration procedure a coupling between the finite element code Plaxis and the constitutive BSP model is required. Firstly, the constitutive BSP model for natural clay programmed in Fortran programming language has to be compiled as a Dynamic Link Library (DLL) and added as a user-defined soil model to the finite element code Plaxis.
The finite element code provides information on effective stress, excess pore-water pressure and state variables for each Gauss integration point at the beginning of each calculation step. In addition, the entire strain and time increments for the current calculation step are given by the finite element code. The global iterative procedure supplies a strain increment for the integration based on the balance between external and internal forces. All information from the global iterative procedure are transferred to the constitutive BSP model at the beginning of the calculation step. Furthermore, the finite element code transfers the constant constitutive BSP model parameters given as a user input. After a successful calculation the stress-strain-time relationship of the constitutive BSP model provides effective stress, excess pore-water pressure and state variables with respect to the given strain increment. The information at the end of the calculation step are again transferred to the finite element code to continue the global iterative procedure.
The Plaxis structure for the implementation of user-defined soil models requires the performance of the following so-called ID tasks within the constitutive model: The state variables have to be initialized once at the very first beginning of the entire calculation procedure. The number of state variables has to be defined as well. For example, state variables defining initial void ratio, initial amount of structure, initial size and rotation of the surfaces and initial value of the damage variable must be specified. Afterwards, within the entire calculation the state variables are stored as internal variables and automatically transferred from one calculation step to the next one. However, the initial stress state of the soil domain is provided by the finite element code based on a user-defined K_0 value or the gravity loading at the beginning of the entire calculation.
Moreover, the main part of the constitutive BSP model deals with the stress-strain relations. That is, the increments and the final values of effective stress, excess pore-water pressure and state variables have to be calculated with respect to the given strain increment provided by the global iterative procedure by calling the constitutive BSP model. For the calculation of the constitutive relations an appropriate integration scheme is essential as described in section 4.4. The state variables are calculated based on the previous values of the state variables and the new stress state. When applying undrained conditions the excess pore-water pressure is calculated as a function of the bulk modulus of water and the total volumetric strain.

However, in this study the elastic material stiffness matrix rather than tangent stiffness matrix has to be calculated by the constitutive BSP model and provided to the finite element code. The elastic material stiffness at the beginning of each global calculation step is required for the global iterative procedure used in the finite element code. Besides, the stiffness matrix attributes have to be defined such as stress-dependence and symmetry. In the present study time-dependence of the stiffness matrix is not considered. If the stress-dependence is activated, the global stiffness matrix is created and decomposed at the beginning of each global calculation step based on the current stress and strain (Modified Newton-Raphson approach).

4.4 Integration of constitutive equations

4.4.1 General formulations

The aim of the procedure is to provide an updated stress state ${}_n\boldsymbol{\sigma}'$ at the end of the calculation step according to Equation 4.8 based on the stress state at the beginning of the calculation step ${}_{n-1}\boldsymbol{\sigma}'$ and a stress increment $\Delta\boldsymbol{\sigma}'$, which has to be properly obtained based on the given strain increment $\Delta\boldsymbol{\varepsilon}$.

$$ {}_n\boldsymbol{\sigma}' \;=\; {}_{n-1}\boldsymbol{\sigma}' + \Delta\boldsymbol{\sigma}' \tag{4.8} $$

Due to the fact that the constitutive equations of the bounding surface plasticity model are highly nonlinear it is not possible to derive exact solutions. Consequently, the constitutive equations have to be numerically integrated to properly approximate the soil behavior. The constitutive equations are often formulated in a way that an infinitesimal increment of stress $\Delta\boldsymbol{\sigma}'$ is related to an infinitesimal increment of strain $\Delta\boldsymbol{\varepsilon}$ via an elastoplastic stiffness matrix $\boldsymbol{D}^{\mathrm{ep}}$ as given in Equation 4.9. Hence, the integration of the constitutive equations follows a certain stress return algorithm. An initially assumed elastic stress predictor increment $\Delta\boldsymbol{\sigma}'_{\mathrm{pred}} = \boldsymbol{D}^{\mathrm{e}} : \Delta\boldsymbol{\varepsilon}$ governed by the elastic stiffness matrix $\boldsymbol{D}^{\mathrm{e}}$ is corrected by a plastic stress corrector increment $\Delta\boldsymbol{\sigma}'_{\mathrm{corr}} = L\,\boldsymbol{D}^{\mathrm{e}} : \{\partial G/\partial\bar{\boldsymbol{\sigma}}'\}$ controlled by the plastic flow rule including the plastic loading index L and the gradient of the plastic potential surface with respect to the image stress state $\{\partial G/\partial\bar{\boldsymbol{\sigma}}'\}$.
For numerical integration the return algorithm requires the knowledge of stress state and internal variables. To obtain the unknown stress increment from a given strain increment

the constitutive equations of the soil model have to be integrated in each Gauss integration point for each calculation step. For a given strain increment the differential equations above have to be integrated by use of a pseudo time T, where ${}_{n-1}T = 0$ is the time at the beginning of the calculation step, ${}_{n}\Delta T = 1$ is the pseudo time increment for the entire calculation step corresponding to the provided strain increment $\Delta\boldsymbol{\varepsilon}$ and ${}_{n}T = 1$ is the time at the end of the calculation step. Consequently, for each calculation step the following condition has to be fulfilled ${}_{n}T = {}_{n-1}T + {}_{n}\Delta T = 1$. That is, within a calculation step the strain increment provided by the finite element code has to be entirely applied. Note: The left subscript n denotes the calculation step number.

$$\begin{aligned} \Delta\boldsymbol{\sigma}' &= \boldsymbol{D}^{\mathrm{ep}} : \Delta\boldsymbol{\varepsilon} \\ &= \boldsymbol{D}^{\mathrm{e}} : \{\Delta\boldsymbol{\varepsilon} - \Delta\boldsymbol{\varepsilon}^{\mathrm{p}}\} \\ &= \boldsymbol{D}^{\mathrm{e}} : \Delta\boldsymbol{\varepsilon} - L\, \boldsymbol{D}^{\mathrm{e}} : \left\{ \frac{\partial G}{\partial \bar{\boldsymbol{\sigma}}'} \right\} \end{aligned} \tag{4.9}$$

where:

$$\boldsymbol{D}^{\mathrm{ep}} = \boldsymbol{D}^{\mathrm{e}} - \frac{\boldsymbol{D}^{\mathrm{e}} : \left\{ \frac{\partial G}{\partial \bar{\boldsymbol{\sigma}}'} \right\} : \left\{ \frac{\partial F}{\partial \bar{\boldsymbol{\sigma}}'} \right\} : \boldsymbol{D}^{\mathrm{e}}}{\left\{ \frac{\partial F}{\partial \bar{\boldsymbol{\sigma}}'} \right\} : \boldsymbol{D}^{\mathrm{e}} : \left\{ \frac{\partial G}{\partial \bar{\boldsymbol{\sigma}}'} \right\} + K_{\mathrm{p}}} \tag{4.10}$$

$$L = \frac{\left\{ \frac{\partial F}{\partial \bar{\boldsymbol{\sigma}}'} \right\} : \boldsymbol{D}^{\mathrm{e}} : \Delta\boldsymbol{\varepsilon}}{\left\{ \frac{\partial F}{\partial \bar{\boldsymbol{\sigma}}'} \right\} : \boldsymbol{D}^{\mathrm{e}} : \left\{ \frac{\partial G}{\partial \bar{\boldsymbol{\sigma}}'} \right\} + K_{\mathrm{p}}} \tag{4.11}$$

$$K_{\mathrm{p}} = \bar{K}_{\mathrm{p}} + \hat{h}\, \frac{\delta}{\langle r - s_{\mathrm{eln}}\, \delta \rangle} = \bar{K}_{\mathrm{p}} + \hat{h} \left\langle \frac{b-1}{b - \{b-1\}\ s_{\mathrm{eln}}} \right\rangle \tag{4.12}$$

$$\bar{K}_{\mathrm{p}} = -\left\{ \frac{\partial F}{\partial \boldsymbol{q}} \right\} : \tilde{\boldsymbol{q}} = -\left\{ \frac{\partial F}{\partial p_{0,\mathrm{s}}}\, \tilde{p}_{0,\mathrm{s}} + \frac{\partial F}{\partial \boldsymbol{\alpha}} : \tilde{\boldsymbol{\alpha}} \right\} \tag{4.13}$$

4.4.2 Explicit integration scheme with automatic error control and sub-stepping approach

The numerical integration of the equations of the present constitutive BSP model is based on the explicit integration scheme with automatic error control and sub-stepping approach, which was proposed by Sloan (1987) and Sloan et al. (2001). The integration scheme is following a second order accurate Forward Euler solution (Modified Euler approach). In this work, the explicit integration scheme originally developed for elastoplastic constitutive models was adapted and refined to accommodate the more complex constitutive equations of the bounding surface plasticity framework. Explicit integration schemes are based on the determination of the final stress of the current calculation step with respect to the current stress state and state variables. That is, the gradients of the yield surface and the plastic potential surface and the hardening/softening rules are evaluated related to the current stress state and state variables. The main advantage of the explicit integration scheme is the straightforward implementation due to the requirement of just first derivatives of the yield surface and plastic potential surface. The explicit integration of the constitutive BSP model is described in the following.

Transfer of initial conditions and entire strain increment

At the beginning of each calculation step the finite element code provides the initial conditions such as stress state ${}_0\boldsymbol{\sigma}'$, hardening variables ${}_0\boldsymbol{q}$ such as ${}_0p_{0,\mathrm{s}}$ and ${}_0\boldsymbol{\alpha}$, structure variable ${}_0S_{\mathrm{i}}$, damage variable ${}_0d$, void ratio ${}_0e$ and position of the projection center ${}_0\boldsymbol{\sigma}'_{\mathrm{pc}}$. Furthermore, the finite element code supplies the entire strain increment $\Delta\boldsymbol{\varepsilon}$ for the current calculation step.

Transfer of initial conditions and entire strain increment $\Delta\boldsymbol{\varepsilon}$

Get initial conditions

$${}_0\boldsymbol{\sigma}',\ {}_0\boldsymbol{q},\ {}_0S_{\mathrm{i}},\ {}_0d,\ {}_0e,\ {}_0\boldsymbol{\sigma}'_{\mathrm{pc}}$$

Get entire strain increment

$$\Delta\boldsymbol{\varepsilon}$$

Automatic error control and sub-stepping approach

The explicit integration scheme proposed by Sloan (1987) and Sloan et al. (2001) incorporates an automatic error control and sub-stepping approach. Dependent on the maximum

relative error ${}_mR$ of the final stress and hardening variables computed during the calculation step, the entire strain increment $\Delta\boldsymbol{\varepsilon}$ is automatically divided into a certain number of sub-steps governed by the variable size of a pseudo time increment ${}^i_m\Delta T$. Note: In the following the left subscript m denotes the sub-step number $[1, m_{\max}]$ and the left superscript i denotes the iteration number of the pseudo time increment $[1, i_{\max}]$ for the sub-stepping with respect to the relative error. The relative error occurs due to the approximate integration of the constitutive equations. Whereat, the estimation of the relative error will be done by comparison of the calculated results of first order and the second order accurate forward Euler solution. The Modified Euler approach will be described in detail in the following section 4.4.3. However, the accuracy of the numerical integration is controlled by the error tolerance R_{Tol}, which in this study is specified as 10^{-4}.
That is, the pseudo time increment will be updated with respect to the relative error. Hence, the strain increment will be sub-divided as long as the relative error ${}_mR$ is larger than the error tolerance R_{Tol} or the maximum number of sub-steps $m_{\max}$ is reached. After each successful calculation of a sub-step the pseudo time would be updated, so that ${}^i_mT = {}^i_{m-1}T + {}^i_m\Delta T$, where ${}^i_{m-1}T$ is the pseudo time at the beginning of the sub-step, ${}^i_m\Delta T$ is the pseudo time increment corresponding to the current strain sub-increment ${}_m\Delta\boldsymbol{\varepsilon}$ and ${}^i_mT$ is the pseudo time at the end of the sub-step. Furthermore, the pseudo time increment will be adjusted during the sub-stepping loop with respect to the relative error achieved during a successful current sub-step to accelerate the computational speed. That is, if the pseudo time increment from the current sub-step was suitable to fulfill the error tolerance, the pseudo time increment in the next sub-step will be slightly increased. The entire calculation step is completed when the pseudo time at the end of any sub-step ${}^i_mT$ reaches the required pseudo time at the end of the entire calculation step ${}_nT$. That means, the entire strain increment is applied, so that ${}^i_mT = {}_nT = 1$. Whereat, the pseudo time is summed up over all sub-steps. In brief, the automatic error control and sub-stepping approach ensures the accuracy of the obtained numerical solution.

Setting of initial time conditions

At the beginning of the calculation step the initial pseudo time is set to zero (${}^i_0T = 0$) and the pseudo time increment is set to one (${}^i_m\Delta T = 1$). Therefore, an entire pseudo time step is assumed. This is, the entire strain increment is applied at once for the first trial.

Setting of initial time conditions

Set initial time and assume entire pseudo time increment

$${}^i_0T = 0 \text{ and } {}^i_m\Delta T = 1$$

Set counting variable for sub-step number $m = 1$

Set counting variable for iteration of pseudo time increment $i = 1$

Sub-stepping loop

After setting the initial conditions at the beginning of the calculation step the "do while" loop for the sub-stepping approach starts. The loop continues as long as the pseudo time at the beginning of the current sub-step does not reach the required pseudo time of the entire calculation step corresponding to the entire strain increment (do while ${}^{i}_{m-1}T < {}_{n}T = 1$). The loop stops when the pseudo time at the end of the current sub-step summed up over all sub-steps reaches the pseudo time at the end of the entire calculation step ${}^{i}_{m}T = {}_{n}T = 1$.

Sub-stepping loop
Do While $\left\{{}^{i}_{m-1}T < 1\right\}$

Calculation of strain sub-increment and elastic trial stress state

At the beginning of each loop the strain sub-increment ${}_{m}\Delta\boldsymbol{\varepsilon}$ will be calculated based on the pseudo time increment ${}^{i}_{m}\Delta T$ as a certain proportion of the entire strain increment $\Delta\boldsymbol{\varepsilon}$ provided by the finite element code. The elastic trial stress increment ${}_{m}\Delta\boldsymbol{\sigma}'_{\text{trial}}$ is calculated using the secant elastic stiffness matrix ${}_{m}\boldsymbol{D}^{\text{e}}_{\text{sec}}$ and the current strain sub-increment ${}_{m}\Delta\boldsymbol{\varepsilon}$. The elastic trial stress ${}_{m}\boldsymbol{\sigma}'_{\text{trial}}$ for the current sub-step is the sum of the stress at the beginning of the sub-step ${}_{m-1}\boldsymbol{\sigma}'$ and the current stress increment ${}_{m}\Delta\boldsymbol{\sigma}'_{\text{trial}}$. The secant elastic stiffness matrix ${}_{m}\boldsymbol{D}^{\text{e}}_{\text{sec}}\left({}_{m-1}\boldsymbol{\sigma}',\ {}_{m-1}e,\ {}_{m}\Delta\boldsymbol{\varepsilon}_{\text{v}}\right)$ is derived as a function of the stress ${}_{m-1}\boldsymbol{\sigma}'$ and void ratio ${}_{m-1}e$ at the beginning of the sub-step and the current volumetric strain sub-increment ${}_{m}\Delta\boldsymbol{\varepsilon}_{\text{v}}$ as given in Equation 4.45. The concept of the secant elastic stiffness matrix as given in section 4.4.5 is employed to accurately find the elastic trial stress state in case of having transition from elastic to the elastoplastic state.

Calculation of strain sub-increment ${}_{m}\Delta\boldsymbol{\varepsilon}$ and elastic trial stress state ${}_{m}\boldsymbol{\sigma}'_{\text{trial}}$
Calculate strain sub-increment

$${}_{m}\Delta\boldsymbol{\varepsilon} = {}^{i}_{m}\Delta T\ \Delta\boldsymbol{\varepsilon}$$

Calculate elastic trial stress increment

$${}_{m}\Delta\boldsymbol{\sigma}'_{\text{trial}} = {}_{m}\boldsymbol{D}^{\text{e}}_{\text{sec}}\left({}_{m-1}\boldsymbol{\sigma}',\ {}_{m-1}e,\ {}_{m}\Delta\boldsymbol{\varepsilon}_{\text{v}}\right) : {}_{m}\Delta\boldsymbol{\varepsilon}$$

Calculate elastic trial stress

$${}_{m}\boldsymbol{\sigma}'_{\text{trial}} = {}_{m-1}\boldsymbol{\sigma}' + {}_{m}\Delta\boldsymbol{\sigma}'_{\text{trial}}$$

Purely elastic model response

For each sub-step the location of the current stress state ${}_{m-1}\boldsymbol{\sigma}'$ at the beginning of the sub-step and the elastic trial stress state ${}_{m}\boldsymbol{\sigma}'_{\mathrm{trial}}$ are checked in relation to the position of the elastic nucleus f_{eln}. This procedure allows to distinguish between a purely elastic and an elastoplastic stress path. However, the elastic nucleus is implicitly defined by the projection center $\boldsymbol{\sigma}'_{\mathrm{pc}}$ specifying the position in the stress space and the constitutive parameter s_{eln} as an indirect measure of the size as given in section 4.4.6. Whereat, the elastic nucleus with respect to the stress at the beginning of the sub-step $f_{\mathrm{eln}}({}_{m-1}\boldsymbol{\sigma}', {}_{m-1}\boldsymbol{q}, {}_{m-1}\boldsymbol{\sigma}'_{\mathrm{pc}})$ and the elastic nucleus with respect to the trial stress $f_{\mathrm{eln}}({}_{m}\boldsymbol{\sigma}'_{\mathrm{trial}}, {}_{m-1}\boldsymbol{q}, {}_{m-1}\boldsymbol{\sigma}'_{\mathrm{pc}})$ are both calculated based on the hardening variables ${}_{m-1}\boldsymbol{q}$ and the position of the projection center ${}_{m-1}\boldsymbol{\sigma}'_{\mathrm{pc}}$ at the beginning of the sub-step.
If both the current and the trial stress are located inside the elastic nucleus, so that $f_{\mathrm{eln}}({}_{m-1}\boldsymbol{\sigma}') < +Tol$ and $f_{\mathrm{eln}}({}_{m}\boldsymbol{\sigma}'_{\mathrm{trial}}) < +Tol$ the material behavior is fully elastic. Due to small deviations and impreciseness in the numerical calculation and for the sake of the numerical stability a positive tolerance value $+Tol$ (here specified as 10^{-7}) is introduced for checking the elastic criterion. In that case, the elastic trial stress state will be accepted as the final stress state of the sub-step, so that ${}_{m}\boldsymbol{\sigma}' = {}_{m}\boldsymbol{\sigma}'_{\mathrm{trial}}$. The hardening variables ${}_{m}\boldsymbol{q} = {}_{m-1}\boldsymbol{q}$, the structure variable ${}_{m}S_{\mathrm{i}} = {}_{m-1}S_{\mathrm{i}}$, the damage variable ${}_{m}d = {}_{m-1}d$ and the projection center ${}_{m}\boldsymbol{\sigma}'_{\mathrm{pc}} = {}_{m-1}\boldsymbol{\sigma}'_{\mathrm{pc}}$ are kept unchanged. The void ratio ${}_{m}e$ at the end of the sub-step is calculated with respect to the increment of the volumetric strain ${}_{m}\Delta\boldsymbol{\varepsilon}^{\mathrm{v}}$. The pseudo time at the end of the current sub-step ${}^{i}_{m}T$ will be updated. However, the pseudo time increment is kept constant for the next sub-step ${}^{i}_{m+1}\Delta T = {}^{i}_{m}\Delta T$. Just in case the pseudo time at the end of the next sub-step ${}^{i}_{m+1}T$ would exceed the maximum value of 1, the pseudo time increment for the next sub-step ${}^{i}_{m+1}\Delta T$ would be adjusted. Finally, the counting variable m for the sub-stepping loop is increased by 1 and the loop starts again (Do While $\{{}^{i}_{m-1}T < 1\}$).

Check for purely elastic model response

If $\{f_{\mathrm{eln}}({}_{m-1}\boldsymbol{\sigma}', {}_{m-1}\boldsymbol{q}, {}_{m-1}\boldsymbol{\sigma}'_{\mathrm{pc}}) < +Tol\}$ AND $\{f_{\mathrm{eln}}({}_{m}\boldsymbol{\sigma}'_{\mathrm{trial}}, {}_{m-1}\boldsymbol{q}, {}_{m-1}\boldsymbol{\sigma}'_{\mathrm{pc}}) < +Tol\}$

Then Do (purely elastic model response)

Update stress

$${}_{m}\boldsymbol{\sigma}' = {}_{m}\boldsymbol{\sigma}'_{\mathrm{trial}}$$

Keep variables unchanged

$${}_{m}\boldsymbol{q} = {}_{m-1}\boldsymbol{q}$$

$${}_{m}S_{\mathrm{i}} = {}_{m-1}S_{\mathrm{i}}$$

$${}_{m}d = {}_{m-1}d$$

$${}_{m}\boldsymbol{\sigma}'_{\mathrm{pc}} = {}_{m-1}\boldsymbol{\sigma}'_{\mathrm{pc}}$$

Update void ratio

$${}_{m}e = {}_{m-1}e - {}_{m}\Delta\boldsymbol{\varepsilon}^{\mathrm{v}} \ \{1 + {}_{m-1}e\}$$

Update time and time step

$${}^{i}_{m}T = {}^{i}_{m-1}T + {}^{i}_{m}\Delta T$$

$${}^{i}_{m+1}\Delta T = \min\left[{}^{i}_{m}\Delta T,\ 1 - {}^{i}_{m}T\right] \text{ (max. entire time } {}^{i}_{m+1}T = 1)$$

Set $m = m + 1$

Go To sub-stepping loop

Else Do (elastoplastic model response)

Elastoplastic transition

If the stress ${}_{m-1}\boldsymbol{\sigma}'$ at the beginning of the sub-step is located within or on the elastic nucleus so that $f_{\mathrm{eln}}({}_{m-1}\boldsymbol{\sigma}',\ {}_{m-1}\boldsymbol{q},\ {}_{m-1}\boldsymbol{\sigma}'_{\mathrm{pc}}) < +Tol$ and the elastic trial tress ${}_{m}\boldsymbol{\sigma}'_{\mathrm{trial}}$ lies outside the elastic nucleus, so that $f_{\mathrm{eln}}({}_{m}\boldsymbol{\sigma}'_{\mathrm{trial}},\ {}_{m-1}\boldsymbol{q},\ {}_{m-1}\boldsymbol{\sigma}'_{\mathrm{pc}}) > +Tol$ the material behavior undergoes a transition from a purely elastic state to an elastoplastic state. Accordingly, the elastic trial stress path intersects the elastic nucleus at the initially unknown intersection stress ${}_{m}\boldsymbol{\sigma}'_{\mathrm{inter}}$. Due to numerical calculation issues the positive tolerance value $+Tol$ (here specified as 10^{-7}) is again used for checking the elastoplastic transition. If both stresses are located outside the elastic nucleus so that $f_{\mathrm{eln}}({}_{m-1}\boldsymbol{\sigma}',\ {}_{m-1}\boldsymbol{q},\ {}_{m-1}\boldsymbol{\sigma}'_{\mathrm{pc}}) > +Tol$ and $F_{\mathrm{eln}}({}_{m}\boldsymbol{\sigma}'_{\mathrm{trial}},\ {}_{m-1}\boldsymbol{q},\ {}_{m-1}\boldsymbol{\sigma}'_{\mathrm{pc}}) > +Tol$ the material behavior is purely elastoplastic. That is, the trial stress path does not intersect the elastic nucleus.

Before starting the elastoplastic calculation, the stress state ${}_{m-1}\boldsymbol{\sigma}'$ and void ratio ${}_{m-1}e$ at the beginning of the sub-step are stored as ${}_{m-1}\boldsymbol{\sigma}'_{\mathrm{reset}}$ and ${}_{m-1}e_{\mathrm{reset}}$, respectively. This is required because in case of having an elastoplastic transition both stress and void ratio will be updated to the corresponding values at the onset of the plastic yielding. The variables ${}_{m-1}\boldsymbol{q}$, ${}_{m-1}S_{\mathrm{i}}$, ${}_{m-1}d$ are not affected by the update to the onset of the plastic yielding due to the purely elastic material behavior until reaching the intersection stress ${}_{m}\boldsymbol{\sigma}'_{\mathrm{inter}}$. The stress and void ratio at the beginning of the sub-step are needed if a stress reversal is identified during the elastoplastic calculation at any plastic loading index $L < 0$. In that

case, the projection center ${}_{m-1}\boldsymbol{\sigma}'_{\mathrm{pc}}$ has to be updated to the stress state at which the stress reversal occurs rather than the stress state at the onset of plastic yielding. That is, the projection center is updated to ${}_{m-1}\boldsymbol{\sigma}'_{\mathrm{pc}} = {}_{m-1}\boldsymbol{\sigma}'_{\mathrm{reset}}$, which corresponds to the stress at the beginning of the sub-step. Afterwards, the calculation of the current sub-step starts again from the beginning of the sub-stepping loop with ${}_{m-1}\boldsymbol{\sigma}'_{\mathrm{reset}}$ and ${}_{m-1}e_{\mathrm{reset}}$. Additionally, an update of the projection center to the last stress reversal causes an update of the elastic nucleus because the projection center is the center of homology of the elastic nucleus and the bounding surface. Therefore, when re-starting the sub-stepping loop an intersection with the elastic nucleus has to be newly calculated based on the reset values of stress ${}_{m-1}\boldsymbol{\sigma}'_{\mathrm{reset}}$ and void ratio ${}_{m-1}e_{\mathrm{reset}}$.

Store stress and void ratio at the beginning of the sub-step for the case of updating the projection center when having stress reversal

$${}_{m-1}\boldsymbol{\sigma}'_{\mathrm{reset}} = {}_{m-1}\boldsymbol{\sigma}'$$

$${}_{m-1}e_{\mathrm{reset}} = {}_{m-1}e$$

If the stress undergoes a transition from a purely elastic state $f_{\mathrm{eln}}({}_{m-1}\boldsymbol{\sigma}', {}_{m-1}\boldsymbol{q}, {}_{m-1}\boldsymbol{\sigma}'_{\mathrm{pc}}) < +Tol$ to an elastoplastic state $f_{\mathrm{eln}}({}_{m}\boldsymbol{\sigma}'_{\mathrm{trial}}, {}_{m-1}\boldsymbol{q}, {}_{m-1}\boldsymbol{\sigma}'_{\mathrm{pc}}) > +Tol$ it is needed to locate the intersection stress state ${}_{m}\boldsymbol{\sigma}'_{\mathrm{inter}}$ of the elastic trial stress path with the elastic nucleus f_{eln}. This offers the opportunity to differentiate between elastic and elastoplastic components of the trial stress path. The intersection stress ${}_{m}\boldsymbol{\sigma}'_{\mathrm{inter}}$ is usually determined according to Equation 4.84 as described in section 4.4.7. Inserting the stress of the current sub-step yields to Equation 4.14, where *int* is an initially unknown scalar stress multiplier. However, due to the Lode angle dependence of the elastic nucleus the analytical closed form solution for the intersection stress is not applicable. Hence, an iterative solution for the determination of the intersection stress as proposed in section 4.4.9 is employed. Nevertheless, the iterative solution requires the analytical solution for the intersection stress as given by Equation 4.84 during the interpolation.

$${}_{m}\boldsymbol{\sigma}'_{\mathrm{inter}} = \{\{{}_{m-1}\boldsymbol{\sigma}' - {}_{m-1}\boldsymbol{\sigma}'_{\mathrm{pc}}\} + {}_{m}int\ {}_{m}\Delta\boldsymbol{\sigma}'_{\mathrm{trial}}\} + {}_{m-1}\boldsymbol{\sigma}'_{\mathrm{pc}} \tag{4.14}$$

To divide the strain sub-increment in a purely elastic part and an elastoplastic part a proportion of the strain sub-increment $\{{}_{m}inter\ {}_{m}\Delta\boldsymbol{\varepsilon}\}$ that causes elastic strain only and moves the stress state from the initial condition ${}_{m-1}\boldsymbol{\sigma}'$ to the intersection stress state ${}_{m}\boldsymbol{\sigma}'_{\mathrm{inter}}$ on the elastic nucleus has to be found.

The following Equation 4.15 has to be satisfied.

$$f_{\mathrm{eln}}\left({}_{m-1}\boldsymbol{\sigma}' + {}_{m}inter\ {}_{m}\boldsymbol{D}^{\mathrm{e}}_{\mathrm{sec}} : {}_{m}\Delta\boldsymbol{\varepsilon},\ {}_{m-1}\boldsymbol{q}\right) = f_{\mathrm{eln}}\left({}_{m}\boldsymbol{\sigma}'_{\mathrm{inter}},\ {}_{m-1}\boldsymbol{q}\right) = 0 \tag{4.15}$$

The proportion is indicated by a scalar strain intersection factor ${}_{m}inter$, which is determined in accordance with Equation 4.108. Inserting the associated variables for the current sub-step leads to the following Equation 4.16. Moreover, the description of the partitioning of the strain increment and the finding of the scalar strain intersection factor ${}_{m}inter$ are presented in section 4.4.7.

$${}_{m}inter = \frac{\kappa}{\{1+{}_{m-1}e\}\ {}_{m}\Delta\varepsilon_{\mathrm{v}}} \ln\left(\frac{|{}_{m}\boldsymbol{\sigma}'_{\mathrm{inter}} - {}_{m-1}\boldsymbol{\sigma}'|}{\left|\frac{1}{{}_{m}K_{\mathrm{sec}}}\ {}_{m}\boldsymbol{D}^{\mathrm{e}}_{\mathrm{sec}} : {}_{m}\Delta\boldsymbol{\varepsilon}\right|}\frac{{}_{m}\Delta\varepsilon_{\mathrm{v}}}{{}_{m-1}p'} + 1\right) \tag{4.16}$$

The void ratio ${}_{m}e_{\mathrm{inter}}$ at the intersection state is calculated with respect to the elastic proportion of the volumetric strain sub-increment $\{{}_{m}inter\ {}_{m}\Delta\varepsilon^{\mathrm{v}}\}$ defined by the scalar strain intersection factor ${}_{m}inter$. The stress ${}_{m-1}\boldsymbol{\sigma}' = {}_{m}\boldsymbol{\sigma}'_{\mathrm{inter}}$ and the void ratio ${}_{m-1}e = {}_{m}e_{\mathrm{inter}}$ are updated with respect to the corresponding values at the intersection state and the onset of plastic yielding. Hence, the updated values serve as the new stress state and void ratio at the beginning of the sub-step. The hardening variables ${}_{m-1}\boldsymbol{q}$, the structure variable ${}_{m-1}S_{\mathrm{i}}$, the damage variable ${}_{m-1}d$ and the projection center ${}_{m-1}\boldsymbol{\sigma}'_{\mathrm{pc}}$ are kept unchanged due to the purely elastic behavior until reaching the intersection state. Finally, the proportion of the strain increment, which causes an elastoplastic response is calculated according to ${}_{m}\Delta\boldsymbol{\varepsilon} = \{1 - inter\}\ {}_{m}\Delta\boldsymbol{\varepsilon}$.

Check for elastoplastic transition

If $\left\{f_{\mathrm{eln}}({}_{m-1}\boldsymbol{\sigma}',\ {}_{m-1}\boldsymbol{q},\ {}_{m-1}\boldsymbol{\sigma}'_{\mathrm{pc}}) < +Tol\right\}$ AND $\left\{f_{\mathrm{eln}}({}_{m}\boldsymbol{\sigma}'_{\mathrm{trial}},\ {}_{m-1}\boldsymbol{q},\ {}_{m-1}\boldsymbol{\sigma}'_{\mathrm{pc}}) > +Tol\right\}$

Then Do (finding intersection state and partitioning of the strain sub-increment)

Call subroutine: iterative solution for intersection stress (see section 4.4.7)

input: ${}_{m-1}\boldsymbol{\sigma}'$, ${}_{m}\Delta\boldsymbol{\sigma}'_{\mathrm{trial}}$, ${}_{m-1}\boldsymbol{q}$, ${}_{m-1}\boldsymbol{\sigma}'_{\mathrm{pc}}$

output: ${}_{m}\boldsymbol{\sigma}'_{\mathrm{inter}}$, ${}_{m}N_{\mathrm{inter}}({}_{m}\theta_{\mathrm{inter}})$

Calculate intersection factor

$${}_{m}inter = \frac{\kappa}{\{1+{}_{m-1}e\}\ {}_{m}\Delta\varepsilon_{\mathrm{v}}} \ln\left(\frac{|{}_{m}\boldsymbol{\sigma}'_{\mathrm{inter}} - {}_{m-1}\boldsymbol{\sigma}'|}{\left|\frac{1}{{}_{m}K^{\mathrm{e}}_{\mathrm{sec}}}\ {}_{m}\boldsymbol{D}^{\mathrm{e}}_{\mathrm{sec}} : {}_{m}\Delta\boldsymbol{\varepsilon}\right|}\frac{{}_{m}\Delta\varepsilon_{\mathrm{v}}}{{}_{m-1}p'} + 1\right)$$

Calculate void ratio wrt. intersection state

$$ {}_{m}e_{\text{inter}} = {}_{m-1}e - {}_{m}inter\ {}_{m}\Delta\boldsymbol{\varepsilon}^{\text{v}}\ \{1 + {}_{m-1}e\} $$

Update stress and void ratio to intersection state

$$ {}_{m-1}\boldsymbol{\sigma}' = {}_{m}\boldsymbol{\sigma}'_{\text{inter}} $$

$$ {}_{m-1}e = {}_{m}e_{\text{inter}} $$

Keep hardening variables ${}_{m-1}\boldsymbol{q}$, structure variable ${}_{m-1}S_{\text{i}}$, damage variable ${}_{m-1}d$ and projection center ${}_{m-1}\boldsymbol{\sigma}'_{\text{pc}}$ unchanged

Calculate proportion of the strain increment which causes an elastoplastic response

$$ {}_{m}\Delta\boldsymbol{\varepsilon} = \{1 - inter\}\ {}_{m}\Delta\boldsymbol{\varepsilon} $$

Else Do (no intersection)

Set intersection factor to zero

$$ {}_{m}inter = 0 $$

Keep strain increment ${}_{m}\Delta\boldsymbol{\varepsilon}$ unchanged

Keep stress state ${}_{m-1}\boldsymbol{\sigma}'$, hardening variables ${}_{m-1}\boldsymbol{q}$, structure variable ${}_{m-1}S_{\text{i}}$, damage variable ${}_{m-1}d$, void ratio ${}_{m-1}e$ and projection center ${}_{m-1}\boldsymbol{\sigma}'_{\text{pc}}$ unchanged

End If (check for elastoplastic transition)

Elastoplastic model response (Modified Euler solution)

For getting the elastoplastic model response with respect to the given strain sub-increment ${}_{m}\Delta\boldsymbol{\varepsilon}$ the second order accurate Forward Euler solution (Modified Euler approach), which is explicitly described in section 4.4.3 is employed. Input parameters for the Modified Euler algorithm are stress ${}_{m-1}\boldsymbol{\sigma}'$, hardening variables ${}_{m-1}\boldsymbol{q}$, structure variable ${}_{m-1}S_{\text{i}}$, damage variable ${}_{m-1}d$, the void ratio ${}_{m-1}e$ and position of the projection center ${}_{m-1}\boldsymbol{\sigma}'_{\text{pc}}$ at the beginning of the sub-step or at the intersection state, respectively. Following the Modified Euler approach for the bounding surface plasticity framework, stress ${}_{m}\boldsymbol{\sigma}'$, hardening variables ${}_{m}\boldsymbol{q}$, structure variable ${}_{m}S_{\text{i}}$ and damage variable ${}_{m}d$ are calculated according to the Equations 4.17-4.20 based on the second order Taylor's expansion.
The first estimations of the increments of stress $\Delta\boldsymbol{\sigma}'_{1\text{st}}$, hardening variables $\Delta\boldsymbol{q}_{1\text{st}}$, structure variable $\Delta S_{\text{i,1st}}$ and damage variable $\Delta d_{1\text{st}}$ are derived based on the stress state ${}_{m-1}\boldsymbol{\sigma}'$, state variables ${}_{m-1}\boldsymbol{q}$, ${}_{m-1}S_{\text{i}}$, ${}_{m-1}d$, void ratio ${}_{m-1}e$ and projection center ${}_{m-1}\boldsymbol{\sigma}'_{\text{pc}}$

at the beginning of the sub-step or the intersection state, respectively. Based on the results of the first estimation the second estimations of the increments of stress $\Delta\boldsymbol{\sigma}'_{2\mathrm{nd}}$ and variables $\Delta\boldsymbol{q}_{2\mathrm{nd}}$, $\Delta S_{\mathrm{i,2nd}}$, $\Delta d_{2\mathrm{nd}}$ are computed.

$$
\begin{aligned}
{}_m\boldsymbol{\sigma}' &= {}_{m-1}\boldsymbol{\sigma}' + \frac{1}{2}\left\{\Delta\boldsymbol{\sigma}'_{1\mathrm{st}} + \Delta\boldsymbol{\sigma}'_{2\mathrm{nd}}\right\} && (4.17)\\
{}_m\boldsymbol{q} &= {}_{m-1}\boldsymbol{q} + \frac{1}{2}\left\{\Delta\boldsymbol{q}_{1\mathrm{st}} + \Delta\boldsymbol{q}_{2\mathrm{nd}}\right\} && (4.18)\\
{}_m S_{\mathrm{i}} &= {}_{m-1}S_{\mathrm{i}} + \frac{1}{2}\left\{\Delta S_{\mathrm{i,1st}} + \Delta S_{\mathrm{i,2nd}}\right\} && (4.19)\\
{}_m d &= {}_{m-1}d + \frac{1}{2}\left\{\Delta d_{1\mathrm{st}} + \Delta d_{2\mathrm{nd}}\right\} && (4.20)
\end{aligned}
$$

Finally, the Modified Euler algorithm provides the stress state ${}_m\boldsymbol{\sigma}'$, hardening variables ${}_m\boldsymbol{q}$, structure variable ${}_m S_{\mathrm{i}}$ and damage variable ${}_m d$ at the end of the sub-step as the mean values of the results from the first and second estimation. However, the void ratio ${}_m e = {}_{m-1}e - {}_m\Delta\boldsymbol{\varepsilon}^{\mathrm{v}}\,\{1 + {}_{m-1}e\}$ at the end of the sub-step is the same for the first and second estimation because of the same predefined volumetric strain increment in both calculation phases.

Elastoplastic model response (Modified Euler solution)

Call Modified Euler algorithm for bounding surface plasticity (see section 4.4.3)

input: ${}_{m-1}\boldsymbol{\sigma}'$, ${}_{m-1}\boldsymbol{q}$, ${}_{m-1}S_{\mathrm{i}}$, ${}_{m-1}d$, ${}_{m-1}e$, ${}_{m-1}\boldsymbol{\sigma}'_{\mathrm{pc}}$, ${}_m\Delta\boldsymbol{\varepsilon}$

output: ${}_m\boldsymbol{\sigma}'$, $\Delta\boldsymbol{\sigma}'_{1\mathrm{st}}$, $\Delta\boldsymbol{\sigma}'_{2\mathrm{nd}}$, ${}_m\boldsymbol{q}$, $\Delta\boldsymbol{q}_{1\mathrm{st}}$, $\Delta\boldsymbol{q}_{2\mathrm{nd}}$, ${}_m S_{\mathrm{i}}$, ${}_m d$, ${}_m e$

Automatic error control and sub-stepping approach

To quantify the accuracy of the Modified Euler solution the relative error ${}_m R$ is introduced. The relative error ${}_m R$ is specified as the difference of the increments of stress and hardening variables calculated in the first and the second estimation as the estimate of error normalized by the magnitude of their final values at the end of the increment. To be more precise, the relative error with respect to stress is defined as the difference of the increments of stress $\Delta\boldsymbol{\sigma}'_{2\mathrm{nd}} - \Delta\boldsymbol{\sigma}'_{1\mathrm{st}}$ normalized by the magnitude of the final stress state ${}_m\boldsymbol{\sigma}'$ at the end of the sub-step.
Furthermore, the same procedure holds true for the relative error with respect to the hardening variables. That is, the differences of the increments of the hardening variables $\Delta\boldsymbol{q}_{2\mathrm{nd}} - \Delta\boldsymbol{q}_{1\mathrm{st}}$ is normalized by the magnitude of the hardening variables ${}_m\boldsymbol{q}$ at the end of

the sub-step. The maximum relative error among stress ${}_mR_\sigma$ and each hardening variable ${}_mR_{p_{0,\mathrm{s}}}$ and ${}_mR_\alpha$ (separation to avoid scaling effects) will become decisive.

Error control

Calculate relative error (1st vs. 2nd estimation)

$$ {}_mR = \frac{1}{2} \max \left[\frac{|\Delta\boldsymbol{\sigma}'_{2\mathrm{nd}} - \Delta\boldsymbol{\sigma}'_{1\mathrm{st}}|}{|{}_m\boldsymbol{\sigma}'|}, \frac{|\Delta\boldsymbol{q}_{2\mathrm{nd}} - \Delta\boldsymbol{q}_{1\mathrm{st}}|}{|{}_m\boldsymbol{q}|} \right] $$

In case the relative error ${}_mR$ is larger than a tolerance value R_{Tol} (here specified as 10^{-4}) the pseudo time increment and the associated size of the strain sub-increment have to be decreased. A new iteration $i+1$ of the calculation with a reduced pseudo time increment ${}^{i+1}_{m-1}T$ starts again from the beginning of the sub-stepping loop with the stress state at the beginning of the sub-step or at the intersection with the elastic nucleus, respectively. Hence, the corresponding values of stress, hardening variables, structure variable, damage variable, void ratio and projection center are considered at the beginning of the new iteration. If an intersection stress was detected during the sub-step the initial pseudo time ${}^{i+1}_{m-1}T$ for starting the new iteration is updated to the corresponding pseudo time at the intersection state, so that ${}^{i+1}_{m-1}T = {}^{i}_{m-1}T + {}_m\mathit{inter}\ {}^{i}_{m}\Delta T$ using the intersection factor ${}_m\mathit{inter}$. In case of having no intersection, the pseudo time ${}^{i+1}_{m-1}T$ at the beginning of the new iteration equals the pseudo time ${}^{i}_{m-1}T$ at the beginning of the current iteration since the intersection factor equals zero ${}_m\mathit{inter} = 0$, so that ${}^{i+1}_{m-1}T = {}^{i}_{m-1}T$.
The pseudo time increment ${}^{i+1}_{m}\Delta T$ for the next iteration is generally calculated based on an extrapolation factor ${}^{i}_{m}\zeta$ using the relation ${}^{i+1}_{m}\Delta T = {}^{i}_{m}\zeta\ {}^{i}_{m}\Delta T$. Considering the error in the Euler method the relative error for the next iteration can be estimated as ${}^{i+1}_{m}R \approx {}^{i}_{m}\zeta^2\ {}^{i}_{m}R$. Combining this equation with the restriction that the relative error for the next iteration is smaller than the tolerance value R_{Tol} results in an extrapolation factor ${}^{i}_{m}\zeta \leq \sqrt{R_{\mathrm{Tol}} \,/\, {}_mR}$. For reasons of having a conservative assumption a reduction factor of 0.9 is introduced to the equation of ${}^{i}_{m}\zeta$. Furthermore, empirical limiting values for the interpolation factor ${}^{i}_{m}\zeta$ are given as a minimum value of 0.1 and a maximum value of 1.1. This empirical limits constrain the value of the pseudo time increment for the next iteration to $0.1\ {}^{i}_{m}\Delta T \leq {}^{i+1}_{m}\Delta T \leq 1.1\ {}^{i}_{m}\Delta T$. Hence, in case of decreasing the pseudo time increment with respect to the relative error larger than the tolerance value the minimum extrapolation factor ${}^{i}_{m}\zeta$ is restricted to a value of 0.1. Additionally, the size of the pseudo time increment has a minimum value ΔT_{min} (here specified as 10^{-10}) to avoid an endless iteration. If the minimum size of the pseudo time increment is reached an error message will be printed. In case the time at the end of the next sub-step ${}^{i}_{m+1}T$ would exceed the maximum value of 1, the pseudo time increment for the next sub-step ${}^{i}_{m+1}\Delta T$ would be adjusted to $1 - {}^{i+1}_{m-1}T$. Finally the counting parameter i for the iteration is increased by 1 and the iteration

starts again from the beginning of the sub-stepping loop. The sub-step number m is kept constant. This procedure will be repeated until an appropriate sub-step size is determined ensuring a successful Modified Euler calculation step so that ${}_{m}R \leq R_{\mathrm{Tol}}$.

Check for sub-stepping via relative error

If $\{{}_{m}R > R_{\mathrm{Tol}}\}$

Then Do (sub-stepping)

Reset stress state ${}_{m-1}\boldsymbol{\sigma}'$, hardening variables ${}_{m-1}\boldsymbol{q}$, structure variable ${}_{m-1}S_{\mathrm{i}}$, damage variable ${}_{m-1}d$, void ratio ${}_{m-1}e$ and projection center ${}_{m-1}\boldsymbol{\sigma}'_{\mathrm{pc}}$

Update pseudo time and time increment

$${}^{i+1}_{m-1}T = {}^{i}_{m-1}T + inter\ {}^{i}_{m}\Delta T \text{ (pseudo time at start of new iteration)}$$

$${}^{i+1}_{m}\zeta = \max\left[0.9\sqrt{\frac{R_{\mathrm{Tol}}}{{}_{m}R}}, 0.1\right] \text{ (extrapolation factor)}$$

$${}^{i+1}_{m}\Delta T = {}^{i}_{m}\zeta\ {}^{i}_{m}\Delta T \text{ (decrease time increment)}$$

$${}^{i+1}_{m}\Delta T = \max\left[{}^{i+1}_{m}\Delta T, \Delta T_{\mathrm{min}}\right] \text{ (min. increment size)}$$

$${}^{i+1}_{m}\Delta T = \min\left[{}^{i+1}_{m}\Delta T,\ 1 - {}^{i+1}_{m-1}T\right] \text{ (max. entire pseudo time } {}^{i+1}_{m}T = 1)$$

Keep m constant

Set $i = i + 1$

Go To sub-stepping loop

Successful Modified Euler calculation

The Modified Euler calculation is successful when the relative error becomes smaller than the tolerance value ${}_{m}R \leq R_{\mathrm{Tol}}$ and the stress ${}_{m}\boldsymbol{\sigma}'$, hardening variables ${}_{m}\boldsymbol{q}$, structure variable ${}_{m}S_{\mathrm{i}}$ and damage variable ${}_{m}d$ at the end of the sub-step are accepted according to the Equations 4.20-4.20. As already mentioned the final void ratio resulting from both estimations of the Modified Euler approach is given as ${}_{m}e = {}_{m-1}e - {}_{m}\Delta\boldsymbol{\varepsilon}^{\mathrm{v}}\ \{1 + {}_{m-1}e\}$.

Successful Modified Euler sub-step

Else Do (accept successful Modified Euler solution)

Accept calculated stress state and variables (see Equations 4.20-4.20)

$${}_{m}\boldsymbol{\sigma}' = {}_{m-1}\boldsymbol{\sigma}' + \frac{1}{2}\ \{\Delta\boldsymbol{\sigma}'_{1\mathrm{st}} + \Delta\boldsymbol{\sigma}'_{2\mathrm{nd}}\}$$

$$ {}_m\boldsymbol{q} = {}_{m-1}\boldsymbol{q} + \frac{1}{2}\left\{\Delta\boldsymbol{q}_{1\mathrm{st}} + \Delta\boldsymbol{q}_{2\mathrm{nd}}\right\} $$

$$ {}_mS_{\mathrm{i}} = {}_{m-1}S_{\mathrm{i}} + \frac{1}{2}\left\{\Delta S_{\mathrm{i},1\mathrm{st}} + \Delta S_{\mathrm{i},2\mathrm{nd}}\right\} $$

$$ {}_md = {}_{m-1}d + \frac{1}{2}\left\{\Delta d_{1\mathrm{st}} + \Delta d_{2\mathrm{nd}}\right\} $$

Drift correction

If the elastoplastic stress state after the successful Modified Euler calculation is located outside the bounding surface $F({}_m\boldsymbol{\sigma}',\ {}_m\boldsymbol{q}) > +Tol$ the stress state has to be returned/projected back to the bounding surface by use of an iterative drift correction algorithm. The drift of the bounding surface arises by reasons of numerical inaccuracy of the integration of the highly non-linear constitutive equations. Whereat, the numerical tolerance value Tol is specified as 10^{-7} in this study.
In this work a so-called consistent drift correction approach is used as detailed described in section 4.4.4 (see e.g. Potts and Gens, 1985; Sloan et al., 2001). This approach is based on the iterative back projection of the stress state along the direction of the plastic flow and with consideration of the updated hardening variables in each iteration. Furthermore, at the end of each iteration the structure variable and the damage variable are adjusted with respect to the corrected plastic strain increment. In case of divergence of the consistent drift correction approach the normal drift correction approach is activated. The normal drift correction approach is based on the back projection of the stress state along the normal to the bounding surface without considering the update of the hardening variables. However, the drift correction is successful if in any iteration the following condition is fulfilled $|F({}_m\boldsymbol{\sigma}',\ {}_m\boldsymbol{q})| \leq +Tol$. Finally, the drift correction results in the final values of stress state ${}_m\boldsymbol{\sigma}'$, hardening variables ${}_m\boldsymbol{q}$, structure variable ${}_mS_{\mathrm{i}}$ and damage variable ${}_md$.

Check for drift correction
If $\{F({}_m\boldsymbol{\sigma}',\ {}_m\boldsymbol{q}) > +Tol\}$

Then Do (drift correction)

Call drift correction algorithm for bounding surface plasticity (see section 4.4.4)

input: ${}_m\boldsymbol{\sigma}'$, ${}_m\boldsymbol{q}$, ${}_mS_{\mathrm{i}}$, ${}_md$, ${}_me$

output: ${}_m\boldsymbol{\sigma}'$, ${}_m\boldsymbol{q}$, ${}_mS_{\mathrm{i}}$, ${}_md$

End If (check for drift correction)

Update of projection center and pseudo time

To ensure that the projection center is always located inside or on the updated bounding surface it has to be adjusted with respect to the incremental change of the hardening variables during the successful Modified Euler calculation. The procedure was already described in section 3.3.9. The update of the projection center is given by ${}_m\boldsymbol{\sigma}'_{\mathrm{pc}} = {}_{m-1}\boldsymbol{\sigma}'_{\mathrm{pc}} + {}_m\Delta\boldsymbol{\sigma}'_{\mathrm{pc}}$. Whereat, the increment of the projection center is calculated by calling a certain subroutine, which includes the associated evolution Equations 3.39 - 3.42 as described in section 3.3.9. The time at the end of the sub-step is updated to ${}^i_m T = {}^i_{m-1}T + {}^i_m\Delta T$ because the pseudo time increment ${}^i_m\Delta T$ and therefore the strain increment ${}_m\Delta\boldsymbol{\varepsilon}$ are successfully applied. For the next sub-step $m+1$ the pseudo time increment ${}^i_{m+1}\Delta T$ is adjusted to accelerate the computational speed by use of the extrapolation factor ${}^i_m\zeta$ following exactly the same procedure as described above (${}_{m+1}R \approx {}^i_m\zeta^2\ {}_mR$). The only difference compared to a decreasing pseudo time increment is that the extrapolation factor is restricted to a maximum value of 1.1. Finally the counting parameter m for the sub-stepping loop is increased by 1 and the loop starts again (Do While $\left\{{}^i_{m-1}T < 1\right\}$).

Update of projection center and pseudo time

Update projection center wrt. updated hardening variables

Call subroutine: increment projection center (see section 3.3.9)

input: ${}_{m-1}\boldsymbol{q}$, ${}_m\Delta\boldsymbol{q}$, ${}_{m-1}\boldsymbol{\sigma}'_{\mathrm{pc}}$

output: ${}_m\Delta\boldsymbol{\sigma}'_{\mathrm{pc}}$

Update ${}_m\boldsymbol{\sigma}_{\mathrm{pc}} = {}_{m-1}\boldsymbol{\sigma}'_{\mathrm{pc}} + {}_m\Delta\boldsymbol{\sigma}'_{\mathrm{pc}}$

Update pseudo time and time increment

${}^i_m T = {}^i_{m-1}T + {}^i_m\Delta T$ (pseudo time at start of new sub-step)

${}^i_m\zeta = \min\left[0.9\sqrt{\frac{R_{\mathrm{Tol}}}{{}_mR}}, 1.1\right]$ (extrapolation factor)

${}^i_{m+1}\Delta T = {}^i_m\zeta\ {}^i_m\Delta T$ (increase time increment)

${}^i_{m+1}\Delta T = \max\left[{}^i_{m+1}\Delta T, \Delta T_{\min}\right]$ (min. increment size)

${}^i_{m+1}\Delta T = \min\left[{}^i_{m+1}\Delta T, 1 - {}^i_m T\right]$ (max. entire pseudo time ${}^i_{m+1}T = 1$)

Set $m = m + 1$

Go To sub-stepping loop

End If (check for sub-stepping via relative error)

End If (check for elastic and elastoplastic model response)

The sub-stepping loop is stopped when the sum of all pseudo time sub-steps reaches the full pseudo time $\{{}^{i}_{m}T = 1\}$), which means that the entire strain increment $\Delta\boldsymbol{\varepsilon}$ is successfully applied.

End Do While (sub-stepping loop)

Transfer of stress and variables to FE-code

At the end of a calculation step the constitutive model returns the final values of the stress ${}_{m}\boldsymbol{\sigma}'$, hardening variables ${}_{m}\boldsymbol{q}$, structure variable ${}_{m}S_{\mathrm{i}}$, damage variable ${}_{m}d$, void ratio ${}_{m}e$ and position of the projection center ${}_{m}\boldsymbol{\sigma}'_{\mathrm{pc}}$ to the finite element code.

Return ${}_{m}\boldsymbol{\sigma}'$, ${}_{m}\boldsymbol{q}$, ${}_{m}S_{\mathrm{i}}$ ${}_{m}d$, ${}_{m}e$, ${}_{m}\boldsymbol{\sigma}'_{\mathrm{pc}}$

4.4.3 Modified Euler approach

For finding the stress ${}_{m}\boldsymbol{\sigma}'$, hardening variables ${}_{m}\boldsymbol{q}$, structure variable ${}_{m}S_{\mathrm{i}}$ and damage variable ${}_{m}d$ at the end of a strain sub-increment the second order accurate explicit Modified Euler approach is used. The Modified Euler integration scheme is based on the second order Taylor's expansion of stress as given in Equation 4.21. In the Taylor's expansion of stress the difference $\boldsymbol{D}^{\mathrm{ep}}_{\mathrm{2nd}} - \boldsymbol{D}^{\mathrm{ep}}_{\mathrm{1st}}$ is the change in the elastoplastic stiffness matrix over a given strain sub-increment for a forward Euler integration.

$$\begin{aligned} {}_{m}\boldsymbol{\sigma}' &= {}_{m-1}\boldsymbol{\sigma}' + \boldsymbol{D}^{\mathrm{ep}}_{\mathrm{1st}} : {}_{m}\Delta\boldsymbol{\varepsilon} + \frac{1}{2}\{\boldsymbol{D}^{\mathrm{ep}}_{\mathrm{2nd}} - \boldsymbol{D}^{\mathrm{ep}}_{\mathrm{1st}}\} : {}_{m}\Delta\boldsymbol{\varepsilon} \\ &= {}_{m-1}\boldsymbol{\sigma}' + \Delta\boldsymbol{\sigma}'_{\mathrm{1st}} + \frac{1}{2}\{\Delta\boldsymbol{\sigma}'_{\mathrm{2nd}} - \Delta\boldsymbol{\sigma}'_{\mathrm{1st}}\} \\ &= {}_{m-1}\boldsymbol{\sigma}' + \frac{1}{2}\{\Delta\boldsymbol{\sigma}'_{\mathrm{1st}} + \Delta\boldsymbol{\sigma}'_{\mathrm{2nd}}\} \end{aligned} \tag{4.21}$$

The Modified Euler approach includes the first (subscript 1st) and second (subscript 2nd) estimation of the stress increment $\Delta\boldsymbol{\sigma}'_{\mathrm{1st}}$ and $\Delta\boldsymbol{\sigma}'_{\mathrm{2nd}}$ associated with the given strain sub-increment ${}_{m}\Delta\boldsymbol{\varepsilon}$. The stress state after the first and the second estimation are defined as $\boldsymbol{\sigma}'_{\mathrm{1st}} = {}_{m-1}\boldsymbol{\sigma}' + \Delta\boldsymbol{\sigma}'_{\mathrm{1st}}$ and $\boldsymbol{\sigma}'_{\mathrm{2nd}} = {}_{m-1}\boldsymbol{\sigma}' + \Delta\boldsymbol{\sigma}'_{\mathrm{2nd}}$, respectively. Whereat, the first estimation is calculated according to $\Delta\boldsymbol{\sigma}'_{\mathrm{1st}} = \boldsymbol{D}^{\mathrm{ep}}_{\mathrm{1st}} : {}_{m}\Delta\boldsymbol{\varepsilon}$. That is, the calculation of the first estimation is based on the stress state ${}_{m-1}\boldsymbol{\sigma}'$, hardening variables ${}_{m-1}\boldsymbol{q}$,

structure variable ${}_{m-1}S_{\mathrm{i}}$, damage variable ${}_{m-1}d$, void ratio ${}_{m-1}e$ and position of the projection center ${}_{m-1}\boldsymbol{\sigma}'_{\mathrm{pc}}$ at the beginning of the Modified Euler calculation step, so that $\boldsymbol{D}^{\mathrm{ep}}_{1\mathrm{st}}({}_{m-1}\boldsymbol{\sigma}',\ {}_{m-1}\boldsymbol{q},\ {}_{m-1}S_{\mathrm{i}},\ {}_{m-1}d,\ {}_{m-1}e,\ {}_{m-1}\boldsymbol{\sigma}'_{\mathrm{pc}})$. Whereas, the second estimation is based on the final results of the first estimation, so that $\boldsymbol{D}^{\mathrm{ep}}_{2\mathrm{nd}}(\boldsymbol{\sigma}'_{1\mathrm{st}}, \boldsymbol{q}_{1\mathrm{st}}, S_{\mathrm{i},1\mathrm{st}}, d_{1\mathrm{st}},\ {}_{m}e, \boldsymbol{\sigma}'_{\mathrm{pc},1\mathrm{st}})$. According to Taylor's expansion of stress, the final value of the stress state derived from a Modified Euler calculation is defined as the mean value of the stresses from the first and the second estimation, so that ${}_{m}\boldsymbol{\sigma}' = {}_{m-1}\boldsymbol{\sigma}' + 1/2\ \{\Delta\boldsymbol{\sigma}'_{1\mathrm{st}} + \Delta\boldsymbol{\sigma}'_{2\mathrm{nd}}\}$. A similar approach is employed for the second order approximation of the hardening variables, structure variable and damage variable as given in Equations 4.22-4.24.

$$ {}_{m}\boldsymbol{q} = {}_{m-1}\boldsymbol{q} + \frac{1}{2}\ \{\Delta\boldsymbol{q}_{1\mathrm{st}} + \Delta\boldsymbol{q}_{2\mathrm{nd}}\} \tag{4.22} $$

$$ {}_{m}S_{\mathrm{i}} = {}_{m-1}S_{\mathrm{i}} + \frac{1}{2}\ \{\Delta S_{\mathrm{i},1\mathrm{st}} + \Delta S_{\mathrm{i},2\mathrm{nd}}\} \tag{4.23} $$

$$ {}_{m}d = {}_{m-1}d + \frac{1}{2}\ \{\Delta d_{1\mathrm{st}} + \Delta d_{2\mathrm{nd}}\} \tag{4.24} $$

Transfer of initial conditions

At the beginning of the Modified Euler calculation the initial values for the stress state ${}_{m-1}\boldsymbol{\sigma}'$, hardening variables ${}_{m-1}\boldsymbol{q}$, structure variable ${}_{m-1}S_{\mathrm{i}}$, damage variable ${}_{m-1}d$, void ratio ${}_{m-1}e$ and position of the projection center ${}_{m-1}\boldsymbol{\sigma}'_{\mathrm{pc}}$ at the beginning of the substep or at the intersection state are taken from the general explicit integration scheme. Moreover, the strain sub-increment ${}_{m}\Delta\boldsymbol{\varepsilon}$ is provided by the general explicit integration scheme.

Transfer of initial conditions

Get initial conditions

${}_{m-1}\boldsymbol{\sigma}',\ {}_{m-1}\boldsymbol{q},\ {}_{m-1}S_{\mathrm{i}},\ {}_{m-1}d,\ {}_{m-1}e,\ {}_{m-1}\boldsymbol{\sigma}'_{\mathrm{pc}},\ {}_{m}\Delta\boldsymbol{\varepsilon}$

1st estimation - 1st elastic trial stress state, plastic stress correction and final stress state

According to the Modified Euler approach the main aim of the first estimation is to provide the increment of stress $\Delta\boldsymbol{\sigma}'_{1\mathrm{st}}$ related to the given strain sub-increment ${}_{m}\Delta\boldsymbol{\varepsilon}$ and the estimation of the corresponding increments of the hardening variables $\Delta\boldsymbol{q}_{1\mathrm{st}}$, structure variable $\Delta S_{\mathrm{i},1\mathrm{st}}$ and damage variable $\Delta d_{1\mathrm{st}}$. A first elastic trial stress increment $\Delta\boldsymbol{\sigma}'_{\mathrm{trial},1\mathrm{st}}$ is calculated based on the elastic stress-strain relation using the strain sub-increment

${}_m\Delta\boldsymbol{\varepsilon}$ and the tangent elastic stiffness matrix $\boldsymbol{D}^{\mathrm{e}}_{1\mathrm{st}}$ at the beginning of the sub-step or at the intersection state, respectively. The definition of the tangent elastic stiffness matrix $\boldsymbol{D}^{\mathrm{e}}_{1\mathrm{st}}\,({}_{m-1}\boldsymbol{\sigma}',\ {}_{m-1}e)$ dependent on stress and void ratio is given by Equation 4.38 in section 4.4.5. The elastic trial stress increment $\Delta\boldsymbol{\sigma}'_{\mathrm{trial,1st}}$ leads to the elastic trial stress $\boldsymbol{\sigma}'_{\mathrm{trial,1st}}$ of the first estimation.

Calculation of elastic trial stress $\boldsymbol{\sigma}'_{\mathrm{trial,1st}}$

Calculate elastic trial stress increment

$$\Delta\boldsymbol{\sigma}'_{\mathrm{trial,1st}} = \boldsymbol{D}^{\mathrm{e}}_{1\mathrm{st}}\,({}_{m-1}\boldsymbol{\sigma}',\ {}_{m-1}e) : {}_m\Delta\boldsymbol{\varepsilon}$$

Calculate elastic trial stress

$$\boldsymbol{\sigma}'_{\mathrm{trial,1st}} = {}_{m-1}\boldsymbol{\sigma}' + \Delta\boldsymbol{\sigma}'_{\mathrm{trial,1st}}$$

Calculation of plasticity modulus

As described by the constitutive equations in section 4.4.1, it is required to calculate the plastic loading index L according to Equation 3.11 to obtain the unknown stress increment $\Delta\boldsymbol{\sigma}'$ from a given plastic strain increment $\Delta\boldsymbol{\varepsilon}^{\mathrm{p}}$. Therefore, the plasticity modulus K_{p} has to be calculated. Within the framework of bounding surface plasticity, the plasticity modulus K_{p} with respect to the current stress state is defined according to Equation 3.6 as a function of the plasticity modulus $\bar{K}_{\mathrm{p}}$ with respect to the image stress state, a distance function $\hat{f}$ and a shape hardening function $\hat{h}$, so that $K_{\mathrm{p}} = \bar{K}_{\mathrm{p}} + \hat{f}\,\hat{h}$.
Consequently, for the determination of the plastic strain increment $\Delta\boldsymbol{\varepsilon}^{\mathrm{p}}$, the stress increment $\Delta\boldsymbol{\sigma}'$ and the final stress state $\boldsymbol{\sigma}'$ of any sub-step, the image stress state $\bar{\boldsymbol{\sigma}}'$ needs to be identified via the projection rule 3.9, which incorporates the similarity ratio b. For deriving the similarity ratio b the approach described in section 4.4.8 is usually applied. The approach is based on substituting the image stress components of the bounding surface formulation by the projection rule and solving the modified equation for the similarity ratio b afterwards. However, due to the Lode angle dependence of the bounding surface F the analytical closed form solution for the similarity ratio b as given by Equation 4.101 in section 4.4.8 is not applicable. Hence, an iterative solution for the determination of the similarity ratio b as proposed in section 4.4.9 is used. Nevertheless, the iterative solution requires the analytical solution during the interpolation.
The similarity ratio $b_{1\mathrm{st}}$ and the corresponding Lode angle dependent variable $N_{1\mathrm{st}}$ for the first estimation are iteratively calculated with respect to the stress state ${}_{m-1}\boldsymbol{\sigma}'$ at the beginning of the sub-step or at the intersection stress state and with respect to the current bounding surface F specified by the hardening variables ${}_{m-1}\boldsymbol{q}$ and the position

of the projection center ${}_{m-1}\boldsymbol{\sigma}'_{\mathrm{pc}}$ at the beginning of the sub-step. By use of the similarity ratio $b_{1\mathrm{st}}$ the image stress state $\bar{\boldsymbol{\sigma}}'_{1\mathrm{st}}$ is computed afterwards employing the projection rule 3.9, so that $\bar{\boldsymbol{\sigma}}'_{1\mathrm{st}} = b_{1\mathrm{st}} \left\{ {}_{m-1}\boldsymbol{\sigma}' - {}_{m-1}\boldsymbol{\sigma}'_{\mathrm{pc}} \right\} + {}_{m-1}\boldsymbol{\sigma}'_{\mathrm{pc}}$.
The plasticity modulus $K_{\mathrm{p},1\mathrm{st}} = \bar{K}_{\mathrm{p},1\mathrm{st}} + \hat{f}_{1\mathrm{st}}\, \hat{h}_{1\mathrm{st}}$ with respect to the current stress state ${}_{m-1}\boldsymbol{\sigma}'$ is calculated according to Equation 3.6 with respect to the image stress state $\bar{\boldsymbol{\sigma}}'_{1\mathrm{st}}$ as given by Equation 3.8, so that $\bar{K}_{\mathrm{p},1\mathrm{st}} = -\left\{ \partial F / \partial_{m-1} p_{0,\mathrm{s}}\, \tilde{p}_{0,\mathrm{s},1\mathrm{st}} + \partial F / \partial_{m-1}\boldsymbol{\alpha} : \tilde{\boldsymbol{\alpha}}_{1\mathrm{st}} \right\}$. Whereat, the bounding surface $F(\bar{\boldsymbol{\sigma}}'_{1\mathrm{st}},\ {}_{m-1}\boldsymbol{q}) = 0$ is evaluated with respect to the hardening variables ${}_{m-1}p_{0,\mathrm{s}}$ and ${}_{m-1}\boldsymbol{\alpha}$ at the beginning of the sub-step or the intersection state, respectively. The gradients $\partial F / \partial_{m-1} p_{0,\mathrm{s}}$ and $\partial F / {}_{m-1}\boldsymbol{\alpha}$ are given by Equations 4.127 and 4.128 in section 4.4.10. Furthermore, the variables $\tilde{p}_{0,\mathrm{s},1\mathrm{st}}$, $\tilde{p}_{0,\mathrm{i},1\mathrm{st}}$, $\tilde{S}_{\mathrm{i},1\mathrm{st}}$ and $\tilde{\boldsymbol{\alpha}}_{1\mathrm{st}}$ are specified by the Equations 3.31, 3.32, 3.35 - 3.36 and 3.15, respectively. The auxiliary variables are calculated as functions of the hardening variables ${}_{m-1}\boldsymbol{q}$, structure variable ${}_{m-1}S_{\mathrm{i}}$ and void ratio ${}_{m-1}e$ at the beginning of the sub-step or the intersection state, respectively. However, the plastic potential surface $G(\bar{\boldsymbol{\sigma}}'_{1\mathrm{st}},\ {}_{m-1}\boldsymbol{q}) = 0$ is evaluated with respect to the variable ${}_{m-1}p_{\alpha}$ (see Equation 3.13) and the same hardening variable ${}_{m-1}\boldsymbol{\alpha}$ at the beginning of the sub-step or the intersection state, respectively. The required gradient of the plastic potential surface with respect to the image stress state $\partial G / \bar{\boldsymbol{\sigma}}'_{1\mathrm{st}}$ is presented in section 4.4.10. The distance function $\hat{f}_{1\mathrm{st}}$ is evaluated according to Equation 3.7 as a function of the similarity ratio $b_{1\mathrm{st}}$ so that $\hat{f}_{1\mathrm{st}} = \left\langle \{b_{1\mathrm{st}} - 1\} \,/\, \{b_{1\mathrm{st}} - \{b_{1\mathrm{st}} - 1\}\ s_{\mathrm{eln}}\} \right\rangle$. The shape hardening function $\hat{h}_{1\mathrm{st}}$ is derived in accordance with Equation 3.37 as a function of the hardening variables ${}_{m-1}p_{0,\mathrm{s}}$ and the damage variable ${}_{m-1}d$ at the beginning of the sub-step, so that $\hat{h}_{1\mathrm{st}} = \{{}_{m-1}p_{0,\mathrm{s}}\}^3\ h_0 \,/\, \{1 + {}_{m-1}d\}$.

Calculation of plasticity modulus $K_{\mathrm{p},1\mathrm{st}}$

Call subroutine: iterative solution for similarity ratio (see section 4.4.8)

input: ${}_{m-1}\boldsymbol{\sigma}'$, ${}_{m-1}\boldsymbol{q}$, ${}_{m-1}\boldsymbol{\sigma}'_{\mathrm{pc}}$

output: $b_{1\mathrm{st}}$, $N_{1\mathrm{st}}(\theta_{1\mathrm{st}})$

Calculate image stress

$$\bar{\boldsymbol{\sigma}}'_{1\mathrm{st}} = b_{1\mathrm{st}} \left\{ {}_{m-1}\boldsymbol{\sigma}' - {}_{m-1}\boldsymbol{\sigma}'_{\mathrm{pc}} \right\} + {}_{m-1}\boldsymbol{\sigma}'_{\mathrm{pc}}$$

Call subroutine: plasticity modulus wrt. stress on the bounding surface

input: $\bar{\boldsymbol{\sigma}}'_{1\mathrm{st}}$, ${}_{m-1}\boldsymbol{q}$, ${}_{m-1}S_{\mathrm{i}}$, ${}_{m-1}e$

output: $\bar{K}_{\mathrm{p},1\mathrm{st}}$, $\tilde{\mathrm{q}}_{1\mathrm{st}}$, $\tilde{S}_{\mathrm{i},1\mathrm{st}}$

Calculate distance function

$$\hat{f}_{1\mathrm{st}} = \left\langle \frac{b_{1\mathrm{st}} - 1}{b_{1\mathrm{st}} - \{b_{1\mathrm{st}} - 1\}\ s_{\mathrm{eln}}} \right\rangle$$

Calculate shape hardening function

$$\hat{h}_{1\mathrm{st}} = \{{}_{m-1}p_{0,\mathrm{s}}\}^3\ \frac{h_0}{1+{}_{m-1}d}$$

Calculate plasticity modulus wrt. current stress

$$K_{\mathrm{p},1\mathrm{st}} = \bar{K}_{\mathrm{p},1\mathrm{st}} + \hat{f}_{1\mathrm{st}}\ \hat{h}_{1\mathrm{st}}$$

Calculation of plastic loading index

The plastic loading index $L_{1\mathrm{st}}$ for the first estimation has to be determined to calculate the plastic strain increment $\Delta\boldsymbol{\varepsilon}^{\mathrm{p}}_{1\mathrm{st}}$ and the increments and updated values for the first estimation of the hardening variables $\Delta\boldsymbol{q}_{1\mathrm{st}}$ and $\boldsymbol{q}_{1\mathrm{st}}$, structure variable $\Delta S_{\mathrm{i},1\mathrm{st}}$ and $S_{\mathrm{i},1\mathrm{st}}$ and damage variable $\Delta d_{1\mathrm{st}}$ and $d_{1\mathrm{st}}$ via the plastic deviatoric strain increment. However, the plastic loading index $L_{1\mathrm{st}}$ is derived from the consistency condition and the non-associated flow rule according to Equation 3.11. The plastic loading index $L_{1\mathrm{st}}$ is a function of the elastic stiffness matrix $\boldsymbol{D}^{\mathrm{e}}_{1\mathrm{st}}({}_{m-1}\boldsymbol{\sigma}',\ {}_{m-1}e)$ at the beginning of the sub-step or the intersection state, plasticity modulus $K_{\mathrm{p},1\mathrm{st}}$ and strain sub-increment ${}_m\Delta\boldsymbol{\varepsilon}$. The gradients of the bounding surface $\partial F/\bar{\boldsymbol{\sigma}}'_{1\mathrm{st}}$ and the plastic potential surface $\partial G/\bar{\boldsymbol{\sigma}}'_{1\mathrm{st}}$ as given in section 4.4.10 are evaluated with respect to the image stress state $\bar{\boldsymbol{\sigma}}'_{1\mathrm{st}}$.

Calculation of plastic loading index $L_{1\mathrm{st}}$

Calculate plastic loading index

$$L_{1\mathrm{st}} = \frac{\left\{\dfrac{\partial F}{\partial \bar{\boldsymbol{\sigma}}'_{1\mathrm{st}}}\right\} : \boldsymbol{D}^{\mathrm{e}}_{1\mathrm{st}}({}_{m-1}\boldsymbol{\sigma}',\ {}_{m-1}e) : {}_m\Delta\boldsymbol{\varepsilon}}{\left\{\dfrac{\partial F}{\partial \bar{\boldsymbol{\sigma}}'_{1\mathrm{st}}}\right\} : \boldsymbol{D}^{\mathrm{e}}_{1\mathrm{st}}({}_{m-1}\boldsymbol{\sigma}',\ {}_{m-1}e) : \left\{\dfrac{\partial G}{\partial \bar{\boldsymbol{\sigma}}'_{1\mathrm{st}}}\right\} + K_{\mathrm{p},1\mathrm{st}}}$$

Update of projection center with respect to stress reversal

Non-monotonic stress paths result in elastoplastic strain even after the stress reversal. To numerically capture this behavior the projection center ${}_{m-1}\boldsymbol{\sigma}'_{\mathrm{pc}}$ needs to be updated to the stress state of the last stress reversal ${}_{m-1}\boldsymbol{\sigma}'_{\mathrm{reset}}$ whenever a stress reversal occurs (Seidalinov and Taiebat, 2014). From an analytical point of view a stress reversal appears whenever $L_{1\mathrm{st}} < 0$. Afterwards, the calculation for the sub-step has to be restarted using the updated projection center and the stress ${}_{m-1}\boldsymbol{\sigma}' = {}_{m-1}\boldsymbol{\sigma}'_{\mathrm{reset}}$, hardening variables ${}_{m-1}\boldsymbol{q}$ and void ratio ${}_{m-1}e = {}_{m-1}e_{\mathrm{reset}}$ at the beginning of the sub-step. The sub-step number m

is kept constant and the calculation starts from the beginning of the sub-stepping loop. It has to be noticed that an update of the projection center causes an update of the elastic nucleus because the projection center is the center of homology between the elastic nucleus and the bounding surface. Therefore, the intersection of the trial stress path with the updated elastic nucleus has to be newly calculated using the resetted values of the stress ${}_{m-1}\boldsymbol{\sigma}'_{\mathrm{reset}}$ and void ratio ${}_{m-1}e_{\mathrm{reset}}$ when restarting the sub-stepping loop.

Check for update of projection center wrt. stress reversal

If $\{L_{1\mathrm{st}} < 0\}$

Then Do (update projection center to last stress reversal state)

Reset projection center, stress state and void ratio

$${}_{m-1}\boldsymbol{\sigma}'_{\mathrm{pc}} = {}_{m-1}\boldsymbol{\sigma}'_{\mathrm{reset}}$$

$${}_{m-1}\boldsymbol{\sigma}' = {}_{m-1}\boldsymbol{\sigma}'_{\mathrm{reset}}$$

$${}_{m-1}e = {}_{m-1}e_{\mathrm{reset}}$$

Keep m constant

Go To sub-stepping loop

End If (check for update of projection center wrt. stress reversal)

Update of variables and calculation of plastic strain sub-increment

If no stress reversal is detected the increments of the hardening variables $\Delta\boldsymbol{q}_{1\mathrm{st}}$ and the structure variable $\Delta S_{\mathrm{i},1\mathrm{st}}$ are calculated based on the plastic loading index $L_{1\mathrm{st}}$, so that $\Delta\boldsymbol{q}_{1\mathrm{st}} = L_{1\mathrm{st}}\,\tilde{\boldsymbol{q}}_{1\mathrm{st}}$ and $\Delta S_{\mathrm{i},1\mathrm{st}} = L_{1\mathrm{st}}\,\tilde{S}_{\mathrm{i},1\mathrm{st}}$. The variables $\Delta p_{0,\mathrm{s},1\mathrm{st}}$, $\Delta p_{0,\mathrm{i},1\mathrm{st}}$, $\Delta S_{\mathrm{i},1\mathrm{st}}$ and $\Delta\boldsymbol{\alpha}_{1\mathrm{st}}$ are specified by the Equations 3.31, 3.32, 3.33 - 3.34 and 3.15, respectively. The update of the hardening variables and the structure variable yield to $\boldsymbol{q}_{1\mathrm{st}} = {}_{m-1}\boldsymbol{q} + \Delta\boldsymbol{q}_{1\mathrm{st}}$ and $S_{\mathrm{i},1\mathrm{st}} = {}_{m-1}S_{\mathrm{i}} + \Delta S_{\mathrm{i},1\mathrm{st}}$. The final value of the void ratio ${}_{m}e$ is computed considering the total volumetric strain increment ${}_{m}\Delta\boldsymbol{\varepsilon}^{\mathrm{v}}$ and the void ratio ${}_{m-1}e$ at the beginning of the sub-step, so that ${}_{m}e = {}_{m-1}e - {}_{m}\Delta\boldsymbol{\varepsilon}^{\mathrm{v}}\ \{1 + {}_{m-1}e\}$. Therefore, the void ratio ${}_{m}e$ at the end of the sub-step is independent of the estimation number. Furthermore, the projection center $\boldsymbol{\sigma}'_{\mathrm{pc},1\mathrm{st}}$ evolves with respect to the evolution of the bounding surface due to the calculated increments of the hardening variables $\Delta\boldsymbol{q}_{1\mathrm{st}}$ to ensure that the projection center is always located inside or on the updated bounding surface. The update of the projection center is given by $\boldsymbol{\sigma}'_{\mathrm{pc},1\mathrm{st}} = {}_{m-1}\boldsymbol{\sigma}'_{\mathrm{pc}} + \Delta\boldsymbol{\sigma}'_{\mathrm{pc},1\mathrm{st}}$. Whereat, the increment of the projection center

$\Delta\boldsymbol{\sigma}'_{\mathrm{pc,1st}}$ is calculated by calling a certain subroutine, which includes the associated evolution Equations 3.39 - 3.42. The plastic strain sub-increment $\Delta\boldsymbol{\varepsilon}^{\mathrm{p}}_{\mathrm{1st}}$ for the first estimation is determined using the non-associated flow rule 3.12, so that $\Delta\boldsymbol{\varepsilon}^{\mathrm{p}}_{\mathrm{1st}} = L_{\mathrm{1st}}\ \{\partial G/\bar{\boldsymbol{\sigma}}'_{\mathrm{1st}}\}$. Whereat, the size of the plastic strain sub-increment is given by the plastic loading index L_{1st} and the direction of the plastic strain sub-increment is governed by the gradient of the plastic potential with respect to the image stress state $\partial G/\bar{\boldsymbol{\sigma}}'_{\mathrm{1st}}$. Based on the plastic deviatoric strain sub-increment the increment of the damage variable Δd_{1st} can be evaluated according to Equation 3.38, so that $\Delta d_{\mathrm{1st}} = a_{\mathrm{dam}}\sqrt{2/3\ \Delta\boldsymbol{e}^{\mathrm{p}}_{\mathrm{1st}} : \Delta\boldsymbol{e}^{\mathrm{p}}_{\mathrm{1st}}}$. Afterwards, the damage variable $d_{\mathrm{1st}} = {}_{m-1}d + \Delta d_{\mathrm{1st}}$ is updated.

Update of variables and calculation of plastic strain sub-increment $\Delta\boldsymbol{\varepsilon}^{\mathrm{p}}_{\mathrm{1st}}$

Calculate increment of hardening variables and structure variable

$$\Delta\boldsymbol{q}_{\mathrm{1st}} = L_{\mathrm{1st}}\ \tilde{\boldsymbol{q}}_{\mathrm{1st}}$$

$$\Delta S_{\mathrm{i,1st}} = L_{\mathrm{1st}}\ \tilde{S}_{\mathrm{i,1st}}$$

Update hardening variables and structure variable

$$\boldsymbol{q}_{\mathrm{1st}} = {}_{m-1}\boldsymbol{q} + \Delta\boldsymbol{q}_{\mathrm{1st}}$$

$$S_{\mathrm{i,1st}} = {}_{m-1}S_{\mathrm{i}} + \Delta S_{\mathrm{i,1st}}$$

Update void ratio

$${}_{m}e = {}_{m-1}e - {}_{m}\Delta\boldsymbol{\varepsilon}^{\mathrm{v}}\ \{1 + {}_{m-1}e\}$$

Update projection center wrt. updated hardening variables

Call subroutine: increment projection center (see section 3.3.9)

input: ${}_{m-1}\boldsymbol{q}$, $\Delta\boldsymbol{q}_{\mathrm{1st}}$, ${}_{m-1}\boldsymbol{\sigma}'_{\mathrm{pc}}$

output: $\Delta\boldsymbol{\sigma}'_{\mathrm{pc,1st}}$

Update $\boldsymbol{\sigma}_{\mathrm{pc,1st}} = {}_{m-1}\boldsymbol{\sigma}'_{\mathrm{pc}} + \Delta\boldsymbol{\sigma}'_{\mathrm{pc,1st}}$

Calculate plastic strain sub-increment

$$\Delta\boldsymbol{\varepsilon}^{\mathrm{p}}_{\mathrm{1st}} = L_{\mathrm{1st}}\ \left\{\frac{\partial G}{\partial\bar{\boldsymbol{\sigma}}'_{\mathrm{1st}}}\right\}$$

Calculate increment of damage variable wrt. plastic deviatoric strain increment

$$\Delta d_{\mathrm{1st}} = a_{\mathrm{dam}}\sqrt{\frac{2}{3}\ \Delta\boldsymbol{e}^{\mathrm{p}}_{\mathrm{1st}} : \Delta\boldsymbol{e}^{\mathrm{p}}_{\mathrm{1st}}}$$

Update damage variable

$$d_{\mathrm{1st}} = {}_{m-1}d + \Delta d_{\mathrm{1st}}$$

Plastic stress correction and calculation of final stress state

After each stress estimation according to the Modified Euler approach, the elastic trial stress increment $\Delta\boldsymbol{\sigma}'$ has to be corrected via a plastic stress correction incorporating the plastic strain increment $\Delta\boldsymbol{\varepsilon}^{\mathrm{p}}$. Hence, the trial stress increment is projected back along the plastic flow direction, so that $\Delta\boldsymbol{\sigma}' = \boldsymbol{D}^{\mathrm{e}} : \{\Delta\boldsymbol{\varepsilon} - \Delta\boldsymbol{\varepsilon}^{\mathrm{p}}\}$.
Inserting the corresponding variables yields $\Delta\boldsymbol{\sigma}'_{1\mathrm{st}} = \boldsymbol{D}^{\mathrm{e}}_{1\mathrm{st}} : \{{}_m\Delta\boldsymbol{\varepsilon} - \Delta\boldsymbol{\varepsilon}^{\mathrm{p}}_{1\mathrm{st}}\}$ for the first estimation . The corrected elastoplastic stress state after the first estimation is given by the following equation, so that $\boldsymbol{\sigma}'_{1\mathrm{st}} = {}_{m-1}\boldsymbol{\sigma}' + \Delta\boldsymbol{\sigma}'_{1\mathrm{st}}$. Finally, at the end of the first estimation the increments of stress $\Delta\boldsymbol{\sigma}'_{1\mathrm{st}}$, hardening variables $\Delta\boldsymbol{q}_{1\mathrm{st}}$, structure variable $\Delta S_{\mathrm{i},1\mathrm{st}}$ and damage variable $\Delta d_{1\mathrm{st}}$ are provided. The increments are needed for the calculation of the Modified Euler second order accurate solution after the second estimation. In addition, the former two components are needed to calculate the relative error in the general explicit integration scheme later on. Moreover, the updated values of the first estimation of the stress state $\boldsymbol{\sigma}'_{1\mathrm{st}}$, hardening variables $\boldsymbol{q}_{1\mathrm{st}}$, structure variable $S_{\mathrm{i},1\mathrm{st}}$, damage variable $d_{1\mathrm{st}}$, void ratio ${}_me$ and position of the projection center $\boldsymbol{\sigma}'_{\mathrm{pc},1\mathrm{st}}$ are supplied. The final values of the variables are needed as the basis of the second estimation within the Modified Euler approach.

Plastic stress correction and calculation of stress increment $\Delta\boldsymbol{\sigma}'_{1\mathrm{st}}$ and stress state $\boldsymbol{\sigma}'_{1\mathrm{st}}$

Calculate plastic stress correction

$$\Delta\boldsymbol{\sigma}'_{1\mathrm{st}} = \boldsymbol{D}^{\mathrm{e}}_{1\mathrm{st}} : \{{}_m\Delta\boldsymbol{\varepsilon} - \Delta\boldsymbol{\varepsilon}^{\mathrm{p}}_{1\mathrm{st}}\}$$

Calculate final stress state after first estimation

$$\boldsymbol{\sigma}'_{1\mathrm{st}} = {}_{m-1}\boldsymbol{\sigma}' + \Delta\boldsymbol{\sigma}'_{1\mathrm{st}}$$

Obtained variables of first estimation

$$\Delta\boldsymbol{\sigma}'_{1\mathrm{st}},\ \Delta\boldsymbol{q}_{1\mathrm{st}},\ \Delta S_{\mathrm{i},1\mathrm{st}},\ \Delta d_{1\mathrm{st}},\ \boldsymbol{\sigma}'_{1\mathrm{st}},\ \boldsymbol{q}_{1\mathrm{st}},\ S_{\mathrm{i},1\mathrm{st}},\ d_{1\mathrm{st}},\ {}_me,\ \boldsymbol{\sigma}'_{\mathrm{pc},1\mathrm{st}}$$

2nd estimation - 2nd elastic trial stress state, plastic stress correction and final stress state

The general procedure of the second estimation of the increments of stress $\Delta\boldsymbol{\sigma}'_{2\mathrm{nd}}$ related to the given strain sub-increment ${}_m\Delta\boldsymbol{\varepsilon}$, hardening variables $\Delta\boldsymbol{q}_{2\mathrm{nd}}$, structure variable $\Delta S_{\mathrm{i},2\mathrm{nd}}$ and damage variable $\Delta d_{2\mathrm{nd}}$ is almost identical to the procedure applied for the first estimation. However, the second estimation is based on the results of the first estimation

such as stress state $\boldsymbol{\sigma}'_{1st}$, hardening variables $\boldsymbol{q}_{1st}$, structure variable $S_{i,1st}$, damage variable d_{1st}, void ratio ${}_m e$, elastic stiffness matrix $\boldsymbol{D}^{e}_{2nd}(\boldsymbol{\sigma}'_{1st},\ {}_m e)$ and projection center $\boldsymbol{\sigma}'_{pc,1st}$. Furthermore, the updated bounding surface and plastic potential surface are considered for the second estimation. The elastic trial stress increment $\Delta\boldsymbol{\sigma}'_{trial,2nd}$ is calculated based on the elastic stress-strain relation as a function of strain sub-increment ${}_m\Delta\boldsymbol{\varepsilon}$ and tangent elastic stiffness matrix $\boldsymbol{D}^{e}_{2nd}(\boldsymbol{\sigma}'_{1st},\ {}_m e)$ with respect to stress state $\boldsymbol{\sigma}'_{1st}$ and void ratio ${}_m e$ after the first estimation. The elastic trial stress state $\boldsymbol{\sigma}'_{trial,2nd}$ of the second estimation is determined afterwards.

Calculation of elastic trial stress $\boldsymbol{\sigma}'_{trial,2nd}$

Calculate elastic trial stress increment

$$\Delta\boldsymbol{\sigma}_{trial,2nd} = \boldsymbol{D}^{e}_{2nd}(\boldsymbol{\sigma}'_{1st},\ {}_m e) : {}_m\Delta\boldsymbol{\varepsilon}$$

Calculate elastic trial stress

$$\boldsymbol{\sigma}'_{trial,2nd} = {}_{m-1}\boldsymbol{\sigma}' + \Delta\boldsymbol{\sigma}'_{trial,2nd}$$

Calculation of plasticity modulus

The similarity ratio b_{2nd} and the corresponding Lode angle dependent variable N_{2nd} for the second estimation are calculated with respect to the stress state $\boldsymbol{\sigma}'_{1st}$ after the first estimation and with respect to the updated bounding surface F specified by the updated hardening variables $\boldsymbol{q}_{1st}$ and the updated position of the projection center $\boldsymbol{\sigma}'_{pc,1st}$ after the first estimation. The image stress state $\bar{\boldsymbol{\sigma}}'_{2nd}$ is computed by use of the similarity ratio b_{2nd} employing the projection rule 3.9, so that $\bar{\boldsymbol{\sigma}}'_{2nd} = b_{2nd}\left\{\boldsymbol{\sigma}'_{1st} - \boldsymbol{\sigma}'_{pc,1st}\right\} + \boldsymbol{\sigma}'_{pc,1st}$.
The plasticity modulus $K_{p,2nd} = \bar{K}_{p,2nd} + \hat{f}_{2nd}\,\hat{h}_{2nd}$ with respect to the stress state $\boldsymbol{\sigma}'_{1st}$ after the first estimation is calculated with respect to the image stress state $\bar{\boldsymbol{\sigma}}'_{2nd}$, so that $\bar{K}_{p,2nd} = -\{\partial F/\partial p_{0,s,1st}\ \tilde{p}_{0,s,2nd} + \partial F/\partial\boldsymbol{\alpha}_{1st} : \tilde{\boldsymbol{\alpha}}_{2nd}\}$. Whereat, the bounding surface $F(\bar{\boldsymbol{\sigma}}'_{2nd}, \boldsymbol{q}_{1st}) = 0$ is evaluated with respect to the hardening variables $p_{0,s,1st}$ and $\boldsymbol{\alpha}_{1st}$ after the first estimation. The gradients $\partial F/\partial p_{0,s,1st}$ and $\partial F/\boldsymbol{\alpha}_{1st}$ are given by Equations 4.127 and 4.128. Furthermore, the variables $\tilde{p}_{0,s,2nd}$, $\tilde{p}_{0,i,2nd}$, $\tilde{S}_{i,2nd}$ and $\tilde{\boldsymbol{\alpha}}_{2nd}$ are calculated as functions of the hardening variables $\boldsymbol{q}_{1st}$, structure variable $S_{i,1st}$ and void ratio ${}_m e$ after the first estimation. However, the plastic potential surface $G(\bar{\boldsymbol{\sigma}}'_{2nd}, \boldsymbol{q}_{1st}) = 0$ is evaluated with respect to the variable $p_{\alpha,1st}$ and the same hardening variable $\boldsymbol{\alpha}_{1st}$ after the first estimation. The required gradient of the plastic potential surface with respect to the image stress state $\partial G/\bar{\boldsymbol{\sigma}}'_{2nd}$ is presented in section 4.4.10. The distance function $\hat{f}_{2nd}$ is evaluated as a function of the similarity ratio b_{2nd}, so that $\hat{f}_{2nd} = \langle\{b_{2nd} - 1\} / \{b_{2nd} - \{b_{2nd} - 1\}\ s_{eln}\}\rangle$. The

shape hardening function $\hat{h}_{2\mathrm{nd}}$ is derived as a function of the hardening variables $p_{0,\mathrm{s},1\mathrm{st}}$ and the damage variable $d_{1\mathrm{st}}$ after the first estimation, so that $\hat{h}_{2\mathrm{nd}} = \{p_{0,\mathrm{s},1\mathrm{st}}\}^3 \; h_0 \,/\, \{1{+}d_{1\mathrm{st}}\}$.

Calculation of plasticity modulus $K_{\mathrm{p},2\mathrm{nd}}$

Call subroutine: iterative solution for similarity ratio (see section 4.4.8)

input: $\boldsymbol{\sigma}'_{1\mathrm{st}}$, $\boldsymbol{q}_{1\mathrm{st}}$, $\boldsymbol{\sigma}'_{\mathrm{pc},1\mathrm{st}}$

output: $b_{2\mathrm{nd}}$, $N_{2\mathrm{nd}}(\theta_{2\mathrm{nd}})$

Calculate image stress

$$\bar{\boldsymbol{\sigma}}'_{2\mathrm{nd}} = b_{2\mathrm{nd}} \left\{\boldsymbol{\sigma}'_{1\mathrm{st}} - \boldsymbol{\sigma}'_{\mathrm{pc},1\mathrm{st}}\right\} + \boldsymbol{\sigma}'_{\mathrm{pc},1\mathrm{st}}$$

Call subroutine: plasticity modulus wrt. stress on the bounding surface

input: $\bar{\boldsymbol{\sigma}}'_{2\mathrm{nd}}$, $\boldsymbol{q}_{1\mathrm{st}}$, $S_{\mathrm{i},1\mathrm{st}}$, ${}_m e$

output: $\bar{K}_{\mathrm{p},2\mathrm{nd}}$, $\tilde{\mathrm{q}}_{2\mathrm{nd}}$, $\tilde{S}_{\mathrm{i},2\mathrm{nd}}$

Calculate distance function

$$\hat{f}_{2\mathrm{nd}} = \left\langle \frac{b_{2\mathrm{nd}} - 1}{b_{2\mathrm{nd}} - \{b_{2\mathrm{nd}} - 1\} \; s_{\mathrm{eln}}} \right\rangle$$

Calculate shape hardening function

$$\hat{h}_{2\mathrm{nd}} = \{p_{0,\mathrm{s},1\mathrm{st}}\}^3 \; \frac{h_0}{1{+}d_{1\mathrm{st}}}$$

Calculate plasticity modulus wrt. current stress

$$K_{\mathrm{p},2\mathrm{nd}} = \bar{K}_{\mathrm{p},2\mathrm{nd}} + \hat{f}_{2\mathrm{nd}} \; \hat{h}_{2\mathrm{nd}}$$

Calculation of plastic loading index

The plastic loading index $L_{2\mathrm{nd}}$ is a function of the elastic stiffness matrix $\boldsymbol{D}^{\mathrm{e}}_{2\mathrm{nd}}(\boldsymbol{\sigma}'_{1\mathrm{st}}, {}_m e)$ with respect to the stress state $\boldsymbol{\sigma}'_{1\mathrm{st}}$ after the first estimation, void ratio ${}_m e$ at the end of the sub-step, plasticity modulus $K_{\mathrm{p},2\mathrm{nd}}$ and strain sub-increment ${}_m\Delta\boldsymbol{\varepsilon}$. The gradients of the bounding surface $\partial F/\bar{\boldsymbol{\sigma}}'_{2\mathrm{nd}}$ and the plastic potential surface $\partial G/\bar{\boldsymbol{\sigma}}'_{2\mathrm{nd}}$ are evaluated with respect to the image stress state $\bar{\boldsymbol{\sigma}}'_{2\mathrm{nd}}$.

Calculation of plastic loading index $L_{2\mathrm{nd}}$

Calculate plastic loading index

$$L_{2\mathrm{nd}} = \frac{\left\{\dfrac{\partial F}{\partial \bar{\boldsymbol{\sigma}}'_{2\mathrm{nd}}}\right\} : \boldsymbol{D}^{\mathrm{e}}_{2\mathrm{nd}}(\boldsymbol{\sigma}'_{1\mathrm{st}}, {}_m e) : {}_m\Delta\boldsymbol{\varepsilon}}{\left\{\dfrac{\partial F}{\partial \bar{\boldsymbol{\sigma}}'_{2\mathrm{nd}}}\right\} : \boldsymbol{D}^{\mathrm{e}}_{2\mathrm{nd}}(\boldsymbol{\sigma}'_{1\mathrm{st}}, {}_m e) : \left\{\dfrac{\partial G}{\partial \bar{\boldsymbol{\sigma}}'_{2\mathrm{nd}}}\right\} + K_{\mathrm{p},2\mathrm{nd}}}$$

Update of projection center with respect to stress reversal

It needs to be checked, if a stress reversal occurs for the second estimation $L_{2\mathrm{nd}} < 0$. This could rarely appear even if a stress reversal was not detected for the first estimation. If a stress reversal occurs, the entire calculation for the sub-step including the first estimation of stress, hardening variables, structure variable and damage variable has to be restarted using the updated projection center ${}_{m-1}\boldsymbol{\sigma}'_{\mathrm{pc}} = {}_{m-1}\boldsymbol{\sigma}'_{\mathrm{reset}}$ and the stress state ${}_{m-1}\boldsymbol{\sigma}' = {}_{m-1}\boldsymbol{\sigma}'_{\mathrm{reset}}$ and void ratio ${}_{m-1}e = {}_{m-1}e_{\mathrm{reset}}$ at the beginning of the sub-step.

Check for update of projection center wrt. stress reversal

If $\{L_{2\mathrm{nd}} < 0\}$

Then Do (update projection center to last stress reversal state)

Reset projection center, stress state and void ratio

$${}_{m-1}\boldsymbol{\sigma}'_{\mathrm{pc}} = {}_{m-1}\boldsymbol{\sigma}'_{\mathrm{reset}}$$

$${}_{m-1}\boldsymbol{\sigma}' = {}_{m-1}\boldsymbol{\sigma}'_{\mathrm{reset}}$$

$${}_{m-1}e = {}_{m-1}e_{\mathrm{reset}}$$

Keep m constant

Go To sub-stepping loop

End If (check for update of projection center wrt. stress reversal)

Calculation of increments of variables and plastic strain sub-increment

For the further calculation of the Modified Euler solution only the increments of hardening variables $\Delta\boldsymbol{q}_{2\mathrm{nd}}$ and structure variable $\Delta S_{\mathrm{i},2\mathrm{nd}}$ are required. The updated values of the hardening variables are not needed. The increments are calculated based on the plastic loading index $L_{2\mathrm{nd}}$, so that $\Delta\boldsymbol{q}_{2\mathrm{nd}} = L_{2\mathrm{nd}}\ \tilde{\boldsymbol{q}}_{2\mathrm{nd}}$ and $\Delta S_{\mathrm{i},2\mathrm{nd}} = L_{2\mathrm{nd}}\ \tilde{S}_{\mathrm{i},2\mathrm{nd}}$. Furthermore, the update of the void ratio is the same as for the first estimation and has not to be calculated again. Also the update of the projection center with respect to the evolution of the bounding surface is not required for the final calculation of the Modified Euler solution. The plastic strain sub-increment $\Delta\boldsymbol{\varepsilon}^{\mathrm{p}}_{2\mathrm{nd}}$ for the second estimation is determined using the non-associated flow rule as a function of plastic loading index $L_{2\mathrm{nd}}$ and gradient of the plastic potential $\partial G/\bar{\boldsymbol{\sigma}}'_{2\mathrm{nd}}$ with respect to the image stress state $\bar{\boldsymbol{\sigma}}'_{2\mathrm{nd}}$, so that $\Delta\boldsymbol{\varepsilon}^{\mathrm{p}}_{2\mathrm{nd}} = L_{2\mathrm{nd}}\ \{\partial G/\bar{\boldsymbol{\sigma}}'_{2\mathrm{nd}}\}$. Based on the plastic deviatoric strain sub-increment the increment of the damage variable $\Delta d_{2\mathrm{nd}}$ can be evaluated, so that $\Delta d_{2\mathrm{nd}} = a_{\mathrm{dam}}\ \sqrt{2/3\ \Delta\boldsymbol{e}^{\mathrm{p}}_{2\mathrm{nd}} : \Delta\boldsymbol{e}^{\mathrm{p}}_{2\mathrm{nd}}}$. The updated value of the damage variable is not needed for the further calculation.

Calculation of increments of variables and plastic strain sub-increment $\Delta\boldsymbol{\varepsilon}^{\mathrm{p}}_{2\mathrm{nd}}$

Calculate increment of hardening variables and structure variable

$$\Delta\boldsymbol{q}_{2\mathrm{nd}} = L_{2\mathrm{nd}}\ \tilde{\boldsymbol{q}}_{2\mathrm{nd}}$$

$$\Delta S_{\mathrm{i},2\mathrm{nd}} = L_{2\mathrm{nd}}\ \tilde{S}_{\mathrm{i},2\mathrm{nd}}$$

Calculate plastic strain sub-increment

$$\Delta\boldsymbol{\varepsilon}^{\mathrm{p}}_{2\mathrm{nd}} = L_{2\mathrm{nd}}\ \left\{\frac{\partial G}{\partial \bar{\boldsymbol{\sigma}}'_{2\mathrm{nd}}}\right\}$$

Calculate increment of damage variable wrt. plastic deviatoric strain increment

$$\Delta d_{2\mathrm{nd}} = a_{\mathrm{dam}}\ \sqrt{\frac{2}{3}\,\Delta\boldsymbol{e}^{\mathrm{p}}_{2\mathrm{nd}} : \Delta\boldsymbol{e}^{\mathrm{p}}_{2\mathrm{nd}}}$$

Plastic stress correction

The plastic stress correction yields $\Delta\boldsymbol{\sigma}'_{2\mathrm{nd}} = \boldsymbol{D}^{\mathrm{e}}_{2\mathrm{nd}} : \{{}_m\Delta\boldsymbol{\varepsilon} - \Delta\boldsymbol{\varepsilon}^{\mathrm{p}}_{2\mathrm{nd}}\}$ for the second estimation. The corrected elastoplastic stress state after the second estimation is not required for the further calculation of the Modified Euler solution. Finally, at the end of the second estimation the increments of stress $\Delta\boldsymbol{\sigma}'_{2\mathrm{nd}}$, hardening variables $\Delta\boldsymbol{q}_{2\mathrm{nd}}$, structure variable $\Delta S_{\mathrm{i},2\mathrm{nd}}$ and damage variable $\Delta d_{2\mathrm{nd}}$ are provided. The increments are needed for the calculation of the Modified Euler second order accurate solution. In addition, the former two components are needed to calculate the relative error in the general explicit integration scheme later on.

Plastic stress correction and calculation of stress increment $\Delta\boldsymbol{\sigma}'_{2\mathrm{nd}}$ and stress state $\boldsymbol{\sigma}'_{2\mathrm{nd}}$

Calculate plastic stress correction

$$\Delta\boldsymbol{\sigma}'_{2\mathrm{nd}} = \boldsymbol{D}^{\mathrm{e}}_{2\mathrm{nd}} : \{{}_m\Delta\boldsymbol{\varepsilon} - \Delta\boldsymbol{\varepsilon}^{\mathrm{p}}_{2\mathrm{nd}}\}$$

Obtained variables of second estimation

$$\Delta\boldsymbol{\sigma}'_{2\mathrm{nd}},\ \Delta\boldsymbol{q}_{2\mathrm{nd}},\ \Delta S_{\mathrm{i},2\mathrm{nd}},\ \Delta d_{2\mathrm{nd}}$$

Calculation and transfer of Modified Euler solution for stress and variables

At the end of the Modified Euler algorithm the second order accurate solutions for the stress state ${}_m\boldsymbol{\sigma}'$, hardening variables ${}_m\boldsymbol{q}$, structure variable ${}_mS_{\mathrm{i}}$ and damage variable ${}_md$ are calculated in accordance with the Equations 4.21- 4.24 by averaging the corresponding increments obtained in the first and in the second estimation $\Delta\boldsymbol{\sigma}'_{1\mathrm{st}}$, $\Delta\boldsymbol{\sigma}'_{2\mathrm{nd}}$, $\Delta\boldsymbol{q}_{1\mathrm{st}}$, $\Delta\boldsymbol{q}_{2\mathrm{nd}}$,

$\Delta S_{\mathrm{i,1st}}$, $\Delta S_{\mathrm{i,2nd}}$ and Δd_{1st}, Δd_{2nd}. The final values are returned back to the general integration scheme. Furthermore, the increments of stress $\Delta\boldsymbol{\sigma}'_{\mathrm{1st}}$, $\Delta\boldsymbol{\sigma}'_{\mathrm{2nd}}$ and hardening variables $\Delta\boldsymbol{q}_{\mathrm{1st}}$, $\Delta\boldsymbol{q}_{\mathrm{2nd}}$ from the first and the second estimation are provided to the general integration scheme for the calculation of the relative error ${}_mR$ to decide if the Modified Euler calculation step is successful. At last, the void ratio ${}_me$ at the end of the sub-step based on the total volumetric strain and independent of the estimation number is also transferred to the general integration scheme.

Calculation of Modified Euler 2nd order accurate solution

Update stress, hardening variables, structure variable and damage variable

$${}_m\boldsymbol{\sigma}' = {}_{m-1}\boldsymbol{\sigma}' + \frac{1}{2}\left\{\Delta\boldsymbol{\sigma}'_{\mathrm{1st}} + \Delta\boldsymbol{\sigma}'_{\mathrm{2nd}}\right\}$$

$${}_m\boldsymbol{q} = {}_{m-1}\boldsymbol{q} + \frac{1}{2}\left\{\Delta\boldsymbol{q}_{\mathrm{1st}} + \Delta\boldsymbol{q}_{\mathrm{2nd}}\right\}$$

$${}_mS_{\mathrm{i}} = {}_{m-1}S_{\mathrm{i}} + \frac{1}{2}\left\{\Delta S_{\mathrm{i,1st}} + \Delta S_{\mathrm{i,2nd}}\right\}$$

$${}_md = {}_{m-1}d + \frac{1}{2}\left\{\Delta d_{\mathrm{1st}} + \Delta d_{\mathrm{2nd}}\right\}$$

Return ${}_m\boldsymbol{\sigma}'$, $\Delta\boldsymbol{\sigma}'_{\mathrm{1st}}$, $\Delta\boldsymbol{\sigma}'_{\mathrm{2nd}}$, ${}_m\boldsymbol{q}$, $\Delta\boldsymbol{q}_{\mathrm{1st}}$, $\Delta\boldsymbol{q}_{\mathrm{2nd}}$, ${}_mS_{\mathrm{i}}$, ${}_md$, ${}_me$

4.4.4 Drift correction

As already mentioned, if the elastoplastic stress state after the successful Modified Euler calculation is positioned outside the bounding surface $F({}_m\boldsymbol{\sigma}',\ {}_m\boldsymbol{q}) > +Tol$ the stress state has to be corrected and returned/projected back to the bounding surface by use of an iterative drift correction algorithm. In the present study a so-called consistent drift correction approach proposed by Potts and Gens (1985) and Sloan et al. (2001) is employed. The consistent drift correction approach is based on the iterative back projection of the elastoplastic stress state along the direction of the plastic flow. The consistent drift correction approach considers that each correction of the stress state due to the corrected plastic strain increment will evoke a correction of the hardening variables influencing the bounding surface. Moreover, the structure variable and the damage variable are updated with respect to the corrected plastic strain increment.

Within the consistent drift correction approach the corrected stress increment ${}^j\Delta\boldsymbol{\sigma}'_{\mathrm{drift}}$ in any iteration j is calculated according to the Equation 4.25. Therein, ${}^j\Delta\boldsymbol{\varepsilon}^{\mathrm{pl}}_{\mathrm{drift}}$ and ${}^jL_{\mathrm{drift}}$ are the corresponding corrected plastic strain increment and the scalar plastic loading index, respectively. It is to be noted that in the following discussion the left superscript j

denotes the iteration number $[1, j_{\max}]$. Thereby, the superscript $j-1$ specifies the initial values at the beginning of the current iteration and the superscript j specifies the increments and the final values at the end of the current iteration.

$$\begin{aligned} {}^{j}\Delta\boldsymbol{\sigma}'_{\text{drift}} &= \boldsymbol{D}^{\text{e}}\left({}^{j-1}\boldsymbol{\sigma}',\ {}_{m}e\right) : {}^{j}\Delta\boldsymbol{\varepsilon}^{\text{pl}}_{\text{drift}} \\ &= {}^{j}L_{\text{drift}}\ \boldsymbol{D}^{\text{e}}\left({}^{j-1}\boldsymbol{\sigma}',\ {}_{m}e\right) : \left\{\frac{\partial G}{\partial\, {}^{j-1}\boldsymbol{\sigma}'}\right\} \end{aligned} \tag{4.25}$$

The corrected scalar plastic loading index ${}^{j}L_{\text{drift}}$ is determined by an expansion of the bounding surface formulation F in a Taylor series while neglecting the second order and above terms as given in Equation 4.26.

$${}^{j}L_{\text{drift}} = \frac{F\left({}^{j-1}\boldsymbol{\sigma}',\ {}^{j-1}\boldsymbol{q}\right)}{\left\{\frac{\partial F}{\partial\, {}^{j-1}\boldsymbol{\sigma}'}\right\} : \boldsymbol{D}^{\text{e}}\left({}^{j-1}\boldsymbol{\sigma}',\ {}_{m}e\right) : \left\{\frac{\partial G}{\partial\, {}^{j-1}\boldsymbol{\sigma}'}\right\} + {}^{j-1}K_{\text{p}}} \tag{4.26}$$

Finally, the corrected stress state ${}^{j}\boldsymbol{\sigma}'$ at the end of the iteration is given by Equation 4.27 as the difference of the stress state ${}^{j-1}\boldsymbol{\sigma}'$ at the beginning of the iteration and the corrected stress increment ${}^{j}\Delta\boldsymbol{\sigma}'_{\text{drift}}$ from the consistent drift correction approach from Equation 4.25.

$${}^{j}\boldsymbol{\sigma}' = {}^{j-1}\boldsymbol{\sigma}' - {}^{j}\Delta\boldsymbol{\sigma}'_{\text{drift}} \tag{4.27}$$

The corrected plastic strain increment during the consistent drift correction causes corresponding increments of the hardening variables ${}^{j}\Delta\boldsymbol{q}_{\text{drift}}$, structure variable ${}^{j}\Delta S_{\text{i,drift}}$ and damage variable ${}^{j}\Delta d_{\text{drift}}$ according to Equations 4.28-4.30.

$${}^{j}\Delta\boldsymbol{q}_{\text{drift}} = {}^{j}L_{\text{drift}}\ {}^{j}\tilde{\boldsymbol{q}}_{\text{drift}} \tag{4.28}$$

$${}^{j}\Delta S_{\text{i,drift}} = {}^{j}L_{\text{drift}}\ {}^{j}\tilde{S}_{\text{i,drift}} \tag{4.29}$$

$${}^{j}\Delta d_{\text{drift}} = a_{\text{dam}}\sqrt{\frac{2}{3}\ {}^{j}\Delta\boldsymbol{e}^{\text{p}}_{\text{drift}} : {}^{j}\Delta\boldsymbol{e}^{\text{p}}_{\text{drift}}} \tag{4.30}$$

Consequently, the corrected variables ${}^{j}\boldsymbol{q}$, ${}^{j}S_{\text{i}}$ and ${}^{j}d$ at the end of the current iteration are given by Equations 4.31-4.33 and are defined as the sum of the variables ${}^{j-1}\boldsymbol{q}$, ${}^{j-1}S_{\text{i}}$ and ${}^{j-1}d$ at the beginning of the iteration and the corrected increment of the variables

${}^{j}\Delta\boldsymbol{q}_{\mathrm{drift}}$, ${}^{j}\Delta S_{\mathrm{i,drift}}$ and ${}^{j}\Delta d_{\mathrm{drift}}$ from the consistent drift correction approach.

$$
\begin{aligned}
{}^{j}\boldsymbol{q} &= {}^{j-1}\boldsymbol{q} + {}^{j}\Delta\boldsymbol{q}_{\mathrm{drift}} && (4.31)\\
{}^{j}S_{\mathrm{i}} &= {}^{j-1}S_{\mathrm{i}} + {}^{j}\Delta S_{\mathrm{i,drift}} && (4.32)\\
{}^{j}d &= {}^{j-1}d + {}^{j}\Delta d_{\mathrm{drift}} && (4.33)
\end{aligned}
$$

In case of divergence of the consistent drift correction approach the normal drift correction approach is activated. Hence, the normal drift correction approach is used whenever $|F\left({}^{j}\boldsymbol{\sigma}',\, {}^{j}\boldsymbol{q}\right)| \geq |F\left({}^{j-1}\boldsymbol{\sigma}',\, {}^{j-1}\boldsymbol{q}\right)|$ anytime after the first iteration. This is, it has to be checked after each iteration if the value of the bounding surface function with respect to the stress state at the end of the current iteration is larger or equal than the value of the bounding surface function with respect to the stress state at the beginning of the current iteration. In that case the normal drift correction is activated and replaces the former consistent drift correction of the current iteration. The normal drift correction approach is based on the back projection of the stress state along the normal to the bounding surface specified by the gradient $\partial F/\partial {}^{j-1}\boldsymbol{\sigma}'$ without considering the update of the hardening variables. When employing the normal drift correction approach the corrected stress increment ${}^{j}\Delta\boldsymbol{\sigma}'_{\mathrm{drift}}$ in any iteration j is derived according to the Equation 4.34.

$$
{}^{j}\Delta\boldsymbol{\sigma}'_{\mathrm{drift}} = {}^{j}L_{\mathrm{drift}} \left\{ \frac{\partial F}{\partial\, {}^{j-1}\boldsymbol{\sigma}'} \right\} \tag{4.34}
$$

The corrected scalar plastic loading index ${}^{j}L_{\mathrm{drift}}$ can be obtained according to Equation 4.35.

$$
{}^{j}L_{\mathrm{drift}} = \frac{F\left({}^{j-1}\boldsymbol{\sigma}',\, {}^{j-1}\boldsymbol{q}\right)}{\left\{ \dfrac{\partial F}{\partial\, {}^{j-1}\boldsymbol{\sigma}'} \right\} : \left\{ \dfrac{\partial F}{\partial\, {}^{j-1}\boldsymbol{\sigma}'} \right\}} \tag{4.35}
$$

Finally, the corrected stress state ${}^{j}\boldsymbol{\sigma}'$ at the end of the iteration is also calculated according to Equation 4.27, but related to the results from the normal drift correction approach from Equation 4.34. However, the hardening variables, structure variable and damage variable are kept constant for the normal drift correction approach. The consistent or normal drift correction are successful if at the end of any iteration the following condition is fulfilled $|F({}_{m}\boldsymbol{\sigma}' = {}^{j}\boldsymbol{\sigma}',\, {}_{m}\boldsymbol{q} = {}^{j}\boldsymbol{q}| \leq +Tol$ (here specified as 10^{-7}). The drift correction results in the final values of the stress state ${}_{m}\boldsymbol{\sigma}'$, hardening variables ${}_{m}\boldsymbol{q}$, structure variable ${}_{m}S_{\mathrm{i}}$ and damage variable ${}_{m}d$. The iterative drift correction algorithm is explained in the following.

Transfer of initial conditions at the beginning of drift correction

At the beginning of the iteration procedure the drift correction algorithm requires the transfer of the initial conditions and variables after the successful Modified Euler calculation. Therefore, the drifted stress state ${}_m\boldsymbol{\sigma}'$, hardening variables ${}_m\boldsymbol{q}$, structure variable ${}_mS_\mathrm{i}$ and damage variable ${}_md$ at the end of the successful Modified Euler calculation are needed. Moreover, the void ratio ${}_me$ at the end of the Modified Euler calculation related to the entire strain sub-increment is required. Hence, the void ratio is kept constant for all iterations. Afterwards, the initial values of the stress state ${}^0\boldsymbol{\sigma}' = {}_m\boldsymbol{\sigma}'$, hardening variables ${}^0\boldsymbol{q} = {}_m\boldsymbol{q}$, structure variable ${}^0S_\mathrm{i} = {}_mS_\mathrm{i}$ and damage variable ${}^0d = {}_md$ at the beginning of the iteration procedure are specified. The initial conditions at the beginning of the iteration are denoted using the left superscript $j = 0$. The initial bounding surface function $F({}^{j=0}\boldsymbol{\sigma}',\ {}^{j=0}\boldsymbol{q})$ is calculated with respect to the drifted stress state ${}^{j=0}\boldsymbol{\sigma}'$ and hardening variables ${}^{j=0}\boldsymbol{q}$ at the beginning of the drift correction.

Transfer and setting of initial conditions

Get initial conditions

$${}_m\boldsymbol{\sigma}',\ {}_m\boldsymbol{q},\ {}_mS_\mathrm{i},\ {}_md,\ {}_me$$

Set stress state, hardening variables, structure variable and damage variable at the beginning of iteration procedure

$${}^{j=0}\boldsymbol{\sigma}' = {}_m\boldsymbol{\sigma}'$$

$${}^{j=0}\boldsymbol{q} = {}_m\boldsymbol{q}$$

$${}^{j=0}S_\mathrm{i} = {}_mS_\mathrm{i}$$

$${}^{j=0}d = {}_md$$

Calculate bounding surface function

$$F({}^0\boldsymbol{\sigma}',\ {}^0\boldsymbol{q})$$

Drift correction iteration - convergence loop

The drift correction is embedded in an iterative do while loop (iteration number j) with respect to the convergence criterion $|F({}^j\boldsymbol{\sigma}',\ {}^j\boldsymbol{q})| \leq +Tol$. Before starting the drift correction loop the counting variable is set to $j = 1$ and a logical variable related to the convergence is set to false. If the maximum number of iterations is reached so that $\{j > j_\mathrm{max} = 100\}$ the iteration is aborted and an error message is shown.

Iterative convergence loop

Set counting variable for iteration number $j = 1$

Set logical variable *convergence* = false

Do While $\{convergence = \text{false}\}$ and $\{j \leq j_{\max}\}$

Consistent drift correction

The consistent drift correction is conducted by the calculation of the scalar plastic loading index ${}^{j}L_{\text{drift}}$ in accordance with Equation 4.26. For the determination of the plastic loading index ${}^{j}L_{\text{drift}}$ in each iteration the bounding surface function $F\left({}^{j-1}\boldsymbol{\sigma}',\ {}^{j-1}\boldsymbol{q}\right)$, gradients of the bounding surface $\partial F/\partial\,{}^{j-1}\boldsymbol{\sigma}'$ and the plastic potential surface $\partial G/\partial\,{}^{j-1}\boldsymbol{\sigma}'$ with respect to the stress state at the beginning of the iteration ${}^{j-1}\boldsymbol{\sigma}'$, elastic stiffness matrix $\boldsymbol{D}^{\text{e}}\left({}^{j-1}\boldsymbol{\sigma}',\ {}_{m}e\right)$ and plasticity modulus ${}^{j-1}K_{\text{p}}$ have to be obtained with respect to the stress state ${}^{j-1}\boldsymbol{\sigma}'$, hardening variables ${}^{j-1}\boldsymbol{q}$, structure variable ${}^{j-1}S_{\text{i}}$ and damage variable ${}^{j-1}d$ at the beginning of the current iteration. Based on the plastic loading index ${}^{j}L_{\text{drift}}$ the increments of stress state ${}^{j}\Delta\boldsymbol{\sigma}'_{\text{drift}}$, hardening variables ${}^{j}\Delta\boldsymbol{q}_{\text{drift}}$, structure variable ${}^{j}\Delta S_{\text{i,drift}}$ and damage variable ${}^{j}\Delta d_{\text{drift}}$ can be calculated with respect to the consistent drift correction approach according to Equation 4.25 and Equations 4.28-4.30, respectively. Moreover, the corrected values of the stress state ${}^{j}\boldsymbol{\sigma}'$, hardening variables ${}^{j}\boldsymbol{q}$, structure variable ${}^{j}S_{\text{i}}$ and damage variable ${}^{j}d$ are determined with respect to the consistent drift correction by employing Equations 4.27 and Equations 4.31-4.33, respectively. At the end of the consistent drift correction the bounding surface function $F({}^{j}\boldsymbol{\sigma}',\ {}^{j}\boldsymbol{q})$ is calculated with respect to the corrected stress state ${}^{j}\boldsymbol{\sigma}'$ and the hardening variables ${}^{j}\boldsymbol{q}$.

Consistent drift correction

Calculate scalar plastic loading index wrt. consistent drift correction

$$
{}^{j}L_{\text{drift}} = \frac{F\left({}^{j-1}\boldsymbol{\sigma}',\ {}^{j-1}\boldsymbol{q}\right)}{\left\{\dfrac{\partial F}{\partial\,{}^{j-1}\boldsymbol{\sigma}'}\right\} : \boldsymbol{D}^{\text{e}}\left({}^{j-1}\boldsymbol{\sigma}',\ {}_{m}e\right) : \left\{\dfrac{\partial G}{\partial\,{}^{j-1}\boldsymbol{\sigma}'}\right\} + {}^{j-1}K_{\text{p}}}
$$

Calculate increments of stress state and variables wrt. consistent drift correction

$$
{}^{j}\Delta\boldsymbol{\sigma}'_{\text{drift}} = {}^{j}L_{\text{drift}}\ \boldsymbol{D}^{\text{e}}\left({}^{j-1}\boldsymbol{\sigma}',\ {}_{m}e\right) : \left\{\frac{\partial G}{\partial\,{}^{j-1}\boldsymbol{\sigma}'}\right\}
$$

$$
{}^{j}\Delta\boldsymbol{q}_{\text{drift}} = {}^{j}L_{\text{drift}}\ {}^{j}\tilde{\boldsymbol{q}}_{\text{drift}}
$$

$$
{}^{j}\Delta S_{\text{i,drift}} = {}^{j}L_{\text{drift}}\ {}^{j}\tilde{S}_{\text{i,drift}}
$$

$$^{j}\Delta d_{\mathrm{drift}} = a_{\mathrm{dam}} \sqrt{\frac{2}{3}\ ^{j}\Delta \boldsymbol{e}^{\mathrm{p}}_{\mathrm{drift}} : {}^{j}\Delta \boldsymbol{e}^{\mathrm{p}}_{\mathrm{drift}}}$$

Correct stress state and variables wrt. consistent drift correction

$$^{j}\boldsymbol{\sigma}' = {}^{j-1}\boldsymbol{\sigma}' - {}^{j}\Delta\boldsymbol{\sigma}'_{\mathrm{drift}}$$

$$^{j}\boldsymbol{q} = {}^{j-1}\boldsymbol{q} + {}^{j}\Delta\boldsymbol{q}_{\mathrm{drift}}$$

$$^{j}S_{\mathrm{i}} = {}^{j-1}S_{\mathrm{i}} + {}^{j}\Delta S_{\mathrm{i,drift}}$$

$$^{j}d = {}^{j-1}d + {}^{j}\Delta d_{\mathrm{drift}}$$

Calculate bounding surface function wrt. corrected stress state and hardening variables from consistent drift correction

$$F(^{j}\boldsymbol{\sigma}', {}^{j}\boldsymbol{q})$$

Normal drift correction

Afterwards, it has to be checked, if the consistent drift correction is diverging. If the bounding surface function with respect to the corrected stress and hardening variables from the consistent drift correction yields a larger or equal value than the bounding surface function with respect to the stress state and hardening variables at the beginning of the current iteration, so that $|F\,(^{j}\boldsymbol{\sigma}', {}^{j}\boldsymbol{q})| \geq |F\,(^{j-1}\boldsymbol{\sigma}', {}^{j-1}\boldsymbol{q})|$, a normal drift correction is required. In this case the former consistent drift correction of the current iteration is abandoned. The absolute values are used because the values of the bounding surface function may become negative during the drift correction procedure. The normal drift correction follows a similar procedure as the consistent drift correction. On the contrary, the scalar plastic loading index $^{j}L_{\mathrm{drift}}$ and the increment of the stress state $^{j}\Delta\boldsymbol{\sigma}'_{\mathrm{drift}}$ with respect to the normal drift correction are calculated in accordance with Equations 4.35 and 4.34, respectively. Therefore, only the bounding surface function $F\,(^{j-1}\boldsymbol{\sigma}', {}^{j-1}\boldsymbol{q})$ with respect to the stress state $^{j-1}\boldsymbol{\sigma}'$, hardening variables $^{j-1}\boldsymbol{q}$, structure variable $^{j-1}S_{\mathrm{i}}$ and damage variable ^{j-1}d at the beginning of the current iteration and the gradient of the bounding surface $\partial F/\partial {}^{j-1}\boldsymbol{\sigma}'$ with respect to the stress state $^{j-1}\boldsymbol{\sigma}'$ at the beginning of the iteration are required during the normal drift correction. However, the corrected stress state $^{j}\boldsymbol{\sigma}'$ is derived using the same Equation 4.27 as for the consistent drift correction. On the contrary, the hardening variables, structure variable and damage variable are kept constant for the current iteration when employing the normal drift correction. At the end of the normal drift correction the bounding surface function $F(^{j}\boldsymbol{\sigma}', {}^{j}\boldsymbol{q})$ is calculated with respect to the corrected stress state $^{j}\boldsymbol{\sigma}'$ and the constant hardening variables $^{j}\boldsymbol{q}$.

Check for normal drift correction

If $|F\,({}^{j}\boldsymbol{\sigma}',\,{}^{j}\boldsymbol{q})| \geq |F\,({}^{j-1}\boldsymbol{\sigma}',\,{}^{j-1}\boldsymbol{q})|$

Then Do (normal drift correction and abandon previous consistent drift correction)

Calculate scalar plastic loading index wrt. normal drift correction

$$ {}^{j}L_{\text{drift}} = \frac{F\,({}^{j-1}\boldsymbol{\sigma}',\,{}^{j-1}\boldsymbol{q})}{\left\{\dfrac{\partial F}{\partial\,{}^{j-1}\boldsymbol{\sigma}'}\right\} : \left\{\dfrac{\partial F}{\partial\,{}^{j-1}\boldsymbol{\sigma}'}\right\}} $$

Calculate increments of stress state wrt. normal drift correction

$$ {}^{j}\Delta\boldsymbol{\sigma}'_{\text{drift}} = {}^{j}L_{\text{drift}} \left\{\frac{\partial F}{\partial\,{}^{j-1}\boldsymbol{\sigma}'}\right\} $$

Correct stress state wrt. normal drift correction

$$ {}^{j}\boldsymbol{\sigma}' = {}^{j-1}\boldsymbol{\sigma}' - {}^{j}\Delta\boldsymbol{\sigma}'_{\text{drift}} $$

Keep variables unchanged

$$ {}^{j}\boldsymbol{q} = {}^{j-1}\boldsymbol{q} $$

$$ {}^{j}S_{\text{i}} = {}^{j-1}S_{\text{i}} $$

$$ {}^{j}d = {}^{j-1}d $$

Calculate bounding surface function wrt. corrected stress state from normal drift correction

$$ F({}^{j}\boldsymbol{\sigma}',\,{}^{j}\boldsymbol{q}) $$

End If (check for normal drift correction)

Check for convergence criterion

After the consistent or normal drift correction it has to be checked, whether the drift of the stress state is corrected sufficiently or if the stress state still is positioned outside the bounding surface. Therefore, the criterion $|F({}^{j}\boldsymbol{\sigma}',\,{}^{j}\boldsymbol{q})| \leq +Tol$ is used. The tolerance value Tol (here specified as 10^{-7}) is introduced to this criterion to overcome the inaccuracy of the numerical calculation. The absolute value is taken because the drift correction may result in negative values of the bounding surface function. If the criterion is fulfilled the drift correction is successful and the logical variable is set *convergence* = true. That is, the do while convergence loop will be exited and the corrected stress state ${}^{j}\boldsymbol{\sigma}'$, hardening variables ${}^{j}\boldsymbol{q}$, structure variable ${}^{j}S_{\text{i}}$ and damage variable ${}^{j}d$ are accepted. If the stress state still is positioned outside the bounding surface the drift correction will be continued

with another iteration. Consequently, the logical variable is kept *convergence* = true, the iteration number is increased by one $j = j + 1$ and the drift correction algorithm starts again from beginning of the convergence loop.

Check for convergence criterion
If $|F({}^{j}\boldsymbol{\sigma}', {}^{j}\boldsymbol{q})| \leq +Tol$

Then Do (successful drift correction)

Set *convergence* = true

Else Do (non-successful drift correction)

Keep *convergence* = false

Set $j = j + 1$

Go To convergence loop

End If (check for convergence criterion)

End Do While (iterative convergence loop)

Transfer of corrected stress state, hardening variables, structure variable and damage variable

Finally, the stress state ${}_{m}\boldsymbol{\sigma}' = {}^{j}\boldsymbol{\sigma}'$, hardening variables ${}_{m}\boldsymbol{q} = {}^{j}\boldsymbol{q}$, structure variable ${}_{m}S_{\mathrm{i}} = {}^{j}S_{\mathrm{i}}$ and damage variable ${}_{m}d = {}^{j}d$ at the end of the sub-step are updated to the corresponding values at the end of the current iteration.

Update stress state, hardening variables, structure variable and damage variable at the end of sub-step

$${}_{m}\boldsymbol{\sigma}' = {}^{j}\boldsymbol{\sigma}'$$

$${}_{m}\boldsymbol{q} = {}^{j}\boldsymbol{q}$$

$${}_{m}S_{\mathrm{i}} = {}^{j}S_{\mathrm{i}}$$

$${}_{m}d = {}^{j}d$$

Return ${}_{m}\boldsymbol{\sigma}'$, ${}_{m}\boldsymbol{q}$, ${}_{m}S_{\mathrm{i}}$, ${}_{m}d$

4.4.5 Tangent and secant elastic stiffness matrix

In general an isotropic hypoelastic form of the elastic stress-strain relationship is used for critical state models. For the sake of simplicity this formulation neglects the definition of the elastic potentials. Since the elastic deformation is small compared to the plastic deformation, the elastic energy dissipation is also small compared to the plastic dissipation. The elastic stress-strain relation is given by Equation 4.36. The elastic strain increment $\Delta\boldsymbol{\varepsilon}^{\mathrm{e}}$ is divided into a deviatoric and a volumetric part as given in Equation 4.37.

$$\Delta\boldsymbol{\sigma}' = \boldsymbol{D}^{\mathrm{e}} : \Delta\boldsymbol{\varepsilon}^{\mathrm{e}} \tag{4.36}$$

$$\Delta\boldsymbol{\varepsilon}^{\mathrm{e}} = \frac{\Delta\boldsymbol{s}}{2\,G^{\mathrm{e}}} + \frac{\Delta p'}{3\,K^{\mathrm{e}}}\,\boldsymbol{I} \tag{4.37}$$

In this work the tangential fourth order tensor of the elastic modulus $\boldsymbol{D}^{\mathrm{e}}$ is assumed to be isotropic and symmetric as specified in Equation 4.38.

$$\boldsymbol{D}^{\mathrm{e}} = \begin{pmatrix} K^{\mathrm{e}}+4/3\,G^{\mathrm{e}} & K^{\mathrm{e}}-2/3\,G^{\mathrm{e}} & K^{\mathrm{e}}-2/3\,G^{\mathrm{e}} & 0 & 0 & 0 \\ & K^{\mathrm{e}}+4/3\,G^{\mathrm{e}} & K^{\mathrm{e}}-2/3\,G^{\mathrm{e}} & 0 & 0 & 0 \\ & & K^{\mathrm{e}}+4/3\,G^{\mathrm{e}} & 0 & 0 & 0 \\ & & & G^{\mathrm{e}} & 0 & 0 \\ & \text{symm.} & & & G^{\mathrm{e}} & 0 \\ & & & & & G^{\mathrm{e}} \end{pmatrix} \tag{4.38}$$

In the three-dimensional finite element software Plaxis 3D the general elastic stress-strain equation $\Delta\boldsymbol{\sigma}' = \boldsymbol{D}^{\mathrm{e}} : \Delta\boldsymbol{\varepsilon}^{\mathrm{e}}$ is defined according to Equation 4.39 with respect to the tensors of stress and strain increments.

$$\begin{pmatrix} \Delta\sigma'_{11} \\ \Delta\sigma'_{22} \\ \Delta\sigma'_{33} \\ \Delta\sigma'_{12} \\ \Delta\sigma'_{23} \\ \Delta\sigma'_{31} \end{pmatrix} = \begin{pmatrix} K^{\mathrm{e}}+4/3\,G^{\mathrm{e}} & K^{\mathrm{e}}-2/3\,G^{\mathrm{e}} & K^{\mathrm{e}}-2/3\,G^{\mathrm{e}} & 0 & 0 & 0 \\ & K^{\mathrm{e}}+4/3\,G^{\mathrm{e}} & K^{\mathrm{e}}-2/3\,G^{\mathrm{e}} & 0 & 0 & 0 \\ & & K^{\mathrm{e}}+4/3\,G^{\mathrm{e}} & 0 & 0 & 0 \\ & & & G^{\mathrm{e}} & 0 & 0 \\ & \text{symm.} & & & G^{\mathrm{e}} & 0 \\ & & & & & G^{\mathrm{e}} \end{pmatrix} \begin{pmatrix} \Delta\varepsilon_{11} \\ \Delta\varepsilon_{22} \\ \Delta\varepsilon_{33} \\ \Delta\gamma_{12} \\ \Delta\gamma_{23} \\ \Delta\gamma_{31} \end{pmatrix} \tag{4.39}$$

The increments of the shear strain are defined as given in Equation 4.40.

$$\Delta\gamma_{12} = \Delta\varepsilon_{12} + \Delta\varepsilon_{21}, \Delta\gamma_{23} = \Delta\varepsilon_{23} + \Delta\varepsilon_{32}, \Delta\gamma_{31} = \Delta\varepsilon_{31} + \Delta\varepsilon_{13} \tag{4.40}$$

Moreover, the elastic bulk modulus K^{e} is assumed to be dependent on the stress state expressed by the effective mean stress p' as specified in Equation 4.41. Furthermore, the elastic bulk modulus K^{e} is defined by the specific volume $v = 1 + e$ and the elastic model parameter κ. The elastic shear modulus G^{e} as given in Equation 4.42 is expressed in terms of the elastic bulk modulus K^{e} and the Poisson's ratio ν.

$$K^{\mathrm{e}} = \frac{1+e}{\kappa}\, p' \tag{4.41}$$

$$G^{\mathrm{e}} = \frac{3\,\{1-2\,\nu\}}{2\,\{1+\nu\}}\, K^{\mathrm{e}} \tag{4.42}$$

Analytically integrating the non-linear stress-dependent equation of the elastic bulk modulus for a given effective mean stress p' and an elastic volumetric strain increment $\Delta\boldsymbol{\varepsilon}^{\mathrm{e}}_{\mathrm{v}}$ results in an exponential function of the elastic secant bulk modulus K_{sec} as given in Equation 4.43. Thereby p' and e are related to the start of the strain increment $\Delta\boldsymbol{\varepsilon}^{\mathrm{e}}_{\mathrm{v}}$. The elastic secant shear modulus G_{sec} is a function of K_{sec} and ν as shown in Equation 4.44.

$$K_{\mathrm{sec}} = \frac{p'}{\Delta\boldsymbol{\varepsilon}^{\mathrm{e}}_{\mathrm{v}}} \left\{ \exp\left(\frac{\{1+e\}\ \Delta\boldsymbol{\varepsilon}^{\mathrm{e}}_{\mathrm{v}}}{\kappa} \right) - 1 \right\} \tag{4.43}$$

$$G^{\mathrm{e}}_{\mathrm{sec}} = \frac{3\,\{1-2\,\nu\}}{2\,\{1+\nu\}}\, K_{\mathrm{sec}} \tag{4.44}$$

The corresponding secant elastic stiffness matrix $\boldsymbol{D}^{\mathrm{e}}_{\mathrm{sec}}$ is finally defined by use of K_{sec} and G_{sec} as specified in Equation 4.45.

$$\boldsymbol{D}^{\mathrm{e}}_{\mathrm{sec}} = \begin{pmatrix} K_{\mathrm{sec}} + 4/3\,G_{\mathrm{sec}} & K_{\mathrm{sec}} - 2/3\,G_{\mathrm{sec}} & K_{\mathrm{sec}} - 2/3\,G_{\mathrm{sec}} & 0 & 0 & 0 \\ & K_{\mathrm{sec}} + 4/3\,G_{\mathrm{sec}} & K_{\mathrm{sec}} - 2/3\,G_{\mathrm{sec}} & 0 & 0 & 0 \\ & & K_{\mathrm{sec}} + 4/3\,G_{\mathrm{sec}} & 0 & 0 & 0 \\ & & & G_{\mathrm{sec}} & 0 & 0 \\ & \text{symm.} & & & G_{\mathrm{sec}} & 0 \\ & & & & & G_{\mathrm{sec}} \end{pmatrix} \tag{4.45}$$

Finally, the elastic stress-strain relation is given by the following Equation 4.46 as a function of the elastic secant bulk modulus and elastic secant shear modulus. To be more specific, the elastic stress-strain behavior is dependent on the current stress state, current void ratio and elastic volumetric strain increment.

$$\begin{aligned} \Delta\boldsymbol{\sigma}' &= \boldsymbol{D}^{\mathrm{e}}_{\mathrm{sec}}\,(K_{\mathrm{sec}}, G_{\mathrm{sec}}) : \Delta\boldsymbol{\varepsilon}^{\mathrm{e}} \\ &= \boldsymbol{D}^{\mathrm{e}}_{\mathrm{sec}}\,(\boldsymbol{\sigma}',\, e,\, \Delta\boldsymbol{\varepsilon}^{\mathrm{e}}_{\mathrm{v}}) : \Delta\boldsymbol{\varepsilon}^{\mathrm{e}} \end{aligned} \tag{4.46}$$

4.4.6 Elastic nucleus

The model response within the elastic nucleus f_{eln} is purely elastic. Whereat, the elastic nucleus is implicitly defined by the projection center $\boldsymbol{\sigma}'_{\text{pc}}$ specifying the position in the stress space and the constitutive parameter s_{eln} as an indirect measure of the size. In the following the formulation of the elastic nucleus $f_{\text{eln}}(\boldsymbol{\sigma}', \boldsymbol{q}, \boldsymbol{\sigma}'_{\text{pc}})$ is derived. It is assumed that the elastic nucleus is homologeous to the bounding surface F with respect to the projection center $\boldsymbol{\sigma}'_{\text{pc}}$ as the center of homology. That allows for the utilization of the radial projection rule. The distance from the projection center $\boldsymbol{\sigma}'_{\text{pc}}$ to the image stress state $\bar{\boldsymbol{\sigma}}'$ on the bounding surface F is specified by the scalar r as given by Equation 4.47 and visualized in Figure 3.4.

$$\left|\bar{\boldsymbol{\sigma}}' - \boldsymbol{\sigma}'_{\text{pc}}\right| = r \tag{4.47}$$

The distance from the stress on the elastic nucleus $\boldsymbol{\sigma}'_{\text{eln}}$ to the image stress state $\bar{\boldsymbol{\sigma}}'$ on the bounding surface F is defined in Equation 4.48 as a certain proportion of the scalar r. The ratio is controlled by the scalar constitutive parameter s_{eln} as displayed in Figure 3.4. Consequently, the ratio r/s_{eln} indirectly defines the size of the elastic nucleus f_{eln}.

$$|\bar{\boldsymbol{\sigma}}' - \boldsymbol{\sigma}'_{\text{eln}}| = \frac{r}{s_{\text{eln}}} \tag{4.48}$$

Therefore, the distance from the projection center $\boldsymbol{\sigma}'_{\text{pc}}$ to the projected stress $\boldsymbol{\sigma}'_{\text{eln}}$ on the elastic nucleus f_{eln} is defined by the term $r - r/s_{\text{eln}}$ as given by Equation 4.49 and displayed in Figure 3.4.

$$\left|\boldsymbol{\sigma}'_{\text{eln}} - \boldsymbol{\sigma}'_{\text{pc}}\right| \;=\; r - \frac{r}{s_{\text{eln}}} = r\left\{1 - \frac{1}{s_{\text{eln}}}\right\} \tag{4.49}$$

The constant value of the similarity ratio b_{eln} between the bounding surface F and the elastic nucleus f_{eln} is given by Equation 4.50.

$$b_{\text{eln}} \;=\; \frac{s_{\text{eln}}}{s_{\text{eln}} - 1} \tag{4.50}$$

The similarity ratio b_{eln} can be derived by combining Equation 4.49 with Equation 4.47 and the projection rule 4.51. By using the similarity ratio b_{eln} in the projection rule it is assumed that the current stress $\boldsymbol{\sigma}'_{\mathrm{eln}}$ lies on the elastic nucleus with $f_{\mathrm{eln}}(\boldsymbol{\sigma}'_{\mathrm{eln}}) = 0$.

$$\bar{\boldsymbol{\sigma}}' = b_{\mathrm{eln}} \left\{ \boldsymbol{\sigma}'_{\mathrm{eln}} - \boldsymbol{\sigma}'_{\mathrm{pc}} \right\} + \boldsymbol{\sigma}'_{\mathrm{pc}} \tag{4.51}$$

Due to a freely moving projection center in the stress space the elastic nucleus is also moving. Hence, the formulations of the elastic nucleus $f_{\mathrm{eln}} = 0$ and the corresponding stress $\boldsymbol{\sigma}'_{\mathrm{eln}}$ have to be updated accordingly. The shifted stress origin of the elastic nucleus $\boldsymbol{\sigma}'_{\mathrm{eln,origin}}$ in the stress space is determined by the projection of the unknown $\boldsymbol{\sigma}'_{\mathrm{eln,origin}}$ towards the origin of the bounding surface. The origin of the bounding surface is fixed at the origin of the stress space indicated by $\mathbf{0}$. The projection as given by Equation 4.52 is conducted via the projection rule 4.50 considering $\boldsymbol{\sigma}'_{\mathrm{eln}} = \boldsymbol{\sigma}'_{\mathrm{eln,origin}}$, $\bar{\boldsymbol{\sigma}}' = \mathbf{0}$ and b_{eln}. Finally, solving the projection rule for the shifted stress origin of the elastic nucleus $\boldsymbol{\sigma}'_{\mathrm{eln,origin}}$ leads to the definition given in Equation 4.53.

$$\mathbf{0} = b_{\mathrm{eln}} \left\{ \boldsymbol{\sigma}'_{\mathrm{eln,origin}} - \boldsymbol{\sigma}'_{\mathrm{pc}} \right\} + \boldsymbol{\sigma}'_{\mathrm{pc}} \tag{4.52}$$

$$\boldsymbol{\sigma}'_{\mathrm{eln,origin}} = \boldsymbol{\sigma}'_{\mathrm{pc}} \left\{ 1 - \frac{1}{b_{\mathrm{eln}}} \right\} \tag{4.53}$$

Equivalent to that approach, the value of $p_{0,\mathrm{s,eln}}$, which defines the size of the elastic nucleus is determined. The unknown mean stress component $p_{0,\mathrm{s,eln}}$ will be projected via the projection rule to the mean stress state $p_{0,\mathrm{s}}$, which specifies the size of the bounding surface. Solving the projection rule for $p_{0,\mathrm{s,eln}}$ needs the setting of $p'_{\mathrm{eln}} = p_{0,\mathrm{s,eln}}$ and $\bar{p}' = p_{0,\mathrm{s}}$ as specified by Equations 4.54 and 4.55.

$$p_{0,\mathrm{s}} = b_{\mathrm{eln}} \left\{ p_{0,\mathrm{s,eln}} - p'_{\mathrm{pc}} \right\} + p'_{\mathrm{pc}} \tag{4.54}$$

$$p_{0,\mathrm{s,eln}} = \frac{p_{0,\mathrm{s}} - p'_{\mathrm{pc}}}{b_{\mathrm{eln}}} + p'_{\mathrm{pc}} \tag{4.55}$$

Due to the shifted origin of the elastic nucleus and the new coordinate system, the use of the elastic nucleus formulation requires some modifications of the stress components as defined by Equations 4.56-4.58. The current stress state $\boldsymbol{\sigma}'$ divided into effective mean stress p' and deviatoric stress $\boldsymbol{s}$ has to be modified with respect to the shifted stress origin of the elastic nucleus $\boldsymbol{\sigma}'_{\mathrm{eln,origin}}(p'_{\mathrm{eln,origin}}, \boldsymbol{s}_{\mathrm{eln,origin}})$. The variable $p_{0,\mathrm{s,eln}}$ has to be modified

with respect to the volumetric component of the shifted stress origin of the elastic nucleus $p'_{\mathrm{eln,origin}}$. From Equation 4.58 it can be seen that the similarity ratio b_{eln} relates the size of the bounding surface F given by the variable $p_{0,\mathrm{s}}$ and the size of the elastic nucleus f_{eln} given by the variable $p_{0,\mathrm{s,eln,mod}}$.

$$
\begin{aligned}
p'_{\mathrm{eln,mod}} &= p' - p'_{\mathrm{eln,origin}} && (4.56)\\
\boldsymbol{s}_{\mathrm{eln,mod}} &= \boldsymbol{s} - \boldsymbol{s}_{\mathrm{eln,origin}} && (4.57)\\
p_{0,\mathrm{s,eln,mod}} &= p_{0,\mathrm{s,eln}} - p'_{\mathrm{eln,origin}} \\
&= \frac{p_{0,\mathrm{s}} - p'_{\mathrm{pc}}}{b_{\mathrm{eln}}} + p'_{\mathrm{pc}} - \left\{ p'_{\mathrm{pc}} \left\{ 1 - \frac{1}{b_{\mathrm{eln}}} \right\} \right\} \\
&= \frac{p_{0,\mathrm{s}}}{b_{\mathrm{eln}}} && (4.58)
\end{aligned}
$$

Inserting the modified values of $p'_{\mathrm{eln,mod}}$, $\boldsymbol{s}_{\mathrm{eln,mod}}$ and $p_{0,\mathrm{s,eln,mod}}$ in the general equation of the elastic nucleus f_{eln} results in the following Equation 4.59. Due to the homology of the bounding surface and the elastic surface the equations $F = 0$ and $f_{\mathrm{eln}} = 0$ are similar. Differences occur related to the reduced size and the shifted origin of the elastic nucleus. The fabric stress tensor $\boldsymbol{\alpha}$, Lode angle θ and Lode angle dependent value of N are the same for the bounding surface and the elastic nucleus due to the homology of both surfaces.

$$
\begin{aligned}
f_{\mathrm{eln}} = {} & \frac{3}{2} \left\{ \boldsymbol{s}_{\mathrm{eln,mod}} - p'_{\mathrm{eln,mod}}\, \boldsymbol{\alpha} \right\} : \left\{ \boldsymbol{s}_{\mathrm{eln,mod}} - p'_{\mathrm{eln,mod}}\, \boldsymbol{\alpha} \right\} \\
& - \left\{ N^2 - \frac{3}{2}\, \boldsymbol{\alpha} : \boldsymbol{\alpha} \right\} p'_{\mathrm{eln,mod}} \left\{ p_{0,\mathrm{s,eln,mod}} - p'_{\mathrm{eln,mod}} \right\} = 0 \qquad (4.59)
\end{aligned}
$$

4.4.7 Intersection stress and intersection factor

For the determination of the transition from the purely elastic state $f_{\mathrm{eln}}\left(\boldsymbol{\sigma}', \boldsymbol{q}\right) < 0$ to the elastoplastic state $f_{\mathrm{eln}}\left(\boldsymbol{\sigma}' + \Delta\boldsymbol{\sigma}'_{\mathrm{trial}},\ \boldsymbol{q}\right) > 0$ it is needed to locate the intersection of an elastic trial stress path with the elastic nucleus f_{eln}. Thereby $\boldsymbol{\sigma}'$ is the initial stress state at the beginning of a (sub-)increment, $\Delta\boldsymbol{\sigma}'_{\mathrm{trial}}$ is an elastic trial stress (sub-)increment and $\boldsymbol{q}$ are the initial hardening variables. The intersection stress $\boldsymbol{\sigma}'_{\mathrm{inter}}$ lies on the elastic nucleus $f_{\mathrm{eln}}\left(\boldsymbol{\sigma}'_{\mathrm{inter}},\ \boldsymbol{q}\right) = 0$. The following non-linear Equation 4.60 has to be satisfied:

$$
f_{\mathrm{eln}}\left(\boldsymbol{\sigma}' + inter\, \boldsymbol{D}^{\mathrm{e}}_{\mathrm{sec}} : \Delta\boldsymbol{\varepsilon},\ \boldsymbol{q}\right) = f_{\mathrm{eln}}\left(\boldsymbol{\sigma}'_{\mathrm{inter}},\ \boldsymbol{q}\right) = 0 \qquad (4.60)
$$

Firstly, the intersection stress $\boldsymbol{\sigma}'_{\mathrm{inter}}$ is calculated according to Figure 4.2.

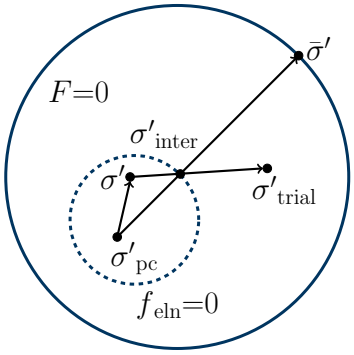

Figure 4.2: Schematic illustration of the determination of the intersection stress within the bounding surface plasticity framework

Based on the intersection stress $\boldsymbol{\sigma}'_{\text{inter}}$ the strain intersection factor *inter* to fulfill Equation 4.60 is determined. The scalar strain intersection factor *inter* is related to the strain increment $\Delta\boldsymbol{\varepsilon}$ and specifies the purely elastic proportion of the trial strain increment *inter* $\Delta\boldsymbol{\varepsilon}$ and the elastoplastic proportion $\{1 - \mathit{inter}\}\ \Delta\boldsymbol{\varepsilon}$.

Calculation of intersection stress $\boldsymbol{\sigma}'_{\text{inter}}$

The intersection stress $\boldsymbol{\sigma}'_{\text{inter}}$ will be calculated based on the current stress $\boldsymbol{\sigma}'$, elastic trial stress $\boldsymbol{\sigma}'_{\text{trial}}$ and projection center $\boldsymbol{\sigma}'_{\text{pc}}$. The projection center defines the position of the elastic nucleus as it is the center of homology between bounding surface and elastic nucleus. Moreover, the similarity ratio b_{eln} indirectly specifies the size of the elastic nucleus. The elastic trial stress increment $\Delta\boldsymbol{\sigma}'_{\text{trial}}$ is the distance between the trial stress $\boldsymbol{\sigma}'_{\text{trial}}$ and the current stress $\boldsymbol{\sigma}'$. Two additional stress increments $\Delta\boldsymbol{\sigma}'_{\text{cur-pc}}$ and $\Delta\boldsymbol{\sigma}'_{\text{int-pc}}$ are introduced. $\Delta\boldsymbol{\sigma}'_{\text{cur-pc}}$ is the distance between the current stress $\boldsymbol{\sigma}'$ and the projection center $\boldsymbol{\sigma}'_{\text{pc}}$ and $\Delta\boldsymbol{\sigma}'_{\text{int-pc}}$ is the distance between the intersection stress $\boldsymbol{\sigma}'_{\text{inter}}$ and the projection center $\boldsymbol{\sigma}'_{\text{pc}}$.

$$\Delta\boldsymbol{\sigma}'_{\text{trial}} = \boldsymbol{\sigma}'_{\text{trial}} - \boldsymbol{\sigma}' \tag{4.61}$$

$$\Delta\boldsymbol{\sigma}'_{\text{cur-pc}} = \boldsymbol{\sigma}' - \boldsymbol{\sigma}'_{\text{pc}} \tag{4.62}$$

$$\Delta\boldsymbol{\sigma}'_{\text{int-pc}} = \boldsymbol{\sigma}'_{\text{inter}} - \boldsymbol{\sigma}'_{\text{pc}} \tag{4.63}$$

The intersection stress $\boldsymbol{\sigma}'_{\text{inter}}$ is the unknown stress to be found. The distance $\Delta\boldsymbol{\sigma}'_{\text{int-pc}}$ between the projection center and the intersection stress can also be expressed in combined terms of the distance $\Delta\boldsymbol{\sigma}'_{\text{cur-pc}}$ between the projection center and the current stress

and an unknown proportion of the elastic trial stress increment $int\ \Delta\boldsymbol{\sigma}'_{\text{trial}}$ as given in Equation 4.64. Therein int is an unknown scalar multiplier, which is related to the trial stress increment $\Delta\boldsymbol{\sigma}'_{\text{trial}}$.

$$\Delta\boldsymbol{\sigma}'_{\text{int-pc}} = \Delta\boldsymbol{\sigma}'_{\text{cur-pc}} + int\ \Delta\boldsymbol{\sigma}'_{\text{trial}} \tag{4.64}$$

The image stress state $\bar{\boldsymbol{\sigma}}'$ on the bounding surface F is related to the intersection stress $\boldsymbol{\sigma}'_{\text{inter}}$ on the elastic nucleus f_{eln} via the radial projection rule 4.65 using the scalar similarity ratio b_{eln} relating elastic nucleus and bounding surface with respect to the projection center $\boldsymbol{\sigma}'_{\text{pc}}$.

$$\bar{\boldsymbol{\sigma}}' = b_{\text{eln}}\ \{\boldsymbol{\sigma}'_{\text{inter}} - \boldsymbol{\sigma}'_{\text{pc}}\} + \boldsymbol{\sigma}'_{\text{pc}} \tag{4.65}$$

Inserting Equations 4.63 and 4.64 in Equation 4.65 leads to the following set of equations:

$$\bar{\boldsymbol{\sigma}}' = b_{\text{eln}}\ \{\Delta\boldsymbol{\sigma}'_{\text{cur-pc}} + int\ \Delta\boldsymbol{\sigma}'_{\text{trial}}\} + \boldsymbol{\sigma}'_{\text{pc}} \tag{4.66}$$

$$\bar{p}' = b_{\text{eln}}\ \{\Delta p'_{\text{cur-pc}} + int\ \Delta p'_{\text{trial}}\} + p'_{\text{pc}} \tag{4.67}$$

$$\bar{\boldsymbol{s}} = b_{\text{eln}}\ \{\Delta\boldsymbol{s}_{\text{cur-pc}} + int\ \Delta\boldsymbol{s}_{\text{trial}}\} + \boldsymbol{s}_{\text{pc}} \tag{4.68}$$

The unknown scalar multiplier int will be determined by use of the bounding surface formulation $F = 0$, which is given in Equation 4.69.

$$F = \frac{3}{2}\ \{\bar{\boldsymbol{s}} - \bar{p}'\,\boldsymbol{\alpha}\} : \{\bar{\boldsymbol{s}} - \bar{p}'\,\boldsymbol{\alpha}\} - \left\{N^2 - \frac{3}{2}\,\boldsymbol{\alpha} : \boldsymbol{\alpha}\right\}\ \bar{p}'\ \{p_{0,\text{s}} - \bar{p}'\} = 0 \tag{4.69}$$

The image stress components $\bar{p}'$ and $\bar{\boldsymbol{s}}$ from Equations 4.67 and 4.68 are inserted in the bounding surface formulation 4.69. To finally obtain the scalar multiplier int the bounding surface formulation $F = 0$ can be formulated in a quadratic Equation 4.70 with respect to the scalar multiplier int. Therein $A_{\text{int}}, B_{\text{int}}, C_{\text{int}}$ are constant model terms.

$$A_{\text{int}}\ int^2 + B_{\text{int}}\ int + C_{\text{int}} = 0 \tag{4.70}$$

Within the multiaxial space the quadratic equation can be subdivided and solved term by term as given in the following.

Former term:

$$\frac{3}{2}\ \{\bar{\boldsymbol{s}} - \bar{p}'\ \boldsymbol{\alpha}\} : \{\bar{\boldsymbol{s}} - \bar{p}'\ \boldsymbol{\alpha}\} \quad = \quad A_{\mathrm{int},1}\ int^2 + B_{\mathrm{int},1}\ int + C_{\mathrm{int},1} \tag{4.71}$$

where:

$$A_{\mathrm{int},1} \quad = \quad \frac{3}{2}\ \{b_{\mathrm{eln}}\}^2\ \{\Delta\boldsymbol{s}_{\mathrm{trial}} - \Delta p'_{\mathrm{trial}}\ \boldsymbol{\alpha}\} : \{\Delta\boldsymbol{s}_{\mathrm{trial}} - \Delta p'_{\mathrm{trial}}\ \boldsymbol{\alpha}\} \tag{4.72}$$

$$B_{\mathrm{int},1} \quad = \quad 3\,b_{\mathrm{eln}}\ \left\{\left\{\boldsymbol{s}_{\mathrm{pc}} + \Delta\boldsymbol{s}_{\text{cur-pc}}\,b_{\mathrm{eln}}\right\} - \left\{p'_{\mathrm{pc}} + \Delta p'_{\text{cur-pc}}\,b_{\mathrm{eln}}\right\}\ \boldsymbol{\alpha}\right\} : \{\Delta\boldsymbol{s}_{\mathrm{trial}} - \Delta p'_{\mathrm{trial}}\ \boldsymbol{\alpha}\} \tag{4.73}$$

$$C_{\mathrm{int},1} \quad = \quad \frac{3}{2}\ \left\{\left\{\boldsymbol{s}_{\mathrm{pc}} + \Delta\boldsymbol{s}_{\text{cur-pc}}\,b_{\mathrm{eln}}\right\} - \left\{p'_{\mathrm{pc}} + \Delta p'_{\text{cur-pc}}\,b_{\mathrm{eln}}\right\}\ \boldsymbol{\alpha}\right\} : \left\{\left\{\boldsymbol{s}_{\mathrm{pc}} + \Delta\boldsymbol{s}_{\mathrm{a}}\,b_{\mathrm{eln}}\right\} - \left\{p'_{\mathrm{pc}} + \Delta p'_{\mathrm{a}}\,b_{\mathrm{eln}}\right\}\ \boldsymbol{\alpha}\right\} \tag{4.74}$$

Latter term:

$$\bar{p}'\ \{p_{0,\mathrm{s}} - \bar{p}'\} \quad = \quad A_{\mathrm{int},2}\ int^2 + B_{\mathrm{int},2}\ int + C_{\mathrm{int},2} \tag{4.75}$$

where:

$$A_{\mathrm{int},2} \quad = \quad -\{b_{\mathrm{eln}}\}^2\ \{\Delta p'_{\mathrm{trial}}\}^2 \tag{4.76}$$

$$B_{\mathrm{int},2} \quad = \quad b_{\mathrm{eln}}\ \Delta p'_{\mathrm{trial}}\ \left\{p_{0,\mathrm{s}} - 2\ \left\{p'_{\mathrm{pc}} + b_{\mathrm{eln}}\ \Delta p'_{\text{cur-pc}}\right\}\right\} \tag{4.77}$$

$$C_{\mathrm{int},2} \quad = \quad p'_{\mathrm{pc}}\,p_{0,\mathrm{s}} + b_{\mathrm{eln}}\ \Delta p'_{\text{cur-pc}}\,p_{0,\mathrm{s}} - \left\{p'_{\mathrm{pc}}\right\}^2 - 2\,b_{\mathrm{eln}}\,p'_{\mathrm{pc}}\,\Delta p'_{\text{cur-pc}} - \{b_{\mathrm{eln}}\}^2\left\{\Delta p'_{\text{cur-pc}}\right\}^2 \tag{4.78}$$

Consequently, the quadratic Equation 4.70 can be further specified by considering the Equations 4.71 and 4.75.

$$A_{\mathrm{int}}\ int^2 + B_{\mathrm{int}}\ int + C_{\mathrm{int}} \quad = \quad 0 \tag{4.79}$$

where:

$$A_{\mathrm{int}} \quad = \quad A_{\mathrm{int},1} - \left\{N^2 - \frac{3}{2}\,\boldsymbol{\alpha} : \boldsymbol{\alpha}\right\}\ A_{\mathrm{int},2} \tag{4.80}$$

$$B_{\mathrm{int}} \quad = \quad B_{\mathrm{int},1} - \left\{N^2 - \frac{3}{2}\,\boldsymbol{\alpha} : \boldsymbol{\alpha}\right\}\ B_{\mathrm{int},2} \tag{4.81}$$

$$C_{\mathrm{int}} \quad = \quad C_{\mathrm{int},1} - \left\{N^2 - \frac{3}{2}\,\boldsymbol{\alpha} : \boldsymbol{\alpha}\right\}\ C_{\mathrm{int},2} \tag{4.82}$$

Solving the quadratic Equation 4.79 for the scalar multiplier *int* yields to Equation 4.83.

$$int_{\max/\min} = \frac{-B_{\text{int}} \pm \sqrt{B_{\text{int}}^2 - 4\, A_{\text{int}}\, C_{\text{int}}}}{2\, A_{\text{int}}} \tag{4.83}$$

Concerning the algebraic sign of the square root two different cases have to be distinguished. In the first case, the current stress lies inside the elastic nucleus and the trial stress lies outside the elastic nucleus. The intersection stress is defined along the direction of the elastic trial stress increment from the current stress to the trial stress state. Hence, the maximum value of the scalar multiplier $int_{\max}$ has to be considered for the determination of the intersection stress (see left hand side of Figure 4.3). In the second case, the current stress lies slightly outside the elastic nucleus but inside a positive numerical tolerance (here specified as 10^{-7}). That is, the elastic trial stress path will twice cross the elastic nucleus. For finding the intersection stress the maximum value of the scalar multiplier $int_{\max}$ is of interest (see right hand side of Figure 4.3). The intersection stress $\boldsymbol{\sigma}'_{\text{inter}}$ on the elastic nucleus can finally be calculated by combining the Equations 4.63 and 4.64 as given by Equation 4.84.

$$\begin{aligned} \boldsymbol{\sigma}'_{\text{inter}} &= \Delta\boldsymbol{\sigma}'_{\text{b}} + \boldsymbol{\sigma}'_{\text{pc}} \\ &= \{\Delta\boldsymbol{\sigma}'_{\text{a}} + int\, \Delta\boldsymbol{\sigma}'_{\text{trial}}\} + \boldsymbol{\sigma}'_{\text{pc}} \\ &= \{\{\boldsymbol{\sigma}' - \boldsymbol{\sigma}'_{\text{pc}}\} + int\, \Delta\boldsymbol{\sigma}'_{\text{trial}}\} + \boldsymbol{\sigma}'_{\text{pc}} \end{aligned} \tag{4.84}$$

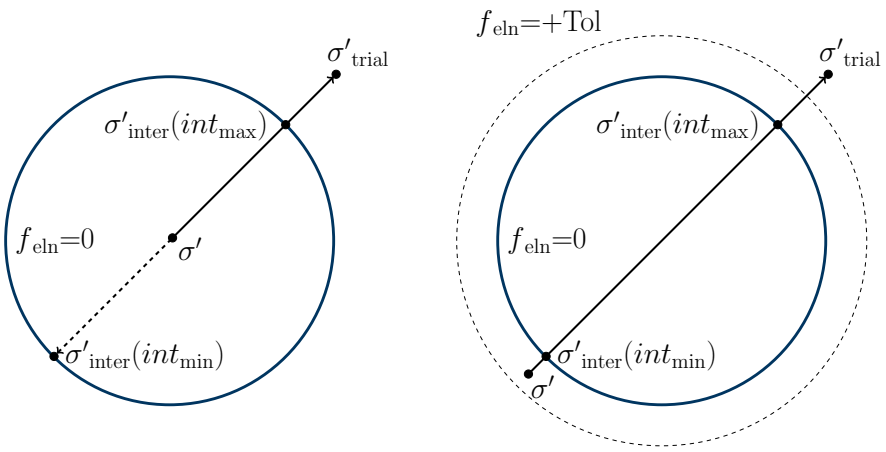

Figure 4.3: Schematic illustration of the intersection stresses obtained via a quadratic equation and the scalar multiplier *int*

4.4.8 Similarity ratio

The similarity ratio b between an imaginary loading surface $f(\boldsymbol{\sigma}') = 0$ and the bounding surface $F(\bar{\boldsymbol{\sigma}}') = 0$ is needed to determine the image stress $\bar{\boldsymbol{\sigma}}'$. The similarity ratio b is calculated according to the following procedure:

The bounding surface formulation is generally defined by Equation 4.85.

$$F = \frac{3}{2} \{\bar{\boldsymbol{s}} - \bar{p}' \boldsymbol{\alpha}\} : \{\bar{\boldsymbol{s}} - \bar{p}' \boldsymbol{\alpha}\} - \left\{ N^2 - \frac{3}{2} \boldsymbol{\alpha} : \boldsymbol{\alpha} \right\} \bar{p}' \{p_{0,\mathrm{s}} - \bar{p}'\} = 0 \quad (4.85)$$

To obtain the similarity ratio b the hydrostatic and the deviatoric image stress components $\bar{p}'$ and $\bar{\boldsymbol{s}}$ in Equation 4.85 have to be substituted by the projection rules as given in Equations 4.86 and 4.87. The modified Equation 4.85 has to be solved for the similarity ratio b afterwards. The projection rules define the image stress components $\bar{p}'$ and $\bar{\boldsymbol{s}}$ on the bounding surface by projecting the current stresses p' and $\boldsymbol{s}$ by means of the projection center $\boldsymbol{\sigma}'_{\mathrm{pc}}$ and the similarity ratio b. The projection center tensor $\boldsymbol{\sigma}'_{\mathrm{pc}}$ can be divided into a hydrostatic part p'_{pc} and a deviatoric part $\boldsymbol{s}_{\mathrm{pc}}$.

$$\bar{p}' = b \left\{ p' - p'_{\mathrm{pc}} \right\} + p'_{\mathrm{pc}} \quad (4.86)$$

$$\bar{\boldsymbol{s}} = b \left\{ \boldsymbol{s} - \boldsymbol{s}_{\mathrm{pc}} \right\} + \boldsymbol{s}_{\mathrm{pc}} \quad (4.87)$$

To finally obtain the similarity ratio b the bounding surface formulation $F = 0$ can be formulated in a quadratic Equation 4.88 with respect to the similarity ratio b. Therein $A_{\mathrm{b}}, B_{\mathrm{b}}, C_{\mathrm{b}}$ are constant model terms.

$$A_{\mathrm{b}}\, b^2 + B_{\mathrm{b}}\, b + C_{\mathrm{b}} = 0 \quad (4.88)$$

Within the multiaxial space the quadratic equation can be subdivided and solved term by term as given in the following.

Former term:

$$\frac{3}{2} \{\bar{\boldsymbol{s}} - \bar{p}' \boldsymbol{\alpha}\} : \{\bar{\boldsymbol{s}} - \bar{p}' \boldsymbol{\alpha}\} = A_{\mathrm{b},1}\, b^2 + B_{\mathrm{b},1}\, b + C_{\mathrm{b},1} \quad (4.89)$$

where:

$$\begin{aligned} A_{\mathrm{b},1} &= \frac{3}{2}\,\{\boldsymbol{s}-\boldsymbol{s}_{\mathrm{pc}}\}:\{\boldsymbol{s}-\boldsymbol{s}_{\mathrm{pc}}\}-3\,\left\{p'-p'_{\mathrm{pc}}\right\}\{\boldsymbol{s}-\boldsymbol{s}_{\mathrm{pc}}\}:\boldsymbol{\alpha} \\ &\quad +\frac{3}{2}\,\left\{p'-p'_{\mathrm{pc}}\right\}^2\,\boldsymbol{\alpha}:\boldsymbol{\alpha} \qquad (4.90) \\ B_{\mathrm{b},1} &= 3\,\{\boldsymbol{s}-\boldsymbol{s}_{\mathrm{pc}}\}:\boldsymbol{s}_{\mathrm{pc}}-3\,\left\{\{\boldsymbol{s}-\boldsymbol{s}_{\mathrm{pc}}\}\,p'_{\mathrm{pc}}+\boldsymbol{s}_{\mathrm{pc}}\,\left\{p'-p'_{\mathrm{pc}}\right\}\right\}:\boldsymbol{\alpha} \\ &\quad +3\,p'_{\mathrm{pc}}\,\left\{p'-p'_{\mathrm{pc}}\right\}\,\boldsymbol{\alpha}:\boldsymbol{\alpha} \qquad (4.91) \\ C_{\mathrm{b},1} &= \frac{3}{2}\,\boldsymbol{s}_{\mathrm{pc}}:\boldsymbol{s}_{\mathrm{pc}}-3\,p'_{\mathrm{pc}}\,\boldsymbol{s}_{\mathrm{pc}}:\boldsymbol{\alpha}+\frac{3}{2}\,\{p'_{\mathrm{pc}}\}^2\,\boldsymbol{\alpha}:\boldsymbol{\alpha} \qquad (4.92) \end{aligned}$$

Latter term:

$$\bar{p}'\,\{p_{0,\mathrm{s}}-\bar{p}'\} = A_{\mathrm{b},2}\,b^2+B_{\mathrm{b},2}\,b+C_{\mathrm{b},2} \qquad (4.93)$$

where:

$$\begin{aligned} A_{\mathrm{b},2} &= -\left\{p'-p'_{\mathrm{pc}}\right\}^2 \qquad (4.94) \\ B_{\mathrm{b},2} &= -\left\{p'-p'_{\mathrm{pc}}\right\}\,\left\{2\,p'_{\mathrm{pc}}-p_{0,\mathrm{s}}\right\} \qquad (4.95) \\ C_{\mathrm{b},2} &= -p'_{\mathrm{pc}}\,\left\{p'_{\mathrm{pc}}-p_{0,\mathrm{s}}\right\} \qquad (4.96) \end{aligned}$$

Consequently, the quadratic Equation 4.88 can be further specified by considering the Equations 4.89 and 4.93.

$$A_{\mathrm{b}}\,b^2+B_{\mathrm{b}}\,b+C_{\mathrm{b}} = 0 \qquad (4.97)$$

where:

$$\begin{aligned} A_{\mathrm{b}} &= A_{\mathrm{b},1}-\left\{N^2-\frac{3}{2}\,\boldsymbol{\alpha}:\boldsymbol{\alpha}\right\}\,A_{\mathrm{b},2} \qquad (4.98) \\ B_{\mathrm{b}} &= B_{\mathrm{b},1}-\left\{N^2-\frac{3}{2}\,\boldsymbol{\alpha}:\boldsymbol{\alpha}\right\}\,B_{\mathrm{b},2} \qquad (4.99) \\ C_{\mathrm{b}} &= C_{\mathrm{b},1}-\left\{N^2-\frac{3}{2}\,\boldsymbol{\alpha}:\boldsymbol{\alpha}\right\}\,C_{\mathrm{b},2} \qquad (4.100) \end{aligned}$$

Solving the quadratic Equation 4.97 for the similarity ratio b yields to Equation 4.101.

$$b_{\mathrm{max/min}} = \frac{-B_{\mathrm{b}}\pm\sqrt{B_{\mathrm{b}}^2-4\,A_{\mathrm{b}}\,C_{\mathrm{b}}}}{2\,A_{\mathrm{b}}} \qquad (4.101)$$

Generally, the algebraic sign of the root in the quadratic equation is related to two image stresses $\bar{\boldsymbol{\sigma}}'(b_{\max})$ and $\bar{\boldsymbol{\sigma}}'(b_{\min})$, which can be projected on the bounding surface in opposite directions (see Figure 4.4). The image stresses $\bar{\boldsymbol{\sigma}}'(b_{\max})$ and $\bar{\boldsymbol{\sigma}}(b_{\min})$ are related to the maximum and the minimum value of the similarity ratio $b_{\max}$ and $b_{\min}$, respectively. It is to be noted that in any case the maximum value of the similarity ratio $b_{\max}$ has to be chosen as the solution of the quadratic equation. Two cases have to be distinguished due to numerical reasons of tolerance.

In the first regular case the projection center is assumed to be located within the bounding surface. The maximum value $b_{\max}$ results in the correct value of the similarity ratio. This is, the image stress state on the bounding surface is projected from the projection center through the current stress state along the desired direction of $\boldsymbol{\sigma}' - \boldsymbol{\sigma}'_{\mathrm{pc}}$ as visualized on the left hand side of Figure 4.4. The minimum value $b_{\min}$ would result in a projection to the opposite direction, which is not reasonable.

In the second case the projection center is assumed to be located outside the bounding surface within the numerical tolerance (here specified as 10^{-7}). However, a projection of the current stress along the desired direction of $\boldsymbol{\sigma}' - \boldsymbol{\sigma}'_{\mathrm{pc}}$ leads to two possible image stresses on the bounding surface. From the right hand side of Figure 4.4 it can be clearly seen that the maximum value of the similarity ratio $b_{\max}$ results in the desired image stress state on the opposite of the bounding surface. Whereas, the minimum value $b_{\min}$ yields an image stress state on the bounding surface, which is just caused by the position of the projection center with respect to the numerical tolerance.

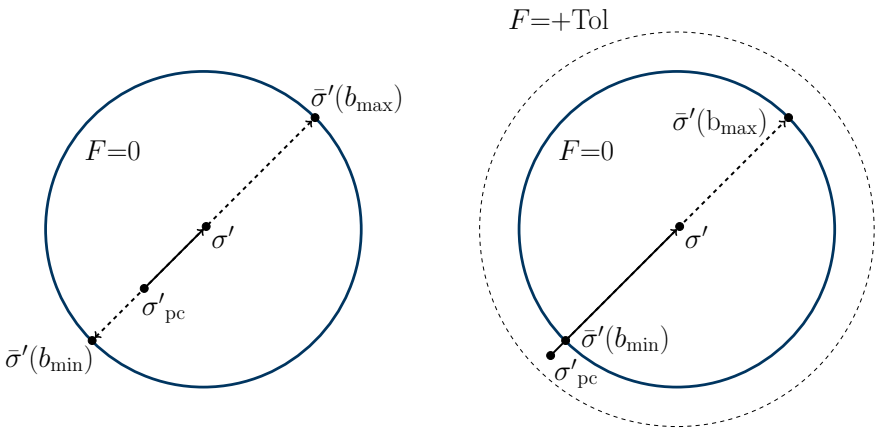

Figure 4.4: Schematic illustration of the image stresses obtained via quadratic equation and similarity ratio b

The similarity ratio b can be calculated by use of the newly proposed approach based on finding an intersection stress on the elastic nucleus which differs from the projection center. After stress initialization or initially after updating the projection center to the last stress reversal state the current stress and the projection center initially coincide. If $\boldsymbol{\sigma}' = \boldsymbol{\sigma}'_{\mathrm{pc}}$ it is mathematically not possible to derive the similarity ratio from the projection rule. The newly proposed procedure makes use of the fact that the projection center acts as the center of homology of the elastic nucleus f_{eln} and the bounding surface F. This holds true even after stress reversal due to the simultaneous update of the elastic nucleus to the last stress reversal state. Therefore, the intersection of the applied strain increment with the elastic nucleus can be calculated and the intersection stress state, which acts as the initial stress state of the Modified Euler stress-strain calculation does not coincide with the projection center anymore. Applying this procedure requires at least a small elastic nucleus anytime (material parameter $s_{\mathrm{eln}} > 1$). Hence, the similarity ratio b can be mathematically derived as described before.
If even after applying the intersection stress algorithm the current stress state coincides with the position of the projection center, the projection parameter has to be manually set to $b = 1$, so that $\bar{\boldsymbol{\sigma}}' = \boldsymbol{\sigma}'$. This special case implies that the current stress lies on the bounding surface $F(\boldsymbol{\sigma}', \boldsymbol{q}) = 0$, the further loading is directed outwards or tangential to the bounding surface, so that $F(\boldsymbol{\sigma}'_{\mathrm{trial}}, \boldsymbol{q}) \geq 0$ and at the same time the projection center is located at once on the bounding surface $F(\boldsymbol{\sigma}'_{\mathrm{pc}}, \boldsymbol{q}) = 0$ and the elastic nucleus $f_{\mathrm{eln}}(\boldsymbol{\sigma}'_{\mathrm{pc}}, \boldsymbol{q}) = 0$. This could happen only after stress initialization.

Calculation of strain intersection factor *inter*

The intersection stress $\boldsymbol{\sigma}'_{\mathrm{inter}}$ is given by the following Equation 4.102 with respect to the strain intersection factor *inter*. The scalar intersection factor *inter* to be found is related to the strain increment $\Delta\boldsymbol{\varepsilon}$. It specifies the proportion of the strain increment $\Delta\boldsymbol{\varepsilon}$ that causes elastic strain only. The stress state is moved from the initial condition $\boldsymbol{\sigma}'$ at the start of a (sub-)increment to the intersection stress state $\boldsymbol{\sigma}'_{\mathrm{inter}}$ on the elastic nucleus.

$$\begin{aligned} \boldsymbol{\sigma}'_{\mathrm{inter}} &= \boldsymbol{\sigma}' + \mathit{inter}\, \Delta\boldsymbol{\sigma}'_{\mathrm{trial}} \\ &= \boldsymbol{\sigma}' + \mathit{inter}\, \boldsymbol{D}^{\mathrm{e}}_{\mathrm{sec}} : \Delta\boldsymbol{\varepsilon} \end{aligned} \tag{4.102}$$

The definition of the elastic secant stiffness matrix $\boldsymbol{D}^{\mathrm{e}}_{\mathrm{sec}}$ is given according to the related section 4.4.5.

The elastic secant bulk modulus K^{e}_{sec} and the elastic secant shear modulus G^{e}_{sec} are defined as follows.

$$K^{e}_{sec} = \frac{p'}{\Delta\varepsilon^{e}_{v}} \left\{ \exp\left(\frac{\{1+e\}\ \Delta\varepsilon^{e}_{v}}{\kappa} \right) - 1 \right\} \tag{4.103}$$

$$G^{e}_{sec} = \frac{3\ \{1-2\,\nu\}}{2\ \{1+\nu\}}\, K^{e}_{sec} \tag{4.104}$$

The elastic volumetric strain increment $\Delta\varepsilon^{e}_{v}$ will be replaced by a proportion of the total volumetric strain increment $inter\ \Delta\varepsilon_{v}$ to introduce the intersection factor $inter$ in the equation of K^{e}_{sec}.

$$K^{e}_{sec} = \frac{p'}{inter\ \Delta\varepsilon_{v}} \left\{ \exp\left(\frac{\{1+e\}\ inter\ \Delta\varepsilon_{v}}{\kappa} \right) - 1 \right\} \tag{4.105}$$

The elastic secant bulk modulus K^{e}_{sec} can be factored out in the Equation **??** of the elastic secant stiffness matrix $\boldsymbol{D}^{e}_{sec}$.

$$\boldsymbol{D}^{e}_{sec} = K^{e}_{sec} \left\{ \frac{1}{K^{e}_{sec}}\, \boldsymbol{D}^{e}_{sec} \right\} \tag{4.106}$$

Inserting Equations 4.105 and 4.106 in Equation 4.102 leads to the following Equation 4.107 of the intersection stress $\boldsymbol{\sigma}'_{inter}$.

$$\boldsymbol{\sigma}'_{inter} = \boldsymbol{\sigma}' + \frac{p'}{\Delta\varepsilon_{v}} \left\{ \exp\left(\frac{\{1+e\}\ inter\ \Delta\varepsilon_{v}}{\kappa} \right) - 1 \right\} \left\{ \frac{1}{K^{e}_{sec}}\, \boldsymbol{D}^{e}_{sec} : \Delta\boldsymbol{\varepsilon} \right\} \tag{4.107}$$

The intersection factor $inter$ can finally be obtained from solving Equation 4.107 for $inter$.

$$inter = \frac{\kappa}{\{1+e\}\ \Delta\varepsilon_{v}} \ln\left(\frac{|\boldsymbol{\sigma}'_{inter} - \boldsymbol{\sigma}'|}{\left| \frac{1}{K^{e}_{sec}}\, \boldsymbol{D}^{e}_{sec} : \Delta\boldsymbol{\varepsilon} \right|} \frac{\Delta\varepsilon_{v}}{p'} + 1 \right) \tag{4.108}$$

In case the volumetric strain increment tends to approach zero $\Delta\boldsymbol{\varepsilon}_{\mathrm{v}} \rightarrow 0$, Equation 4.108 is modified to Equation 4.109 considering a limiting value for *inter* using the l'Hospital rule.

$$inter = \frac{\kappa}{\{1+e\}} \ln \left(\frac{|\boldsymbol{\sigma}'_{\mathrm{inter}} - \boldsymbol{\sigma}'|}{\left| \frac{1}{K^{\mathrm{e}}_{\mathrm{sec}}} \boldsymbol{D}^{\mathrm{e}}_{\mathrm{sec}} : \Delta\boldsymbol{\varepsilon} \right|} \frac{1}{p'} \right) \tag{4.109}$$

4.4.9 Lode angle dependence

In the current study the bounding surface F is assumed to be dependent on the Lode angle θ as already discussed in section 3.3.6. Whereat, the Lode angle dependence is introduced to the bounding surface formulation by the Lode-angle dependent variable $N(\theta)$. As a consequence an analytical closed form solution for the similarity ratio b as given by Equation 4.101 in section 4.4.8 is not applicable. The analytical solution of the similarity ratio b requires to know the Lode angle dependent variable $N(\theta)$. However, the Lode angle dependent variable $N(\theta)$ is governed by the image stress state $\bar{\boldsymbol{\sigma}}'(b)$ as a function of the similarity ratio b itself. Hence, an iterative solution for the determination of the similarity ratio is used.

Moreover, the elastic nucleus f_{eln} is also Lode angle dependent due to the homology to the bounding surface F. Again, the analytical solution for the intersection stress $\boldsymbol{\sigma}'_{\mathrm{inter}}$ as given by Equations 4.83 and 4.84 in section 4.4.7 is not employable. The analytical solution of the intersection stress $\boldsymbol{\sigma}'_{\mathrm{inter}}$ requires to know the Lode angle dependent variable $N(\theta)$ while the Lode angle dependent variable $N(\theta)$ is governed by the image stress state $\bar{\boldsymbol{\sigma}}'(\boldsymbol{\sigma}'_{\mathrm{inter}})$ with respect to the intersection stress $\boldsymbol{\sigma}'_{\mathrm{inter}}$ itself. Consequently, an iterative solution for the determination of the intersection stress $\boldsymbol{\sigma}'_{\mathrm{inter}}$ with respect to the Lode angle dependence given by the variable $N(\theta)$ is needed as well.

Both iterative solutions for the similarity ratio and the intersection stress are described in the following. The iterative solutions are based on the Pegasus interpolation algorithm proposed by Dowell and Jarratt (1972). Advantages of the Pegasus algorithm are an unconditional convergence, no requirement of derivatives and the achievement of the convergence in four to five iterations. It is to be noted that in the following discussion the right subscript k specifies the interpolation variables and the left superscript l denotes the iteration number $[1, l_{\max}]$.

Iterative solution for similarity ratio with respect to Lode angle dependence

The interpolation variable $N(\theta)$ generally serves as the governing variable of the iterative solution for the similarity ratio b with respect to the Lode angle dependence. For each estimated interpolation variable N used during the iterative Pegasus interpolation algorithm the following estimation algorithm is employed: The similarity ratio b according to the analytical solution given by Equation 4.101 as a function of the estimated interpolation variable N, the image stress state $\bar{\boldsymbol{\sigma}}' = b\left\{\boldsymbol{\sigma}' - \boldsymbol{\sigma}'_{\mathrm{pc}}\right\} + \boldsymbol{\sigma}'_{\mathrm{pc}}$ and the corresponding Lode angle dependent variable N_{calc} according to Equations 3.23 and 3.26-3.27 as a function of the image stress state $\bar{\boldsymbol{\sigma}}'$ on the bounding surface are derived. The estimated value of the interpolation variable N before the estimation algorithm should coincide with the calculated value N_{calc} after a successful iteration employing the Pegasus algorithm. Hence, as an error measure the difference E of the estimated and the calculated value of the interpolation variable is obtained so that $E = N - N_{\mathrm{calc}}$. During the iterative Pegasus interpolation algorithm the difference should be minimized by updating the value of the interpolation variable N. That is, the absolute value of the difference should become smaller than or equal to a positive tolerance value Tol (here specified as 10^{-7}) so that $\{|E| \leq +Tol\}$. If the difference is larger than the tolerance value the interpolation variable N will be adjusted for the next iteration by applying a linear interpolation procedure.
At the beginning of the Pegasus interpolation algorithm the starting values for the interpolation variables $N_{k-1} = N_{\mathrm{e}}$ and $N_k = N_{\mathrm{c}}$ are set to define the upper and the lower initial boundaries of the interpolation, respectively. Hence, the possible range of the image stress state, which has to be calculated is constrained.

Initial conditions

Set starting values for interpolation variables

$$N_{k-1} = N_{\mathrm{e}}$$

$$N_k = N_{\mathrm{c}}$$

Afterwards, the following components are calculated with respect to the lower boundary value of the interpolation variable N_{k-1}. The similarity ratio b_{k-1} as a function of N_{k-1}, the image stress state $\bar{\boldsymbol{\sigma}}'_{k-1} = b_{k-1}\left\{\boldsymbol{\sigma}' - \boldsymbol{\sigma}'_{\mathrm{pc}}\right\} + \boldsymbol{\sigma}'_{\mathrm{pc}}$ as a function of the similarity ratio b_{k-1} and the corresponding Lode angle dependent variable $N_{\mathrm{calc},k-1}$ as a function of the image stress state $\bar{\boldsymbol{\sigma}}'_{k-1}$ on the bounding surface are derived. Furthermore, the difference $E_{k-1} = N_{k-1} - N_{\mathrm{calc},k-1}$ is calculated.

Estimation algorithm wrt. lower boundary $k-1$

Call subroutine: similarity ratio

input: $\boldsymbol{\sigma}'$, $\boldsymbol{q}$, $\boldsymbol{\sigma}'_{\mathrm{pc}}$, N_{k-1}

output: b_{k-1}

Calculate image stress

$$\bar{\boldsymbol{\sigma}}'_{k-1} = b_{k-1}\left\{\boldsymbol{\sigma}' - \boldsymbol{\sigma}'_{\mathrm{pc}}\right\} + \boldsymbol{\sigma}'_{\mathrm{pc}}$$

Calculate auxiliary variable $N_{\mathrm{calc},k-1}$

$$N_{\mathrm{calc},k-1} = \frac{2\,n_{\mathrm{cs}}}{\{1+n_{\mathrm{cs}}\} - \{1-n_{\mathrm{cs}}\}\,\cos(3\,\theta_{k-1})}\,N_{\mathrm{c}}$$

where: $\cos(3\,\theta_{k-1}) = \sqrt{6}\,\mathrm{tr}(\bar{\boldsymbol{n}}^3_{\mathrm{r}\alpha,k-1})$ as function of $\bar{\boldsymbol{\sigma}}'_{k-1}$

Calculate corresponding difference

$$E_{k-1} = N_{k-1} - N_{\mathrm{calc},k-1}$$

The same estimation algorithm is repeated, but with respect to the upper boundary value of the interpolation variable N_k. The similarity ratio b_k as a function of N_k, the image stress state $\bar{\boldsymbol{\sigma}}'_k = b_k\left\{\boldsymbol{\sigma}' - \boldsymbol{\sigma}'_{\mathrm{pc}}\right\} + \boldsymbol{\sigma}'_{\mathrm{pc}}$ as a function of the similarity ratio b_k and the corresponding Lode angle dependent variable $N_{\mathrm{calc},k}$ as a function of the image stress state $\bar{\boldsymbol{\sigma}}'_k$ are calculated. Moreover, the difference $E_k = N_k - N_{\mathrm{calc},k}$ is evaluated.

Estimation algorithm wrt. upper boundary k

Call subroutine: similarity ratio

input: $\boldsymbol{\sigma}'$, $\boldsymbol{q}$, $\boldsymbol{\sigma}'_{\mathrm{pc}}$, N_k

output: b_k

Calculate image stress

$$\bar{\boldsymbol{\sigma}}'_k = b_k\left\{\boldsymbol{\sigma}' - \boldsymbol{\sigma}'_{\mathrm{pc}}\right\} + \boldsymbol{\sigma}'_{\mathrm{pc}}$$

Calculate auxiliary variable $N_{\mathrm{calc},k}$

$$N_{\mathrm{calc},k} = \frac{2\,n_{\mathrm{cs}}}{\{1+n_{\mathrm{cs}}\} - \{1-n_{\mathrm{cs}}\}\,\cos(3\,\theta_k)}\,N_{\mathrm{c}}$$

where: $\cos(3\,\theta_k) = \sqrt{6}\,\mathrm{tr}(\bar{\boldsymbol{n}}^3_{\mathrm{r}\alpha,k})$ as function of $\bar{\boldsymbol{\sigma}}'_k$

Calculate corresponding difference

$$E_k = N_k - N_{\mathrm{calc},k}$$

In addition to the estimations with respect to the lower and the upper boundaries of the interpolation variable N_{k-1} and N_k, a further estimation will be conducted with respect to an interpolated value N_{k+1} of the Lode angle dependent interpolation variable,

so that $N_{k+1} = \{N_k\, E_{k-1} - N_{k-1}\, E_k\} / \{E_{k-1} - E_k\}$. The linear interpolation between the boundary values N_{k-1} and N_k is based on the differences E_{k-1} and E_k between the estimated and the calculated values of the interpolation variable. Consequently, the similarity ratio b_{k+1} as a function of the interpolated value of the variable N_{k+1}, the image stress state $\bar{\boldsymbol{\sigma}}'_{k+1} = b_{k+1} \left\{\boldsymbol{\sigma}' - \boldsymbol{\sigma}'_{\mathrm{pc}}\right\} + \boldsymbol{\sigma}'_{\mathrm{pc}}$ as a function of the similarity ratio b_{k+1} and the corresponding Lode angle dependent variable $N_{\mathrm{calc},k+1}$ as a function of the image stress state $\bar{\boldsymbol{\sigma}}'_{k+1}$ are determined. Again, the difference $E_{k+1} = N_{k+1} - N_{\mathrm{calc},k+1}$ is calculated as an error measure.

Estimation algorithm wrt. interpolation $k+1$

Calculate interpolation variable N_{k+1}

$$N_{k+1} = \frac{N_k\, E_{k-1} - N_{k-1}\, E_k}{E_{k-1} - E_k}$$

Call subroutine: similarity ratio

input: $\boldsymbol{\sigma}'$, $\boldsymbol{q}$, $\boldsymbol{\sigma}'_{\mathrm{pc}}$, N_{k+1}

output: b_{k+1}

Calculate image stress

$$\bar{\boldsymbol{\sigma}}'_{k+1} = b_{k+1} \left\{\boldsymbol{\sigma}' - \boldsymbol{\sigma}'_{\mathrm{pc}}\right\} + \boldsymbol{\sigma}'_{\mathrm{pc}}$$

Calculate auxiliary variable $N_{\mathrm{calc},k+1}$

$$N_{\mathrm{calc},k+1} = \frac{2\, n_{\mathrm{cs}}}{\{1 + n_{\mathrm{cs}}\} - \{1 - n_{\mathrm{cs}}\}\, \cos(3\, \theta_{k+1})}\, N_{\mathrm{c}}$$

where: $\cos(3\, \theta_{k+1}) = \sqrt{6}\, \mathrm{tr}(\bar{\boldsymbol{n}}^3_{\mathrm{r}\alpha,k+1})$ as function of $\bar{\boldsymbol{\sigma}}'_{k+1}$

Calculate corresponding difference

$$E_{k+1} = N_{k+1} - N_{\mathrm{calc},k+1}$$

Before starting the iterative interpolation loop the counting variable $l = 1$ is set to one and the first iteration starts if $\{|E_{k+1}| > +Tol\}$ holds true. The interpolation loop is called and repeated until the criterion $\{|E_{k+1}| \leq +Tol\}$ is fulfilled. If the maximum number of iterations is reached so that $\{l > l_{\max} = 10\}$ the iterative interpolation is aborted and an error message is shown.

Iterative interpolation loop

Set counting variable for iteration number $l = 1$

Do While $\{|E_{k+1}| > +Tol\}$ and $\{l \leq l_{\max}\}$

At the beginning of each iteration the lower boundary value of the interpolation variable N_{k-1} and the corresponding difference E_{k-1} are adjusted with respect to the former boundary values and the interpolated values dependent on the sign convention of the solution. Furthermore, the upper boundary value of the interpolation variable N_k and the corresponding difference E_k are updated towards the interpolated values N_{k+1} and E_{k+1}, respectively. The procedure ensures to always have function values with opposite signs during the iteration procedure.

Update boundaries wrt. sign convention of interpolation

If $\{E_{k+1}\, E_k < 0\}$

Update lower boundary value of interpolation variable and difference

$$N_{k-1} = N_k$$

$$E_{k-1} = E_k$$

End If (update wrt. 1st sign convention criterion)

If $\{E_{k+1}\, E_k > 0\}$

Update lower boundary of difference

$$N_{k-1} = N_{k-1}$$

$$E_{k-1} = \frac{E_{k-1}\, E_k}{E_k + E_{k+1}}$$

End If (update wrt. 2nd sign convention criterion)

Update upper boundary of interpolation variable and difference

$$N_k = N_{k+1}$$

$$E_k = E_{k+1}$$

After the update of the boundary values of the interpolation variables N_{k-1} and N_k and the corresponding differences E_{k-1} and E_k an additional estimation with respect to the newly interpolated value of the Lode angle dependent interpolation variable $N_{k+1} = \{N_k\, E_{k-1} - N_{k-1}\, E_k\} / \{E_{k-1} - E_k\}$ is conducted. Consequently, the similarity ratio b_{k+1} as a function of the interpolated value of the variable N_{k+1}, the image stress state $\bar{\boldsymbol{\sigma}}'_{k+1} = b_{k+1} \left\{\boldsymbol{\sigma}' - \boldsymbol{\sigma}'_{\mathrm{pc}}\right\} + \boldsymbol{\sigma}'_{\mathrm{pc}}$ as a function of the similarity ratio b_{k+1} and the corresponding Lode angle dependent variable $N_{\mathrm{calc},k+1}$ as a function of the image stress state $\bar{\boldsymbol{\sigma}}'_{k+1}$ are determined. Again, the difference $E_{k+1} = N_{k+1} - N_{\mathrm{calc},k+1}$ is calculated as an error measure. Finally, the iteration number is increased by one, so that $l = l + 1$ and a new iteration is started. The calculation proceeds from the beginning of the iterative interpolation loop with checking if the criterion $\{|E_{k+1}| \leq +Tol\}$ is fulfilled.

Estimation algorithm wrt. interpolation $k+1$

Calculate interpolation variable N_{k+1}

$$N_{k+1} = \frac{N_k\, E_{k-1} - N_{k-1}\, E_k}{E_{k-1} - E_k}$$

Call subroutine: similarity ratio

input: $\boldsymbol{\sigma}'$, $\boldsymbol{q}$, $\boldsymbol{\sigma}'_{\mathrm{pc}}$, N_{k+1}

output: b_{k+1}

Calculate image stress

$$\bar{\boldsymbol{\sigma}}'_{k+1} = b_{k+1}\left\{\boldsymbol{\sigma}' - \boldsymbol{\sigma}'_{\mathrm{pc}}\right\} + \boldsymbol{\sigma}'_{\mathrm{pc}}$$

Calculate auxiliary variable $N_{\mathrm{calc},k+1}$

$$N_{\mathrm{calc},k+1} = \frac{2\, n_{\mathrm{cs}}}{\{1+n_{\mathrm{cs}}\} - \{1-n_{\mathrm{cs}}\}\, \cos(3\,\theta_{k+1})}\, N_{\mathrm{c}}$$

where: $\cos(3\,\theta_{k+1}) = \sqrt{6}\,\mathrm{tr}(\bar{\boldsymbol{n}}^3_{\mathrm{r}\alpha,k+1})$ as function of $\bar{\boldsymbol{\sigma}}'_{k+1}$

Calculate corresponding difference

$$E_{k+1} = N_{k+1} - N_{\mathrm{calc},k+1}$$

Set $l = l+1$

Go To iterative interpolation loop

End Do While (interpolation loop)

When fulfilling the criterion $\{|E_{k+1}| \leq +Tol\}$ the iterative Pegasus interpolation algorithm is successful and the solution for the similarity ratio with respect to Lode angle dependence is accepted. Therefore, the similarity ratio $b = b_{k+1}$ and the Lode angle dependent variable $N = N_{k+1}$ are transferred to the Modified Euler calculation.

Setting and transfer of variables

Set similarity ratio b and Lode angle dependent variable N

$$b = b_{k+1}$$

$$N = N_{k+1}$$

Return b and N

Iterative solution for intersection stress with respect to Lode angle dependence

For obtaining the solution for the intersection stress $\boldsymbol{\sigma}'_{\mathrm{inter}}$ with respect to the Lode angle dependence the same iterative Pegasus interpolation algorithm is employed. The intersection stress $\boldsymbol{\sigma}'_{\mathrm{inter}}$ is calculated according to the analytical solution given by Equations 4.83 and 4.84 as a function of the estimated interpolation variable N. The image stress state $\bar{\boldsymbol{\sigma}}' = b_{\mathrm{eln}} \left\{\boldsymbol{\sigma}'_{\mathrm{inter}} - \boldsymbol{\sigma}'_{\mathrm{pc}}\right\} + \boldsymbol{\sigma}'_{\mathrm{pc}}$ is derived as a function of the constant similarity ratio b_{eln} and projected from the position of the projection center $\boldsymbol{\sigma}'_{\mathrm{pc}}$ through the calculated intersection stress state $\boldsymbol{\sigma}'_{\mathrm{inter}}$ onto the bounding surface. The corresponding Lode angle dependent variable N_{calc} is evaluated according to Equations 3.23 and 3.26-3.27 as a function of the image stress state $\bar{\boldsymbol{\sigma}}'$ on the bounding surface. The entire iterative Pegasus interpolation algorithm to obtain the iterative solution for the intersection stress with respect to Lode angle dependence is given in the following part:

Initial conditions

Set starting values for interpolation variables

$$N_{k-1} = N_{\mathrm{e}}$$

$$N_{k} = N_{\mathrm{c}}$$

Estimation algorithm wrt. lower boundary $k-1$

Call subroutine: intersection stress

input: $\boldsymbol{\sigma}'$, $\Delta\boldsymbol{\sigma}'_{\mathrm{trial}}$, $\boldsymbol{q}$, $\boldsymbol{\sigma}'_{\mathrm{pc}}$

output: $\boldsymbol{\sigma}'_{\mathrm{inter},k-1}$

Calculate image stress state wrt. intersection stress

$$\bar{\boldsymbol{\sigma}}'_{k-1} = b_{\mathrm{eln}} \left\{\boldsymbol{\sigma}'_{\mathrm{inter},k-1} - \boldsymbol{\sigma}'_{\mathrm{pc}}\right\} + \boldsymbol{\sigma}'_{\mathrm{pc}}$$

Calculate auxiliary variable $N_{\mathrm{calc},k-1}$

$$N_{\mathrm{calc},k-1} = \frac{2\, n_{\mathrm{cs}}}{\{1+n_{\mathrm{cs}}\} - \{1-n_{\mathrm{cs}}\}\, \cos(3\,\theta_{k-1})}\, N_{\mathrm{c}}$$

where: $\cos(3\,\theta_{k-1}) = \sqrt{6}\, \mathrm{tr}(\bar{\boldsymbol{n}}^{3}_{\mathrm{r}\alpha,k-1})$ as function of $\bar{\boldsymbol{\sigma}}'_{k-1}$

Calculate corresponding difference

$$E_{k-1} = N_{k-1} - N_{\mathrm{calc},k-1}$$

Estimation algorithm wrt. upper boundary k

Call subroutine: intersection stress

input: $\boldsymbol{\sigma}'$, $\Delta\boldsymbol{\sigma}'_{\mathrm{trial}}$, $\boldsymbol{q}$, $\boldsymbol{\sigma}'_{\mathrm{pc}}$

output: $\boldsymbol{\sigma}'_{\mathrm{inter},k}$

Calculate image stress state wrt. intersection stress

$$\bar{\boldsymbol{\sigma}}'_k = b_{\mathrm{eln}} \left\{\boldsymbol{\sigma}'_{\mathrm{inter},k} - \boldsymbol{\sigma}'_{\mathrm{pc}}\right\} + \boldsymbol{\sigma}'_{\mathrm{pc}}$$

Calculate auxiliary variable $N_{\mathrm{calc},k}$

$$N_{\mathrm{calc},k} = \frac{2\, n_{\mathrm{cs}}}{\{1 + n_{\mathrm{cs}}\} - \{1 - n_{\mathrm{cs}}\}\, \cos(3\,\theta_k)}\, N_{\mathrm{c}}$$

where: $\cos(3\,\theta_k) = \sqrt{6}\, \mathrm{tr}(\bar{\boldsymbol{n}}^3_{\mathrm{r}\alpha,k})$ as function of $\bar{\boldsymbol{\sigma}}'_k$

Calculate corresponding difference

$$E_k = N_k - N_{\mathrm{calc},k}$$

Estimation algorithm wrt. interpolation $k+1$

Calculate interpolation variable N_{k+1}

$$N_{k+1} = \frac{N_k\, E_{k-1} - N_{k-1}\, E_k}{E_{k-1} - E_k}$$

Call subroutine: intersection stress

input: $\boldsymbol{\sigma}'$, $\Delta\boldsymbol{\sigma}'_{\mathrm{trial}}$, $\boldsymbol{q}$, $\boldsymbol{\sigma}'_{\mathrm{pc}}$

output: $\boldsymbol{\sigma}'_{\mathrm{inter},k+1}$

Calculate image stress state wrt. intersection stress

$$\bar{\boldsymbol{\sigma}}'_{k+1} = b_{\mathrm{eln}} \left\{\boldsymbol{\sigma}'_{\mathrm{inter},k+1} - \boldsymbol{\sigma}'_{\mathrm{pc}}\right\} + \boldsymbol{\sigma}'_{\mathrm{pc}}$$

Calculate auxiliary variable $N_{\mathrm{calc},k+1}$

$$N_{\mathrm{calc},k+1} = \frac{2\, n_{\mathrm{cs}}}{\{1 + n_{\mathrm{cs}}\} - \{1 - n_{\mathrm{cs}}\}\, \cos(3\,\theta_{k+1})}\, N_{\mathrm{c}}$$

where: $\cos(3\,\theta_{k+1}) = \sqrt{6}\, \mathrm{tr}(\bar{\boldsymbol{n}}^3_{\mathrm{r}\alpha,k+1})$ as function of $\bar{\boldsymbol{\sigma}}'_{k+1}$

Calculate corresponding difference

$$E_{k+1} = N_{k+1} - N_{\mathrm{calc},k+1}$$

Iterative interpolation loop

Set counting variable for iteration number $l = 1$

Do While $\{|E_{k+1}| > +Tol\}$ and $\{l \leq l_{\max}\}$

Update boundaries wrt. sign convention of interpolation

If $\{E_{k+1}\, E_k < 0\}$

Update lower boundary value of interpolation variable and difference

$$N_{k-1} = N_k$$

$$E_{k-1} = E_k$$

End If (update wrt. 1st sign convention criterion)

If $\{E_{k+1}\, E_k > 0\}$

Update lower boundary of difference

$$N_{k-1} = N_{k-1}$$

$$E_{k-1} = \frac{E_{k-1}\, E_k}{E_k + E_{k+1}}$$

End If (update wrt. 2nd sign convention criterion)

Update upper boundary value of interpolation variable and difference

$$N_k = N_{k+1}$$

$$E_k = E_{k+1}$$

Estimation algorithm wrt. interpolation $k+1$

Calculate interpolation variable N_{k+1}

$$N_{k+1} = \frac{N_k\, E_{k-1} - N_{k-1}\, E_k}{E_{k-1} - E_k}$$

Call subroutine: intersection stress

input: $\boldsymbol{\sigma}'$, $\Delta\boldsymbol{\sigma}'_{\mathrm{trial}}$, $\boldsymbol{q}$, $\boldsymbol{\sigma}'_{\mathrm{pc}}$

output: $\boldsymbol{\sigma}'_{\mathrm{inter},k+1}$

Calculate image stress state wrt. intersection stress

$$\bar{\boldsymbol{\sigma}}'_{k+1} = b_{\mathrm{eln}} \left\{\boldsymbol{\sigma}'_{\mathrm{inter},k+1} - \boldsymbol{\sigma}'_{\mathrm{pc}}\right\} + \boldsymbol{\sigma}'_{\mathrm{pc}}$$

Calculate auxiliary variable $N_{\mathrm{calc},k+1}$

$$N_{\mathrm{calc},k+1} = \frac{2\, n_{\mathrm{cs}}}{\{1 + n_{\mathrm{cs}}\} - \{1 - n_{\mathrm{cs}}\}\, \cos(3\, \theta_{k+1})}\, N_{\mathrm{c}}$$

where: $\cos(3\, \theta_{k+1}) = \sqrt{6}\, \mathrm{tr}(\bar{\boldsymbol{n}}^3_{\mathrm{r}\alpha,k+1})$ as function of $\bar{\boldsymbol{\sigma}}'_{k+1}$

Calculate corresponding difference

$$E_{k+1} = N_{k+1} - N_{\mathrm{calc},k+1}$$

Set $l = l + 1$

Go To iterative interpolation loop

End Do While (interpolation loop)

When fulfilling the criterion $\{|E_{k+1}| \leq +Tol\}$ the iterative Pegasus interpolation algorithm is successful and the solution for the intersection stress with respect to Lode angle dependence is accepted. Therefore, the similarity ratio $\boldsymbol{\sigma}'_{\text{inter}} = \boldsymbol{\sigma}'_{\text{inter},k+1}$ and the Lode angle dependent variable $N_{\text{inter}} = N_{k+1}$ are transferred to the general integration scheme.

Setting and transfer of variables

Set intersection stress $\boldsymbol{\sigma}'_{\text{inter}}$ and Lode angle dependent variable N_{inter}

$$\boldsymbol{\sigma}'_{\text{inter}} = \boldsymbol{\sigma}'_{\text{inter},k+1}$$

$$N_{\text{inter}} = N_{k+1}$$

Return $\boldsymbol{\sigma}'_{\text{inter}}$ and N_{inter}

4.4.10 Gradients

The gradients of the bounding surface with respect to the hardening variables $\partial F/\partial \boldsymbol{q}$ and the gradient of the plastic potential surface with respect to the image stress state $\partial G/\partial \bar{\boldsymbol{\sigma}}'$ are required for the calculation of the plasticity modulus $\bar{K}_{\text{p}}$ with respect to the image stress state on the bounding surface. Moreover, the gradients of the bounding surface and the plastic potential surface with respect to the image stress state $\partial F/\partial \bar{\boldsymbol{\sigma}}'$ and $\partial G/\partial \bar{\boldsymbol{\sigma}}'$ are used for the calculation of the scalar plastic loading index L, which incorporates the plasticity modulus $\bar{K}_{\text{p}}$ as well. Finally, to obtain the plastic strain increment $\Delta\boldsymbol{\varepsilon}^{\text{p}}$ the flow rule is employed, which considers the gradient of the plastic potential surface with respect to the image stress state $\partial G/\partial \bar{\boldsymbol{\sigma}}'$ and the plastic loading index L. The updates of the hardening variables, the strcuture variable and the damage variable are also governed by the scalar plastic loading index L and the gradient of the plastic potential surface with respect to the image stress state $\partial G/\partial \bar{\boldsymbol{\sigma}}'$.

Gradient of F and G with respect to $\bar{\sigma}'$

Use of the following equations for F and G:

$$F = \frac{3}{2}\{\bar{\boldsymbol{s}} - \bar{p}'\,\boldsymbol{\alpha}\} : \{\bar{\boldsymbol{s}} - \bar{p}'\,\boldsymbol{\alpha}\} - \left\{N^2 - \frac{3}{2}\,\boldsymbol{\alpha} : \boldsymbol{\alpha}\right\} \bar{p}'\ \{p_{0,\text{s}} - \bar{p}'\} = 0 \quad (4.110)$$

$$G = \frac{3}{2}\{\bar{\boldsymbol{s}} - \bar{p}\,\boldsymbol{\alpha}\} : \{\bar{\boldsymbol{s}} - \bar{p}'\,\boldsymbol{\alpha}\} - \left\{M^2 - \frac{3}{2}\,\boldsymbol{\alpha} : \boldsymbol{\alpha}\right\} \bar{p}'\ \{p_{\alpha} - \bar{p}'\} = 0 \quad (4.111)$$

Gradient of F with respect to $\bar{\boldsymbol{\sigma}}'$:

$$\frac{\partial F}{\partial \bar{\boldsymbol{\sigma}}'} = \frac{\partial F}{\partial \bar{\boldsymbol{s}}}\,\frac{\partial \bar{\boldsymbol{s}}}{\partial \bar{\boldsymbol{\sigma}}'} + \frac{\partial F}{\partial \bar{p}'}\,\frac{\partial \bar{p}'}{\partial \bar{\boldsymbol{\sigma}}'} + \frac{\partial F}{\partial \theta}\,\frac{\partial \theta}{\partial \bar{\boldsymbol{\sigma}}'} \tag{4.112}$$

$$\begin{aligned}\frac{\partial F}{\partial \bar{\boldsymbol{\sigma}}'} = {} & 3\,\{\bar{\boldsymbol{s}} - \bar{p}'\,\boldsymbol{\alpha}\} \\ & - \left\{\{\bar{\boldsymbol{s}} - \bar{p}'\,\boldsymbol{\alpha}\} : \{\boldsymbol{\alpha}\} + \frac{1}{3}\,\left\{N^2 - \frac{3}{2}\,\boldsymbol{\alpha} : \boldsymbol{\alpha}\right\}\,\{p_{0,\mathrm{s}} - 2\,\bar{p}'\}\right\}\,\boldsymbol{I} \\ & + \frac{\partial F}{\partial \theta}\,\frac{\partial \theta}{\partial \boldsymbol{\sigma}'}\end{aligned} \tag{4.113}$$

Gradient of G with respect to $\bar{\boldsymbol{\sigma}}'$:

$$\frac{\partial G}{\partial \bar{\boldsymbol{\sigma}}'} = \frac{\partial G}{\partial \bar{\boldsymbol{s}}}\,\frac{\partial \bar{\boldsymbol{s}}}{\partial \bar{\boldsymbol{\sigma}}'} + \frac{\partial G}{\partial \bar{p}'}\,\frac{\partial \bar{p}'}{\partial \bar{\boldsymbol{\sigma}}'} + \frac{\partial G}{\partial \theta}\,\frac{\partial \theta}{\partial \bar{\boldsymbol{\sigma}}'} \tag{4.114}$$

$$\begin{aligned}\frac{\partial G}{\partial \bar{\boldsymbol{\sigma}}'} = {} & 3\,\{\bar{\boldsymbol{s}} - \bar{p}'\,\boldsymbol{\alpha}\} \\ & - \left\{\{\bar{\boldsymbol{s}} - \bar{p}'\,\boldsymbol{\alpha}\} : \{\boldsymbol{\alpha}\} + \frac{1}{3}\,\left\{M^2 - \frac{3}{2}\,\boldsymbol{\alpha} : \boldsymbol{\alpha}\right\}\,\{p_{\alpha} - 2\,\bar{p}'\}\right\}\,\boldsymbol{I} \\ & + \frac{\partial G}{\partial \theta}\,\frac{\partial \theta}{\partial \boldsymbol{\sigma}'}\end{aligned} \tag{4.115}$$

Gradient of $\boldsymbol{F}$ and $\boldsymbol{G}$ with respect to θ

Use of the following equations for N:

$$N(\theta) = \Theta_{\mathrm{n}}\;N_{\mathrm{c}} = \frac{2\,n_{\mathrm{cs}}}{\{1 + n_{\mathrm{cs}}\} - \{1 - n_{\mathrm{cs}}\}\,\cos(3\,\theta)}\,N_{\mathrm{c}} \tag{4.116}$$

Use of the following equations for M:

$$M(\theta) = \Theta_{\mathrm{m}}\;M_{\mathrm{c}} = \frac{2\,m_{\mathrm{cs}}}{\{1 + m_{\mathrm{cs}}\} - \{1 - m_{\mathrm{cs}}\}\,\cos(3\,\theta)}\,M_{\mathrm{c}} \tag{4.117}$$

Gradient of F with respect to θ:

$$\frac{\partial F}{\partial \theta} = \frac{\partial F}{\partial N}\,\frac{\partial N}{\partial \theta} \tag{4.118}$$

$$\frac{\partial F}{\partial \theta} = 6\,N^2\,\bar{p}'\,\{p_{0,\mathrm{s}} - \bar{p}'\}\,\left\{\frac{1 - n_{\mathrm{cs}}}{2\,n_{\mathrm{cs}}}\right\}\,\Theta_{\mathrm{n}}\,\sin(3\,\theta) \tag{4.119}$$

Gradient of G with respect to θ:

$$\frac{\partial G}{\partial \theta} = \frac{\partial G}{\partial M}\,\frac{\partial M}{\partial \theta} \tag{4.120}$$

$$\frac{\partial G}{\partial \theta} = 6\,M^2\,\bar{p}'\,\{p_\alpha - \bar{p}'\}\,\left\{\frac{1-m_{\rm cs}}{2\,m_{\rm cs}}\right\}\,\Theta_{\rm m}\sin(3\,\theta) \tag{4.121}$$

Gradient of θ with respect to $\bar{\boldsymbol{\sigma}}'$

Use of the following equations for θ:

$$\cos(3\,\theta) = \sqrt{6}\,{\rm tr}(\bar{\boldsymbol{n}}^3_{{\rm r}\alpha}) \tag{4.122}$$

$$\bar{\boldsymbol{n}}_{{\rm r}\alpha} = \frac{\bar{\boldsymbol{r}}-\boldsymbol{\alpha}}{|\bar{\boldsymbol{r}}-\boldsymbol{\alpha}|} = \frac{\bar{\boldsymbol{r}}-\boldsymbol{\alpha}}{\sqrt{\{\bar{\boldsymbol{r}}-\boldsymbol{\alpha}\}:\{\bar{\boldsymbol{r}}-\boldsymbol{\alpha}\}}} \tag{4.123}$$

Gradient of θ with respect to $\bar{\boldsymbol{\sigma}}'$:

$$\frac{\partial \theta}{\partial \bar{\boldsymbol{\sigma}}'} = \frac{-3\,\left\{\bar{\boldsymbol{n}}^2_{{\rm r}\alpha} - {\rm tr}(\bar{\boldsymbol{n}}^3_{{\rm r}\alpha})\,\bar{\boldsymbol{n}}_{{\rm r}\alpha} - \frac{1}{3}\,\boldsymbol{I}\,\{1+{\rm tr}(\bar{\boldsymbol{n}}^2_{{\rm r}\alpha}\,\boldsymbol{\alpha}) - {\rm tr}\,(\bar{\boldsymbol{n}}^3_{{\rm r}\alpha})\,{\rm tr}(\bar{\boldsymbol{n}}_{{\rm r}\alpha}\,\boldsymbol{\alpha})\}\right\}}{\sqrt{\frac{3}{2}\,\{\bar{\boldsymbol{s}}-\bar{p}'\,\boldsymbol{\alpha}\}:\{\bar{\boldsymbol{s}}-\bar{p}'\,\boldsymbol{\alpha}\}}\,\sqrt{1-6\,{\rm tr}^2(\bar{\boldsymbol{n}}^3_{{\rm r}\alpha})}} \tag{4.124}$$

Combined terms $\dfrac{\partial F}{\partial \theta}\,\dfrac{\partial \theta}{\partial \bar{\boldsymbol{\sigma}}'}$ and $\dfrac{\partial G}{\partial \theta}\,\dfrac{\partial \theta}{\partial \bar{\boldsymbol{\sigma}}'}$

$$\frac{\partial F}{\partial \theta}\,\frac{\partial \theta}{\partial \bar{\boldsymbol{\sigma}}'} = 6\,N^2\,\bar{p}'\,\{p_{0,{\rm s}}-\bar{p}'\}\,\left\{\frac{1-n_{\rm cs}}{2\,n_{\rm cs}}\right\}\,\Theta_{\rm n} \times \frac{-3\,\left\{\bar{\boldsymbol{n}}^2_{{\rm r}\alpha} - {\rm tr}(\bar{\boldsymbol{n}}^3_{{\rm r}\alpha})\,\bar{\boldsymbol{n}}_{{\rm r}\alpha} - \frac{1}{3}\,\boldsymbol{I}\,\{1+{\rm tr}(\bar{\boldsymbol{n}}^2_{{\rm r}\alpha}\,\boldsymbol{\alpha}) - {\rm tr}\,(\bar{\boldsymbol{n}}^3_{{\rm r}\alpha})\,{\rm tr}(\bar{\boldsymbol{n}}_{{\rm r}\alpha}\,\boldsymbol{\alpha})\}\right\}}{\sqrt{\frac{3}{2}\,\{\bar{\boldsymbol{s}}-\bar{p}'\,\boldsymbol{\alpha}\}:\{\bar{\boldsymbol{s}}-\bar{p}'\,\boldsymbol{\alpha}\}}} \tag{4.125}$$

$$\frac{\partial G}{\partial \theta}\,\frac{\partial \theta}{\partial \bar{\boldsymbol{\sigma}}'} = 6\,M^2\,\bar{p}'\,\{p_\alpha-\bar{p}'\}\,\left\{\frac{1-m_{\rm cs}}{2\,m_{\rm cs}}\right\}\,\Theta_{\rm m} \times \frac{-3\,\left\{\bar{\boldsymbol{n}}^2_{{\rm r}\alpha} - {\rm tr}(\bar{\boldsymbol{n}}^3_{{\rm r}\alpha})\,\bar{\boldsymbol{n}}_{{\rm r}\alpha} - \frac{1}{3}\,\boldsymbol{I}\,\{1+{\rm tr}(\bar{\boldsymbol{n}}^2_{{\rm r}\alpha}\,\boldsymbol{\alpha}) - {\rm tr}\,(\bar{\boldsymbol{n}}^3_{{\rm r}\alpha})\,{\rm tr}(\bar{\boldsymbol{n}}_{{\rm r}\alpha}\,\boldsymbol{\alpha})\}\right\}}{\sqrt{\frac{3}{2}\,\{\bar{\boldsymbol{s}}-\bar{p}'\,\boldsymbol{\alpha}\}:\{\bar{\boldsymbol{s}}-\bar{p}'\,\boldsymbol{\alpha}\}}} \tag{4.126}$$

Gradient of $\boldsymbol{F}$ with respect to $\boldsymbol{p_{0,s}}$

$$\frac{\partial F}{\partial p_{0,\mathrm{s}}} = -\bar{p}' \left\{ N^2 - \frac{3}{2}\,\boldsymbol{\alpha} : \boldsymbol{\alpha} \right\} \tag{4.127}$$

Gradient of $\boldsymbol{F}$ with respect to $\boldsymbol{\alpha}$

$$\frac{\partial F}{\partial \boldsymbol{\alpha}} = -3\,\bar{p}'\,\{\bar{\boldsymbol{s}} - \bar{p}'\,\boldsymbol{\alpha}\} + 3\,\bar{p}'\,\{p_{0,\mathrm{s}} - \bar{p}'\}\,\boldsymbol{\alpha} \tag{4.128}$$

4.5 Summary

The numerical analysis of mechanized tunneling in natural clay requires the availability of an adequate constitutive soil model in the finite element code. Consequently, the numerical implementation of the constitutive BSP model and the integration of the constitutive equations were discussed in this chapter.

The global iterative procedure as used in the finite element code Plaxis to find the appropriate strain field which satisfies the global static equilibrium condition was shortly introduced in this chapter. The global iterative procedure employed by the Plaxis software is based on a Modified Newton-Raphson approach. Whereat, the global stiffness matrix is formed based on the elastic stiffness matrix and the strain interpolation matrix integrated over the volume. Furthermore, the global stiffness matrix is kept constant during an entire global calculation step of the Modified Newton-Raphson approach. Moreover, the communication between the finite element code Plaxis and the user-defined constitutive BSP model was described. The interaction between the finite element code and the constitutive BSP model compiled as a Dynamic Link Library (DLL) allows for the coupling of global iterative procedure and integration procedure via so-called ID Tasks.

The integration procedure for any estimated strain increment provides an appropriate stress increment to balance the difference between external body forces and internal reactions. In this chapter the time integration of the constitutive equations was emphasized. Hence, an explicit integration scheme with automatic error control and sub-stepping approach using the second order accurate Forward Euler solution (Modified Euler approach) was intensively discussed. The explicit integration scheme, which is based on the determination of the final stress of the current calculation step with respect to the current stress state and hardening variables, was adapted and further modified to be applicable to the constitutive BSP model.

Moreover, the coupled consistent and normal drift correction approach was presented in detail. Additionally, the following subroutines, which are needed for the integration scheme were presented such as determination of the tangent and the secant elastic stiffness matrix, calculation of the elastic nucleus to decide for purely elastic material behavior, analytical finding of the intersection stress state and computation of the intersection factor to account for elastoplastic transition, analytical evaluation of the similarity ratio to obtain the corresponding image stress state and Lode angle dependence of the bounding surface, which becomes relevant for the iterative solution of intersection stress and similarity ratio. Finally, particular incremental formulations were evaluated such as the gradients of the bounding surface and plastic potential with respect to stress and Lode angle, the gradient of the Lode angle with respect to stress and the gradients of the bounding surface with respect to hardening variables. The gradients are required for the calculation of the plasticity modulus with respect to the image stress state on the bounding surface, scalar plastic loading index, plastic strain increment, flow rule, update of the hardening variables, structure variable and damage variable.
In conclusion, employing the global iterative Modified Newton-Raphson procedure in combination with the proposed explicit forward Euler time integration procedure makes the constitutive BSP model available in the three-dimensional state-of-the-art finite element code Plaxis for conducting numerical simulations of mechanized tunneling. To ensure realistic and reliable predictions of the system response induced by mechanized tunneling an adequate calibration of the constitutive BSP model parameters and validation of the constitutive BSP model are essential. Hence, in the next chapters the calibration and validation of the constitutive BSP model against a number of geotechnical laboratory tests on natural and reconstituted clay samples under oedometric and triaxial boundary conditions will be presented . In advance to the parameter calibration, the sensitivity of model responses regarding the numerical simulations of geotechnical laboratory tests to the constitutive model parameters of the BSP model is investigated. Therefore, a global sensitivity analysis (GSA) is employed to guarantee a most appropriate parameter calibration.

5 Sensitivity analysis regarding BSP model parameters

5.1 Concept

Realistic and reliable predictions of the system behavior induced by mechanized tunneling in natural clay deposits require numerical simulations and a sophisticated constitutive model. The employed constitutive BSP model as described in chapter 3 accounts for the complex constitutive behavior of natural clay, which is governed by the current state, stress-strain history and structure. The constitutive BSP model in particular accounts for non-associated flow, inherent and stress-induced anisotropy, structure and destructuruation as well as the behavior under non-monotonic and cyclic loading. Therefore, a multitude of constitutive model parameters are needed to mathematically describe the constitutive behavior in an accurate manner. Accordingly, the number of constitutive BSP model parameters, their correlations and the superimposed influence on the BSP model responses make the calibration against geotechnical laboratory testing data demanding and complicated. Nevertheless, the realistic numerical simulation of mechanized tunneling requires a very precise knowledge of the constitutive BSP model parameters, which are often hard to access and to determine. Hence, more advanced approaches for the calibration such as parameter identification by means of applying an automated inverse numerical analysis (Tarantola, 2005) have to be utilized rather than using the common one-at-time variation of the parameters.
It is to be mentioned that the applicability of the inverse analysis may be restricted by the number of constitutive BSP model parameters to be identified and the number of BSP model responses to be back-calculated and to be fitted against the measurements. A multitude of constitutive model parameters may lead to non-unique solutions and non-distinct constitutive model parameter sets obtained from the optimization procedure. That is, different combinations of constitutive model parameters lead to the same minimum of the objective function or the same BSP model response.

Hence, the current chapter is mainly focusing on global sensitivity analysis (GSA) as a sophisticated approach to enhance the subsequent calibration of the constitutive BSP model parameters via inverse analysis by providing information on the geotechnical laboratory test and even the loading stage to be selected to most properly identify a particular constitutive BSP model parameter. However, the constitutive BSP model parameters which have a distinct definition with respect to the experimental data, so-called measurable parameters, can be directly determined and assessed from the corresponding geotechnical laboratory tests. This already will reduce the number of constitutive BSP model parameters to be identified via inverse analysis. Moreover, the GSA provides additional information on the following issues before performing a constitutive parameter identification.

- Optimal design of geotechnical experiments (type of test, loading stages) to ensure an efficient calibration of the constitutive BSP model parameters
- Reduction of the number of experimental data from geotechnical laboratory tests to be considered in the objective function of the inverse analysis
- Reduction of the dimensions of the inverse analysis problem with respect to the number of constitutive model parameters to be considered

At first, the general ability of the constitutive BSP model is discussed with respect to the stress-strain BSP model responses obtained from the numerical simulation of several geotechnical laboratory tests on natural Bothkennar clay to better interpret the results of the GSA. Afterwards, the sensitivity of the various numerical BSP model responses to the constitutive BSP model parameters is evaluated by employing the variance-based GSA as introduced by Sobol' (1993) and further developed by Saltelli et al. (2008). The GSA is suitable for highly non-linear problems and explores the whole input parameter space giving more comprehensive information than the local sensitivity analysis (LSA). In brief, the superimposed impact of other constitutive BSP model parameters is considered in the analysis of the relative influence.
The current study is particularly focusing on the influence of the constitutive BSP model parameters related to non-associated flow, inherent and stress-induced anisotropy, initial structure and destructuration, bounding surface plasticity and especially size of the purely elastic domain, degradation of stiffness and accumulation of plastic strain. In addition, a local parameter variation is conducted to gain additional knowledge on the influence of the change of the constitutive BSP model parameters on the stress-strain BSP model response. However, the results of the local parameter variation are not explicitly shown but incorporated in the analysis of the results of the GSA.

At the end of the chapter, recommendations are given regarding the adequate choice of geotechnical laboratory tests to be preferentially considered in the calibration of the constitutive BSP model parameters.

5.2 Global sensitivity analysis

5.2.1 Variance-based GSA

A comprehensive review of the global sensitivity analysis techniques can be found in Saltelli et al. (2008). The employed variance-based GSA (Sobol', 1993; Homma and Saltelli, 1996; Jansen, 1999; Saltelli et al., 2008; Mara and Tarantola, 2012) is aimed to quantify the impact of the variance of the input parameter vector $\boldsymbol{P} = \left\{p_1, ..., p_{N_{\mathrm{cp}}}\right\}$ on the variance of a particular model output y. The output variance is composed of the sum of the contributions of each individual input parameter and additionally the superimposed influence (interactions) of all input parameters specified by several higher order interaction terms.

The first order sensitivity index $S_{n_{\mathrm{cp}}}$ quantifies the sensitivity of a certain model output y to a particular input parameter $p_{n_{\mathrm{cp}}}$ without accounting for the interactions between the different input parameters on the BSP model response. Thereby $n_{\mathrm{cp}} = 1, ..., N_{\mathrm{cp}}$ specifies the n_{cp}-th constitutive BSP model parameter of the constitutive BSP model parameter vector $\boldsymbol{P} = \left\{p_1, ..., p_{N_{\mathrm{cp}}}\right\}$ and N_{cp} is the number of constitutive BSP model parameters considered in the sensitivity analysis. To capture the entire effect of a particular input parameter $p_{n_{\mathrm{cp}}}$ on the variance of the model output y in a single sensitivity measure, Homma and Saltelli (1996) introduced the sophisticated total effect sensitivity index $S_{\mathrm{T}_{n_{\mathrm{cp}}}}$.

That is, the total effect sensitivity index $S_{\mathrm{T}_{n_{\mathrm{cp}}}}$ covers both the first order effect as well as the higher order superimposed effects (interactions) induced by the other remaining input parameters. Consequently, the first order sensitivity index $S_{n_{\mathrm{cp}}}$ and the total effect sensitivity index $S_{\mathrm{T}_{n_{\mathrm{cp}}}}$ are the most prominent indicators of sensitivity in the employed variance-based GSA. Generally, the total effect sensitivity index $S_{\mathrm{T}_{n_{\mathrm{cp}}}}$ is larger than the first order sensitivity index $S_{n_{\mathrm{cp}}}$ due to the consideration of the interaction effects. The larger the difference between both values $S_{\mathrm{T}_{n_{\mathrm{cp}}}} - S_{n_{\mathrm{cp}}}$ the larger the interaction effects. However, in case of having no interaction effects of the different input parameters on the BSP model response both values are equal.

The numerical procedure for the calculation of the first order and the total effect sensitivity index $S_{n_{\mathrm{cp}}}$ and $S_{\mathrm{T}_{n_{\mathrm{cp}}}}$ is explained in the following. Initially, two independent matrices

$\boldsymbol{A}_{\mathrm{s}}$ and $\boldsymbol{B}_{\mathrm{s}}$ (with dimensions $R_{\mathrm{s}}, N_{\mathrm{cp}}$) including R_{s} random sets of the input constitutive model parameter vector are generated by employing a proper sampling method. In the current study, the Monte Carlo sampling method is employed to randomly generate uniformly distributed sample points within the predefined range of variation of the constitutive BSP model parameters (Saltelli, 2002). Afterwards, additional matrices $\boldsymbol{C}_{n_{\mathrm{cp}}}$ are defined. The matrices $\boldsymbol{C}_{n_{\mathrm{cp}}}$ for each input parameter have the same arrays as the matrix $\boldsymbol{B}_{\mathrm{s}}$ but for each model input parameter the n_{cp}-th column is replaced by the n_{cp}-th column of the matrix $\boldsymbol{A}_{\mathrm{s}}$. Finally, the first order sensitivity index $S_{n_{\mathrm{cp}}}$ and the total effect sensitivity index $S_{\mathrm{T}_{n_{\mathrm{cp}}}}$ are estimated according to Saltelli (2002) and Jansen (1999) as given by Equations 5.1-5.2. Therein $\boldsymbol{y}_{\mathrm{A}}$, $\boldsymbol{y}_{\mathrm{B}}$ and $\boldsymbol{y}_{\mathrm{C}_{\boldsymbol{n}_{\mathrm{cp}}}}$ denote vectors containing the functions of the model output y associated to the input matrices $\boldsymbol{A}_{\mathrm{s}}$, $\boldsymbol{B}_{\mathrm{s}}$ and $\boldsymbol{y}_{\mathrm{C}_{\boldsymbol{n}_{\mathrm{cp}}}}$, respectively. Furthermore, $\bar{y}_{\mathrm{A}}$ and $\bar{y}_{\mathrm{B}}$ are the corresponding mean value estimates for the components of $\boldsymbol{y}_{\mathrm{A}}$ and $\boldsymbol{y}_{\mathrm{B}}$.

$$S_{n_{\mathrm{cp}}} = \frac{\left(\boldsymbol{y}_{\mathrm{A}}^{\mathrm{T}}\, \boldsymbol{y}_{\mathrm{C}_{\boldsymbol{n}_{\mathrm{cp}}}}\right) - R_{\mathrm{s}}\left(\bar{y}_{\mathrm{A}}\right)^{2}}{\left(\boldsymbol{y}_{\mathrm{A}}^{\mathrm{T}}\, \boldsymbol{y}_{\mathrm{A}}\right) - R_{\mathrm{s}}\left(\bar{y}_{\mathrm{A}}\right)^{2}} \tag{5.1}$$

$$S_{\mathrm{T}_{n_{\mathrm{cp}}}} = \frac{\left(\boldsymbol{y}_{\mathrm{B}} - \boldsymbol{y}_{\mathrm{C}_{\boldsymbol{n}_{\mathrm{cp}}}}\right)^{\mathrm{T}}\left(\boldsymbol{y}_{\mathrm{B}} - \boldsymbol{y}_{\mathrm{C}_{\boldsymbol{n}_{\mathrm{cp}}}}\right)}{\left(2\, \boldsymbol{y}_{\mathrm{B}}^{\mathrm{T}}\, \boldsymbol{y}_{\mathrm{B}}\right) - 2\, R_{\mathrm{s}}\left(\bar{y}_{\mathrm{B}}\right)^{2}} \tag{5.2}$$

It is worth mentioning that the GSA incorporating the Monte Carlo based approach requires $R_{\mathrm{s}}\left(2 + N_{\mathrm{cp}}\right)$ runs of model evaluation. Two times R_{s} runs are needed for the model evaluation with respect to the input matrices $\boldsymbol{A}_{\mathrm{s}}$ and $\boldsymbol{B}_{\mathrm{s}}$. Moreover, additional N_{cp} times R_{s} runs are needed for the model evaluation with respect to the input matrices $\boldsymbol{C}_{n_{\mathrm{cp}}}$ being different for each constitutive BSP model parameter. The number of random sample sets R_{s} is strongly dependent on the complexity of the constitutive BSP model and the numerical model of the designed geotechnical laboratory test. The larger the degree of complexity the more sample sets are necessary to ensure reliable BSP model responses in terms of stable mean values and variances. The required number of random sample sets to be generated has to be determined by a convergence analysis to estimate the uncertainty of the sensitivity measures.

For the evaluation of the sensitivity of a certain BSP model response to the constitutive BSP model parameters the normalized total effect sensitivity index $S_{\mathrm{T}_{n_{\mathrm{cp}}},\mathrm{norm}}$ as defined by the Equations 5.3-5.4 is used. That is, the total effect sensitivity index $S_{\mathrm{T}_{n_{\mathrm{cp}}}}$ of a particular constitutive BSP model parameter is normalized by the sum of the total effect sensitivity indices $\sum S_{\mathrm{T}_{n_{\mathrm{cp}}}}$ of all N_{cp} constitutive BSP model parameters. The normalized sensitivity index allows to better evaluate the development of the influence and to com-

pare the relative importance of a certain constitutive BSP model parameter on the BSP model response during different loading stages of a geotechnical laboratory test.

$$S_{\mathrm{T}_{n_{\mathrm{cp}}},\mathrm{norm}} = S_{\mathrm{T}_{n_{\mathrm{cp}}}} / \sum_{n_{\mathrm{cp}}}^{N_{\mathrm{cp}}} S_{\mathrm{T}_{n_{\mathrm{cp}}}} \tag{5.3}$$

$$\sum_{n_{\mathrm{cp}}}^{N_{\mathrm{cp}}} S_{\mathrm{T}_{n_{\mathrm{cp}}},\mathrm{norm}} = 1 \tag{5.4}$$

5.2.2 Constitutive BSP model parameters

The constitutive BSP model parameters with respect to the critical state soil mechanics and the Modified Cam-Clay model are measurable and can be directly determined from the results of the associated geotechnical laboratory tests. Bothkennar clay is chosen as a typical representative of natural clay behavior. The experimental data on Bothkennar clay from a depth of 5.3-6.2 m are provided by Smith (1992a) and Smith et al. (1992b). The calibration of the measurable constitutive BSP model parameters via direct determination will be intensively discussed in the next chapter 6. The constitutive BSP model parameters, which are derived by direct determination from the corresponding geotechnical laboratory tests are summarized in the following.

- Swelling parameter $\kappa = 0.022$
- Poisson's ratio $\nu = 0.2$
- Compression parameter $\lambda = 0.255$
- Critical state stress ratio $M_{\mathrm{c}} = 1.40$ in triaxial compression
- Critical state stress ratio $M_{\mathrm{e}} = 1.04$ in triaxial extension

The current study is particularly focusing on the evaluation of the influence of the following non-measurable constitutive BSP model parameters related to non-associated flow ($N_{\mathrm{c}}, N_{\mathrm{e}}$), inherent anisotropy ($\alpha_0$), stress-induced anisotropy ($c_\alpha, s_\alpha, z_\alpha$), initial structure ($S_{\mathrm{i},0}$), destructuration ($k_{\mathrm{i}}, A$), elastic nucleus ($s_{\mathrm{eln}}$), stiffness degradation and accumulation of plastic strain (h_0, a_{dam}). Among these non-measurable constitutive BSP model parameters some can be analytically calculated.

- The model parameter N_{e} controlling the shape of the bounding surface in extension is always defined in a way that $N_{\mathrm{e}}/N_{\mathrm{c}} = M_{\mathrm{e}}/M_{\mathrm{c}}$ to ensure the uniqueness of the critical state line.

- The model parameter α_0 controlling the initial rotation is set to either $\alpha_0 = \alpha_{K_0} = 0.25$ according to Dafalias (1986c) and Dafalias et al. (2006) for the tests starting from an initial anisotropic stress or $\alpha_0 = 0$ for the tests starting from an initial isotropic stress.
- The model parameters $s_\alpha = z_\alpha = 5.3$ which are controlling the bounding attractor of the fabric stress tensor are obtained according to Dafalias and Taiebat (2014).

The parameters defining the initial conditions such as initial void ratio $e_0 = 1.86$ and the coefficient of earth pressure at rest $K_0 = 0.5$ are specified according to the in situ data of Bothkennar clay from a depth of 5.3-6.2 m. The yield stress ratio is switched between $YSR = 1$ and $YSR = 3$ for the geotechnical laboratory tests starting from normally consolidated and overconsolidated initial stress conditions, respectively. Hence, YSR indirectly defines the initial size of the bounding surface with respect to the stress state at the beginning of the test. For the one-dimensional compression (oedometer) test the parameter $p_{0,\mathrm{s,init}} = 55$ kPa is directly defined to specify the initial size of the bounding surface.

In conclusion, the number of the remaining constitutive BSP model parameters to be included in the GSA equals $N_{\mathrm{cp}} = 8$. To be more specific, the constitutive BSP model parameter vector yield: $\boldsymbol{P} = \{p_1, ..., p_{N_{\mathrm{cp}}}\} = \{N_{\mathrm{c}}, c_\alpha, S_{\mathrm{i},0}, k_{\mathrm{i}}, A, s_{\mathrm{eln}}, h_0, a_{\mathrm{dam}}\}$. The range of variation of the different constitutive BSP model parameters is chosen based on the author's experience gained during the research on the hierarchical BSP model and limited available literature data on the manual BSP model parameter calibration related to other natural clays (Dafalias et al., 2002, 2006; Taiebat et al., 2010, 2011; Seidalinov, 2012; Dafalias and Taiebat, 2013, 2014; Seidalinov and Taiebat, 2014; Rezania et al., 2016). Furthermore, Gras et al. (2017a) and Gras et al. (2017b) suggested permissible ranges of model parameters for natural fine-grained materials.

A reference constitutive BSP model parameter set for Bothkennar clay based on the author's experience and the corresponding ranges of variation are given in Table 5.1.

Table 5.1: Overview of the constitutive BSP model parameters – reference values and range of variation. Whereat, the constant values are chosen according to the experimental data on Bothkennar clay (Smith, 1992a; Smith et al., 1992b).

Type	Parameter	Unit	Reference	Range of variation
Critical state soil mechanics MCC	κ	[-]	0.022	–
	ν	[-]	0.2	–
	λ	[-]	0.255	–
	M_{c}	[-]	1.40	–
	M_{e}	[-]	1.04	–
Non-associated flow rule	N_{c}	[-]	1.20	$[1.1, 1.4]$
	N_{e}	[-]	0.89	$N_{\mathrm{e}} = N_{\mathrm{c}} \{M_{\mathrm{e}}/M_{\mathrm{c}}\}$
Anisotropy and rotational hardening	α_0	[-]	$\alpha_{\mathrm{K}_0} = 0.25$ (aniso.)	–
			0 (iso.)	–
	c_α	[-]	50	[0,150]
	$s_\alpha = z_\alpha$	[-]	5.3	–
Structure and destructuration	$S_{\mathrm{i},0}$	[-]	6	[1,10]
	k_{i}	[-]	1	[0,1.5]
	A	[-]	0.5	[0,1]
Bounding surface plasticity	s_{eln}	[-]	1.1	[1,1.4]
	h_0	[-]	200	[100,500]
	a_{dam}	[-]	50	[0,100]
Initial conditions	e_0	[-]	1.86	–
	K_0	[-]	0.5	–
	YSR	[-]	1 (NC)	–
			3 (OC)	–
	$p_{0,\mathrm{s,init}}$	[kPa]	55	–

5.2.3 Numerical testing program

In the course of the GSA numerical simulations of the following geotechnical laboratory tests on natural clay are conducted to guarantee a most efficient calibration of the constitutive BSP model parameters afterwards. All geotechnical laboratory tests are numerically simulated by use of an integration point algorithm.

- Drained oedometer test: The initial effective stress is assumed to be anisotropic with respect to the experimentally determined value of $K_0 = 0.5$. Hence, defining an initial effective axial stress of 10 kPa implies an initial effective radial stress of 5 kPa. Consequently, the initial bounding surface is rotated specified by $\alpha_0 = \alpha_{K_0} = 0.25$. Moreover, the natural clay manifests a structure induced increase of the yield stress given by the constitutive BSP model parameter $p_{0,s,init} = 55$ kPa. Hence, the test starts from anisotropic initial stress conditions inside the initial bounding surface. The radial strain is fixed to zero during the entire test by applying an associated strain boundary condition. The oedometer test is numerically examined using a multi-staged axial loading and unloading as listed below as a changing total axial stress boundary condition. Since the excess pore-water pressure is assumed to be zero during the entire simulation the effective stress equals the total stress.
  - σ'_a=20-50-100-200-400 kPa
  - σ'_a=400-200-100-50-20 kPa
  - σ'_a=20-50-100-200-400-1,000 kPa
  - σ'_a=1,000-400-200-100-50-20 kPa
- Drained isotropic compression test: The initial effective stress is assumed to be isotropic, so the effective mean stress equals $p' = 10$ kPa. Therefore, the initial BS is not rotated specified by $\alpha_0 = 0$. Similar to the oedometer test the yield stress is defined by the constitutive model parameter $p_{0,s,init} = 55$ kPa. Hence, the test starts from isotropic initial stress conditions inside the initial bounding surface. The isotropic compression test is numerically conducted using a multi-staged isotropic loading and unloading as listed below. The axial and radial total stress boundary conditions are changing in the same manner to induce isotropic loading and unloading. Since the excess pore-water pressure is assumed to be zero during the entire simulation the effective stress equals the total stress.
  - p'=20-50-100-200-400 kPa
  - p'=400-200-100-50-20 kPa

  - p'=20-50-100-200-400-1,000 kPa
  - p'=1,000-400-200-100-50-20 kPa

- Six monotonic undrained triaxial tests (CAU and CIU tests): The initial effective stress as listed below and the initial rotation of the bounding surface differ with respect to the consolidation history. The initial condition at the beginning of the undrained shearing is either anisotropically consolidated (CAU with $\alpha_0 = \alpha_{K_0} = 0.25$) or isotropically consolidated (CIU with $\alpha_0 = 0$) and either normally consolidated (NC with $YSR = 1$) or overconsolidated (OC with $YSR = 3$). However, the consolidation procedure is not explicitly taken into account in the numerical simulation. The monotonic undrained triaxial tests are numerically simulated by applying radial stress and axial strain boundary conditions. The total radial stress boundary is kept constant during undrained shearing. The axial strain pattern in compression and extension is applied as a changing axial strain boundary condition. As undrained conditions are selected a constant volume is assumed and the generation of excess-pore water pressure is allowed during undrained shearing. The CAU tests are sheared in triaxial compression (CAUC tests) as well as triaxial extension (CAUE tests). The CIU tests are sheared in triaxial compression (CAUC tests) only. The samples are sheared until reaching an axial strain of $\varepsilon_a = \pm 20\,\%$ in triaxial compression and extension, respectively.
  - CAU, NC: $\sigma'_a = 82.1$ kPa, $\sigma'_r = 41.1$ kPa, $\varepsilon_{a,compr} = 20\,\%$ and $\varepsilon_{a,ext} = -20\,\%$
  - CAU, OC: $\sigma'_a = 27.4$ kPa, $\sigma'_r = 13.7$ kPa, $\varepsilon_{a,compr} = 20\,\%$ and $\varepsilon_{a,ext} = -20\,\%$
  - CIU, NC: $\sigma'_a = 55$ kPa, $\sigma'_r = 55$ kPa, $\varepsilon_{a,compr} = 20\,\%$
  - CIU, OC: $\sigma'_a = 18.3$ kPa, $\sigma'_r = 18.3$ kPa, $\varepsilon_{a,compr} = 20\,\%$
- Two cyclic undrained triaxial tests (CAUcyc and CIUcyc tests): The initial effective stress as listed below and the initial rotation of the bounding surface differ with respect to the consolidation history. The initial condition at the beginning of the cyclic undrained shearing is either anisotropically consolidated (CAUcyc with $\alpha_0 = \alpha_{K_0} = 0.25$) or isotropically consolidated (CIUcyc with $\alpha_0 = 0$). In both tests the cyclic undrained shearing is starting from normally consolidated conditions on the initial bounding surface assuming zero excess pore-water pressure. Again the total radial stress boundary is kept constant during the cyclic undrained shearing. The cyclic loading is numerically conducted by cyclically changing the total axial stress boundary in accordance with the cyclic shear stress amplitude $\Delta q_{cyc} = \Delta\sigma_a = \pm 10$ kPa. As undrained conditions are selected a constant volume is assumed and

the generation of excess-pore water pressure is allowed during undrained shearing. The effects of time-dependency and cyclic loading frequency are not considered in the numerical simulation. However, five cycles of undrained triaxial shearing around the average cyclic shear stress $q = 0$ kPa for the CIUcyc test and $q = 16$ kPa for the CAUcyc test are conducted. The number of cycles and the magnitude of the cyclic stress amplitude are chosen in a way that the critical state is never reached for any combination of the constitutive model parameters. Since a load-controlled test has to be numerically simulated a stress path reaching the critical state will cause an abort of the test because the prescribed axial load cannot be applied anymore.

- CIUcyc, NC: $\sigma'_{\mathrm{a}} = 55$ kPa, $\sigma'_{\mathrm{r}} = 55$ kPa, $\Delta q_{\mathrm{cyc}} = \Delta\sigma_{\mathrm{a}} = \pm 10\,\mathrm{kPa}$
- CAUcyc, NC: $\sigma'_{\mathrm{a}} = 75.3$ kPa, $\sigma'_{\mathrm{r}} = 59.4$ kPa, $\Delta q_{\mathrm{cyc}} = \Delta\sigma_{\mathrm{a}} = \pm 10\,\mathrm{kPa}$

An overview of the numerical testing program including information on the type of test, the loading pattern, the drainage conditions, the initial consolidation conditions, the initial stress state and the initial rotation of the plastic potential surface and the bounding surface is given in Table 5.2.

Table 5.2: Overview of the numerical testing program

No.	Type	Loading pattern		Drainage	Consolidation	Stress & rotation	
1	Oed.	L-UL-RL-L-UL		D	OC $p_{0,\mathrm{s,init}} = 55\,\mathrm{kPa}$	aniso. $\eta_0 = \eta_{\mathrm{K_0}}$	$\alpha_0 = \alpha_{\mathrm{K_0}}$
2	Iso. compr.	L-UL-RL-L-UL		D	OC $p_{0,\mathrm{s,init}} = 55\,\mathrm{kPa}$	iso. $\eta_0 = 0$	$\alpha_0 = 0$
3	Triax	Monotonic	Compr.	U	NC	aniso. $\eta_0 = \eta_{\mathrm{K_0}}$	$\alpha_0 = \alpha_{\mathrm{K_0}}$
4			Ext.				
5			Compr.		$YSR = 3$		
6			Ext.				
7			Compr.		NC	iso. $\eta_0 = 0$	$\alpha_0 = 0$
8					$YSR = 3$		
9		Cyclic	$\Delta q_{\mathrm{cyc}} = 10$ kPa	U	NC	$\eta_0 = 0$	$\alpha_0 = 0$
10			$\Delta q_{\mathrm{cyc}} = 10$ kPa			$\eta_0 = \alpha_{\mathrm{K_0}}$	$\alpha_0 = \alpha_{\mathrm{K_0}}$

5.2.4 Settings of GSA

The GSA is used to find the most appropriate geotechnical laboratory tests and even loading stages within a certain test to most accurately identify a particular constitutive BSP model parameter. For each selected BSP model response the corresponding $N_{\mathrm{cp}} = 8$ total effect sensitivity indices $S_{\mathrm{T}_{n_{\mathrm{cp}}}}$ related to the chosen $N_{\mathrm{cp}} = 8$ constitutive BSP model parameters and the associated $N_{\mathrm{cp}} = 8$ normalized total effect sensitivity indices $S_{\mathrm{T}_{n_{\mathrm{cp}}},\mathrm{norm}}$ are calculated and evaluated. The required number R_{s} of random sets of the parameter vector $\boldsymbol{P}$ used as the input for the GSA is obtained from a convergence analysis. That is, the convergence analysis proofs if a certain number of random sets of $\boldsymbol{P}$ is sufficient to result in a steady state with respect to the total effect sensitivity indices $S_{\mathrm{T}_{n_{\mathrm{cp}}}}$ derived in the GSA. The convergence analysis incorporating the sensitivity analysis of all geotechnical laboratory tests chosen in the current study yield $R_{\mathrm{s}} = 500$. The following BSP model responses related to the particular geotechnical laboratory tests are chosen.

- Oedometer test
  - Void ratio increment Δe wrt. effective axial stress increment $\Delta\sigma'_{\mathrm{a}}$
- Drained isotropic compression test
  - Void ratio increment Δe wrt. effective mean stress increment $\Delta p'$
- Monotonic undrained triaxial tests
  - Deviatoric stress increment Δq wrt. axial strain increment $\Delta\varepsilon_{\mathrm{a}}$
  - Effective mean stress increment $\Delta p'$ wrt. axial strain increment $\Delta\varepsilon_{\mathrm{a}}$
  - Excess pore-water pressure increment $\Delta(\Delta p_{\mathrm{w}})$ wrt. axial strain increment $\Delta\varepsilon_{\mathrm{a}}$
- Cyclic undrained triaxial tests
  - Axial strain increment $\Delta\varepsilon_{\mathrm{a}}$ induced in each quarter cycle including the peaks of the cyclic shear stress
  - Effective mean stress increment $\Delta p'$ induced in each quarter cycle including the peaks of the cyclic shear stress
  - Excess pore-water pressure increment $\Delta(\Delta p_{\mathrm{w}})$ induced in each quarter cycle including the peaks of the cyclic shear stress

5.3 General ability of the BSP model

In this section the general stress-strain behavior obtained from the numerical simulations of geotechnical laboratory tests employing the BSP model is presented. For that purpose, a reference parameter set is defined according to Table 5.1 in a way to activate the decisive features of the constitutive BSP model regarding non associated flow, inherent and stress-induced anisotropy, initial structure and destructuration and behavior under non-monotonic and cyclic loading such as stiffness degradation and accumulation of plastic strain. Hence, the results of the numerical simulations of the various geotechnical laboratory tests show the general ability of the constitutive BSP model with respect to different induced stress paths. However, the BSP model responses significantly differ for other combinations of the constitutive BSP model parameters.

5.3.1 Oedometer test

The results of the numerical simulation of the oedometer test confirm that the BSP model is generally able to reproduce the mechanical behavior of natural clay under oedometric conditions. The corresponding effective axial stress vs. void ratio behavior is displayed in Figure 5.1a. The structure imparts additional stiffness and strength to natural clay resulting in an enlarged initial bounding surface. That is, the BSP model response within

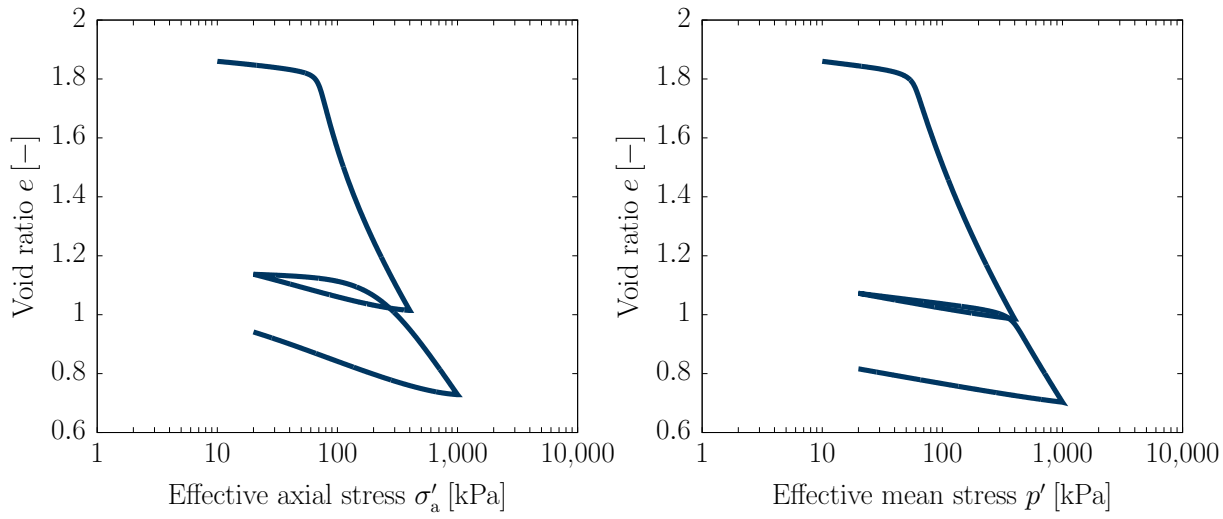

Figure 5.1: a) Effective axial stress vs. void ratio behavior from oedometer test b) effective mean stress vs. void ratio behavior from isotropic compression test

the bounding surface before reaching the yield stress is very stiff and predominantly elastic dependent on the distance of the current stress to the bounding surface. When the effective stress path is approaching to the bounding surface the BSP model response underlies a smooth elastoplastic transition. That is, plasticity is induced even for stress states within the bounding surface. After reaching the bounding surface the interparticle bonding is progressively destroyed. The BSP model via the evolution of the structure variable S_{i} is suitable to model the corresponding abrupt degradation of stiffness and the associated significant decrease of the void ratio.
Furthermore, the BSP model is appropriate to simulate the hysteresis behavior during the unloading-reloading cycle. The BSP model response is purely elastic immediately after stress reversal since the effective stress path is initially moving inside the updated elastic nucleus. After crossing the elastic nucleus the BSP model again considers a smooth elastoplastic transition while moving towards the bounding surface during either unloading or reloading. When reaching the bounding surface the BSP model response adopts the virgin compression behavior.

5.3.2 Isotropic compression test

The numerical simulation of the isotropic compression test leads to a BSP model response which is quite similar to the oedometer test. The associated effective mean stress vs. void ratio behavior is shown in Figure 5.1b.
However, compared to the oedometer test some differences related to the volumetric stress-strain behavior can be detected. Since the effective stress path of the isotropic compression test is just moving on the effective mean stress axis just volumetric plastic strain is generated. Whereas, the K_0-loading path of the oedometer test causes both volumetric and deviatoric plastic strains. Therefore, during isotropic compression destructuration is governed by the evolution of the volumetric plastic strain only. Consequently, the shape of the effective stress-void ratio curve during progressive destructuration is slightly different for both tests. Furthermore, due to the position and distance of the effective stress fixed to the effective mean stress axis in relation to the bounding surface and the occurrence of just volumetric strain and the missing deviatoric strain component, the BSP model response during the unloading-reloading cycle is predominantly elastic. This leads to less pronounced hysteresis effects in the simulation of the isotropic compression test compared to the oedometer test.

5.3.3 Monotonic undrained triaxial tests

Moreover, the BSP model generally allows for the adequate numerical simulation of the mechanical behavior of natural clay obtained from monotonic undrained triaxial tests. Whereat, the undrained triaxial behavior significantly differs with respect to the consolidation stress and the applied strain direction. The corresponding effective stress path, axial strain vs. deviatoric stress behavior and axial strain vs. excess pore-water pressure behavior are given in Figures 5.2 and 5.3 for an anisotropic consolidation stress and in Figures 5.4 and 5.5 for an isotropic consolidation stress.

CAUC, NC

The initial bounding surface represents the stress history, the initial amount of structure and the inherent anisotropy related to the anisotropic consolidation stress. The shape of the bounding surface is represented by a distorted and rotated ellipse. The effective stress path evolving under undrained shearing in triaxial compression starting from normally consolidated anisotropic stress conditions as given in Figure 5.2 initially follows the shape of the evolving bounding surface until reaching the maximum peak deviatoric stress. The BSP model response is elastoplastic immediately at the beginning of the undrained shearing since the stress is initially located on the bounding surface and the strain increment is directed outwards. Hence, the bounding surface underlies expansion, shrinkage and rotation due to isotropic hardening, destructuration and rotational hardening with respect to the induced plastic straining. However, the effective stress path is following the initial bounding surface while the deviatoric stress increases until reaching the maximum peak value indicating a small amount of induced plasticity.
Afterwards, the BSP model allows for softening behavior by use of the non-associated flow rule as also shown in Figure 5.3a. Consequently, the deviatoric stress decreases until reaching the critical state. That is, the effective stress path is following the non-associated and evolving bounding surface until reaching the intersection stress with the plastic potential surface at the critical state. However, the progressive destructuration simultaneously takes place in addition to the softening. Consequently, as a result of the superimposed softening and destructuration the computed deviatoric stress is very strongly decreasing after reaching the maximum peak value. Moreover, the destructuration is causing the migration of the effective stress path close to the critical state towards the stress origin indicated by a significant decrease of the deviatoric and effective mean stress.

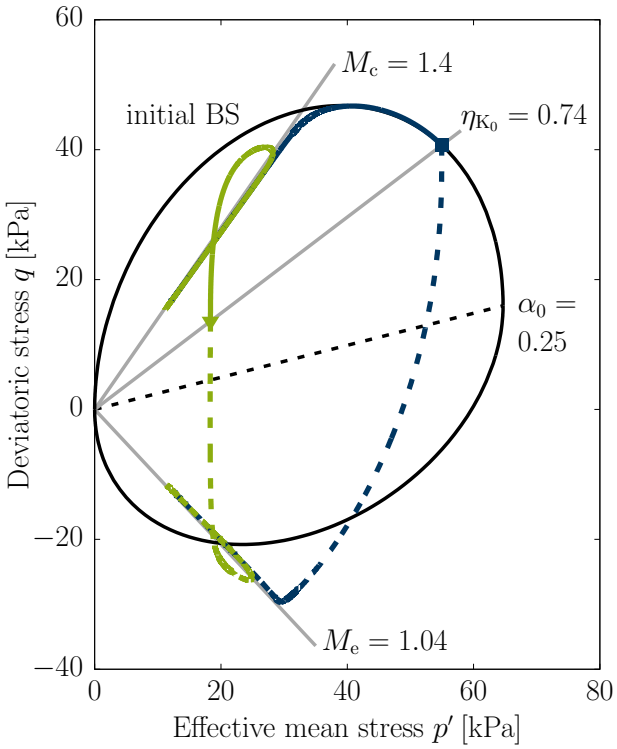

Figure 5.2: Effective mean stress vs. deviatoric stress path from CAU tests

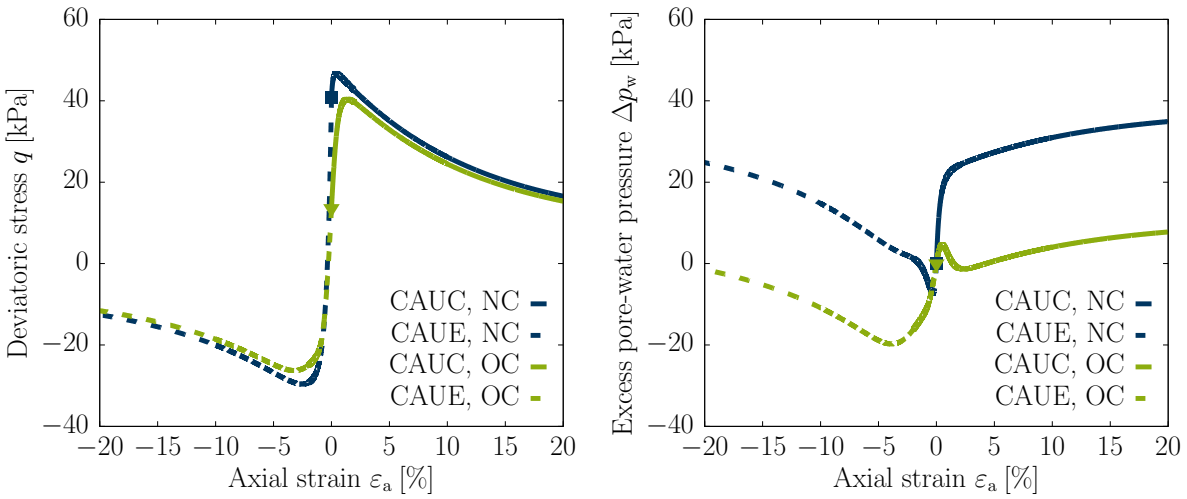

a) b)

Figure 5.3: a) Axial strain vs. deviatoric stress behavior and b) axial strain vs. excess pore-water pressure behavior from CAU tests

The excess pore-water pressure is continuously increasing with increasing axial strain suggesting just contractive internal behavior until reaching the critical state as visualized in Figure 5.3b. The contractive soil behavior is related to the direction of the normal to the plastic potential surface with a positive volumetric component. The destructuration has a striking impact on the increase of the excess pore-water pressure. That is, the excess pore-water pressure counteracts the high potential of structured clay for the restricted volume decrease during destructuration by additional plasticity.
However, the stress-strain behavior and the evolution of the excess pore-water pressure indicate that the shearing induced by the applied 20 % of axial strain is not sufficient to fully complete the destructuration. That is, the deviatoric stress and the excess pore-water pressure are not getting fully constant yet.

CAUE, NC

The effective stress path developed under undrained shearing in triaxial extension starting from normally consolidated anisotropic initial stress conditions as visualized in Figure 5.2 and the associated stress-strain behavior for undrained shearing in triaxial extension as given in Figure 5.3a emphasize the features of the BSP model. That is, the initial BSP model response is purely elastic and stiff since the strain increment is directed towards the extension side and the effective stress path is moving within the elastic nucleus, which is initialized at the corresponding anisotropic consolidation stress. After crossing the elastic nucleus the BSP model response becomes elastoplastic while the effective stress path is approaching to the bounding surface on the extension side.
The applied strain increment directed in triaxial extension results in an associated stress increment significantly deviating from the initial stress ratio. Consequently, the rotational hardening is strongly activated while moving to the bounding surface on the extension side. Hence, the effective stress path is following the rotating bounding surface. The chosen rotational hardening rule incorporating the Lode angle dependence ensures the uniqueness of the critical state in triaxial compression and extension. That is, the critical state is reached at the same effective mean stress. At the same time the rotational hardening rule is limiting the excessive rotation in the vicinity of the critical state by use of the bounding attractor.
When the bounding surface is reached the effective stress path is following the continuously evolving bounding surface until reaching the minimum peak deviatoric stress. This is followed by destructuration resulting in an increase of the deviatoric stress compared to the minimum peak deviatoric stress. The magnitude of the increase of the deviatoric stress is

decisively governed by the destructuration. The evolution of the excess pore-water pressure as shown in Figure 5.3b suggests a change from dilative to contractive internal behavior after changing from predominantly elastic to elastoplastic BSP model response. That is, the increments of the excess pore-water pressure are changing from negative to positive. Again, the magnitude of excess pore-water pressure increase is strongly dependent on the amount of structure degradation.

CAUC, OC

When starting the monotonic undrained shearing test in triaxial compression from overconsolidated initial stress conditions within the initial bounding surface the initial BSP model response is purely elastic since the effective stress path as shown in Figure 5.2 is starting within the elastic nucleus. This is because the projection center which governs the position of the elastic nucleus is initialized at the consolidation stress. Whereat, the size of the elastic nucleus is defined as a certain ratio related to the initial size of the bounding surface. This results in a quite large domain of purely elastic BSP model response. Moreover, the elastic nucleus follows the rotation of the bounding surface due to the homology of both surfaces. From the development of the excess pore-water pressure as given in Figure 5.3b it becomes obvious that the internal behavior initially is contractive causing an increase of the excess pore-water pressure. The internal behavior is contractive since the soil response is predominantly elastic. However, the BSP model response gradually becomes elastoplastic after the effective stress path crosses the elastic nucleus and approaches to the evolving bounding surface on the compression side.
After reaching the bounding surface the effective stress path follows the continuously evolving bounding surface trying to bring back the stress to the critical state. When comparing to the effective stress path it becomes obvious that the initial bounding surface is significantly evolving due to isotropic softening, destructuration and rotational hardening. Again, softening and destructuration occur simultaneously. After reaching a certain maximum peak deviatoric stress the softening and the destructuration lead to an asymptotic decrease of the deviatoric stress with increasing strain as shown in Figure 5.3a. The magnitude of the maximum peak deviatoric stress and the size of the predominantly elastic BSP model response strongly depend on the relative position of the overconsolidated initial stress and the effective stress path to the bounding surface. The BSP model response switches to dilative material behavior due to stress states on the dry side of the critical state. Hence, the direction of the normal to the plastic potential surface leads to negative volumetric plastic strain. The excess pore-water pressure decreases.

After reaching the maximum peak deviatoric stress the destructuration again controls the migration of the effective stress path along the critical state towards the stress origin. The BSP model response again changes to contractive material behavior because of destructuration. The destructuration gains a potential for decreasing volume which is counteracted by the positive excess pore-water pressure.
When comparing the stress-strain behavior during the monotonic undrained tests in triaxial compression starting from either normally consolidated or overconsolidated initial stress conditions it becomes obvious that both curves are converging to the same deviatoric stress.

CAUE, OC

The effective stress path as given in Figure 5.2 obtained from an undrained shearing test in triaxial extension starting from overconsolidated anisotropic initial stress conditions develops qualitatively similar to the equivalent test in triaxial compression but with a different direction. The initial BSP model response is purely elastic since the test is starting from a stress state within the elastic nucleus. Until reaching the evolving bounding surface the BSP model response underlies an elastoplastic transition.
After reaching the minimum peak deviatoric stress, the effective stress path continues to follow the evolving bounding surface towards the critical state. As a possible drawback a hook-type shape of the effective stress path occurs when reaching the critical state in triaxial extension.
Subsequently, destructuration causes a significant increase of the deviatoric stress accompanied by a decrease of the effective mean stress as visualized in Figure 5.3a. The internal behavior switches from dilative to contractive. That is, the increments of the excess pore-water pressure developed during the test are changing from negative to positive. Hence, the behavior is qualitatively similar to the behavior when starting from normally consolidated initial stress conditions but with an enlarged dilative domain. This is because the destructuration becomes relevant not until a certain magnitude of axial strain is exceeded. However, the stress-strain behavior is qualitatively similar to the undrained shearing test in triaxial extension starting from normally consolidated anisotropic initial stress conditions. After a predominantly elastic soil behavior until reaching the minimum peak deviatoric stress softening and destructuration are initiated. Again, both curves are converging to the same deviatoric stress.

CIUC, NC

For the monotonic undrained shearing test in triaxial compression starting from normally consolidated isotropic initial stress conditions the initial bounding surface is not rotated theoretically assuming that the inherent anisotropy is fully erased after isotropic consolidation. The effective stress path as given in Figure 5.4 again follows the evolving bounding surface.

Compared to the undrained triaxial test starting from anisotropic initial stress conditions the rotational hardening induced by plastic straining is much more pronounced since the initial bounding surface is not rotated and the induced stress ratio remarkably deviates from the isotropic consolidation stress ratio. That is, the initial isotropy allows for a larger potential for the evolution of anisotropy with respect to the induced stress ratio. Hence, the effective stress path deviates from the shape of the initial bounding surface.

However, the further evolution of the effective stress path, the stress-strain behavior and the generation of excess pore-water pressure as shown in Figures 5.4 and 5.5 are qualitatively very similar compared to the undrained shearing starting from anisotropic consolidation stress conditions.

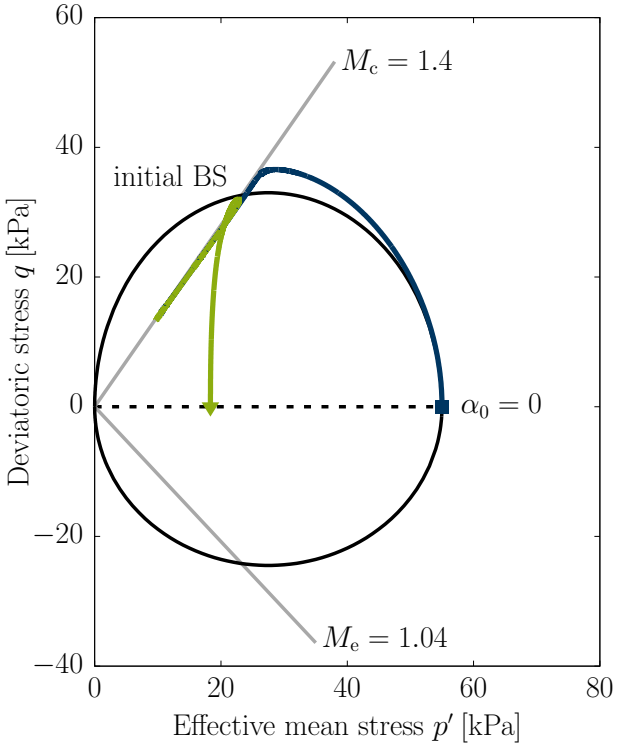

Figure 5.4: Effective mean stress vs. deviatoric stress path from CIU tests

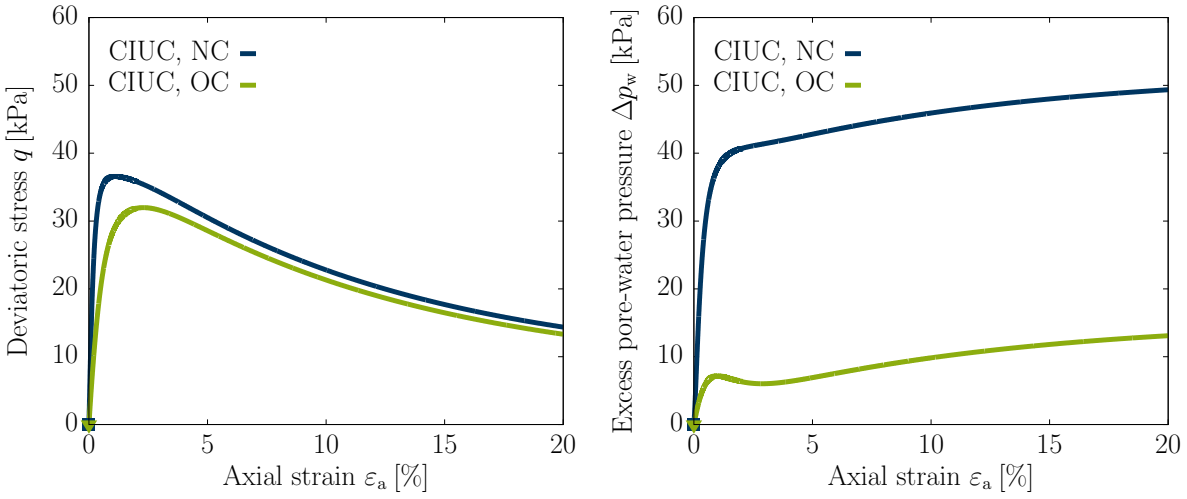

a) b)

Figure 5.5: a) Axial strain vs. deviatoric stress behavior and b) axial strain vs. excess pore-water pressure behavior from CIU tests

CIUC, OC

The effective stress path obtained during undrained shearing in triaxial compression starting from isotropic and overconsolidated initial stress conditions as given in Figure 5.2 does qualitatively not differ from the corresponding undrained shearing test starting from an anisotropic consolidation stress. Moreover, the stress-strain behavior and the evolution of the excess pore-water pressure as shown in Figure 5.5 are qualitatively similar no matter from which consolidation stress ratio the undrained shearing starts.
However, the behavior above the critical state line and the softening are not that pronounced since the isotropic and overconsolidated initial stress conditions by chance is quite similar to the effective mean stress corresponding to intersection between the critical state line and the initial bounding surface. Hence, the evolution of the effective stress path on the dry side is limited.

5.3.4 Cyclic undrained triaxial tests

Furthermore, the numerical simulations confirm that the BSP model is suitable to adequately simulate the mechanical behavior of natural clay observed in undrained triaxial tests under cyclic loading. The undrained triaxial behavior under cyclic loading significantly differs with respect to the consolidation stress.

The corresponding effective stress path, axial strain vs. deviatoric stress behavior and axial strain vs. excess pore-water pressure behavior are given in Figures 5.6 - 5.7.

CIUcyc, NC

The effective stress path of a cyclic undrained triaxial test starting from normally consolidated isotropic initial stress conditions as given in Figure 5.6 initially follows the non-rotated bounding surface. After stress reversal, the effective stress path is directed inwards to the bounding surface. During the further cyclic loading the effective stress path moves within the bounding surface and continuously migrates towards the stress origin with a decreasing effective mean stress. The incremental reduction of the effective mean stress becomes smaller with an increasing number of cycles. The migration and the shape of the effective stress path are governed by the development of the excess pore-water pressure as displayed in Figure 5.7b. An overall increase of the excess pore-water pressure can be observed suggesting a predominantly contractive internal behavior. Since the effective stress path is still far away from critical state the normal to the bounding surface at the image stress always manifests a positive volumetric component and the effective

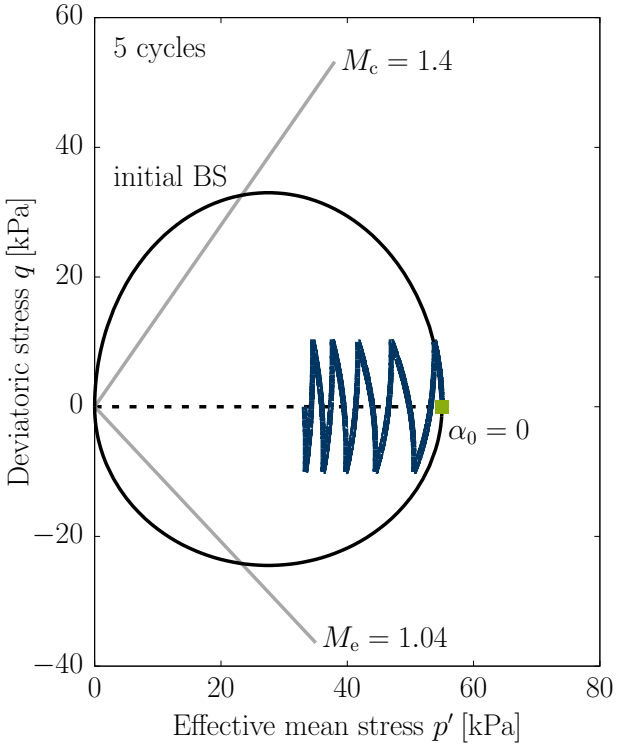

Figure 5.6: Effective mean stress vs. deviatoric stress path from CIUcyc test

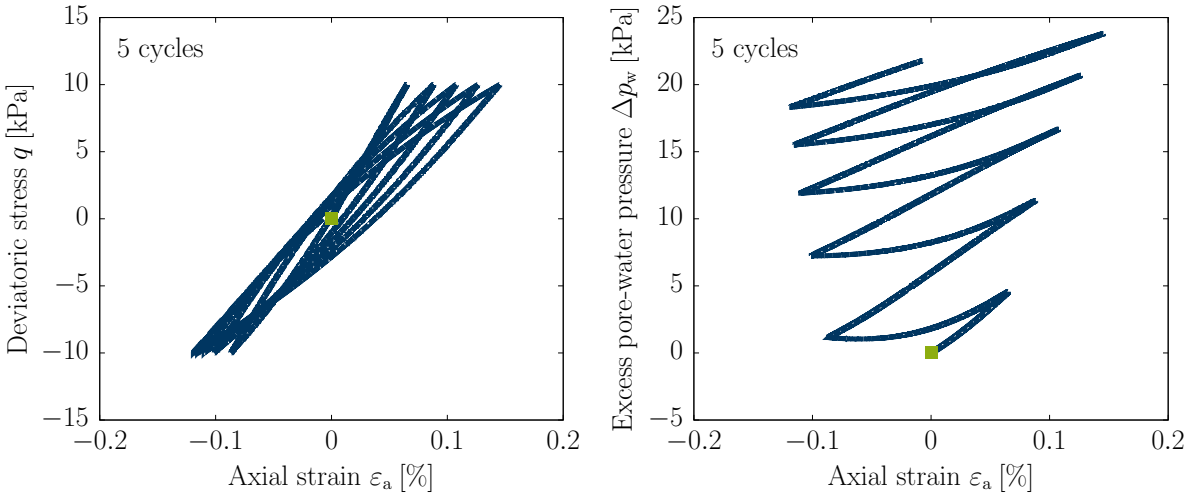

a) b)

Figure 5.7: a) Axial strain vs. deviatoric stress behavior and b) axial strain vs. excess pore-water pressure behavior from CIUcyc test

mean stress is continuously decreasing. Even when decreasing the shear stress during the progress of each cycle the BSP model response becomes elastoplastic when the effective stress path is approaching to the bounding surface on the extension side. Consequently, the excess pore-water pressure already starts to significantly slow down the decrease even while the shear stress is still decreasing. Hence, the effective mean stress is decreasing while it would be constant if purely elastic response is predicted.

The corresponding stress-strain behavior as visualized in Figure 5.7a covers the accumulation of strain during cyclic loading. This is, the BSP model accounts for the progressive stiffness degradation, soil damping and dissipation of energy by the evolution of the damage variable as a function of plastic straining. The larger the stiffness degradation and the destructuration the larger the excess pore-water pressure, the larger the reduction of effective mean stress and the larger the strain. Whereat, the stiffness reduction becomes more relevant at a higher number of cycles because of the dependence on the accumulated plastic strain.

Under the current initial and boundary conditions and the chosen constitutive BSP model parameter set the development of strain in compression is higher than in extension. However, the axial strain accumulates in compression as well as in extension with increasing number of cycles but with a different magnitude. The direction and magnitude of strain is strongly dependent on the relative position and distance of the cyclic effective stress path with respect to the bounding surface. Hence, the average cyclic shear stress corresponding

to the consolidation and the cyclic shear stress amplitude are of high importance. The shape of the bounding surface and especially its inherent and stress-induced rotation control the preferred direction of strain.
The elastic nucleus and its update to the last stress reversal as incorporated in the BSP model allow for the simulation of purely elastic soil behavior immediately after stress reversal occurs. Hence, the BSP model response is purely elastic and very stiff after stress reversal and smoothly becomes elastoplastic when approaching to the bounding surface on the opposite.

CAUcyc, NC

The development of the effective stress path during the cyclic undrained triaxial test starting from normally consolidated anisotropic initial stress conditions with an initial stress ratio of $\eta_0 = \alpha_{K_0}$ as given in Figure 5.8 is qualitatively similar to the test starting from an isotropic consolidation stress. The effective stress path again migrates by means of effective mean stress reduction as a consequence of the increasing excess pore-water pressure during undrained cyclic loading.

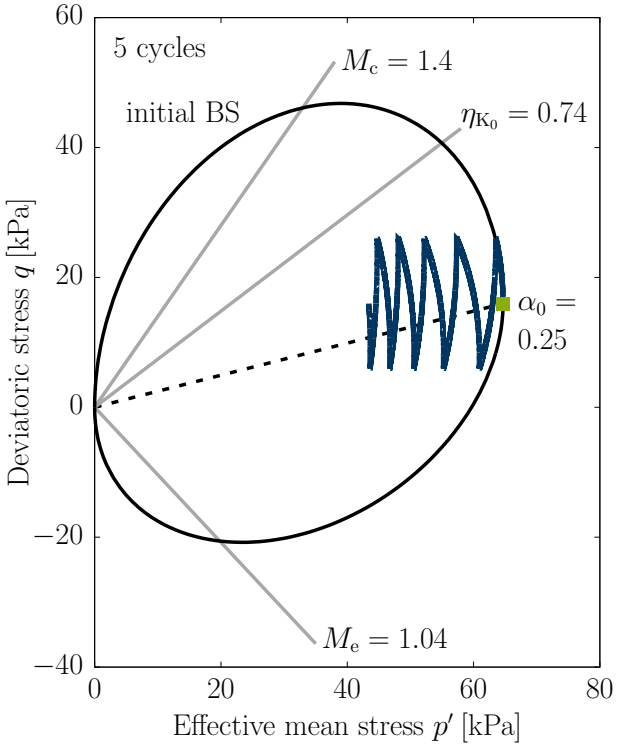

Figure 5.8: Effective mean stress vs. deviatoric stress path from CAUcyc test

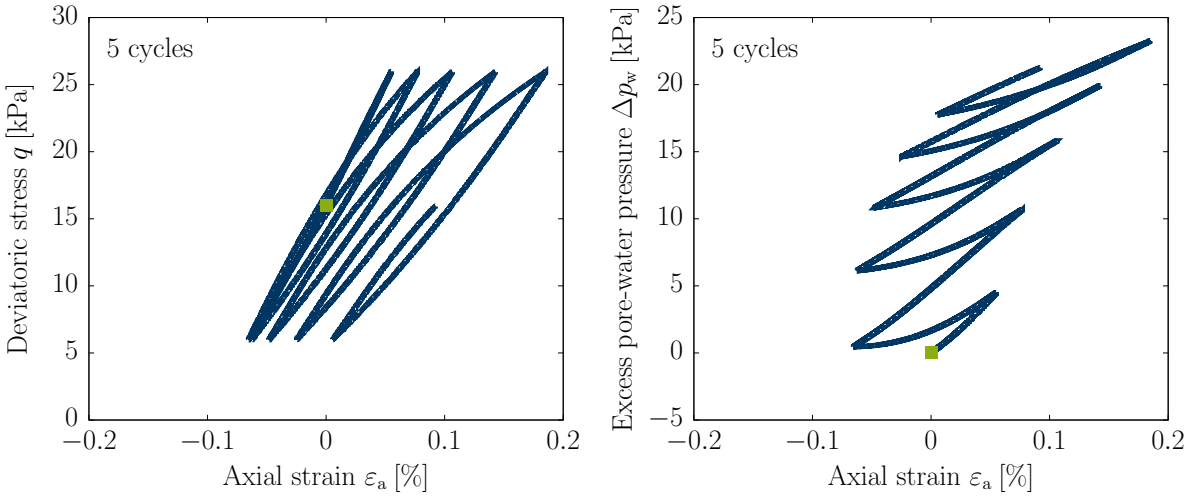

a) b)

Figure 5.9: a) Axial strain vs. deviatoric stress behavior and b) axial strain vs. excess pore-water pressure behavior from CAUcyc test

The most obvious differences with respect to the stress-strain behavior when starting the cyclic undrained shearing from anisotropic consolidation stress conditions in the compression domain are explained in the following. Due to the fact that the anisotropic initial stress is located on the rotation line $\eta_0 = \alpha_{K_0}$ and the cyclic stress amplitude is smaller than the average deviatoric stress, the effective stress path moves in the positive deviatoric stress domain only. Consequently, the axial strain is predominantly developing in compression rather than in extension as visible in Figure 5.9a. The decrease of the shear stress during the progress of each cycle causes just a minor development of strain in extension due to the large relative distance of the effective stress path to the bounding surface on the opposite. That is, when evaluating the strain accumulation after applying the positive and negative cyclic stress amplitude it can be observed that with increasing number of cycles the axial strain accumulates in compression but becomes smaller in extension.

5.4 Results of GSA

In this section the results of the GSA with respect to the corresponding geotechnical laboratory tests and the associated BSP model responses are presented. The focus is set on the analysis of the relative influence of the chosen specific constitutive BSP model parameters related to the following properties:

- Non-associated flow and the shape of the bounding surface given by N_{c} and N_{e}
- Stress-induced anisotropy and rate of rotation given by c_{α}
- Initial structure given by $S_{\mathrm{i},0}$, rate of destructuration given by k_{i} and the ratio of the volumetric and the deviatoric plastic strain components given by A
- Size of the elastic nucleus given by s_{eln} defining the elastic domain
- Behavior under non-monotonic and cyclic loading with the initial shape hardening stiffness given by h_0 and the rate of stiffness degradation and the rate of evolution of the damage variable given by a_{dam}

The influence of a particular constitutive BSP model parameter on a specific BSP model response within a certain loading-unloading stage of the geotechnical laboratory test is evaluated relatively to the influence of the other constitutive BSP model parameters on the same BSP model response. The sensitivity is represented by the normalized total effect sensitivity index $S_{\mathrm{T}_{n_{\mathrm{cp}}},\mathrm{norm}}$.

5.4.1 Oedometer test

The results of the GSA related to the oedometer test are displayed in Figure 5.10. That is, the normalized sensitivity $S_{\mathrm{T}_{n_{\mathrm{cp}}},\mathrm{norm}}$ of the void ratio increment Δe to the constitutive BSP model parameters wrt. to the applied effective axial stress increment $\Delta\sigma'_{\mathrm{a}}$ is evaluated. However, the results of the GSA regarding the isotropic compression test are qualitatively similar compared to the oedometer test, so that the results are not explicitly shown but the main differences are discussed.

Non-associated flow and shape of bounding surface

There is a small to medium relative influence (between 5% to 20%) of N_{c} and N_{e} on the increment of the volumetric strain during unloading and reloading. Since the plasticity modulus K_{p} with respect to the current stress, the plasticity modulus $\bar{K}_{\mathrm{p}}$ related to the image stress on the bounding surface, the distance of the current stress to the bounding surface and the loading index L and the shape of the elastic nucleus are defined as functions of N_{c} and N_{e} the shape of the bounding surface controls the magnitude of elastic and plastic strain developing during unloading and reloading. The larger the values of N_{c} and N_{e} the more plasticity is induced, the larger the volume increase during unloading and the larger the hysteresis of the volumetric strain during unloading and reloading cycles.

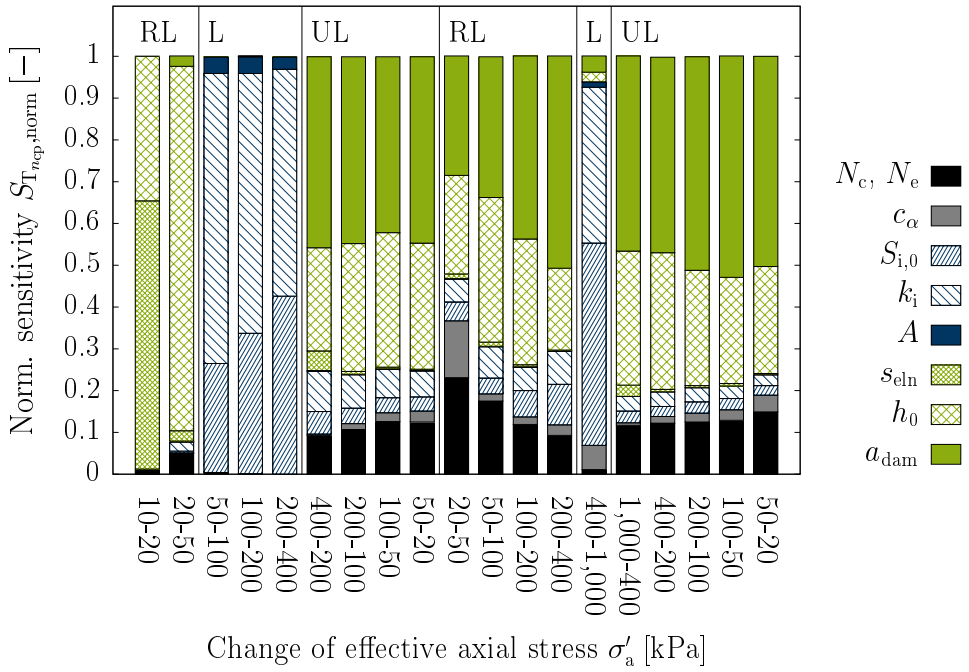

Figure 5.10: Normalized sensitivity $S_{T_{n_{cp}},norm}$ of void ratio increment Δe to constitutive BSP model parameters wrt. effective axial stress increment $\Delta\sigma'_a$ (oedometer test)

Stress-induced anisotropy

The sensitivity of the increment of the volumetric strain to the rate of rotation represented by c_α is negligible during the entire oedometer test. Because at the beginning of the test the rotated bounding surface with $\alpha_0 = \alpha_{K_0}$ is already in an equilibrium state with respect to the anisotropic stress, further rotation is just slightly induced since the stress ratio is not significantly changing during the oedometer test. During loading the stress ratio is kept constant following $\eta_{K_{0,pl}}$. Whereas, during the initial purely elastic part of the unloading and reloading the stress ratio switches to $\eta_{K_{0,el}}$. Hence, during elastoplastic transition and more pronounced during further loading an adjustment of the rotation is required but without any significant relative influence ($< 10\%$) on the increment of the volumetric strain.

For the isotropic compression test the sensitivity of the increment of the volumetric strain to the rotational hardening represented by c_α is null since the isotropic compression does not induce any deviatoric strain since the stress path is moving along the effective mean stress axis only. Consequently, no rotation of the initially non-rotated bounding surface with $\alpha_0 = 0$ is induced.

Initial structure and destructuration

The increment of volumetric strain is most sensitive (up to almost 100%) to the initial structure and the destructuration in any part of the test where the stress path reaches the bounding surface after exceeding the yield stress and the structure is not yet fully destroyed. If further loading in the outward direction to the bounding surface is induced elastoplastic strain develops and destructuration as a function of plastic straining is initiated.

The relative influence of the magnitude of the initial structure represented by $S_{\mathrm{i},0}$ on the increment of the volumetric strain gets larger (up to 50%) with increasing stress due to the developing plastic strain. That is, $S_{\mathrm{i},0}$ strongly governs how much structure is left after a certain stress is applied during destructuration. The larger the amount of initial structure the larger the total amount of volumetric strain at the same stress state during oedometric loading. Furthermore, the larger the value of $S_{\mathrm{i},0}$ the larger the rate of volume change since destructuration is more strongly activated.

Whereas, the relative influence of the rate of destructuration represented by k_{i} is largest (up to 70%) directly after initiating destructuration where the rate of plastic straining is largest due to lower stress-dependent stiffness. The relative influence is decreasing with increasing stress and decreasing amount of structure since the remaining amount of structure is more relevant. The larger the value of k_{i} the larger the incremental increase of the volumetric strain during oedometric loading until the fully destructured state is reached and the larger the hysteresis of the volumetric strain during unloading-reloading since more destructuration occurs even when the effective stress path is moving inside the bounding surface.

The relative influence of the ratio between the volumetric and deviatoric plastic strains affecting the destructuration represented by A is relatively small (less than 5%) compared to the other two constitutive BSP model parameters governing the destructuration. The smaller the value of A the larger the portion of the volumetric plastic strain participating in the destructuration. Consequently, the smaller the value of A the larger the rate of destructuration during the oedometric loading since the evolution of the volumetric plastic strain is larger than the evolution of the deviatoric plastic strain because of the boundary conditions of the test.

Since the increment of volumetric strain at a stress of 1,000 kPa is still sensitive to the constitutive BSP model parameters controlling the destructuration it can be stated that the structure is not yet fully destroyed.

Moreover, the increment of volumetric strain is sensitive to destructuration even during unloading-reloading since the BSP model allows for the development of plastic strain even for stress paths moving within the bounding surface. The relative influence of destructuration on the increment of volumetric strain gets much smaller (between 5% to 20%) as compared to the virgin loading. This is because the magnitude of elastoplastic strain developed during unloading-reloading cycles is small and the relative influence of the constitutive BSP model parameters related to the cyclic behavior becomes more dominant at the same time. However, during reloading the relative influence of destructuration is increasing with decreasing distance to the bounding surface since more plasticity is induced the closer the stress path approaches to the bounding surface.
For the isotropic compression test the relative influence of $S_{\mathrm{i},0}$ and k_{i} becomes smaller as compared to the oedometer test since the deviatoric stress-strain component is missing and the relative influence of A is increasing simultaneously. That is, the ratio between the volumetric and the deviatoric plastic strains affecting the destructuration represented by A plays a more significant role (more than 25%). Since no deviatoric plastic strain is developed during the isotropic compression test just the volumetric plastic strain is contributing to the evolution of the destructuration. Therefore, the value of A directly controls the portion of volumetric plastic strain participating in the development of the destructuration with respect to the entire amount of volumetric plastic strain developed during isotropic compression. Consequently, the smaller the value of A the larger the rate of destructuration during the isotropic compression test. The relative influence of A is decreasing with increasing stress as it holds true for the value of k_{i}.

Size of elastic nucleus

The relative influence of the size of the elastic nucleus represented by s_{eln} on the increment of volumetric strain is most significant (up to 65%) immediately after starting the test from overconsolidated initial stress conditions within the elastic nucleus located within the bounding surface. That is, dependent on the size of the elastic nucleus the volumetric strain is either fully elastic if the stress path up to 20 kPa moves within the elastic nucleus or elastoplastic in case of crossing the elastic nucleus. However, s_{eln} always becomes important whenever a stress reversal occurs and the projection center and the elastic nucleus are updated to the last stress reversal. The relative importance is low (below 5%) within the present simulation of the oedometer test because the load increment after stress reversal is either that large so that the stress path is moving far beyond the elastic nucleus and other constitutive BSP model parameters are relatively more dominant with

respect to the change of the volumetric strain, or the distance to the bounding surface is that large so that the BSP model response is predominantly elastic anyway. To sum up, the larger the size of the elastic nucleus the longer the stress path moves within the elastic nucleus causing a stiffer BSP model response. However, the incremental change of the volumetric strain due to a change in the size of the elastic nucleus is relatively small. Thus, a calibration becomes complicated.

Behavior under non-monotonic and cyclic loading

The cyclic behavior becomes most significant when the effective stress path is moving within the bounding surface and outside the elastic nucleus.
The initial shape hardening stiffness represented by h_0 is most influencing on the development of the volumetric strain (up to 90%) when the stress path is firstly crossing the elastic nucleus. At that part of the test, the plasticity modulus K_p with respect to the current stress is mainly governed by the initial shape hardening stiffness since plastic straining is not yet strongly developed and hence the damage variable and the destructuration play no major role. During the following unloading-reloading the relative influence of the initial shape hardening stiffness is almost constant at approximately 30-40%. The relative influence of h_0 decreases with smaller distance to the bounding surface because the destructuration becomes more influencing since the plastic straining increases. The larger the value of h_0 the stiffer the BSP model response after stress reversal and the smaller the hysteresis during unloading-reloading.
The sensitivity of the increment of the volumetric strain to a_dam which governs the rate of stiffness degradation and the rate of evolution of the damage variable reaches values up to 40-50% during unloading-reloading. The relative influence of a_dam increases with decreasing distance to the bounding surface since the magnitude of accumulated plastic strain is increasing. The larger the value of a_dam the softer the BSP model response due to stiffness degradation, the larger the induced plasticity after stress reversal and the larger the hysteresis of the volumetric strain during unloading-reloading.
For the isotropic compression test the sensitivity of the increment of the volumetric strain to the damage parameter a_dam is null since the isotropic compression does not induce any deviatoric plastic strain since the stress path is moving along the effective mean stress axis only. Consequently, by definition no evolution of the damage variable and no stiffness reduction are induced.

5.4.2 Monotonic undrained triaxial tests

CAUC, NC

The results of the GSA related to the CAUC, NC test are displayed in Figure 5.11. That is, the normalized sensitivity $S_{\mathrm{T}_{n_{\mathrm{cp}}},\mathrm{norm}}$ of the increments of deviatoric stress Δq, effective mean stress $\Delta p'$ and excess pore-water pressure $\Delta(\Delta p_{\mathrm{w}})$ to the constitutive BSP model parameters wrt. to the applied axial strain increment $\Delta\varepsilon_{\mathrm{a}}$ is evaluated.

Non-associated flow and shape of bounding surface

At the beginning of the test at small axial strain the increments of the deviatoric stress, effective mean stress and excess pore-water pressure are highly sensitive (up to 90%) to the shape of the bounding surface on the compression side represented by N_{c}. This is because the maximum peak deviatoric stress indicating the peak undrained shear strength in compression is governed by the shape of the bounding surface. Moreover, the effective stress path which is directly correlated to the development of the excess pore-water pressure is following the shape of the bounding surface while approaching to the critical state line from the wet side. Moreover, the softening behavior is governed by the shape of the bounding surface with respect to the shape of the plastic potential surface.
The smaller the value of N_{c} the flatter the shape of the effective stress path migrating towards the critical state line with decreasing effective mean stress due to the larger developed excess pore-water pressure. Hence, the smaller the value of N_{c} the smaller the maximum peak deviatoric stress. The relative influence of the shape of the bounding surface on the BSP model responses mentioned above drastically decreases with increasing strain since the relative influence of the destructuration takes over.

Stress-induced anisotropy

The sensitivity of the increments of the deviatoric stress, effective mean stress and excess pore-water pressure to the rate of rotation represented by c_α is negligible during the entire test. Because the rotated initial bounding surface with $\alpha_0 = \alpha_{\mathrm{K}_0}$ is already in an equilibrium state with respect to the anisotropic stress at the beginning of the test and the anisotropic stress ratio is already close to the critical state, just a small amount of further rotation is induced.

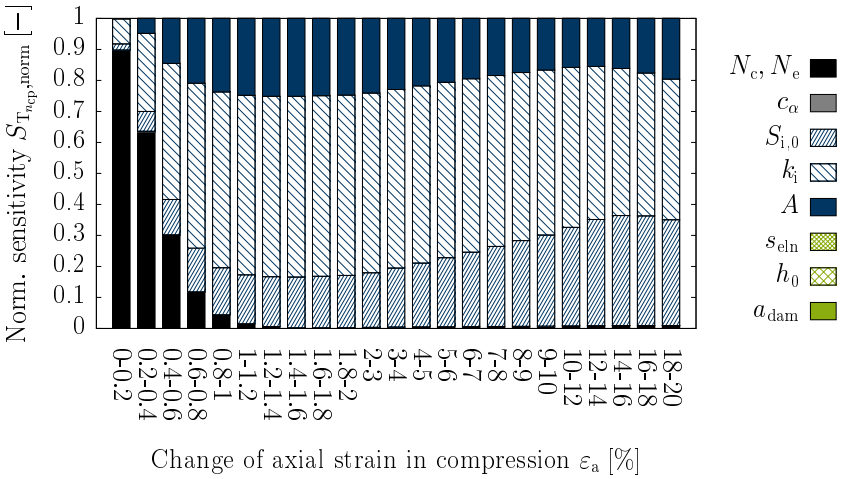

a) Normalized sensitivity $S_{T_{n_{cp}},norm}$ of deviatoric stress increment Δq

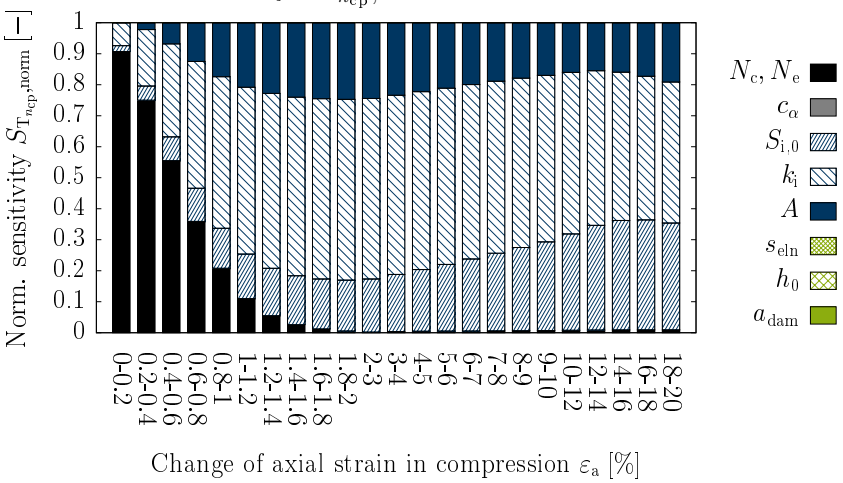

b) Normalized sensitivity $S_{T_{n_{cp}},norm}$ of effective mean stress increment $\Delta p'$

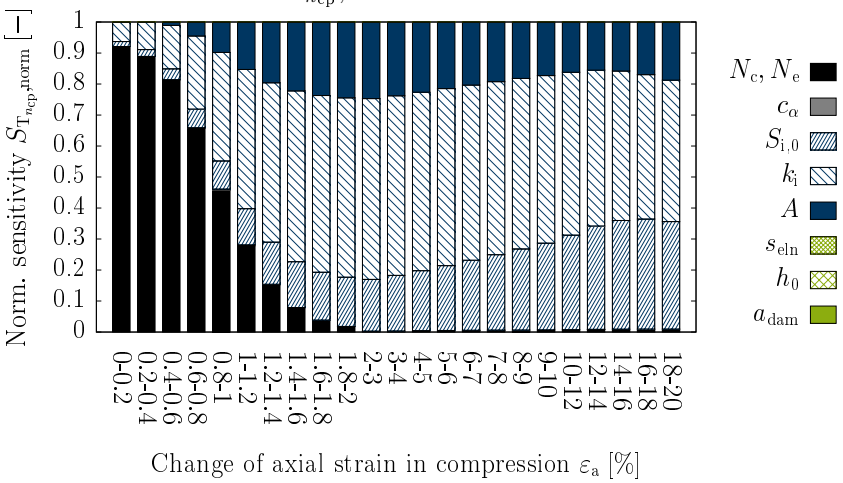

c)Normalized sensitivity $S_{T_{n_{cp}},norm}$ of excess pore-water pressure increment $\Delta(\Delta p_w)$

Figure 5.11: Normalized sensitivity $S_{T_{n_{cp}},norm}$ of various BSP model responses to constitutive BSP model parameters wrt. effective axial stress increment $\Delta\varepsilon_a$ (CAUC, NC test)

Initial structure and destructuration

The destructuration significantly influences (up to almost 100%) the evolution of the increments of the deviatoric stress, effective mean stress and excess pore-water pressure during the test. The influence of destructuration is qualitatively and quantitatively almost the same for all of the above mentioned BSP model responses.
Whereat, the relative influence of the magnitude of the initial structure represented by $S_{\mathrm{i},0}$ becomes most relevant at larger axial strain (up to 35% at 20% of axial strain) in the vicinity of the critical state. The initial amount of structure mainly controls how much the effective stress path after reaching the maximum peak deviatoric stress moves in the vicinity of the critical state line towards the stress origin and how much the undrained shear strength decreases. The larger the magnitude of initial structure the more pronounced the effective stress path migration. That is, the larger the value of $S_{\mathrm{i},0}$ the larger the developed excess pore-water pressure and the associated effective mean stress reduction and the larger the decrease of the deviatoric stress after reaching the maximum peak value representing the residual undrained shear strength in compression. In case of having no initial structure the effective stress path does not migrate at all after reaching the critical state line. That is, the excess pore-water pressure, effective mean stress and deviatoric stress do not evolve anymore.
The relative influence of the rate of destructuration represented by k_{i} is increasing rapidly after initiation of the destructuration where the development of the increment of the plastic strain is largest, becomes most relevant (up to 55%) at intermediate axial strain and decreases at larger axial strain (45% at 20% of axial strain). The larger the rate of destructuration the more contractive the internal behavior and hence the flatter the shape of the effective stress path towards the critical state line due to the increasing excess pore-water pressure accompanied by the decreasing effective mean stress. Hence, a larger value of k_{i} leads to a smaller maximum peak deviatoric stress since the bounding surface is already shrinking due to destructuration. Close to the critical state line a larger value of k_{i} leads to a more distinct migration of the effective stress path towards the stress origin due to more pronounced generation of excess pore-water pressure and a larger decrease of deviatoric stress.
The relative influence of the ratio between the volumetric and the deviatoric plastic strains affecting the destructuration represented by A follows the same trend as the parameter k_{i} but is less dominant (max. 25% at intermediate axial strain and 20% at 20% of axial strain). The larger the value of A the larger the influence of the deviatoric plastic strain on the destructuration.

It can be stated that the larger the value of A the larger the effects of destructuration such as migration of the effective stress path towards the stress origin due to increasing excess pore-water pressure and the larger the decrease of the deviatoric stress after reaching the maximum peak value. If just volumetric plastic strain is involved, so that $A = 0$, destructuration stops when reaching the critical state line where the increment of volumetric plastic strain becomes zero.

Size of elastic nucleus

The sensitivity of the increments of the deviatoric stress, effective mean stress and excess pore-water pressure to the size of the elastic nucleus represented by s_{eln} is negligible since the test is starting from normally consolidated initial stress conditions and no stress reversal occurs.

Behavior under non-monotonic and cyclic loading

The sensitivity of the increments of the deviatoric stress, effective mean stress and excess pore-water pressure to the cyclic behavior represented by h_0 and a_{dam} is negligible during the test since no non-monotonic or cyclic loading is induced and the effective stress path is exclusively moving on the updated bounding surface.

CAUE, NC

The results of the GSA related to the CAUE, NC test are displayed in Figure 5.12. That is, the normalized sensitivity $S_{\mathrm{T}_{n_{\mathrm{cp}}},\mathrm{norm}}$ of the increment of deviatoric stress Δq, effective mean stress $\Delta p'$ and excess pore-water pressure $\Delta(\Delta p_{\mathrm{w}})$ to the constitutive BSP model parameters wrt. to the applied axial strain increment $\Delta\varepsilon_{\mathrm{a}}$ is evaluated.

Non-associated flow and shape of bounding surface

The relative influence of the shape of the bounding surface on the extension side represented by N_{e} is largest when the effective stress path approaches to the bounding surface on the extension side and follows the updated surface towards the critical state line from the wet side. That is, the shape of the bounding surface governs at which stress state the effective stress path reaches the bounding surface and how the effective stress path develops afterwards.

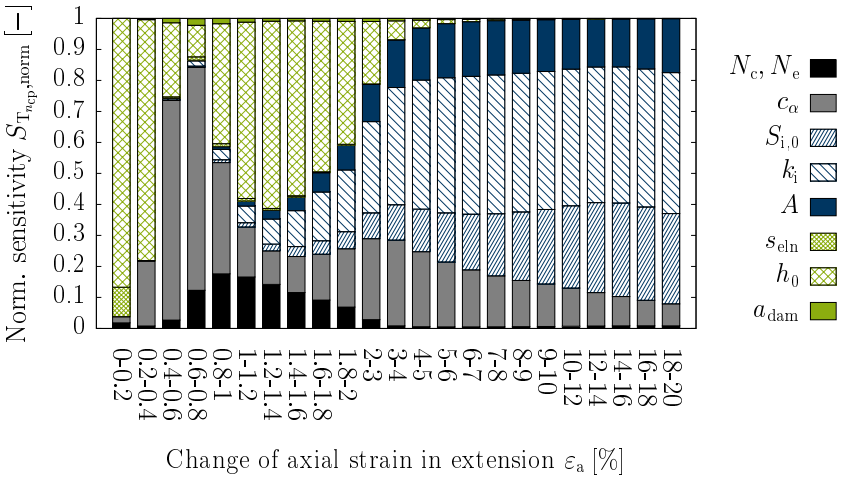

a) Normalized sensitivity $S_{T_{n_{cp}},norm}$ of deviatoric stress increment Δq

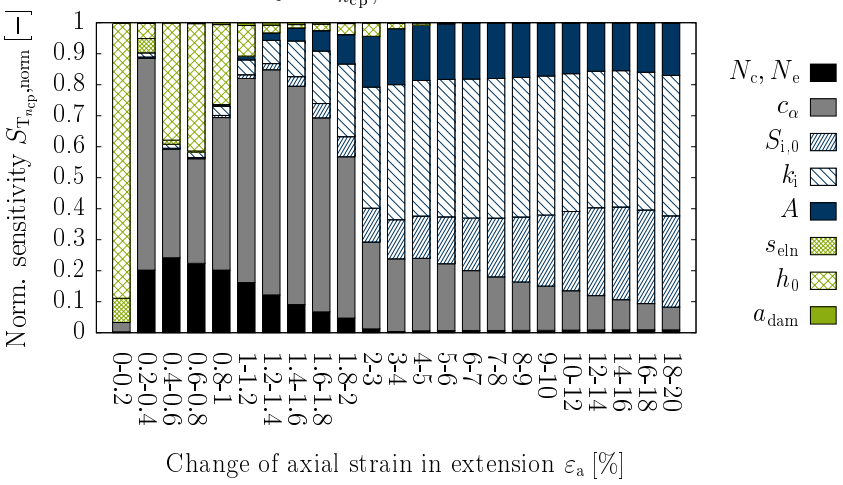

b) Normalized sensitivity $S_{T_{n_{cp}},norm}$ of effective mean stress increment $\Delta p'$

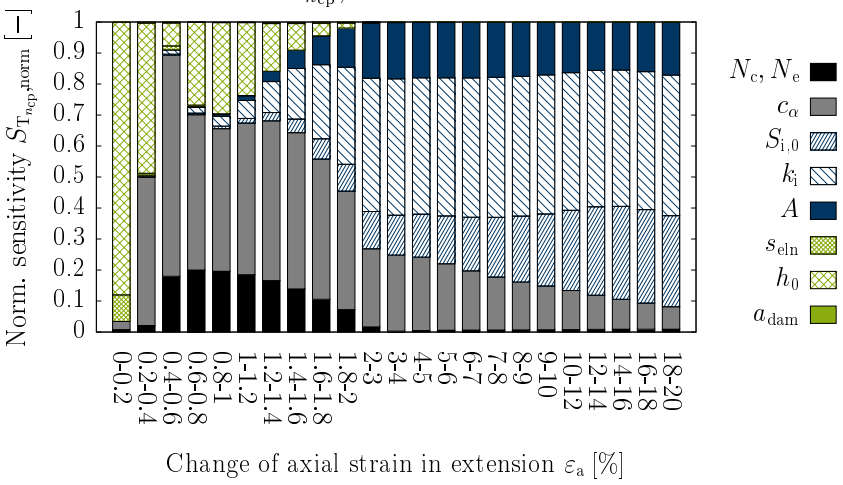

c)Normalized sensitivity $S_{T_{n_{cp}},norm}$ of excess pore-water pressure increment $\Delta(\Delta p_w)$

Figure 5.12: Normalized sensitivity $S_{T_{n_{cp}},norm}$ of various BSP model responses to constitutive BSP model parameters wrt. effective axial stress increment $\Delta\varepsilon_a$ (CAUE, NC test)

With an increasing value of N_e the shape of the effective stress path becomes steeper leading to larger absolute values of the minimum peak deviatoric stress indicating the peak undrained shear strength in extension and the excess pore-water pressure. Whereat, the increments of the effective mean stress and excess pore-water pressure show the largest sensitivity to the shape of the bounding surface (up to 20%). However, the changes in the deviatoric stress are slightly less sensitive to N_e.

Stress-induced anisotropy

The sensitivity of the increments of the deviatoric stress, effective mean stress and excess pore-water pressure to the rate of rotation represented by c_α is very striking (up to 70%). The stress-induced anisotropy and the corresponding rotation are strongly activated because the stress ratio is changing from compression to extension. At larger axial strain the rotation is not that relevant anymore since just slight changes of the stress ratio occur in the vicinity of the critical state line. The relative influence of the rotation becomes most relevant when the effective stress path is approaching to the bounding surface on the extension side. That is, the rotation controls at which stress state the effective stress path reaches the bounding surface accompanied by generation of significant plasticity. Furthermore, the rotation governs how the effective stress paths evolves after reaching the bounding surface while approaching to the critical state line. That is, the effective stress path is following the rotating bounding surface with respect to the wet side of the critical state.
A larger rate of rotation leads to a steeper shape of the effective stress path and larger absolute values of the minimum peak deviatoric stress representing the undrained peak shear strength in extension and the excess pore-water pressure. However, the changes of the excess pore-water pressure and the associated effective mean stress are more affected than the changes of the deviatoric stress. The rate of rotation impacts the increase of the excess pore-water pressure after reaching the minimum peak value changing from dilative to contractive internal behavior. However, the increase of the deviatoric stress is less affected.

Initial structure and destructuration

The relative influence of destructuration becomes significant not before applying a larger amount of axial strain. That is, when the effective stress path approaches to the bounding surface on the extension side the development of plastic strain is initiated causing

destructuration. Afterwards, the effective stress path is moving on the bounding surface and in the vicinity of the critical state line towards the stress origin resulting in significant plastic strain accompanied by the damage of the structure. The sensitivity of the increments of the deviatoric stress, effective mean stress and excess pore-water pressure to destructuration develops from 30% at 2% of axial strain to more than 90% at 20% of axial strain. Whereat, the relative influence of the destructuration is qualitatively and quantitatively almost the same for all of the above mentioned BSP model responses.
The relative influence of the initial value of the structure represented by $S_{\mathrm{i},0}$ becomes more dominant and continuously increases with increasing axial strain (up to 30% at 20% of axial strain). The larger the initial structure the smaller the absolute values of the minimum peak deviatoric stress and excess pore-water pressure developed while approaching to the critical state line. Afterwards, the larger the initial amount of structure the more pronounced the migration of the effective stress path in the vicinity of the critical state line towards the stress origin. Moreover, the larger the value of $S_{\mathrm{i},0}$ the larger the increase of the deviatoric stress and the excess pore-water pressure after reaching their minimum peak values. Again, when assuming a fully destructured clay the evolution of the effective stress path stops when reaching the critical state line.
Whereas, the relative influence of the rate of destructuration represented by k_{i} is getting most relevant (up to 45%) at intermediate strain where the rate of plastic straining is largest. The relative influence becomes almost constant afterwards. The larger the value of k_{i} the smaller the absolute values of the minimum peak deviatoric stress and excess pore-water pressure while approaching to the critical state line. Afterwards, the larger the rate of destructuration the more distinct the migration of the effective stress path towards the stress origin. Furthermore, the larger the value of k_{i} the larger the increase of the deviatoric stress and the excess pore-water pressure after reaching their minimum peak values.
The ratio between the volumetric and the deviatoric plastic strains affecting the destructuration represented by A has a smaller relative influence (up to 20%). The larger the ratio the more involved the deviatoric plastic strain. That is, the larger the value of A the more pronounced the increase of the deviatoric stress after reaching its minimum peak value and the more remarkable the evolution of the excess pore-water pressure from negative to even positive values. Again, if just volumetric plastic strain is involved, so that $A = 0$, destructuration stops after reaching the critical state line.

Size of elastic nucleus

The size of the elastic nucleus becomes relevant just directly after the beginning of the undrained shearing in extension. This is because the effective stress path initially moves inside the elastic nucleus which is initialized with respect to the initial stress on the bounding surface. Hence, the size of the elastic nucleus controls when the BSP model response switches from elastic to elastoplastic. However, the relative influence of s_{eln} on the increments of the deviatoric stress, effective mean stress and excess pore-water pressure is small (below 10%) since the effective stress path quickly crosses the elastic nucleus and the BSP model response becomes elastoplastic. The larger the elastic nucleus the steeper the initial effective stress path showing a more stiff response and the larger the decrease of the deviatoric stress and excess pore-water pressure due to the larger elastic domain.

Behavior under non-monotonic and cyclic loading

The relative influence of the initial shape hardening stiffness represented by h_0 on the increments of the deviatoric stress, effective mean stress and excess pore-water pressure is most relevant (up to 90%) initially after the effective stress path is crossing the elastic nucleus until it reaches the bounding surface. That is, the larger the initial shape hardening stiffness the smaller the plasticity modulus K_{p} with respect to the current stress and the less pronounced the plastic BSP model response inside the bounding surface. The behavior becomes more stiff and less elastoplastic while moving inside the bounding surface. Consequently, the effective stress path is steeper when the value of the initial shape hardening stiffness is larger showing less change of the effective mean stress until reaching the bounding surface. In total, a larger value of h_0 leads to larger absolute values of the minimum peak deviatoric stress and the minimum peak excess pore-water pressure due to the already induced increments while moving inside the bounding surface.
The sensitivity of the increments of the deviatoric stress, effective mean stress and excess pore-water pressure to the rate of evolution of the damage variable represented by a_{dam} is negligible during the test since no non-monotonic or cyclic loading is induced. Therefore, accumulation of plastic strain affecting the evolution of the damage variable is not remarkable.

CAUC, OC

The results of the GSA related to the CAUC, OC test are displayed in Figure 5.13. That is, the normalized sensitivity $S_{\mathrm{T}_{n_{\mathrm{cp}}},\mathrm{norm}}$ of the increments of deviatoric stress Δq, effective mean stress $\Delta p'$ and excess pore-water pressure $\Delta(\Delta p_{\mathrm{w}})$ to the constitutive BSP model parameters wrt. to the applied axial strain increment $\Delta\varepsilon_{\mathrm{a}}$ is evaluated.

Non-associated flow and shape of bounding surface

The increments of the deviatoric stress, effective mean stress and excess pore-water pressure are sensitive to the shape of the bounding surface when the effective stress path reaches the bounding surface and follows the updated surface returning the stress back towards the critical state line from the dry side.
The increment of the deviatoric stress is most sensitive (more than 75%) to N_{c} since the shape of the bounding surface governs the maximum peak deviatoric stress. The increment of the effective mean stress is just slightly less sensitive (up to 70%) because the shape of the bounding surface also governs the evolution of the effective stress path while returning the stress back to the critical state line. On the contrary, the increment of the excess pore-water pressure is relatively less influenced (up to 45%) by the shape of the bounding surface since the relative influence of the initial shape hardening stiffness is more prominent. However, the shape of the bounding surface governs both the increase of the excess pore-water pressure until reaching the maximum peak deviatoric stress and the subsequent decrease during softening when the stress is returned to the critical state line.
The larger the value of N_{c} the larger the maximum peak deviatoric stress indicating the peak undrained shear strength in compression and the effective stress path is adjusting accordingly.

Stress-induced anisotropy

The sensitivity of the increments of the deviatoric stress, effective mean stress and excess pore-water pressure to the rate of rotation represented by c_{α} is negligible during the test as already seen for the CAUC, NC test. Due to the initial rotation of the bounding surface with $\alpha_0 = \alpha_{\mathrm{K}_0}$, the relative location of the initial anisotropic stress with respect to the critical state line and the amount of overconsolidation further rotation is by definition just slightly induced when bringing back the effective stress path to the critical state line.

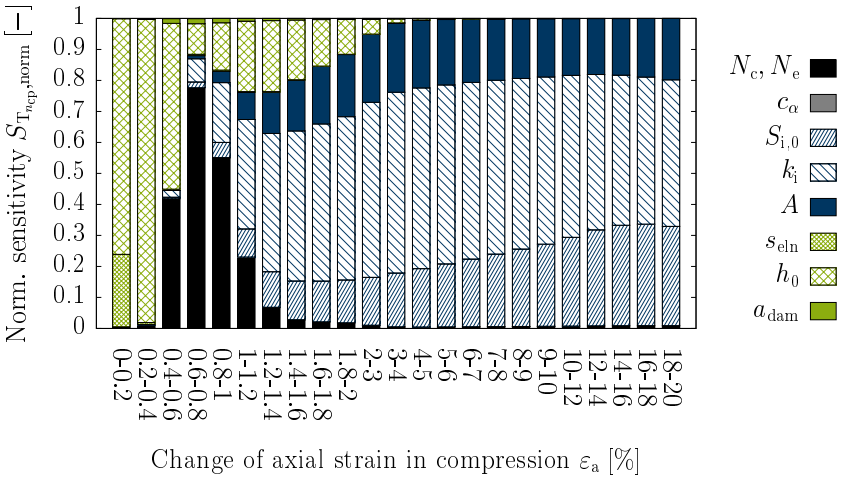

a) Normalized sensitivity $S_{T_{n_{cp}},norm}$ of deviatoric stress increment Δq

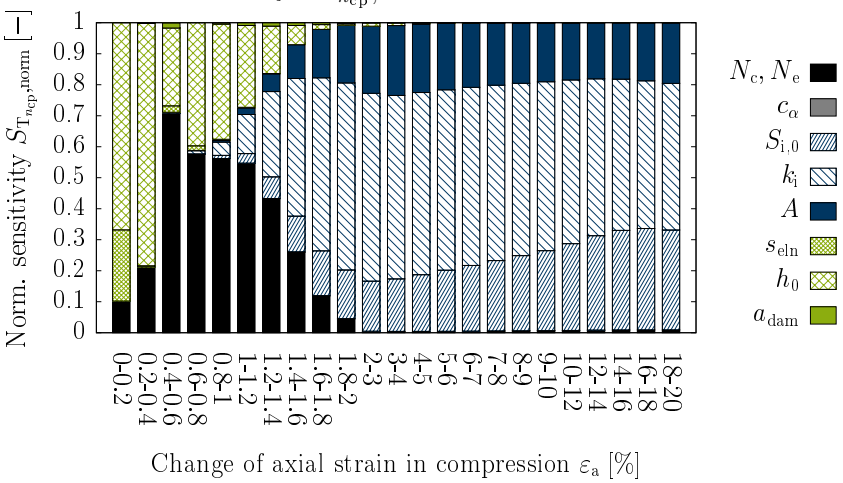

b) Normalized sensitivity $S_{T_{n_{cp}},norm}$ of effective mean stress increment $\Delta p'$

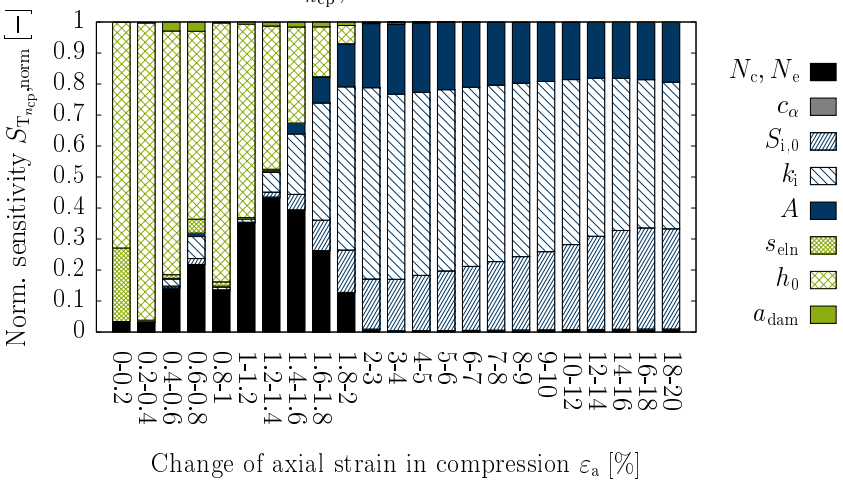

c)Normalized sensitivity $S_{T_{n_{cp}},norm}$ of excess pore-water pressure increment $\Delta(\Delta p_w)$

Figure 5.13: Normalized sensitivity $S_{T_{n_{cp}},norm}$ of various BSP model responses to constitutive BSP model parameters wrt. effective axial stress increment $\Delta\varepsilon_a$ (CAUC, OC test)

Initial structure and destructuration

Destructuration significantly becomes important when the effective stress path is moving on the evolving bounding surface and in the vicinity of the critical state line towards the stress origin. However, the relative influence of destructuration on the increments of the deviatoric stress, effective mean stress and excess pore-water pressure is qualitatively and quantitatively almost the same as for the CAUC, NC test. In contrast, destructuration is initiated at larger strain since the effective stress path has to approach to the bounding surface from the overconsolidated stress state to induce plasticity.
To sum up, the relative influence of the magnitude of the initial structure represented by $S_{\mathrm{i},0}$ becomes most relevant (up to 35%) at larger axial strain. The relative influence of the rate of the destructuration represented by k_{i} becomes important after the initiation of destructuration and reaches the maximum of up to 55% at intermediate strain where the rate of plastic straining is largest. The relative influence of the ratio between the volumetric and the deviatoric plastic strains affecting the destructuration represented by A follows the same trend and is largest with max. 25% at intermediate axial strain.
The larger the initial amount of structure the flatter the shape of the effective stress path while returning the stress back to the critical state line and hence the smaller the absolute value of the maximum peak deviatoric stress since destructuration is activated more significantly. Moreover, the larger the value of $S_{\mathrm{i},0}$ the more pronounced the migration of the effective stress path in the vicinity of the critical state line towards the stress origin. That is, the decrease of the deviatoric stress after reaching its maximum peak value and the increase of the excess pore-water pressure after reaching its minimum peak value after softening are much more pronounced when the initial structure becomes larger. Again, when assuming a fully destructured clay the effective stress path stops evolving when the critical state is reached. Moreover, the larger the value of k_{i} and A the more pronounced the above mentioned destructuration effects.

Size of elastic nucleus

The relative influence of the size of the elastic nucleus represented by s_{eln} on the increments of the deviatoric stress, effective mean stress and excess pore-water pressure is most significant (up to 25%) when starting the test from overconsolidated initial stress conditions within the elastic nucleus located within the bounding surface. This is much more pronounced when comparing to the CAUE, NC test (below 10%).

The larger the size of the elastic nucleus the steeper the initial effective stress path and the larger the increase of the deviatoric stress and excess pore-water pressure due to the larger elastic domain.

Behavior under non-monotonic and cyclic loading

The relative influence of the initial shape hardening stiffness represented by h_0 on the increments of the deviatoric stress, effective mean stress and excess pore-water pressure is again most relevant (80% up to almost 100%) initially after the effective stress path is crossing the elastic nucleus until it reaches the bounding surface as observed in the CAUE, NC test. To recall, the larger the initial shape hardening stiffness the less distinct the elastoplastic BSP model response while moving inside the bounding surface. The larger the initial shape hardening stiffness the steeper the effective stress path inside the bounding surface due to the more dominant stiff behavior. In total, a larger value of h_0 causes larger maximum peak values of the deviatoric stress and the excess pore-water pressure.
The sensitivity of the increments of the deviatoric stress, effective mean stress and excess pore-water pressure to the rate of evolution of the damage variable represented by a_{dam} is negligible during the test since no non-monotonic or cyclic loading is induced as already observed for the CAUE, NC test.

CAUE, OC

The results of the GSA related to the CAUE, OC test are displayed in Figure 5.14. That is, the normalized sensitivity $S_{\mathrm{T}_{n_{\mathrm{cp}}},\mathrm{norm}}$ of the increments of deviatoric stress Δq, effective mean stress $\Delta p'$ and excess pore-water pressure $\Delta(\Delta p_{\mathrm{w}})$ to the constitutive BSP model parameters wrt. to the applied axial strain increment $\Delta\varepsilon_{\mathrm{a}}$ is evaluated.

Non-associated flow and shape of bounding surface

The relative influence of the shape of the bounding surface on the extension side represented by N_{e} becomes most relevant when the effective stress path approaches to the bounding surface on the extension side and follows the updated surface while bringing back the stress to the critical state line from the dry side. That is, the shape of the bounding surface governs at which stress state the effective stress path reaches the bounding surface and how the effective stress path evolves afterwards. The larger the value of N_{e}

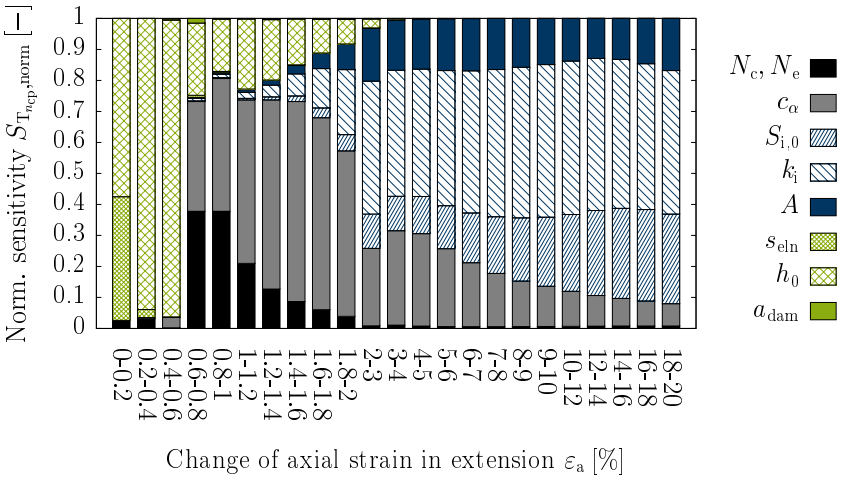

a) Normalized sensitivity $S_{T_{n_{cp}},norm}$ of deviatoric stress increment Δq

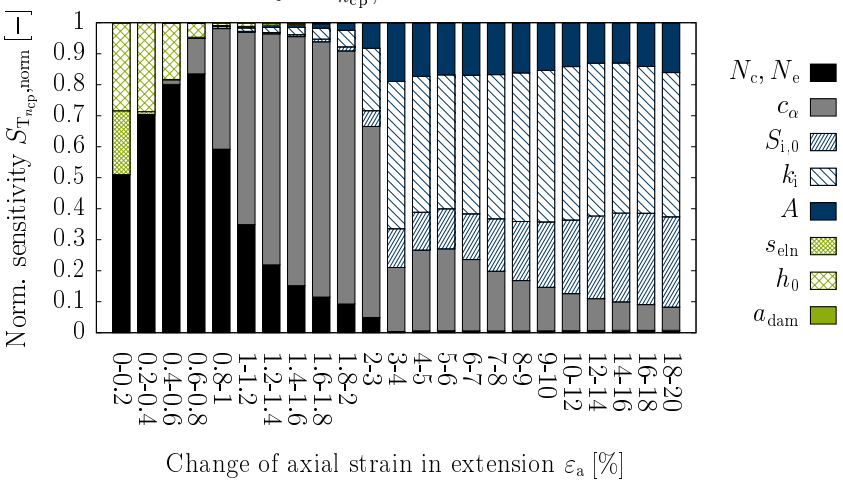

b) Normalized sensitivity $S_{T_{n_{cp}},norm}$ of effective mean stress increment $\Delta p'$

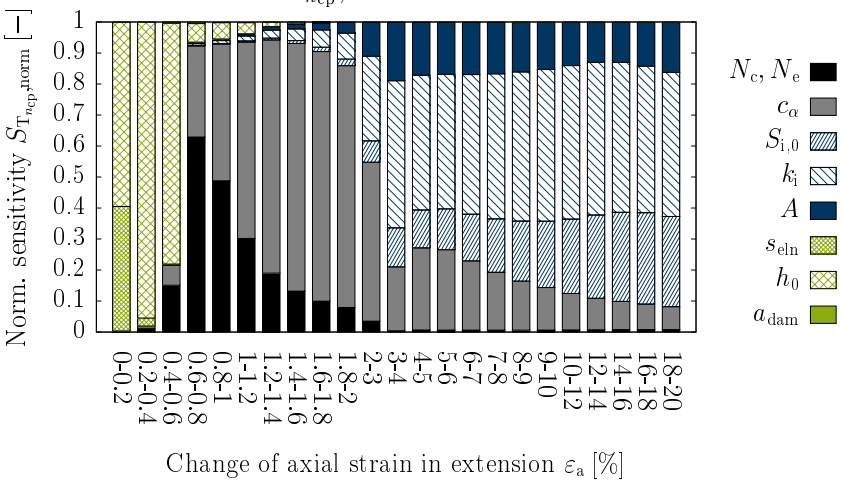

c)Normalized sensitivity $S_{T_{n_{cp}},norm}$ of excess pore-water pressure increment $\Delta(\Delta p_w)$

Figure 5.14: Normalized sensitivity $S_{T_{n_{cp}},norm}$ of various BSP model responses to constitutive BSP model parameters wrt. effective axial stress increment $\Delta\varepsilon_a$ (CAUE, OC test)

the steeper the shape of the effective stress path and the larger the absolute values of the minimum peak deviatoric stress and excess pore-water pressure.
The increment of the effective mean stress shows the largest sensitivity to the shape of the bounding surface (up to 85%). The shape of the bounding surface governs at which stress state plasticity starts to be induced more significantly. However, when plasticity occurs the effective stress path shows an increase of the effective mean stress while the effective mean stress is kept constant when just purely elastic BSP model response occurs. The relative influence of the shape of the bounding surface on the corresponding change of the excess pore-water pressure is a little less (up to 65%) since the rotation plays a more significant role. Whereas, the changes of the deviatoric stress are less sensitive (up to 35%) to N_e since the rotation and the initial shape hardening stiffness are relevant at the same time.

Stress-induced anisotropy

The relative influence of the rotational hardening represented by c_α on the increment of the deviatoric stress (up to 65%), the increment of the effective mean stress (up to 80%) and the increment of the excess pore-water pressure (up to 80%) becomes most relevant when the effective stress path is approaching to the bounding surface on the extension side and is moving on the updated bounding surface to return the stress back to the critical state line. As for the CAUE, NC test the stress-induced anisotropy and the corresponding rotation are strongly activated because the stress ratio is changing from compression to extension. At larger axial strain the rotation becomes relatively less relevant since just slight changes of the stress ratio occur in the vicinity of the critical state line and the relative importance of destructuration takes over. In contrast to the CAUE, NC test the effective stress path is moving on the bounding surface with respect to the dry side of the critical state.
The rotation governs the stress state where the plasticity starts to be induced more significantly and the BSP model response is distinctly changed. However, when the rate of rotation tends to zero the effective stress path does not show a significant increase of the effective mean stress until reaching the critical state line. Moreover, the rotation of the bounding surface governs how the effective stress path evolves on the dry side of the critical state after reaching the bounding surface and influences the minimum peak deviatoric stress. The larger the value of c_α the steeper the shape of the effective stress path and the larger the absolute values of the minimum peak deviatoric stress and excess pore-water pressure developed during undrained shearing. The minimum peak values are

reached at lower axial strain when the rate of rotation is larger. Furthermore, the rotational hardening governs the increase of the deviatoric stress and the excess pore-water pressure after reaching their minimum peak values. The larger the value of c_α the faster and more pronounced are the increase of the deviatoric stress and excess pore-water pressure.

Initial structure and destructuration

The sensitivity of the increments of the deviatoric stress, effective mean stress and excess pore-water pressure to the destructuration is qualitatively and quantitatively similar compared to the CAUE, NC test. That is, the destructuration becomes significant after applying a larger amount of axial strain where the effective stress path is moving on the bounding surface and in the vicinity of the critical state line towards the stress origin. The results from the local parameter variation regarding the effect of $S_{\mathrm{i},0}$, k_{i} and A on the stress-strain behavior are also very similar to the CAUE, NC test and described in that section.

Size of elastic nucleus

The relative influence of the size of the elastic nucleus represented by s_{eln} on the increment of the deviatoric stress (up to 40%) and the excess pore-water pressure (up to 40%) is most significant when starting the test from overconsolidated initial stress conditions located within the elastic nucleus. However, the sensitivity of the increment of the effective mean stress is less dominant (up to 20%). This is because the transition from elastic to elastoplastic behavior will not induce pronounced changes of stiffness due to overconsolidation and the effective mean stress remains almost constant.
Compared to the CAUE, NC test (less than 10%) and the CAUC, OC test (25%) the relative influence of the size of the elastic nucleus is more significant. Due to the relative position and size of the elastic nucleus with respect to the bounding surface the effective stress path moves inside the elastic nucleus for a larger portion of the first axial strain increment and the constitutive BSP model parameters controlling the elastoplastic behavior inside the bounding surface such as h_0 become relatively less important. The results from the local parameter variation regarding the effect of s_{eln} on the stress-strain behavior are very similar to the CAUE, NC test and described in that section.

Behavior under non-monotonic and cyclic loading

The relative influence of the initial shape hardening stiffness represented by h_0 is most relevant for the increments of the deviatoric stress and excess pore-water pressure (up to 95%) initially after the effective stress path is crossing the elastic nucleus until it reaches the bounding surface as already found for the CAUE, NC and CAUC, OC tests. However, the sensitivity of the increment of the effective mean stress to the initial shape hardening stiffness is much less (up to 30%). Since the BSP model response is anyway predominantly elastic while the effective stress path is moving within the bounding surface and the changes of the effective mean stress are small the shape of the bounding surface becomes more relevant by defining at which stress state plasticity starts to be induced more significantly. The sensitivity of the increment of the deviatoric stress, the effective mean stress and the excess pore-water pressure to the rate of evolution of the damage variable represented by a_{dam} is negligible as already observed for the CAUE, NC and CAUC, OC tests since no non-monotonic or cyclic loading is induced.

5.4.3 Cyclic undrained triaxial test

CAUcyc, NC

The results of the GSA related to the CAUcyc, NC, $\eta_0 = \alpha_{\mathrm{K}_0}$ test are displayed in Figure 5.15. That is, the normalized sensitivity $S_{\mathrm{T}_{n_{\mathrm{cp}}},\mathrm{norm}}$ of the increments of axial strain $\Delta\varepsilon_{\mathrm{a}}$, effective mean stress $\Delta p'$ and excess pore-water pressure $\Delta(\Delta p_{\mathrm{w}})$ to the constitutive BSP model parameters wrt. to the number of cycles and loading quarters is evaluated. However, the results of the GSA regarding the CIUcyc, NC test are qualitatively similar compared to the CAUcyc, NC test, so that the results are not explicitly shown but the main differences are discussed.

Non-associated flow and shape of bounding surface

At the very beginning of the test the increments of the excess pore-water pressure and effective mean stress are sensitive to the shape of the bounding surface represented by N_{c} and N_{e} since it governs how the effective stress path develops when moving on the bounding surface. Furthermore, the shape of the bounding surface controls the distance between the effective stress path and the bounding surface during cyclic loading. The distance is regulating the amount of induced plasticity.

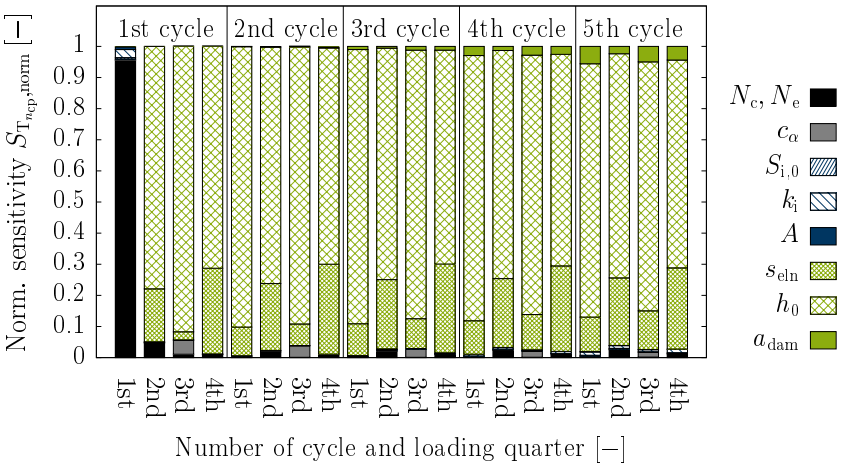

a) Normalized sensitivity $S_{\mathrm{T}_{n_{\mathrm{cp}}},\mathrm{norm}}$ of axial strain increment $\Delta\varepsilon_{\mathrm{a}}$

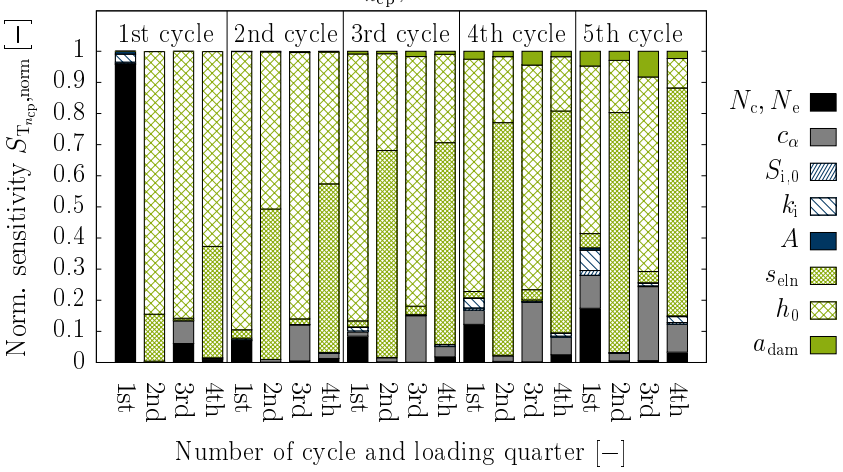

b) Normalized sensitivity $S_{\mathrm{T}_{n_{\mathrm{cp}}},\mathrm{norm}}$ of effective mean stress increment $\Delta p'$

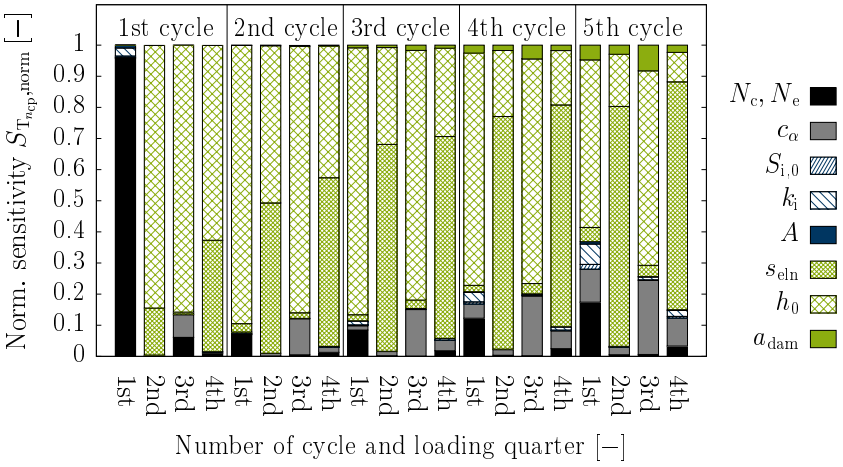

c)Normalized sensitivity $S_{\mathrm{T}_{n_{\mathrm{cp}}},\mathrm{norm}}$ of excess pore-water pressure increment $\Delta(\Delta p_{\mathrm{w}})$

Figure 5.15: Normalized sensitivity $S_{\mathrm{T}_{n_{\mathrm{cp}}},\mathrm{norm}}$ of various BSP model responses to constitutive BSP model parameters wrt. number of cycles and loading quarters (CAUcyc, NC test)

Consequently, the increments of the excess pore-water pressure and effective mean stress are most sensitive in the 1st quarter of the 1st cycle (up to 95%) when the undrained shearing is starting from normally consolidated initial stress conditions. Afterwards, the shape of the bounding surface becomes relevant (between 10% to 20%) in the loading quarters where the effective stress path approaches to or moves on the bounding surface on the compression side only. This is because the effective stress path is cycling just in the compression domain and the extension side of the bounding surface does not significantly become relevant. On the contrary, for the CIUcyc test the shape of the bounding surface becomes just slightly relevant (between 3% to 10%) after the first quarter but then in each second cyclic loading quarter where the effective stress path approaches to or moves on the bounding surface on the compression or the extension side, respectively. That is due to the fact that the effective stress path is cycling around the effective mean stress axis towards both the compression and extension domain. To sum up, the relative influence of N_c and N_e is largest in the first cycle, decreases in the second cycle and becomes larger with increasing number of cycles (up to 10% in the 5th cycle) since the distance to the bounding surface decreases when the effective stress path migrates towards the stress origin with a decreasing effective mean stress. The lower the values of N_c and N_e the larger the positive excess pore-water pressure and the more pronounced the migration of the effective stress path towards the stress origin. However, the relative influence of the shape of the bounding surface on the increment of the axial strain is relevant only for the 1st quarter of the 1st cycle up to 95%. When evaluating the entire first cycle other constitutive BSP model parameters are more influencing, so that the relative influence of the shape of the bounding surface on the increment of the axial strain becomes negligible. In general it can be stated that the lower the value of N_c the more pronounced the evolution of axial strain. This effect becomes more pronounced with larger number of cycles since the distance to the bounding surface is decreasing and more plasticity is induced.

Stress-induced anisotropy

The relative influence of the stress-induced anisotropy and the rate of rotation represented by c_α on the increments of the excess pore-water pressure and effective mean stress reaches values up to 25% when cycling around an anisotropic stress state. The rotation becomes most relevant in the cyclic loading quarters where the effective stress path moves in the direction of the bounding surface on the extension side. That is, the stress ratio is significantly changing and rotation is activated. For the other loading quarters the relative

influence is significantly smaller. Generally, it can be stated that the relative influence of the rate of rotation grows with increasing number of cycles (from 5% to 25%).
During the CIUcyc test the rotation is much less activated when cycling around an isotropic stress state. That is, the relative influence of the rate of rotation on the increments of the excess pore-water pressure, effective mean stress and axial strain is relatively small (below 5%) during the entire test even though the bounding surface is initially not rotated with $\alpha_0 = 0$. The rotation becomes slightly relevant in each second cyclic loading quarter where the rotational hardening is activated due to the occurrence of stress reversal.
In general there is a tendency that the larger the rate of rotation the smaller the development of positive excess pore-water pressure and the less pronounced the migration of the effective stress path towards the stress origin. Moreover, the larger the value of c_α the larger the accumulation of axial compression strain during cyclic loading. However, for the CIUcyc test the axial strain accumulates in both compression and extension. The larger the number of cycles the more pronounced the above mentioned effects.

Initial structure and destructuration

The relative influence of the destructuration on the increments of the excess pore-water pressure, effective mean stress and axial strain becomes relevant where plastic strain is developed during the undrained cyclic loading. Hence, destructuration mainly occurs within the cyclic loading quarters where the effective stress path gets close to the bounding surface on the compression side. Since the destructuration is dependent on the developed plastic strain the above mentioned BSP model responses become more sensitive to the increment of destructuration with an increasing number of cycles where the distance of the effective stress path to the bounding surface gets smaller. The relative influence of the destructuration on the increments of the excess pore-water pressure and the effective mean stress reaches a little more than 10% within the 5th cycle, whereas the relative influence on the increment of the axial strain is almost negligible, i.e. below 5% only. Whereas, for the CIUcyc test the sensitivity of destructuration is even larger up to 25% and 10% since the relative influence of the shape of the bounding surface, initial shape hardening stiffness and rotational hardening is much smaller.
However, the quantity of the initial structure represented by $S_{\mathrm{i},0}$ is not that influencing (far below 5%) since the structure is anyway not fully destroyed. Just a very low value of $S_{\mathrm{i},0}$ representing an unstructured to slightly structured clay significantly changes the BSP model response. There is a tendency that the larger the initial structure the more

pronounced the destructuration effects such as increasing excess pore-water pressure, migration of the effective mean stress and accumulated axial strain.
Whereas, the relative influence of the rate of destructuration controlled by k_{i} is most significant (up to 10%). Since the developed strain is very small the value of k_{i} becomes relatively more important since it strongly controls how fast the destructuration occurs. The larger the rate of destructuration the larger the generated excess pore-water pressure and the more pronounced the migration of the effective stress path towards the stress origin due to the associated reduction of the effective mean stress. Moreover, the larger the value of k_{i} the larger the accumulated axial strain especially at a higher number of cycles.
The relative influence of the ratio between the volumetric and the deviatoric plastic strains affecting the destructuration represented by A is almost negligible (below 5%). There is a tendency that the volumetric plastic strain is more relevant during undrained cyclic loading since a smaller value of A causes more pronounced destructuration effects.

Size of elastic nucleus

The size of the elastic nucleus represented by s_{eln} is influencing the increments of the excess pore-water pressure and effective mean stress as well as the increment of the axial strain since it governs the proportion of the elastic and plastic strains developed during the undrained cyclic loading. The larger the elastic domain the less plasticity is induced to the system which becomes most relevant immediately after stress reversal. The larger the size of the elastic nucleus the smaller the developed positive excess pore-water pressure and the less pronounced the migration of the effective stress path towards the stress origin due to the reduction of the effective mean stress. Moreover, the larger the value of s_{eln} the stiffer the BSP model response and the smaller the evolved axial strain.
The increments of the excess pore-water pressure and effective mean stress become most sensitive to the size of the elastic nucleus (up to 75%) within the 5th cycle. Generally, it can be stated that the relative influence of the size of the elastic nucleus grows with increasing number of cycles (from 35% to 75%) because the effective stress path cycles closer to the bounding surface. Moreover, the relative influence of the size of the elastic nucleus is larger for cyclic loading quarters after stress reversal after unloading with a smaller value of deviatoric stress rather than stress reversals after loading. For the cyclic loading quarters in between the relative sensitivity significantly reduces (below 5%) since the effective stress path mostly left the elastic nucleus already within the subsequent cyclic loading quarter. The relative influence of the size of the elastic nucleus on the increment

of the axial strain is significantly lower and oscillates between 20% and 30%. Again the axial strain becomes most sensitive for the cyclic loading quarters after stress reversal after unloading. However, even for the cyclic loading quarters in between the relative sensitivity reaches values between 5% to 15%.

Behavior under non-monotonic and cyclic loading

The initial shape hardening stiffness represented by h_0 is significantly affecting (up to 85% to 95%) the increments of the excess pore-water pressure, effective mean stress and axial strain. The relative influence is largest when the effective stress path is moving within the bounding surface and the soil behavior is elastoplastic but not directly after stress reversal where the effective stress path is at least partly moving within the elastic nucleus representing a purely elastic behavior. Hence, in the cyclic loading quarters after stress reversal the relative influence of h_0 is reduced. Moreover, the relative influence of h_0 on the increments of the excess pore-water pressure and effective mean stress decreases (from 90% to 65%) with an increasing number of cycles. Since the elastoplastic transition zone between the elastic nucleus and the bounding surface becomes smaller with respect to the continuously migrating effective stress path the relative influence of the elastic nucleus becomes larger. However, the sensitivity of the increment of the axial strain to the initial shape hardening stiffness is less affected by the increasing number of cycles (decreases from 95% to 80%). The smaller the initial shape hardening stiffness the larger the positive excess pore-water pressure accumulated during cyclic loading and the more distinct the migration of the effective stress path towards the stress origin due to the reduction of the effective mean stress. Furthermore, the smaller the value of h_0 the larger the accumulated axial strain and the more pronounced the damping and the energy dissipation since more plasticity is induced. Additionally, the difference between the development of compression and extension strain becomes much more significant with a smaller value of h_0.
The sensitivity of the increments of the excess pore-water pressure, effective mean stress and axial strain to the rate of evolution of the damage variable represented by a_{dam} increases with an increasing number of cycles since the plastic deviatoric strain is accumulating. To be more specific, the relative influence of a_{dam} on the increments of the excess pore-water pressure and effective mean stress reaches up to 10 % in the 5th cycle. The sensitivity is largest for the loading quarters where the effective stress path experiences an elastoplastic transition within the bounding surface but not directly after the stress reversal occurs. The relative influence of the rate of evolution of the damage variable on the increment of the axial strain qualitatively follows the same trend but quantitatively

differs by reaching a maximum value of 5% in the 5th cycle. The larger the rate of evolution of the damage variable the larger the developed positive excess pore-water pressure and the associated reduction of the effective mean stress. Moreover, the larger the value of a_{dam} the larger the stiffness degradation and the corresponding accumulated axial compression strain. Whereas for the CIUcyc test both the axial compression and extension strain accumulate during undrained cyclic loading.

5.5 Recommendations

In the following recommendations are given for an adequate BSP model parameter calibration based on the results of the GSA. For additional knowledge on the specific influence of the change of a particular constitutive BSP model parameter on the BSP model response such as stress-strain behavior and evolution of excess pore-water pressure it is referred to the former sections where the results of the local parameter variation are intensively discussed.

- The elastoplastic compression parameter λ and the elastic swelling parameter κ can be derived from experimental data of a one-dimensional compression (oedometer) test or preferably isotropic compression test incorporating a virgin loading-unloading path. Whereat, the elastic swelling parameter κ has to be ascertained from the unloading path directly after stress reversal since plasticity will be induced to the system during further unloading. Both compression and swelling parameters are related to the intrinsic material properties of reconstituted clay. If just experimental data on natural clay are available the elastoplastic compression parameter λ can be determined from the virgin loading path at large stress where the destructuration is fully completed and the compression curves converge. The elastic swelling parameter κ is rather less affected by the structure and can be identified from the very first part of any unloading-reloading path initially after stress reversal.

- The Poisson's ratio ν can be obtained from the experimental data of one-dimensional compression (oedometer) test with an elastic K_0-unloading path conducted preferentially on reconstituted clay or alternatively on natural clay. The measurement of the radial stress allows for the determination of the effective stress ratio q/p'.

- The critical state stress ratios M_{c} and M_{e} describing the slope of the critical state line in compression and extension can be determined from experimental data of CAU or CIU tests in triaxial compression and extension on natural clay.

- The constitutive BSP model parameter N_c related to the non-associated flow and the shape of the bounding surface can be preferentially calibrated against the experimental data of the CAUC, NC, test on natural clay. The increments of the deviatoric stress, effective mean stress and excess pore-water pressure are highly sensitive (up to 90%) to the changes of N_c at the beginning of the test starting from anisotropic and normally consolidated initial stress conditions up to a small amount ($< 1\%$) of the applied axial strain. Hence, for the calibration of N_c the maximum peak deviatoric stress and the effective stress path following the shape of the bounding surface have to be fitted. Alternatively, a CIUC, NC test can be used to calibrate N_c. However, the increments of the effective mean stress and the excess pore-water pressure are also most sensitive (up to 90%) to the change of N_c at the beginning of the test. Whereat, the increment of the deviatoric stress is additionally influenced by the anisotropy already at small strain and hence less sensitive.

- The constitutive BSP model parameter N_e defining the shape of the bounding surface in triaxial extension is always defined as $N_e = N_c \{M_e/M_c\}$ to ensure the uniqueness of the critical state line. Consequently, during calibration of N_c the coupled influence of N_e on the BSP model response has to be additionally considered.

- The constitutive BSP model parameter α_0 related to the inherent anisotropy and controlling the initial rotation of the bounding surface and the plastic potential surface is set to $\alpha_0 = \alpha_{K_0}$ representing anisotropic initial stress conditions. This underlies the assumption that the rotation of the plastic potential surface under K_0-loading during deposition and sedimentation has been stabilized at $\alpha \to \alpha_b = \alpha_{K_0}$. The value of α_{K_0} is calculated according to Equations 5.5-5.7 as proposed by Dafalias (1986c) and Dafalias et al. (2006). For isotropic initial stress conditions the value is set to $\alpha_0 = 0$ and the surfaces are initially not rotated.

$$\alpha_{K_0} = \frac{3/2\, B\, \eta_{K_0}^3 + \eta_{K_0}^2 + \{2\ \{1 - \{\kappa/\lambda\}\} - B\, M_c^2\}\, 3/2\, \eta_{K_0} - M_c^2}{3\ \{1 - \{\kappa/\lambda\}\}} \tag{5.5}$$

$$B = -\frac{2\ \{1+\nu\}}{9\ \{1-2\,\nu\}}\,\frac{\kappa}{\lambda} \tag{5.6}$$

$$\eta_{K_0} = \frac{3\ \{1-K_0\}}{\{1+2\,K_0\}} \tag{5.7}$$

- The constitutive BSP model parameter c_α controlling the rate of rotation can be most accurately identified by using the experimental data of the CAUE, NC test on

natural clay. The increments of the deviatoric stress, effective mean stress and excess pore-water pressure are most sensitive (up to 70%) to the changes of c_α when the effective stress path is approaching to the bounding surface on the extension side. The stress-induced anisotropy and the corresponding rotation are strongly activated because the stress ratio is changing from compression to extension. Hence, for the calibration of c_α the value of the minimum peak deviatoric stress and the evolution of the effective stress path while approaching to the bounding surface on the extension side have to be fitted. However, for the CAUE, OC test on natural clay, which can be alternatively used for calibration of c_α, the rotation is relevant (up to 80%) even at larger axial strain since the effective stress path is moving on the bounding surface with respect to the dry side of the critical state. The results, which were figured out for the CAUE tests should hold true for CIUE tests on natural clay as well. This kind of tests were not investigated within this study due to the expected similarities.

- The constitutive BSP model parameters s_α and z_α which are controlling the bounding attractor of the fabric stress tensor have to be mathematically determined to ensure a correct simulation of the K_0-loading path. This is, Equation 5.8 has to be solved for $s_\alpha = z_\alpha$ with respect to a given α_{K_0} obtained according to Equation 5.5.

$$\alpha = \alpha_{\mathrm{b}} = \alpha_{\mathrm{K}_0} = \pm \frac{M_{\mathrm{c}}}{z_\alpha} \left\{ 1 - \exp\left(-s_\alpha \frac{|\eta_{\mathrm{K}_0}|}{M_{\mathrm{c}}} \right) \right\} \tag{5.8}$$

- The constitutive BSP model parameter $S_{\mathrm{i},0}$, k_{i} and A involved in the destructuration are best to calibrate against the experimentally obtained volume change during virgin loading phases in either one-dimensional compression (oedometer) or isotropic compression tests on natural clay. The volume change during virgin loading phases in those tests is almost exclusively influenced by destructuration (up to 100%). However, the superimposed effects on the destructuration caused by the constitutive BSP model parameters $S_{\mathrm{i},0}$, k_{i} and even A occur simultaneously and cannot be decoupled. It is strongly recommended to calibrate all of the constitutive model parameters $S_{\mathrm{i},0}$, k_{i} and A related to destructuration on the same geotechnical laboratory test.

  - The constitutive BSP model parameter $S_{\mathrm{i},0}$ defining the magnitude of the initial structure should be calibrated against the volumetric behavior related to virgin loading phases of the one-dimensional compression (oedometer) test at larger stress, where the sensitivity of the volumetric behavior is largest (up to 50%). That is $S_{\mathrm{i},0}$ governs if and how much structure is remaining at larger stress since the structure is successively destroyed.

- However, for the isotropic compression test the relative influence of $S_{i,0}$ on the volume change is lower (around 40%) since the influence of A increases due to the missing deviatoric component of plastic strain.
- The constitutive BSP model parameter k_i controlling the rate of destructuration should be calibrated against the volumetric behavior related to virgin loading phases of the one-dimensional compression (oedometer) test directly after initiation of destructuration, where the rate of plastic straining is largest due to lower stress-dependent stiffness and the sensitivity of the volumetric behavior is largest (up to 70%).
- However, for the isotropic compression test the relative influence of k_i on the volume change is lower (around 50%) since the influence of A increases due to the missing deviatoric component of plastic strain.
- The calibration of the constitutive BSP model parameter A controlling the ratio of the volumetric and deviatoric plastic strains involved in destructuration is not that straightforward since its effects on the BSP model responses occur simultaneously to the effects caused by the more dominant constitutive BSP model parameters $S_{i,0}$ and k_i and cannot be decoupled. Hence, the relative importance of A on the BSP model response is not that large and it can be stated that the calibration of A is relatively not that important compared to the other constitutive BSP model parameters $S_{i,0}$ and k_i governing the destructuration. Nevertheless, the volume change during the initial virgin loading phase of the isotropic compression test on natural clay can be somewhat used for calibration of A since the relative importance of A on the volume change is largest (up to 25%). Compared to the one-dimensional compression (oedometer) test (less than 5%) the relative influence of A becomes more significant due to the missing deviatoric plastic strain. Therefore, A directly controls the portion of volumetric plastic strain participating in the development of the destructuration with respect to the entire amount of volumetric plastic strain developed during isotropic compression.

Alternatively, $S_{i,0}$, k_i and A can be calibrated against the experimental data of CAUC and CIUC tests on natural clay when the effective stress path is moving in the vicinity of the critical state. The relative importance of $S_{i,0}$, k_i and A on the increments of the deviatoric stress, effective mean stress and excess pore-water pressure are around 35%, 55% and 20%-25%, respectively, dependent on the applied strain.

However, due to the vicinity of the critical state and the relatively large applied strain the condition of the sample is not known and the calibration is not recommended.

- The calibration of the constitutive BSP model parameter s_{eln} controlling the size of the elastic nucleus is strongly dependent on the magnitude of the stress or strain increment applied after stress reversal. Nevertheless, s_{eln} can be calibrated against the evolution of the excess pore-water pressure and the corresponding effective mean stress migration after each stress reversal in the cyclic undrained triaxial tests on natural clay independently of the initial stress ratio. The calibration is most effective at larger number of cycles since the increment of the excess pore-water pressure and the effective mean stress become more sensitive (up to 75% within 5th cycle in this study) to the size of the elastic nucleus with increasing number of cycles. The relative influence of the size of the elastic nucleus on the increment of the axial strain is significantly smaller (up to 20-30%) and is not recommended to use for calibration of s_{eln}. Generally, for estimation of s_{eln} any geotechnical laboratory test incorporating either a stress reversal or starting from overconsolidated initial stress conditions is suitable. However, it can be stated that the calibration of s_{eln} becomes relevant for geotechnical applications with complex cyclic loading but is relatively not that important for simpler non-monotonic stress paths with smaller number of stress reversals and for larger stress or strain increments.

- For the calibration of the constitutive BSP model parameter h_0 related to the initial shape hardening stiffness there are several convenient tests available. The common characteristic of these tests is the existence of stress reversal and a stress path moving within the bounding surface and outside the elastic nucleus.

  - The most simple but not most accurate option is to calibrate h_0 against the experimentally obtained volume change during one-dimensional compression (oedometer) test on natural clay starting from overconsolidated initial stress conditions within the elastic nucleus. However, it has to be stated that the effects of h_0 on the volume change occur simultaneously to the effects caused by a_{dam} and cannot be decoupled. However, the advantage of this option is to calibrate both constitutive BSP model parameters h_0 and a_{dam} on the same geotechnical laboratory test. Though, the relative influence of h_0 on the volume change is largest (up to 90%) when the stress path is firstly crossing the elastic nucleus. However, the total volume changes due to variation of h_0 are relatively small and therefore not most appropriate for the calibration of h_0. During the

following unloading-reloading cycles the relative influence of h_0 on the volume change decreases to an almost constant value between 30%-40%. That is, to calibrate h_0 the volume change of any unloading-reloading phase of the one-dimensional compression (oedometer) test has to be fitted by variation of h_0. However, it is not recommended to use the isotropic compression test on a natural clay for calibration of h_0 since the total volume change due to variation of h_0 is relatively small in all unloading-reloading cycles.

- Alternatively, h_0 can be calibrated against the experimental data of CAUC or CIUC, OC tests on natural clay starting from overconsolidated initial stress conditions. The relative influence of h_0 on the increments of the deviatoric stress, effective mean stress and excess pore-water pressure is most relevant (80% up to almost 100%) initially after the effective stress path is crossing the elastic nucleus and moves within the bounding surface until it reaches the bounding surface. Hence, for calibration of h_0 the evolution of the effective stress path has to be fitted by variation of h_0.

- Another possibility is to calibrate h_0 against experimental data of CAUE or CIUE tests on natural clay independently of the consolidation stress. The relative influence of the initial shape hardening stiffness on the increments of the deviatoric stress, effective mean stress and excess pore-water pressure is most relevant (up to 90%) initially after the effective stress path is crossing the elastic nucleus and moves within the bounding surface until it reaches the bounding surface. Hence, for calibration of h_0 the evolution of the effective stress path has to be fitted by variation of h_0.

- Generally, cyclic undrained tests on natural clay, such as the evaluated CIUcyc, NC and CAUcyc, NC, $\eta_0 = \alpha_{K_0}$, can be used for calibration of h_0. Whereat, h_0 is significantly affecting (up to 85% to 95%) the increments of the axial strain, effective mean stress and excess pore-water pressure. The relative influence is largest when the effective stress path is moving within the bounding surface and the soil behavior is elastoplastic but not directly after stress reversal where the stress path is moving within the elastic nucleus representing a purely elastic behavior. Hence, in the cyclic loading quarters after stress reversal the relative influence of h_0 is slightly reduced. For the calibration of h_0 one of the earlier cycles should be used since the relative influence of h_0 on the increment of the excess pore-water pressure and the effective mean stress significantly decreases with an increasing number of cycles.

- The calibration of the constitutive BSP model parameter a_{dam} related to the rate of evolution of the damage variable using cyclic undrained triaxial tests is not that straightforward since a certain amount of deviatoric plastic strain has to be developed to induce a distinct stiffness degradation. The amount of deviatoric plastic strain developed during undrained cyclic loading depends on the cyclic shear stress amplitude and the average cyclic shear stress. Nevertheless, the experimental data of cyclic undrained triaxial tests on natural clay, such as the evaluated CIUcyc, NC and CAUcyc, NC with $\eta_0 = \alpha_{\mathrm{K_0}}$ tests, can be used for calibration of a_{dam} since the sensitivity of the increments of the excess pore-water pressure, effective mean stress and axial strain to the rate of evolution of the damage variable increases with an increasing number of cycles due to the accumulation of plastic deviatoric strain. Therefore, to even better calibrate a_{dam} against the experimental data of cyclic undrained triaxial tests with a small cyclic stress amplitude as it was investigated in this study a larger number of cycles is required.
  To be more specific, the relative influence of a_{dam} on the increments of the excess pore-water pressure and the corresponding effective mean stress reaches just up to 20% (CIUcyc, NC) and 10% (CAUcyc, NC, $\eta_0 = \alpha_{\mathrm{K_0}}$) in the 5th cycle. The sensitivity is largest for the loading quarters where the effective stress path experiences an elastoplastic transition within the bounding surface but not directly after the stress reversal occurs. The relative influence of the rate of evolution of the damage variable on the increment of the axial strain qualitatively follows the same trend but quantitatively differs by reaching a maximum value of 10% (CIUcyc, NC) and 5% (CAUcyc, NC, $\eta_0 = \alpha_{\mathrm{K_0}}$) in the 5th cycle and is therefore much less convenient for the calibration of a_{dam}. As an alternative, if no experimental data from cyclic tests are available the one-dimensional compression (oedometer) test on natural clay can be used for calibration of a_{dam} since the sensitivity of the volume change to the variation of a_{dam} is quite large (up to 40%-50%) during the unloading-reloading cycles. The relative influence of a_{dam} increases with decreasing distance to the bounding surface during the unloading-reloading cycles since the magnitude of accumulated plastic strain is increasing.

5.6 Summary

In this chapter, the global sensitivity analysis (GSA) was presented as a sophisticated approach and suitable tool to enhance the subsequent calibration of the constitutive BSP model parameters via inverse analysis by providing information on the geotechnical laboratory test and even the loading stage to be selected to most properly identify a particular constitutive BSP model parameter. Initially, the general ability of the constitutive BSP model with respect to the numerical simulations of geotechnical laboratory tests related to Bothkennar clay as a typical representative for natural clay behavior was discussed to better interpret the results of the GSA. The subsequent GSA and the local parameter variation analysis were evaluated with respect to the sensitivity of the various numerical BSP model responses regarding the geotechnical laboratory tests such as increment of stress, strain and excess pore-water pressure to the constitutive BSP model parameters. In conclusion, based on the results of the GSA recommendations were given regarding the adequate choice of the geotechnical laboratory tests to be preferentially selected for the calibration of a particular constitutive BSP model parameter.

To sum up, the so-called measurable constitutive BSP model parameters κ, λ, ν, M_{c} and M_{e} related to the critical state soil mechanics and the Modified Cam-Clay model can be experimentally determined and directly assessed from the results of the associated geotechnical laboratory or field tests. Furthermore, the parameters related to the initial conditions such as initial void ratio e_0, coefficient of earth pressure at rest K_0, yield stress ratio YSR and preconsolidation stress $p_{0,\mathrm{s,init}}$ can be directly determined from the experimental results of the associated geotechnical laboratory or field test. In addition to this, some non-measurable constitutive BSP model parameters such as $N_{\mathrm{e}}/N_{\mathrm{c}} = M_{\mathrm{e}}/M_{\mathrm{c}}$ related to the shape of the bounding surface on the extension side and $\alpha_0 = \alpha_{\mathrm{K}_0}$ and $s_\alpha = z_\alpha$ related to the inherent and stress-induced anisotropy can be analytically calculated.

The remaining non-measurable constitutive BSP model parameters N_{c} related to non-associated flow and the shape of the bounding surface, c_α related to the stress-induced anisotropy and the rate of rotation, $S_{\mathrm{i},0}$ related to the initial structure, k_{i} and A related to destructuration, s_{eln} related to the size of the elastic nucleus defining the purely elastic domain, h_0 related to the initial shape hardening stiffness and a_{dam} related to the degradation of stiffness and accumulation of plastic strain have to be calibrated against the experimental data of geotechnical laboratory tests using inverse analysis.

The calibration of the constitutive BSP model parameters with respect to the natural Onsøy clay is investigated in the next chapter.

6 Calibration of BSP model parameters

In this chapter the calibration of the constitutive BSP model parameters is presented. The natural Onsøy clay is chosen as a representative for the typical natural clay behavior. The chapter starts with an introduction on the available experimental data on Onsøy clay from RUB, NGI and KIT. Special focus is set on oedometer tests and undrained triaxial tests under monotonic and cyclic loading.

Afterwards, the calibration of the constitutive BSP model parameters which is composed of two consecutive processes is presented. The first process contains the constitutive BSP model parameter calibration via direct determination. That is, the measurable constitutive BSP model parameters, which originally have an explicit definition with respect to the experimental data can be directly determined and assessed from the corresponding geotechnical laboratory test. Furthermore, some constitutive model parameters can be obtained by employing analytical equations. In the second process the remaining non-measurable constitutive BSP model parameters have to be calibrated against the introduced experimental data on Onsøy clay via automated inverse analysis. Therefore, the parameter identification by means of applying an inverse numerical analysis using a particle swarm optimization (PSO) algorithm is employed. The methodology of the inverse analysis adopted and applied in the current study is discussed. Furthermore, the corresponding components such as particle swarm optimization algorithm, constitutive BSP model parameters to be optimized and identified, numerical testing program and multi-objective function are introduced.

The chapter closes with a summary on the particular constitutive BSP model parameter set for natural Onsøy clay identified from the combined calibration via direct determination and automated inverse analysis using the particle swarm optimization. Concluding, the corresponding BSP model response regarding the geotechnical laboratory test is presented by comparison of numerical and experimental results.

6.1 Experimental data on Onsøy clay

Special consideration is given to the experimental data on natural Onsøy clay from oedometer tests and undrained triaxial tests under monotonic and cyclic loading as summarized in the following.

- Constant rate of strain (CRS) oedometer tests on natural samples from a depth of 10.8-10.9 m (Block No. 26C) taken from NGI (Bamberg, 2009).
- Multiple-stage loading (MLS) oedometer tests on natural and reconstituted samples from a depth of 9.9-10.3 m conducted at RUB (Lieske, 2015; Müthing et al., 2017a; Müthing, 2017b).
- Monotonic anisotropically consolidated undrained triaxial tests in compression and extension (CAUC and CAUE) on natural clay samples from a depth of 10.5-10.6 m (Block No. 26A) provided by NGI/KIT (Wichtmann et al., 2013; Wichtmann, 2016).
- Cyclic undrained triaxial tests under anisotropic initial stress condition on natural clay samples from a depth of 10.9-11.0 m (Block No. 26D) provided by NGI/KIT (Wichtmann et al., 2013; Wichtmann, 2016).

It is to be mentioned that the experimental data are provided by different research groups such as the Ruhr-Universität Bochum (RUB), the Norwegian Geotechnical Institute (NGI) and the Karlsruhe Institute of Technology (KIT). However, the testing materials originate from similar sites and depths but manifesting slightly different in situ conditions such as void ratio, natural water content, stress state and stress/strain history as well as degree of structure. Further differences may occur due to the disturbance by sampling, transport and sample preparation. The effect of sample disturbance on the mechanical behavior of Onsøy clay was discussed by Lunne et al. (2006).In spite of these differences, the calibration conducted in the current study provides an adequate constitutive BSP model parameter set.
The natural Onsøy clay samples used by NGI/KIT (Wichtmann et al., 2013; Wichtmann, 2016) and by NGI (Bamberg, 2009) originate from the same sampling block from a depth of 10.5-11.0 m. The Onsøy clay samples used by RUB (Lieske, 2015; Müthing et al., 2017a; Müthing, 2017b) are provided by the NGI and originate from a slightly lower depth of 9.9-10.3 m and probably from a different borehole or even sampling site. Nevertheless, the material characteristics are very similar as shown in Table 6.1.

Table 6.1: Material characteristics of investigated Onsøy clay samples

Parameter	**Unit**	**RUB** (2015, 2017)	**NGI/KIT** (2013, 2016)	**NGI** (2009)
Depth	[m]	9.9-10.3	10.5-10.6	10.8-10.9
w_L	[%]	67.4	62.9-63.0	
w_P	[%]	29.6	29.3-32.6	
I_P	[%]	37.8	32.6-33.7	
ρ_s	$[\mathrm{g/cm^3}]$	2.77	2.78	

On the contrary, other tests by the NGI (Lunne et al., 2003) were conducted on samples from a larger depth of 11.4-11.5 m. However, they did not further specify the material characteristics of the samples from that particular depth.

CRS oedometer test

Bamberg (2009) performed various CRS oedometer tests to analyze the compression behavior of natural Onsøy clay. However, the CSR-Oed-B1-35 oedometer test is chosen for the constitutive BSP model parameter calibration in the present work. An overview of the CSR-Oed-B1-35 oedometer test on natural Onsøy clay from a depth of 10.8-10.9 m is presented in Table 6.2.
The oedometer test is conducted by applying a constant rate of axial strain $\dot{\varepsilon}_{\mathrm{a,max}} = 0.5\,\%/\mathrm{h}$. The strain rate is chosen in a way to avoid the excessive generation of excess pore-water pressure during the test. The fully water-saturated sample manifests an initial void ratio $e_0 = 1.91$. The testing procedure is composed of three phases such as a loading

Table 6.2: Overview of CSR-Oed-B1-35 oedometer test on natural Onsøy clay from a depth of 10.8-10.9 m (Bamberg, 2009)

Test No.	e_0 [-]	$\dot{\varepsilon}_\mathrm{a}$ [%/h]	$\sigma'_{\mathrm{a,L}}$ [kPa]	$\sigma'_{\mathrm{a,UL}}$ [kPa]	$\sigma'_{\mathrm{a,RL}}$ [kPa]
CSR-Oed-B1-35	1.91	0.5	205	70	720

phase until the effective axial stress reaches a value of $\sigma'_{\mathrm{a,L}} = 205\,\mathrm{kPa}$, followed by an unloading phase so the effective axial stress is decreased to $\sigma'_{\mathrm{a,UL}} = 70\,\mathrm{kPa}$ and a reloading phase with an increase of the effective axial stress to $\sigma'_{\mathrm{a,RL}} = 720\,\mathrm{kPa}$.

MLS oedometer test

Lieske (2015), Müthing et al. (2017a) and Müthing (2017b) performed MLS oedometer tests on reconstituted (MLS-Oed-rec) and natural (MLS-Oed-struc) samples to investigate the influence of the structure on the compression behavior. An overview of the MLS-Oed-rec and the MLS-Oed-struc oedometer tests on reconstituted and natural Onsøy clay from a depth of 9.9-10.3 m is presented in Table 6.3.
The reconstituted sample material is produced by mixing the natural sample material at a natural water content which corresponds to the liquid limit. Hence, the reconstitution procedure is in accordance with the suggestions of Burland (1990). Both samples are initially fully water-saturated exhibiting a similar initial void ratio e_0. The total load is applied at the top of the sample. The oedometer tests are examined using a multi-staged loading with a magnitude of the total axial stress $\sigma_{\mathrm{a,L}}$ of 10-20-50-100-200-400 kPa followed by a multi-staged unloading phase with a magnitude of the total axial stress $\sigma_{\mathrm{a,UL}}$ of 200-100-50-20-10 kPa. After each loading stage the clay sample is free to consolidate for 12 hours under the corresponding constant total load. The excess pore-water pressure converged to zero after each consolidation stage. Hence, the total and the effective axial stresses are equal at the end of each stage to have $\sigma'_{\mathrm{a,L}} = \sigma_{\mathrm{a,L}}$ and $\sigma'_{\mathrm{a,UL}} = \sigma_{\mathrm{a,UL}}$.
As a special feature the oedometer device is equipped with strain gauges to allow for the measurement of the total radial stress σ_{r} during one-dimensional compression. Consequently, the effective radial stress σ'_{r} can be back calculated afterwards. Hence, the

Table 6.3: Overview of MLS-Oed-rec and MLS-Oed-struc oedometer tests on reconstituted and natural Onsøy clay from a depth of 9.9-10.3 m (Lieske, 2015; Müthing et al., 2017a; Müthing, 2017b)

Test No.	e_0	$\sigma'_{\mathrm{a,L}}$	$\sigma'_{\mathrm{a,UL}}$
	[-]	[kPa]	[kPa]
MLS-Oed-rec	1.78	10-20-50-100-200-400	200-100-50-20-10
MLS-Oed-struc	1.82	10-20-50-100-200-400	200-100-50-20-10

experimental results are suitable to conduct an effective stress path analysis resulting in the determination of the coefficient of earth pressure at rest K_0 during elastoplastic loading and the Poisson's ratio ν during elastic unloading.

Monotonic CAUC and CAUE tests

Wichtmann et al. (2013) and Wichtmann (2016) conducted various CAUC and CAUE triaxial tests on natural Onsøy clay samples to investigate the undrained shear strength characteristics of the material. However, the CAUC-2 test in triaxial compression and the CAUE-8 in triaxial extension are chosen for the constitutive BSP model parameter calibration in the current study. To show the scatter in the laboratory test results the CAUC-6 and CAUC-10 tests in triaxial compression starting from the same anisotropic stress state are also mentioned. For reasons of comparison the CAUE-32 test in triaxial extension starting from more overconsolidated anisotropic initial stress conditions is also mentioned. An overview of the monotonic undrained triaxial tests on natural Onsøy clay from a depth of 10.5-10.6 m is given in Table 6.4.
The fully water-saturated samples of all tests are initially reconsolidated to the anisotropic effective in situ stress state $(\sigma'_{\mathrm{a}}, \sigma'_{\mathrm{r}})$. The void ratio $e_{\mathrm{consol.}}$ at the beginning of undrained shearing is determined via the measured water content after reconsolidation. The samples are sheared with a constant axial strain rate $\dot{\varepsilon}_{\mathrm{a,max}} = 1.4\,\%/\mathrm{h}$ until reaching axial strain values of $\varepsilon_{\mathrm{a,max,c}} = 20.0\,\%$ and $\varepsilon_{\mathrm{a,max,e}} = -20\,\%$ for triaxial compression and extension, respectively. The axial strain rate is chosen in a way to guarantee a homogeneous pore-water distribution in the sample.

Table 6.4: Overview of the monotonic undrained triaxial tests on natural Onsøy clay from a depth of 10.5-10.6 m (Wichtmann et al., 2013; Wichtmann, 2016)

Test No.	σ'_{a} [kPa]	σ'_{r} [kPa]	$e_{\mathrm{consol.}}$ [-]	$\dot{\varepsilon}_{\mathrm{a}}$ [%/h]	$\varepsilon_{\mathrm{a,max}}$ [%]
CAUC-2	68.1	40.9	1.74	1.4	20
CAUE-8	68.1	40.9	1.74	1.4	-20
CAUC-6	68.1	40.9	1.78	1.4	20
CAUC-10	68.1	40.9	1.76	1.4	20
CAUE-32	48.1	28.8	1.83	1.4	-20

Cyclic undrained triaxial tests

Wichtmann et al. (2013) and Wichtmann (2016) examined undrained cyclic triaxial tests under various initial shear stress conditions $q_{0,\mathrm{cyc}}$ and cyclic shear stress amplitudes Δq_{cyc} to investigate the undrained triaxial behavior under cyclic loading. However, the CAUcyc-40 test is chosen for the constitutive BSP model parameter calibration in the current study. An overview of the CAUcyc-40 triaxial test on natural Onsøy clay from a depth of 10.9-11.0 m is given in Table 6.5.

The fully water-saturated sample is initially reconsolidated to the anisotropic effective in situ stress state ($\sigma'_{\mathrm{a}} = 68.1\,\mathrm{kPa}, \sigma'_{\mathrm{r}} = 40.8\,\mathrm{kPa}$). The void ratio $e_{\mathrm{consol.}} = 1.75$ at the beginning of undrained shearing is determined via the measured water content after the reconsolidation. A cyclic axial loading is applied with a loading frequency 0.01 Hz. The undrained cyclic loading starts from the anisotropic effective in situ stress state with $q_{0,\mathrm{cyc}} = 27.3\,\mathrm{kPa}$ and a cyclic shear stress amplitude of $\Delta q_{\mathrm{cyc}} = \Delta\sigma_{\mathrm{a}} = \pm 22.6\,\mathrm{kPa}$ is chosen. The cyclic shear stress amplitude is achieved by cyclically applying a total axial stress increment $\Delta\sigma_{\mathrm{a}} = \pm 22.6\,\mathrm{kPa}$. Consequently, the total radial stress σ_{r} is kept constant during the test.

Table 6.5: Overview of the cyclic undrained triaxial test on natural Onsøy clay from a depth of 10.9-11.0 m (Wichtmann et al., 2013; Wichtmann, 2016)

Test No.	σ'_{a}	σ'_{r}	$e_{\mathrm{consol.}}$	$q_{0,\mathrm{cyc}}$	Δq_{cyc}	f
	[kPa]	[kPa]	[-]	[kPa]	[kPa]	[Hz]
CAUcyc-40	68.1	40.8	1.75	27.3	± 22.6	0.01

6.2 Experimental determination

6.2.1 BSP model parameters

The constitutive BSP model parameters with respect to the critical state soil mechanics and the Modified Cam-Clay model are measurable and can be directly determined from the results of the associated geotechnical laboratory tests.

- Swelling parameter κ
- Compression parameter λ
- Poisson's ratio ν
- Critical state stress ratio in compression M_{c}
- Critical state stress ratio in extension M_{e}
- $S_{\mathrm{i},0}$ defining the initial structure

Swelling parameter κ and compression parameter λ

In the present work the elastic swelling parameter κ and the elastoplastic compression parameter λ are determined from the volumetric behavior observed in oedometer tests. The volumetric behavior is represented by the semi-logarithmic effective axial stress σ'_{a} versus void ratio e diagram as shown in Figure 6.1a. In the present study $\kappa = 0.015$ and $\lambda = 0.16$ are obtained from the results of the CSR-Oed-B1-35 oedometer test on natural Onsøy clay. Whereat, κ and λ are calculated related to the effective axial stress σ'_{a} due to the lack of information on the effective radial stress σ'_{r} during the CSR-Oed-B1-35 oedometer test. This approximation is justifiable if assuming an almost constant K_0 value during the test.
It is to be noted that the elastic swelling parameter κ has to be preferentially evaluated in the very first part of the reloading/unloading path. This is because the material experiences a transition from purely elastic to elastoplastic behavior during further reloading/unloading. However, it can be stated that there is a slight deviation between the slope observed in the initial reloading phase and the unloading phase. Whereat, during the initial reloading the material behavior is softer showing a higher value of $\kappa = 0.017 - 0.020$ up to an axial stress level of 10-20 kPa. Whereas, the material behavior is stiffer during the unloading phase resulting in a differing value of $\kappa = 0.012$. This observation qualitatively and quantitatively conforms to the test results obtained by Mehli (2015). However,

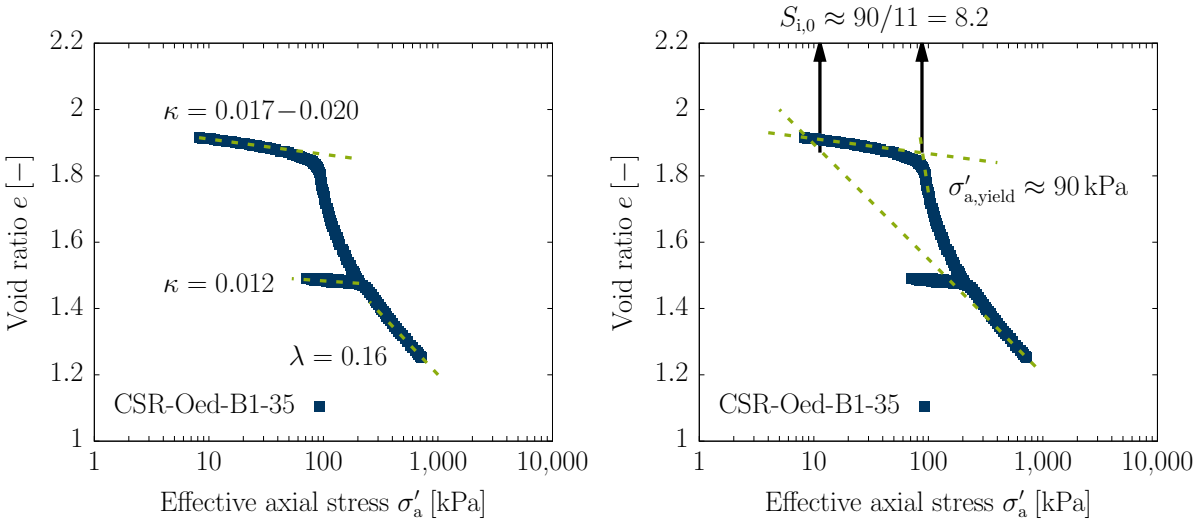

Figure 6.1: Determination of a) swelling parameter κ and compression parameter λ and b) effective axial yield stress $\sigma'_{a,yield}$ and first estimation of $S_{i,0}$ defining the initial structure from CSR-Oed-B1-35 oedometer test on natural Onsøy clay from a depth of 10.8-10.9 m (Bamberg, 2009)

in the present study an average value of $\kappa = 0.015$ is chosen, knowing that the material behavior might be modeled imprecisely dependent on the stress state.

In general, the elastoplastic compression parameter λ is related to the intrinsic material properties of a reconstituted and fully destructured sample. Nevertheless, in the present study λ is obtained from the same test on the natural Onsøy clay sample due to the absence of test results on a corresponding reconstituted sample under CRS conditions. Therefore, it is assumed that the destructuration process is almost completed at large effective axial stress in the range of $\sigma'_a = 600 - 700\,kPa$.

For reasons of comparison the volumetric behavior obtained from the MLS-Oed-struc and MLS-Oed-rec oedometer tests on natural and reconstituted Onsøy clay is displayed in Figure 6.2a. The swelling parameter $\kappa = 0.014$ (reconstituted) and $\kappa = 0.017$ (natural) and the compression parameter $\lambda = 0.18$ ascertained from the MLS-Oed-struc and MLS-Oed-rec oedometer tests match well with the parameters obtained from the CSR-Oed-B1-35 oedometer test. Moreover, it is confirmed that the elastic swelling index κ has to be evaluated in the first part of the reloading/unloading path only.

The elastoplastic compression parameter λ determined from the volumetric behavior of the reconstituted clay sample likewise fits well the intrinsic compression line as shown in Figure 6.3.

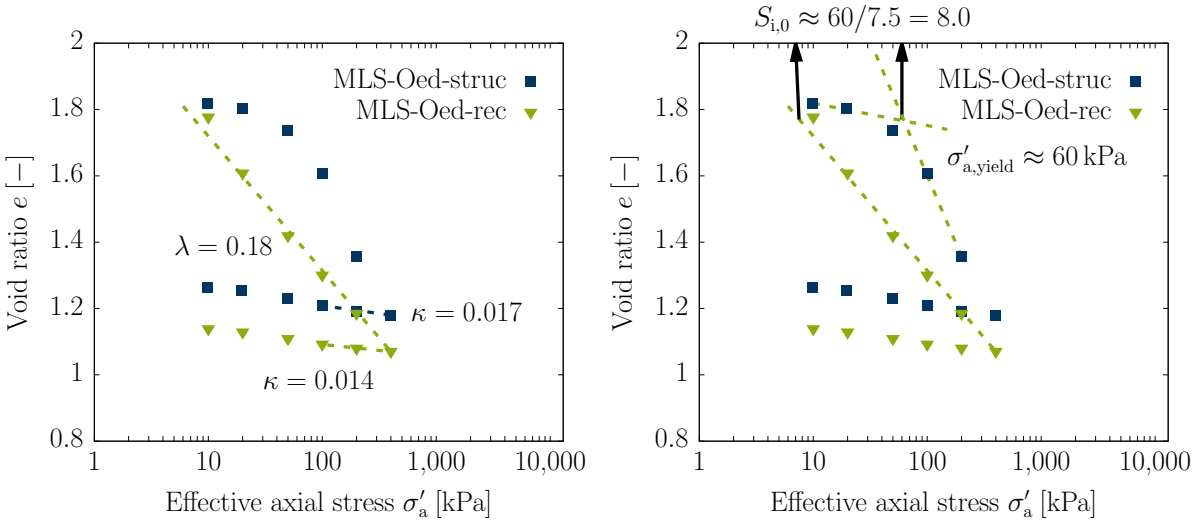

Figure 6.2: Determination of a) swelling parameter κ and compression parameter λ and b) effective axial yield stress $\sigma'_{a,yield}$ and first estimation of $S_{i,0}$ defining the initial structure from MLS-Oed-struc and MLS-Oed-rec oedometer tests on natural and reconstituted Onsøy clay from a depth of 9.9-10.3 m (Lieske, 2015; Müthing et al., 2017a; Müthing, 2017b)

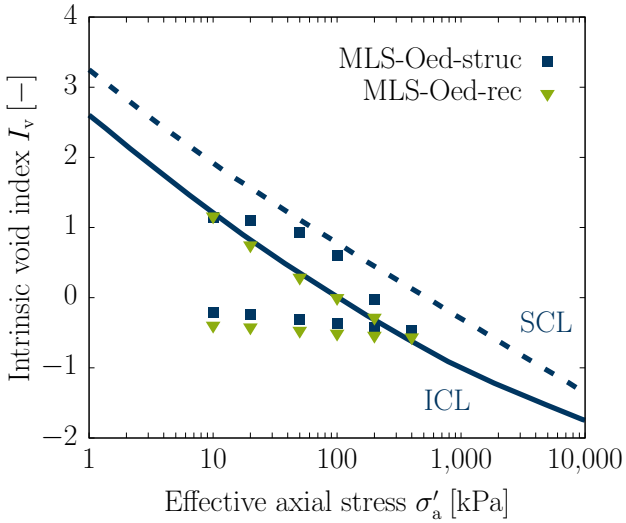

Figure 6.3: Classification of natural Onsøy clay with respect to ICL and SCL from oedometer tests MLS-Oed-struc (RUB) and MLS-Oed-rec (RUB)

Poisson's ratio ν

The Poisson's ratio ν is derived from the MLS-Oed-struc and MLS-Oed-rec oedometer tests on structured and reconstituted Onsøy clay. The measurement of the radial stress allows for the determination of the effective stress ratio q/p'. As an approximation the initial part of the $K_{0,\mathrm{ur}}$-unloading path after the anisotropic K_0-loading is assumed to be purely elastic. Hence, the corresponding increment of the effective stress ratio $\Delta q/\Delta p'$ is considered for the determination of the Poisson's ratio ν according to Equations 6.1-6.2.

$$\Delta q = \frac{3\ \{1-2\,\nu\}}{1+\nu}\,\Delta p' \tag{6.1}$$

$$\nu = \frac{\{3-\Delta q/\Delta p'\}}{\{6+\Delta q/\Delta p'\}} \tag{6.2}$$

The value of the Poisson's ratio obtained from the MLS-Oed-struc oedometer test on natural Onsøy clay is $\nu = 0.30$ as visualized in Figure 6.4a. However, the value of the Poisson's ratio obtained from the MLS-Oed-rec oedometer test on reconstituted Onsøy clay is slightly smaller between $\nu = 0.25$ and $\nu = 0.20$ as shown in Figure 6.5a.

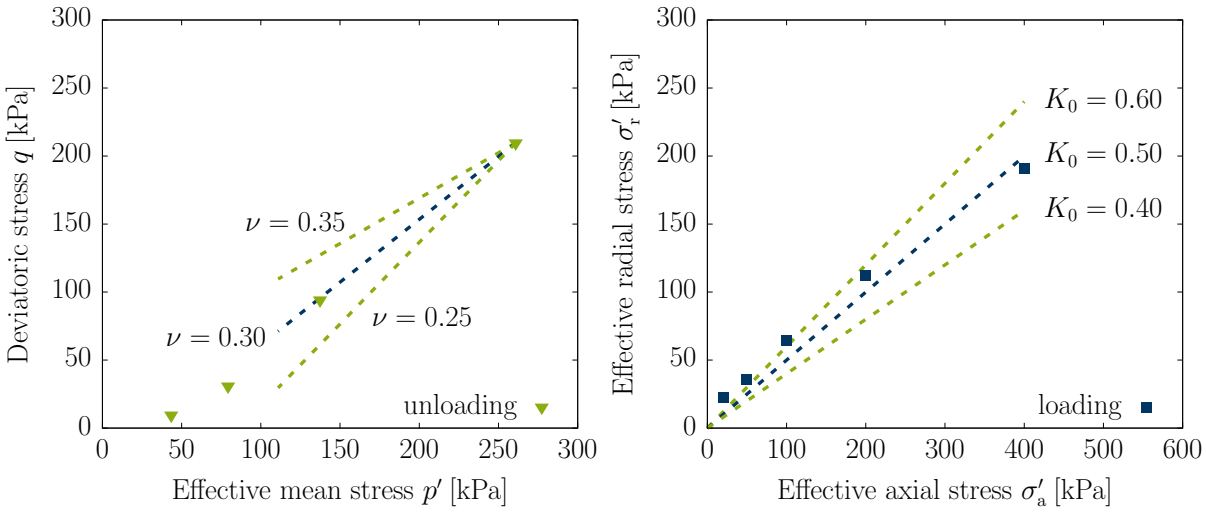

a) b)

Figure 6.4: Determination of a) Poisson's ratio ν and b) coefficient of earth pressure at rest K_0 from MLS-Oed-struc oedometer test on natural Onsøy clay from a depth of 9.9-10.3 m (Lieske, 2015; Müthing et al., 2017a; Müthing, 2017b)

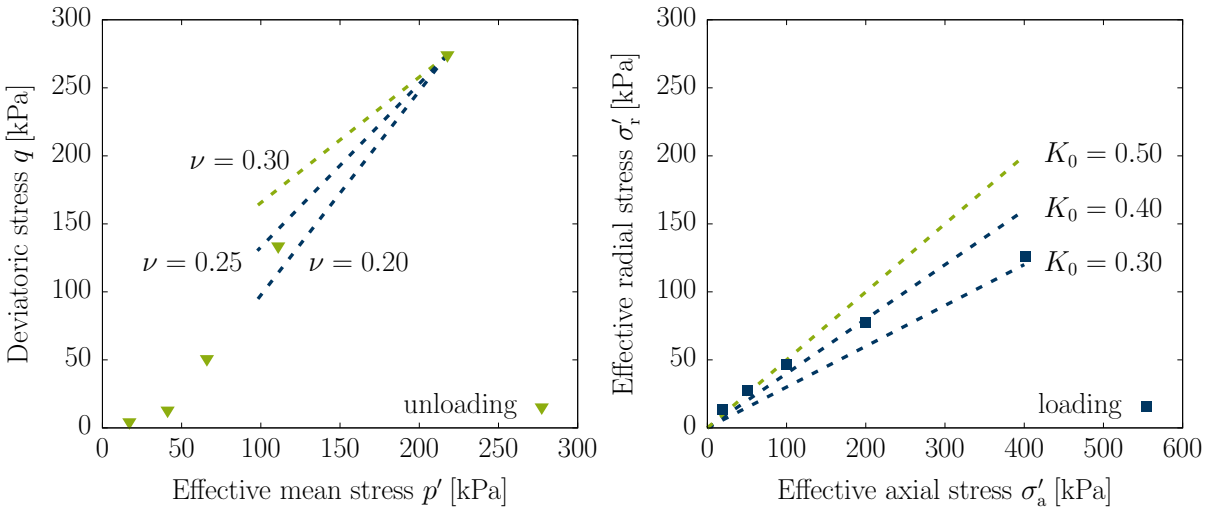

a) b)

Figure 6.5: Determination of a) Poisson's ratio ν and b) coefficient of earth pressure at rest K_0 from MLS-Oed-rec oedometer test on reconstituted Onsøy clay from a depth of 9.9-10.3 m (Lieske, 2015; Müthing et al., 2017a; Müthing, 2017b)

In the present study an average value of $\nu = 0.25$ is chosen, again knowing that the material behavior might be modeled imprecisely especially when destructuration is activated and the Poisson's ratio is decreasing.

Critical state stress ratios M_c and M_e in triaxial compression and extension

The values of the critical state stress ratios M_c and M_e are generally obtained from monotonic undrained triaxial tests in compression and extension, respectively. However, the anisotropically consolidated CAUC-2 and CAUE-8 tests on natural Onsøy clay are chosen in the present work. Anyway, the consolidation history before the undrained shearing should not affect the values of M_c and M_e. Furthermore, undrained triaxial tests are preferred over drained triaxial tests due to the less required time to conduct the test and the smaller magnitude of applied strain to reach the critical state.
The effective p', q stress paths of the CAUC-2 and CAUE-8 tests as visualized in Figure 6.6 allow for the direct determination of the critical state stress ratios $M_c = 1.44$ in triaxial compression and $M_e = 0.95$ in triaxial extension. The values of M_c and M_e are evaluated at 20 % of triaxial compression strain and -20 % of triaxial extension strain, respectively.

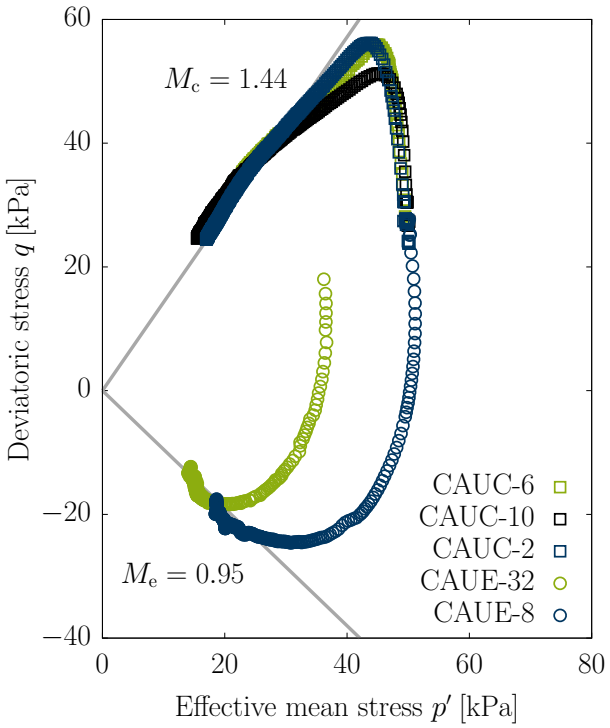

Figure 6.6: Determination of critical state stress ratios M_c and M_e from monotonic undrained triaxial tests on natural Onsøy clay from a depth of 10.5-10.9 m (Wichtmann et al., 2013; Wichtmann, 2016)

It is to be mentioned that the results of further undrained triaxial tests on different samples from the same block show a certain scatter of the effective stress path (Wichtmann et al., 2013; Wichtmann, 2016). Hence, there is a certain variation of the peak deviatoric stress, critical state stress ratio and magnitude of strain when reaching the critical state.

Constitutive BSP model parameter $S_{i,0}$

The amount of initial structure of the Onsøy clay is captured by the initialization of the structure variable S_i specified by an appropriate setting of the constitutive BSP model parameter $S_{i,0}$. As a first guess, the amount of initial structure can be related to the stress sensitivity S_σ as proposed by Cotecchia and Chandler (1997) and Cotecchia and Chandler (2000). Hence, the value of the constitutive BSP model parameter $S_{i,0}$ defining the initial structure can be estimated as the ratio between the effective axial yield stress $\sigma'_{a,yield}$ related to the structured state and the effective axial yield stress $\sigma'_{a,yield,rec}$ associated to the reconstituted state at the same void ratio.
In the present study an initial value of $S_{i,0} = 8.2$ is obtained from the CSR-Oed-B1-35

oedometer test on structured Onsøy clay as shown in Figure 6.1b. Whereat, the corresponding effective axial stress versus void ratio curve with respect to the reconstituted state is assumed to be the extrapolation of the stress-void ratio curve associated to the destructured state of the natural clay sample at large stress. The assumption is needed due to the lack of test results on the associated reconstituted clay. In comparison, the value of the constitutive model parameter $S_{\mathrm{i},0} = 8.0$ derived from the MLS-oed-struc and MLS-oed-rec oedometer tests on structured and reconstituted Onsøy clay as shown in Figure 6.2b is in good agreement. Due to the fact that the determination of the constitutive BSP model parameter $S_{\mathrm{i},0}$ following the approach of stress sensitivity is quite uncertain and represents just the oedometer loading case $S_{\mathrm{i},0}$ is incorporated in the inverse numerical analysis as well.

6.2.2 Initial conditions

The parameters defining the initial and in situ conditions can be also directly determined from the results of the associated geotechnical laboratory tests and field measurements.

- Initial void ratio e_0
- Coefficient of earth pressure at rest K_0
- Yield stress ratio YSR

Initial void ratio e_0

The void ratio e as an internal BSP model variable is initialized via an appropriate setting of the initial void ratio e_0, which is adapted to the initial conditions of the particular geotechnical laboratory test or boundary value problem.

Coefficient of earth pressure at rest K_0

The coefficient of earth pressure at rest K_0 for the elastoplastic loading defined according to Equation 6.3 is also determined from the MLS-Oed-struc oedometer test on natural Onsøy clay accounting for the measurement of the radial stress.

$$K_0 = \frac{\sigma'_{\mathrm{r}}}{\sigma'_{\mathrm{a}}} \tag{6.3}$$

The K_0 value can be determined by plotting the effective axial stress σ'_{a} versus the effective radial stress σ'_{r} as visualized in Figure 6.4b. It can be seen that the K_0 value is varying with the stress level. Whereat, the results at larger stress levels are more reliable due to the smaller relative error of the measurements and the smaller relative influence of the friction as compared to smaller stress levels. For the further analysis of the current study a value of $K_0 = 0.5$ is chosen since the initialization of the stress state demands for one constant value. The coefficient of earth pressure at rest K_0 is in accordance with the literature data for this specific depth as reported by Lunne et al. (2003) and displayed in Figure 2.5b in section 2.1. However, the value of $K_0 = 0.30 - 0.40$ obtained from the associated MLS-Oed-rec oedometer test on reconstituted Onsøy clay as given in Figure 6.5b is smaller. The K_0 value is used for the initialization of the anisotropic effective stress state of each stress point in the entire soil domain of a geotechnical boundary value problem.

Yield stress ratio YSR

The yield stress ratio $YSR \approx 1.35$ may be calculated according to Equation 6.4.

$$YSR = \frac{\sigma'_{\mathrm{a,yield}}}{\sigma'_{\mathrm{vertical,in\,situ}}} \tag{6.4}$$

Whereat, the effective vertical in situ stress $\sigma'_{\mathrm{vertical,in\,situ}}$ is derived with respect to the given depth of the associated soil sample and the unit weight under buoyancy γ'. According to Lunne et al. (2003) the value of the unit weight under buoyancy of natural Onsøy clay below the groundwater Table is assumed as $\gamma' = 6.35\,\mathrm{kN/m^3}$. Additionally, for the calculation of the mechanized tunneling boundary value problem the unit weight above the groundwater Table is assumed to be $\gamma = 16.35\,\mathrm{kN/m^3}$.
The effective axial yield stress $\sigma'_{\mathrm{a,yield}}$ is obtained from the distinct change in the stress-strain behavior observed in the CSR-Oed-B1-35 oedometer test on natural Onsøy clay. To be more specific, $\sigma'_{\mathrm{a,yield}}$ is determined from the semi-logarithmic effective axial stress-void ratio behavior as visualized in Figure 6.1b as suggested by Casagrande. Hence, in the present study $\sigma'_{\mathrm{a,yield}} \approx 90\,\mathrm{kPa}$ is defined as the effective stress state at the intersection of the tangents of the pre-yield and the post-yield behavior. The derived values of the effective axial yield stress $\sigma'_{\mathrm{a,yield}}$ and the yield stress ratio YSR from the CSR-Oed-B1-35 oedometer test are in good agreement with the literature data for this specific depth as reported by Lunne et al. (2003) and displayed in Figure 2.6 in chapter 2.1.

However, the value of the effective axial yield stress $\sigma'_{\mathrm{a,yield}} = 60\,\mathrm{kPa}$ determined from the MLS-Oed-struc oedometer test is somewhat lower than the value of the former test. This hypothesizes either different in situ conditions or a loss of structure during sampling, transport and sample preparation.
The yield stress ratio YSR can be used to initialize the size of the bounding surface via the isotropic hardening variable $p_{0,\mathrm{s}}$. This approach becomes especially relevant for the numerical analysis of geotechnical boundary value problems. To be more specific, for any stress point in the soil domain having an initial effective stress state $\boldsymbol{\sigma}'$ a corresponding stress state $\boldsymbol{\sigma}'_{\mathrm{BS,init}}$ on the initial bounding surface can be obtained via YSR as given in Equation 6.5. Accordingly, the initial value of the isotropic hardening variable $p_{0,\mathrm{s}}$ for any integration point can be calculated by solving the initial bounding surface formulation $F(\boldsymbol{\sigma}'_{\mathrm{BS,init}}) = 0$ for $p_{0,\mathrm{s}}$ as given in Equation 6.6.

$$\boldsymbol{\sigma}'_{\mathrm{BS,init}} = YSR\,\boldsymbol{\sigma}' \tag{6.5}$$

$$p_{0,\mathrm{s}} = \frac{3/2\,\left\{\boldsymbol{s}_{\mathrm{BS,init}} - p'_{\mathrm{BS,init}}\,\boldsymbol{\alpha}\right\} : \left\{\boldsymbol{s}_{\mathrm{BS,init}} - p'_{\mathrm{BS,init}}\,\boldsymbol{\alpha}\right\}}{\left\{M^2 - 3/2\,\left\{\boldsymbol{\alpha} : \boldsymbol{\alpha}\right\}\right\}\,p'_{\mathrm{BS,init}}} + p'_{\mathrm{BS,init}} \tag{6.6}$$

Alternatively, the isotropic hardening variable $p_{0,\mathrm{s}}$ controlling the size of the bounding surface may be directly initialized by an appropriate setting of the associated parameter $p_{0,\mathrm{s,init}}$, which has to account for the stress history of the natural structured clay. This alternative procedure is usually utilized for the numerical simulation of geotechnical laboratory tests rather than boundary value problems (BVP) since the value of $p_{0,\mathrm{s,init}}$ is not constant for the entire soil domain of the BVP.

6.3 Analytical determination

Among the non-measurable constitutive BSP model parameters some can be analytically calculated.

- N_{e} defining the shape of the bounding surface in triaxial extension
- α_0 defining the initial rotation of the bounding surface and the plastic potential surface
- $s_\alpha = z_\alpha$ controlling the bounding attractor of the fabric stress tensor

Constitutive BSP model parameter N_e

The constitutive BSP model parameter N_e controlling the shape of the bounding surface in extension is always defined according to Dafalias and Taiebat (2013) in a way that $N_e/N_c = M_e/M_c$ holds true to ensure the uniqueness of the critical state line. That is, the constitutive BSP model parameter is calculated by $N_e = N_c \{M_e/M_c\}$.

Constitutive BSP model parameter α_0

The initial rotation of the plastic potential surface is governed by the initialization of the anisotropic fabric stress tensor $\boldsymbol{\alpha}$ specified by a proper choice of the constitutive model parameter α_0. However, in the present study the bounding surface manifests the same rotation as the plastic potential surface governed by the same fabric stress tensor $\boldsymbol{\alpha}$. It is assumed that $\alpha_0 = \alpha_{K_0}$. This underlies the assumption that the rotation of the plastic potential surface under the K_0-loading during deposition and sedimentation has been stabilized at $\alpha \to \alpha_b = \alpha_{K_0}$.
The value of α_{K_0} is calculated according to Equations 6.7-6.9 as proposed by Dafalias (1986c) and Dafalias et al. (2006) independently of the rotational hardening rule. The closed-form relation incorporates the dilatancy expression for a drained K_0-loading path. A value of $K_0 = 0.5$ is inserted in accordance with the calibration before. Hence, the constitutive model parameter $\alpha_0 = \alpha_{K_0} = 0.23$ defines the initial rotation of the bounding surface and the plastic potential surface with respect to $K_0 = 0.5$.

$$\alpha_{K_0} = \frac{3/2\, B\, \eta_{K_0}^3 + \eta_{K_0}^2 + \{2\ \{1 - \{\kappa/\lambda\}\} - B\, M_c^2\}\, 3/2\, \eta_{K_0} - M_c^2}{3\ \{1 - \{\kappa/\lambda\}\}} \tag{6.7}$$

$$B = -\frac{2\ \{1+\nu\}}{9\ \{1-2\,\nu\}}\,\frac{\kappa}{\lambda} \tag{6.8}$$

$$\eta_{K_0} = \frac{3\ \{1-K_0\}}{\{1+2\,K_0\}} \tag{6.9}$$

It has to be mentioned that using the same fabric stress tensor $\boldsymbol{\alpha}$ for both surfaces causes the stabilization of the bounding surface and the plastic potential surface at the same rotation α_{K_0}, which is lower than the stress ratio η_{K_0} associated to the K_0-loading path. The general problem of the differences in the stress path is schematically illustrated in Figure 6.7.

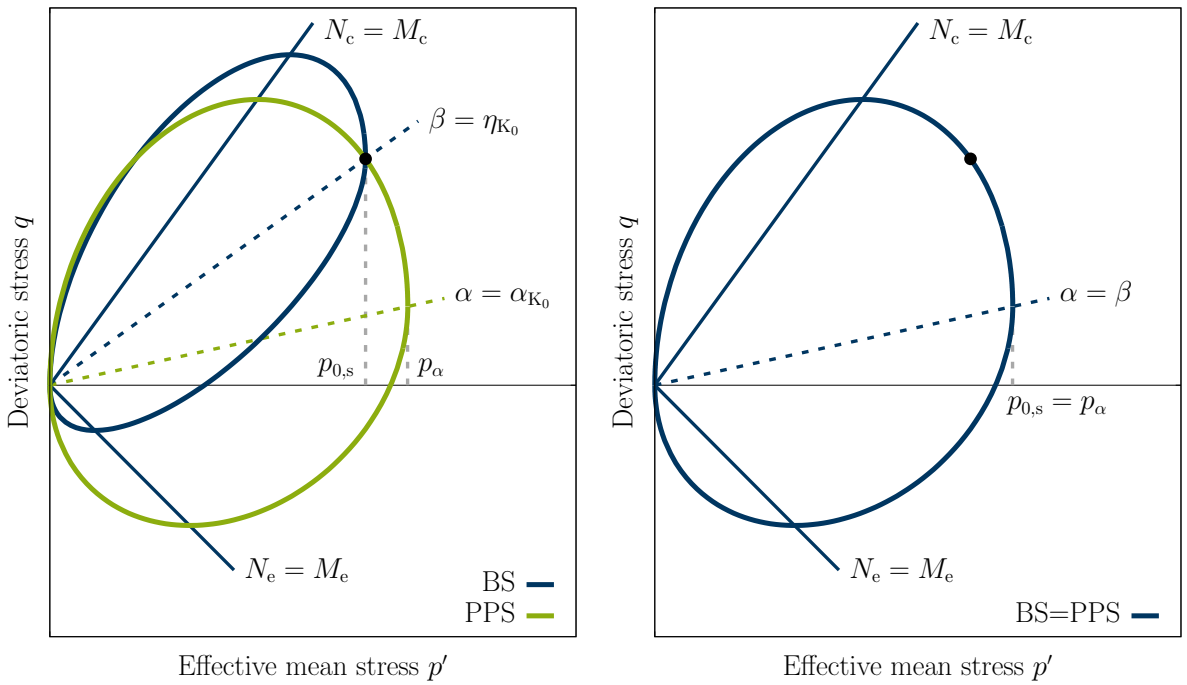

Figure 6.7: Schematic illustration of the rotation of the bounding surface BS and the plastic potential surface PPS a) $\alpha \neq \beta$ and b) $\alpha = \beta$

This may result in non-realistic material behavior under undrained shearing starting from a K_0-consolidated stress state on the bounding surface. This effect occurs because the undrained stress path is following the bounding surface, which is initially insufficiently rotated due to $\alpha_{K_0} < \eta_{K_0}$. Figure 6.7a shows the case if different fabric stress tensors $\boldsymbol{\alpha}$ and $\boldsymbol{\beta}$ are used for the plastic potential surface (PPS) and the bounding surface (BS), respectively. On the contrary, Figure 6.7b displays the case where both surfaces coincide due to the same fabric stress tensor $\boldsymbol{\alpha}$. However, the initial choice of the rotation does not drastically influence the model response because during further loading under a different stress ratio deviating from the consolidation stress ratio the surfaces will adjust themselves governed by the rotational hardening rule.

Constitutive BSP model parameters s_α and z_α

The constitutive BSP model parameters s_α and z_α, which are controlling the bounding attractor of the fabric stress tensor have to be mathematically determined solving Equation 6.10 to ensure a correct simulation of the K_0-loading path.

$$\alpha = \alpha_{\mathrm{b}} = \alpha_{\mathrm{K}_0} = \pm \frac{M_{\mathrm{c}}}{z_\alpha} \left\{ 1 - \exp\left(-s_\alpha \frac{|\eta_{\mathrm{K}_0}|}{M_{\mathrm{c}}} \right) \right\} \tag{6.10}$$

The calculation of s_α and z_α again underlies the assumption that in case of sufficiently large loading under the constant stress ratio η_{K_0} the rotation stabilizes at $\alpha \to \alpha_{\mathrm{b}} = \alpha_{\mathrm{K}_0}$ and the increment of rotation becomes zero, so that $\Delta\alpha = 0$. Consequently, α_{K_0} can be defined as given in Equation 6.10 by zeroing the increment of rotation in the Equations 3.15 and 3.17 as discussed in chapter 3. Furthermore, Dafalias and Taiebat (2014) figured out that the setting of $s_\alpha = z_\alpha$ is an appropriate assumption. In conclusion, Equation 6.10 has to be solved for $s_\alpha = z_\alpha$ with respect to a given α_{K_0} obtained according to Equation 6.7. Here, $\alpha_{\mathrm{K}_0} = 0.23$ is inserted in accordance with the calibration before. This leads to a graphical determination of the constitutive BSP model parameters $s_\alpha = z_\alpha = 6.1$ as shown in Figure 6.8.

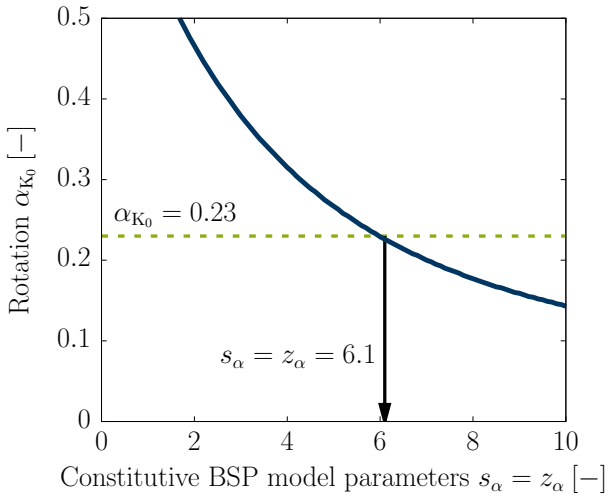

Figure 6.8: Graphical determination of the constitutive model parameters s_α and z_α for a given α_{K_0}

6.4 Inverse analysis

6.4.1 Concept

The calibration of the non-measurable constitutive BSP model parameters is conducted by employing the advanced concept of inverse numerical analysis as visualized in Figure 6.9. In brief, the constitutive BSP model parameters are identified via an inverse numerical analysis utilizing the particle swarm optimization (PSO) algorithm as proposed by Kennedy and Eberhart (1995) to minimize the objective function $F(\boldsymbol{P})$. Thereby $\boldsymbol{P} = \{p_1, ..., p_{N_{\mathrm{cp}}}\}$ specifies the constitutive BSP model parameter vector containing N_{cp} constitutive BSP model parameters which have to be identified.

The parameter identification by means of an automated inverse analysis is based on the mathematical solution of a constrained non-linear optimization problem. Initially, a particular geotechnical problem to be solved inversely such as a laboratory test, field test or boundary value problem has to be defined. The geotechnical problem is numerically simulated by a so-called adequate forward model considering the geometrical boundary conditions, the constitutive model describing the soil behavior, the physical processes and

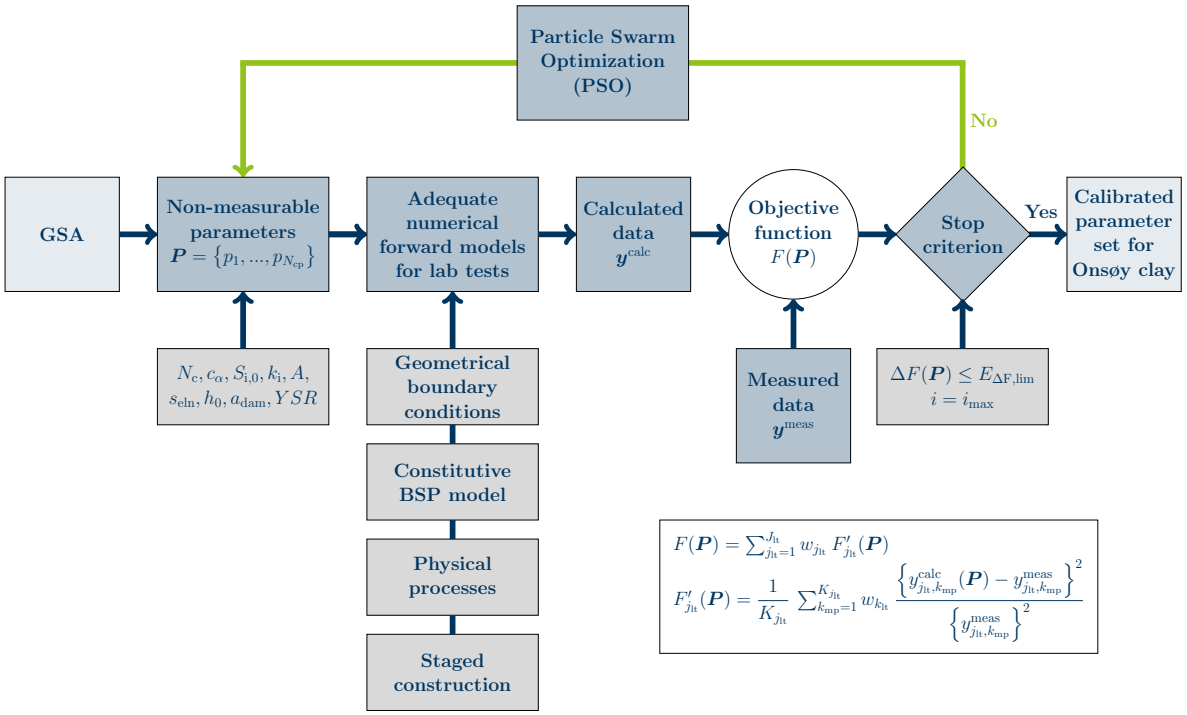

Figure 6.9: The concept of an adequate constitutive model parameter calibration based on the inverse numerical analysis approach

the staged construction. The objective function to be minimized provides a measure for the difference between the measurement and the numerical solution obtained from the corresponding numerical forward model. In the direct approach as originally introduced by Cividini et al. (1981) an initial subset of constitutive model parameters is iteratively changed according to the particular selected optimization strategy until the numerical solution and the measurements are matching sufficiently. That is, the defined objective function is properly minimized or a certain stop criteria is fulfilled. Finally, the iterative procedure results in a calibrated constitutive model parameter set.
The so-called forward calculations are the basis of the parameter identification. The oedometer test CSR-Oed-B1-35, the monotonic undrained triaxial tests CAUC-2 and CAUE-8 and the cyclic undrained triaxial test CAUcyc-40 are consecutively considered for the inverse analysis. Initially, the numerical simulation of a particular geotechnical laboratory test is conducted with respect to an initial constitutive BSP model parameter set. The initial parameter set is composed of the directly determined values of the measurable parameters according to Table 6.8 and an initial guess of the non-measurable parameters. The measurable parameters are assumed to be constant, whereas the non-measurable parameters may have to be optimized during the inverse analysis. Therefore, multiple simulations of the same geotechnical laboratory test with varying constitutive BSP model parameter sets are incorporated in the optimization procedure. Hence, an appropriate range of variation of the constitutive BSP model parameters with upper and lower bounds as given in Table 6.6 has to be defined in advance.
After each simulation, the relevant numerically calculated model responses are evaluated against the measured experimental data of the particular geotechnical laboratory test via an adequate objective function. The objective function quantifies the deviation of the calculated data from the measurement data. The objective function based on the normalized weighted least-squares approach is separately defined for each particular geotechnical laboratory test. If the value of the objective function does not fulfill a defined stop criterion the particle swarm optimization procedure is activated. The stop criterion may comprise the following conditions.

- The difference between the numerically calculated and the measured reference data are below a certain tolerance. That is, the value of the objective function is smaller than a certain tolerated error, so that $F(\boldsymbol{P}) \leq E_{\mathrm{F,tol}}$.

- The incremental minimization of the value of the objective function reaches a steady state. That is, the incremental changes of the minimum of the objective function are below a certain limit value, so that $\Delta F(\boldsymbol{P}) \leq E_{\Delta \mathrm{F,lim}}$.

- The maximum number of iterations of the PSO is reached so $i = i_{\max}$.

However, the constitutive BSP model parameters are identified considering the recommendations regarding the adequate choice of the geotechnical laboratory tests to be preferentially selected for the calibration of each non-measurable constitutive BSP model parameter. That is, a particular constitutive BSP model parameter is identified with respect to that geotechnical laboratory test or even testing phase where the BSP model response has the highest sensitivity to the variation of this particular constitutive BSP model parameter. Whereas, the constitutive BSP model parameters with a low relative influence on the BSP model response of that particular geotechnical laboratory test can be neglected. Hence, the particle swarm optimization is consecutively employed for each required geotechnical laboratory test to guarantee a most precise identification of the constitutive BSP model parameters. The results of the former PSO are successively incorporated in the consecutive PSO of the next geotechnical laboratory test.

6.4.2 Particle swarm optimization

The particle swarm optimization (PSO) was developed by Kennedy and Eberhart (1995) as an evolutionary population-based algorithm employing the concept of swarm intelligence. However, the PSO is a well accepted stochastic approach for solving complex optimization problems since the finding of the global minimum is emphasized rather than getting stuck to the finding of local minima. The gradient-free PSO is used to find the global minimum of the nonlinear objective function in the search space. The search of the minimum of the objective function is conducted by utilizing a population of individuals (swarm of particles) with a certain swarm intelligence in the N_{cp}-dimensional space. Whereat, N_{cp} is the number of constitutive BSP model parameters to be optimized. Moreover, the PSO is employed because it is robust against the initial guess of the constitutive BSP model parameters. A particle swarm consists of M_{sw} number of particles. Whereat, each particle represents a potential solution of the optimization problem in the N_{cp}-dimensional constitutive BSP model parameter space. To be more specific, a particle represents a certain constitutive BSP model parameter set used to find the global mimimum of the objective function, which incorporates the selected experimental data from the geotechnical laboratory tests.
During the iterative optimization process each particle m_{sw} mathematically updates its position $\boldsymbol{X}_{m_{\mathrm{sw}}}$ in the N_{cp}-dimensional constitutive BSP model parameter space with respect to the information on its previous own local best position $\boldsymbol{X}_{m_{\mathrm{sw}}}^{\mathrm{Local}}$ and the shared

information on the previous global best position $\boldsymbol{X}^{\mathrm{Global}}$ among all particles belonging to the swarm. Therein $m_{\mathrm{sw}} = 1, ..., M_{\mathrm{sw}}$ denotes the m_{sw}-th particle. To be more specific, each particle m_{sw} belonging to the swarm is defined by its current position $\boldsymbol{X}_{m_{\mathrm{sw}}}(i) = \left\{x_1(i), ..., x_{N_{\mathrm{cp}}}(i)\right\}$ in the N_{cp}-dimensional constitutive BSP model parameter space and its current velocity $\boldsymbol{V}_{m_{\mathrm{sw}}}(i) = \left\{v_1(i), ..., v_{N_{\mathrm{cp}}}(i)\right\}$, which governs the evolution of the particle towards the best position. Therein $i = 1, ..., i_{\max}$ denotes the i-th iterative evolution of the particle. Hence, the updated position $\boldsymbol{X}_{m_{\mathrm{sw}}}(i)$ of a particular particle m_{sw} is defined according to Equation 6.11 as the sum of its former position $\boldsymbol{X}_{m_{\mathrm{sw}}}(i-1)$ and its current velocity $\boldsymbol{V}_{m_{\mathrm{sw}}}(i)$. Furthermore, the current velocity $\boldsymbol{V}_{m_{\mathrm{sw}}}(i)$ of a particular particle m_{sw} is composed of three terms as defined in Equation 6.12. The first term known as momentum includes the former velocity $\boldsymbol{V}_{m_{\mathrm{sw}}}(i-1)$ of a particular particle m_{sw} multiplied by an inertia weight coefficient $\Omega(i)$ to control the influence of the former velocity. Whereat, $\Omega(i)$ can be assumed to be constant or linearly decreasing between its maximum and minimum values with increasing iteration number. The second term known as cognitive component and the third term known as social component account for the evolution of the particle from its former position $\boldsymbol{X}_{m_{\mathrm{sw}}}(i-1)$ towards the local own best position $\boldsymbol{X}^{\mathrm{Local}}_{m_{\mathrm{sw}}}$ and towards the global best position $\boldsymbol{X}^{\mathrm{Global}}$ among all particles within the entire swarm. c_1 and c_2 are constant learning factors and r_1 and r_2 are independent random numbers between zero and one used to weight the preference of the evolution towards the local or global minima.

$$\boldsymbol{X}_{m_{\mathrm{sw}}}(i) = \boldsymbol{X}_{m_{\mathrm{sw}}}(i-1) + \boldsymbol{V}_{m_{\mathrm{sw}}}(i) \tag{6.11}$$

$$\begin{aligned}\boldsymbol{V}_{m_{\mathrm{sw}}}(i) = {} & \Omega(i)\, \boldsymbol{V}_{m_{\mathrm{sw}}}(i-1) + c_1\, r_1\, \left\{\boldsymbol{X}^{\mathrm{Local}}_{m_{\mathrm{sw}}} - \boldsymbol{X}_{m_{\mathrm{sw}}}(i-1)\right\} \\ & + c_2\, r_2\, \left\{\boldsymbol{X}^{\mathrm{Global}} - \boldsymbol{X}_{m_{\mathrm{sw}}}(i-1)\right\}\end{aligned} \tag{6.12}$$

The PSO algorithm generally works according to the following scheme. At first the particle swarm with a certain number of particles M_{sw} is randomly initialized. That is, for each single particle m_{sw} of the swarm the initial position and initial velocity of motion is randomly set. Afterwards, an iterative optimization loop including the evolution of the particle swarm towards the best position is conducted and repeated until the value of the objective function fulfills the stop criterion.

At the beginning of each iteration the global best position $\boldsymbol{X}^{\mathrm{Global}}$ is determined. Whereat, $\boldsymbol{X}^{\mathrm{Global}}$ among all particles of the entire swarm is evaluated with respect to the minimum value of the objective function. In the following the velocity $\boldsymbol{V}_{m_{\mathrm{sw}}}(i)$ and the position $\boldsymbol{X}_{m_{\mathrm{sw}}}(i)$ of each particle m_{sw} belonging to the swarm are updated according to the cor-

responding functions 6.11 - 6.12 considering the local own best position $\boldsymbol{X}_{m_{\mathrm{sw}}}^{\mathrm{Local}}$ and the global best position $\boldsymbol{X}^{\mathrm{Global}}$. Afterwards, for each particle m_{sw} the value of the objective function $F(\boldsymbol{P}) = F(\boldsymbol{X}_{m_{\mathrm{sw}}}(i))$ is derived by conducting the forward calculation composed of the numerical simulations of the chosen geotechnical laboratory tests and comparing the numerically calculated data with the selected measurement reference data. If the value of the objective function derived in the current iteration is less than the own minimum value obtained in former iterations, so that $F(\boldsymbol{X}_{m_{\mathrm{sw}}}(i)) < F(\boldsymbol{X}_{m_{\mathrm{sw}}}^{\mathrm{Local}})$ the current position of the particle is stored as the own best position. If any local minimum value is smaller than the global minimum value, so that $F(\boldsymbol{X}_{m_{\mathrm{sw}}}(i)) < F(\boldsymbol{X}^{\mathrm{Global}})$ the global best position is updated accordingly. Finally, it is checked if the stop criterion is met. If the stop criterion is fulfilled the optimization is successfully completed while otherwise a new iterations starts.

6.4.3 Constitutive BSP model parameters

The number of non-measurable constitutive BSP model parameters which have to be identified via inverse analysis utilizing the particle swarm optimization is chosen to $N_{\mathrm{cp}} = 9$ in the present work. To be more specific, the constitutive BSP model parameter vector yield $\boldsymbol{P} = \{p_1, ..., p_{N_{\mathrm{cp}}}\} = \{N_{\mathrm{c}}, c_\alpha, S_{\mathrm{i},0}, k_{\mathrm{i}}, A, s_{\mathrm{eln}}, h_0, a_{\mathrm{dam}}, p_{0,\mathrm{s,init}}/YSR\}$. Within the numerical simulation of the geotechnical laboratory test the hardening variable $p_{0,\mathrm{s}}$ controlling the size of the rotated bounding surface is initialized either by an appropriate setting of the associated parameter $p_{0,\mathrm{s,init}}$ or by setting of an adequate value of the yield stress ratio YSR. Both parameters have to account for the stress history of the natural structured clay. Consequently, either $p_{0,\mathrm{s,init}}$ or YSR are incorporated in the inverse numerical analysis as well. The range of variation of the constitutive BSP model parameters are chosen according to the author's experience and the available literature data related to other natural clays. However, the lower and upper bounds are adopted if the achieved solution corresponds to a constitutive BSP model parameter on the parameter space boundary. The defined ranges of variation of the constitutive BSP model parameters for the optimization problem are summarized in Table 6.6.

6.4.4 Numerical testing program

The oedometer test CSR-Oed-B1-35, the monotonic undrained triaxial tests CAUC-2 and CAUE-8 and the cyclic undrained triaxial test CAUcyc-40 are considered as the inverse problems to be solved for the calibration of the constitutive BSP model parameters. All

Table 6.6: Overview of the range of variation of the constitutive BSP model parameters calibrated via inverse analysis using particle swarm optimization

Parameter	Unit	Range
N_c	[-]	[1.10,1.44]
N_e	[-]	$N_c\,\{M_e/M_c\}$
c_α	[-]	[0,100]
$S_{i,0}$	[-]	[2,12]
k_i	[-]	[0.5,1.5]
A	[-]	[0,1]
s_{eln}	[-]	[1,1.5]
h_0	[-]	[50,500]
a_{dam}	[-]	[0,100]
$p_{0,s,init}$	[kPa]	[60,90]
YSR	[-]	[1.2,1.4]

geotechnical laboratory tests are numerically simulated by use of an integration point algorithm. The initial effective stress state as well as the loading and displacement patterns as discussed in section 6.1 are applied as corresponding stress and strain boundary conditions according to Tables 6.2, 6.4 and 6.5. Furthermore, the drained and undrained hydraulic boundary conditions are defined in accordance with the real conditions of the geotechnical laboratory tests. However, the consolidation procedure is not explicitly taken into account in the numerical simulation. That is, the numerical simulation of undrained triaxial shearing starts from the initial effective stress state initially assuming zero excess pore-water pressure. Moreover, the effects of time-dependence, strain rate and cyclic loading frequency are not considered in the numerical simulations.

6.4.5 Objective function

A multitude of BSP model responses which have to be matched may result in a complex and composite objective function. A strategy for multi-objective decision making (MODM) and a multi-objective optimization has to be applied considering the preferences and constraints given by the decision maker (Papon et al., 2005). The objective function

$F(\boldsymbol{P})$ to be minimized is formulated following the concept of normalized weighted least-squares as given in Equations 6.13-6.14. The objective function $F(\boldsymbol{P})$ used in the current study is a composite multi-objective function formulated as the sum of the error measures $F'_{j_{\mathrm{lt}}}(\boldsymbol{P})$ with respect to the J_{lt} sets of measurement data obtained from J_{lt} different geotechnical laboratory tests. Thereby $\boldsymbol{P} = \left\{p_1, ..., p_{n_{\mathrm{cp}}}\right\}$ specifies the vector containing N_{cp} constitutive BSP model parameters, which has to be identified as already discussed before. Moreover, the importance of a particular geotechnical laboratory test j_{lt} can be emphasized by the user-defined setting of a corresponding positive weighting factor $w_{j_{\mathrm{lt}}}$ and $j_{\mathrm{lt}} = 1, ..., J_{\mathrm{lt}}$ denotes the j_{lt}-th geotechnical laboratory test.

$$F(\boldsymbol{P}) = \sum_{j_{\mathrm{lt}}=1}^{J_{\mathrm{lt}}} w_{j_{\mathrm{lt}}} \, F'_{j_{\mathrm{lt}}}(\boldsymbol{P}) \tag{6.13}$$

$$F'_{j_{\mathrm{lt}}}(\boldsymbol{P}) = \frac{1}{K_{j_{\mathrm{lt}}}} \sum_{k_{\mathrm{mp}}=1}^{K_{j_{\mathrm{lt}}}} w_{k_{\mathrm{lt}}} \frac{\left\{y^{\mathrm{calc}}_{j_{\mathrm{lt}},k_{\mathrm{mp}}}(\boldsymbol{P}) - y^{\mathrm{meas}}_{j_{\mathrm{lt}},k_{\mathrm{mp}}}\right\}^2}{\left\{y^{\mathrm{meas}}_{j_{\mathrm{lt}},k_{\mathrm{mp}}}\right\}^2} \tag{6.14}$$

The error measure $F'_{j_{\mathrm{lt}}}(\boldsymbol{P})$ is defined as the mean value of the sum of the normalized weighted squared errors of $K_{j_{\mathrm{lt}}}$ measurement points related to a particular geotechnical laboratory test j_{lt}, $y^{\mathrm{meas}}_{j_{\mathrm{lt}},k_{\mathrm{mp}}}$ denotes the experimental measurement data and $y^{\mathrm{calc}}_{j_{\mathrm{lt}},k_{\mathrm{mp}}}(\boldsymbol{P})$ denotes the corresponding numerically calculated BSP model responses with respect to the constitutive BSP model parameter set $\boldsymbol{P}$. The number of measurement points $K_{j_{\mathrm{lt}}}$ is different for each geotechnical laboratory test j_{lt} since they are adopted with respect to the volumetric and deviatoric stress-strain behavior and the evolution of the excess pore-water pressure obtained in the corresponding test. Hence, the mean value is used for the error measure by applying the term $1/K_{j_{\mathrm{lt}}}$. The squared difference between the data from the numerical calculation and the measurements $\left\{y^{\mathrm{calc}}_{j_{\mathrm{lt}},k_{\mathrm{mp}}}(\boldsymbol{P}) - y^{\mathrm{meas}}_{j_{\mathrm{lt}},k_{\mathrm{mp}}}\right\}^2$ related to a particular measurement point k_{mp} is normalized by $\left\{y^{\mathrm{meas}}_{j_{\mathrm{lt}},k_{\mathrm{mp}}}\right\}^2$ to eliminate scaling effects and $k_{\mathrm{mp}} = 1, ..., K_{j_{\mathrm{lt}}}$ denotes the k_{mp}-th measurement point of the associated laboratory test j_{lt}. The normalization is needed since the measured quantities may manifest different orders of magnitude. Furthermore, the importance of each measurement point k_{mp} can be highlighted by the user-defined setting of the corresponding weighting factor $w_{k_{\mathrm{mp}}}$. The constitutive BSP model parameters are identified with respect to one particular laboratory test at each time. That is, one inverse analysis including the particle swarm optimization is conducted per test (e.g. oedometer test, CAUC test, CAUE test and CAUcyc tests). A weighting of the importance of the different measurement points is neglected in the current study, so that $w_{j_{\mathrm{lt}}} = w_{k_{\mathrm{mp}}} = 1$. Since the number of measurement points $K_{j_{\mathrm{lt}}}$

is chosen in dependence of the volumetric and deviatoric stress-strain behavior and the evolution of excess pore-water pressure it varies for each geotechnical laboratory test j_{lt}.

- CSR-Oed-B1-35 oedometer test: Eight measurement points with respect to the effective axial stress σ'_{a} vs. void ratio e behavior are chosen, so that $\boldsymbol{y}^{\mathrm{meas}}_{\mathrm{oed}} = (e_1, ..., e_8)$. The effective axial stress at which the void ratio is evaluated is selected to be σ'_{a} = 75, 100, 150, 205, 70, 205, 400, 720 kPa. The measurement points are chosen in a way to capture the predominantly elastic preyield behavior inside the bounding surface, the elastoplastic transition, the postyield behavior including the progressive degradation of the structure, the unloading and reloading behavior within the bounding surface and the behavior of the fully destructured material at large stress.

- CAUC-2 monotonic undrained triaxial compression test: Two times seven measurement points each related to the axial strain ε_{a} vs. deviatoric stress q behavior and the axial strain ε_{a} vs. excess pore-water pressure Δp_{w} behavior are selected, so that $\boldsymbol{y}^{\mathrm{meas}}_{\mathrm{CAUC}} = (q_1, ..., q_7, \Delta p_{\mathrm{w},1}, ..., \Delta p_{\mathrm{w},7})$. The measurement points with respect to the deviatoric stress and the excess pore-water pressure are evaluated at the same axial strain. The axial strain at which the deviatoric stress and the excess pore-water pressure are evaluated is chosen to be 0.3, 0,6, 1.5, 3.0, 5.0, 10.0, 20.0%. The measurement points are selected in a way to consider the pre-peak deviatoric stress-strain behavior, the maximum deviatoric peak stress and the post-peak softening and destructuration behavior. Furthermore, the continuous evolution of the excess pore-water pressure during undrained shearing is taken into consideration. However, measurement points with respect to the effective mean stress are not explicitly defined. The development of the effective mean stress is directly related to the development of the deviatoric stress and the excess pore-water pressure by the effective stress concept.

- CAUE-8 monotonic undrained triaxial extension test: Two times nine measurement points with respect to the axial strain ε_{a} vs. deviatoric stress q behavior and the axial strain ε_{a} vs. excess pore-water pressure Δp_{w} behavior are selected, so that $\boldsymbol{y}^{\mathrm{meas}}_{\mathrm{CAUE}} = (q_1, ..., q_9, \Delta p_{\mathrm{w},1}, ..., \Delta p_{\mathrm{w},9})$. The measurement points with respect to the deviatoric stress and the excess pore-water pressure are evaluated at the same axial strain state. The axial strain at which the deviatoric stress and the excess pore-water pressure are evaluated is selected to be 0.1, 0.3, 0.5, 0.7, 1.0, 2.0, 5.0, 10.0, 20.0%. The measurement points are chosen in a way to capture the development of the negative excess pore-water pressure during undrained shearing up to the peak value where a reversal of the excess pore-water pressure takes place. The post-peak

increase of the excess pore-water pressure until reaching positive values is taken into consideration as well. Moreover, the chosen measurement points account for the deviatoric stress-strain behavior firstly showing a continuous decrease of the deviatoric stress towards the critical state in extension with increasing axial strain followed by a slight increase of the deviatoric stress in the vicinity of the critical state.

- CAUcyc-40 cyclic undrained triaxial test: Ten measurement points with respect to the axial strain ε_{a} vs. deviatoric stress q behavior within the first five cycles are selected, so that $\boldsymbol{y}^{\mathrm{meas}}_{\mathrm{CAUcyc}} = (\varepsilon_{\mathrm{a},1}, ..., \varepsilon_{\mathrm{a},10})$. The axial strain is evaluated at the maximum and minimum peak values of the deviatoric stress of each cycle, which are predefined by the cyclic stress amplitude Δq_{cyc}. The measurement points are selected in a way to account for the degradation of stiffness and the accumulation of plastic strain during undrained cyclic loading.

In this study the errors in the experiments and in the measurement technique are neglected. Hence, it is assumed that the testing data are certain, which is obviously not the case in reality.

6.4.6 Settings of PSO

To sum up, $N_{\mathrm{cp}} = 9$ constitutive BSP model parameters have to be identified by the particle swarm optimization. The required number of swarm particles $M_{\mathrm{sw}} = 250$ and the number of iterations $i_{\max} = 50$ are derived from several trial and error runs of the particle swarm optimization. The values are chosen in a way that for any case the objective function is sufficiently minimized and convergence towards the tolerated limiting value $E_{\Delta \mathrm{F,lim}} = 10^{-6}$ of the incremental change is ensured.
However, the application of a specific value for the tolerated error $E_{\mathrm{F,tol}}$ is neglected since it is strongly dependent on the formulation of the objective function. Hence, the evolution of the particles stops if either a steady state is achieved, so that $\Delta F(\boldsymbol{P}) = \Delta F(\boldsymbol{X}^{\mathrm{Global}}) \leq E_{\Delta \mathrm{F,lim}}$ or the maximum number of iterations is reached, so that $i = i_{\max}$. Since the focus is set on finding the global minimum of the objective function the learning parameters $c_1 = 1$ and $c_2 = 2$ are chosen in a way to prefer a particle evolution towards the global minimum rather than the local own best position. Moreover, the value of the inertia weight $\Omega = 0.9$ is kept constant during the iterations. A summary of the PSO parameters related to the settings of the particle swarm optimization is given in Table 6.7.

Table 6.7: Settings of the particle swarm optimization

PSO parameter	**Value** [-]
Number of constitutive BSP model parameters N_{cp}	9
Number of swarm particles M_{sw}	250
Limiting value $E_{\Delta \mathrm{F,lim}}$	10^{-6}
Maximum number of iterations i_{max}	50
Inertia weight Ω	0.9
Learning parameter c_1	1
Learning parameter c_2	2

6.5 Results of calibration

6.5.1 BSP model parameter set for natural Onsøy clay

The resulting constitutive BSP model parameter set for natural Onsøy clay identified from the combined calibration via direct experimental and analytical determination and automated inverse analysis using the particle swarm optimization is summarized in Table 6.8. The specific value of each constitutive BSP model parameter and the corresponding test used for direct determination and inverse analysis are given in accordance with the recommendations regarding the most suitable geotechnical laboratory tests based on the global sensitivity analysis. To conclude, the adequate constitutive BSP model parameter set for natural Onsøy clay represents the common input for the most accurate numerical approximation considering all geotechnical laboratory tests.

6.5.2 BSP model performance regarding monotonic tests

The comparison between the numerically simulated material behavior of natural Onsøy clay and the associated measurements regarding the oedometer test CSR-Oed-B1-35, the undrained triaxial tests CAUC-2 and CAUE-8 and the cyclic undrained triaxial tests CAUcyc-40 is visualized in Figures 6.10 to 6.15. It can be observed that the numerically simulated material behavior of the monotonic geotechnical laboratory tests such as CSR-Oed-B1-35 oedometer test, CAUC-2 test and CAUE-8 test closely matches the experimental measurements as visualized in Figures 6.10 to 6.12.

Table 6.8: Overview of the calibrated constitutive BSP model parameter set related to natural Onsøy clay (opt. is the abbreviation for optimized)

Type	Parameter	Unit	Value	Test No./Equation
Critical state soil mechanics MCC	κ	[-]	0.015	CSR-Oed-B1-35
	ν	[-]	0.25	MLS-Oed-struc/rec
	λ	[-]	0.16	CSR-Oed-B1-35
	M_c	[-]	1.44	CAUC-2
	M_e	[-]	0.95	CAUE-8
Non-associated flow rule	N_c	[-]	1.35	opt. for CAUC-2 & CAUE-8
	N_e	[-]	0.89	$N_e = N_c \{M_e/M_c\}$
Anisotropy and rotational hardening	$\alpha_0 = \alpha_{K_0}$	[-]	0.23	Equation 6.7
	c_α	[-]	15	opt. for CAUE-8
	$s_\alpha = z_\alpha$	[-]	6.1	Equation 6.10
Structure and destructuration	$S_{i,0}$	[-]	8.5	opt. for Oed-B1-35
	k_i	[-]	1.2	opt. for Oed-B1-35, CAUC-2/CAUE-8
	A	[-]	0.3	opt. for CAUE-8
Bounding surface plasticity	s_{eln}	[-]	1.3	opt. for CAUE-8
	h_0	[-]	250	opt. for Oed-B1-35, CAUC-2/CAUE-8
	a_{dam}	[-]	20	opt. for Oed-B1-35
Initial conditions	e_0	[-]		adapted to particular test/BVP
	K_0	[-]	0.5	MLS-Oed-struc
	$p_{0,s,init}$	[kPa]	68	opt. for Oed-B1-35
	YSR	[-]	1.35	opt. for CAUC-2 & CAUE-8
Additional parameters	γ	[kN/m^3]	16.35	Lunne et al. (2003)
	γ'	[kN/m^3]	6.35	Lunne et al. (2003)

This observation holds true for the axial stress vs. void ratio behavior for the CSR-Oed-B1-35 oedometer test and the effective stress path, the axial strain vs. deviatoric stress behavior and the axial strain vs. excess pore-water pressure behavior for the CAUC-2 and the CAUE-8 tests.

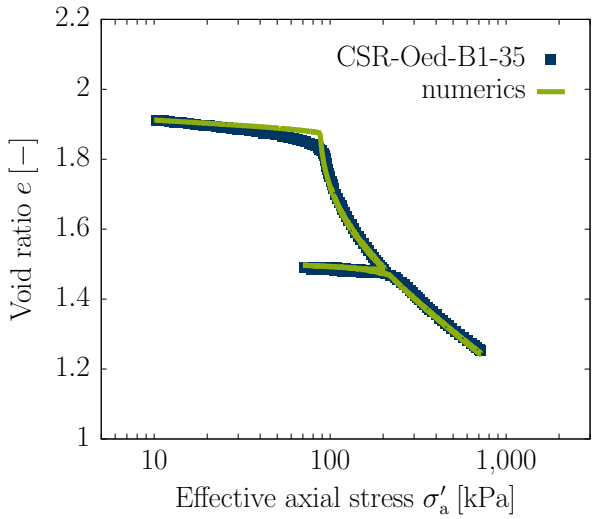

Figure 6.10: Numerically simulated effective axial stress vs. void ratio behavior from the CSR-Oed-B1-35 oedometer test on natural Onsøy clay in comparison with the associated measurements

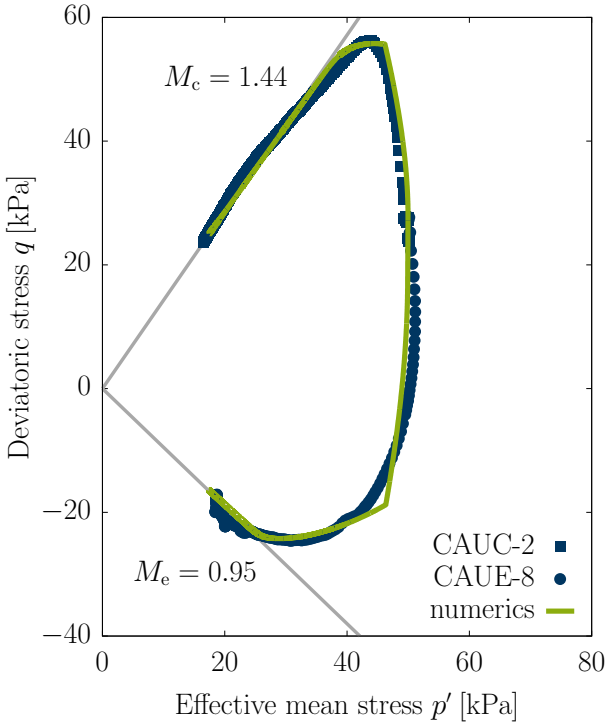

Figure 6.11: Numerically simulated effective p', q stress path from the CAUC-2 and CAUE-8 tests on natural Onsøy clay in comparison with the associated measurements

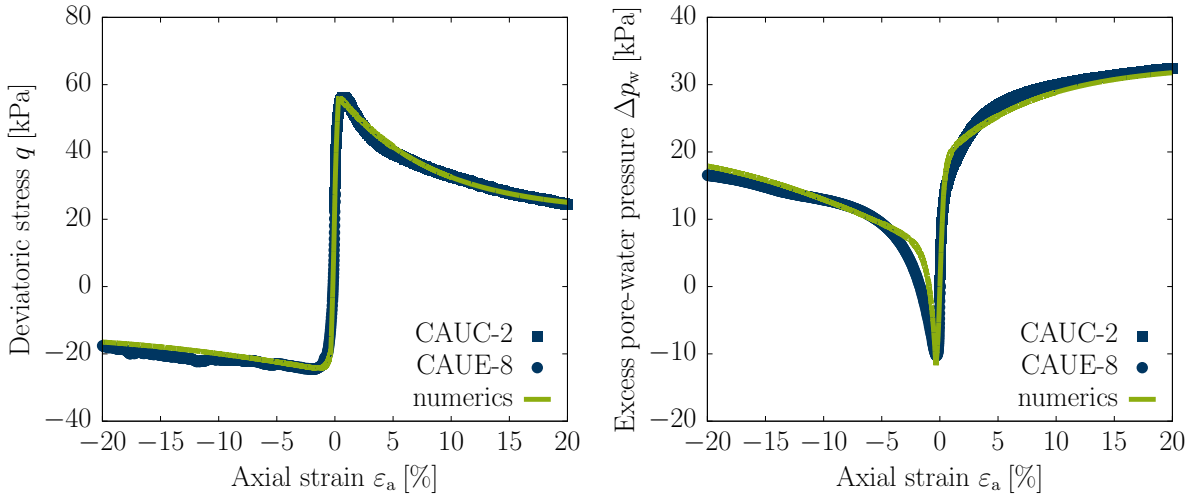

a) b)

Figure 6.12: Numerically simulated a) axial strain vs. deviatoric stress behavior and b) axial strain vs. excess pore-water pressure behavior from the CAUC-2 and CAUE-8 tests on natural Onsøy clay in comparison with the associated measurements

Especially, the typical destructuration behavior of natural clay can be adequately simulated both in the oedometer test after reaching the yield stress and in the CAU tests in compression and extension after reaching the peak deviatoric stress. It has to be noted that for an adequate simulation of the CAUC-2 and the CAUE-8 tests (as well as the CAUcyc-40 test) the constitutive BSP model parameter $S_{i,0}$ governing the initial structure at the beginning of the tests has to be reduced to $S_{i,0,CAU} = 2.9$. That is, the initial structure of the samples is already partly destroyed after reconsolidation to the anisotropic in situ stress state and before starting the undrained triaxial shearing. The decreased amount of initial structure from $S_{i,0,oed} = 8.5$ to $S_{i,0,CAU} = 2.9$ also corresponds to the reduced initial void ratio from $e_{0,oed} = 1.91$ to $e_{consol.,\,CAU} = 1.74$ at the beginning of the CAU tests when comparing to the oedometer test. The other constitutive BSP model parameters of the parameter set are kept the same.

For an adequate numerical simulation of the CAU tests the consideration of non-associated flow by proper setting of N_c and N_e different from M_c and M_e becomes necessary. To be more precise, an appropriate prediction of the peak deviatoric stress and peak excess pore-water pressure, the effective stress path following the shape of the bounding surface until reaching the critical state and the softening behavior afterwards requires the consideration of non-associated flow.

The stiffer axial stress vs. void ratio behavior obtained from the numerical simulation of the CSR-Oed-B1-35 oedometer test during the initial reloading path before reaching the yield stress arises from the averaged setting of $\kappa = 0.015$ as discussed before and the choice of $h_0 = 250$ focusing on a stiffer stress-strain behavior during cyclic loading.

6.5.3 BSP model performance regarding cyclic test

When evaluating the results of the numerical simulation of the CAUcyc-40 test in comparison to the experimental measurements some discrepancies can be observed. For convenience, in Figures 6.13 to 6.15 the results of the cyclic test are shown separately with the experimental measurement data on the left a) and the numerical simulations on the right b).

The numerically simulated effective p', q stress path as shown in Figure 6.13b deviates from the experiments as shown in Figure 6.13a. It is evident that the effective stress path observed in the experiment is significantly inclined towards the bottom right corner of the p', q plane when the deviatoric stress is decreased below its initial deviatoric stress level $q_{0,\mathrm{cyc}} = 27.3\,\mathrm{kPa}$ until reaching its minimum peak value. The decrease of the excess pore-water pressure and the associated development of even negative excess pore-water

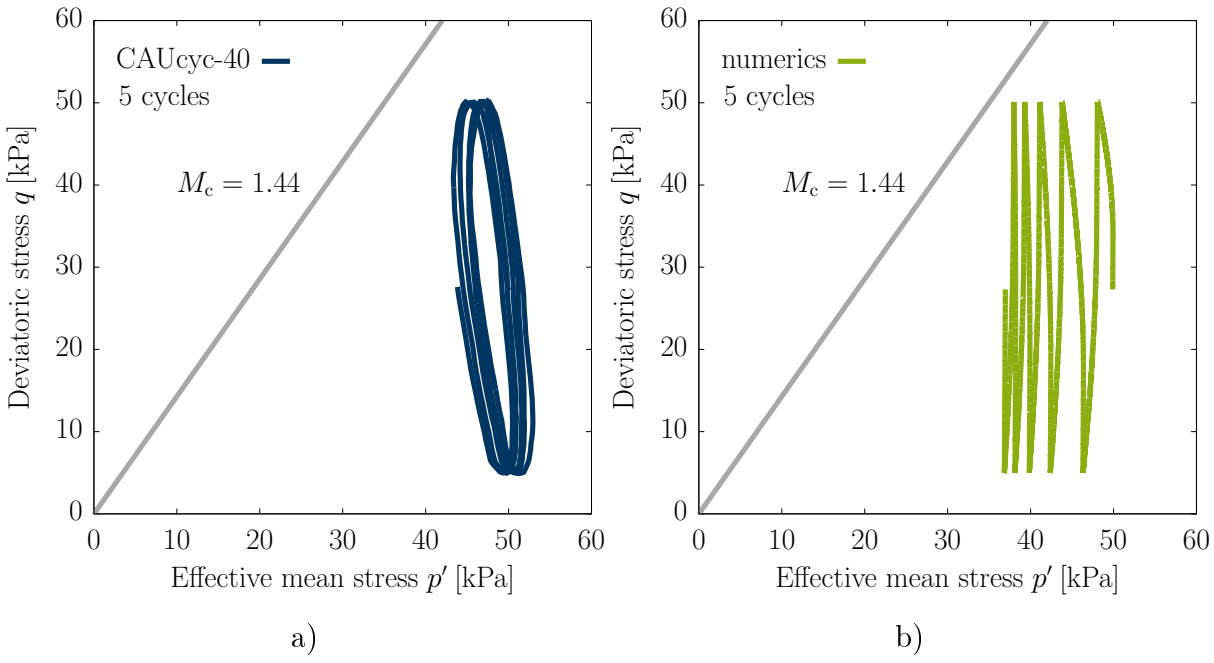

Figure 6.13: Effective p', q stress path of the CAUcyc-40 test on natural Onsøy clay: a) experimental measurements b) numerical simulation results

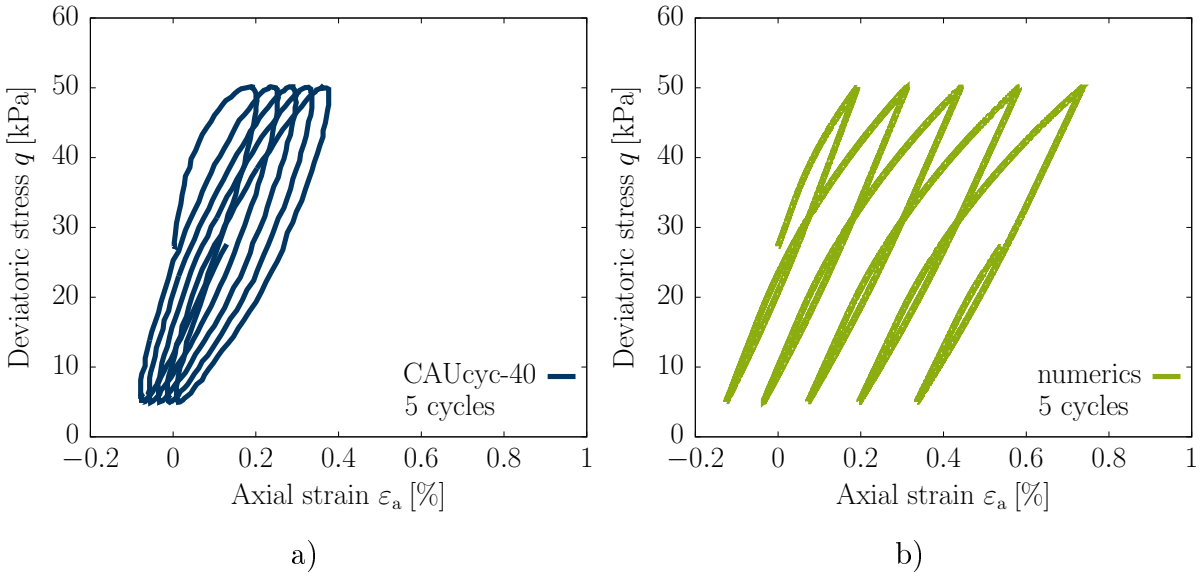

Figure 6.14: Axial strain vs. deviatoric stress behavior of the CAUcyc-40 test on natural Onsøy clay: a) experimental measurements b) numerical simulation results

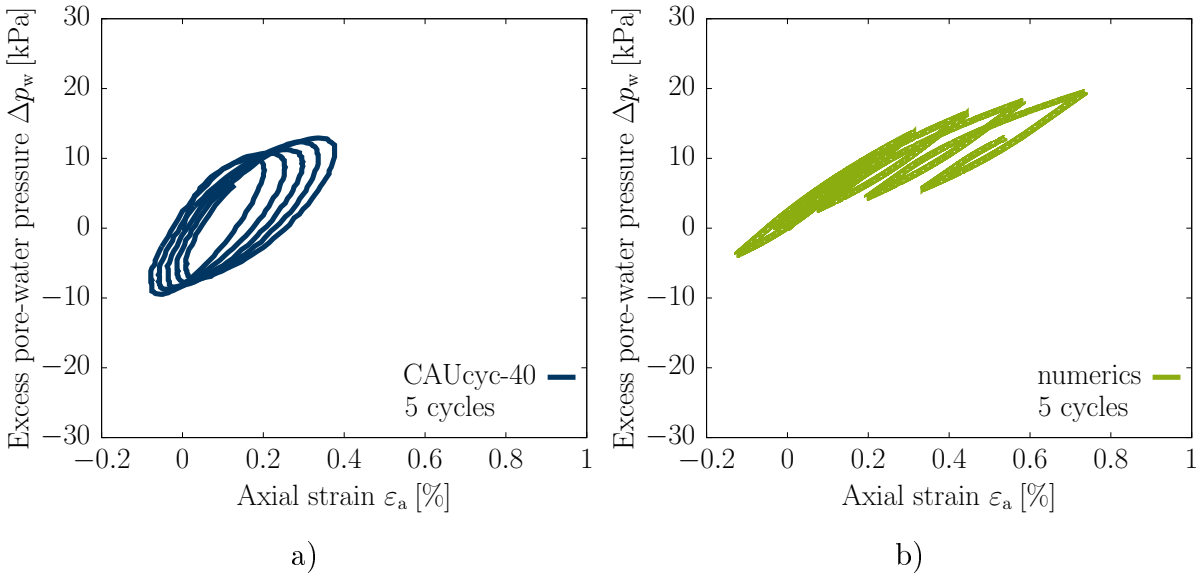

Figure 6.15: Axial strain vs. excess pore-water pressure behavior of the CAUcyc-40 test on natural Onsøy clay: a) experimental measurements b) numerical simulation results

pressure is much larger in the experiments than in the numerical simulations as shown in Figures 6.15a and 6.15b, respectively. Consequently, the effective mean stress is increasing during these unloading phases. Whereas, the numerically simulated effective stress path is continuously migrating to the stress origin due to continuous reduction of the effective mean stress during the entire cyclic loading. To sum up, the inclined slope of the effec-

tive stress path when decreasing the deviatoric stress cannot be reproduced with the BSP model even though inherent and stress-induced anisotropy are incorporated. However, the experimentally observed inclination of the effective stress path towards the left upper corner of the p', q plane when increasing the deviatoric stress from its minimum to maximum peak value during the cyclic triaxial test can be captured quite well with the BSP model. The experimentally observed development of the excess pore-water pressure showing an accumulated positive increase can be qualitatively reproduced by the numerical simulations. Since the accumulated positive excess pore-pressure during cyclic loading is slightly higher in the numerical simulations than in the experiment and the excess pore-water pressure decrease during unloading cannot adequately be reproduced, the migration of the effective stress path to the stress origin is more pronounced in the numerical simulations. As Wichtmann (2016) already stated plausibility and reliability of the effective stress path of the experiments may be questionable. Due to the relatively large loading frequency compared to the low permeability of the clay, the excess pore-water pressure measured at the bottom of the sample might be not representative for the probably inhomogeneous distribution of the excess pore-water pressure. One may expect to have a continuous migration of the effective stress path to the stress origin as seen in Zergoun and Vaid (1994) and Hyodo et al. (1994) rather than observing a temporary increase of the effective mean stress. Hence, the anomalies of the experimental excess pore-water pressure measurements in a certain degree may be an explanation for the deviations between the results from the experiment and the numerical simulation.

The numerically simulated effective stress path also effects the axial strain vs. deviatoric stress behavior reproduced by the BSP model. Figure 6.14 confirms that the accumulation of axial strain towards compression as well as the general inclination of the stress-strain path as observed in the measurements are qualitatively reproduced by the BSP model. The accumulation of strain towards compression results from the anisotropic initial stress conditions and the cyclic shear stress amplitude allowing for cyclic loading in the positive deviatoric stress regime only. Whereat, the general inclination of the stress-strain path is mainly governed by a correct setting of κ and ν. The lower the values the steeper the inclination. Nevertheless, the quantity of the numerically simulated accumulated axial compression strain after 5 cycles is much higher (by factor 2) compared to the measurements. A much softer clay response is numerically simulated. This observation in the numerical simulations directly corresponds to the more pronounced decrease of the effective mean stress since the effective stress path migrates closer to the critical state in compression. Consequently, a higher amount of plasticity and compression strain is developed and accumulated during cyclic loading.

Moreover, the numerically simulated evolution of the axial strain when decreasing the deviatoric stress below its initial level $q_{0,\mathrm{cyc}} = 27.3\,\mathrm{kPa}$ until reaching its minimum peak value deviates from the experimental measurements. The axial compression strain does not develop that strongly towards the extension side in the numerical simulations. Since the effective stress path is not moving close to the bounding surface on the extension side, low amount of plasticity is induced to the system and predominantly elastic stress-strain behavior is numerically modeled during that particular part of the test. Hence, a less significant hysteresis behavior is simulated during cyclic loading compared to the experiment.
In has to be noted that the former observations complicate the identification and calibration of the constitutive BSP model parameters related to cyclic behavior such as s_{eln}, h_0 and a_{dam}. The choice of higher values of s_{eln} and h_0 would lead to a stiffer stress-strain behavior during the numerical simulation of cyclic loading. At the same time the chosen values of s_{eln} and h_0 affect the numerical model response of the monotonic tests. The choice of a lower value of a_{dam} would lead to a less pronounced degradation of stiffness and accumulation of strain during the numerical simulation of cyclic loading. However, the value of a_{dam} is chosen in a way to considerably mobilize the stiffness degradation and accumulation of strain in the mechanized tunneling boundary value problem investigated later in this thesis.

6.6 Summary

In this chapter the calibration of the constitutive BSP model parameters for natural Onsøy clay as a representative for typical natural clay behavior was presented. The calibration of the constitutive model parameters was conducted in two consecutive steps via direct experimental and analytical determination and additionally by an automated inverse analysis using the particle swarm optimization. The constitutive BSP model parameters were calibrated against various experimental data from RUB and further data on Onsøy clay from NGI and KIT.
Whereat, the direct experimental determination from the corresponding geotechnical laboratory tests comprises the measurable constitutive BSP model parameters, which originally have a distinct definition with respect to the experimental data. Furthermore, some constitutive BSP model parameters can be obtained by employing analytical equations. The remaining non-measurable constitutive BSP model parameters were calibrated against the experimental data on Onsøy clay by means of applying an automated inverse

numerical analysis using a particle swarm optimization (PSO) algorithm. The suitable geotechnical laboratory tests for the calibration according to Table 6.8 were selected separately for each constitutive BSP model parameter based on the particular recommendations as the outcome of the GSA.
In conclusion, an adequate constitutive BSP model parameter set for the natural Onsøy clay was developed as summarized in Table 6.8. Finally, the corresponding numerically simulated material behavior of the geotechnical laboratory tests was compared to the experimental measurements. The constitutive BSP parameter set for natural Onsøy clay will be employed for the further analysis of the influence of the material properties of natural clay on the system behavior induced by the mechanized tunneling process. Therefore, the concept of the hierarchical model family will be discussed in the next chapter.

7 Hierarchical BSP model family

In this chapter the concept of the hierarchical BSP model family is introduced. The concept will be used, at a later stage of this study, to evaluate the influence of specific natural clay properties on the system behavior induced by mechanized tunneling. After a short description of the concept, the influence of the level of complexity of the hierarchical BSP model on the numerical BSP model response regarding geotechnical laboratory tests on natural Onsøy clay is evaluated in this chapter. The chosen geotechnical laboratory tests on Onsøy clay as a representative for a typical natural clay are the same as already used for calibration.

7.1 Concept

The required level of complexity of the employed constitutive BSP model for an adequate numerical analysis of mechanized tunneling can be elaborated based on the spatial and construction stage dependent evolution of the influence of specific natural clay properties on the corresponding system behavior. In the present study, the influence of specific natural clay properties (e.g. inherent and stress-induced anisotropy, destructuration, elastoplastic transition and hysteresis, stiffness degradation and accumulative effects under cyclic loading) on the system behavior induced by mechanized tunneling is evaluated by employing the concept of the hierarchical BSP model family. Concluding, the concept allows for the evaluation of the required degree of complexity of the constitutive BSP model for the numerical analysis of a specific simulation model response (e.g. surface settlements and ground movements, stress distribution, generation of excess pore-water pressure in the entire soil domain) in the design and construction phases of mechanized tunneling in natural clay deposits. To be more specific, the proposed approach enables to define rational and practical recommendations if typical mechanical properties of natural clay behavior have to be considered in the numerical analysis of a particular model response in the analysis of mechanized tunneling. The hierarchical structure of the constitutive BSP model offers the possibility to activate or deactivate particular properties

of natural clay behavior by a proper setting of the corresponding constitutive BSP model parameters. That is, the hierarchical complexity of the constitutive BSP model varies for different numerical simulation runs within the same hierarchical BSP model family. Afterwards, the numerical model responses of the different simulation runs regarding the different model extensions are compared to each other. Finally, the differences are evaluated with respect to the relative importance of a particular natural clay property related to a specific simulation model response.
Consequently, the hierarchical BSP model family is divided into four model extensions as listed below. The corresponding constitutive BSP model parameters are shown in Table 7.1. It is to be noted that all four model extensions exhibit a Lode angle dependence of the plastic potential and a non-associated flow rule. Hence, the basic model is called extended MCC model.

- Extended Modified Cam-Clay (**MCC**) → basic model, elastoplasticity, isotropic hardening and softening, non-associated flow
- **Saniclay** → additional inherent and stress-induced anisotropy
- **Saniclay D** → additional destructuration
- **Saniclay D + BSP** → additional bounding surface plasticity incorporating stress-strain hysteresis and elastoplastic transition, stiffness degradation and accumulative effects under non-monotonic or cyclic loading

The proper setting of the constitutive BSP model parameters to deactivate the particular properties of natural Onsøy clay is described in the following. In brief, the bounding surface plasticity is switched to conventional elastoplasticity by increasing the value of the constitutive BSP model parameter governing the size of the elastic nucleus and the initial value of the shape hardening function to $s_{\mathrm{eln}} = 100$ and $h_0 = 10,000$. Additionally, by adjusting $a_{\mathrm{dam}} = 0$ the degradation of stiffness and accumulation of plastic strain induced by cyclic loading are disabled. Furthermore, the destructuration is disabled by setting the constitutive BSP model parameter for the initial structure to $S_{\mathrm{i},0} = 1$. Likewise, the inherent and the stress-induced anisotropy are deactivated by adjusting the constitutive BSP model parameters for the initial rotation and the rate of rotation to $\alpha_0 = 0$ and $c_\alpha = 0$, respectively. The other BSP model parameters of the adequate constitutive BSP model parameter set for the natural Onsøy clay are kept the same for all four model extensions as derived from the model calibration in section 6.5.1.

Table 7.1: Constitutive BSP model parameters related to natural Onsøy clay wrt. the hierarchical BSP model family

Type	Parameter	Unit	Ext. MCC	Saniclay	Saniclay D	Saniclay D+BSP
Critical state soil mechanics MCC	κ	[-]	0.015	0.015	0.015	0.015
	ν	[-]	0.25	0.25	0.25	0.25
	λ	[-]	0.16	0.16	0.16	0.16
	M_{c}	[-]	1.44	1.44	1.44	1.44
	M_{e}	[-]	0.95	0.95	0.95	0.95
Non-associated flow rule	N_{c}	[-]	1.35	1.35	1.35	1.35
	N_{e}	[-]	0.89	0.89	0.89	0.89
Anisotropy and rotational hardening	α_0	[-]	0	0.23	0.23	0.23
	c_α	[-]	0	15	15	15
	$s_\alpha = z_\alpha$	[-]	-	6.1	6.1	6.1
Structure and destructuration	$S_{\mathrm{i},0}$	[-]	1	1	8.5	8.5
	k_{i}	[-]	-	-	1.2	1.2
	A	[-]	-	-	0.3	0.3
Bounding surface plasticity	s_{eln}	[-]	100	100	100	1.3
	h_0	[-]	10,000	10,000	10,000	250
	a_{dam}	[-]	0	0	0	20

It is to be highlighted that the aim of the study is not to separately calibrate each model extension of the BSP model family to have the best fit with the experimental results in each case, but rather to explicitly show the influence of the specific natural clay properties on the BSP model response when not accounting for that particular feature in the numerical simulation. However, all four model extensions intend to reproduce the structured natural Onsøy clay behavior starting from anisotropic, overconsolidated initial stress conditions. Hence, each model extension, even the basic MCC model extension, aims to represent the natural clay with a certain degree of initial bonding modeled by an enlarged size of the initial yield or bounding surface. Therefore, the yield stress ratio

$YSR = 1.35$ (CAU tests) and $p_{0,\mathrm{s,init}} = 68\,\mathrm{kPa}$ (oedometer test) are kept the same for all four model extensions of the BSP model family. That is, the non-rotated surfaces of the MCC model extension are not adjusted in size. The initial void ratio e_0 is adapted to the particular geotechnical laboratory test, but kept the same for all four model extensions of the BSP model family.

7.2 Influence of hierarchical BSP model complexity

7.2.1 Numerical testing program

For a better understanding, the influence of the level of complexity of the hierarchical BSP model is evaluated with respect to the numerical BSP model response regarding the same geotechnical laboratory tests on natural Onsøy clay as presented in section 6.1. Namely, CSR-Oed-B1-35 oedometer test (see Table 6.2), CAUC-2 and CAUE-8 monotonic undrained triaxial tests (see Table 6.4) and CAUcyc-40 cyclic undrained triaxial test (see Table 6.5) are numerically simulated.

7.2.2 Oedometer test

As the most important model responses related to the CSR-Oed-B1-35 oedometer test the numerically simulated effective p', q stress path (see Figure 7.1) and the effective axial stress vs. void ratio behavior (see Figure 7.2) are analyzed for all four hierarchical model extensions.

Effective stress path

Since all four model extensions intend to reproduce the structured natural Onsøy clay behavior with a certain degree of initial interparticle bonding governed by an enlarged size of the initial yield or bounding surface the magnitude of the yield stress is in the same order. A fully reconstituted clay without any bonding would exhibit a decisively smaller yield stress. The effective stress path of all hierarchical model extensions follows the slope of the elastic stress ratio $\eta_{\mathrm{K}_{0,\mathrm{el}}} = 1.20$, entirely while moving inside the initial yield surface $\mathrm{YS}_{\mathrm{init}}$ or just initially while moving inside the elastic nucleus for the Saniclay D+BSP model extension.

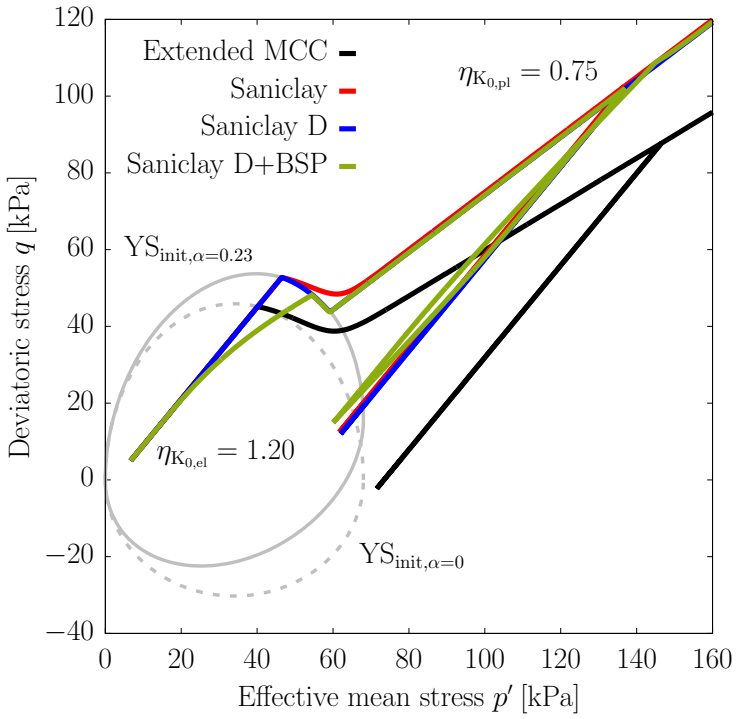

Figure 7.1: Zoom of the numerically simulated effective p', q stress path wrt. the CSR-Oed-B1-35 oedometer test on natural Onsøy clay for all four hierarchical model extensions

The elastic stress ratio $\eta_{K_{0,el}} = 1.20$ is related to $K_{0,el} = 0.33$ according to Equations 7.1 and 7.2.

$$K_{0,el} = \frac{\nu}{1-\nu} = 0.33 \tag{7.1}$$

$$\eta_{K_{0,el}} = \frac{3\,(1-K_{0,el})}{(1+2\,K_{0,el})} = 1.20 \tag{7.2}$$

$$\eta_{K_{0,pl}} = \frac{3\,(1-K_0)}{(1+2\,K_0)} = 0.75 \tag{7.3}$$

When using the Saniclay D+BSP model extension a smooth elastoplastic transition already starts before reaching the initial bounding surface after crossing the elastic nucleus. Hence, the slope of the effective stress path is smoothly adjusting towards the elastoplastic stress ratio $\eta_{K_{0,pl}} = 0.75$ already while moving inside the bounding surface. Whereat, $\eta_{K_{0,pl}}$ is calculated according to Equation 7.3 inserting $K_0 = 0.5$ as given in Table 6.8. Consequently, the effective stress path is crossing the already evolving bounding surface at a different stress state with larger effective mean stress and smaller deviatoric stress. Furthermore, the initial bounding surface is already slightly updated in size and rotation due to isotropic and rotational hardening as well as destructuration since plasticity is

induced while moving inside. Whereas, the initial yield surface for the other hierarchical model extensions is kept constant until the effective stress path is reaching it. It is to be mentioned that for the MCC model extension the effective stress path is crossing the non-rotated initial yield surface $\mathrm{YS}_{\mathrm{init},\alpha=0}$ at a lower yield stress. That arises from the missing rotation and the initial size of $\mathrm{YS}_{\mathrm{init},\alpha=0}$, which is defined by the same constant parameter $p_{0,\mathrm{s,init}} = 68\,\mathrm{kPa}$ as for the Saniclay model extensions, but related to the effective mean stress axis instead of the rotation axis. Consequently, plasticity is induced at a slightly smaller stress level.

After reaching the initial yield surface $\mathrm{YS}_{\mathrm{init},\alpha=0.23}$ or the updated bounding surface the slope of the effective stress path quickly adjusts from the elastic stress ratio $\eta_{\mathrm{K}_{0,\mathrm{el}}} = 1.20$ to the elastoplastic stress ratio $\eta_{\mathrm{K}_{0,\mathrm{pl}}} = 0.75$ for the three Saniclay model extensions. By employing the bounding attractor $\boldsymbol{\alpha}_{\mathrm{b}}$ and by a proper setting of the constitutive BSP model parameters s_α and z_α an adequate modeling of the elastoplastic K_0-loading path is ensured since the rotation of the plastic potential surface is correctly adjusted for loading under the constant stress ratio η_{K_0}. However, since $\alpha_0 = \alpha_{\mathrm{K}_0} = 0.23$ is used for initialization the rotation of the plastic potential surface is already correctly stabilized with respect to the corresponding K_0-loading from the beginning of the test. This underlies the assumption that the rotation of the plastic potential surface under K_0-loading during deposition and sedimentation has been stabilized at α_{K_0}. While adjusting to the slope of the elastoplastic stress ratio $\eta_{\mathrm{K}_{0,\mathrm{pl}}} = 0.75$ the effective stress paths of the three Saniclay model extensions are following the continuously updated yield surface or bounding surface. Whereat, the slight deviation in the effective stress paths of the three Saniclay model extensions mainly originate from the plasticity induced destructuration which is missing in the pure Saniclay model.

However, the simulated elastoplastic stress ratio of the MCC model extension is different compared to the Saniclay model extensions and the effective stress path is inappropriately modeled. The slope of the effective stress path is influenced by the rotation of the plastic potential surface. Since the plastic potential surface of the MCC model extension is initially not rotated with $\alpha_0 = 0$ and rotational hardening is not incorporated it is not possible to adjust the rotation for loading under the constant stress ratio η_{K_0}.

During unloading and reloading, the effective stress paths of all hierarchical model extensions follow the slope of the elastic stress ratio $\eta_{\mathrm{K}_{0,\mathrm{el}}} = 1.20$, entirely while moving inside the already updated yield surfaces or just initially while moving inside the updated elastic nucleus for the Saniclay D+BSP model extension. However, an elastoplastic hysteresis during unloading and reloading is captured only by the Saniclay D+BSP model extension.

Effective stress-strain behavior

The effective axial stress-void ratio behavior predicted by the four hierarchical model extensions is purely elastic and very stiff at the beginning of the oedometer test when starting from overconsolidated initial stress conditions, entirely while moving inside the initial yield surface until reaching the yield stress or just initially while moving inside the elastic nucleus for the Saniclay D+BSP model extension. However, the effects of elasto-plastic transition starting from crossing the elastic nucleus until reaching the already updated bounding surface on the volumetric behavior are small since low plasticity is introduced at that early stage of the test. Concluding, all four model extensions are able to capture the effects of the initial structure of natural Onsøy clay on the stress-strain behavior by a proper setting of the initial size of the yield or bounding surface via the parameter $p_{0,\mathrm{s,init}} = 68\,\mathrm{kPa}$. The initial interparticle bonding, which is thereby simulated, imparts additional stiffness and strength, so that a higher effective stress can be applied without causing yielding.

After reaching the yield stress the model response of all four model extensions is elasto-plastic. The model response of the MCC model extension and the pure Saniclay model extension is much stiffer compared to the model extensions where destructuration and corresponding stiffness reduction are considered. The effective axial stress-void ratio curves of the MCC model extension and the pure Saniclay model extension are almost the same

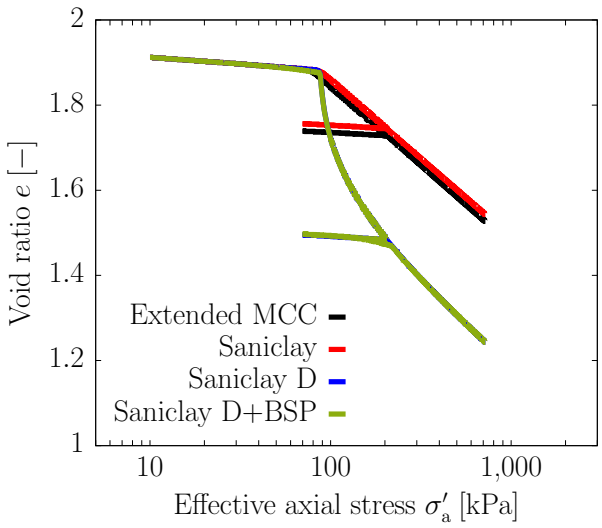

Figure 7.2: Numerically simulated effective axial stress vs. void ratio behavior wrt. the CSR-Oed-B1-35 oedometer test on natural Onsøy clay for all four hierarchical model extensions

since they are both mainly governed by the elastoplastic compression parameter λ with respect to the reconstituted state. That is, the stress-induced anisotropy does not play a major role for the stress-strain behavior during the oedometer test. However, due to the non-rotated yield surface of the MCC model extension the effective stress path reaches the yield surface at a smaller effective yield stress. Therefore, its stress-strain curve is just shifted parallel towards a smaller stress level at the same void ratio. Nevertheless, both model extensions are not capable to reproduce the destructuration behavior. An adjustment of the elastoplastic compression parameter λ is not constructive because it is continuously changing during the destructuration process. Consequently, the volumetric behavior under oedometric conditions is inappropriately reproduced and the decrease of stiffness and void ratio are underestimated when not using at least the Saniclay D model extension accounting for destructuration with plastic straining.

Whereas, the two Saniclay D and Saniclay D+BSP model extensions considering the destructuration show a significant decrease of the void ratio after yielding. Hence, the stress-induced reduction of the stiffness due to progressive structure degradation is adequately reproduced by those model extensions. When the structure is fully destroyed the effective axial stress-void ratio curve approaches towards the compression curve of the reconstituted state mainly governed by the elastoplastic compression parameter λ.

During unloading and reloading, the effective axial stress-void ratio behavior predicted by the four hierarchical model extensions is purely elastic and very stiff, entirely while moving inside the already updated yield surface or just initially while moving inside the updated elastic nucleus for the Saniclay D+BSP model extension. However, with respect to the applied test conditions with just small magnitude of effective axial stress reduction during unloading, the stress-strain behavior during unloading and reloading does not significantly differ for the four model extensions. Since plasticity is not strongly induced the hysteresis effects of the stress-strain behavior are small and the Saniclay D+BSP model extension is not necessarily needed.

7.2.3 Monotonic undrained triaxial compression test

As the most important model responses related to the CAUC-2 test the numerically simulated effective p', q stress path (see Figure 7.3), axial strain vs. deviatoric stress behavior and axial strain vs. excess pore-water pressure behavior (see Figure 7.4) are analyzed for all four hierarchical model extensions.

Effective stress path and excess pore-water pressure

Since the CAUC-2 test starts from anisotropic slightly overconsolidated initial stress conditions inside the yield surface or elastic nucleus the model response of all four model extensions is purely elastic at the beginning of the test. Hence, the effective stress paths under undrained shearing show a linear increase of the deviatoric stress while the effective mean stress remains constant, along with an increase of the excess pore-water pressure due to the contractive internal behavior. The three elastoplastic model extensions maintain an elastic model response until the effective stress path is reaching the non-rotated initial yield surface $\mathrm{YS}_{\mathrm{init},\alpha=0}$ for the MCC model extension or the rotated initial yield

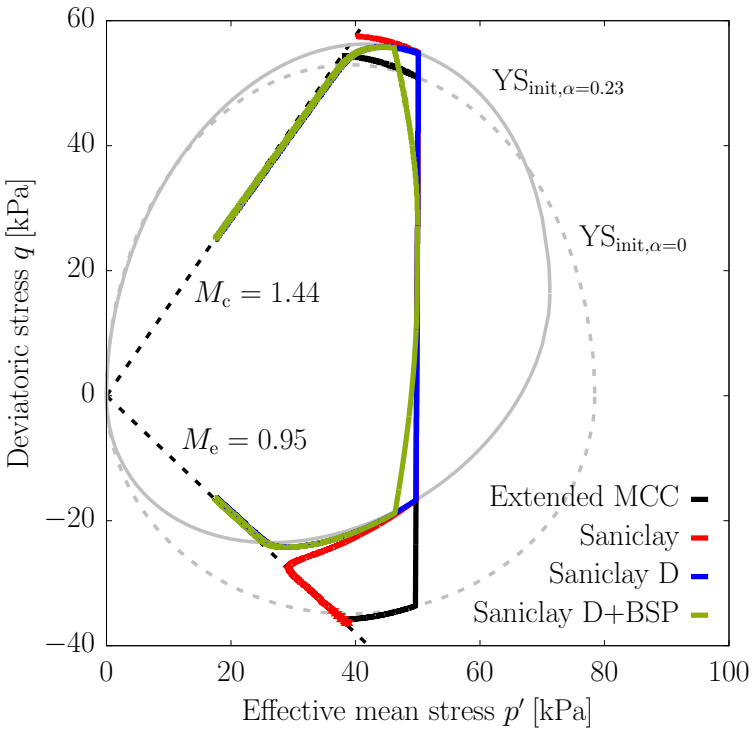

Figure 7.3: Numerically simulated effective p', q stress path wrt. the CAUC-2 and CAUE-8 tests on natural Onsøy clay for all four hierarchical model extensions

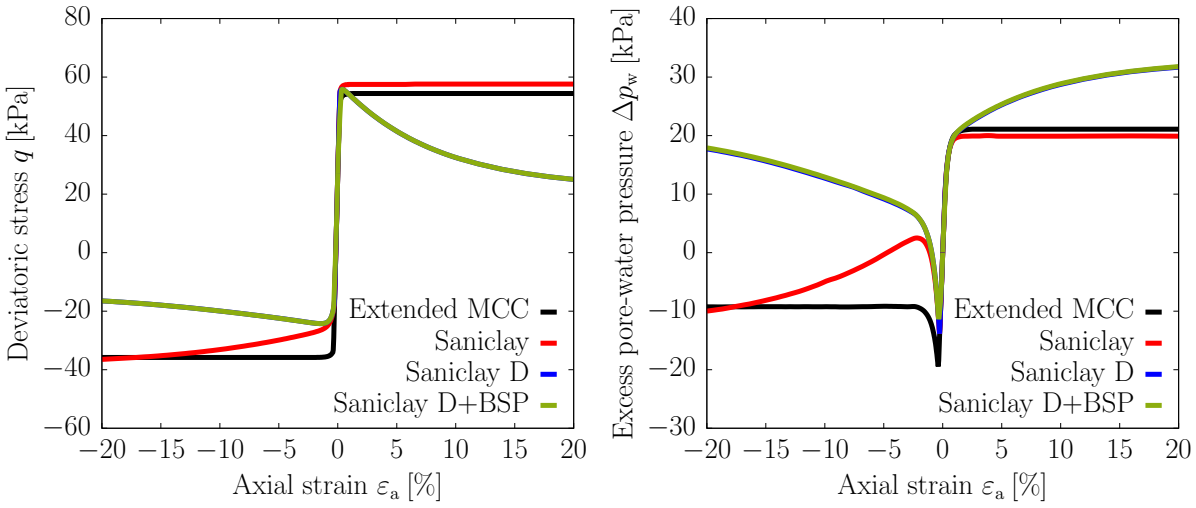

Figure 7.4: Numerically simulated a) axial strain vs. deviatoric stress behavior and b) axial strain vs. excess pore-water pressure behavior wrt. the CAUC-2 and CAUE-8 tests on natural Onsøy clay for all four hierarchical model extensions

surface $YS_{init,\alpha=0.23}$ for the two elastoplastic Saniclay model extensions. Because all four models reproduce the structured natural Onsøy clay behavior with a certain degree of initial bonding represented by an enlarged initial size of the yield or bounding surface, the magnitude of yield stress and undrained shear strength is in the same order for all four model extensions. A fully reconstituted clay without any bonding would exhibit a decisively smaller yield stress and undrained shear strength. However, it is to be mentioned that for the MCC model extension the effective stress path is crossing the non-rotated initial yield surface $YS_{init,\alpha=0}$ at a lower deviatoric yield stress. That arises from the missing rotation and the initial size of the yield surface $YS_{init,\alpha=0}$, which is defined by the same constant yield stress ratio $YSR = 1.35$ as for the Saniclay model extensions, but related to the effective mean stress axis instead of the rotation axis. Consequently, plasticity is induced at a smaller deviatoric stress when not considering the model extensions incorporating inherent anisotropy.

Whereas, the Saniclay D+BSP model extension response gradually becomes elastoplastic after the effective stress path is crossing the elastic nucleus and approaching to the already evolving bounding surface. Due to the induced plasticity, the typical effective stress path under undrained shearing is reproduced, showing a reduction of the effective mean stress due to increasing excess pore-water pressure until reaching the peak deviatoric stress on the evolving bounding surface.

Since the amount of plasticity induced before reaching the bounding surface is small, the evolution of the excess pore-water pressure is quite similar for all four model extensions. After reaching the initial yield surface or the updated bounding surface relevant plasticity is induced and the effective stress paths of all four model extensions follow the evolving yield or bounding surface until approaching to the critical state. Evoked by plastic straining the surfaces may underlie expansion, shrinkage and rotation due to isotropic hardening, softening, destructuration and rotational hardening dependent on their particular activated features. It is to be noted that all four model extensions generally allow for the simulation of softening behavior by use of the non-associated flow rule.
Anyway, under the present test conditions the effective stress paths simulated by the MCC model extension and the pure Saniclay model extension follow their expanded yield surface caused by predominantly isotropic hardening resulting in an increase of the deviatoric stress until reaching the peak value at critical state. The softening behavior is suppressed for both model extensions. Moreover, both model extensions do not account for destructuration. When reaching the critical state, the effective stress path freezes and the excess pore-water pressure stops developing. The responses of the MCC model extension and the pure Saniclay model extension are qualitatively nearly the same beside the smaller peak deviatoric stress predicted by the MCC model extension due the lack of initial rotation as mentioned before. Therefore, the peak undrained shear strength in triaxial compression is underestimated when not considering the model extensions incorporating inherent anisotropy. Anyway, the stress-induced anisotropy does not play a major role for the undrained triaxial compression test. This is, the applied loading path in triaxial compression does not require generation of significant rotation of the initial surface.
On the contrary, the two Saniclay D and Saniclay D+BSP model extensions considering the destructuration are suitable to capture the expected decrease of deviatoric and effective mean stress and the migration of the effective stress path near the critical state towards the stress origin. The ongoing destructuration process simultaneously takes place in addition to softening both leading to shrinkage of the yield or bounding surface indicating a significant loss of undrained shear strength. The destructuration process causes a continuous increase of the excess pore-water pressure to counteract the potential volume decrease which is restricted in undrained conditions. However, the influence of the Saniclay D+BSP model extension is small since the undrained shearing after reaching the bounding surface represents a virgin loading path. Concluding, the residual undrained shear strength is significantly overestimated and the generation of excess pore-water pressure is underestimated when not using at least the Saniclay D model extension accounting for destructuration.

Effective stress-strain behavior

The stress-strain behavior reproduced by the four hierarchical model extensions is purely elastic and stiff at the beginning of the CAUC-2 test when starting from overconsolidated initial stress conditions, entirely while moving inside the initial yield surface YS_{init} until reaching the yield stress or just initially while moving inside the elastic nucleus for the Saniclay D+BSP model extension. Hence, the stress-strain behavior under undrained shearing predicted by the three elastoplastic model extensions is quite similar until reaching the yield surface except the different magnitude of the deviatoric yield stress arising from the different initial rotation.
Due to the incorporated plasticity while moving inside the bounding surface the model response of the Saniclay D+BSP model extension is slightly softer until reaching the peak deviatoric stress state. Hence, the stiffness is overestimated when not using the Saniclay D+BSP model extension for undrained shearing in triaxial compression starting from overconsolidated initial stress conditions like discussed here.
After reaching the yield surface or the bounding surface only the two Saniclay D and Saniclay D+BSP model extensions considering the destructuration are able to accurately simulate the progressive loss of structure and the associated stiffness and strength degradation under continuous undrained shearing. That is, the deviatoric stress is continuously decreasing with ongoing application of axial strain. The critical state would be reached at significantly higher magnitude of axial strain and not before the entire structure is destroyed, which is not achieved after applying 20% of axial compression strain in the CAUC-2 test.
Whereas, the MCC model extension and the pure Saniclay model extension are not suitable to capture the destructuration effects showing a constant deviatoric stress after reaching the critical state already at a small axial strain. However, due to the different initial size of the rotated and non-rotated yield surfaces the critical state is reached at a smaller deviatoric stress when using the MCC model extension. To sum up, the residual undrained shear strength and stiffness are significantly overestimated when not using at least the Saniclay D model extension accounting for destructuration, whenever it comes to undrained loading paths in triaxial compression after reaching the yield stress.

7.2.4 Monotonic undrained triaxial extension test

As the most important model responses related to the CAUE-8 test the numerically simulated effective p', q stress path (see Figure 7.3), axial strain vs. deviatoric stress behavior and axial strain vs. excess pore-water pressure behavior (see Figure 7.4) are analyzed for all four hierarchical model extensions.

Effective stress path and excess pore-water pressure

Again, as the CAUE-8 test starts from anisotropic slightly overconsolidated initial stress conditions inside the yield surface or elastic nucleus the model response of all four model extensions is purely elastic at the beginning of the test. Hence, the effective stress paths under undrained shearing show a linear decrease of the deviatoric stress while the effective mean stress remains constant. The three elastoplastic model extensions exhibit an elastic model response until the effective stress path is reaching the non-rotated initial yield surface $\mathrm{YS}_{\mathrm{init},\alpha=0}$ for the MCC model extension or the rotated initial yield surface $\mathrm{YS}_{\mathrm{init},\alpha=0.23}$ for the two elastoplastic Saniclay model extensions. Compared to the CAUC-2 test in triaxial compression the CAUE-8 test in triaxial extension initially causes dilative internal behavior. All four model extensions predict dilative internal behavior at the beginning of the test resulting in the development of negative excess pore-water pressure while the soil behavior is elastic.
A large difference of the magnitude of the deviatoric yield stress can be observed when comparing the elastoplastic MCC model extension and the two elastoplastic Saniclay model extensions. Due to the non-rotated initial yield surface the yielding simulated by the MCC model extension starts at a much smaller deviatoric yield stress causing a more pronounced generation of negative excess pore-water pressure. Consequently, the elastic domain is overestimated when not considering the model extensions incorporating inherent anisotropy, whenever it comes to undrained shearing in triaxial extension. Whereas, the Saniclay D+BSP model extension response gradually becomes elastoplastic while the effective stress path is approaching to the evolving bounding surface on the extension side. Consequently, the effective stress path reaches the evolving bounding surface at a slightly smaller effective mean stress but also slightly smaller deviatoric stress which is almost negligible when comparing to the elastoplastic Saniclay model extensions. Furthermore, the developed negative excess pore-water pressure is slightly less pronounced.
After reaching the initial yield surfaces or the updated bounding surface, significant plasticity is induced and the effective stress path of all four model extensions follows the evolv-

ing yield surface or bounding surface until approaching to the critical state. Moreover, the evolution of the excess pore-water pressure reproduced by all four model extensions suggests a change from dilative to contractive internal behavior after the transition from (predominantly) elastic to elastoplastic behavior. That is, the increments of the excess pore-water pressure are changing from negative to positive causing a corresponding decrease of the effective mean stress. This counteracting increase of the excess pore-water pressure under undrained conditions is again evoked by the transferred energy balancing the volumetric behavior due to induced plasticity.

However, some most relevant differences can be observed in the responses of the particular model extensions after exceeding the yield stress and occurrence of plasticity until reaching the critical state. That is, only the two Saniclay D and Saniclay D+BSP model extensions are capable to account for the destructuration effects. The plastic straining induced destructuration results in undrained shear strength reduction represented by shrinkage of the yield or bounding surface. Consequently, the effective stress path is migrating towards the stress origin in the vicinity of the critical state. The excess pore-water pressure reproduced by those model extensions is continuously increasing due to the contractive internal behavior induced by the damage of structure. However, the influence of the Saniclay D+BSP model extension is again small since the undrained shearing after reaching the bounding surface represents a predominantly virgin loading path which is captured by the Saniclay D model extension in the same manner. On the contrary, the MCC model extension and the pure Saniclay model extension are not suitable to simulate the destructuration behavior as described before. To sum up, the residual undrained shear strength is significantly overestimated when not using at least the Saniclay D model extension accounting for destructuration whenever it comes to undrained loading paths in triaxial extension after reaching the yield stress.

That is, the MCC model extension shows contractive internal behavior with increasing excess pore-water pressure just while the effective stress path is moving on the isotropically hardening yield surface until reaching the critical state. After reaching the minimum peak deviatoric stress at the critical state the effective stress path freezes and the excess pore-water pressure stops developing. The pure Saniclay model extension even simulates another change to dilative internal behavior with again decreasing excess pore-water pressure after approaching to the critical state. Due to the incorporated rotational hardening the effective stress path migrates close to the critical state with decreasing deviatoric stress and increasing effective mean stress. The chosen rotational hardening rule incorporating the Lode angle dependence ensures the uniqueness of the critical state in triaxial compression and extension. That is, the critical state is reached at the same effective mean stress.

A possible drawback is the hook-type shape of the effective stress path when reaching the critical state in triaxial extension. After reaching the minimum peak deviatoric stress at the critical state the effective stress path freezes and the excess pore-water pressure stops developing. However, the magnitude of peak deviatoric stress and excess pore-water pressure when reaching the critical state are the same for the MCC model extension and the pure Saniclay model extension.

Effective stress-strain behavior

The initial stress-strain behavior of the CAUE-8 test is qualitatively similar to the behavior arising in the CAUC-2 test, but related to triaxial extension. That is, the stress-strain behavior reproduced by the four hierarchical model extensions is purely elastic and very stiff at the beginning of the test when starting from overconsolidated initial stress conditions, entirely while moving inside the initial yield surface until reaching the yield stress or just initially while moving inside the elastic nucleus for the Saniclay D+BSP model extension. The stress-strain behavior under undrained shearing predicted by the three elastoplastic model extensions is almost identical until reaching the yield surface, except the significantly smaller value of the deviatoric yield stress predicted by the MCC model extension arising from the different initial rotation.
The Saniclay D+BSP model extension simulates a smooth elastoplastic transition behavior while the effective stress path is moving inside the bounding surface. Due to the incorporated plasticity, the model response of the bounding surface model extension is slightly softer. However, the overall influence of the Saniclay D+BSP model extension is small due to the predominantly virgin loading path after reaching the bounding surface. To sum up, the stiffness is just slightly overestimated when not using the Saniclay D+BSP model extension for undrained shearing in triaxial extension starting from overconsolidated initial stress conditions.
When significant plasticity is induced and the effective stress path is approaching to the critical state along the evolving yield or bounding surface, the stress-strain behavior of the four model extensions start to considerably deviate. Only the two Saniclay D and Saniclay D+BSP model extensions considering the destructuration are able to accurately simulate the progressive loss of structure and the associated stiffness and undrained strength degradation during undrained shearing. That is, the deviatoric stress is continuously increasing with ongoing application of axial strain. The critical state would be reached at significantly higher magnitude of axial strain and not before the entire structure is destroyed, which is not achieved after applying 20% of axial extension strain in the CAUE-8 test.

Whereas, the MCC model extension and the pure Saniclay model extension are not suitable to account for destructuration resulting in constant deviatoric stress during further undrained shearing after once reaching the critical state. The pure Saniclay model extension simulates a decreasing deviatoric stress until reaching the critical state at a much larger axial strain than the MCC model extension. However, the deviatoric stress when reaching the critical state is almost the same for both model extensions. To sum up, the residual undrained strength and stiffness are significantly overestimated when not using at least the Saniclay D model extension accounting for destructuration, whenever it comes to undrained loading paths in triaxial extension after reaching the yield stress.

7.2.5 Cyclic undrained triaxial test

As the most important model responses related to the CAUcyc-40 test the numerically simulated effective p', q stress path (see Figure 7.5), axial strain vs. deviatoric stress behavior and axial strain vs. excess pore-water pressure behavior (see Figure 7.6) are analyzed for all four hierarchical model extensions.

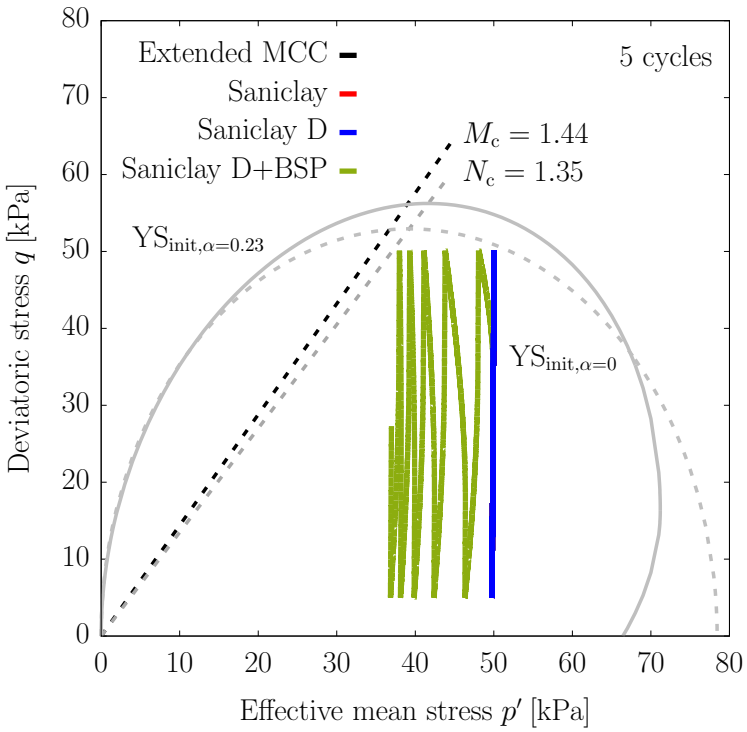

Figure 7.5: Numerically simulated effective p', q stress path wrt. the CAUcyc-40 test on natural Onsøy clay for all four hierarchical model extensions

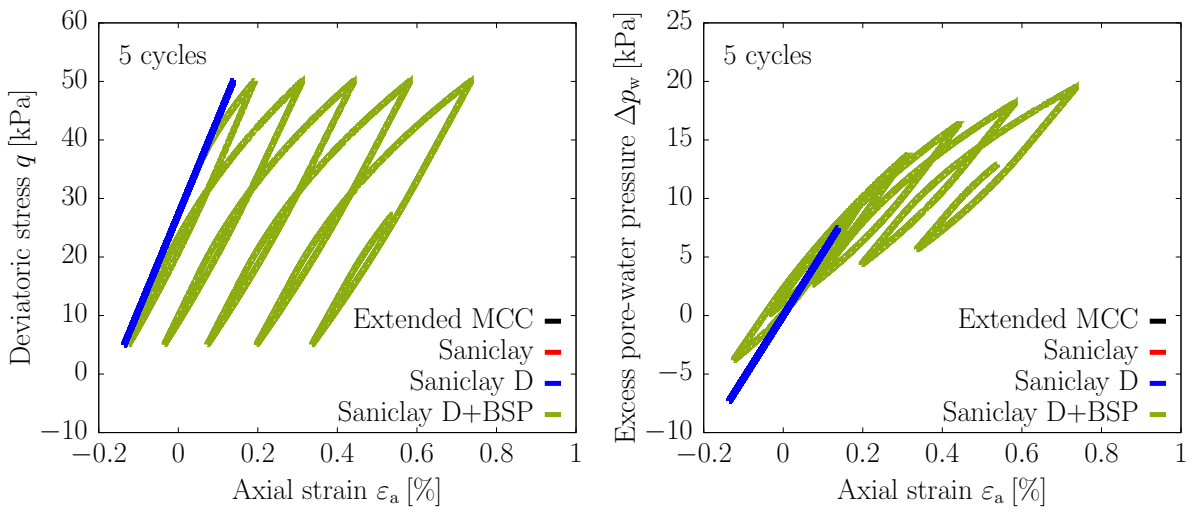

Figure 7.6: Numerically simulated a) axial strain vs. deviatoric stress behavior and b) axial strain vs. excess pore-water pressure behavior wrt. the CAUcyc-40 test on natural Onsøy clay for all four hierarchical model extensions

Effective stress path and excess pore-water pressure

For all hierarchical model extensions the effective stress path stays inside the initial yield surface or updated bounding surface. Hence, according to the model formulation, just for the Saniclay D+BSP model extension an elastoplastic model response during cyclic loading is possible. Therefore, just the Saniclay D+BSP model extension is suitable for an adequate simulation of the expected effective stress path migration towards the effective mean stress origin during undrained cyclic loading.

To be more precise, the continuous effective stress path migration is caused by an accumulative increase of the mean value of the excess pore-water pressure. Among all four model extensions, just the Saniclay D+BSP model extension is able to adequately simulate the accumulative increase of the mean value of the excess pore-water pressure. During undrained shearing energy is transferred to plasticity to compensate the restriction of a constant volume while the sample still wants to deform by means of decreasing volume. Undrained conditions require a resulting zero total volumetric strain increment as the sum of the elastic and the plastic strain components. Accordingly, balancing this contractive internal behavior results in a counteracting increase of the excess pore-water pressure and associated simultaneous decrease of the effective mean stress. Due to the fact that the Saniclay D+BSP model extension allows for plasticity and accumulation of plastic

strain when the effective stress path is moving within the bounding surface, it is able to adequately reproduce the effective stress path under undrained cyclic loading.
Moreover, the evolution of the projection center and the elastic nucleus to the last stress reversal, both included in the Saniclay D+BSP model extension only, enable accurate modeling of the effective stress path under cyclic loading. Since the position of the elastic nucleus is updated in case of a stress reversal the migration of the effective stress path towards the stress origin is restricted due to purely elastic behavior under constant effective mean stress always initially after stress reversal until passing the elastic nucleus again. Afterwards, elastoplastic model response including accumulation of excess pore-water pressure and plastic strain is activated, so that the migration of the effective stress path towards the stress origin continuous until next stress reversal.
For the other hierarchical model extensions the model response inside the initial yield surface $\mathrm{YS}_{\mathrm{init}}$ is purely elastic and no plasticity is induced during undrained cyclic loading. The purely elastic response will not result in any change of the effective mean stress due to the restriction of a constant volume under undrained conditions and the linear elastic relationship via the Hooke‘s law between strain and stress. Consequently, an additional counteracting accumulative increase of the mean value of the excess pore-water pressure is not required and mobilized. Hence, the effective stress path is freezing under constant effective mean stress. To sum up, the magnitude of excess pore-water pressure is underestimated and the corresponding effective mean stress level is overestimated when not using the Saniclay D+BSP model extension for cyclic loading cases like discussed here.

Effective stress-strain behavior

Again, just the Saniclay D+BSP model extension is able to accurately simulate the progressive stiffness degradation and the accumulation of plastic axial strain in compression during cyclic loading due to the elastoplastic model response when moving within the bounding surface. Whereat, the cyclic stress-strain behavior is controlled by the included distance function $\hat{f}$, the shape hardening function $\hat{h}$ and the damage variable d as a function of plastic straining governing the plasticity modulus K_{p}. With increasing number of cycles plastic strain accumulates and stiffness progressively decreases, so that the stress-strain behavior becomes more soft indicated by a flatter axial strain-deviatoric stress curve. Again, the evolution of the projection center and the elastic nucleus allow for adequate modeling of the hysteretic stress-strain behavior during unloading and reloading cycles showing a purely elastic and stiff model response initially after stress reversal followed by an elastoplastic transition when crossing the elastic nucleus.

The other model extensions show elastic model response only when moving inside the yield surface during cyclic loading. That is, the stiffness is kept constant independently of the number of cycles and no accumulation of axial strain takes place. Consequently, the model response is purely elastic and much too stiff and the magnitude of axial strain is significantly underestimated when not using the Saniclay D+BSP model extension for cyclic loading cases.

7.3 Summary

In this chapter the concept of the hierarchical BSP model family was introduced as a tool to evaluate the required level of complexity of the employed BSP model for an adequate numerical analysis of mechanized tunneling in natural clay deposits. Consequently, the hierarchical BSP model family is divided into four model extensions and the corresponding constitutive BSP parameters are listed in Table 7.1.

- Extended Modified Cam-Clay (**MCC**) → basic model, elastoplasticity, isotropic hardening and softening, non-associated flow
- **Saniclay** → additional inherent and stress-induced anisotropy
- **Saniclay D** → additional destructuration
- **Saniclay D + BSP** → additional bounding surface plasticity incorporating stress-strain hysteresis and elastoplastic transition, stiffness degradation and accumulative effects under non-monotonic and cyclic loading

For a better understanding, the influence of the level of complexity of the hierarchical BSP model on the model response of numerical simulations of geotechnical laboratory tests on natural Onsøy clay was exemplarily evaluated in this chapter. That is, the influence of specific natural clay properties (e.g. inherent and stress-induced anisotropy, destructuration, stiffness degradation and accumulative effects under cyclic loading) on the system behavior of the CSR-Oed-B1-35 oedometer test, the CAUC-2 and CAUE-8 monotonic undrainded triaxial tests and the CAUcyc-40 cyclic undrained triaxial test on natural Onsøy clay was analyzed by employing the concept of the hierarchical BSP model family. The main findings are summarized in the following.
All four hierarchical model extensions can adequately reproduce the initial effective stress path starting from anisotropic slightly overconsolidated initial stress conditions and the corresponding purely elastic stress-strain behavior while moving inside the initial yield

surface or the elastic nucleus for the Saniclay D+BSP model extension. This applies to the oedometer test as well as the undrained triaxial tests. However, the model response of the Saniclay D+BSP model extension is slightly softer due to the incorporated plasticity already while moving inside the bounding surface. Hence, the magnitude of strain is slightly underestimated when not using the Saniclay D+BSP model extension for tests starting from slightly overconsolidated initial stress conditions until yielding. However, the overall influence of the Saniclay D+BSP model extension in the oedometer test and the monotonic undrained triaxial tests is quite small due to the predominantly virgin loading path inducing significant destructuration after reaching the bounding surface.
Initializing the four different model extensions by an enlarged size of the initial yield or bounding surface allows for an adequate modeling of the initial interparticle bonding of the natural Onsøy clay. That is, the additional stiffness and strength resulting in an increased yield stress can be adequately simulated. A fully reconstituted clay without any bonding would exhibit a decisively smaller yield stress and undrained shear strength. Nevertheless, due to the missing rotation of the yield surface of the MCC model extension the predicted yield stress might significantly deviate.
Due to the incorporated initial rotation and adequate stress-induced rotational hardening the three Saniclay model extensions are suitable for a realistic modeling of the elastoplastic K_0-loading path arising in the oedometer test. Whereas, the effective stress path predicted by the MCC model extension is inappropriate. Moreover, only the bounding surface model extension is capable to simulate realistic elastoplastic hysteresis during unloading and reloading because of the updated projection center and elastic nucleus after each stress reversal.
After changing to elastoplastic model repsonse only the two Saniclay D and Saniclay D+BSP model extensions are suitable to capture the progressive loss of structure and the associated stiffness and strength degradation. However, destructuration has the most striking influence on the model response in the considered tests. Consequently, the volumetric behavior under oedometric conditions is inappropriately reproduced and the decrease of stiffness and void ratio are underestimated when not using at least the Saniclay D model extension accounting for destructuration after reaching the yield stress. Furthermore, the residual undrained shear strength and stiffness are significantly overestimated and the excess pore-water pressure is underestimated whenever it comes to undrained loading paths in triaxial compression and extension after reaching the yield stress.
Regarding the modeling of the soil behavior under cyclic loading, the Saniclay D+BSP model extension is the only model that is capable to accurately capture the accumulation of plastic strain, degradation of stiffness with increasing number of cycles and elastoplastic

hysteresis during unloading and reloading cycles. The other model extensions only show elastic and much too stiff model response when moving inside the yield surface during cyclic loading. Hence, the magnitude of axial strain is significantly underestimated when not using the Saniclay D+BSP model extension for cyclic loading cases.
Concluding, the required level of complexity of the constitutive BSP model is strongly dependent on the mechanical and hydraulic boundary conditions, the initial consolidation conditions and the induced loading of the investigated geotechnical laboratory test which governs the elastic or elastoplastic BSP model response. The concept of the hierarchical BSP model family will be used in the next chapter to evaluate the required degree of complexity of the constitutive BSP model for the numerical analysis of a specific model response (e.g. surface settlements, ground movements, spatial stress and excess pore-water pressure in the soil domain) induced by mechanized tunneling in natural clay deposits.

8 Numerical model for mechanized tunneling

The basis for reliable predictions of the physical processes involved in mechanized tunneling are the design and development of an adequate numerical three-dimensional (3D) simulation model in a finite element code such as PLAXIS 3D. A 3D model is required to adequately simulate the multiaxial stress distribution and the corresponding strain behavior resulting from the various spatially distributed construction processes involved in mechanized tunneling. The advanced 3D simulation model needs to consider the most decisive complex interactions between soil, shield machine and lining. Moreover, the simulation model needs to account for the spatial and staged construction dependent processes (e.g. support of the tunnel face, grouting of the annular gap, bedding of the lining) involved in mechanized tunneling. However, since the present study is focusing on the investigation of the influence of the soil mechanical properties of natural clay on the system behavior induced by mechanized tunneling a most complex and most detailed modeling of the subprocesses involved in mechanized tunneling is not intended.

The current chapter is focusing on the introduction of an adequate numerical 3D tunnel simulation model as developed and employed in this study. The geometry and boundary conditions of the synthetic numerical model are arbitrarily chosen with respect to an imaginary mechanized tunnel excavation in a water-saturated natural Onsøy clay deposit. The mechanized tunneling is assumed to be conducted utilizing an EPB shield machine. Furthermore, the consideration of the corresponding staged construction to adequately model mechanized tunneling is intensively discussed. The adequate numerical tunnel simulation model is developed based on the main findings of the state-of-the art literature review on the numerical modeling of mechanized tunneling as presented in chapter 2.4. For the theoretical details on numerical modeling of specific subsystems involved in mechanized tunneling it is again referred to chapter 2.4.

8.1 Numerical 3D tunnel simulation model

8.1.1 Geometry, discretization, initial and boundary conditions

Within this study an excavation of a single horizontal tunnel is investigated utilizing the finite element code PLAXIS 3D. The diameter of the excavated area of the tunnel is set to $D = 10$ m. The overburden depth above the crown of the excavated area is set to simulate a shallow tunnel ($H/D = 1$) according to the definition by Leca and New (2007). Whereat, H/D represents the ratio of the overburden depth H to the diameter D of the excavated area. Moreover, so-called greenfield conditions are considered.
The dimensions of the symmetric numerical 3D tunnel simulation model are chosen in accordance with the recommendations of the German geotechnical society (DGGT, 2014). Symmetric boundary conditions are applied. That is, the model dimensions in longitudinal Y-direction, transverse X-direction and vertical Z-direction are set to $Y = 200$ m, $X = 100$ m, $Z = 45$ m. The dimension in longitudinal Y-direction corresponds to 100 excavation steps each with an advance of the shield machine of 2 m. The dimension in transverse X-direction is twice the recommended distance from the tunnel center to the transverse model boundaries of five times the diameter of the excavated area. The dimension in vertical Z-direction is based on the recommended distance from the tunnel center to the lower model boundary of three times the diameter of the excavated area. The recommendations by DGGT (2014) are developed in a way to avoid boundary effects on the simulation results of mechanized tunneling. The 3D numerical tunnel simulation model is displayed in Figure 8.1.
To constrain the simulation model the following mechanical displacement boundary conditions are utilized. The bottom of the model is vertically fixed in its position and the model sides in transverse and longitudinal direction are constrained perpendicular to the outer model boundary. That is, the normal deformations are restricted while the in-plane displacements are permitted.
In addition to the recommendations by DGGT (2014), the required dimensions of the tunnel simulation model are determined in advance by analyzing the incremental change of strain and stress at the model boundaries. That is, negligible incremental changes of strain and stress at the model boundaries imply a sufficiently large tunnel simulation model. These preparatory analyses revealed that the chosen size of the tunnel simulation model as well as the applied mechanical and hydraulic boundary conditions impose no significant restriction on the mechanical and hydraulic conditions at the excavation zone. For reasons of simplification the entire ground domain is assumed to be a homogeneous

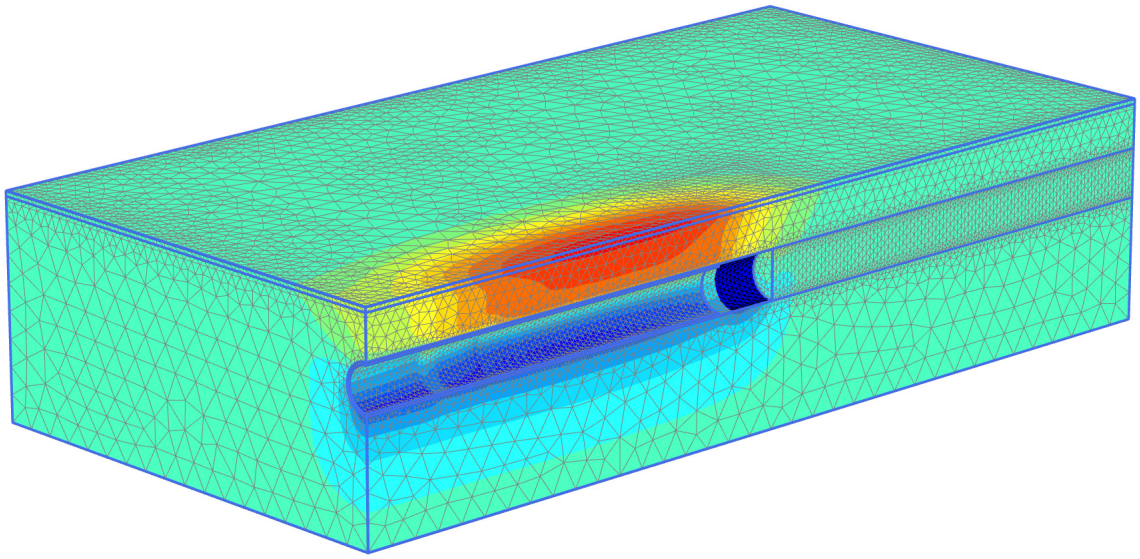

Figure 8.1: 3D numerical tunnel simulation model wrt. a tunnel excavation state where the shield machine has reached the synthetic measurement section (TBM at $Y = 100$ m)

layer consisting of natural Onsøy clay. The soil properties of the natural Onsøy clay with respect to the constitutive BSP model as well as the initialization of the state variables are chosen in accordance to the calibrated parameter sets with respect to the hierarchical model family extensions as discussed in chapters 6 and 7. The initial void ratio $e_0 = 1.91$ is chosen in accordance to the CSR-Oed-B1-35 oedometer test.
However, two different scenarios are investigated: 1.) normally consolidated conditions with $YSR = 1$ throughout the total height of the soil domain, just the upper 1 m is assumed to be overconsolidated with $YSR = 2$; 2.) overconsolidated conditions with $YSR = 2$ at the top 1 m, underlaid by overconsolidated conditions with $YSR = 1.35$ with respect to the calibration in chapter 6 and Figure 2.6 in chapter 2.1 and Table 2.2 in chapter 2.1.5. However, by reason of simplicity the corresponding initial K_0 value is kept constant for the entire soil domain independently of the YSR value.
According to Lunne et al. (2003) the value of the unit weight under buoyancy of natural Onsøy clay below the groundwater Table is assumed to be $\gamma' = 6.35\,\mathrm{kN/m^3}$ and the unit weight above the groundwater Table is assumed to be $\gamma = 16.35\,\mathrm{kN/m^3}$. The water table is assumed to be constant at a depth of 2 m below the ground surface during the entire tunnel excavation. However, hydraulic flow is not considered in the current study.
In the 3D tunnel simulation model the soil domain is discretized into a multitude of soil volume elements (112,893) and nodes (179,084). Whereat, the soil volume elements are defined according to Brinkgreve et al. (2016): 10-node tetrahedral elements numerically

integrated over four Gauss points and three translational degrees of freedom per node. The same holds true for the volume elements representing the concrete lining. A huge magnitude of elements is required to adequately discretize the nearfield around the tunnel. That is, an accurate model prediction requires an increased fineness of the numerical mesh. However, the required accuracy and fineness of the numerical mesh is determined with respect to the relative incremental change of strain and stress to avoid mesh dependency. As a consequence the mesh is automatically refined in the nearfield of the excavation area.
The shell elements employed to model the shield machine are also defined according to Brinkgreve et al. (2016): 6-node triangular elements numerically integrated over three Gauss points with five degrees of freedom per node such as one axial displacement, two transverse displacements and two rotations. However, the six nodes are compatible with the 6-noded triangular side of the 10-node tetrahedral soil volume elements.
To model the soil-structure interaction in the contact areas between soil and shield machine and soil and lining specific interface elements according to van Langen and Vermeer (1991) and Brinkgreve et al. (2016) are utilized: 12-node triangular elements numerically integrated over six Gauss points with three translational degrees of freedom per node. The interface elements manifest pairs of nodes instead of single nodes, whereat the distance between the nodes of each node pair is zero (zero thickness element). However, the six node pairs are compatible with the 6-noded triangular side of the 10-node tetrahedral soil volume elements and the 6-node triangular shell elements.

8.1.2 Numerical subsystems

Within the current study the following most decisive subsystems involved in mechanized tunneling are considered in the numerical analysis.

- Homogeneous ground domain is represented by soil volume elements. Whereat, the stress-strain behavior is simulated by the adequate constitutive BSP model for natural clay based on the bounding surface plasticity as presented in chapter 3.
- Sequential advance of the shield machine with an excavation step length of 2 m is represented by following a numerical staged construction process which will be described in the following.
- Shield machine is represented by elastic shell elements. The entire length of the shield machine is assumed to be 10 m. Whereat, each of the five shield machine segments has a length of 2 m which is identical to the advance of the shield machine

in each excavation step. The shell elements manifest a certain axial rigidity ($E\,A$) and flexural rigidity ($E\,I$) with respect to their thickness $d_{\text{shield}} = 0.1\,\text{m}$ but no torsional rigidity. A simplified isotropic linear-elastic material behavior is assumed and a corresponding elastic constitutive model is employed. The material properties of the shield such as Young's modulus $E_{\text{shield}} = 210 \times 10^6\,\text{kN/m}^2$, Poisson's ratio $\nu_{\text{shield}} = 0.3$ and unit weight $\gamma_{\text{shield}} = 78.5\,\text{kN/m}^3$ are assigned with respect to the used steel material. The material is assumed to be impermeable. Due to the conicity of the shield and overcutting an annular steering gap between the shield and the adjacent soil develops.

- Precast concrete lining segments are represented by volume elements without consideration of joints. Each lining segment has a length of 2 m which is identical to the advance of the shield machine in each excavation step and a thickness of $d_{\text{lining}} = 0.5\,\text{m}$. A simplified isotropic linear-elastic material behavior is assumed and a corresponding elastic constitutive model is employed. The material properties of the lining such as the Young's modulus $E_{\text{lining}} = 30 \times 10^6\,\text{kN/m}^2$, the Poisson's ratio $\nu_{\text{lining}} = 0.2$ and the unit weight $\gamma_{\text{lining}} = 25\,\text{kN/m}^3$ are assigned with respect to the used reinforced concrete material. The material is assumed to be impermeable.

- Soil-structure interaction/contact modeling between soil and shield machine as well as soil and lining is represented by utilizing interface elements. Whereat, the material properties of the interface element are explicitly defined with respect to the adjacent soil but with reduced shear strength. The soil vs. concrete structure interaction as well as the soil vs. steel interaction with respect to the shear strength is controlled by applying the factor $R_{\text{inter}} = 2/3$ to reduce the effective friction angle of the adjacent soil from $\varphi' = 35.5°$ (corresponds to $M_{\text{c}} = 1.44$) to $\varphi'_{\text{inter}} = 23.7°$. The interfaces are assumed to be impermeable.

- Tunnel face support is represented by a distributed surface load. The required value of the resulting face support force S_{ci} for a circular tunnel face acting at the tunnel axis and the resulting face support pressure $s_{\text{invert/crown}}$ are calculated according to the recommendation by DAUB (2016) based on Equations 2.15 and 2.16 respectively as discussed in section 2.4. Whereat, the resulting support force due to earth pressure is calculated by assuming an active kinematic failure mechanism at the tunnel face after Horn (1961) and Anagnostou and Kovari (1996) composed of sliding wedge and prism. However, silo effects are not considered in the calculation of the vertical effective stress. The input parameters for the calculation are chosen in accordance to the calibrated parameter set with respect to the BSP model as dis-

cussed in chapter 7. The required friction angle of the soil in front of the tunnel face is determined based on the corresponding constitutive parameter $M_c = 1.44$ representing the critical stress ratio in triaxial compression. Based on the calculations the following value of the face support pressure at the crown of the excavated area $s_{face,crown,H/D=1} = 85\,kN/m^2$ is applied within the numerical simulations. The value is determined with respect to the minimum required face support force as a lower limit. However, support pressure deviations of $\pm 30\,kN/m^2$ are not considered in the calculations. Whereat, the gradient of the linear increase of the face support pressure from crown to invert of the excavated area $16.35\,kN/m^2$/m-depth is calculated based on the unit weight of the earth paste acting as support medium. However, the quantity of the surface load representing the face support is kept constant during the entire tunnel excavation.

- Tail void grouting pressure is represented by a distributed surface load without consideration of the thin grouting layer and time-dependent behavior of the grouting material due to computational costs. The surface load is applied to the corresponding soil volume elements over the length of two excavation steps in the sections directly behind the shell elements which represent the shield machine. Therefore, the volume loss at the tail void due to the lining installation inside the shield is incorporated. Consequently, the adjacent soil in that grouting domain is allowed to freely move considering the applied support pressure boundary conditions. It is generally recommended that the value of the grouting pressure has to be higher than the face pressure at the same depth to avoid support material flow from the tunnel face toward the annular gap. Within this study the value of the grouting pressure is chosen based on practical experience by increasing the corresponding value of the face pressure at the crown of the excavated area by $50\,kN/m^2$. Moreover, the grouting pressure linearly increases from crown to invert of the excavated area with a gradient of $12\,kN/m^2$/m-depth, which is determined based on the assumed unit weight of the liquid grouting material. Hence, the following value of the grouting pressure at the crown of the excavated area $s_{grout,crown,H/D=1} = 135\,kN/m^2$ is applied within the numerical simulations. However, the quantity of the distributed surface load representing the grouting pressure is kept constant during the entire tunnel excavation.

- Volume loss due to overcutting and conicity of the machine is considered by contraction of the corresponding shell elements representing the shield machine (Brinkgreve et al., 2016). However, the annular gap of several cm thickness between the shield

machine and the adjacent soil is also partly backfilled with grouting material during the phase of excavation with respect to the sequential advance of the machine. Furthermore, stress redistribution will occur in the nearfield of the excavated area. Hence, due to the supported annular gap and the stress redistribution during excavation it is assumed that just a certain movement of the adjacent soil toward the excavated area occurs. The movement is assumed to be significantly lower than the entire size of the annular gap developed due to overcutting and conicity. A maximum tunnel volume loss ratio of 0.5% is assumed which corresponds to a unique radial deformation of the soil towards the excavated area of $\Delta u_{\mathrm{VL}} = 1.25\,\mathrm{cm}$. Hence, a maximum contraction factor of 0.5% is employed in the numerical simulation model. The reduction of the diameter develops over the first 8 m length of the shield machine applying a linear contraction from 0% at the tunnel face to 0.5% after 8 m length. Whereas, the last 2 m length to the tail of the shield machine have a constant diameter with a constant contraction factor of 0.5%. Moreover, for reasons of consistency, the contraction factor of 0.5% initially has to be applied to the area behind the grouting domain representing the lining segments as well.

Nonetheless, further subsystems such as machine steering processes including re-meshing and jack thrust forces are not taken into account.

8.1.3 Staged construction

For the numerical 3D simulation of mechanized tunneling the step-by-step or staged construction approach is employed as already applied in many other numerical studies using three-dimensional models. The numerical simulation starts with an initialization phase (O) where the effective stress state is calculated and the state variables of the constitutive BSP model are initialized.

(0) The initial effective stress field of the soil domain is calculated based on a so-called K_0-procedure as already described in chapter 4. That is, the effective vertical stress in each stress point is calculated in a way to be in equilibrium with the self-weight of the soil. The effective horizontal stress is calculated accordingly based on the user-defined K_0 value. Moreover, the following variables of the BSP model are initialized: initial void ratio, initial amount of structure, initial size and rotation of the bounding surface based on the initial stress eventually modified by a given preconsolidation stress or YSR value, initial size of the intrinsic reference surface, initial position of the projection center and initial value of the damage parameter.

Afterwards, an additional so-called plastic nil step phase in which no additional load is applied is conducted. The plastic nil step using the constitutive BSP model allows the system to correct and equilibrate small out-of-balance forces when the stress field was not in equilibrium after the K_0-procedure. However, additional displacements occuring during the plastic nil step are ignored for further computational phases starting from a zero displacement field. For more information it is referred to Brinkgreve et al. (2016).

For the simulation of mechanized tunneling in a water-saturated clay deposit so-called fully undrained and fully drained analyses are taken into consideration. The fully undrained analysis incorporates a computational phase which allows for the full generation of excess pore-water pressure induced by tunnel excavation and advance with changing boundary and loading conditions. That is, the dissipation of excess pore-water pressure is prohibited within this computational phase and a constant soil volume is assumed. The fully undrained analysis is applicable when investigating the short-term construction since natural clays show a slow excess pore-water pressure dissipation due to low hydraulic permeability and low stiffness. Furthermore, fully drained analyses implying an instantaneous dissipation of the excess pore-water pressure are conducted for reasons of comparison. Consolidation processes by incorporating coupled hydro-mechanical computational phases are not considered within the current study but might be investigated in further studies.
However, the initial position of the shield machine is set to an initial advancement of 30 m. Moreover, the following processes (A) to (E) involved in mechanized tunneling are numerically simulated. It is to be noted that the current position of the shield machine/tunnel face is indicated by i_{TBM}.

(A) The excavation of a certain soil volume is simulated by removing/deactivating the corresponding ground volume elements in front of the shield machine at position $i_{\mathrm{TBM}} + 1$. Whereat, the excavation length of 2 m corresponds to the width of one lining ring.

(B) To ensure the face stability the distributed mechanical surface load representing the face support pressure is shifted to the new position of the tunnel face $i_{\mathrm{TBM}} + 1$.

(C) The sequential advance of the shield machine from position i_{TBM} to $i_{\mathrm{TBM}} + 1$ is simulated by shifting (activating/deactivating) all five shell elements representing the shield machine by one position. The contraction of the shell elements to take into account the overcutting and the conicity of the shield has to be adopted in similar manner. The same holds true for the interface elements to model the contact properties between shield and soil.

(D) Besides, the distributed mechanical surface load acting on the soil volume elements over two segments directly behind the shield representing the grouting pressure is shifted each by one position because the tail void space is moving along with the advance of the shield machine. It is to be noted that neither shell elements nor interface elements are activated where the distributed mechanical surface load is applied.

(E) A new ring of lining segments is installed at the former position of the mechanical surface load by activating the corresponding volume elements. The interface elements to model the contact properties between lining and soil have to be assigned to the new lining ring.

The procedure (A) to (E) is repeated until the aimed advance of the machine is reached.

8.2 Summary

In this chapter the development of an adequate numerical 3D model for the simulation of mechanized tunneling utilizing the finite element code PLAXIS 3D was discussed. The description highlighted the geometry of the system, the initial and boundary conditions and the mesh discretization. Whereat, the geometry and the boundary conditions of the synthetic numerical simulation model are chosen with respect to an imaginary mechanized tunnel excavation in a water-saturated natural Onsøy clay deposit.
The chapter dealed with the numerical modeling of the considered subsystems such as sequential advance, shield machine and precast concrete lining, soil-structure interaction, tunnel face support, tail void grouting and volume loss. Special consideration was also given to the numerical simulation of the staged construction of mechanized tunneling and the fully undrained and fully drained analyses.
The presented numerical tunnel simulation model is suitable for the analysis of the excavation of a single horizontal tunnel for a given overburden depth. Hence, the developed numerical tunnel simulation model allows for the assessment of the influence of the soil properties of natural clay on the system behavior caused by mechanized tunneling as discussed in the following chapter.

9 Natural clay behavior with application to mechanized tunneling

This chapter deals with the evaluation of the influence of the mechanical properties of natural clay on the numerical model response induced by mechanized tunneling. For the numerical investigation an imaginary shallow mechanized tunnel excavation in a water-saturated natural Onsøy clay deposit under so-called greenfield conditions is considered. In particular, the spatial and construction stage dependent evolution of the influence of the mechanical properties of natural clay on the system behavior arising from the continuous construction process of the tunnel is analyzed. Whereat, special focus is set on the relevant natural clay properties such as inherent and stress-induced anisotropy, initial structure and its progressive destructuration and the behavior under non-monotonic or cyclic loading such as stress-strain hysteresis and elastoplastic transition, stiffness degradation and accumulation of plastic strain.

It has to be noted that the numerical tunnel simulations employing the constitutive BSP model is not validated against any case study about mechanized tunneling in natural clay. However, the constitutive BSP model was calibrated and validated on the element level against various geotechnical laboratory tests on natural Onsøy clay. The study showed a sufficient level of accuracy when comparing numerical and experimental results. From a practical point of view the transferability of the BSP model to the mechanized tunneling simulation is justified since the stress-strain behavior of natural clay is adequately reproduced in the element tests under consideration of the initial stress conditions, drainage conditions and effective stress paths as they are expected for the mechanized tunneling application in water-saturated natural clay deposits. Furthermore, the study illustrated the superiority of the more advanced BSP model extensions with higher level of complexity in capturing various aspects of the typical constitutive behavior of natural clays.

Hence, the reliability of the outcome of the numerical study on mechanized tunneling in natural clay deposits using the hierarchical BSP model family apporach is given especially in qualitative manner even without comparison to any case study.

At first, the numerical analysis is introduced more detailed. Therefore, the numerical setup, the investigated scenarios regarding the consolidation and drainage conditions, the synthetic measurement section used for evaluation, the significant construction stages and the assessed model responses regarding mechanized tunneling are discussed. The subsequent section of this chapter presents the numerical results regarding the various model responses. Initially a qualitative and quantitative description and analysis of the general model responses such as surface settlements, ground movements, evolution of effective stress path and generation of excess pore-water pressure induced by mechanized tunneling is given. Furthermore, the required degree of complexity of the constitutive BSP model for the numerical analysis of mechanized tunneling in natural clay deposits is assessed. That is, the numerical model responses of the different simulation runs with varying hierarchical complexity of the four model extensions are compared to each other and evaluated with respect to the relative importance of a particular natural clay property related to a specific model response arising from mechanized tunneling. To better understand the spatial and construction stage dependent evolution of the influence of the mechanical properties on the system behavior the evolution of the state variables of the BSP model corresponding to destructuration, stress-induced anisotropy and stiffness degradation and accumulation effects under non-monotonic or cyclic loading are evaluated.

The chapter closes with the development of practical recommendations regarding the main objective if typical mechanical properties of natural clay behavior (e.g. inherent and stress-induced anisotropy, structure and destructuration, elastoplastic hysteresis, stiffness degradation and accumulative effects under non-monotonic or cyclic loading) have to be considered in the numerical analysis of a particular model response in the design and construction phases of mechanized tunneling.

9.1 Numerical analysis

9.1.1 Setup

The corresponding numerical analysis is conducted by using the adequate numerical 3D model for the simulation of mechanized tunneling incorporating the relevant subsystems as discussed in chapter 8. Moreover, the concept of the hierarchical BSP model family as introduced in chapter 7 and the adequate constitutive BSP model parameter set related to natural Onsøy clay as calibrated in chapter 6 are applied. Thus, four hierarchical BSP model extensions are considered as listed below. The results of each model extension are marked with the corresponding color.

- Extended Modified Cam-Clay (**MCC**) → basic model, elastoplasticity, isotropic hardening and softening, non-associated flow
- **Saniclay** → additional inherent and stress-induced anisotropy
- **Saniclay D** → additional destructuration
- **Saniclay D + BSP** → additional bounding surface plasticity incorporating stress-strain hysteresis and elastoplastic transition, stiffness degradation and accumulative effects under non-monotonic or cyclic loading

9.1.2 Scenarios

The following scenarios with respect to the consolidation and drainage conditions are numerically investigated. Consequently, fully undrained and fully drained analyses are conducted starting from normally and overconsolidated initial stress conditions.

- **NC, D** → normally consolidated conditions, drained conditions
- **OC, D** → overconsolidated conditions, drained conditions
- **NC, UD** → normally consolidated conditions, undrained conditions
- **OC, UD** → overconsolidated conditions, undrained conditions

9.1.3 Synthetic measurement section

To trace the spatial and construction stage dependent variation of the model responses with advancing excavation a synthetic transverse measurement section is defined in the middle of the numerical model ($Y = 100$ m) to assure no influence of the model boundaries on the numerical measurements.

9.1.4 Construction stages

For the evaluation of the spatial and construction stage dependent evolution of the influence of the mechanical properties on the system behavior arising from the continuous construction process of the tunnel the model responses are analyzed with respect to the following significant construction stages (1) to (6).

(1) Tunnel excavation begins from initial state (calculation phase 2)

(2) TBM face reaches the measurement section at $Y = 100$ m (calculation phase 37)

(3) TBM tail reaches the measurement section and grouting starts in the measurement section (calculation phase 42)

(4) Grouting ends and installation of lining starts in the measurement section (calculation phase 44)

(5) TBM face reaches $Y = 118$ m (calculation phase 46)

(6) TBM face reaches $Y = 198$ m (calculation phase 86) and steady state is reached in the measurement section

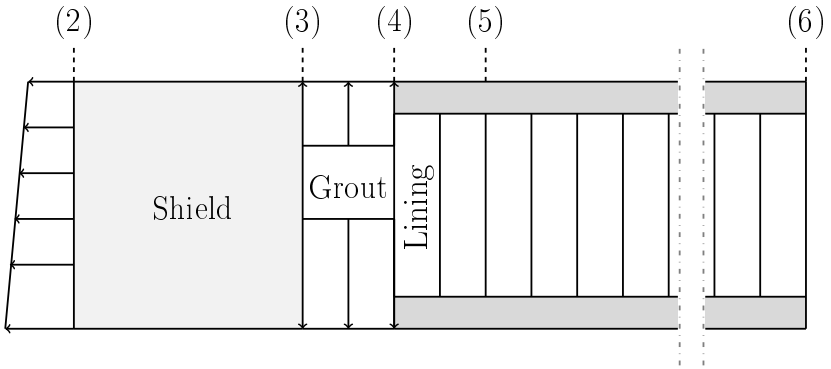

Figure 9.1: Significant construction stages

9.1.5 Model responses

For the assessment of the influence of the mechanical properties of natural clay on the system behavior induced by the mechanized tunneling process the following relevant numerical model responses are chosen.

- Surface settlements, vertical soil displacements and void ratio
  - Transverse settlement trough in the synthetic measurement section ($Y = 100$ m) for construction state (TBM at $Y = 118$ m) and steady state wrt. the final tunnel excavation state (TBM at $Y = 198$ m)
  - Longitudinal settlement trough along the tunnel axis Y ($X = 0$ m) wrt. tunnel excavation state where the shield machine has reached the synthetic measurement section (TBM at $Y = 100$ m)
  - Evolution of surface settlements s of a fixed synthetic measurement point ($Y = 100$m, $X = 0$m) traced over the developing distance ΔY between the advancing shield machine and the measurement point
  - Evolution of vertical soil displacements u_{v} via transverse contour plots in the synthetic measurement section ($Y = 100$ m) wrt. the significant construction stages (1) to (6) using the Saniclay D+BSP model extension
  - Evolution of void ratio e via transverse contour plots in the synthetic measurement section ($Y = 100$ m) wrt. the significant construction stages (1) to (6) using the Saniclay D+BSP model extension
- Effective stress path
  - Evolution of effective stress path (Effective mean stress p' vs. deviatoric stress $|\boldsymbol{s}|$) wrt. the continuous tunnel excavation for representative stress points around the tunnel
    - 1 m above the tunnel crown ($Y = 100$ m, $X = 0$ m, $Z = -9$ m)
    - 1 m beside the tunnel side ($Y = 100$ m, $X = -6$ m, $Z = -15$ m)
    - 1 m below the tunnel invert ($Y = 100$ m, $X = 0$ m, $Z = -21$ m)
    - 5 m above the tunnel crown ($Y = 100$ m, $X = 0$ m, $Z = -5$ m)

- Excess pore-water pressure
  - Evolution of excess pore-water pressure Δp_{w} traced over the developing distance ΔY between the advancing shield machine and representative measurement points:
    - 1 m above the tunnel crown ($Y = 100\,\mathrm{m}$, $X = 0\,\mathrm{m}$, $Z = -9\,\mathrm{m}$)
    - 1 m beside the tunnel side ($Y = 100\,\mathrm{m}$, $X = -6\,\mathrm{m}$, $Z = -15\,\mathrm{m}$)
    - 1 m below the tunnel invert ($Y = 100\,\mathrm{m}$, $X = 0\,\mathrm{m}$, $Z = -21\,\mathrm{m}$)
    - 5 m above the tunnel crown ($Y = 100\,\mathrm{m}$, $X = 0\,\mathrm{m}$, $Z = -5\,\mathrm{m}$)
  - Evolution of excess pore-water pressure Δp_{w} via transverse contour plots in the synthetic measurement section ($Y = 100\,\mathrm{m}$) wrt. the significant construction stages (1) to (6) using the Saniclay D+BSP model extension
- State variables of the BSP model and plastic strain
  - Evolution of state variables and plastic strain via transverse contour plots in the synthetic measurement section ($Y = 100\,\mathrm{m}$) wrt. the significant construction stages (1) to (6) using the Saniclay D+BSP model extension
    - Structure variable S_{i}
    - Rotational hardening variable $|\boldsymbol{\alpha}|$
    - Damage variable d
    - Plastic strain $|\boldsymbol{\varepsilon}^{\mathrm{p}}|$

9.2 Results and evaluation

9.2.1 Surface settlements, vertical soil displacements and void ratio

The surface settlements and the ground movements play the most significant role for the design and construction stages of mechanized tunneling in urban areas. Therefore, the transverse and longitudinal surface settlements as well as the vertical soil displacements and the void ratio related to the volumetric behavior are evaluated.

9.2.1.1 Transverse settlement trough

The transverse settlement trough in the synthetic measurement section ($Y = 100$ m) for a) construction state (TBM at $Y = 118$ m) and b) steady state wrt. the final tunnel excavation state (TBM at $Y = 198$m) is displayed in Figures 9.2 to 9.5 for the investigated four scenarios with respect to the consolidation and drainage conditions. Positive values represent surface settlements and negative values surface heave. The maximum settlements always occur above the tunnel axis ($X = 0$ m) independently of the used model extension and the investigated scenario.

NC, D scenario

The tunnel excavation in a natural clay deposit starting from normally consolidated initial stress conditions assuming drained conditions obviously shows the largest settlements $s = 67.9$ mm at the construction state (5) and $s = 74.5$ mm at the steady state (6) when using the most sophisticated Saniclay D+BSP model extension as visualized in Figure 9.2. The Saniclay D model extension results in slightly smaller settlements $s = 66.1$ mm at the construction state (5) and $s = 72.0$ mm at the steady state (6). Whereas, the MCC and the Saniclay model extensions, which do not account for destructuration, lead to significant smaller settlements $s = 26.1$ mm and $s = 30.9$ mm at the construction state (5). Moreover, the MCC and Saniclay model extensions evidence certain incremental upward displacements while moving from the construction state (5) to the steady state (6) as confirmed by the slightly smaller final settlements of $s = 22.7$ mm and $s = 28.0$ mm. That is, the maximum settlements predicted by the MCC and the Saniclay model extensions are 55-70% smaller compared to the most sophisticated Saniclay D+BSP model extension representing a significant underestimation.
The aforementioned differences of the settlement behavior mainly arise from the plasticity induced destructuration, which is incorporated in the Saniclay D and the Saniclay D+BSP model extensions while it is missing in the MCC and the Saniclay model extensions. The structure decreases with increasing plastic straining. Plastic straining is strongly induced during stress redistribution caused by the excavation process conditioning a volume loss around the machine due to overcutting and conicity of the shield machine, soil removal and corresponding stress release and buoyancy effects, application of the support pressures and the compressible behavior of the lining. Along with that, the stiffness of natural clay progressively decreases with increasing destructuration which explains the larger settlements compared to the model extensions which do not account for destructuration.

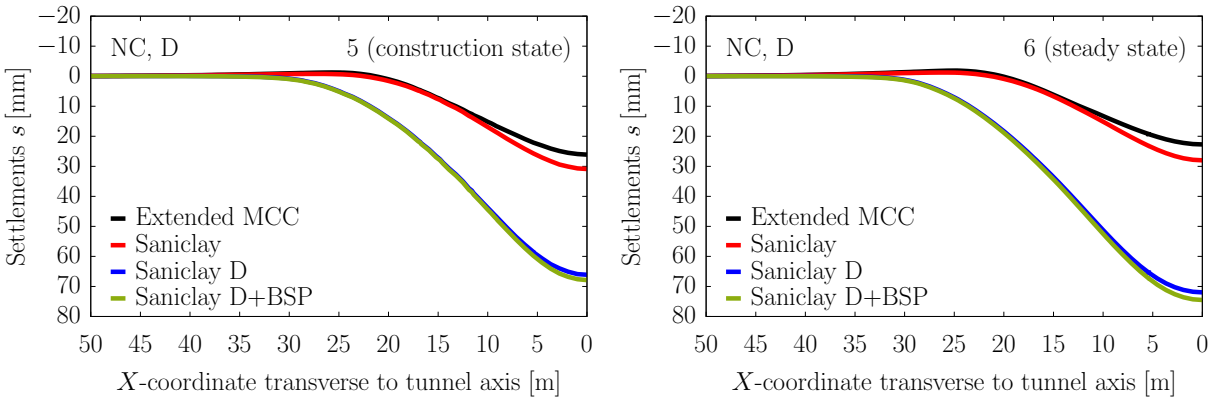

Figure 9.2: Transverse settlement trough in the synthetic measurement section (Y = 100 m) for a) construction state (TBM at $Y = 118$ m) and b) steady state wrt. the final tunnel excavation state (TBM at $Y = 198$ m) for NC, D scenario

The difference regarding the settlements between the Saniclay model extension and the MCC model extension is about 16-18%. That is, considering the inherent and stress-induced anisotropy with an initial and stress-induced rotation of the bounding surface leads to an increase of the settlements since the rotational hardening is slightly activated during the stress redistribution around the excavation zone.
However, the differences in the settlement behavior between Saniclay D and Saniclay D+BSP are almost negligible (3-4%). This means that stress-strain hysteresis and elasto-plastic transition, stiffness degradation and accumulative effects under non-monotonic and cyclic loading are not significantly mobilized. That is, the model response is either anyway elastoplastic due to the normally consolidated initial stress located on the bounding surface or anyway predominantly elastic and very stiff in the soil domains where stress release occurs. Elastoplastic transition zones are not that distinctly formed to cause additional plastic strain and conditionally induce destructuration, rotational hardening and stiffness degradation while the effective stress path is moving inside the bounding surface. Thus, the Saniclay D and the Saniclay D+BSP model extensions act almost the same and just slightly larger settlements are induced by the Saniclay D+BSP model extension.
Furthermore, the transverse settlement trough of the Saniclay D and the Saniclay D+BSP model extensions is much steeper due to the larger maximum settlements compared to the settlement trough of the MCC and Saniclay model extensions. Hence, the inclination of the settlement trough is underestimated when using the MCC and the Saniclay model extensions. Whereat, the gradient of the settlement trough decisively governs the damage assessment of edifices and urban infrastructure related to mechanized tunneling.

However, the surface area affected by settlements is wider for the Saniclay D and Saniclay D+BSP model extensions since the MCC and the Saniclay model extensions even show heave of the ground surface adjacent to the settlement trough with minimum values up to $s = -1.2$ mm to $s = -1.9$ mm. The heave of the adjacent ground surface originates from the stress release of the soil below the tunnel during the excavation process and the lining installation in combination with the low overburden and the water-saturated clay deposit resulting in incremental upward displacements of the soil and even heave when using the MCC and Saniclay model extensions. Whereat, heave at the ground surface is suppressed by the superimposed effect of destructuration when using the Saniclay D and the Saniclay D+BSP model extensions.
The width of the influenced surface area (defined as restricted by settlements less than 1 mm) with respect to the Saniclay D and the Saniclay D+BSP model extensions is about 30 m transverse to the tunnel axis. The transition from settlements to heave is reached at a transverse distance to the tunnel axis of about 20 m for the MCC and the Saniclay model extensions. The width of the influenced surface area in transverse direction (defined as restricted by heave less than 1 mm) combined of settlement and heave is about 30 m which corresponds to the width of the influenced surface area predicted by the Saniclay D+BSP model extension.

OC, D scenario

Whereas, when starting the tunnel excavation from overconsolidated initial stress conditions assuming drained conditions maximum settlements $s = 6.1$ mm at the construction state (5) and $s = 0.8$ mm at the steady state (6) are reached when using the Saniclay D+BSP model extension as displayed in Figure 9.3. The magnitude of the settlements at the construction state (5) is about 9% of the corresponding value of the normally consolidated NC, D scenario only. For normally consolidated initial stress conditions the model response is predominantly elastoplastic and soft and the stiffness is governed by both the elastoplastic compression parameter λ and the elastic swelling parameter κ. On the contrary, for overconsolidated initial stress conditions the model response is predominantly elastic and much stiffer since the initial stress is located inside the bounding surface or even inside the elastic nucleus for the Saniclay D+BSP model extension and the effective stress path is mostly moving inside the bounding surface afterwards. The stiffness is mainly controlled by the elastic swelling parameter κ in this case. Since the elastoplastic behavior is much softer than the elastic behavior a larger magnitude of settlements is obtained for the normally consolidated NC, D scenario.

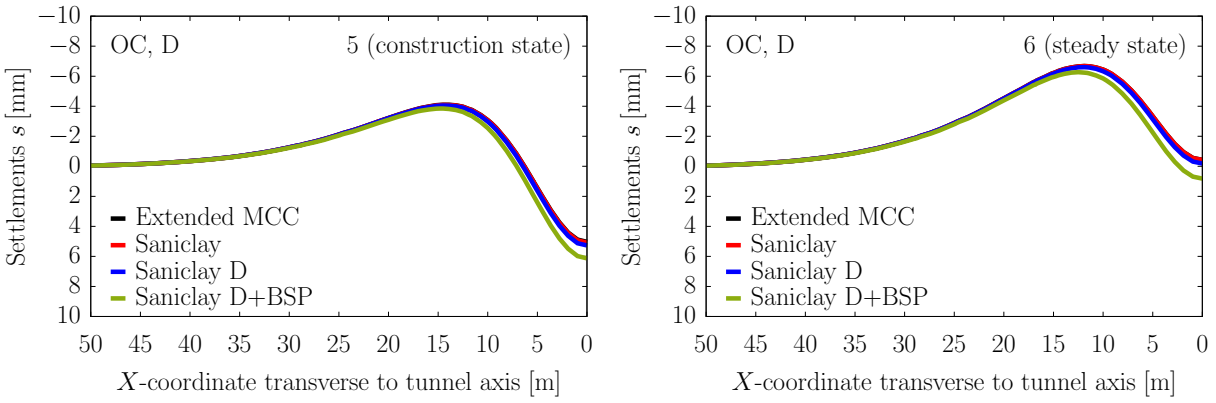

Figure 9.3: Transverse settlement trough in the synthetic measurement section ($Y = 100\,\text{m}$) for a) construction state (TBM at $Y = 118\,\text{m}$) and b) steady state wrt. the final tunnel excavation state (TBM at $Y = 198\,\text{m}$) for OC, D scenario

There is no striking difference in the transverse settlement trough noticeable related to the construction state (5) and the steady state (6) between the three elastoplastic MCC, Saniclay and Saniclay D model extensions. To conclude, the inherent and stress-induced anisotropy as well as the progressive destructuration are rather irrelevant regarding the transverse settlement behavior since just a small amount of plasticity is induced constrained to a limited area in the nearfield of the tunnel.

Compared to the maximum settlements predicted by the Saniclay D+BSP model extension the settlements of the MCC, Saniclay and Saniclay D model extensions at the construction state (5) are up to 13-18% smaller and hence slightly underestimated when using those model extensions only. However, the qualitative shape of the transverse settlement trough is very similar for all four model extensions. To sum up, the behavior under non-monotonic or cyclic loading is mobilized to a certain extent. The difference of the settlements originate from the BSP concept which allows for the development of plastic strain even for an effective stress path moving inside the bounding surface. Whereat, the shape hardening function $\hat{h}$ and the damage variable d control the initial stiffness and its degradation with plastic straining. Consequently, remarkable amount of plasticity is induced even while moving inside the bounding surface and the model response becomes more soft. Conditionally, destructuration and rotational hardening are activated in a certain manner since they are also governed by plastic straining. Whereas, for the three elastoplastic model extensions the model response is elastic for effective stress paths inside the bounding surface and thus the model response is more stiff.

The ground surface adjacent to the settlement trough experiences heave with minimum values up to $s = -3.9\,\text{mm}$ at the construction state (5) and $s = -6.3\,\text{mm}$ at the steady state (6) when using the Saniclay D+BSP model extension. Concluding, the entire ground surface experiences incremental upward displacements while moving from the construction state (5) to the steady state (6). That is, the settlements decrease and the heave of the adjacent ground surface increases. These phenomena hold true for all four model extensions. To be more specific, during tunnel excavation and installation of lining the soil below the tunnel exhibits a stress release. The stress release during shield machine advance is caused by so-called buoyancy effects during soil removal denoting upward forces resulting from the difference in weight of the shield machine / installed lining and the excavated soil. By reason of stress release upward displacements of the soil below the tunnel and associated uplift of the relatively stiff lining are induced as visualized in Figure 9.9. The counterbalancing forces are relatively small due to the fact that a shallow tunnel with a low overburden depth ($H/D = 1$) is considered resulting in smaller overburden pressure. Higher vertical stress on the tunnel lining caused by a larger overburden depth would prevent such uplift effects. Since the mechanized tunneling takes place in a water-saturated clay deposit hydrostatic buoyant forces occur which intensifies the upward displacements of the soil and the uplift of the lining due to reduced unit weights of the overburden and the lining.

For the MCC, Saniclay and Saniclay D model extensions the settlements entirely turn into heave of the ground surface while moving from the construction state (5) to the steady state (6). In addition, the maximum heave is up to 5-6% larger for the MCC, Saniclay and Saniclay D model extensions compared to the Saniclay D+BSP model extension. The explanation is that the already occurred settlements from the construction state (5) are superimposed with the incremental upward displacements afterwards resulting in a slightly smaller total amount of heave when considering the Saniclay D+BSP model extension. The width of the influenced surface area in transverse direction (defined as restricted by heave less than 1 mm) with respect to all four model extensions is about 35 m transverse to the tunnel axis at the construction state (5) and the steady state (6). Concluding, the influenced surface area in transverse direction under overconsolidated initial stress conditions assuming drained conditions is 17% wider than under normally consolidated initial stress conditions due to the fact that the heave effects are spatially spreaded more widely than the settlement effects.

NC, UD scenario

Tunnel excavation starting from normally consolidated initial stress conditions assuming undrained conditions produces maximum settlements $s = 12.2$ mm at the construction state (5) and $s = 13.6$ mm at the steady state (6) when using the Saniclay D and Saniclay D+BSP model extensions as displayed in Figure 9.4. The magnitude of the settlements at both the construction state (5) and the steady state (6) is about 18% of the settlements from the drained NC, D scenario only. The distinct difference of the magnitude of settlements is caused by the generation of excess pore-water pressure as shown in Figures 9.14 to 9.21 and the corresponding evolution of the effective mean stress as shown in Figures 9.13 to 9.15 during mechanized tunneling in assumed undrained conditions. The evolution of the effective mean stress in the nearfield around the tunnel leads to effects counteracting the general downward displacements originating from the excavation process and associated volume loss around the shield machine as well as the compressibility and destructuration of natural clay induced by plastic straining. The smaller the effective stress transferred to the soil skeleton the smaller the corresponding mechanical deformations. This counteracting effects result in smaller settlements at the ground surface as compared to the drained NC, D scenario.
Since the Saniclay D and Saniclay D+BSP model extensions lead to almost identical model responses regarding the transverse settlement trough the relevance of the behavior under non-monotonic or cyclic loading is negligible. The MCC and the Saniclay model extensions, which do not account for destructuration, lead to smaller settlements $s = 12.9$ mm

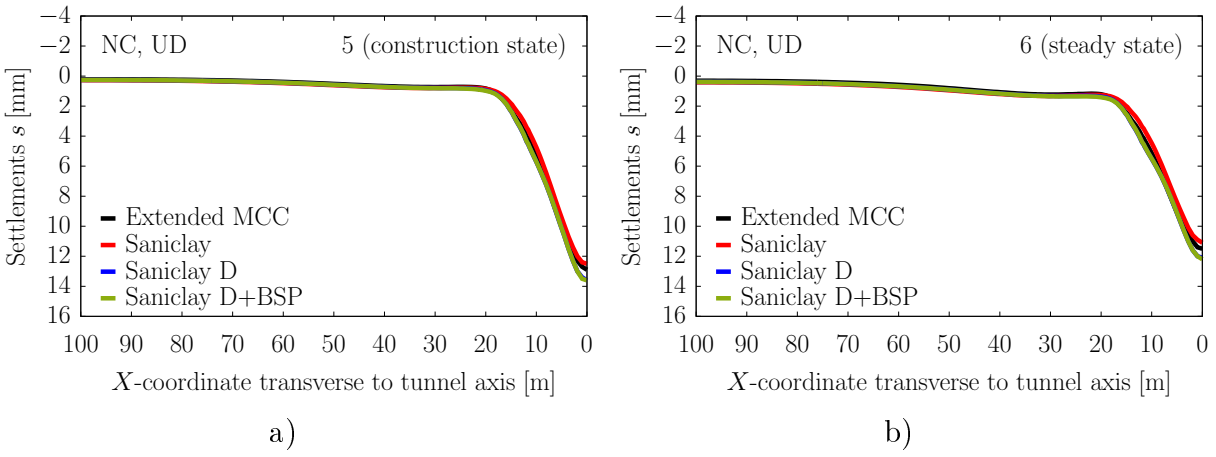

Figure 9.4: Transverse settlement trough in the synthetic measurement section ($Y = 100$ m) for a) construction state (TBM at $Y = 118$ m) and b) steady state wrt. the final tunnel excavation state (TBM at $Y = 198$ m) for NC, UD scenario

and $s = 12.5$ mm at the construction state (5) and $s = 11.5$ mm and $s = 11.1$ mm at the steady state (6). This corresponds to an underestimation of the settlements of 8-9% when using the MCC and the Saniclay model extensions only. Compared to the drained NC, D scenario with an underestimation of 55-70% the effects of destructuration become noticeable, but by far not as significant. Moreover, the difference regarding the settlements between the Saniclay model extension and the MCC model extension is about 3% only. However, the MCC model extension shows slightly larger settlements. Nevertheless, the effects of inherent and stress-induced anisotropy can be judged negligible.
The qualitative shape of the transverse settlement trough is very similar for all four model extensions. Furthermore, all model extensions exhibit incremental upward displacements while moving from the construction state (5) to the steady state (6) resulting in a decrease of the settlements by 11%. Total heave effects at the ground surface can not be observed for any of the four model extensions. The width of the influenced surface area in transverse direction (defined as restricted by settlement less than 1 mm) with respect to all four model extensions is about 20 m transverse to the tunnel axis at the construction state (5) and 46 m at the steady state (6). To summarize, the influenced surface area in transverse direction under normally consolidated initial stress conditions assuming undrained conditions is 33% narrower at the construction state and 53% wider at the steady state than compared to assumed drained conditions. That is, the induced soil displacements are differently transferred when assuming undrained conditions due to the development of excess pore-water pressure which is not allowed to dissipate.

OC, UD scenario

Whereas, when starting the tunnel excavation from overconsolidated initial stress conditions assuming undrained conditions maximum settlements $s = 8.1$mm at the construction state (5) and $s = 6.8$ mm at the steady state (6) are reached when using the Saniclay D+BSP model extension as displayed in Figure 9.5. When comparing with the drained OC, D scenario the following main differences can be observed. The magnitude of the settlements at the construction state (5) is about 33% larger compared to the drained OC, D scenario when applying the Saniclay D+BSP model extension. The ground surface experiences relatively small incremental upward displacements while moving from the construction state (5) to the steady state (6) of about 14-18%. That is, the settlements just slightly decrease and the ground surface does not experience heave at all. However, the shape of the transverse settlement trough of the adjacent ground surface looks similar for both scenarios.

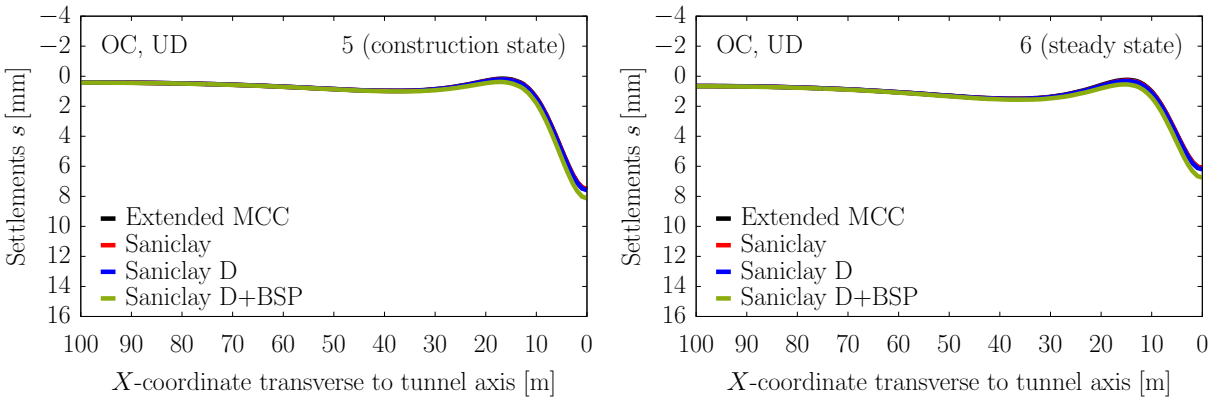

Figure 9.5: Transverse settlement trough in the synthetic measurement section (Y = 100 m) for a) construction state (TBM at $Y = 118$ m) and b) steady state wrt. the final tunnel excavation state (TBM at $Y = 198$ m) for OC, UD scenario

As for the overconsolidated, drained OC, D scenario, there is again no striking difference noticeable in the transverse settlement trough related to the construction state (5) and the steady state (6) between the three elastoplastic MCC, Saniclay and Saniclay D model extensions. That leads to the conclusion that the inherent and stress-induced anisotropy as well as the progressive destructuration are rather unimportant regarding the transverse settlement behavior for tunneling in overconsolidated natural clay deposits independently of the drainage conditions.

Compared to the maximum settlements of the Saniclay D+BSP model extension the settlements of the MCC, Saniclay and Saniclay D model extensions at the construction state (5) and at the steady state (6) are up to 6-10% smaller and hence underestimated. However, the qualitative shape of the transverse settlement trough is very similar for all four model extensions. It must be noted that the width of the influenced surface area in transverse direction is difficult to determine due to the saddle-shaped development. Nevertheless, the transverse settlement trough firstly falls below the defined limit of 1 mm settlement at a distance of 10-12 m transverse to the tunnel axis at both the construction state (5) and the steady state (6). Deducing, the consideration of the soil behavior under non-monotonic or cyclic loading is of moderate importance regarding the transverse settlements when it comes to mechanized tunneling in overconsolidated natural clay deposits again independently of the drainage conditions.

9.2.1.2 Longitudinal settlement trough

The longitudinal settlement trough along the tunnel axis Y ($X = 0$ m) wrt. a tunnel excavation state where the shield machine has reached the synthetic measurement section (TBM at $Y = 100$m) is shown in Figure 9.6 for the four investigated scenarios a) NC, D b) OC, D c) NC, UD d) OC, UD. Positive values represent surface settlements and negative values surface heave. The current position of the shield machine is indicated by a dashed vertical line at $Y = 100$m. The analysis of the longitudinal settlement behavior is focusing on the evaluation of the influenced surface area (defined as restricted by settlement and heave less than 1 mm) in longitudinal direction ahead of the shield machine.

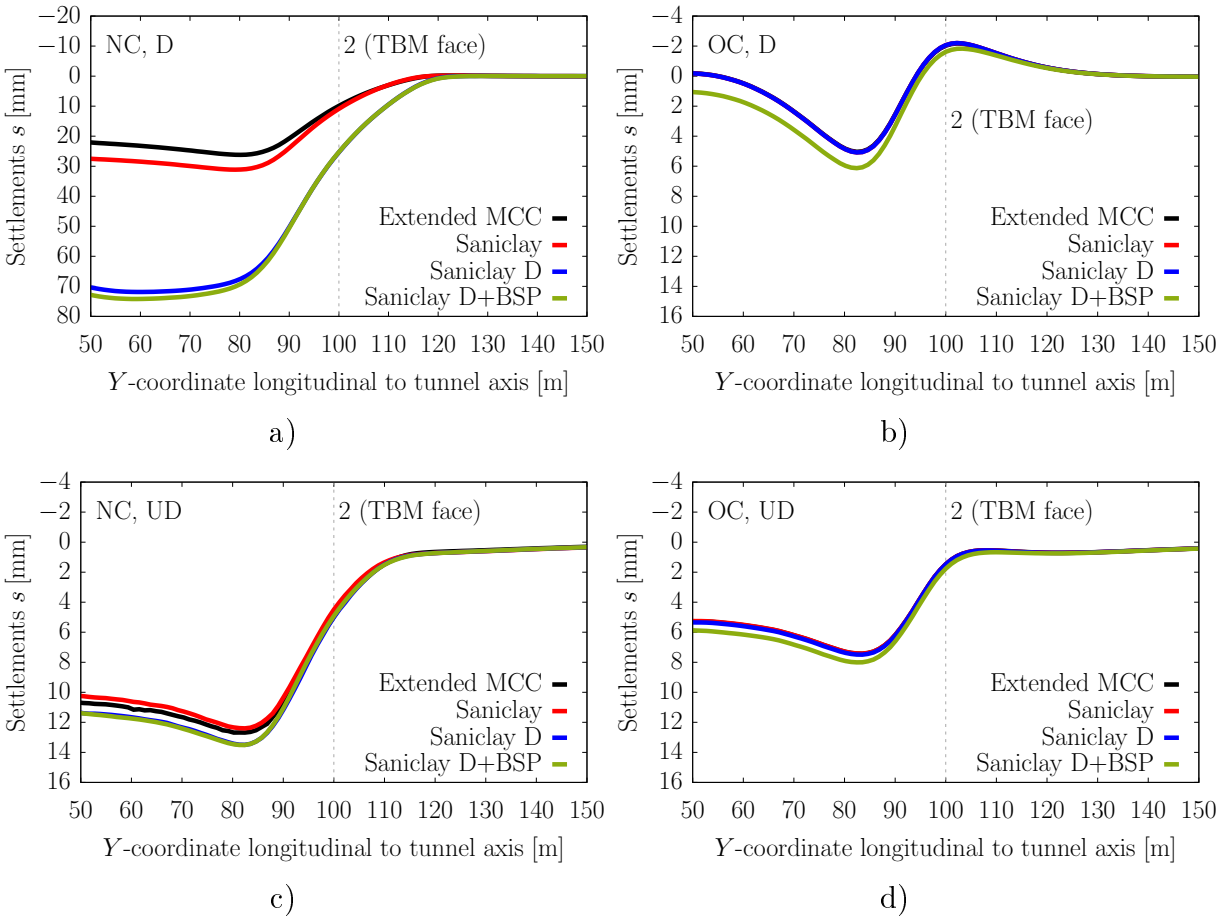

Figure 9.6: Longitudinal settlement trough along the tunnel axis Y ($X = 0$ m) wrt. a tunnel excavation state where shield machine has reached the synthetic measurement section (TBM at $Y = 100$ m) for a) NC, D b) OC, D c) NC, UD d) OC, UD scenarios

NC, D scenario

The length of the influenced surface area in longitudinal direction ahead of the shield machine is about 20 m when using the Saniclay D and the Saniclay D+BSP model extensions in the NC, D scenario as visualized in Figure 9.6a. In contrast, the length of the influenced surface area decreases by about 25% to values of 14-16 m when not accounting for the destructuration of the natural clay by using the MCC and Saniclay model extensions only. That is, a pronounced activation of the destructuration will lead to a noticeable enlargement of the influenced surface area in longitudinal direction ahead of the shield machine. This could become important when discussing safety measures for the reinforcement of the area ahead of the shield machine (e.g. anchoring in terms of spiles, installation of piperoof, elevation grouting). However, in the investigated case of a shallow tunnel with an overburden depth of $H/D = 1$ the maximum distance ahead of the shield machine corresponds to twice the tunnel diameter. In the context of damage assessment, the maximum inclination of the longitudinal settlement trough might be decisive.
In accordance with the results from the analysis of the transverse settlement behavior the most significant impact on the shape of the settlement trough is generated by the destructuration. Therefore, not considering destructuration effects will result in a flatter shape of the longitudinal settlement trough causing an underestimation of the damage potential. In addition, not accounting for inherent and stress-induced anisotropy will also lead to flatter longitudinal settlement troughs but not that impactful.

Other scenarios

Whereas, for the other scenarios the length of the influenced surface area in longitudinal direction ahead of the shield machine is almost independent of the employed model extension showing values of about 14-16 m (OC, D), 12-14 m (NC, UD) and 2-4 m (OC, UD) as displayed in Figure 9.6b-d. Whereat, the overconsolidated, drained OC, D scenario conversely shows heave of the ground surface in front of the shield machine. For the undrained NC, UD and OC, UD scenarios the ground surface in front of the shield machine settles as observed for the normally consolidated, drained NC, D scenario. The much smaller influenced surface area detected for the overconsolidated, undrained OC, UD scenario is caused by the saddle-shaped development of the settlements lying in a narrow band between +1 mm and -1 mm rated as irrelevant.

To sum up, mechanized tunneling in normally consolidated clay deposits assuming drained conditions leads to the largest influenced surface area in longitudinal direction ahead of the shield machine. This statement is generally in accordance with the findings from the analysis of the length of the influenced surface area in transverse direction. That is, mechanized tunneling assuming drained conditions exhibits larger influenced surface area than assuming undrained conditions. However, the width of the influenced surface area in transverse direction is larger for overconsolidated conditions while the length of the influenced surface area in longitudinal direction ahead of the shield machine is larger for normally consolidated conditions. That is, heave effects are more pronounced in the adjacent sideward areas transverse to the tunnel axis than in the area straight above the tunnel axis.

9.2.1.3 Evolution of surface settlements s

The evolution of the surface settlements s of a fixed synthetic measurement point ($Y = 100\,\text{m}$, $X = 0\,\text{m}$) traced over the developing distance ΔY between the advancing shield machine and the measurement point is illustrated in Figure 9.7 for the four investigated scenarios. Positive values represent surface settlements and negative values surface heave. The position of the shield machine is developing in relation to the fixed measurement point at the ground surface. The dashed vertical lines indicate when a particular construction stage of the mechanized tunneling process (2) to (5) reaches the measurement section. However, the construction stage (6) where the shield machine reaches $Y = 198\,\text{m}$ (corresponds to $\Delta Y = 98\,\text{m}$) is out of the range of the diagram since a constant settlement and hence the steady state is already achieved earlier.
When the tunnel excavation begins from the initial state (1) where the shield machine is located $\Delta Y = -70\,\text{m}$ away from the measurement section the surface settlements in the synthetic measurement point at $Y = 100\,\text{m}$ and $X = 0\,\text{m}$ are zero.
While the shield machine approaches to the measurement section surface settlements start to develop in the measurement point for the normally consolidated NC, D and NC, UD scenarios as shown in Figure 9.7a and 9.7c. Whereat, the distance of the shield machine to the measurement point at the time when remarkable settlements larger than 1 mm are observed corresponds to the length of the influenced area in longitudinal direction ahead of the shield machine as derived in the former section. In contrast, for the overconsolidated OC, D and OC, UD scenarios the measurement point experiences heave and incremental upward displacements when the shield machine approaches as displayed in Figure 9.7b and 9.7d. The heave effects related to the overconsolidated, drained OC, D scenario have

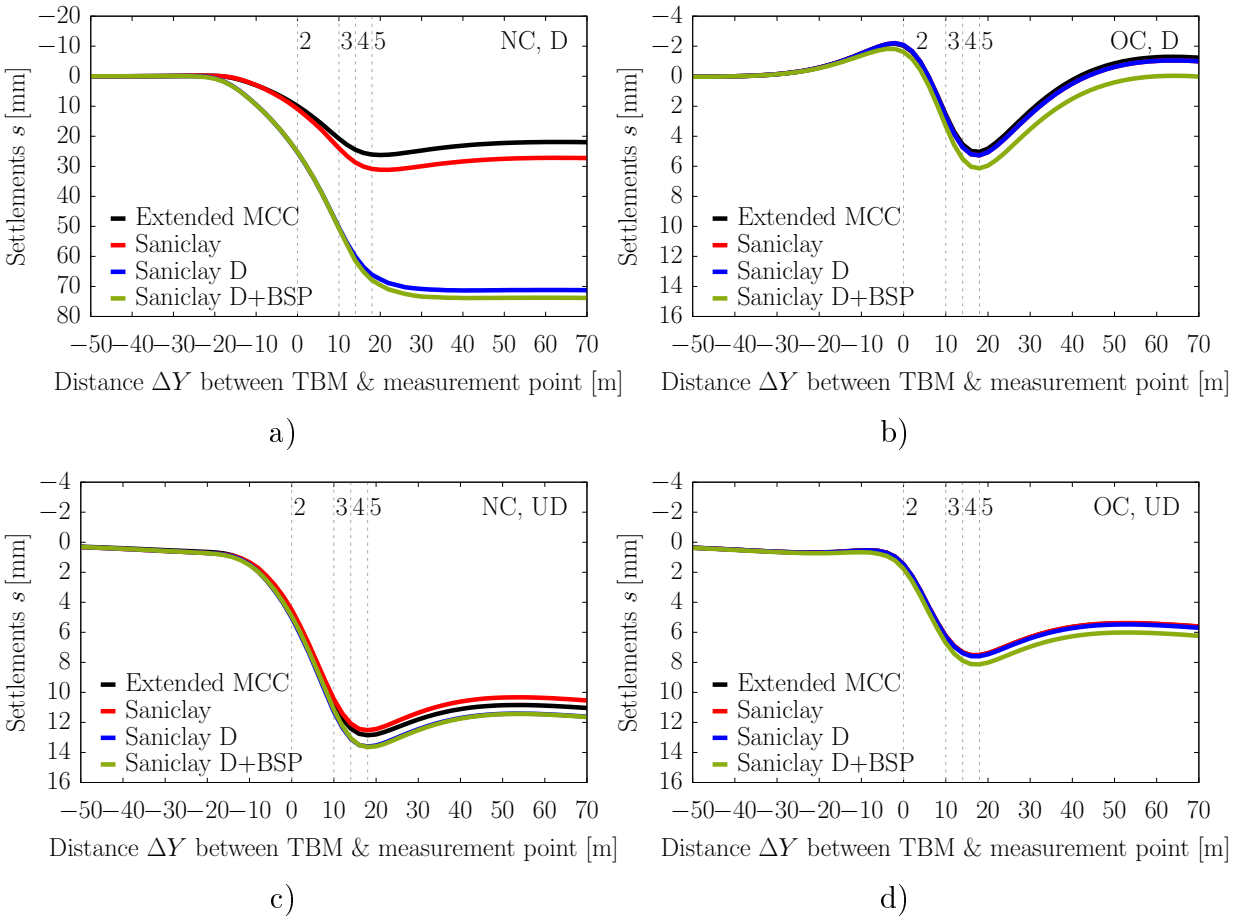

Figure 9.7: Evolution of surface settlements s of a fixed synthetic measurement point ($Y = 100$ m, $X = 0$ m) traced over the developing distance ΔY between the advancing shield machine and the measurement point for a) NC, D b) OC, D c) NC, UD d) OC, UD scenarios

minimum values of $s = -1.8$ mm for the Saniclay D+BSP model extension and slightly larger values of $s = -2.2$ mm for the other model extensions which do not account for the soil behavior under non-monotonic or cyclic loading. As an explanation, the heave effects arising in overconsolidated soil conditions with low overburden may be caused by the applied face support pressure at the tunnel face pushing the stiff elastic soil domain in front of the shield machine upwards. Add to this uplift effects of the overconsolidated stiff soil body prior to the arrival of the shield machine may occur due to the shallow overburden depth. Since the soil behavior for the Saniclay D+BSP model extension is a little softer due to introduced plasticity the heave effects diminish. Due to the predominantly elastic soil behavior there are less counteracting settlements induced by plasticity than seen for the normally consolidated scenarios.

When the shield machine reaches the measurement section at $Y = 100$ m at construction stage (2) approximately 34-39% of the maximum settlements related to the specific model extension have already been developed for the normally consolidated NC, D and NC, UD scenarios. However, the magnitude is partly dependent on the applied face support pressure. The amount of settlements in front of the shield machine and above might slightly reduce for larger face support pressure. Whereas, for the overconsolidated OC, D and OC, UD scenarios the generation of settlements is about to start when the shield machine reaches the measurement section (2) due to the previous heave effects and incremental upward displacements.

In the following the shield machine sequentially advances and the settlements are evolving caused by the volume loss of 0.5% due to overcutting and conicity of the shield machine and the existence of an annular steering gap between the shield and the adjacent soil. The volume loss initiates stress redistribution and elastoplastic behavior in the soil domain above the tunnel. When the tail of the shield machine reaches the measurement section at construction stage (3) approximately 68-79% of the maximum settlements related to the specific model extension have already been developed for the normally consolidated, drained NC, D scenario and up to 82-84% for the undrained NC, UD and OC, UD scenarios. Because of the previous heave at construction stage (2) the settlements for the overconsolidated, drained OC, D scenario is just about 50-54%. The advance of the shield machine from (2) to (3) corresponds to the length of the shield machine of 10 m and 5 sequential excavation steps of 2 m each.

Between the construction stages (3) to (4) tail void grouting pressure is applied in the area of the measurement section over 4 m and 2 sequential excavation steps of 2 m each. Due to the stress redistribution in the nearfield of the grouting zone further settlements are generated. At construction stage (4) approximately 82-93% of the maximum settlements related to the specific model extension have already been developed for the normally consolidated NC, D scenario and up to 96-97% for the undrained NC, UD and OC, UD scenarios. Even for the overconsolidated, drained OC, D scenario 90% of the maximum settlements have been developed. The lower value of 82% for the normally consolidated, drained NC, D scenario results from the Saniclay D and Saniclay D+BSP model extensions since the ongoing destructuration process is not yet completed.

Afterwards, the shield machine sequentially advances and the precast concrete lining is successively installed. At construction stage (4) the installation of lining starts in the measurement section. The shield machine reaches $Y = 118$ m (corresponds to $\Delta Y = 18$ m) at construction stage (5) and $Y = 198$ m (corresponds to $\Delta Y = 98$ m) at construction stage (6). During the shield machine advance from (4) to (6) the tunnel below the synthetic

measurement point is permanently supported by the precast lining elements. It can be seen that between construction stages (4) and (5) and hence latest 4 m and two excavation steps after grouting is finished the maximum settlements are reached for all scenarios. Subsequently, incremental upward displacements and heave effects of the soil due to stress release caused by buoyancy effects during soil removal and uplift of the lining establish for these three scenarios when moving from construction stage (5) till the steady state (6) resulting in smaller surface settlements or even heave at the steady state as already discussed in the former sections. As explained before, the Saniclay D and Saniclay D+BSP model extensions in the NC, D scenario have an exceptional character since the maximum settlements are reached at a later stage $\Delta Y = 30$ m due to the ongoing destructuration process during lining installation. However, also the steady state is already reached at this stage for the Saniclay D and Saniclay D+BSP model extensions in the NC, D scenario since the maximum settlements show a constant behavior afterwards.

Regarding the evolution of the influence of the mechanical properties of natural clay on the settlements with respect to the construction stages of mechanized tunneling the following statements can be made by investigating the differences in the settlement evolution predicted by the specific model extensions.

The destructuration strikingly increases the surface settlements already when the shield machine is approaching to the measurement section even until passing construction stage (5) and further advance as observed for the NC, D scenario in Figure 9.7a. During the construction stages (1/2) to (5/6) the soil experiences the following processes such as volume loss due to overcutting and conicity of the shield machine, stress release and buoyancy effects during soil removal, application of grouting pressure and installation of compressible lining leading to significant plastic straining. The findings can qualitatively be confirmed for the undrained NC, UD scenario as shown in Figure 9.7c but showing a much lower quantity.

The influence of the inherent and stress-induced anisotropy on the surface settlements comes into picture while the face of the shield machine is passing the measurement section (2), during shield machine advance (2) to (3), during grouting (3) to (4) until the initial installation of the lining (4) to (5) as noticed for the NC, D scenario in Figure 9.7a. During these construction stages plasticity is induced to the soil domain in the nearfield of the excavation zone. However, during further advancement of the shield machine (5) to (6) the influence of anisotropy becomes negligible since the curves predicted by the MCC and the Saniclay model extensions are almost parallel. The consideration of stress-induced anisotropy results in larger amount of surface settlements for the NC, D scenario.

However, the undrained NC, UD scenario as visualized in Figure 9.7c shows opposing trend regarding the effects of the stress-induced anisotropy on the magnitude of the surface settlements and exhibit a much lower quantity of the impact.
The influence of the behavior under non-monotonic or cyclic loading such as elastoplastic hysteresis and transition, stiffness degradation and accumulative effects on the settlements becomes most relevant between the construction stages (3) to (4) where the grouting pressure is applied to the surrounding soil and (4) to (6) where the soil experiences incremental upward displacements and even heave as monitored especially for the overconsolidated OC, D and OC, UD scenarios in Figure 9.7b and 9.7d. However, a low impact can also be detected for the normally consolidated, drained NC, D scenario between construction stage (3) where grouting is starting until the maximum settlements are reached. In any case the consideration of the behavior under non-monotonic or cyclic loading leads to larger surface settlements due to the additionally induced plasticity.

9.2.1.4 Evolution of vertical soil displacements u_v

The evolution of the vertical soil displacements u_v in the synthetic measurement section ($Y = 100\,\mathrm{m}$) wrt. the significant construction stages (1) to (6) is shown exemplarily for the Saniclay D+BSP model extension via transverse contour plots in Figures 9.8 to 9.11 for the investigated four scenarios. Positive values represent downward displacements and negative values upward displacements. The contour plots give an overall impression of the spatial distribution of the vertical soil displacements induced by mechanized tunneling. The results confirm the findings made in the previous sections.

NC, D scenario

For the NC, D scenario the contour plots in Figure 9.8 impressively show the evolution of the downward soil displacements in the area above the tunnel continuously increasing with advancing shield machine from construction stage (1) to (6). The stress redistribution caused by the volume loss around the machine, the application of the support pressures and the compressibility of the lining lead to downward soil displacements above the tunnel. Consequently, the downward soil displacements in the domain above the tunnel accumulate to surface settlements. The vertical soil displacements propagate under an angle of approximately 60° to the vertical from the tunnel side in upward direction to the ground surface. The width of the influenced surface area in transverse direction with respect to the tunnel axis develops from 28 m at the construction stage (2) up to 30 m

at the steady state (6). However, the rather coarse resolution especially in the mm-range of smaller vertical soil displacements has to be considered when visually evaluating the contour plots. In the area below the tunnel (20 m below the invert) and less pronounced at the side of the tunnel (15-20 m next to the side) the development of upward soil displacements can be clearly observed. The upward soil displacements below the tunnel are almost continuously increasing with the ongoing mechanized tunneling process (2) to (6) with the exception of the construction from stage (3) to (4) where the grouting pressure is applied downwards. Because of the stress release due to buoyancy effects upward soil displacements below and sidewards the tunnel and associated uplift of the lining are induced.

OC, D scenario

Excessive upward soil displacements due to stress release and uplift effects can be identified from the contour plots in Figure 9.9 for the OC, D scenario. The development of the upward soil displacements starts when the shield machine is approaching to the measurement section. When the shield machine reaches the measurement section (2) a wide soil domain around the excavated area (10 m up from crown to ground surface, 17.5 m next to side and 20 m below invert) exhibits upward soil displacements. Hence, the upward soil displacements accumulate to heave at the ground surface with a width of the influenced surface area of 26.5 m with respect to the tunnel axis. However, while the shield machine is moving through the measurement section from construction stages (2) to (4) an almost vertical funnel/chimney of downward soil displacements is forming in the soil domain directly above the tunnel with a width of approximately 5-7 m with respect to the tunnel axis which approximately corresponds to the tunnel radius. This leads to the saddle-shaped transverse settlement-heave trough as discussed in a former section.
The downward soil displacements in the funnel above the tunnel and the corresponding surface settlements are continuously increasing while moving from (2) to (4). Due to the continuing heave and uplift effects while moving from construction stage (4) to (6) the width of the funnel with respect to the tunnel axis reduces to 2.5 m and the downward soil displacements in the funnel above the tunnel and the associated settlements decrease. At the same time, the soil domain influenced by the upward soil displacements successively increases to a lateral dimension of 23 m next to the tunnel side and a vertical dimension of 23 m below the tunnel invert, This results in a final width of the influenced surface area at the steady state (6) of 35 m with respect to the tunnel axis, which corresponds to the findings regarding the transverse settlement trough. The upward soil displacements

below and sidewards the tunnel sequentially increase during shield machine advance except of the construction from stage (3) to (4) where the grouting is applied. Whereat, the magnitude of the maximum upward soil displacements directly below the tunnel and its evolution over the construction stages (2) to (6) is approximately the same when comparing both drained scenarios NC, D and OC, D for the particular consolidation conditions. This leads to associated increasing heave of the ground surface adjacent to the settlement trough above the funnel.

NC, UD scenario

For the NC, UD scenario the distribution of the vertical soil displacements in the soil domain is subdivided into downward soil displacements above the tunnel and upward soil displacements in a balloon-shaped area below the tunnel as seen in the contour plots in Figure 9.10. The downward soil displacements above the tunnel and the corresponding surface settlements are continuously increasing while moving from (2) to (4) due to volume loss, support pressures and compressibility of the lining. Due to stress release and uplift effects while moving from construction stage (4) to (6) the upward soil displacements below the tunnel increase and hence the downward soil displacements above the tunnel and the associated settlements decrease. The width of the influenced surface area in transverse direction successively increases from 15 m when the shield machine reaches the measurement section (2) to 20 m at construction stage (5) and finally to 46 m at the steady state (6). Again, the upward soil displacements below the tunnel are almost continuously increasing with the ongoing mechanized tunneling process (2) to (6) with the exception of construction from stage (3) to (4) where the grouting pressure is applied downwards. Whereat, the magnitude of the maximum upward soil displacements directly below the tunnel and its evolution over the construction stages (2) to (6) is 35-45% smaller than in the corresponding drained NC, D scenario. The balloon-shaped area of upward soil displacements extends to 20 m below the tunnel and 12 m in width with respect to the tunnel axis when reaching the steady state (6).

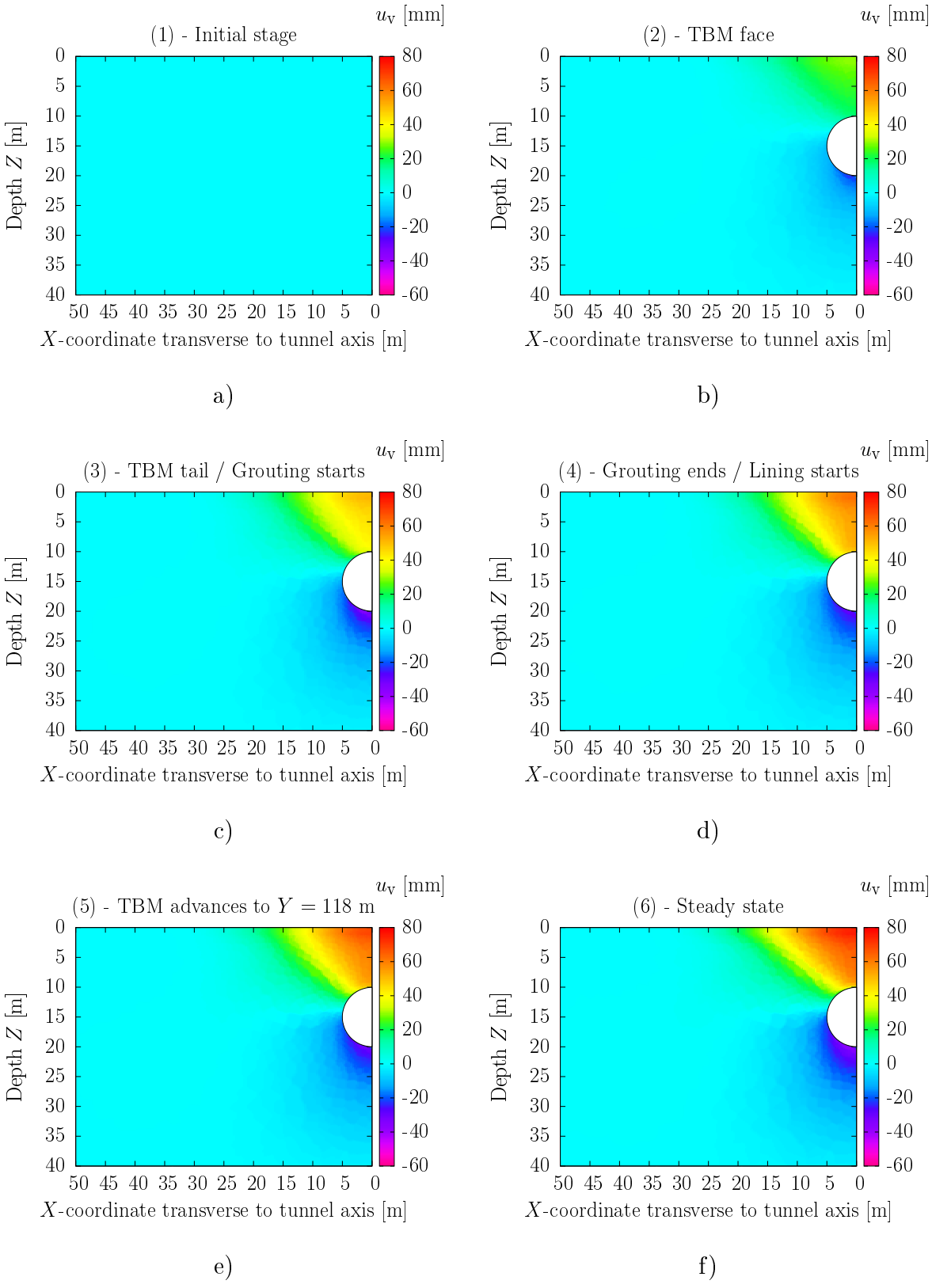

Figure 9.8: Evolution of vertical soil displacements u_v in the synthetic measurement section ($Y = 100$ m) using the Saniclay D+BSP model extension for NC, D scenario wrt. the significant construction stages (1) to (6)

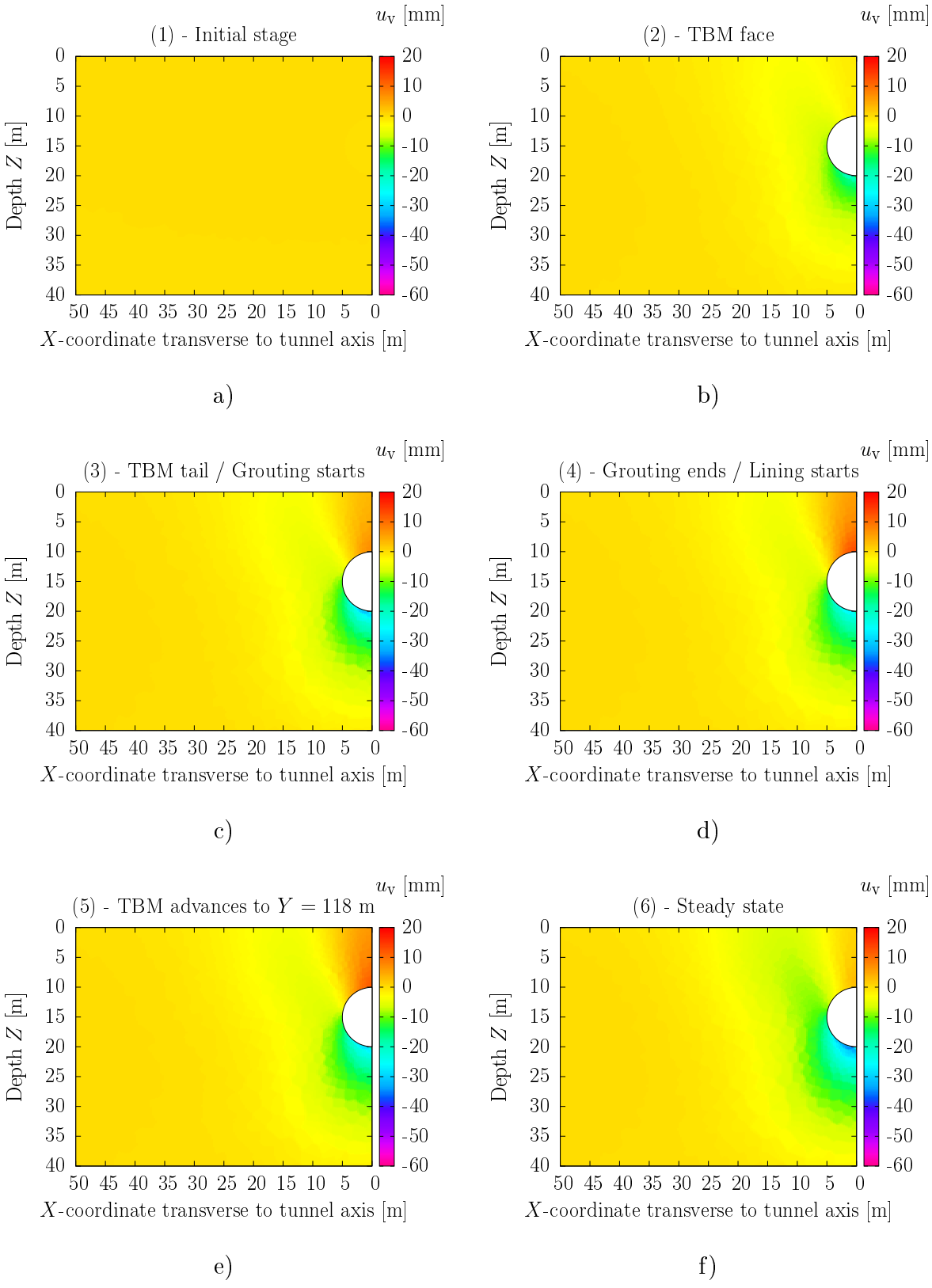

Figure 9.9: Evolution of vertical soil displacements u_v in the synthetic measurement section ($Y = 100$ m) using the Saniclay D+BSP model extension for OC, D scenario wrt. the significant construction stages (1) to (6)

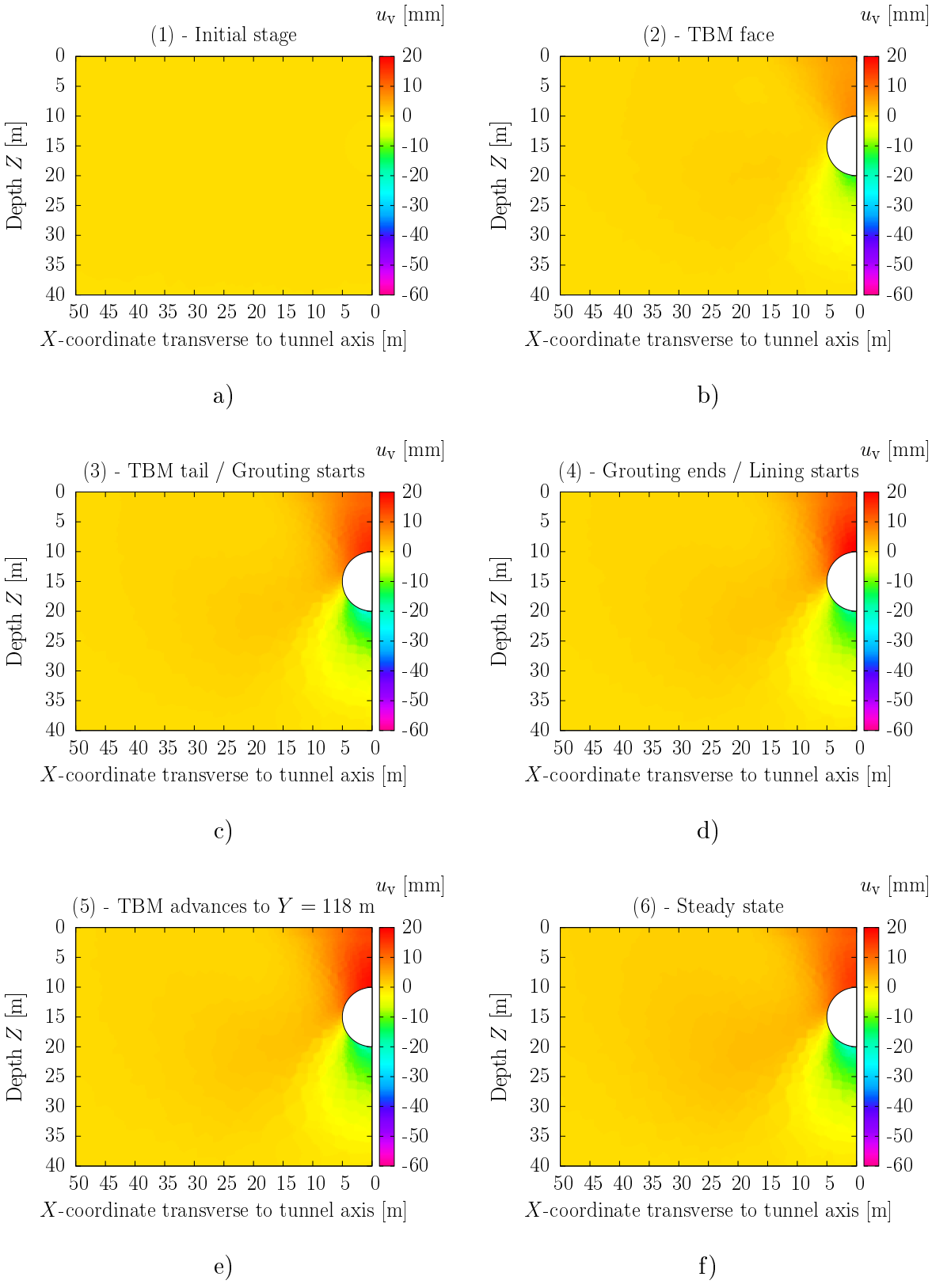

Figure 9.10: Evolution of vertical soil displacements u_v in the synthetic measurement section ($Y = 100$ m) using the Saniclay D+BSP model extension for NC, UD scenario wrt. the significant construction stages (1) to (6)

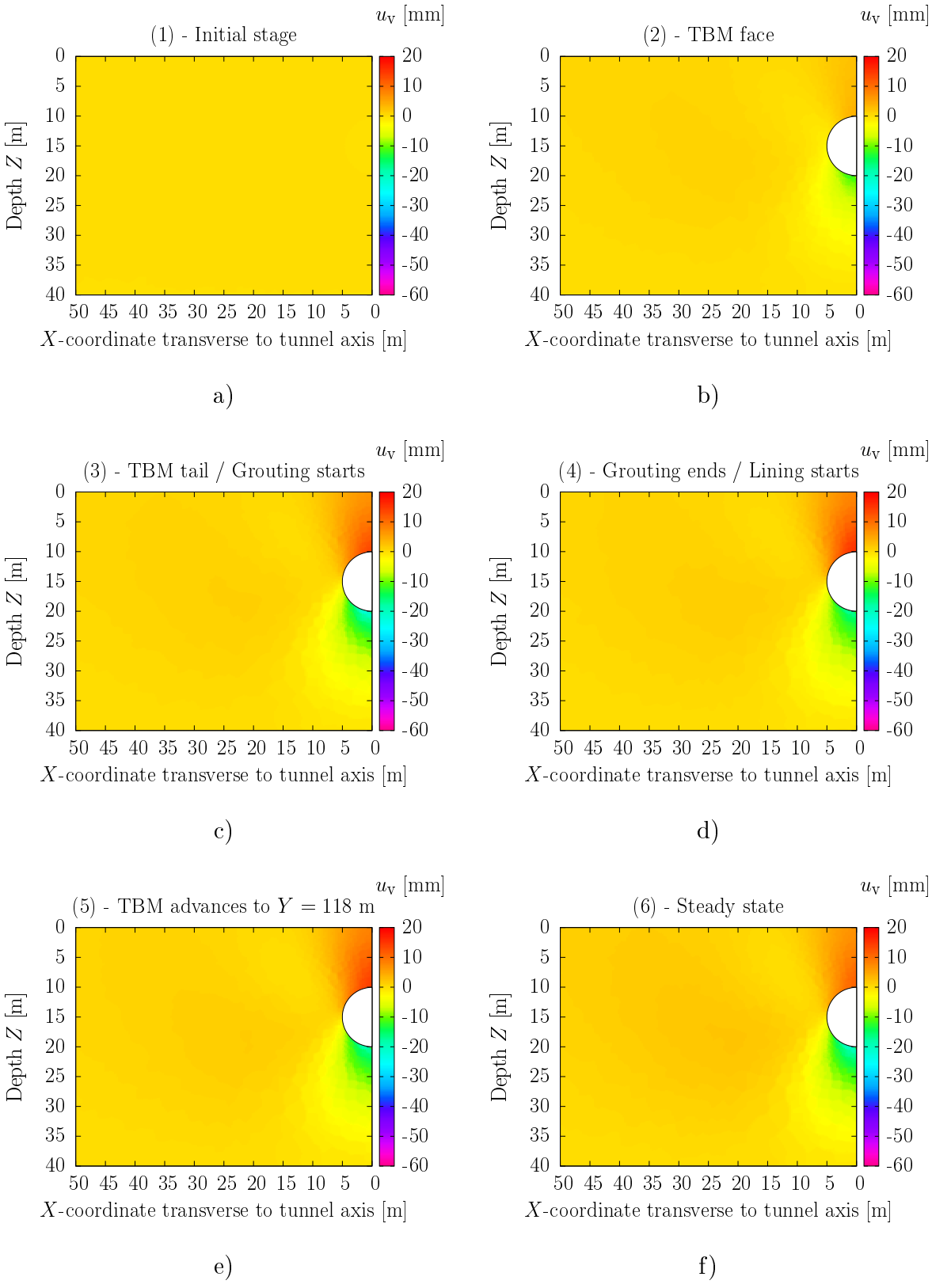

Figure 9.11: Evolution of vertical soil displacements u_v in the synthetic measurement section ($Y = 100$ m) using the Saniclay D+BSP model extension for OC, UD scenario wrt. the significant construction stages (1) to (6)

OC, UD scenario

The distribution of the vertical soil displacements in the soil domain for the OC, UD scenario as shown in the contour plots in Figure 9.11 is quite similar to the normally consolidated NC, UD scenario showing downward soil displacements above the tunnel and upward soil displacements in a balloon-shaped area below the tunnel. Even the evolution of the vertical soil displacements over the construction stages (2) to (6) is qualitatively the same. Whereat, the magnitude of the maximum downward soil displacements directly above the tunnel is 20-30% smaller when comparing to the corresponding normally consolidated NC, UD scenario. Whereas, the magnitude of the maximum upward soil displacements directly below the tunnel and its evolution over the construction stages (2) to (6) is approximately the same when comparing both undrained NC, UD and OC, UD scenarios for the particular consolidation conditions. The dimensions of the balloon-shaped area of upward soil displacements are similar compared to the normally consolidated NC, UD scenario. The width of the influenced surface area in transverse direction is about 12 m as already discussed in the section regarding the transverse settlement behavior.

9.2.1.5 Evolution of void ratio e

The evolution of the void ratio e in the synthetic measurement section ($Y = 100$m) wrt. the significant construction stages (1) to (6) is presented exemplarily for the Saniclay D+BSP model extension in Figure 9.12 for the investigated NC, D scenario. To visualize the volumetric soil behavior around the tunnel the evolution of the void ratio is investigated starting from an initial void ratio of $e_0 = 1.910$.

NC, D scenario

Induced by the volume loss around the tunnel, compaction of the adjacent and overlying soil occurs for the NC, D scenario. Hence, the void ratio is continuously decreasing to minimum values of $e = 1.882$ at construction stage (2) and $e = 1.858$ at construction stage (3) while the shield machine is passing the measurement section. During the application of grouting from construction stage (3) to (4) the soil volume and the void ratio remains almost constant. The compressible behavior of the lining leads to further decrease of the void ratio showing minimum values of $e = 1.847$ at construction stage (5) and $e = 1.808$ at construction stage (6). To sum up, the void ratio ultimately reduces by 6% only compared to the initial value $e_0 = 1.910$. However, the decrease of the void ratio significantly takes

place in an area propagating diagonally in upward direction from the upper tunnel quarter to the ground surface. Whereas, the area vertically above the tunnel is relatively less influenced by volume changes compared to the area at the upper side. This may be explained by the stress redistribution around the tunnel from the crown to the sides and corresponding arching effects. Thus, the area vertically above the tunnel shows a more elastic behavior and thus smaller volume change than the sides. The overconsolidated upper layer of 1 m thickness is not affected by volume changes.
Due to the stress release in the area below the tunnel and the corresponding dilative behavior an increase of the soil volume indicated by an increase of the void ratio up to a maximum value of $e = 1.933$ can be observed while excavating from construction stage (2) to (3). Because of the application of grouting the maximum void ratio below the tunnel invert decreases to a minimum value of $e = 1.922$ while moving from construction stage (3) to (4). Afterwards, due to further stress release and additional uplift effects the void ratio below the tunnel invert again increases to maximum value of $e = 1.927$ at construction stage (6). However, it can be seen that the incremental changes of the void ratio below the tunnel are relatively small.

OC, D scenario

The OC, D scenario is not explicitly shown due to relatively small changes of the void ratio in a range of $1.895 \leq e \leq 1.932$. That is the magnitude of volume change is around 1% compared to the initial value $e_0 = 1.910$. The volumetric behavior and therefore the distribution of the void ratio is qualitatively similar to the normally consolidated NC, D scenario but with smaller magnitude due to the predominantly elastic behavior. However, for the area below the tunnel even the quantitative distribution of the void ratio is similar to the NC, D scenario.

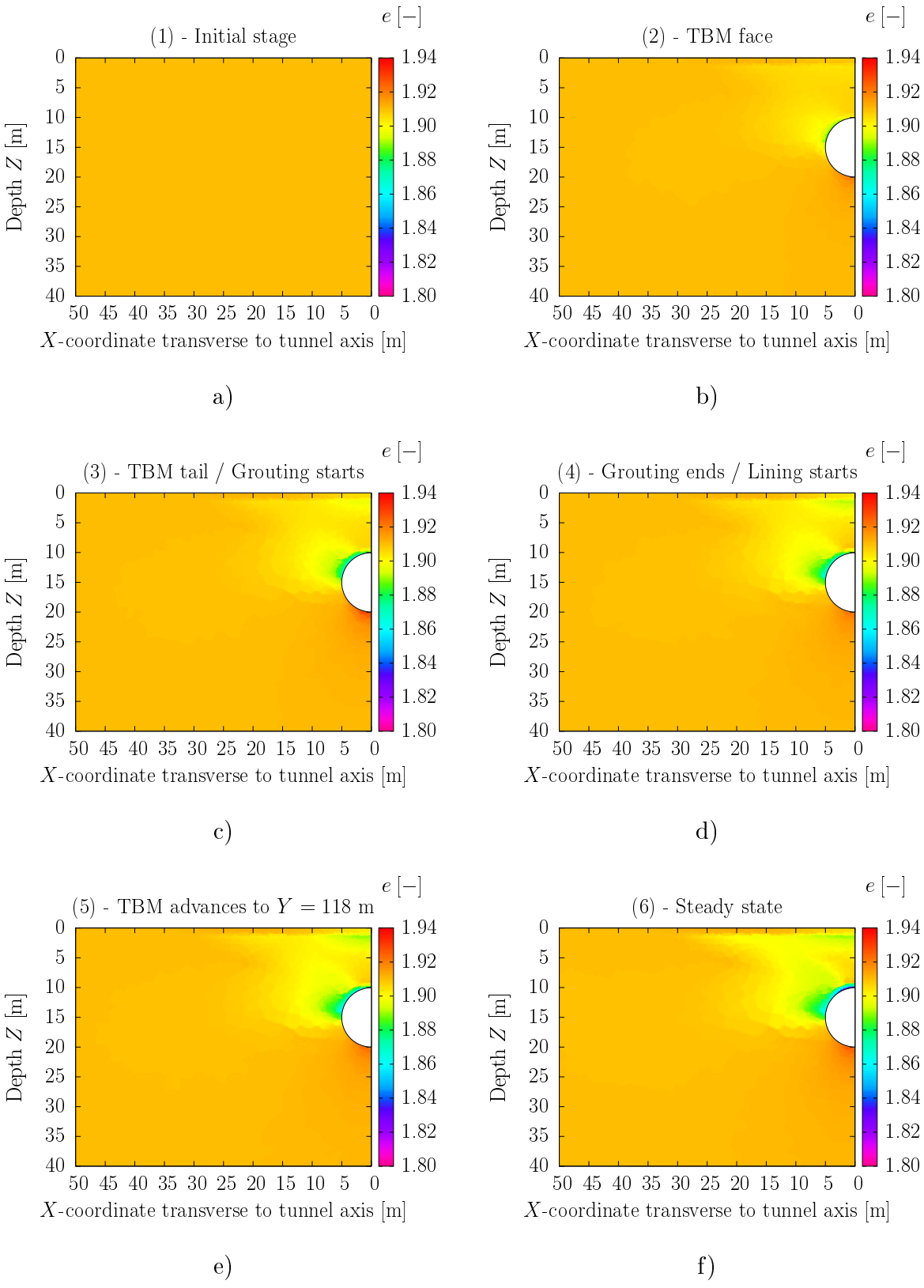

Figure 9.12: Evolution of void ratio e in the synthetic measurement section ($Y = 100$ m) using the Saniclay D+BSP model extension for NC, D scenario wrt. the significant construction stages (1) to (6)

9.2.2 Effective stress path and excess pore-water pressure

The mechanized tunneling process causes significant stress redistribution in the soil domain due to appearance of volume loss around the tunnel, stress release due to excavation and soil removal, application of face support and grouting pressures as well as compressibility and uplift effects of the tunnel lining. The unbalance in stress around the tunnel is compensated by stress redistribution in the nearfield of the tunnel. To better understand the stress redistribution in the soil domain evolving during mechanized tunneling this section covers the analysis of effective stress paths of representative stress points around the tunnel. The most distinct stress changes are expected to occur in the nearfield of the tunnel. Consequently, stress points with 1 m distance to the tunnel crown, side and invert are considered for analysis. Additionally, a stress point midway between tunnel crown and ground surface is analyzed. The evolution of the effective stress paths (effective mean stress p' vs. deviatoric stress $|\boldsymbol{s}|$) while the shield machine is advancing from initial state at construction stage (1) to steady state at construction stage (6) is visualized in Figures 9.13, 9.15, 9.17 and 9.19 with respect to the representative stress points.

Beside the surface settlements, the magnitude and distribution of the effective stress and excess pore-water pressure in the vicinity of the lining are also relevant for the design of mechanized tunneling in natural clay. In particular, the effective stress and excess pore-water pressure in the nearfield of the excavated tunnel govern the bedding of the lining and the acting external lining forces to be used for the design of the precast concrete lining segments. Hence, the associated internal forces, bending moments and radial displacements of the lining segments are correlated to the magnitude and distribution of the effective stress and excess pore-water pressure developed during mechanized tunneling in natural clay deposits.

For the general description of the effective stress path evolution during mechanized tunneling the most complex Saniclay D+BSP model extension is used as reference model. However, the differences compared to the less complex model extensions are discussed afterwards. Regardless of the used model extension and soil conditions, any effective stress path begins from the initial K_0-consolidation stress at construction stage (1). It has to be noted that the distinct characteristics of the effective stress paths are not always strictly allocated to a particular construction stage (1) to (6) due to neighboring effects of the adjacent soil which are hurrying ahead.

Moreover, for the scenarios assuming undrained conditions the evolution of the corresponding excess pore-water pressure Δp_{w} during mechanized tunneling is discussed as shown in Figures 9.14, 9.16, 9.18 and 9.20 with respect to the representative stress points.

To recall, when the soil wants to deform by means of decrease or increase of volume energy is transferred to plasticity to compensate the restriction of a constant volume in assumed undrained conditions. Undrained conditions require a resulting zero total volumetric strain increment as the sum of the elastic and the plastic strain components. Accordingly, balancing contractive internal behavior results in counteracting increase of excess pore-water pressure. On the contrary, dilative internal behavior is balanced by decreasing excess pore-water pressure.
In addition, the spatial and construction stage dependent evolution of the excess pore-water pressure Δp_{w} in the synthetic measurement section ($Y = 100\,\mathrm{m}$) wrt. the significant construction stages (1) to (6) is presented exemplarily for the Saniclay D+BSP model in Figures 9.21 and 9.22 for the investigated scenarios assuming undrained conditions.

9.2.2.1 Above the tunnel

NC, D scenario

The evolution of the effective stress path for a stress point 1 m above the tunnel crown starting from normally consolidated conditions and assuming drained conditions is given in Figure 9.13a. When the shield machine is approaching to the measurement section (1) to (2) the effective stress path directly above the later excavation area is initially following the bounding surface showing an increase of deviatoric stress and a decrease of effective mean stress. Elastoplastic soil behavior is induced due to the normally consolidated initial stress. The applied face support pressure generally balances the soil in front of the shield machine but allows for small inward displacements at the upper tunnel face. Since the soil starts moving towards the face of the shield machine the unbalanced effective horizontal stress in longitudinal tunnel direction decreases while the other stress components just slightly decrease. Hence, the deviatoric stress increases and the effective mean stress decreases. The initial course of the effective stress path for the different model extensions depends on the inherent rotation of the bounding surface. Noticeable differences can be observed for the Saniclay D and Saniclay D+BSP model extensions since the induced destructuration simultaneously shrinks the size of the evolving bounding surface. While the effective mean stress is continuously decreasing, the deviatoric stress experiences rapidly oscillating shearing behavior when the shield machine comes very close to the measurement section due to superimposed effects of volume loss, stress release due to soil removal and face support pressure hurrying ahead. All four model extensions qualitatively show a similar effective stress path evolution but with slightly different quantity.

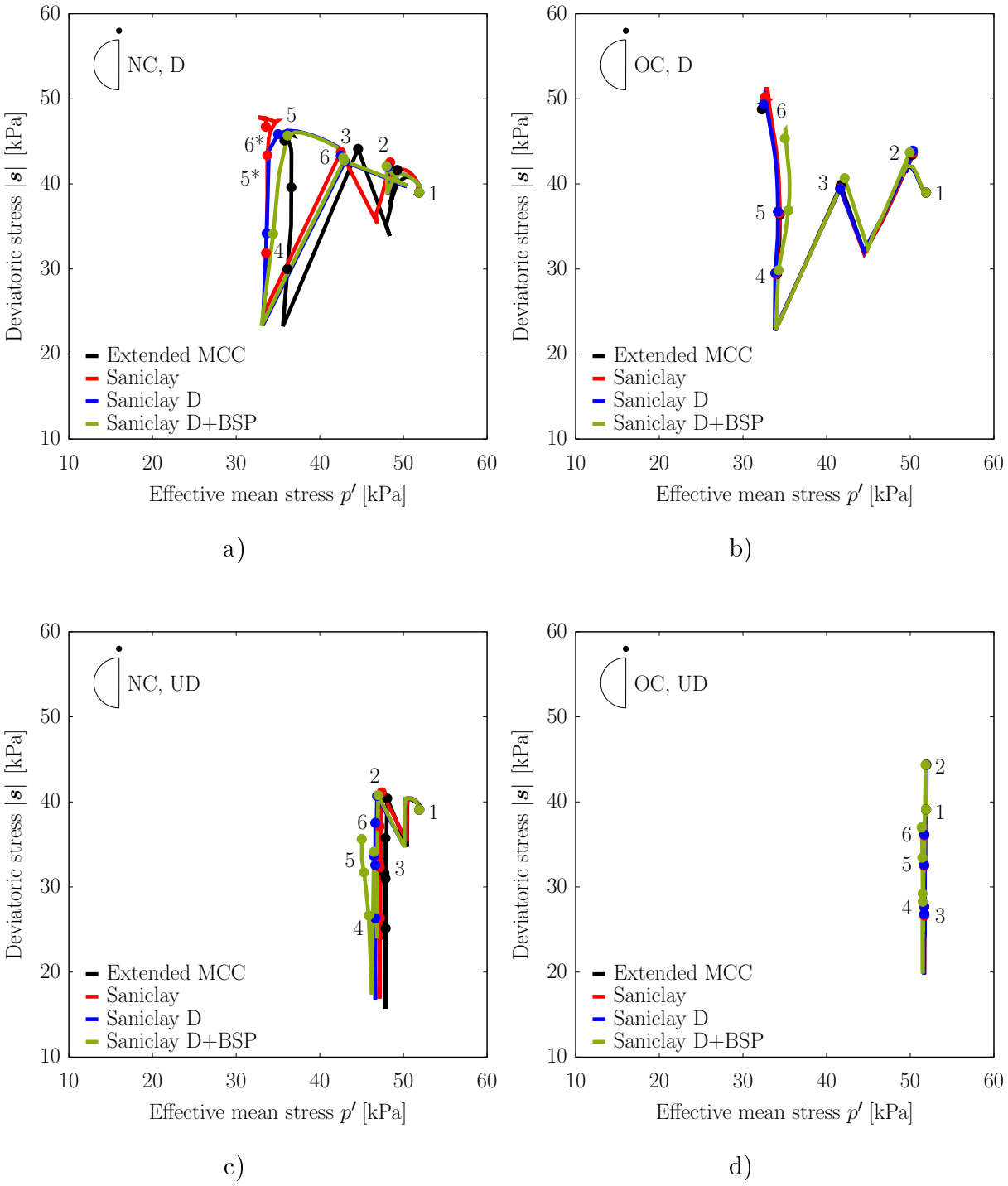

Figure 9.13: Effective mean stress p' vs. deviatoric stress $|\boldsymbol{s}|$ path for stress point 1 m above the tunnel crown wrt. the continuous tunnel excavation for a) NC, D b) OC, D c) NC, UD, d) OC, UD scenarios

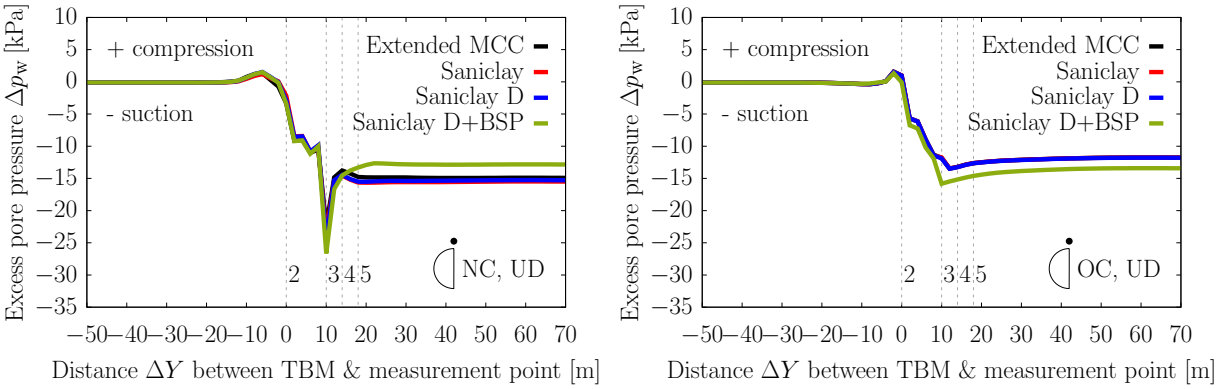

Figure 9.14: Evolution of excess pore-water pressure Δp_w traced over the developing distance ΔY between the advancing shield machine and fixed measurement point 1 m above the tunnel crown for a) NC, UD and b) OC, UD scenarios

When the shield machine is passing the measurement section (2) to (3) developing volume loss takes place directly underneath the stress point 1 m above the tunnel crown. Accordingly, the soil directly above the tunnel crown experiences an increase of effective horizontal stress in longitudinal tunnel direction. However, the effective vertical stress and the effective horizontal stress in transverse tunnel direction are just slightly varying when using the Saniclay D and Saniclay D+BSP model extensions. Hence, the deviatoric stress decreases accompanied by increasing effective mean stress. Whereas, for the MCC and Saniclay model extensions the effective vertical stress decreases at the same time. Since no counteracting destructuration is superimposed arching and corresponding stress redistribution from the vertical to the longitudinal tunnel direction appear. Consequently, more pronounced decrease of the deviatoric stress is generated. Moreover, decreasing effective mean stress is noticed because the decrease of the effective vertical stress is larger than the corresponding increase of the effective horizontal stress in longitudinal tunnel direction.

Even before reaching construction stage (3) the soil directly above the face of the shield machine is already affected by the applied grouting pressure in the neighboring soil domain. The applied grouting pressure generally equilibrates the soil above the shield machine but allows for small vertical inward displacements. Consequently, the effective vertical and horizontal stresses decrease due to stress relaxation and a reduction of the effective mean stress is noticed. Since the decrease of the effective horizontal stress is more pronounced than the decrease of the effective vertical stress the deviatoric stress increases. This behavior is predicted by all four model extensions.

Further tunnel excavation supported by constant grouting pressure (3) to (4) leads to additional significant decrease of the effective mean stress and deviatoric stress indicating predominantly elastic unloading behavior of the soil directly above the tunnel crown due to developing arching effects and stress redistribution in the overlying soil layers. Hence, the soil domain directly above the tunnel crown experiences further stress relaxation given by a decrease of effective vertical and horizontal stresses. Anyhow, the degree of effective vertical stress reduction is dominating. That is why the deviatoric stress is strikingly decreasing. Again, this behavior is predicted by all four model extensions. Whereat, the model extensions incorporating inherent and stress-induced anisotropy show slightly larger reduction of the effective mean stress due to the rotated bounding surface and plastic potential surface while the magnitude of deviatoric stress reduction is the same for all model extensions.

Due to upward movements and uplift effects of the entire tunnel lining during installation of lining and further shield machine advance (4) to (6) the soil above the tunnel crown is pushed upwards. Hence, the effective vertical stress is again increasing while the effective horizontal stress decreases in both longitudinal and transverse tunnel direction at the same time. The soil is reloaded in vertical direction while stress relaxation occurs in horizontal directions. Hence, a striking increase of the deviatoric stress is observed even before reaching construction stage (4) due to lining installation effects in the neighboring soil domain. The impact of the elastoplastic soil behavior after stress reversal as captured by the Saniclay D+BSP model extension only leads to increasing effective mean stress. That is, the increase of the effective vertical stress is larger than the decrease of the effective horizontal stress. For the other model extensions the soil behavior is predominantly elastic and the effective mean stress remains almost constant. That is, the increase of the effective vertical stress and the decrease of the effective horizontal stresses are balanced. After reaching the bounding surface the soil behavior is elastoplastic causing destructuration indicated by an effective stress path following the evolving bounding surface showing decrease of deviatoric stress and increase of effective mean stress until reaching the steady state (6) when using the Saniclay D and Saniclay D+BSP model extensions. That is, all stresses are increasing, whereat the increment of increase of the effective horizontal stress is larger. On the contrary, the MCC and Saniclay model extensions are not capable to predict the destructuration behavior.

To sum up, the qualitative evolution of the effective stress path is very similar for all four model extensions. It can be recognized that the effective stress path of the Saniclay D and Saniclay D+BSP model extensions are very similar despite the reloading part inside the bounding surface after stress reversal (3/4) to (5). The Saniclay and MCC

model extensions show larger deviations due to the absence of destructuration effects especially between construction stages (5) to (6). The effects of stress-induced anisotropy come into picture while the shield machine is passing the measurement section (1) to (3) and grouting takes place (3) to (4). Regarding a most accurate design of the lining, destructuration, anisotropy and non-monotonic or cyclic behavior have to be considered to adequately predict the effective stress in the soil domain above the tunnel when having normally consolidated initial stress conditions and assuming drained conditions.

OC, D scenario

The evolution of the effective stress path for a stress point 1 m above the tunnel crown starting from overconsolidated conditions and assuming drained conditions is given in Figure 9.13b. The effective stress path is qualitatively very similar when comparing to the normally consolidated NC, D scenario. Because the same subprocesses of mechanized tunneling are involved, the qualitative stress changes become alike almost independently of the consolidation conditions but related to predominantly elastic behavior. It is to be noted that the elastoplastic destructuration behavior indicated by an effective stress path following the evolving bounding surface showing a decrease of deviatoric stress and increase of effective mean stress until reaching the steady state (6) vanishes in overconsolidated conditions due to predominantly elastic behavior.
Due to overconsolidation the soil behavior predicted by the elastoplastic MCC, Saniclay and Saniclay D model extensions is nearly purely elastic for the entire construction process (1) to (6). Hence, the evolution of the effective stress path is almost identical for the MCC, Saniclay and Saniclay D model extensions since the plasticity induced anisotropy and destructuration do not become relevant. Nevertheless, the effective stress path simulated by the Saniclay D+BSP model extension slightly deviates due to the induced plasticity during unloading and especially reloading cycles. Regarding a most accurate design of the lining non-monotonic or cyclic behavior has to be considered to adequately predict the effective stress in the soil domain above the tunnel when having overconsolidated initial stress conditions and assuming drained conditions.

NC, UD scenario

The evolution of the effective stress path for a stress point 1 m above the tunnel crown starting from normally consolidated conditions and assuming undrained conditions is given in Figure 9.13c. The corresponding evolution of excess pore-water pressure Δp_{w}

traced over the developing distance ΔY between the advancing shield machine and the representative measurement points is displayed in Figure 9.14a. Moreover, the spatial distribution of the excess pore-water pressure Δp_{w} wrt. the significant construction stages (1) to (6) is visualized exemplarily for the Saniclay D+BSP model extension in Figure 9.21.

When the shield machine is approaching to the measurement section (1) to (2) the effective stress path is initially following the bounding surface showing an increase of deviatoric stress and a decrease of effective mean stress as for the drained NC, D scenario. Elastoplastic soil behavior is induced due to the normally consolidated initial stress conditions. Because of the tunneling effects hurrying ahead the soil domain above the tunnel experiences contractive internal behavior and counteracting positive excess pore-water pressure up to 1.5 kPa is generated. Also when the shield machine comes very close to the measurement section the evolution of the effective stress path is qualitatively similar when comparing to the drained NC, D scenario. While the effective mean stress is continuously decreasing, the deviatoric stress experiences rapidly oscillating shearing behavior due to superimposed effects of volume loss, stress release due to soil removal and face support pressure hurrying ahead. However, the peaks of the deviatoric stress changes are larger for assumed undrained than for drained conditions. The soil domain above the tunnel manifests dilative internal behavior due to deviatoric shearing and simultaneous decrease of effective mean stress. Consequently, counteracting negative excess pore-water pressure develops up to -3.5 kPa when reaching construction stage (2). All four model extensions qualitatively and quantitatively show similar effective stress path evolution and development of excess pore-water pressure while the shield machine is approaching to the measurement section (1) to (2). However, the Saniclay D and Saniclay D+BSP model extensions incorporating destructuration show the largest decrease of the effective mean stress. Moreover, the Saniclay model extension accounting for anisotropy exhibits larger effective mean stress decrease than the less complex MCC model extension.

When the shield machine is passing the measurement section from (2) to (3) volume loss and stress release due to soil removal continuously take place underneath the stress point 1 m above the tunnel crown. The soil directly above the tunnel crown experiences decrease of effective vertical stress and associated increase of effective horizontal stresses due to stress redistribution. Therefore, the deviatoric stress is strikingly decreasing down to values around 25 kPa one excavation step before reaching construction stage (3). Since the material behavior is predominantly elastic the effective mean stress remains almost constant in assumed undrained conditions. The negative excess pore-water pressure develops up to -9 kPa initially after passing construction stage (2) because of the still dilative

internal behavior and stays almost constant during further excavation (2) to (3) varying between -9 kPa and -11 kPa. Again, the evolution of the effective stress path and the development of excess pore-water pressure is qualitatively and quantitatively alike for all four model extensions.

The initial application of grouting pressure (3) leads to an increase of the effective vertical stress accompanied by decreasing effective horizontal stresses. That is, the applied upward grouting pressure is larger than the effective vertical stresses previously developed in the soil under assumed undrained conditions. Concluding, the deviatoric stress is again rapidly increasing immediately when reaching construction stage (3) coming along with decreasing effective mean stress. However, the internal behavior is dilative due to deviatoric shearing and simultaneous decrease of effective mean stress. Hence, remarkable generation of counteracting negative excess pore-water pressure up to a minimum value of -26.5 kPa is observed for the Saniclay D+BSP model extension. Whereas, the other model extensions show less pronounced negative excess pore-water pressure between -22.5 kPa (MCC), -23.5 kPa (Saniclay) and -24.5 kPa (Saniclay D). That corresponds to 84-93% compared to the Saniclay D+BSP model extension. The influence of the grouting pressure on the effective stress path and the excess pore-water pressure is qualitatively similar for all four model extensions.

Further tunnel excavation supported by constant grouting pressure (3) to (4) initially leads to additional significant decrease of deviatoric stress directly above the tunnel crown due to developing arching effects and stress redistribution especially in longitudinal tunnel direction. That is, the effective vertical stress is decreasing while the effective horizontal stress in longitudinal tunnel direction increases and the effective horizontal stress in transverse tunnel direction is just slightly affected. The effective mean stress is slightly decreasing for the Saniclay D+BSP model extension and slightly increasing for the other model extensions. Since the internal behavior turns from dilative to contractive the previously generated negative excess pore-water pressure increases from the minimum value to -14.5 kPa at construction stage (4) for the Saniclay D+BSP model extension.

As for the drained NC, D scenario upward movements and uplift effects of the entire tunnel lining occur during the installation of lining and further shield machine advance (4) to (6). Hence, the effective vertical stress is increasing while the effective horizontal stress decreases in both longitudinal and transverse tunnel direction at the same time. The soil is reloaded in vertical direction while stress relaxation occurs in horizontal directions resulting in striking increase of the deviatoric stress even before reaching construction stage (4). The impact of the elastoplastic soil behavior after stress reversal as captured by the Saniclay D+BSP model extension leads to decreasing effective mean stress. Whereas,

for the elastoplastic MCC, Saniclay and Saniclay D model extensions the effective mean stress remains constant due to purely elastic behavior. Since the Saniclay D+BSP model extension allows for plasticity with ongoing shield machine advance the negative excess pore-water pressure is further increasing. The steady state value of the negative excess pore-water pressure of -13 kPa is reached two excavation steps after the shield machine has passed construction stage (5). Afterwards, the soil behavior becomes elastic even for the Saniclay D+BSP model extension resulting in constant effective mean stress and excess pore-water pressure. That is, the excess pore-water pressure is not dissipated due to assumed undrained conditions. For the other model extensions, the negative excess pore-water pressure is again slightly decreasing from construction stage (4) until reaching the steady state value of about -15 kPa at construction stage (5). That corresponds to 15-20% higher values compared to the Saniclay D+BSP model extension.
To sum up, the qualitative and even quantitative evolution of the effective stress path and the generation of excess pore-water pressure are very similar for all four model extensions. It can be recognized that the stress paths of the Saniclay D and Saniclay D+BSP model extensions are nearly identical despite the reloading part inside the bounding surface after stress reversal. The Saniclay and MCC model extensions show larger deviations when remarkable elastoplastic soil behavior occurs while the shield machine is approaching to the measurement section (1) to (2). Compared to the drained NC, D scenario the effective mean stress changes during mechanized tunneling are much smaller due to the predominantly elastic unloading reloading cycles where the effective mean stress remains almost constant in assumed undrained conditions. It is to be noted that the elastoplastic destructuration behavior almost vanishes in assumed undrained conditions. Regarding a most accurate design of the lining non-monotonic or cyclic behavior has to be considered to adequately predict the effective stress in the soil domain above the tunnel when having normally consolidated initial stress conditions and assuming undrained conditions.

OC, UD scenario

The evolution of the effective stress path for a stress point 1 m above the tunnel crown starting from overconsolidated conditions and assuming undrained conditions is given in Figure 9.13d. The corresponding evolution of excess pore-water pressure Δp_{w} traced over the developing distance ΔY between the advancing shield machine and the representative measurement points is displayed in Figure 9.14b. Moreover, the spatial distribution of the excess pore-water pressure Δp_{w} wrt. the significant construction stages (1) to (6) is visualized exemplarily for the Saniclay D+BSP model extension in Figure 9.22.

Due to overconsolidation and the associated predominantly elastic behavior the effective mean stress remains almost constant during mechanized tunneling in assumed undrained conditions and just the deviatoric stress is changing during construction stages (1) to (6). While the shield machine is approaching to the measurement section (1) to (2) the deviatoric stress is increasing followed by a decrease of the deviatoric stress during further shield machine advance (2) to (3). The application of grouting (3) leads to increasing deviatoric stress. Ongoing shield machine advance (3) to (4) under the protection of grouting pressure initially decreases the deviatoric stress until the installation of lining (4) and the proceeding shield machine advance (4) to (6) again raise the deviatoric stress. To sum up, the non-monotonic or cyclic deviatoric stress reversals governed by the different construction stages (1) to (6) are qualitatively similar compared to the other three scenarios.
Moreover, the development of excess pore-water pressure is qualitatively alike as compared to the normally consolidated NC, UD scenario. However, the generation of excess pore-water pressure starts just before the shield machine reaches the measurement section for overconsolidated conditions while it begins earlier for normally consolidated conditions. The dilative internal behavior is dominating causing remarkable generation of negative excess pore-water pressure. However, the quantity is smaller than in the normally consolidated case since less plasticity has to be counterbalanced by generation of excess pore-water pressure. The minimum value of negative excess pore-water pressure at construction stage (3) is about -15.5 kPa for the Saniclay D+BSP model. This correponds to 60% compared to the normally consolidated NC, UD scenario. The negative excess pore-water pressure generated by the other model extensions is again 15% less pronounced. It can be observed that the contractive internal behavior developed after construction stage (3) is less distinct in overconsolidated conditions than in normally consolidated conditions. Due to predominantly elastic behavior counteracting development of excess pore-water pressure is not strongly mobilized. The steady state values of excess pore-water pressure are about -13.5 kPa for the Saniclay D+BSP model extension and -12 kPa for the other model extensions, which corresponds to a difference of about 11%.
To conclude, the qualitative and even quantitative evolution of the effective stress path and the generation of excess pore-water pressure are very similar for all four model extensions and the influence of destructuration, stress-induced anisotropy and non-monotonic or cyclic behavior is small.

9.2.2.2 Between the tunnel and the ground surface

The soil domain midway between tunnel crown and ground surface is generally less affected by stress changes induced by mechanized tunneling than the nearfield of the tunnel.

NC, D scenario

The evolution of the effective stress path for a stress point 5 m above the tunnel crown starting from normally consolidated conditions and assuming drained conditions is given in Figure 9.15a. While the shield machine is approaching to the measurement section (1) to (2) an initial increase of deviatoric stress and a decrease of effective mean stress can be detected as for the stress point directly above the tunnel due to horizontal movements towards the face of the shield machine. However, due to the relatively large vertical distance to the shield machine the upper soil domain is less influenced by excavation effects hurrying ahead.
Whereas, a noticeable decrease of the deviatoric stress is observed when the shield machine is passing below the measurement point (2) to (4). That is, the induced volume loss around the shield machine results in arching effects in the soil midway between tunnel crown and ground surface. The arching leads to stress redistribution to the side and to the longitudinal tunnel direction indicated by decreasing effective vertical stress and increasing effective horizontal stress in both transverse and longitudinal direction. Hence, the deviatoric stress is decreasing. However, destructuration leads to intensification of the increase of the effective horizontal stress while the decrease of the effective vertical stress remains constant. This leads to smaller deviatoric stress accompanied with increasing effective mean stress. When not accounting for destructuration the changes of the effective mean stress are even smaller. That means, the loss in effective vertical stress is transferred to gain of effective horizontal stress in similar magnitude.
As for the stress directly above the tunnel crown, also the upper soil layers are affected by upward movements and uplift effects of the entire tunnel lining during installation of lining and further shield machine advance (4) to (6). Initially when lining installation starts (4) to (5) stress reversal occurs and the soil behavior during initial reloading is predominantly elastic. The deviatoric stress is increasing while the effective mean stress remains almost constant for all four model extensions. That is, the increase of the effective vertical stress and the decrease of the effective horizontal stress are balanced. With further shield machine advance (5) to (6) the soil behavior becomes elastoplastic again and the effective stress path is following the bounding surface. The increase of the deviatoric

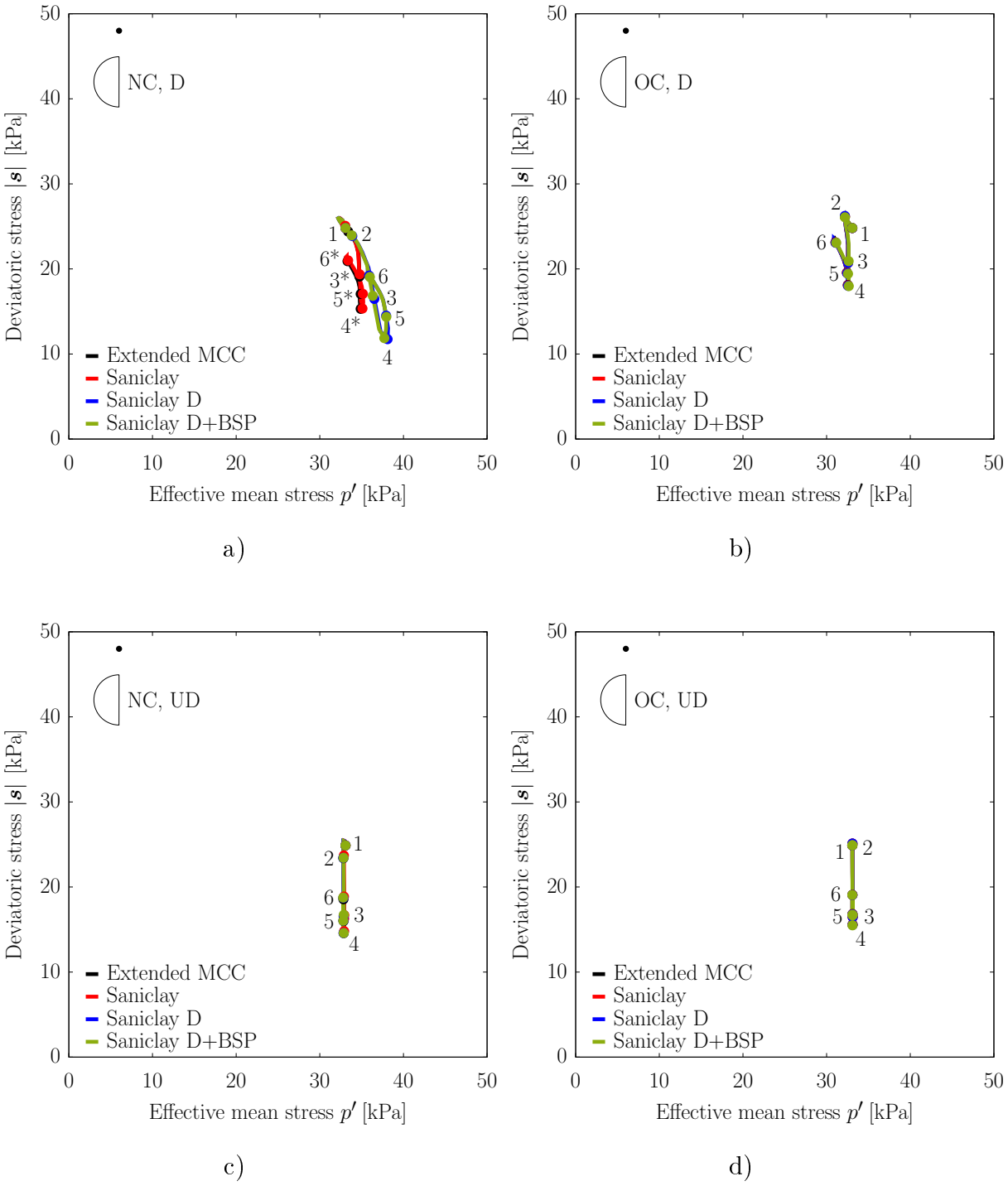

Figure 9.15: Effective mean stress p' vs. deviatoric stress $|\boldsymbol{s}|$ path for stress point 5 m above the tunnel crown wrt. the continuous tunnel excavation for a) NC, D b) OC, D c) NC, UD, d) OC, UD scenarios

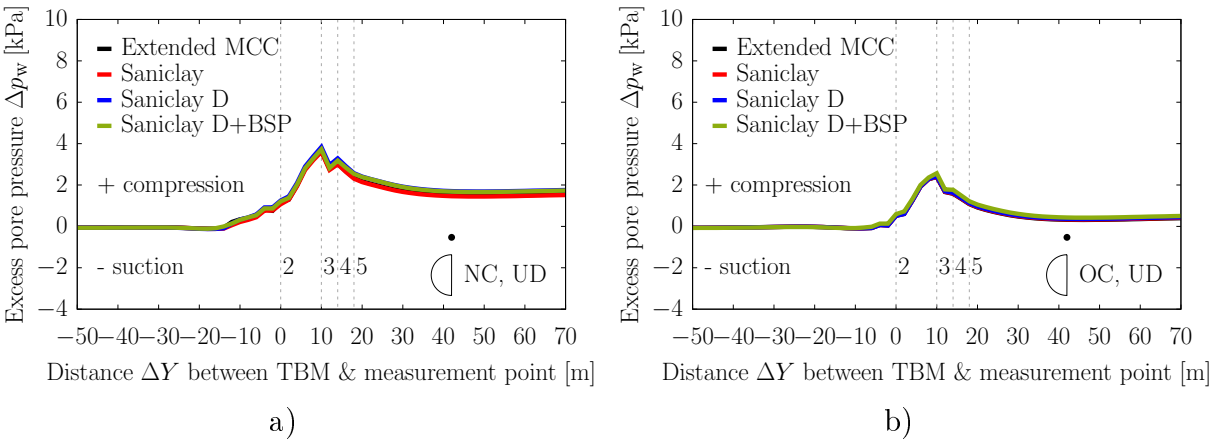

a) b)

Figure 9.16: Evolution of excess pore-water pressure Δp_w traced over the developing distance ΔY between the advancing shield machine and fixed measurement point 5 m above the tunnel crown for a) NC, UD and b) OC, UD scenarios

stress continues. Since the decrease of the effective horizontal stresses is larger than the increase of the effective vertical stress the effective mean stress decreases as well.
To conclude, the qualitative evolution of the effective stress path is very similar for all four model extensions. It can be recognized that the effective stress paths of the Saniclay D and Saniclay D+BSP model extensions are very similar, so that non-monotonic or cyclic behavior is not strongly mobilized. Whereas, the destructuration has a quite perceptible influence especially when the shield machine is passing the measurement section (1) to (4). The Saniclay and MCC model extensions show larger deviations while the shield machine is crossing the measurement section due to absence of destructuration. However, anisotropy does not have any impact.

OC, D scenario

The evolution of the effective stress path for a stress point 5 m above the tunnel crown starting from overconsolidated conditions and assuming drained conditions is given in Figure 9.15b. Whereat, the qualitative evolution of the effective stress path is alike when comparing to the normally consolidated NC, D scenario. Again, because the same subprocesses of mechanized tunneling are involved the qualitative stress changes become alike almost independently of the consolidation conditions but related to predominantly elastic behavior. Nevertheless, especially the decrease of the deviatoric stress is smaller for overconsolidated conditions due to the absence of plasticity and corresponding effects such as destructuration. Moreover, it is to be highlighted that arching effects and stress redistri-

bution to the tunnel side during the passing of the shield machine below the measurement point (2) to (4) lead to a noticeable decrease of the deviatoric stress while the effective mean stress remains almost constant in overconsolidated conditions. Hence, the decrease of the effective vertical stress and the associated increase of the effective horizontal stress are balanced when assuming overconsolidated soil conditions and predominantly elastic material behavior.
To sum up, for overconsolidated conditions of the soil domain midway between tunnel crown and ground surface all four model extensions show almost the same evolution of the effective stress path. To conclude, the effects governed by plasticity such as inherent and stress-induced anisotropy, destructuration as well as stiffness degradation and plastic strain accumulation during non-monotonic or cyclic loading do not come into picture due to purely elastic soil behavior. Even for the Saniclay D+BSP model extension very low plasticity is induced because of the small effective stress changes and the corresponding large distance to the bounding surface.

NC, UD scenario

The evolution of the effective stress path for a stress point 5 m above the tunnel crown starting from normally consolidated conditions and assuming undrained conditions is given in Figure 9.15c. The corresponding evolution of excess pore-water pressure Δp_{w} traced over the developing distance ΔY between the advancing shield machine and the representative measurement points is displayed in Figure 9.16a. Moreover, the spatial distribution of the excess pore-water pressure Δp_{w} wrt. the significant construction stages (1) to (6) is visualized exemplarily for the Saniclay D+BSP model extension in Figure 9.21.
Because the same subprocesses of mechanized tunneling are involved, the qualitative stress changes become alike when comparing to the drained NC, D scenario. Arching effects and stress redistribution to the tunnel side during the passing of the shield machine below the measurement point (1) to (4) lead to a noticeable decrease of the deviatoric stress while the effective mean stress remains almost constant in assumed undrained conditions due to predominantly elastic behavior. Hence, the decrease of effective vertical stress and the associated increase of effective horizontal stress are balanced. Whereas, upward movements and uplift effects of the entire tunnel lining during installation of lining and further shield machine advance (4) to (6) result in increasing deviatoric stress accompanied by constant effective mean stress due to still predominantly elastic soil behavior. Again, the increase of effective vertical stress and the decrease of effective horizontal stress are balanced.

The generation of excess pore-water pressure Δp_w in the normally consolidated soil domain midway between tunnel crown and ground surface is very less pronounced during the construction stages (1) to (6). Since the soil behavior is predominantly elastic less counteracting excess pore-water pressure is developed. However, the internal behavior 5 m above the tunnel crown is contractive during tunnel excavation in construction stages (1) to (4). Hence, positive excess pore-water pressure of relatively small magnitude is generated. Anyhow, the application of grouting (3) leads to dilative internal behavior resulting in slight reduction of the positive excess pore-water pressure in between. Further, shield machine advance (4) to (6) causes dilative internal behavior and the positive excess pore-water pressure again decreases.
Summarizing, the evolution of the effective stress path and the development of excess pore-water pressure is qualitatively and quantitatively alike for all four model extensions. Hence, the influence of anisotropy, destructuration and behavior under non-monotonic or cyclic loading is very small.

OC, UD scenario

The evolution of the effective stress path for a stress point 5 m above the tunnel crown starting from overconsolidated conditions and assuming undrained conditions is given in Figure 9.15d. The corresponding evolution of excess pore-water pressure Δp_w traced over the developing distance ΔY between the advancing shield machine and the representative measurement points is displayed in Figure 9.16b. Moreover, the spatial distribution of the excess pore-water pressure Δp_w wrt. the significant construction stages (1) to (6) is visualized exemplarily for the Saniclay D+BSP model extension in Figure 9.22.
However, the evolution of the effective stress path and the generation of excess pore-water pressure are qualitatively very similar to the normally consolidated NC, UD scenario. Due to the even more elastic soil behavior because of overconsolidation the quantity of the deviatoric stress and excess pore-water pressure peaks is smaller. Moreover, the qualitative and quantitative evolution of the effective stress path and the generation of excess pore-water pressure are very similar for all four model extensions. Again, the influence of destructuration, anisotropy and non-monotonic or cyclic behavior is negligible.

9.2.2.3 Beside the tunnel

NC, D scenario

The evolution of the effective stress path for a stress point 1 m beside the tunnel side starting from normally consolidated conditions and assuming drained conditions is given in Figure 9.17a. Initially, the effective stress path at the side of the later excavation area is following the bounding surface exhibiting an increase of deviatoric stress and a decrease of effective mean stress. Due to excavation effects hurrying ahead the soil starts moving towards the face of the shield machine and the longitudinal and transverse settlement trough start to form. Especially the effective horizontal stress in transverse tunnel direction adjacent to the sliding wedge decreases while the other stress components underlie small stress release only. Again, the initial course of the effective stress path for the different model extensions depends on the inherent rotation of the bounding surface. Since the induced destructuration simultaneously shrinks the size of the evolving bounding surface differences can be observed for the Saniclay D and Saniclay D+BSP model extensions resulting in larger decrease of the effective mean stress.
When the shield machine is very close to and passing through the measurement section (2) the soil next to the tunnel side is pushed by the shield machine in transverse and longitudinal direction. Therefore, the soil experiences gain of effective horizontal stress coming along with loss of effective vertical stress resulting in decreasing deviatoric stress. A larger incremental increase of the effective horizontal stress compared to the incremental decrease of the effective vertical stresses leads to increasing effective mean stress.
Further advance of the shield machine passing through the measurement section (2) to (3) causes stress redistribution in the upper soil layers above the tunnel. Due to arching the stresses of the upper soil are transferred to the lower soil domain beside the tunnel. Consequently, the effective vertical stress increases at the tunnel side. At the same time, the soil next to the tunnel side experiences volume loss and associated sideward movements resulting in decreasing effective horizontal stress. The superimposed effects cause an increase of deviatoric stress accompanied with decreasing effective mean stress.
The initial application of grouting (3) mainly leads to an increase of the effective horizontal stress in transverse tunnel direction and the effective vertical stress in same order while the effective horizontal stress in longitudinal tunnel direction is slightly decreasing. Hence, the effective mean stress is increasing while the deviatoric stress remains almost constant. During ongoing shield machine advance under the support of grouting pressure (3) to (4) and even up to construction stage (5) the soil next to the tunnel side continues the effective stress path with increasing deviatoric stress accompanied with decreasing

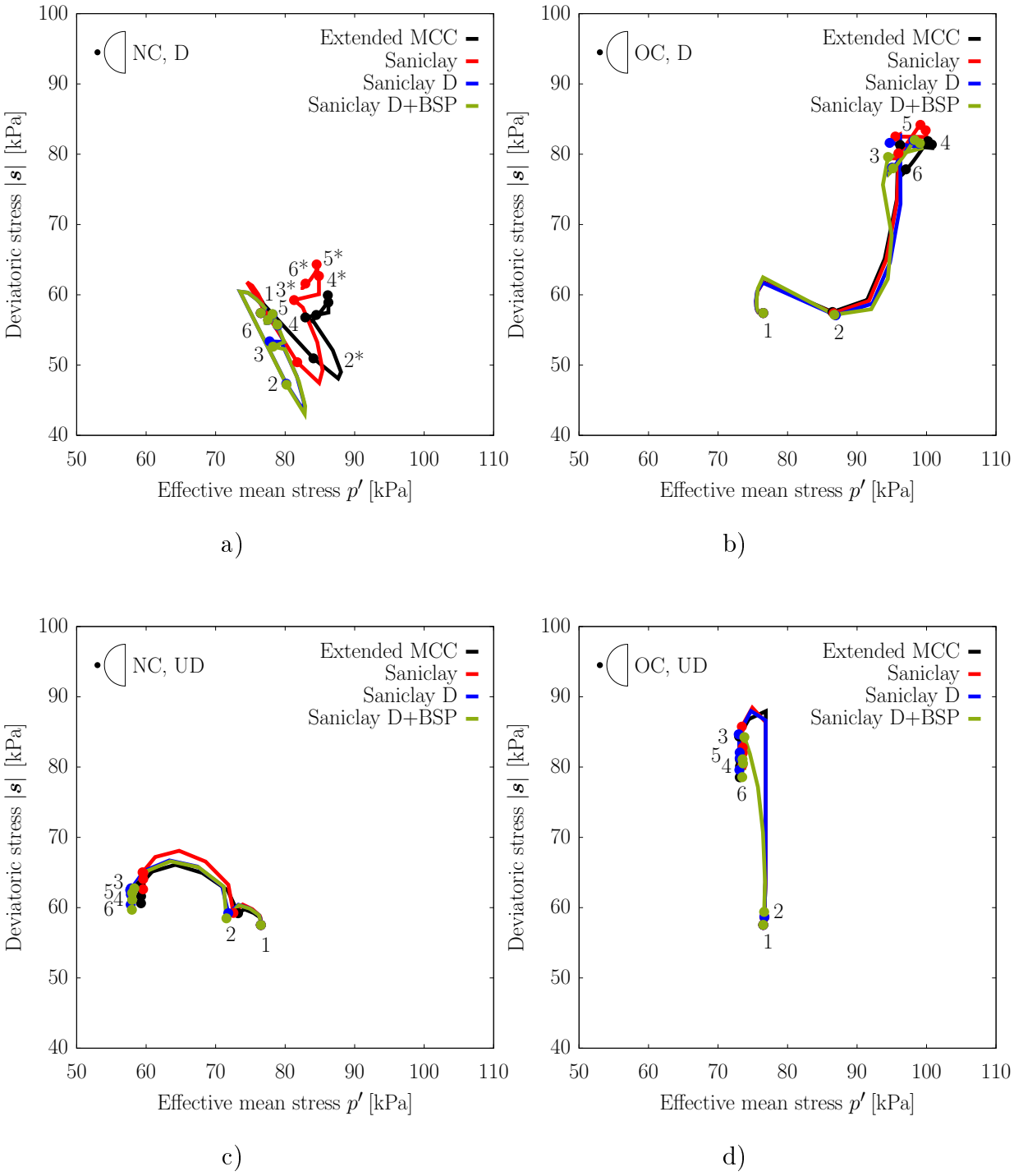

Figure 9.17: Effective mean stress p' vs. deviatoric stress $|\boldsymbol{s}|$ path for stress point 1 m beside the tunnel side wrt. the continuous tunnel excavation for a) NC, D b) OC, D c) NC, UD, d) OC, UD scenarios

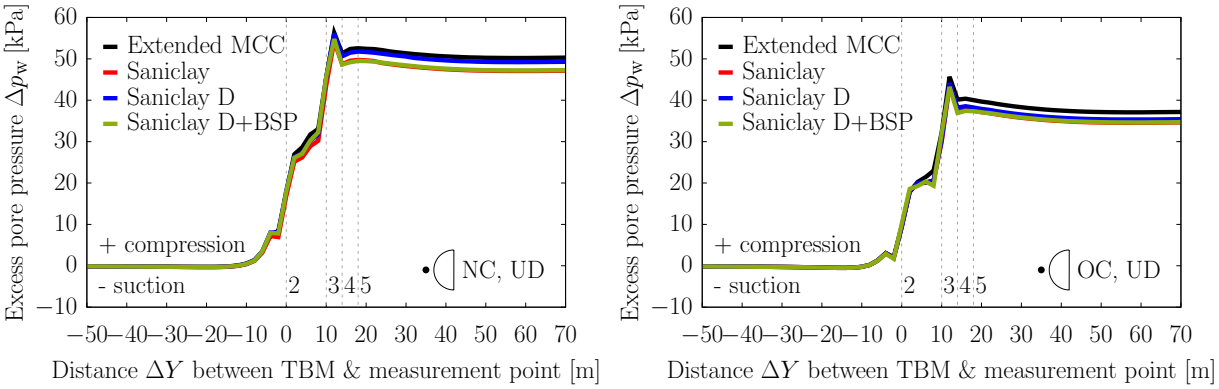

Figure 9.18: Evolution of excess pore-water pressure Δp_w traced over the developing distance ΔY between the advancing shield machine and fixed measurement point 1 m beside the tunnel side for a) NC, UD and b) OC, UD scenarios

effective mean stress. However, further shield machine advance and lining installation (5) to (6) induce a decrease of the effective vertical stress because of buoyancy effects during soil removal and uplift effects while the effective horizontal stress just slightly decrease. That is, the deviatoric stress and effective mean stress are decreased.
Concluding, the qualitative shape of the effective stress paths is the same for all four model extensions. The consideration of the stress-induced destructuration process influences the quantity of the effective stress path at the tunnel side especially when the degradation of stiffness leads to larger decrease of the deviatoric stress and smaller increase of the effective mean stress. However, even the effect of anisotropy is remarkable indicated by larger changes of the deviatoric stress and smaller changes of the effective mean stress when comparing to the isotropic MCC model extension. Whereas, the effects of non-monotonic or cyclic behavior are not that relevant because of the induced predominantly elastoplastic soil behavior. Regarding a most accurate design of the lining destructuration and anisotropy have to be considered to adequately predict the effective stress in the soil domain beside the tunnel when having normally consolidated initial stress conditions and assuming drained conditions.

OC, D scenario

The evolution of the effective stress path for a stress point 1 m beside the tunnel side starting from overconsolidated conditions and assuming drained conditions is given in Figure 9.17b. Whereat, the evolution of the effective stress path is qualitatively and quanti-

tatively quite different when comparing to the normally consolidated NC, D scenario. Tunneling induced arching effects and stress redistribution to the tunnel sides are much more pronounced in overconsolidated conditions than in normally consolidated conditions. Consequently, the effective vertical stress is continuously increasing while the shield machine is approaching and crossing the measurement section (1) to (4). When the shield machine is approaching to the measurement section (1) to (2) the effective horizontal stress is also increasing due to the excavation effects hurrying ahead. Whereat, the incremental increase of the effective horizontal stress rises the closer the shield machine comes to the measurement section. Therefore, the deviatoric stress is initially increasing and decreasing afterwards accompanied by continuously increasing effective mean stress. However, due to overconsolidation the initial model response is predominantly elastic and therefore almost the same for all model extensions.

Further advance of the shield machine passing through the measurement section (2) to (3) causes even more distinct stress redistribution in the upper soil layers above the tunnel. Beside the effective vertical stress also the effective horizontal stress moderately increases due to stress transfer to the tunnel side. Consequently, the deviatoric stress and effective mean stress are slightly increasing. With further shield machine advance the volume loss and associated sideward movements of the soil next to the tunnel side comes into picture. The corresponding decrease of the effective horizontal stress and the still increasing effective vertical stress result into a remarkable increase of deviatoric stress accompanied with a slight increase of effective mean stress. However, the effects of non-monotonic and cyclic behavior becomes obvious during reloading. Due to allowance of elastoplasticity and its associated effects such as destructuration the increase in effective vertical stress is smaller for the Saniclay D+BSP model extension resulting in smaller increase of deviatoric stress and effective mean stress. Moreover, even when initially starting from overconsolidated conditions the stress redistribution to the tunnel side causes elastoplastic soil behavior also for the MCC, Saniclay and Saniclay D model extensions at a certain construction stage. This is indicated by small differences of the effective stress path predicted by the elastoplastic MCC, Saniclay and especially Saniclay D model extensions. Compared to the normally consolidated conditions the stress redistribution is much more striking for overconsolidated conditions showing much larger increase of the deviatoric stress as compared to the normally consolidated NC, D scenario.

The initial application of grouting (3) leads to an increase of effective horizontal stress in transverse tunnel direction and effective vertical stress in same order while the effective horizontal stress in longitudinal tunnel direction is just slightly increasing. Hence, the effective mean stress is increasing while the deviatoric stress remains almost constant.

The soil behavior is very similar to the normally consolidated NC, D scenario since the current stress conditions are not overconsolidated anymore.
During ongoing shield machine advance under the support of grouting pressure (3) to (4) and even up to construction stage (5) the soil next to the tunnel side experiences an effective stress path with increasing deviatoric stress accompanied with decreasing effective mean stress. The effective horizontal stress is redistributed from transverse to longitudinal direction due to arching effects. That is, the effective horizontal stress in transverse direction is decreasing while the effective horizontal stress in longitudinal direction is increasing and the effective vertical stress remains almost constant.
Moreover, as for the normally consolidated NC, D scenario, further shield machine advance and lining installation (5) to (6) induce a decrease of effective vertical and horizontal stresses because of buoyancy effects during soil removal and uplift effects while the effective horizontal stress stays constant. That is, deviatoric stress and effective mean stress are decreased until reaching a steady state (6).
To conclude, since the model responses are almost identical, the plasticity induced destructuration and anisotropy do not become relevant. Whereas, the effective stress path simulated by the Saniclay D+BSP model extension slightly deviates due to the induced plasticity during unloading and reloading cycles. Regarding a most accurate design of the lining non-monotonic or cyclic behavior has to be considered to adequately predict the effective stress in the soil domain beside the tunnel when having overconsolidated initial stress conditions and assuming drained conditions.

NC, UD scenario

The evolution of the effective stress path for a stress point 1 m beside the tunnel side starting from normally consolidated conditions and assuming undrained conditions is given in Figure 9.17c. The corresponding evolution of excess pore-water pressure Δp_{w} traced over the developing distance ΔY between the advancing shield machine and the representative measurement points is displayed in Figure 9.18a. Moreover, the spatial distribution of the excess pore-water pressure Δp_{w} wrt. the significant construction stages (1) to (6) is visualized exemplarily for the Saniclay D+BSP model extension in Figure 9.21.
The evolution of the effective stress path and the corresponding development of the excess pore-water pressure are qualitatively and quantitatively very similar for all four model extensions. As for the drained NC, D scenario, the effective stress path at the side of the later excavation area is initially following the bounding surface exhibiting an increase of deviatoric stress and a decrease of effective mean stress when approaching to the measure-

ment section (1) to (2). Again, the effective horizontal stress in transverse tunnel direction adjacent to the sliding wedge decreases while the other stress components underlie small stress release only. Whereat, the initial course of the effective stress path for the different model extensions depends on the inherent rotation of the bounding surface. Because of the tunneling effects hurrying ahead the soil domain beside the tunnel experiences contractive internal behavior and counteracting positive excess pore-water pressure up to 8 kPa is generated.

When the shield machine is very close to and passing through the measurement section (2) the soil next to the tunnel side is pushed by the shield machine mainly in transverse direction. Hence, the soil experiences a gain of effective horizontal stress in transverse direction accompanied by a decrease of the other stress components leading to decreasing deviatoric stress and effective mean stress. However, the internal behavior is still contractive and the positive excess pore-water pressure increases up to 18 kPa.

Further advance of the shield machine passing through the measurement section (2) to (3) causes volume loss and associated sideward movements resulting in significant decrease of effective horizontal stress in transverse tunnel direction as well as effective vertical stress. The changes of the effective horizontal stress in longitudinal direction are small. Initially, the decrease of the effective horizontal stress in transverse tunnel direction is larger resulting in increasing deviatoric stress accompanied with decreasing effective mean stress. Afterwards, the decrease of the effective vertical stress becomes larger causing a decrease of the deviatoric stress coming along with a reduction of effective mean stress. Still, the internal behavior is contractive and the positive excess pore-water pressure increases up to 46 kPa.

The application of grouting (3) to (4) mainly leads to an increase of effective horizontal stress in transverse tunnel direction while the other stress components slightly decrease in same order. Hence, the deviatoric stress is decreasing while the effective mean stress remains almost constant. The internal behavior next to the tunnel side is still contractive and the positive excess pore-water pressure increases to the maximum value of 55 kPa.

Continuing shield machine advance (4) to (5) leads to an increase of deviatoric stress with almost constant effective mean stress due to predominantly elastic reloading soil behavior. However, the internal behavior switches from contractive to dilative and positive excess pore-water pressure initially slightly drops to about 49 kPa and 47.5 kPa at the steady state. However, further shield machine advance and lining installation (5) to (6) induce predominantly elastic unloading behavior. Therefore, a slight decrease of deviatoric stress is observed while the effective mean stress remains almost constant. Consequently, the excess pore-water pressure stays at the same magnitude.

Concluding, the qualitative and quantitative shape of the effective stress path and the evolution of the excess pore-water pressure is the same for all four model extensions and the influence of anisotropy, destructuration and non-monotonic or cyclic effects are very small and almost negligible.

OC, UD scenario

The evolution of the effective stress path for a stress point 1 m beside the tunnel side starting from overconsolidated conditions and assuming undrained conditions is given in Figure 9.17d. The corresponding evolution of excess pore-water pressure Δp_{w} traced over the developing distance ΔY between the advancing shield machine and the representative measurement points is displayed in Figure 9.18b. Moreover, the spatial distribution of the excess pore-water pressure Δp_{w} wrt. the significant construction stages (1) to (6) is visualized exemplarily for the Saniclay D+BSP model extension in Figure 9.22.
When the shield machine is approaching to the measurement section (1) to (2) the stress changes are very small for all model extensions. Due to the initial elastic reloading the deviatoric stress is increasing while the effective mean stress remains almost constant.
Further shield machine advance from construction stage (2) to (3) causes volume loss around the tunnel and stress redistribution from the tunnel crown to the side. That leads to significantly increasing effective vertical stress and decreasing effective horizontal stress in transverse tunnel direction resulting in striking increase of the deviatoric stress. However, for the Saniclay D+BSP model extension the soil behavior is just initially purely elastic resulting in constant effective mean stress under assumed undrained conditions. Afterwards, the soil behavior turns elastoplastic and decreasing effective mean stress can be observed. On the contrary, the soil behavior predicted by the three elastoplastic model extensions is purely elastic until reaching the bounding surface again. After intersection the effective stress path follows the bounding surface resulting in decreasing deviatoric stress and effective mean stress. However, the stress state when reaching construction stage (3) is almost the same for all four model extensions.
The evolution of the effective stress path from construction stage (3) to (6) is qualitatively very similar to the normally consolidated NC, UD scenario. That is, the deviatoric stress is decreasing during application of grouting (3) to (4), increasing during lining installation (4) to (5) and again decreasing during further shield machine advance (5) to (6) while the effective mean stress remains almost constant due to the predominantly elastic unloading and reloading behavior.

The generation of excess pore-water pressure is qualitatively very similar to the normally consolidated NC, UD scenario but shows smaller magnitude due to more elastic soil behavior. While the shield machine is moving from construction stage (1) to (4) the internal behavior is contractive and counteracting positive excess pore-water pressure is generated up to a maximum value of 43.5 kPa. This corresponds to 79% compared to the maximum excess pore-water pressure observed in the NC, UD scenario. At the steady state the excess pore-water pressure reaches a reduced value of 35 kPa.
Summarizing, since the model responses are almost identical the plasticity induced destructuration and anisotropy do not become relevant. Nevertheless, the effective stress path simulated by the Saniclay D+BSP model extension slightly deviates due to the induced plasticity during unloading and reloading cycles. Regarding a most accurate design of the lining non-monotonic or cyclic behavior has to be considered to adequately predict the effective stress in the soil domain beside the tunnel when having overconsolidated initial stress conditions and assuming undrained conditions.

9.2.2.4 Below the tunnel

NC, D scenario

The evolution of the effective stress path for a stress point 1 m below the tunnel invert starting from normally consolidated conditions and assuming drained conditions is given in Figure 9.19a. While the shield machine is approaching to and passing through the measurement section (1) to (3) the soil domain directly below the excavation zone experiences predominantly elastic unloading due to stress release caused by buoyancy effects during soil removal and volume loss represented by a remarkable decrease of the effective mean stress and deviatoric stress. The soil shows upward deformations and stress relaxation. That is, especially the effective vertical stress is decisively decreasing accompanied by a smaller decrease of the effective horizontal stress. Whereat, the effect of unloading is largest shortly before the shield machine is reaching the measurement section. The stress release and unloading behavior of the soil below the shield machine are slowed down while the shield machine is passing the measurement section (2) to (3) because of already influencing neighboring grouting effects balancing the stress.
When grouting pressure is applied (3) to (4) the soil below the shield machine is pushed downwards. Hence, the effective vertical stress increases, whereas the effective horizontal stress just slightly changes. This leads to increasing deviatoric stress and effective mean stress. Continuing tunnel excavation and installation of lining (4) to (6) in combination

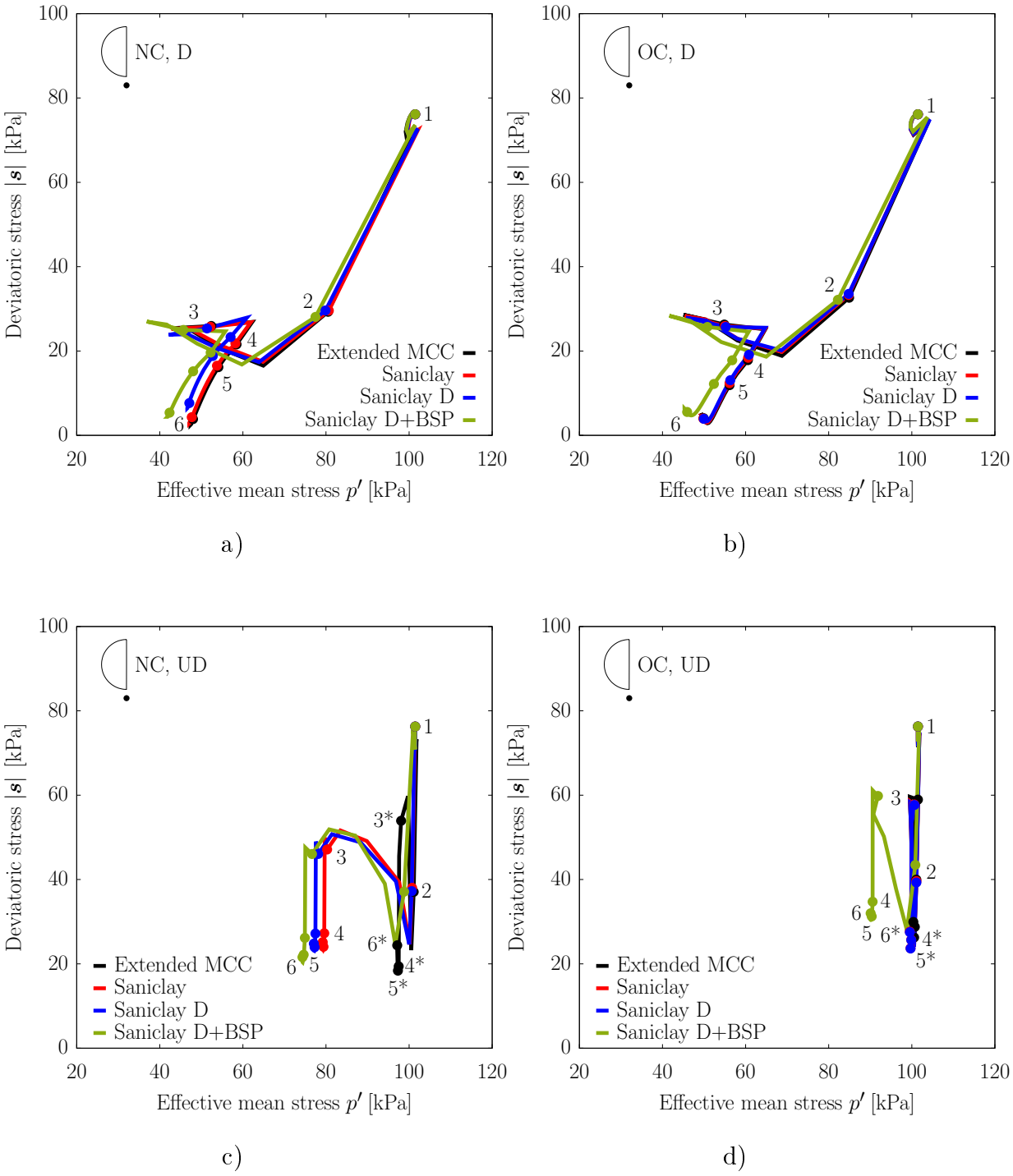

Figure 9.19: Effective mean stress p' vs. deviatoric stress $|\boldsymbol{s}|$ path for stress point 1 m below the tunnel invert wrt. the continuous tunnel excavation for a) NC, D b) OC, D c) NC, UD, d) OC, UD scenarios

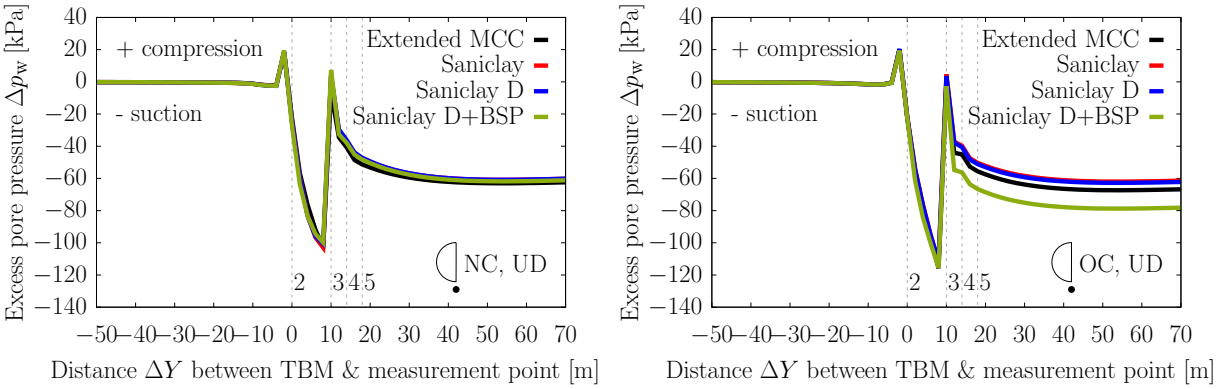

Figure 9.20: Evolution of excess pore-water pressure Δp_w traced over the developing distance ΔY between the advancing shield machine and fixed measurement point 1 m below the tunnel invert for a) NC, UD and b) OC, UD scenarios

with the low overburden depth and the water-saturated clay deposit again causes buoyancy effects due to soil removal and uplift effects. Consequently, further unloading of the soil below the tunnel invert is evoked by stress release.

In general, the qualitative and quantitative evolution of the effective stress path is very similar for all four model extensions since the material behavior is predominantly elastic. However, the Saniclay D+BSP model extension shows slightly different elastoplastic unloading-reloading behavior while moving inside the bounding surface. The small differences of the effective stress path predicted by the Saniclay D model extension compared to the MCC and Saniclay model extensions arise from elastoplastic material behavior induced by the application of grouting pressure causing a certain destructuration. Since the effective stress paths predicted by the MCC and Saniclay model extensions are almost identical it is confirmed that the soil domain below the tunnel invert is rather less influenced by inherent and stress-induced anisotropy due to predominantly elastic soil behavior.

To sum up, the impact of anisotropy is small for the soil domain below the tunnel invert, but the destructuration and the non-monotonic or cyclic behavior of the soil becomes more relevant. Regarding a most accurate design of the lining destructuration and non-monotonic or cyclic behavior have to be considered to adequately predict the effective stress in the soil domain below the tunnel when having normally consolidated initial stress conditions and assuming drained conditions.

OC, D scenario

The evolution of the effective stress path for a stress point 1 m below the tunnel invert starting from overconsolidated conditions and assuming drained conditions is given in Figure 9.19b. The evolution of the effective stress path is qualitatively and quantitatively very similar when comparing to the normally consolidated NC, D scenario. That is, irrespective of the consolidation condition the soil behavior below the tunnel invert is predominantly elastic. However, when considering overconsolidated soil conditions, the soil behavior predicted by the MCC, Saniclay and Saniclay D model extensions is purely elastic for the entire construction process (1) to (6).
To sum up, the plasticity induced anisotropy and destructuration do not become relevant. Consequently, the model responses are almost identical. On the contrary, the effective stress path simulated by the Saniclay D+BSP model extension slightly deviates due to the induced plasticity during unloading and reloading cycles. Regarding a most accurate design of the lining non-monotonic or cyclic behavior has to be considered to adequately predict the effective stress in the soil domain below the tunnel when having overconsolidated initial stress conditions and assuming drained conditions.

NC, UD scenario

The evolution of the effective stress path for a stress point 1 m below the tunnel invert starting from normally consolidated conditions and assuming undrained conditions is given in Figure 9.19c. The corresponding evolution of excess pore-water pressure Δp_{w} traced over the developing distance ΔY between the advancing shield machine and the representative measurement points is displayed in Figure 9.20a. Moreover, the spatial distribution of the excess pore-water pressure Δp_{w} wrt. the significant construction stages (1) to (6) is visualized exemplarily for the Saniclay D+BSP model extension in Figure 9.21. The evolution of the effective stress path is qualitatively alike for the three Saniclay model extensions but slightly differs quantitatively. However, the effective stress path predicted by the MCC model extension is rather different due to less induced plasticity because of the non-rotated bounding surface. Whereas, the development of the excess pore-water pressure is qualitatively and quantitatively almost the same for all four model extensions. Compared to the drained NC, D scenario the deviatoric stress changes during mechanized tunneling are qualitatively similar. However, the evolution of the effective mean stress is quite different since it remains almost constant when it comes to elastic soil behavior in assumed undrained conditions.

To be more detailed, while the shield machine is moving one step before and one step behind the measurement section (1) to (2) the deviatoric stress is significantly decreasing. That is, the effective vertical stress is decisively decreasing due to buoyancy effects during soil removal and volume loss accompanied by smaller increase of the effective horizontal stress. At the same time the effective mean stress is just slightly decreasing for the Saniclay D+BSP model extension due to the predominantly elastic unloading behavior caused by stress release combined with assumed undrained conditions. For the elastoplastic model extensions which do not incorporate plastic behavior during non-monotonic or cyclic loading the effective mean stress remains almost constant. Beside some preceding development of positive excess pore-water pressure due to initial compressive internal behavior, the stress release during excavation (1) to (3) leads to dilative internal behavior and corresponding generation of negative excess pore-water pressure up to -100 kPa.
Afterwards, neighboring grouting effects evoke decreasing effective horizontal stress in longitudinal tunnel direction even before reaching construction stage (3). However, the effective vertical stress is still decreasing due to volume loss. To conclude, the deviatoric stress is increasing while the effective mean stress is decreasing. The decrease of the effective mean stress is most pronounced for the three Saniclay model extensions where plasticity induced effects such as destructuration and anisotropy come into picture. Whereas, the MCC model extension shows elastic reloading only represented by increasing deviatoric stress and constant effective mean stress.
When grouting pressure is applied (3) the soil below the shield machine is pushed downwards to be balanced. That is, the effective vertical stress is again increasing coming along with decreasing effective horizontal stress. The change of the deviatoric stress and effective mean stress is small. Since the internal behavior switches from dilative to contractive the excess pore-water pressure strikingly increases up to positive values of 7 kPa for the Saniclay D+BSP model extension.
Ongoing tunnel excavation and installation of lining (3) to (6) in combination with the low overburden depth and the water-saturated clay deposit cause buoyancy effects due to soil removal and uplift effects. Consequently, further unloading of the soil below the tunnel invert is evoked by stress release and rapid decrease of the deviatoric stress occurs. Since the soil behavior is predominantly elastic and undrained conditions are assumed the effective mean stress stays almost constant during unloading. Further stress release once more causes dilative behavior and again negative excess pore-water pressure is generated converging to a steady state value of -60 kPa.

To sum up, the impact of the stress-induced destructuration and the non-monotonic or cyclic behavior on the effective stress path is somehow noticeable for the soil domain below the tunnel invert. Moreover, the influence of the initial rotation of the bounding surface on the evolution of the effective stress path is quite striking. The fact if the effective stress path reaches the bounding surface during unloading or not governs the decision if purely elastic or elastoplastic material behavior occurs. On the other side, the development of the excess pore-water pressure is almost independent of destructuration, anisotropy and non-monotonic or cyclic behavior. Regarding a most accurate design of the lining destructuration, anisotropy and non-monotonic or cyclic behavior have to be considered to adequately predict the effective stress in the soil domain below the tunnel when having normally consolidated initial stress conditions and assuming undrained conditions.

OC, UD scenario

The evolution of the effective stress path for a stress point 1 m below the tunnel invert starting from normally consolidated conditions and assuming undrained conditions is given in Figure 9.19d. The corresponding evolution of excess pore-water pressure Δp_{w} traced over the developing distance ΔY between the advancing shield machine and the representative measurement points is displayed in Figure 9.20b. Moreover, the spatial distribution of the excess pore-water pressure Δp_{w} wrt. the significant construction stages (1) to (6) is visualized exemplarily for the Saniclay D+BSP model extension in Figure 9.22.

The non-monotonic or cyclic deviatoric stress reversals governed by the different construction stages (1) to (6) are qualitatively similar when comparing to the normally consolidated NC, UD scenario, but the evolution of the effective mean stress strongly deviates due to overconsolidation. To be more precise, for the three elastoplastic model extensions which do not account for non-monotonic or cyclic behavior the effective mean stress remains almost constant during mechanized tunneling in assumed undrained conditions due to the associated predominantly elastic behavior. Just the deviatoric stress is changing during construction stages (1) to (6) as described for the normally consolidated NC, UD scenario. To recall, the deviatoric stress is decreasing due to stress release during excavation (1) to (2/3), increasing due to preceding grouting effects (2/3) and again decreasing due to stress release during continuous tunnel excavation and installation of lining (3) to (6). However, for the Saniclay D+BSP model extension incorporating elastoplastic hysteresis, stiffness degradation and accumulation of plastic strain during non-monotonic or cyclic loading the effective mean stress is decreasing when moving from construction stage

(2) to (3). That indicates elastoplastic soil behavior. For the other construction stages the soil behavior predicted by the Saniclay D+BSP model extension is also predominantly elastic as for the other model extensions due to the larger distance to the bounding surface during unloading.

The generation of excess pore-water pressure is qualitatively very similar to the normally consolidated NC, UD scenario. That is, after initial generation of positive excess pore-water pressure due to preceding effects before reaching the measurement section (2), the stress release during excavation (2) to (3) causes the development of negative excess pore-water pressure up to a value of -116 kPa. Compared to the normally consolidated NC, UD scenario the negative excess pore-water pressure is about 16% more pronounced due to even more elastic material behavior during excavation. Application of grouting (3) results in an increase of the excess pore-water pressure up to still negative values of -3 kPa for the Saniclay D+BSP model extension. However, for the other elastoplastic model extensions considering purely elastic reloading the increase in excess pore-water pressure due to grouting is even higher up to positive values of 5 kPa. Further differences between the Saniclay D+BSP model and the other model extensions occur when it comes to continuing tunnel excavation and installation of lining (4) to (6). That is, the development of negative excess pore-water pressure is more pronounced for the Saniclay D+BSP model extension represented by a steady state value of -78 kPa compared to -60 kPa to -65 kPa for the other model extensions which corresponds to the steady state value obtained for the normally consolidated NC, UD scenario.

To conclude, the influence of the non-monotonic or cyclic behavior on the evolution of the effective stress path and the generation of excess pore-water pressure becomes relevant while the shield machine is moving from construction stage (2) to (6). The effects of destructuration and anisotropy are much smaller or even negligible. Regarding a most accurate design of the lining non-monotonic or cyclic behavior has to be considered to adequately predict the effective stress in the soil domain below the tunnel when having overconsolidated initial stress conditions and assuming undrained conditions.

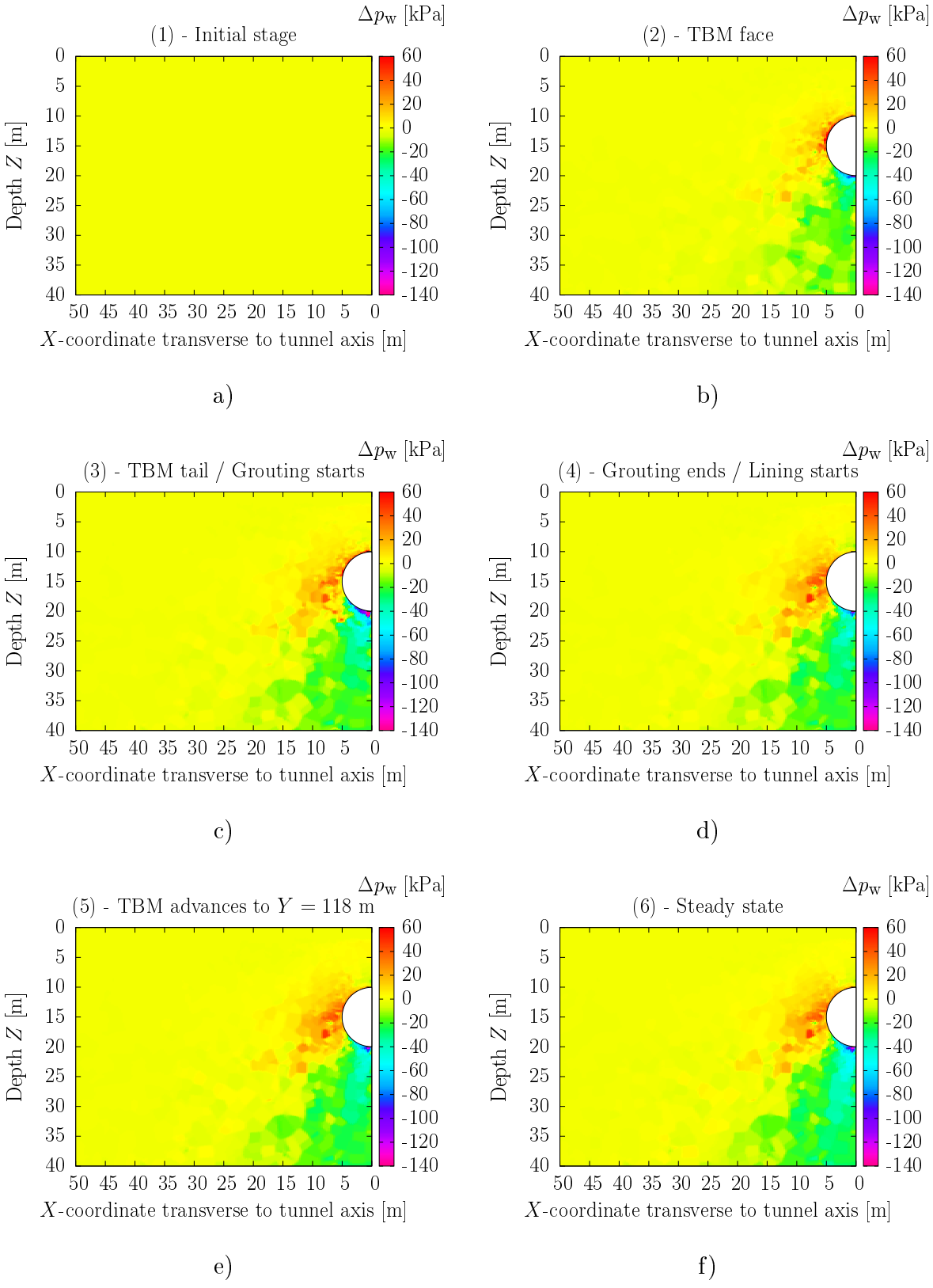

Figure 9.21: Evolution of excess pore-water pressure Δp_w in the synthetic measurement section ($Y = 100$ m) using the Saniclay D+BSP model extension for NC, UD scenario wrt. the significant construction stages (1) to (6)

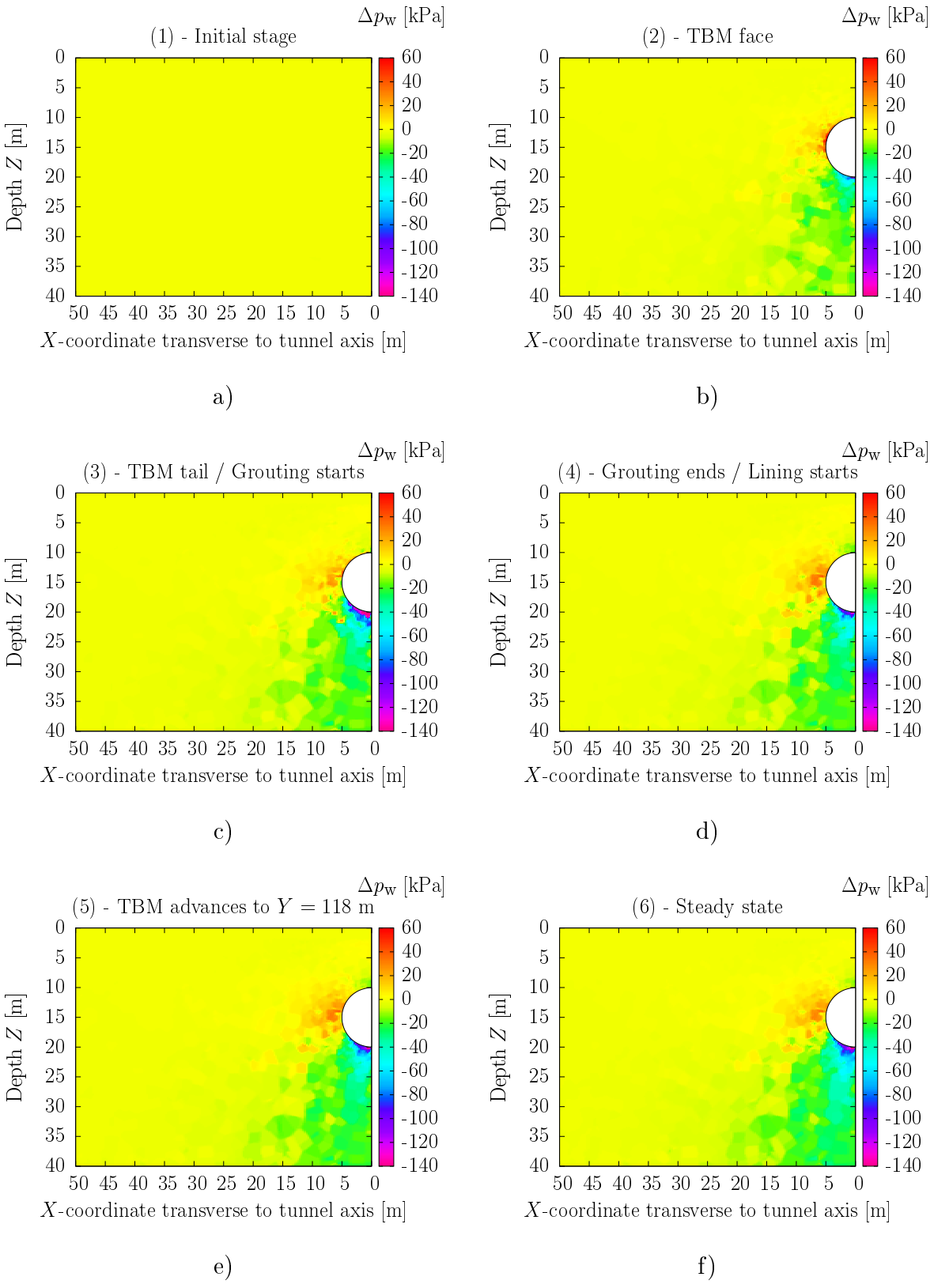

Figure 9.22: Evolution of excess pore-water pressure Δp_w in the synthetic measurement section ($Y = 100$ m) using the Saniclay D+BSP model extension for OC, UD scenario wrt. the significant construction stages (1) to (6)

9.2.3 State variables of the BSP model and plastic strain

For the assessment of the required complexity of the constitutive BSP model it is important to understand the spatial and construction stage dependent evolution of the state variables of the BSP model corresponding to destructuration, stress-induced anisotropy as well as elastoplastic hysteresis, stiffness degradation and accumulation of plastic strain under non-monotonic or cyclic loading induced by mechanized tunneling.

9.2.3.1 Evolution of plastic strain $|\boldsymbol{\varepsilon}^{\mathrm{p}}|$

Since the mechanical properties of natural clay such as destructuration, stress-induced anisotropy and elastoplastic hysteresis, stiffness degradation and accumulation effects under non-monotonic or cyclic loading are strongly dependent on the induced plasticity the evolution of plastic strain $|\boldsymbol{\varepsilon}^{\mathrm{p}}|$ due to mechanized tunneling is initially investigated. The evolution of the plastic strain $|\boldsymbol{\varepsilon}^{\mathrm{p}}|$ in the synthetic measurement section ($Y = 100$ m) wrt. the significant construction stages (1) to (6) is presented exemplarily for the Saniclay D+BSP model extension in Figures 9.23 to 9.26 for the four investigated scenarios.

NC, D scenario

For the NC, D scenario as shown in Figure 9.23 the stress redistribution due to volume loss in the nearfield above and beside the tunnel results in elastoplastic soil behavior and remarkable plastic straining while the shield machine is crossing the measurement section. This is indicated by an increasing maximum value of the plastic strain $|\boldsymbol{\varepsilon}^{\mathrm{p}}| = 1.6\%$ at construction stage (2) and $|\boldsymbol{\varepsilon}^{\mathrm{p}}| = 3.7\%$ at construction stage (3). Whereat, the maximum plasticity is induced in the nearfield of the upper tunnel quarter. Plasticity mainly propagates from the upper tunnel side diagonally towards the ground surface as well as sidewards. In contrast, the area vertically above the tunnel is less affected by plasticity and predominantly elastic behavior occurs since stress is redistributed to the sides due to arching effects. However, the shallow area directly below the overconsolidated upper layer is considerably influenced by plasticity. Here, stress redistribution occurs since arching effects are not mobilized due to low overburden. Moreover, relative movements and shearing of the soil layers with different stiffness and strength takes place. During the application of grouting from construction stage (3) to (4) a small amount of additional plasticity is generated since the support pressure keeps the soil above the tunnel in equilibrium. However, the sideward propagation of the plasticity slightly increases because the lateral

support pressure is pushing the adjacent soil. Moreover, some effects of the grouting on the plasticity may already hurrying ahead while the shield machine is still approaching to the measurement section. During installation of lining and successive advance of the shield machine the compressible behavior of the lining causes further stress redistribution in the nearfield of the tunnel. Hence, more plasticity is induced represented by maximum values of the plastic strain $|\boldsymbol{\varepsilon}^{\mathrm{p}}| = 4.0\%$ at construction stage (5) and $|\boldsymbol{\varepsilon}^{\mathrm{p}}| = 6.3\%$ at construction stage (6). Associated to this, the area influenced by plasticity increases. In the area below the tunnel the soil behavior is predominantly elastic due to stress release during excavation and uplift effects of the lining. Only in the nearfield below the tunnel in an outer ring of 1-2 m thickness plasticity is induced while the shield machine is approaching and crossing the measurement section (1) to (3).

OC, D scenario

For the OC, D scenario as shown in Figure 9.24 noticeable plastic straining due to stress redistribution caused by volume loss and prior grouting effects takes place in the nearfield around the entire tunnel only. This is indicated by an increasing maximum value of the plastic strain $|\boldsymbol{\varepsilon}^{\mathrm{p}}| = 0.38\%$ at construction stage (2) and $|\boldsymbol{\varepsilon}^{\mathrm{p}}| = 0.60\%$ at construction stage (3). Whereat, the noticeable propagation of plasticity is restricted to an area of 1-2 m around the tunnel. It can be observed that the maximum magnitude of the plastic strain is just 10% of the maximum value obtained in the normally consolidated NC, D scenario and the area affected by plasticity is relatively small. That is, because of the overconsolidation the majority of the soil behavior is predominantly elastic as long as just small stress changes occur and plasticity develops in a limited area in the nearfield of the tunnel only. Nevertheless, the magnitude and spatial distribution of the plasticity induced below the tunnel is qualitatively and quantitatively similar for both scenarios. Afterwards, the magnitude and distribution of the plastic strain remain constant during further application of grouting, installation of lining and continuing advance of the shield machine (3) to (6) since the stress release and uplift of the lining cause predominantly elastic behavior.

NC, UD scenario

For the NC, UD scenario the generation of excess pore-water pressure and associated effective stress changes take place caused by volume loss and prior grouting effects when the shield machine is passing the measurement section. Consequently, plastic straining

occurs in the nearfield of 1-2 m around the entire tunnel but especially in the lower tunnel quarter where the largest amount of plasticty is induced as displayed in Figure 9.25. From the lower tunnel side plasticity propagates diagonally downward to a maximum extension of 6 m. In addition, the distribution of the plastic strain above the tunnel is qualitatively similar to the findings from the drained NC, D scenario but in a diluted form. That is, plasticity propagates from the upper tunnel side diagonally towards the ground surface as well as sidewards. The area vertically above the tunnel is less affected by plasticity while in contrast the shallow area directly below the overconsolidated upper layer is considerably influenced by plasticity. The induced plasticity during the excavation process is indicated by an increasing maximum value of the plastic strain $|\boldsymbol{\varepsilon}^{\mathrm{p}}| = 0.65\%$ at construction stage (2) and $|\boldsymbol{\varepsilon}^{\mathrm{p}}| = 0.86\%$ at construction stage (3). The maximum magnitude of the plastic strain is just 14% of the maximum value obtained from the drained NC, D scenario. That is, assumed undrained conditions mainly trigger a small amount of elastoplastic behavior during mechanized tunneling. As figured out for the OC, D scenario the magnitude and spatial distribution of the plastic strain remain constant during further application of grouting, installation of lining and continuing advance of the shield machine (3) to (6) since the stress release and uplift of the lining cause predominantly elastic behavior.

OC, UD scenario

For the OC, UD scenario the noticeable development of plasticity due to the generation of excess pore-water pressure and associated effective stress changes just appears in the area around the lower tunnel quarter while the shield machine is moving from construction stage (1) to (3) as visualized in Figure 9.26. The area around the upper tunnel quarter is nearly unaffected by plasticity showing predominantly elastic behavior only. From the lower tunnel side plasticity is propagating diagonally downward to a maximum extension of 3 m. This means, due to overconsolidation the area influenced by plasticity is smaller than compared to the normally consolidated NC, UD scenario. The induced plasticity during the excavation process is represented by an increasing maximum value of the plastic strain $|\boldsymbol{\varepsilon}^{\mathrm{p}}| = 0.17\%$ at construction stage (2) and $|\boldsymbol{\varepsilon}^{\mathrm{p}}| = 0.94\%$ at construction stage (3). The maximum magnitude of the plastic strain is similar to the normally consolidated NC, UD scenario, but more than 50% larger than compared to the overconsolidated, drained OC, D scenario. As observed for the NC, UD and OC, D scenarios the magnitude and spatial distribution of the plastic strain remain constant during further application of grouting, installation of lining and continuing advance of the shield machine (3) to (6) since the stress release and uplift of the lining causes predominantly elastic behavior.

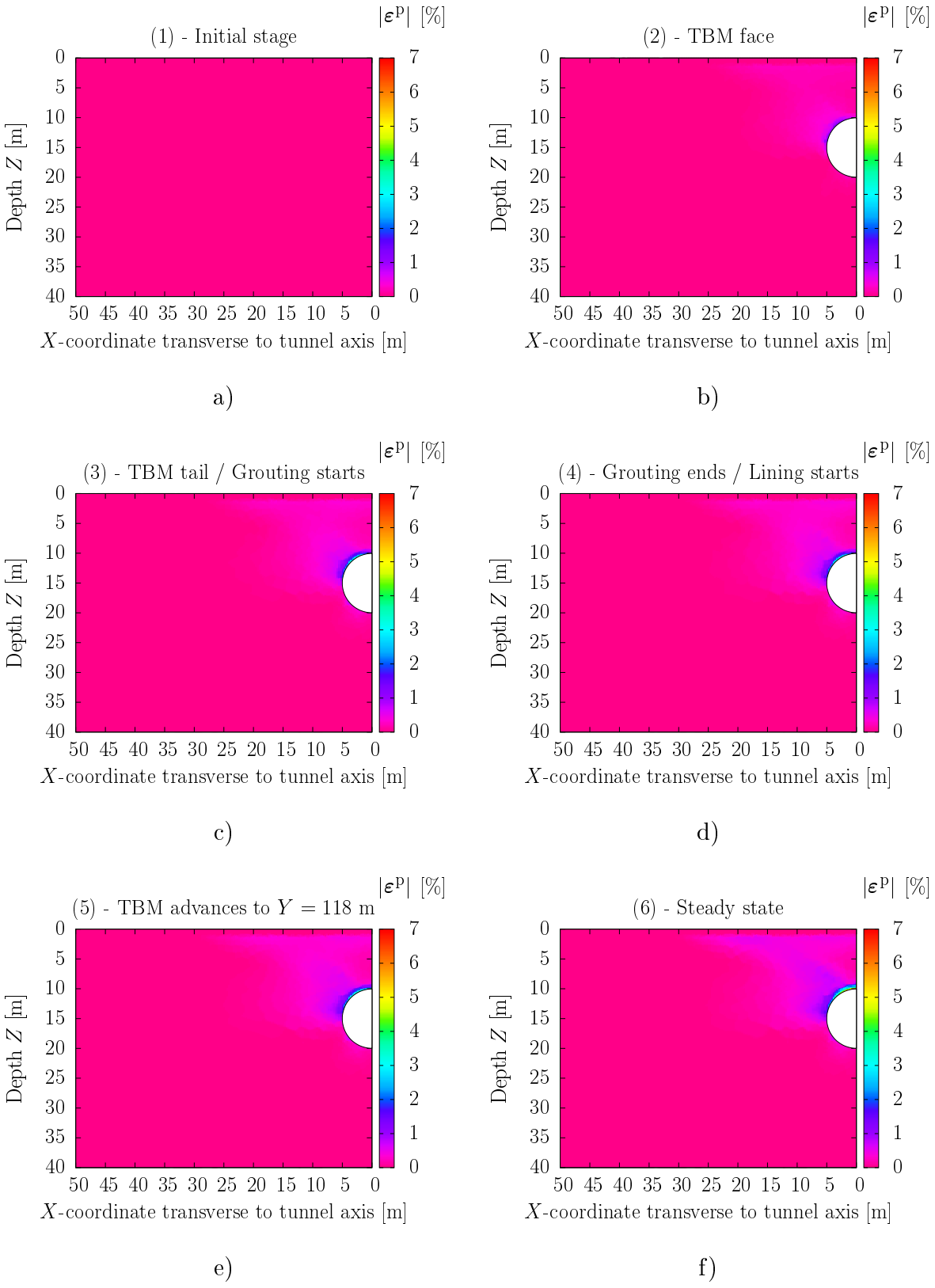

Figure 9.23: Evolution of the plastic strain $|\boldsymbol{\varepsilon}^{\mathrm{p}}|$ in the synthetic measurement section ($Y = 100$ m) using the Saniclay D+BSP model extension for NC, D scenario wrt. the significant construction stages (1) to (6)

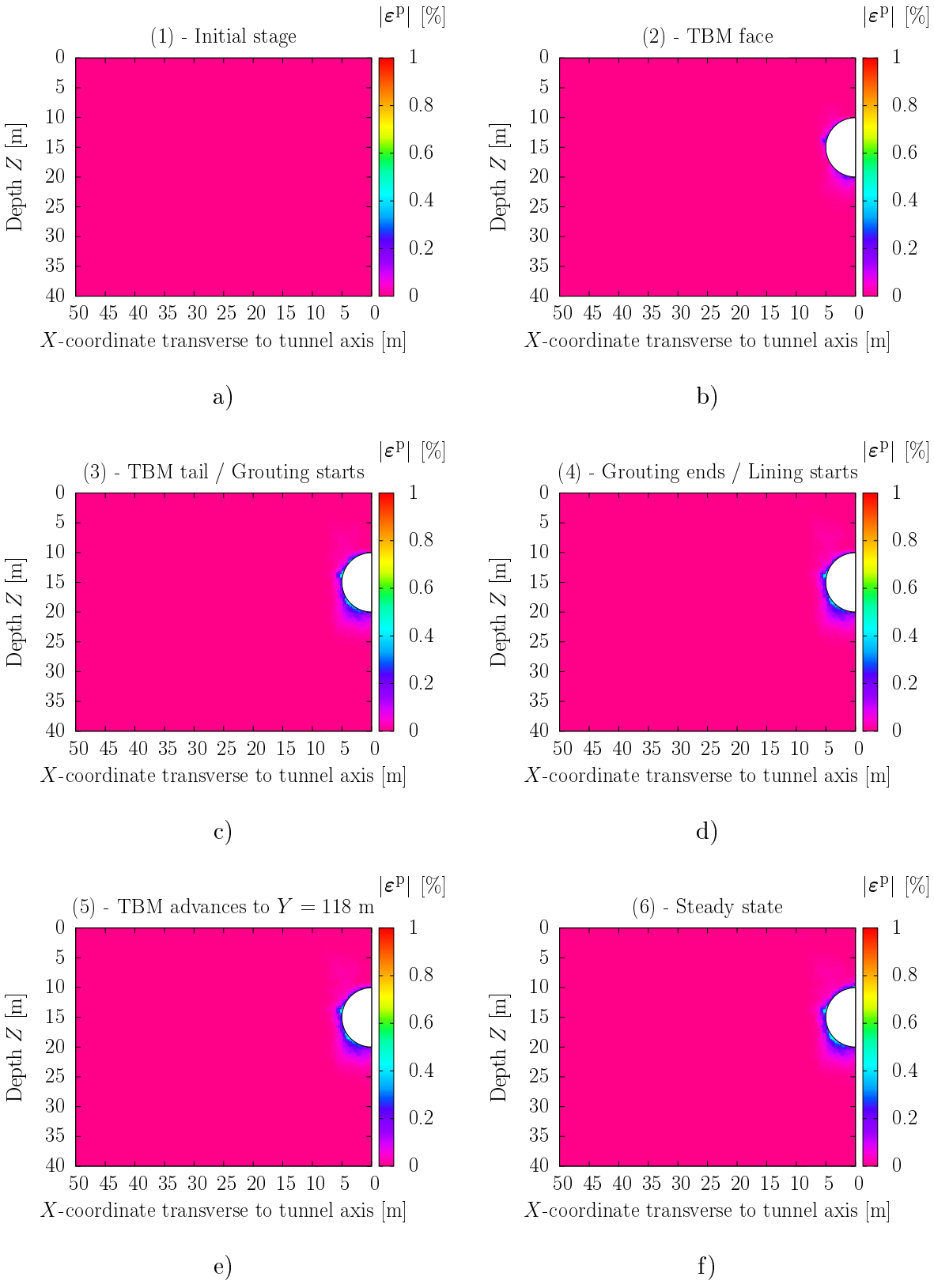

Figure 9.24: Evolution of the plastic strain $|\boldsymbol{\varepsilon}^{\mathrm{p}}|$ in the synthetic measurement section ($Y = 100$ m) using the Saniclay D+BSP model extension for OC, D scenario wrt. the significant construction stages (1) to (6)

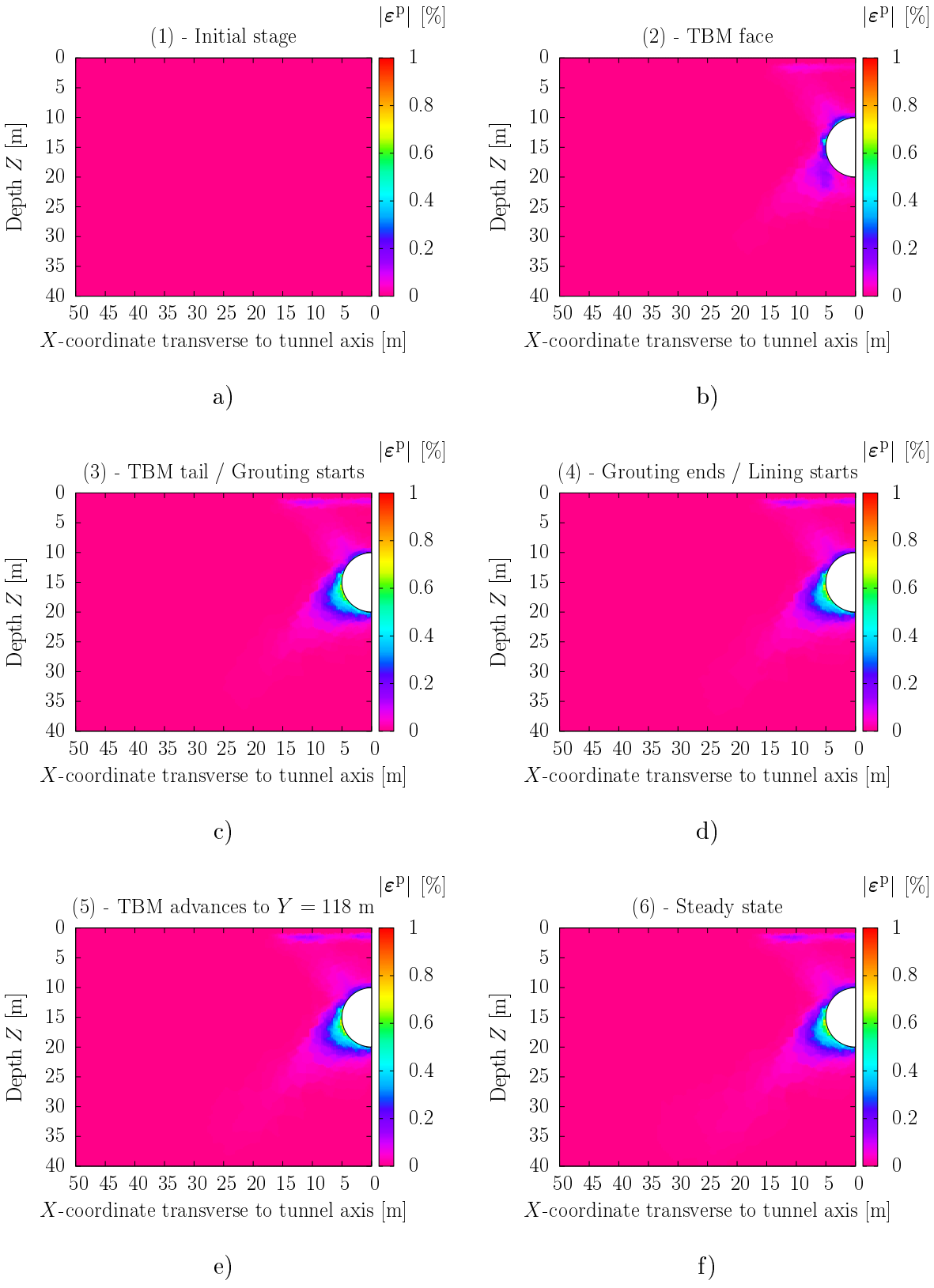

Figure 9.25: Evolution of the plastic strain $|\boldsymbol{\varepsilon}^{\mathrm{p}}|$ in the synthetic measurement section ($Y = 100\,\mathrm{m}$) using the Saniclay D+BSP model extension for NC, UD scenario wrt. the significant construction stages (1) to (6)

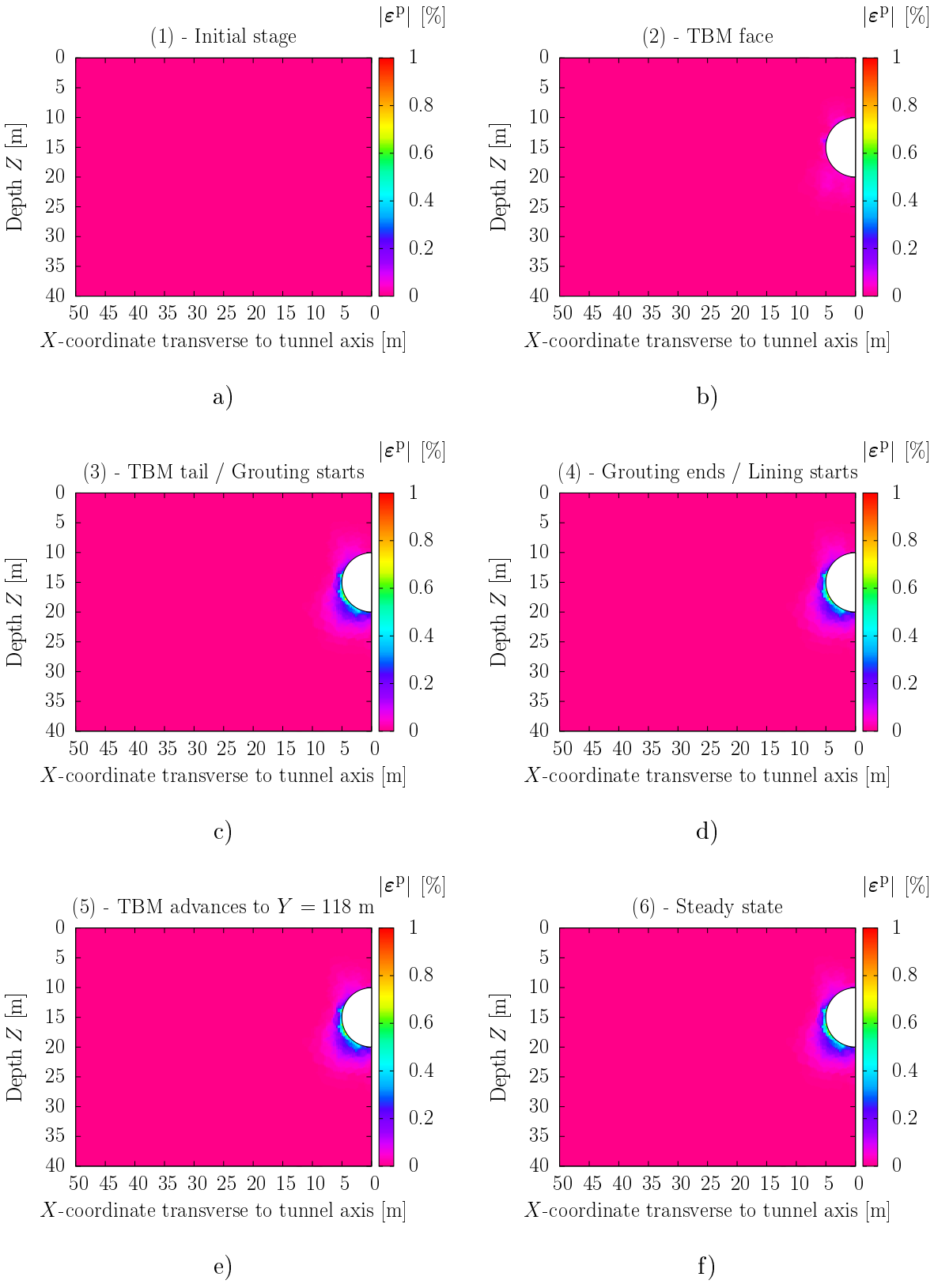

Figure 9.26: Evolution of the plastic strain $|\boldsymbol{\varepsilon}^{\mathrm{p}}|$ in the synthetic measurement section ($Y = 100\,\mathrm{m}$) using the Saniclay D+BSP model extension for OC, UD scenario wrt. the significant construction stages (1) to (6)

9.2.3.2 Evolution of structure variable S_i

The evolution of the structure variable S_i in the synthetic measurement section (Y = 100 m) wrt. the significant construction stages (1) to (6) is presented exemplarily for the Saniclay D+BSP model extension in Figures 9.27 to 9.30 for the investigated scenarios. To visualize the effects of destructuration and progressive reduction of the stiffness and strength the evolution of the structure variable is investigated starting from an initial value of $S_{\mathrm{i},0} = 8.5$. Whereat, the destructuration is defined as a decaying function of the volumetric and deviatoric plastic strain increments. Consequently, the magnitude of destructuration and its spatial distribution in the soil domain is in accordance with the findings regarding the evolution of the plastic straining as discussed in the former section. However, due to the calibrated constitutive BSP model parameter $A = 0.3$ the components of the plastic strain increment influencing the destructuration are partitioned to 70% volumetric and 30% deviatoric.

NC, D scenario

For the NC, D scenario as visualized in Figure 9.27 the induced plastic straining leads to a significant destructuration while the shield machine is crossing the measurement section. The progressive loss of structure is marked by a decreasing minimum value of the structure variable $S_\mathrm{i} = 7.0$ at construction stage (2) and $S_\mathrm{i} = 5.7$ at construction stage (3). With decreasing structure variable the size of the bounding surface decreases. During the application of grouting from construction stage (3) to (4) the structure remains almost constant since rather low further plasticity is induced. Whereas, during installation of lining and ongoing advance of the shield machine the destructuration continuous showing minimum values of the structure variable $S_\mathrm{i} = 5.2$ at construction stage (5) and $S_\mathrm{i} = 3.8$ at construction stage (6). To sum up, the structure variable ultimately reduces by 55% compared to the initial value $S_{\mathrm{i},0} = 8.5$ representing a striking destructuration of the interparticle bonding by mechanical loading during the mechanized tunneling process from construction stage (1) to (6). The spatial distribution is equivalent to the area influenced by plasticity, but destructuration is affected more by volumetric plastic strain than deviatoric plastic strain due to a calibrated $A = 0.3$. That is, the most significant destructuration occurs above the upper tunnel quarter, mainly propagating from the upper tunnel side diagonally to the ground surface and the sides. However, also the nearfield of 1-2 m below the tunnel is slightly affected by destructuration. Anyway, the fully destructured state with $S_\mathrm{i} = 1$ is not reached during mechanized tunneling in any of the scenarios.

Other scenarios

Due to the relatively small amount of induced plasticity compared to the NC, D scenario the other scenarios exhibit associated small changes of the structure only even when allowing for elastoplastic behavior inside the bounding surface as shown in Figures 9.28 to 9.30. The destructuration is represented by the structure variable in a range of $7.7 \leq S_\mathrm{i} \leq 8.5$ for the OC, D and the NC, UD scenarios and $8.0 \leq S_\mathrm{i} \leq 8.5$ for the OC, UD scenario. Hence, the structure variable decreases by 6-9.5% at the utmost compared to the initial value $S_{\mathrm{i},0} = 8.5$. To conclude, the effects of destructuration become noticeable, but by far not as significant as for the NC, D scenario. The soil response is predominantly elastic and less plasticity is induced. Whereat, the spatial distribution is equivalent to the area influenced by plasticity. For the OC, D scenario the noticeable destructuration appears in an area of maximum 1-2 m around the entire tunnel with a maximum at the tunnel side. For the NC, UD and OC, UD scenarios assuming undrained conditions an influenced area of 1 m around the entire tunnel can be detected but the noticeable destructuration occurs at the lower tunnel quarter propagating diagonally downward to a maximum extension of 6 m (NC, UD) and 3 m (OC, UD). It can be ascertained that the structure variable is successively decreasing while the shield machine is approaching and crossing the measurement section (1) to (3). Whereas, the minimum value and the spatial distribution of S_i remain constant during application of grouting pressure, installation of lining and further advance of the shield machine (3) to (6) since no remarkable plasticity is induced anymore.

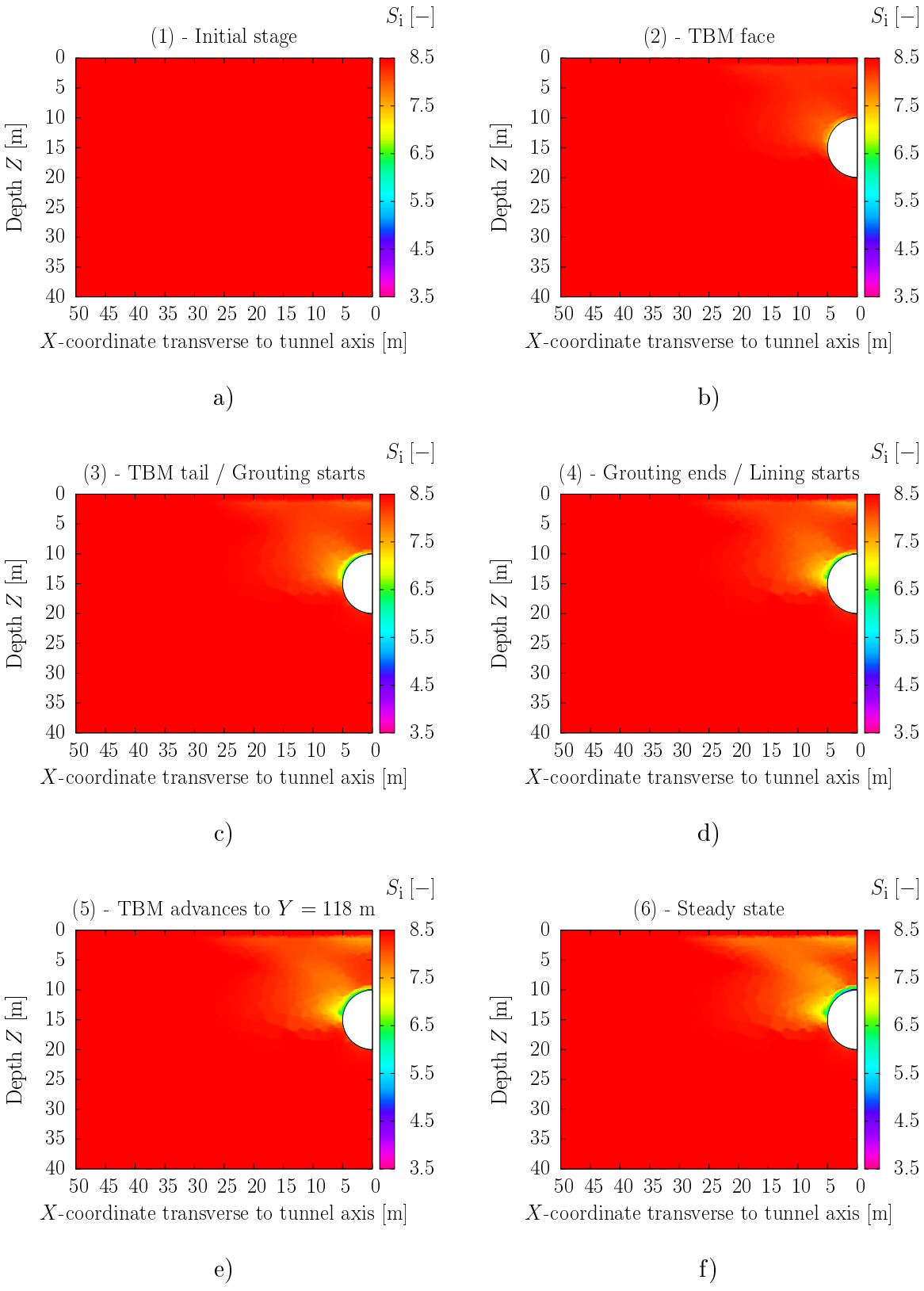

Figure 9.27: Evolution of the structure variable S_i in the synthetic measurement section ($Y = 100$ m) using the Saniclay D+BSP model extension for NC, D scenario wrt. the significant construction stages (1) to (6)

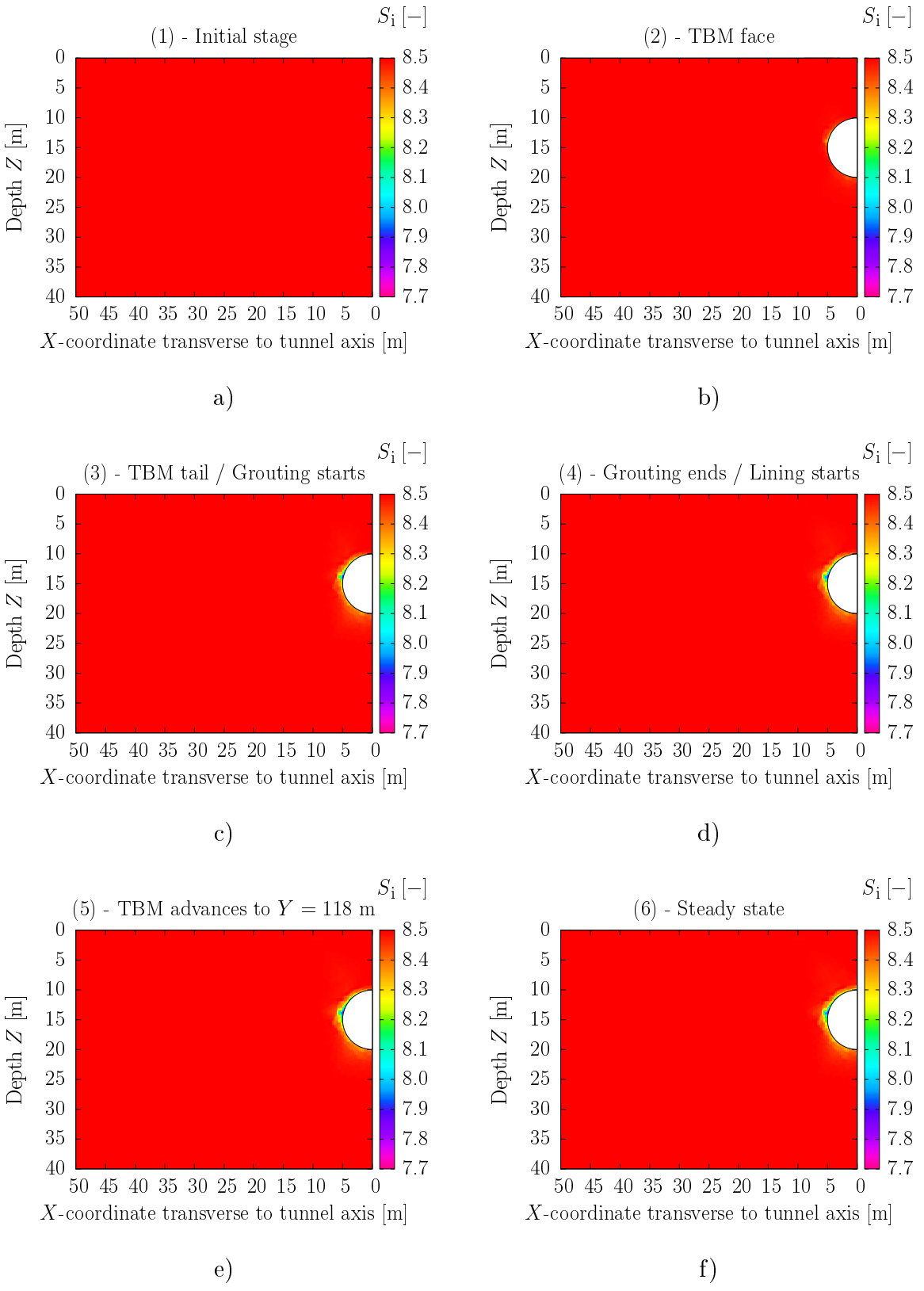

Figure 9.28: Evolution of the structure variable S_i in the synthetic measurement section ($Y = 100$ m) using the Saniclay D+BSP model extension for OC, D scenario wrt. the significant construction stages (1) to (6)

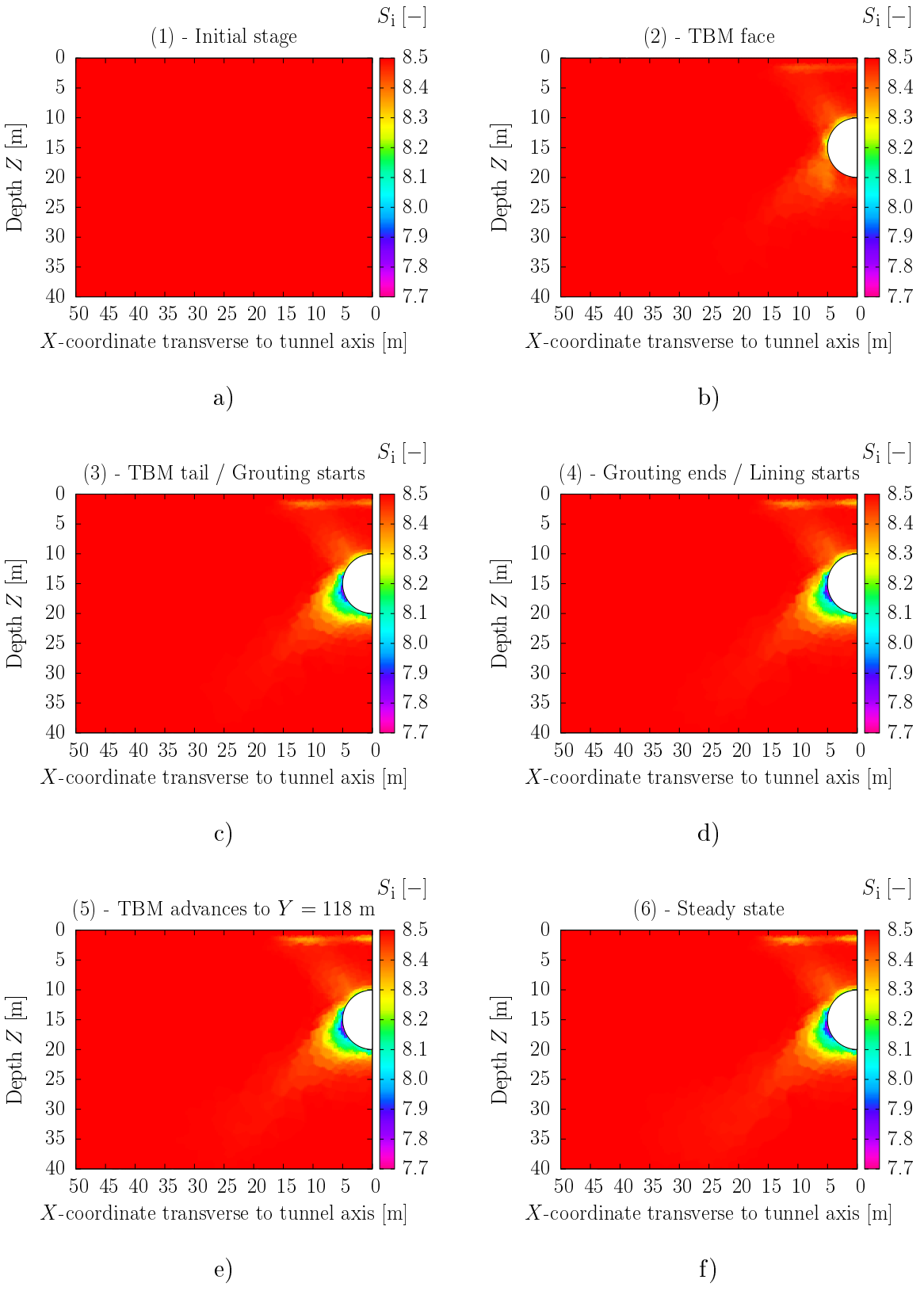

Figure 9.29: Evolution of the structure variable S_i in the synthetic measurement section ($Y = 100$ m) using the Saniclay D+BSP model extension for NC, UD scenario wrt. the significant construction stages (1) to (6)

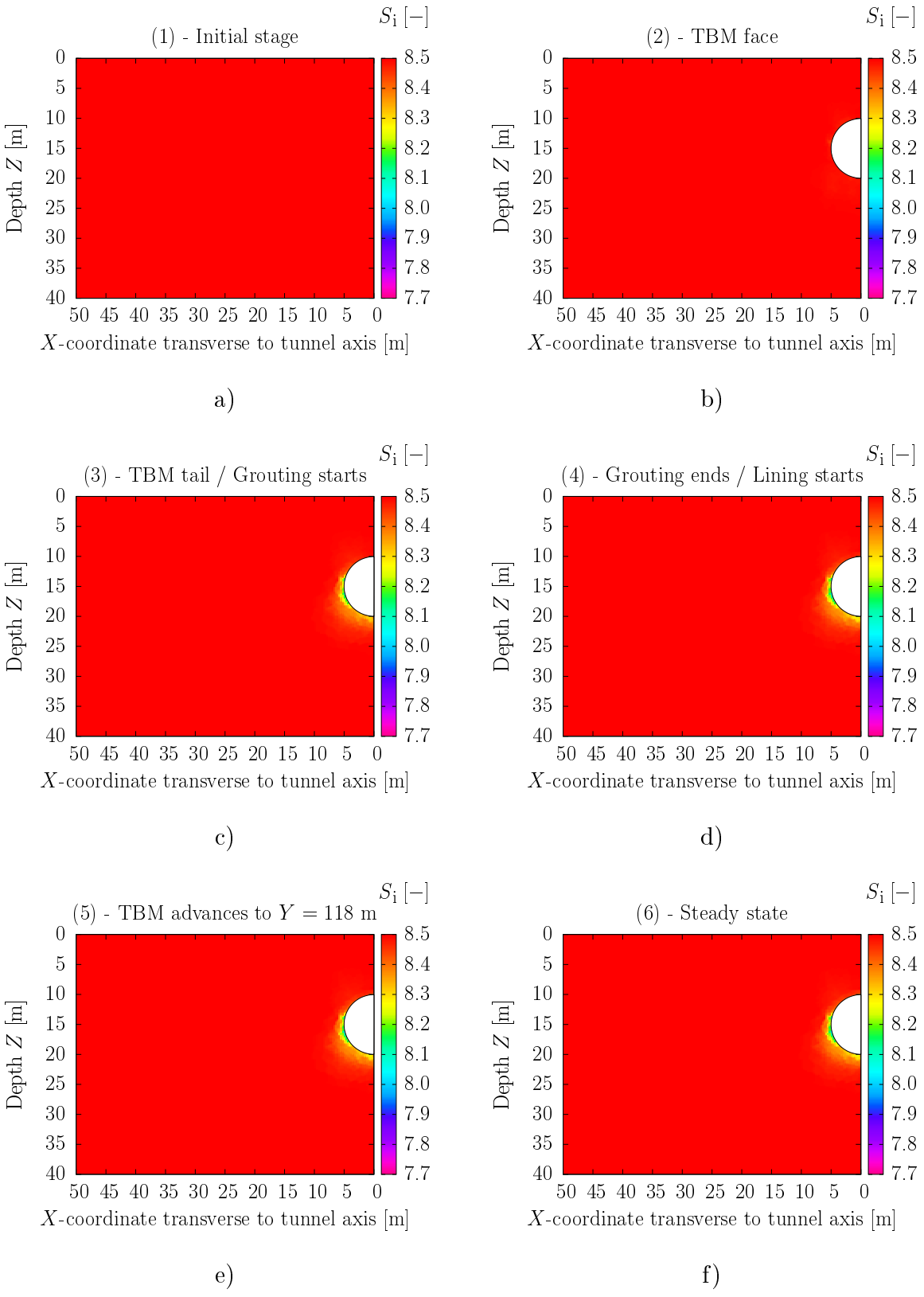

Figure 9.30: Evolution of the structure variable S_i in the synthetic measurement section ($Y = 100$ m) using the Saniclay D+BSP model extension for OC, UD scenario wrt. the significant construction stages (1) to (6)

9.2.3.3 Evolution of rotational hardening variable $|\boldsymbol{\alpha}|$

The evolution of the rotational hardening variable $|\boldsymbol{\alpha}|$ in the synthetic measurement section ($Y = 100$m) wrt. the significant construction stages (1) to (6) is presented exemplarily for the Saniclay D+BSP model extension in Figure 9.31 for the investigated NC, D scenario. To illustrate the effects of stress-induced anisotropy the evolution of the rotational hardening variable is analyzed starting from an initial value of $|\boldsymbol{\alpha}| = 0.23$ indicating a certain inherent anisotropy. That is, the initial bounding and plastic potential surface are rotated. The evolution of the rotational hardening variable is controlled by the rotational hardening rule as a function of the volumetric and deviatoric plastic strain increments as well as the change of the stress ratio. To recall, the bounding surface and the plastic potential surface rotate towards the bounding attractor which is for each loading case defined with respect to a certain fixed stress ratio. If the target value is reached and the stress ratio does not change no further rotation will appear. Any consecutive change in the stress ratio will again influence the bounding attractor and induce rotation of the surfaces. Moreover, the rotational hardening by definition decelerates for highly overconsolidated stress states.

NC, D scenario

For the NC, D scenario the changes of the stress ratio and the plastic straining in the nearfield around the tunnel cause small evolution of anisotropy indicated by a continuous decrease of the rotational hardening variable while the shield machine is moving from construction stage (1) to (6) as visualized in Figure 9.31. Whereat, the evolution of anisotropy in the nearfield of the upper tunnel quarter is more pronounced than close to the lower tunnel quarter. Anyhow, the induced rotation is most distinct in a trough-shaped area near the ground surface above the tunnel indicated by a continuous decrease of the rotational hardening variable from its initial value $|\boldsymbol{\alpha}| = 0.230$ (1) to $|\boldsymbol{\alpha}| = 0.221$ (2), $|\boldsymbol{\alpha}| = 0.213$ (3), $|\boldsymbol{\alpha}| = 0.184$ (4) and $|\boldsymbol{\alpha}| = 0.178$ (5) and $|\boldsymbol{\alpha}| = 0.177$ (6) due to relative movements and shearing of the soil layers with different stiffness and strength and the small stress level close to the surface. To conclude, the rotational hardening variable ultimately reduces by 23% compared to the initial value $|\boldsymbol{\alpha}| = 0.230$ but in a very limited area at the ground surface above the tunnel and in the nearfield of the tunnel only. The continuous decrease of the rotational hardening variable at the ground surface and in the nearfield of the tunnel during mechanized tunneling evidences induced rotation from a more anisotropic to a more isotropic state due to the arising effective stress paths.

Other scenarios

The other scenarios are not explicitly shown since the rotational hardening variable $|\boldsymbol{\alpha}|$ is just slightly changing because of the small variation of the stress ratio and the small amount of plasticity which is induced. The stress-induced anisotropy is represented by the rotational hardening variable in a range of $0.227 \leq |\boldsymbol{\alpha}| \leq 0.231$ for the OC, D scenario, $0.220 \leq |\boldsymbol{\alpha}| \leq 0.230$ for the NC, UD scenario and $0.226 \leq |\boldsymbol{\alpha}| \leq 0.230$ for the OC, UD scenario. Hence, the rotational hardening variable varies, even when allowing for elastoplastic behavior inside the bounding surface, by just 4% (NC, UD) and 1.5-2% (OC, D and OC, UD) at the utmost compared to the initial value $|\boldsymbol{\alpha}| = 0.230$. To conclude, the effects of stress-induced anisotropy are noticeable for the NC, UD scenario but by far not as significant as for the NC, D scenario. For the overconsolidated OC, D and OC, UD scenarios the effects are almost negligible since the ratio $\bar{p}/p_{0,\mathrm{s}}$ as incorporated in the rotational hardening rule slows down the evolution for overconsolidated clay.

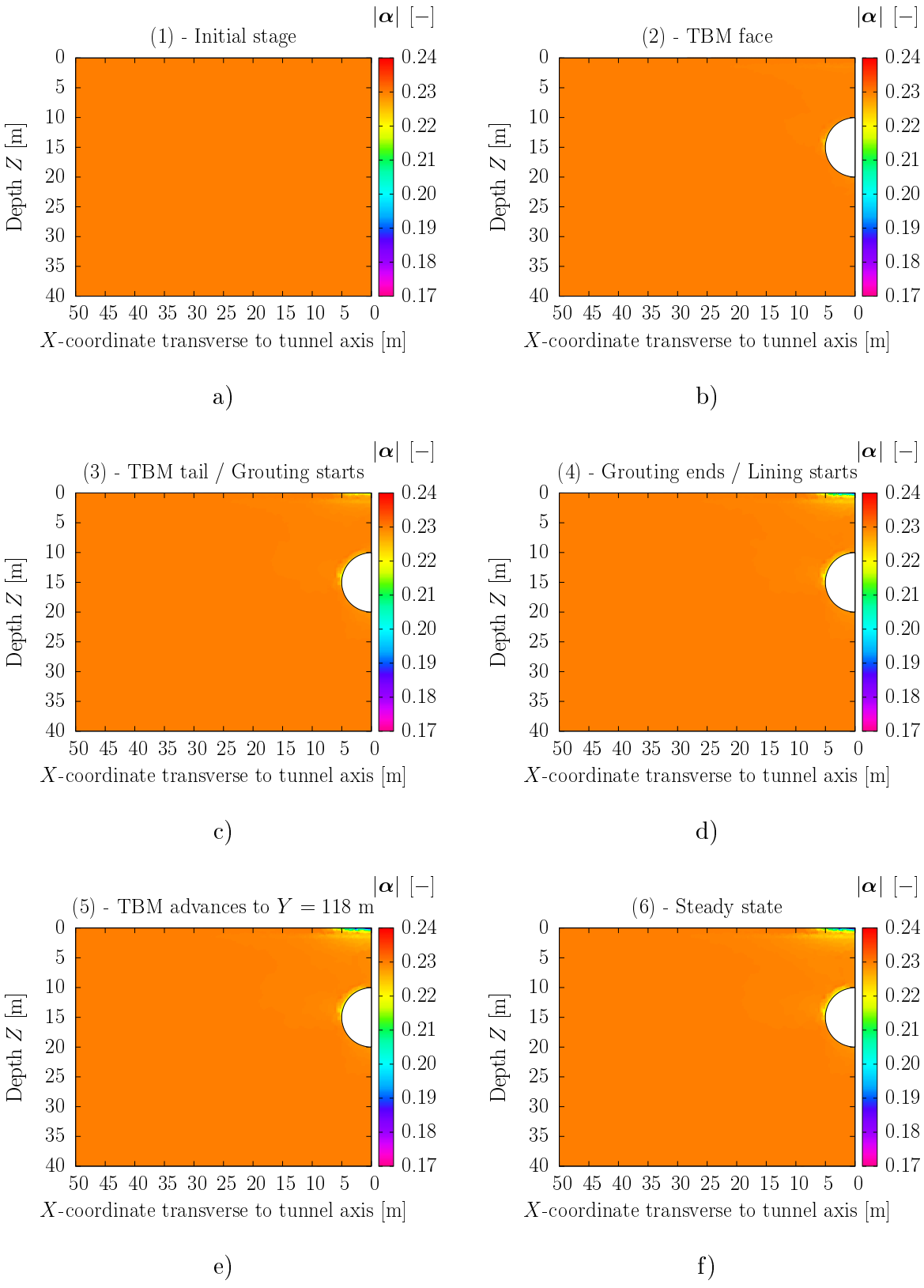

Figure 9.31: Evolution of the rotational hardening variable $|\boldsymbol{\alpha}|$ in the synthetic measurement section ($Y = 100\,\mathrm{m}$) using the Saniclay D+BSP model extension for NC, D scenario wrt. the significant construction stages (1) to (6)

9.2.3.4 Evolution of damage variable d

The evolution of the damage variable d in the synthetic measurement section ($Y = 100\,\mathrm{m}$) wrt. the significant construction stages (1) to (6) is presented exemplarily for the Saniclay D+BSP model in Figures 9.32 to 9.35 for the investigated scenarios. To highlight the effects of stiffness degradation and accumulation of plastic strain with respect to non-monotonic or cyclic loading the evolution of the damage variable is analyzed. To recall, the shape hardening function $\hat{h}$ controls the degradation of stiffness, the accumulation of plastic strain and accordingly the evolution of the elastoplastic stress-strain response loops during non-monotonic or cyclic loading governed by the evolving damage variable d. The evolution of the damage variable is defined as a function of the deviatoric plastic strain increment. With increasing accumulated plastic deviatoric strain $\boldsymbol{e}^{\mathrm{p}}$ during non-monotonic or cyclic loading the damage variable d increases and the shape hardening function $\hat{h}$ decreases. Consequently, the plasticity modulus K_{p} and the stiffness degrade and the model response becomes more soft and more plasticity is induced. Hence, the stiffness degradation and the spatial distribution of the evolving damage variable in the soil domain are in accordance with the findings regarding the evolution of plasticity but limited to the deviatoric component only. However, it has to be noted that the plasticity modulus K_{p} is dependent on the distance function $\hat{f}$ as well which is not considered in the current analysis.

NC, D scenario

For the NC, D scenario the induced deviatoric plastic straining leads to stiffness degradation while the shield machine is crossing the measurement section as visualized in Figure 9.32. The progressive stiffness degradation is marked by a successively increasing maximum value of the damage variable $d = 0.17$ at construction stage (2) and $d = 0.41$ at construction stage (3). During the application of grouting from construction stage (3) to (4) the damage variable just slightly increases to $d = 0.44$. However, when installing the lining and advancing with the shield machine the stiffness degradation continuous resulting in a maximum value of the damage variable $d = 0.47$ at construction stage (5) and $d = 0.74$ at construction stage (6). The spatial distribution is in accordance with the area influenced by plasticity but constrained to the deviatoric component only. That is, the most significant stiffness degradation occurs at the upper tunnel quarter, mainly propagating from the upper tunnel side diagonally to the ground surface and the sides.

Other scenarios

Again, due to the relatively small accumulation of deviatoric plastic strain compared to the NC, D scenario the other scenarios show associated small degradation of stiffness as shown in Figures 9.33 to 9.35. The corresponding damage variable continuously evolves up to a maximum value of $d = 0.15$ for the NC, UD scenario and $d = 0.10$ for the overconsolidated OC, D and OC, UD scenarios when mechanized tunneling advances from construction stage (1) to (4). Whereat, the largest amount of damage is generated while the shield machine is crossing the measurement section from construction stage (2) to (3). Compared to the NC, D scenario the magnitude of the degradation of stiffness due to accumulation of deviatoric plastic strain amounts only 13-20% for the other scenarios. The evolution of the spatial distribution of the damage variable is similar to that of the deviatoric plastic strain as already discussed before. That is, for the OC, D scenario the noticeable stiffness degradation arises in an area of maximum 1-2 m around the entire tunnel with a maximum at the tunnel side. For the NC, UD and OC, UD scenarios assuming undrained conditions the noticeable stiffness degradation develops at the lower tunnel quarter propagating diagonally downward to a maximum extension of 6 m (NC, UD) and 3 m (OC, UD). During installation of lining and further advance of the shield machine (4) to (6) no more noticeable degradation appears due to the predominantly elastic soil behavior.

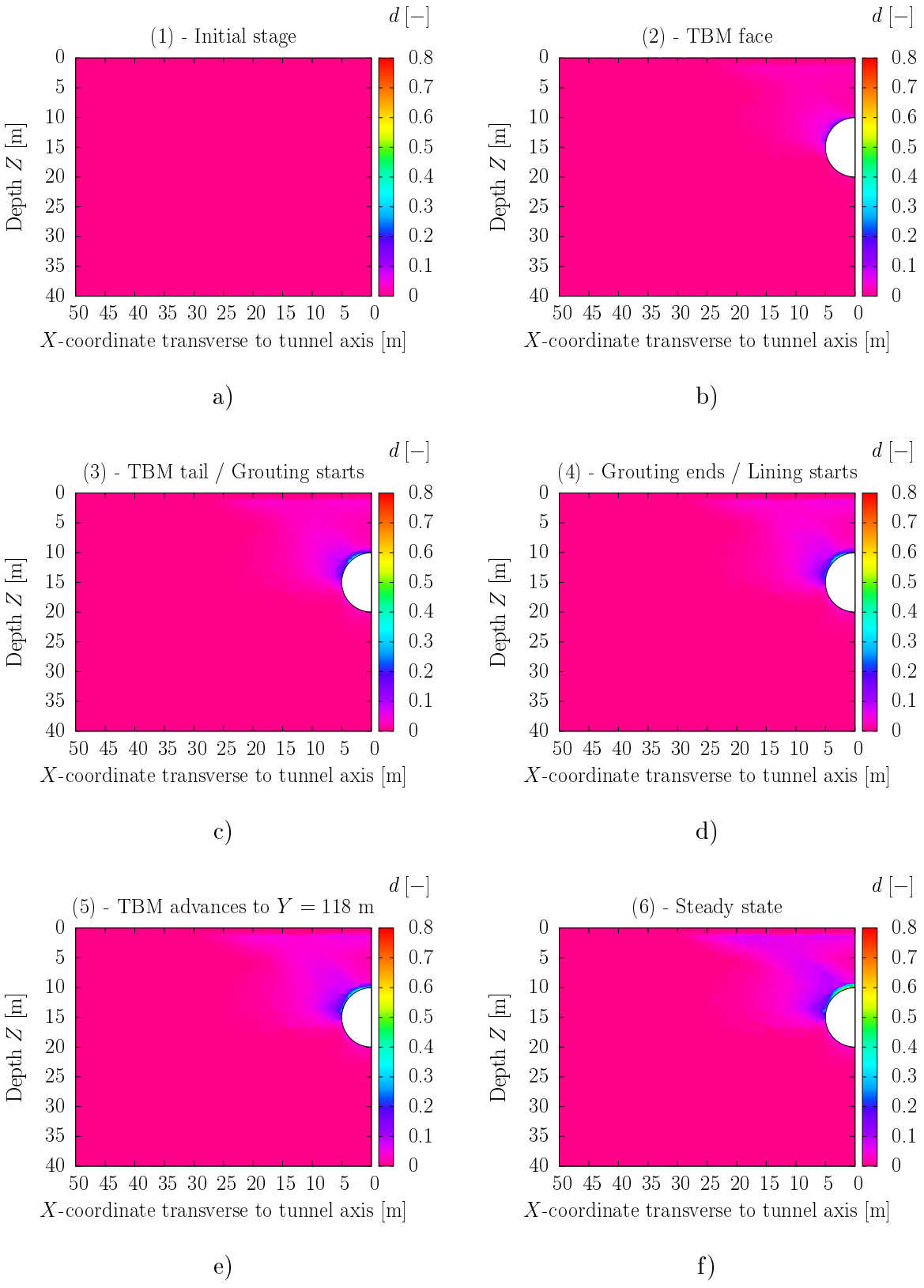

Figure 9.32: Evolution of the damage variable d in the synthetic measurement section ($Y = 100$ m) using the Saniclay D+BSP model extension for NC, D scenario wrt. the significant construction stages (1) to (6)

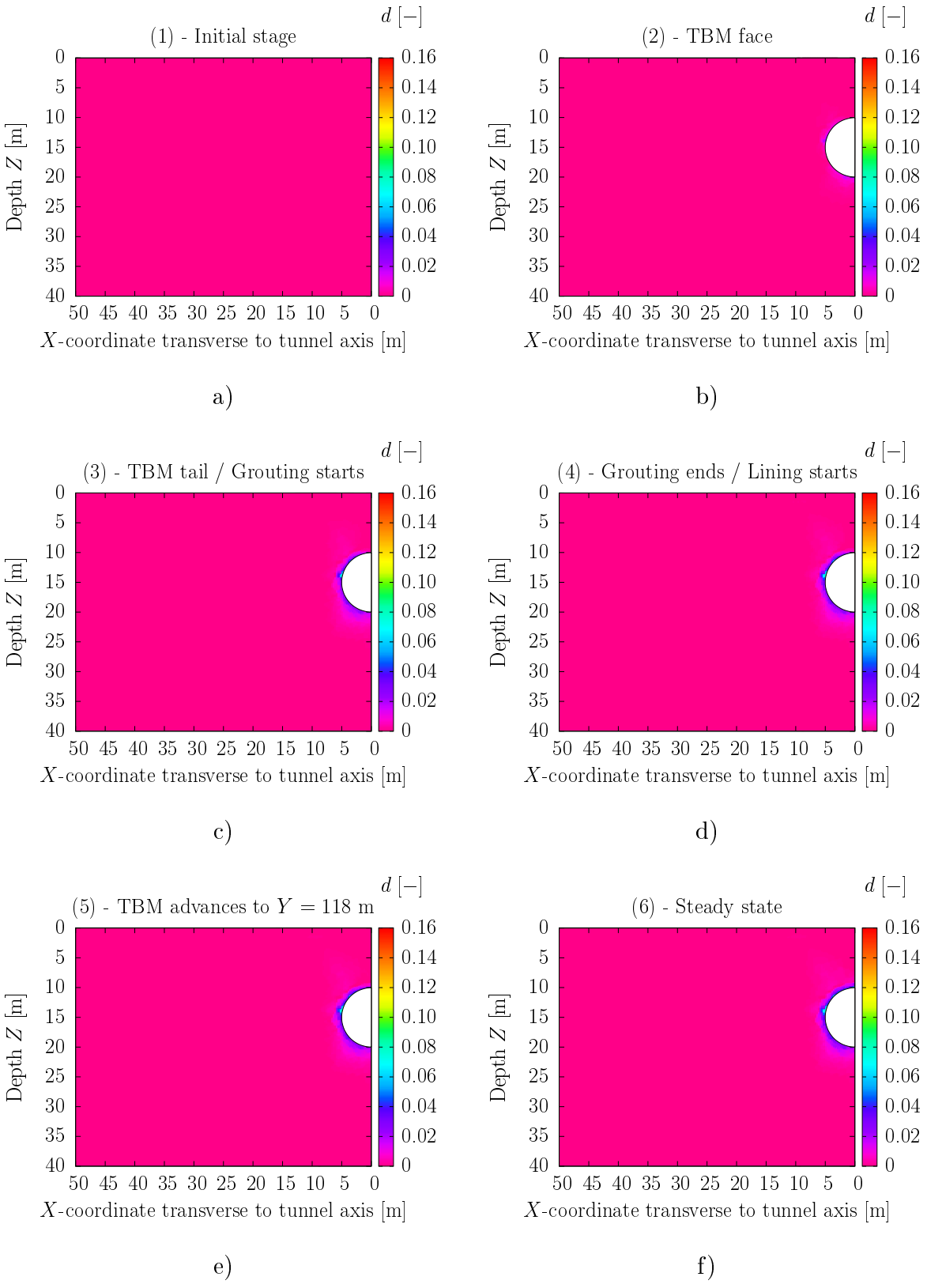

Figure 9.33: Evolution of the damage variable d in the synthetic measurement section ($Y = 100$ m) using the Saniclay D+BSP model extension for OC, D scenario wrt. the significant construction stages (1) to (6)

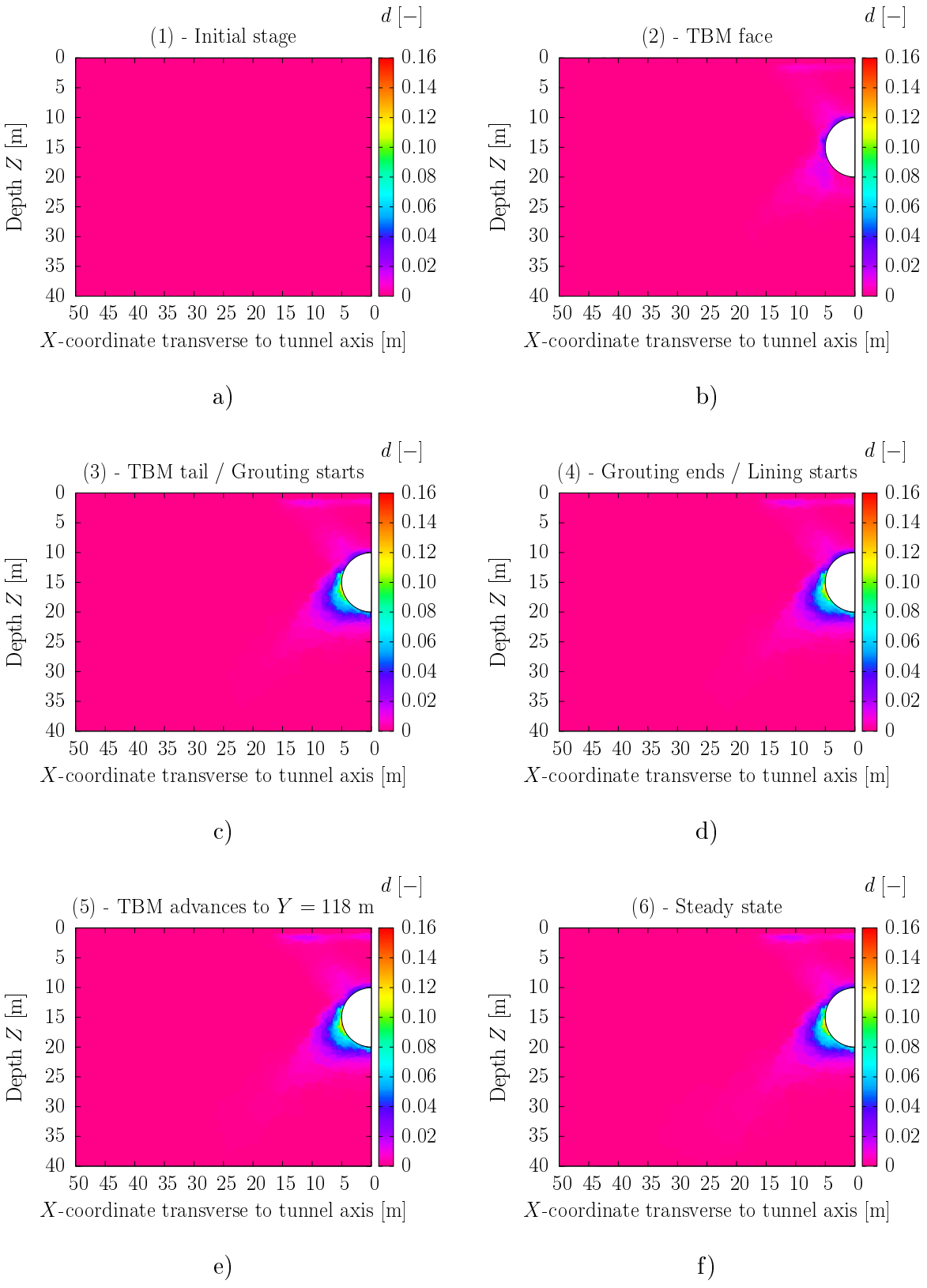

Figure 9.34: Evolution of the damage variable d in the synthetic measurement section ($Y = 100$ m) using the Saniclay D+BSP model extension for NC, UD scenario wrt. the significant construction stages (1) to (6)

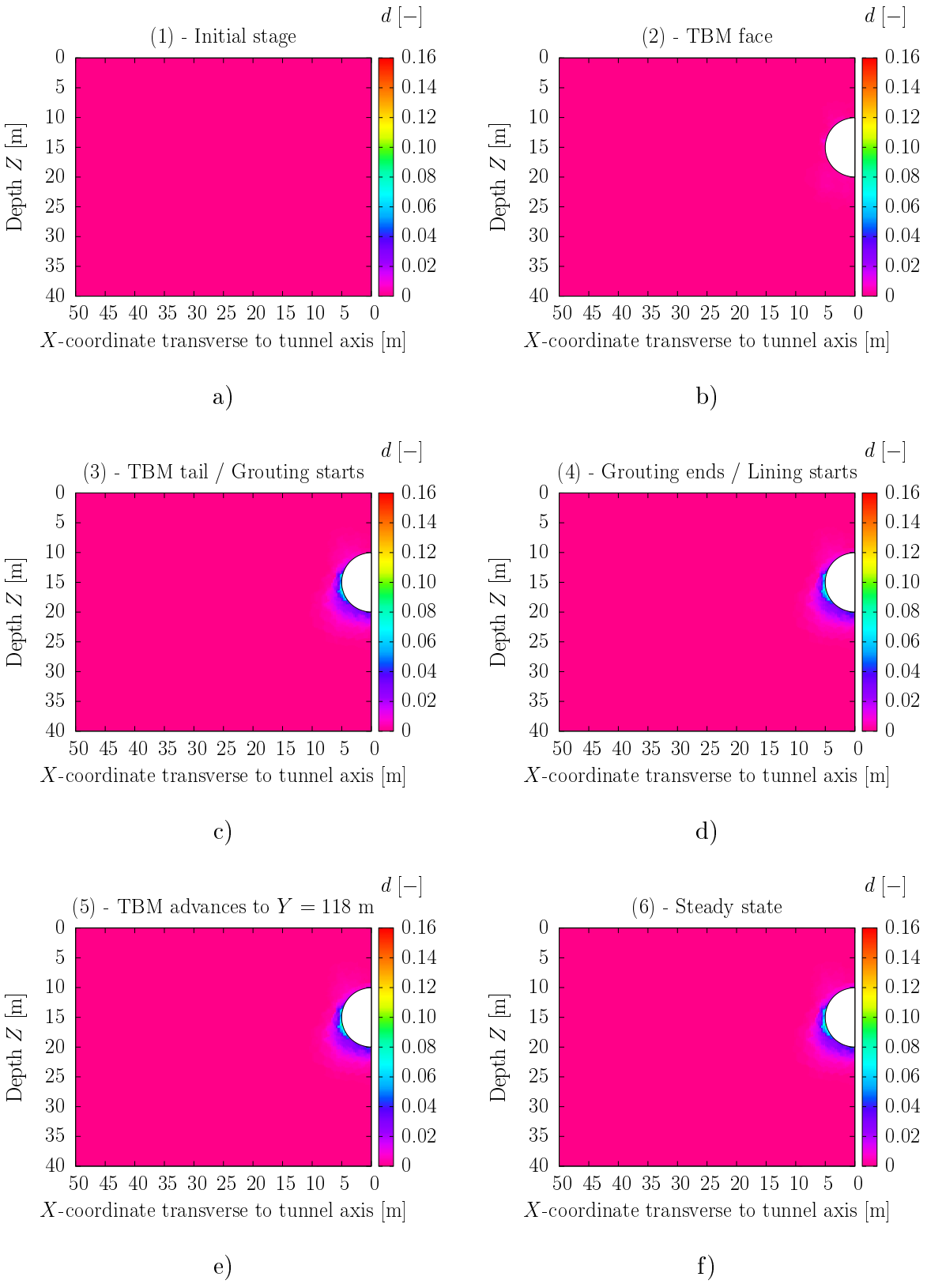

Figure 9.35: Evolution of the damage variable d in the synthetic measurement section ($Y = 100$ m) using the Saniclay D+BSP model extension for OC, UD scenario wrt. the significant construction stages (1) to (6)

9.3 Practical recommendations regarding surface settlements

In this section the influence of the mechanical properties of natural clay on the numerical model response induced by mechanized tunneling was investigated utilizing the concept of the hierarchical BSP model family. Whereat, a synthetic shallow mechanized tunnel excavation in a water-saturated natural Onsøy clay deposit under greenfield conditions was considered. In particular, the spatial and construction stage dependent evolution of the influence of the mechanical properties of natural clay such as inherent and stress-induced anisotropy, initial structure and its progressive destructuration and the behavior under non-monotonic or cyclic loading such as stress-strain hysteresis and elastoplastic transition, stiffness degradation and accumulation of plastic strain on the system behavior evoked by mechanized tunneling such as surface settlements, ground movements, evolution of effective stress path and generation of excess pore-water pressure was analyzed. Moreover, the required degree of complexity of the constitutive BSP model utilized for the numerical analysis of mechanized tunneling in natural clay deposits was assessed by comparison of the numerical model responses of the different simulation runs with varying hierarchical complexity of the four model extensions and subsequent evaluation with respect to the relative importance of a particular natural clay property related to a specific model response arising from mechanized tunneling.

In the following, the study closes with the development of practical recommendations regarding the degree of complexity of the constitutive BSP model for the numerical analysis of mechanized tunneling in natural clay deposits and the main objective if typical mechanical properties of natural clay behavior have to be considered to obtain a particular model response caused by mechanized tunneling. However, the recommendations are focusing on the surface settlements due to the high practical relevance. Whereat, a more specific and universally valid statement regarding restricted spatial areas of influence where the particular property has to be considered during numerical analysis becomes very difficult since the spatial distribution of the plastic straining and of the conditionally induced destructuration, rotational hardening and stiffness degradation in the soil domain is strongly dependent on the initial consolidation and drainage conditions.

It has to be noted that the recommendations are developed based on the particular boundary conditions of the imaginary mechanized tunneling case numerically investigated in the present study such as diameter of the excavated tunnel area of $D = 10$ m, shallow tunnel with small overburden depth of $H/D = 1$, fully water-saturated and homogeneous

natural Onsøy clay deposit with a corresponding calibrated BSP model parameter set and greenfield conditions. However, it is expected that the findings and developed recommendations can be qualitatively transferred to mechanized tunneling cases with slightly differing boundary conditions as well which possibly has to be numerically confirmed afterwards. The influence of elementary changes of the boundary conditions has to be numerically analyzed in further studies anyway.

9.3.1 Initial structure and destructuration

Aiming for an adequate modeling of natural clay behavior necessarily requires to consider the initial structure since the interparticle bonding imparts additional stiffness and strength and consequently governs the surface settlements and soil displacements. The initial structure and the corresponding yielding characteristics can be captured by any hierarchical model extension by a proper initialization of an enlarged size of the initial yield or bounding surface. A fully reconstituted or destructured clay without any bonding would exhibit a much softer behavior.

Normally consolidated initial stress conditions

For an accurate prediction of the transverse and longitudinal surface settlements due to mechanized tunneling in mainly normally consolidated natural clay deposits it is required to consider the progressive destructuration. Whereat, normally consolidated initial stress conditions actually might become relevant in natural clay deposits since the overconsolidation ratio significantly decreases with increasing overburden depth even down to $YSR = 1$ in the area where the tunnel excavation takes place as shown in Figure 2.5 in section 2.1. To be more precise, due to destructuration the maximum surface settlements will significantly increase and the transverse settlement trough and the longitudinal settlement trough hurrying ahead of the shield machine become more steep. Whereat, especially the gradient and inclination of the settlement trough as well as the maximum settlements decisively govern the damage assessment of edifices and urban infrastructure related to mechanized tunneling. Concluding, it is mandatory to account for destructuration of initial structure when it comes to the analysis of surface settlements in the design phase of mechanized tunneling in natural clay to not underestimate the damage potential.
The influence of destructuration on the settlement behavior as described above is most pronounced when assuming drained rather than undrained conditions. For example, under the numerically investigated boundary conditions the following observation can be made:

The maximum settlements when not considering destructuration are underestimated by about 55-70% for assumed drained conditions and just 8-9% for undrained conditions. Due to the generation of excess pore-water pressure the associated change of the effective stress and the propagation of the induced plasticity from the tunnel towards the ground surface are less pronounced for assumed undrained conditions. Moreover, the magnitude of the maximum surface settlements incorporating destructuration is quite striking with $s = 74.5$mm when assuming drained conditions. Whereas, the magnitude of the maximum surface settlements assuming undrained conditions is much smaller with $s = 13.6$ mm corresponding to just about 18% when comparing to drained conditions.

The width of the transverse surface area affected by settlements when including destructuration is varying between 3-times the tunnel diameter in assumed drained conditions and 2-times to 4.5-times in undrained conditions dependent on the construction stage. However, when assuming drained conditions heave of the adjacent ground surface occurs when neglecting destructuration causing a reduction of the width of the pure settlement trough from 3-times to 2-times the tunnel diameter. Whereas, heave at the ground surface is suppressed by the superimposed effect of destructuration. Nevertheless, the width of the entire influenced surface area combining surface settlements and heave is of same width. Whereat, the width of the influenced surface area is less affected by destructuration assuming undrained conditions.

The length of the influenced surface area in longitudinal direction ahead of the shield machine when including destructuration is varying between 2-times the tunnel diameter in assumed drained conditions and 1-times to 1.5-times in undrained conditions. However, when assuming drained conditions the length of the influenced surface area decreases by about 25% to 1.5-times the tunnel diameter when not accounting for destructuration. That is, a pronounced activation of the destructuration will lead to a noticeable enlargement of the influenced surface area in longitudinal direction ahead of the shield machine. This could become important when discussing safety measures for the reinforcement of the area ahead of the shield machine (e.g. compensation grouting). Whereat, the length of the influenced surface area is less affected by destructuration assuming undrained conditions.

The progressive destructuration of the interparticle bonding should be considered already when the shield machine is approaching to the measurement section (1/2) even until the shield machine is passing construction stage (5) and further advance since the surface settlements are strikingly increasing during that construction processes when compared to the case when not accounting for loss of structure. During the construction stages (1/2) to (5/6) the soil experiences the following processes such as tunnel face support, volume

loss due to overcutting and conicity of the shield machine, stress release and buoyancy effects during soil removal, application of grouting pressure and installation of compressible lining leading to significant plastic straining affecting the destructuration process.
To be more specific, under the numerically investigated boundary conditions and assuming drained conditions the structure variable S_i ultimately reduces by 55% compared to the initial value representing a striking destructuration of the interparticle bonding by mechanical loading during the mechanized tunneling process from construction stage (1) to (5/6). The spatial distribution is equivalent to the area influenced by plasticity, but destructuration is affected more by volumetric than deviatoric plastic strain due to the calibrated corresponding BSP model parameter. That is, the most significant destructuration occurs above the upper tunnel quarter, mainly propagating from the upper tunnel side diagonally to the ground surface and the sides. The area vertically above the tunnel is less affected by loss of structure due to predominantly elastic behavior because of stress redistribution and arching effects. However, also the nearfield of 1-2 m below the tunnel is slightly affected by destructuration.
On the contrary, due to the relatively low amount of induced plasticity the structural changes are small when assuming undrained conditions. The maximum magnitude of plastic strain is just about 14% as compared to assumed drained conditions and plasticity is much less propagated. The structure variable S_i decreases by just 9.5% at the utmost compared to the initial value while the shield machine is approaching and crossing the measurement section (1) to (3) and remains constant during application of grouting pressure, installation of lining and further advance of the shield machine (3) to (6) since no remarkable plasticity is induced anymore. Loss of structure occurs at the lower tunnel quarter propagating diagonally downward to a maximum extension of 6 m in accordance with the spatial distribution of plastic strain.
To sum up, for mechanized tunneling in natural clay deposits with mainly normally consolidated initial stress conditions in the tunnel excavation area and assumed drained conditions it is mandatory to consider the progressive destructuration of the initial structure to adequately predict the surface settlements. For assumed fully undrained conditions the necessity of accounting for destructuration has to be decided from case to case in terms of risk assessment with respect to the importance of the aboveground edifices and urban infrastructure. Nevertheless, the drainage conditions with application to mechanized tunneling in natural clay deposits will be neither fully drained nor fully undrained but somehow affected by consolidation and time-dependent dissipation of excess pore-water pressure.

Hence, it is strongly recommended to always consider destructuration when numerically modeling mechanized tunneling in natural clay deposits to be independent of the in situ drainage conditions of the natural clay.

Overconsolidated initial stress conditions

On the contrary to normally consolidated initial stress conditions, the influence of destructuration on the magnitude of surface settlements and the shape of the transverse and longitudinal settlement trough is negligible when conducting mechanized tunneling in overconsolidated natural clay deposits independently of the drainage condition. To be more detailed, the maximum surface settlements are underestimated by maximum up to 4% and far less than 0.5 mm in total when not accounting for destructuration.
Since the initial stress is located inside the bounding surface or even inside the elastic nucleus and the mechanized tunneling induced effective stress path is mostly moving inside the bounding surface afterwards the soil behavior is predominantly elastic and stiff. Hence, under the numerically investigated boundary conditions just a small amount of plasticity constrained to a limited area in the nearfield of the tunnel is induced. The maximum magnitude of plastic strain is, even when allowing for elastoplastic behavior inside the bounding surface, just about 10% (drained) to 15% (undrained) as compared to normally consolidated conditions assuming drained conditions and plasticity is much less propagated.
Whereat, plastic straining strongly governs the progressive damage of the interparticle bonding and loss of structure. Due to the predominantly elastic and stiff behavior and the small amount of induced plasticity and destructuration the magnitude of the surface settlements at construction state (5), where the shield machine has already passed the measurement section, is just about 9% (drained) to 12% (undrained) as compared to normally consolidated conditions assuming drained conditions.
The structure variable S_i is, even when allowing for elastoplastic behavior inside the bounding surface, decreasing by just 6-9.5% at the utmost compared to the initial value. To conclude, the effects of destructuration become noticeable, but by far not that significant as for normally consolidated initial stress conditions and assumed drained conditions. Whereat, the spatial distribution of the structure degradation is equivalent to the area influenced by plasticity. That is, for assumed drained conditions the noticeable propagation of plasticity is restricted to an area of 1-2 m around the tunnel being largest at the lower tunnel side. However, for assumed undrained conditions the noticeable propagation of plasticity is restricted to an area of 1 m around the tunnel being largest at the lower

tunnel quarter but propagating diagonally downward to a maximum extension of 3 m. Concluding, it is not compulsory to account for the progressive degradation of structure when aiming for an adequate prediction of the surface settlements caused by mechanized tunneling in overconsolidated natural clay deposits. However, during the entire excavation and construction process it has to be guaranteed that overconsolidation is existent in large part of the soil domain which is influenced by mechanized tunneling and the corresponding soil behavior remains predominantly elastic. Whereat, the magnitude of overconsolidation and yield stress ratio has to be experimentally obtained by corresponding field and laboratory tests. Any external trigger or changing boundary condition which will cause effective stress paths distinctly exceeding the initial bounding surface will induce significant plasticity and destructuration is strongly activated. Consequently, the surface settlements will strikingly increase and the settlement trough becomes more steep. Based on these considerations, it is strongly recommended to always consider destructuration when numerically modeling mechanized tunneling in natural clay deposits independently of the initial consolidation stress and drainage conditions. Just to be prepared for external trigger and changing boundary conditions causing distinct plasticity during the excavation and construction process in regard to safety issues, damage assessment and risk management since the influence of destructuration on the surface settlements is extensive when it comes to remarkable plastic straining during mechanized tunneling

9.3.2 Inherent and stress-induced anisotropy

Normally consolidated initial stress conditions

The influence of the inherent and stress-induced anisotropy on the maximum surface settlements and the shape of the transverse and longitudinal settlement trough is remarkable when assuming drained conditions for mechanized tunneling in a mainly normally consolidated natural clay deposit. That is, under the investigated boundary conditions the maximum surface settlements are underestimated by about 16-18% when not accounting for the initial rotation and the plastic straining induced rotational hardening of the bounding surface and the plastic potential surface. Furthermore, the shape of the transverse settlement trough and the longitudinal settlement trough hurrying ahead of the shield machine are predicted slightly too flat. However, compared to destructuration the effect of anisotropy on the maximum surface settlements is much less pronounced. Whereas, for assumed undrained conditions the impact of anisotropy on the maximum surface settlements strongly reduces and becomes negligible indicated by just 3% of difference of the

maximum values. However, the consequences are inverted and the nonconsideration of anisotropy even leads to a slight overestimate of the maximum surface settlements. The influence of anisotropy on the shape of the transverse and longitudinal settlement trough is also negligible when conducting mechanized tunneling in mainly normally consolidated natural clay deposits assuming undrained conditions.
With respect to the excavation and construction stages of mechanized tunneling the influence of the inherent and stress-induced anisotropy on the surface settlements comes into picture while the shield machine is passing the measurement section (2) until the initial installation of the lining (4/5). During these construction stages plasticity is induced to the soil domain in the nearfield of the excavation zone. However, during further advancement of the shield machine (5) to (6) the influence of anisotropy becomes irrelevant. For assumed drained conditions, this is indicated by the rotational hardening variable $|\boldsymbol{\alpha}|$ ultimately reducing by 23% compared to the initial value but in a very limited area at the ground surface above the tunnel and in the nearfield of the tunnel only. The continuous decrease of the rotational hardening variable evidences induced rotation from a more anisotropic to a more isotropic state due to the arising effective stress path.
To conclude, for mechanized tunneling in natural clay deposits with mainly normally consolidated initial stress conditions in the tunnel excavation area it is required to consider the inherent and stress-induced anisotropy to adequately predict the surface settlements especially for assumed drained conditions. Due to the variability and uncertainty of the drainage conditions of natural clay during mechanized tunneling the recommendation holds true for any tunnel excavation in a water-saturated clay deposit. However, the initial choice of the rotation does not drastically influence the model response because during further loading under a different stress ratio deviating from the initial stress ratio the surfaces will adjust themselves governed by the rotational hardening rule.

Overconsolidated initial stress conditions

The influence of inherent and stress-induced anisotropy on the magnitude of surface settlements and the shape of the transverse and longitudinal settlement trough is negligible when conducting mechanized tunneling in overconsolidated natural clay deposits independently of the drainage conditions. To be more detailed, the maximum surface settlements are underestimated by maximum up to 2% and far less than 0.5 mm in total when not accounting for anisotropy. Due to overconsolidation the effective stress path is predominantly moving inside the bounding surface. Hence, the initial rotation of the bounding surface and the plastic potential surface is mainly governing the stress state where signif-

icant yielding starts. Moreover, due to the small amount of induced plasticity constrained to a limited area in the nearfield of the tunnel and the small variation of the stress ratio the rotational hardening is not remarkably mobilized. In addition, the rotational hardening is by definition slowed down for overconsolidated clay.
To be more specific, under the numerically investigated boundary and overconsolidated initial stress conditions the rotational hardening variable $|\boldsymbol{\alpha}|$ representing the stress-induced anisotropy is, even when allowing for elastoplastic behavior inside the bounding surface, just slightly varying between 1.5-2% at the utmost compared to the initial anisotropic value.
Concluding, it is not mandatory to account for the inherent and stress-induced anisotropy with respect to an adequate prediction of the surface settlements caused by mechanized tunneling in overconsolidated natural clay deposits independently of the drainage conditions. Even when it somehow comes to a transition from overconsolidated to normally consolidated conditions by having mechanized tunneling induced effective stress paths reaching the bounding surface and significant plasticity is induced afterwards, the impact of anisotropy on the settlement behavior is still moderate with respect to safety issues, damage assessment and risk management.

9.3.3 Non-monotonic or cyclic behavior

Normally consolidated initial stress conditions

For mechanized tunneling in mainly normally consolidated natural clay deposits the influence of the behavior under non-monotonic or cyclic loading on the settlement behavior is negligible since under the numerically investigated boundary conditions the maximum surface settlements are underestimated by just about 3-4% when not accounting for stress-strain hysteresis and elastoplastic transition, stiffness degradation and accumulation of plastic strain assuming drained conditions. Therefore, the shape of the transverse and longitudinal settlement trough is also not significantly affected. Moreover, the influence of the non-monotonic or cyclic behavior becomes even less for assumed undrained conditions.
That is because mechanized tunneling in natural clay as the chosen engineering application generates just a little amount of non-monotonic or cyclic loading. To be more specific, the model response is either anyway elastoplastic due to the normally consolidated initial stress located on the bounding surface. Or the model response is anyway predominantly elastic and very stiff in the soil domains where stress release occurs since the induced

effective stress changes inside the bounding surface are not that pronounced and the distance to the bounding surface on the opposite remains large. Elastoplastic transition zones are not that distinctly formed to cause additional plastic strain and conditionally induce destructuration, rotational hardening and stiffness degradation while the effective stress path is moving inside the bounding surface. However, the influence of the behavior under non-monotonic or cyclic loading on the settlements becomes most relevant between the construction stages (3) to (4) where the grouting pressure is applied to the surrounding soil and (4) to (6) where the soil experiences incremental upward displacements.
To draw a conclusion, for mechanized tunneling in mainly normally consolidated natural clay deposits it is not compulsory to account for the behavior under non-monotonic or cyclic loading such as stress-strain hysteresis and elastoplastic transition, stiffness degradation and accumulation of plastic strain independently of the drainage conditions.

Overconsolidated initial stress conditions

For mechanized tunneling in natural clay deposits with overconsolidated initial stress conditions the influence of the behavior under non-monotonic or cyclic loading on the maximum surface settlements and the shape of the transverse and longitudinal settlement trough becomes remarkable. To be more specific, under the investigated boundary conditions the maximum surface settlements are underestimated by about 13-18% (drained conditions) and 6-10% (undrained conditions) when not taking into consideration the elastic nucleus updated to the last stress reversal, stress-strain hysteresis and elastoplastic transition, stiffness degradation and accumulation of plastic strain. Consequently, a remarkable amount of plasticity is induced while moving inside the bounding surface and the model response becomes more soft. Conditionally, destructuration, rotational hardening and stiffness degradation are activated in a certain manner since they are also governed by plastic straining. However, the total effect on the maximum surface settlements is still in the millimeter range because the magnitude of the surface settlements is considerably smaller when having overconsolidated initial stress conditions.
Moreover, when neglecting the behavior under non-monotonic or cyclic loading, the shape of the transverse settlement trough and the longitudinal settlement trough hurrying ahead of the shield machine are predicted slightly too flat independently of the drainage conditions. Even more important, when not incorporating the behavior under non-monotonic or cyclic loading for mechanized tunneling in an overconsolidated and water-saturated clay deposit with small overburden depth the settlements entirely turn into heave of the ground surface during installation of lining when assuming drained conditions and the

maximum heave is overestimated up to 5-6%. Again, as for the normally consolidated initial stress conditions the influence of the behavior under non-monotonic or cyclic loading such as elastoplastic hysteresis and transition, stiffness degradation and accumulative effects on the settlements becomes most relevant between the construction stages (3) to (4) where the grouting pressure is applied to the surrounding soil and (4) to (6) where the soil experiences incremental upward displacements and even heave. In any case the consideration of the behavior under non-monotonic or cyclic loading leads to larger surface settlements due to the additionally induced plasticity.

To conclude, when aiming for an adequate prediction of the surface settlements arising from mechanized tunneling in overconsolidated natural clay deposits it is recommended to consider the behavior under non-monotonic or cyclic loading independently of the drainage conditions. However, the necessity of accounting for elastoplastic hysteresis and transition, stiffness degradation and accumulative effects might be decided from case to case in terms of risk assessment with respect to the importance of the aboveground edifices and urban infrastructure since the total magnitude of surface settlements is relatively small for mechanized tunneling in overconsolidated natural clay deposits.

10 Conclusions and outlook

Mechanized tunneling is a very common massumedethod to conduct subsurface infrastructural projects particularly in urban areas due to the limited surface space. Especially mechanized tunneling in natural clay deposits is challenging due to the complex constitutive soil behavior governed by current state, stress-strain history and structure. Hence, realistic and reliable predictions of the system behavior induced by mechanized tunneling such as surface settlements require sophisticated understanding of the constitutive behavior of natural clay.

The aim of the present study was to propose a concept for an adequate numerical analysis of mechanized tunneling in natural clay to achieve realistic and reliable predictions of the system behavior such as surface settlements and the distribution of stress and excess pore-water pressure in the soil domain. Whereas, the current study was focusing on the required complexity of constitutive modeling of natural clay which should be performed as simple as possible but not simpler to still guarantee realistic and reliable predictions of the system behavior induced by mechanized tunneling. That is, an adequate analysis concept was developed based on the assessment of the necessity of a certain level of complexity of an appropriate constitutive bounding surface plasticity (BSP) model for natural clay to be employed in the numerical analysis of mechanized tunneling. Therefore, the spatial and construction stage dependent evolution of the influence of the particular soil mechanical properties of natural clay (e.g. inherent and stress-induced anisotropy, initial structure and progressive destructuration, behavior under non-monotonic or cyclic loading incorporating stress-strain hysteresis and elastoplastic transition, stiffness degradation and accumulative effects) on the numerical model response induced by mechanized tunneling was evaluated based on the concept of the hierarchical BSP model family. The present study concludes with the development of practical recommendations if typical mechanical properties of natural clay have to be considered in the numerical analysis of mechanized tunneling with respect to realistic and reliable predictions of surface settlements in design and construction phases.

The structure of natural clay is characterized by fabric referring to the arrangement and orientation of particles, aggregates and contacts and by interparticle bonding. Anisotropic fabric which is formed during deposition results in inherent anisotropy of the constitutive behavior. Interparticle bonding imparts additional strength and stiffness to clay compared to its intrinsic properties. Accordingly, natural clay can sustain higher stresses without yielding. Furthermore, plastic straining initiated after exceeding the yield stress induces anisotropy of the constitutive behavior with respect to the loading direction. In addition, plastic straining causes destructuration which is defined as progressive damage of interparticle bonding causing a certain loss of strength and stiffness. Moreover, natural clay under non-monotonic or cyclic loading arising from the construction processes of mechanized tunneling shows smooth elastoplastic transition and hysteresis of the stress-strain behavior during unloading/reloading cycles and underlies certain stiffness degradation and accumulation of plastic strain with increasing number of cycles. Hence, inherent and stress-induced anisotropy, interparticle bonding and its destructuration and the behavior under non-monotonic or cyclic loading have significant impact on the stress-strain behavior of natural clay and the generation of excess pore-water pressure which was intensively discussed in the state-of-the-art literature review.

Achieving realistic and reliable predictions of the system behavior resulting from mechanized tunneling requires an appropriate numerical 3D simulation model developed in a state-of-the-art model code. The numerical simulation model has to account for the most decisive subsystems as it was explicitly debated in the state-of-the-art review. The following components of an appropriate 3D simulation model for mechanized tunneling were considered in the present study: ground domain represented by soil volume elements; sequential advance; shield machine by elastic shell elements; lining segments by elastic volume elements; soil-structure interaction/contact modeling between soil, shield machine and lining by interface elements; tunnel face support by distributed surface load; tail void grouting pressure by distributed surface load; tunnel volume loss due to overcutting and conicity of the shield machine by contraction of the shield and lining elements; tunnel volume loss at the tail void by contraction of the lining elements.

Furthermore, it is essential to employ a sophisticated constitutive model which accounts for the complex constitutive behavior of natural clay such as inherent and stress-induced anisotropy as well as initial structure and destructuration with special consideration of the non-monotonic or cyclic nature of the loading. In the state-of-the-art literature review it was revealed that the inherent and stress-induced anisotropy can be suitably captured by introducing an anisotropic fabric stress tensor whose evolution is controlled by a sophisticated rotational hardening rule that the current amount of structure and

the destructuration process can be properly taken into consideration by introducing a structure variable and an intrinsic reference surface and that the BSP concept offers a platform to capture the fundamental aspects of the mechanical behavior of natural clay under non-monotonic or cyclic stress paths.

Hence, a sophisticated constitutive BSP model of hierarchical structure accounting for the following features was employed in the present work: non-linear and stress-dependent elasticity; isotropic hardening and softening with respect to volumetric plastic strain; non-associated flow rule; Lode-angle dependence, inherent and stress-induced anisotropy by use of an anisotropic fabric stress tensor and rotational hardening; initial structure and stress-induced destructuration by applying the concept of intrinsic reference surface and evolving structure variable, bounding surface plasticity concept with updated projection center in case of having stress reversal, stiffness degradation and accumulation of plastic strain by use of an evolving damage variable.

To conduct numerical simulations of mechanized tunneling the developed constitutive BSP model was efficiently and robustly implemented in a 3D state-of-the-art finite element code by numerical integration of the constitutive equations incorporating the modified Euler approach with automatic error control and sub-stepping approach.

This study provided the coupling of an appropriate 3D simulation model for mechanized tunneling with a sophisticated constitutive BSP model for natural clay, which was not given in the already existing numerical studies. The appropriate 3D tunnel simulation model allowed for an enhanced analysis of the influence of the soil mechanical properties of natural clay on the system behavior induced by mechanized tunneling considering the spatial stress-strain behavior and excess pore-water pressure distribution in the entire ground domain. The application of the sophisticated constitutive BSP model enhanced the analysis compared to the existing research.

However, the number of constitutive BSP model parameters, their correlations and the superimposed influence on the BSP model responses make the calibration against geotechnical laboratory testing data demanding and complicated. Since the realistic numerical simulation of mechanized tunneling requires a very precise knowledge of the constitutive BSP model parameters a more advanced calibration using identification via inverse analysis was applied in the present study. Beforehand, a global sensitivity analysis (GSA) was additionally conducted to provide information on the geotechnical laboratory test and even the loading stage to be selected to most properly identify a particular constitutive BSP model parameter. To sum up, the so-called measurable constitutive BSP model parameters κ, ν, λ, M_{c} and M_{e} related to the critical state soil mechanics and the Modified Cam-Clay model can be experimentally determined and directly assessed from the results

of the associated geotechnical laboratory or field tests. Furthermore, the parameters related to the initial conditions such as initial void ratio e_0, coefficient of earth pressure at rest K_0, yield stress ratio YSR, and preconsolidation stress $p_{0,\mathrm{s,init}}$ can be directly determined from the experimental results of the associated geotechnical laboratory or field test. In addition to this, some non-measurable constitutive BSP model parameters such as $N_\mathrm{e}/N_\mathrm{c} = M_\mathrm{e}/M_\mathrm{c}$ related to the shape of the bounding surface on the extension side and $\alpha_0 = \alpha_{\mathrm{K}_0}$ and $s_\alpha = z_\alpha$ related to the inherent and stress-induced anisotropy can be analytically calculated. The remaining non-measurable constitutive BSP model parameters N_c related to non-associated flow and the shape of the bounding surface, c_α related to the stress-induced anisotropy and the rotational hardening, $S_{\mathrm{i},0}$ related to the initial structure, k_i and A related to destructuration, s_eln related to the size of the elastic nucleus defining the purely elastic domain, h_0 related to the initial shape hardening stiffness and a_dam related to the degradation of stiffness and accumulation of plastic strain have to be calibrated against the experimental data of geotechnical laboratory tests using inverse analysis. In conclusion, based on the results of the GSA recommendations were given regarding the adequate choice of the geotechnical laboratory tests to be preferentially selected for the calibration of a particular constitutive BSP model parameter.

Afterwards, a constitutive BSP model parameter set for the natural Onsøy clay being representative for the typical natural clay behavior was calibrated via direct experimental and analytical determination and additionally by an automated inverse analysis using the particle swarm optimization (PSO). The constitutive BSP model parameters were calibrated against experimental data from RUB and further literature data on Onsøy clay from NGI and KIT based on the particular recommendations as the outcome of the GSA. The evaluation of the influence of the constitutive properties of natural clay on the system behavior resulting from mechanized tunneling was conducted by employing the concept of the hierarchical BSP model family. In conclusion, using the hierarchical BSP model family concept offers the opportunity to understand the influence of the complexity level of the constitutive BSP model on the numerical model responses caused by mechanized tunneling. Moreover, it enables to evaluate the necessity of a certain degree of complexity of the constitutive BSP model. To be more specific, the proposed approach allows to define rational recommendations if typical mechanical properties of natural clay (e.g. inherent and stress-induced anisotropy, destructuration, behavior under non-monotonic or cyclic loading incorporating stress-strain hysteresis and elastoplastic transition, stiffness degradation and accumulative effects) have to be considered in the numerical analysis of specific numerical model responses in design and construction phases of mechanized tunneling.

The hierarchical structure of the constitutive BSP model for natural clay used in the present study is listed below.

- Extended Modified Cam-Clay (**MCC**) → basic model, elastoplasticity, isotropic hardening and softening, non-associated flow
- **Saniclay** → additional inherent and stress-induced anisotropy
- **Saniclay D** → additional destructuration
- **Saniclay D + BSP** → additional bounding surface plasticity incorporating stress-strain hysteresis and elastoplastic transition, stiffness degradation and accumulative effects under non-monotonic or cyclic loading

For a better understanding, the influence of the level of complexity of the hierarchical BSP model on the model response regarding numerical simulations of geotechnical laboratory tests on natural Onsøy clay was exemplarily evaluated before conducting the numerical analysis with respect to the mechanized tunneling application case. Whereat, destructuration has the largest impact on the BSP model response when it comes to elastoplastic loading due to the striking stiffness and strength degradation governed by plastic straining. Anisotropy becomes relevant when the induced effective stress path remarkably deviates from the current stress ratio. The behavior under non-monotonic or cyclic loading significantly affects the model BSP response during unloading-reloading and when it comes to cyclic loading inside the bounding surface since stress-strain hysteresis, stiffness degradation and accumulation of plastic strain are properly captured. Concluding, the required level of complexity of the constitutive BSP model is strongly dependent on the mechanical and hydraulic boundary conditions, the initial consolidation conditions and the induced loading of the geotechnical laboratory test which governs the elastic or elastoplastic BSP model response.
The influence of the mechanical properties of natural clay on the numerical model response induced by a synthetic shallow mechanized tunneling excavation in a homogeneous, water-saturated natural Onsøy clay deposit under greenfield conditions was numerically investigated with respect to normally and overconsolidated initial stress conditions and assumed fully drained and fully undrained conditions. In particular, the spatial and construction stage dependent evolution of the influence of the mechanical properties of natural clay such as inherent and stress-induced anisotropy, initial structure and its progressive destructuration and the behavior under non-monotonic or cyclic loading incorporating stress-strain hysteresis and elastoplastic transition, stiffness degradation and accumulation of plastic strain on the system behavior evoked by mechanized tunneling was analyzed. The surface

settlements, the spatial distribution of ground movements, void ratio and plastic strain in the soil domain, the evolution of the effective stress paths and the generation of excess pore-water pressure in the nearfield around the tunnel and midway between tunnel crown and ground surface were evaluated as the most decisive model responses induced by mechanized tunneling. Moreover, the spatial and construction stage dependent evolution of the state variables of the BSP model corresponding to destructuration, stress-induced anisotropy and the behavior under non-monotonic or cyclic loading was investigated.
It has to be noted that the numerical tunnel simulations employing the constitutive BSP model is not validated against any case study about mechanized tunneling in natural clay. However, the constitutive BSP model was calibrated and validated on the element level against various geotechnical laboratory tests on natural Onsøy clay. The study showed a sufficient level of accuracy when comparing numerical and experimental results. From a practical point of view the transferability of the BSP model to the mechanized tunneling simulation is justified since the stress-strain behavior of natural clay is adequately reproduced in the element tests under consideration of the initial stress conditions, drainage conditions and effective stress paths as they are expected for the mechanized tunneling application in water-saturated natural clay deposits. Furthermore, the study illustrated the superiority of the more advanced BSP model extensions with higher level of complexity in capturing various aspects of the typical constitutive behavior of natural clays. Hence, the reliability of the outcome of the numerical study on mechanized tunneling in natural clay deposits using the hierarchical BSP model family apporach is given especially in qualitative manner even without comparison to any case study.
For an adequate prediction of the surface settlements induced by mechanized tunneling in natural clay deposits the following recommendations can be concluded regarding the complexity of the constitutive BSP model to be selected for the numerical analysis.

- It is required to consider the initial structure when aiming for an adequate modeling of natural clay behavior since the interparticle bonding imparts additional stiffness and strength and consequently governs the surface settlements and soil displacements. The initial structure and the corresponding yielding characteristics can be captured by any hierarchical model extension by a proper initialization of an enlarged size of the initial yield or bounding surface. A fully reconstituted or destructured clay without any bonding would exhibit a much softer behavior.

- It is mandatory to consider the progressive destructuration of the initial structure to adequately predict the surface settlements for mechanized tunneling in natural clay deposits with mainly normally consolidated initial stress conditions in the

tunnel excavation area and assumed drained conditions. To be more precise, due to destructuration the maximum surface settlements will significantly increase and the transverse settlement trough and the longitudinal settlement trough hurrying ahead of the shield machine become more steep. Whereat, especially the gradient and inclination of the settlement trough as well as the maximum settlements decisively govern the damage assessment of edifices and urban infrastructure related to mechanized tunneling. For assumed undrained conditions the necessity of accounting for destructuration has to be decided from case to case in terms of risk assessment with respect to the importance of the aboveground edifices and urban infrastructure since the influence of destructuration on the surface settlements is not that striking as compared to assumed drained conditions. Nevertheless, the drainage conditions with application to mechanized tunneling in natural clay deposits will be neither fully drained nor fully undrained but somehow affected by consolidation and time-dependent dissipation of excess pore-water pressure. Hence, it is strongly recommended to always consider destructuration when numerically modeling mechanized tunneling in natural clay deposits to be independently of the in situ drainage conditions of the natural clay.

- It is not compulsory to account for the progressive degradation of structure when aiming for an adequate prediction of the surface settlements caused by mechanized tunneling in overconsolidated natural clay deposits. Due to overconsolidation the soil behavior is predominantly elastic and stiff and just a small amount of plasticity constrained to a limited area in the nearfield of the tunnel is induced. Nevertheless, it is strongly recommended to always consider destructuration when numerically modeling mechanized tunneling in natural clay deposits independently of the initial consolidation stress and drainage conditions. Just to be prepared for external trigger and changing boundary conditions causing distinct plasticity during the excavation and construction process in regard to safety issues, damage assessment and risk management since the influence of destructuration on the surface settlements is extensive when it comes to remarkable plastic straining during mechanized tunneling.

- It is required to consider the inherent and stress-induced anisotropy to adequately predict the surface settlements for mechanized tunneling in natural clay deposits with mainly normally consolidated initial stress conditions in the tunnel excavation area and especially for assumed drained conditions. Due to the variability and uncertainty of the drainage conditions of natural clay during mechanized tunnel-

ing the recommendation holds true for any tunnel excavation in a water-saturated clay deposit. To be more specific, the maximum surface settlements are underestimated when not accounting for the initial rotation and the plastic straining induced rotational hardening of the bounding surface and the plastic potential surface. Furthermore, the shape of the transverse settlement trough and the longitudinal settlement trough hurrying ahead of the shield machine are predicted slightly too flat. Compared to destructuration the effect of anisotropy on the maximum surface settlements is much less pronounced.

- It is not mandatory to account for the inherent and stress-induced anisotropy with respect to an adequate prediction of the surface settlements caused by mechanized tunneling in overconsolidated natural clay deposits independently of the drainage conditions since the soil behavior is predominantly elastic and stiff and just a small amount of plasticity constrained to a limited area in the nearfield of the tunnel is induced. Even when it anyhow comes to transition from overconsolidated to normally consolidated conditions of the natural clay by having mechanized tunneling induced effective stress path reaching the bounding surface and significant plasticity is induced afterwards, the impact of anisotropy on the settlement behavior is still moderate with respect to safety issues, damage assessment and risk management.

- It is not compulsory to account for the behavior under non-monotonic or cyclic loading such as stress-strain hysteresis and elastoplastic transition, stiffness degradation and accumulation of plastic strain to adequately predict the surface settlements for mechanized tunneling in mainly normally consolidated natural clay deposits independently of the drainage conditions. That is because mechanized tunneling in natural clay as the chosen engineering application generates just a little amount of non-monotonic or cyclic loading and elastoplastic transition zones are not that distinctly formed to cause additional plastic strain and conditionally induce destructuration, rotational hardening and stiffness degradation while the effective stress path is moving inside the bounding surface.

- It is recommended to consider the behavior under non-monotonic or cyclic loading when aiming for an adequate prediction of the surface settlements arising from mechanized tunneling in overconsolidated natural clay deposits independently of the drainage conditions. In any case the consideration of the behavior under non-monotonic or cyclic loading leads to larger surface settlements due to the additionally induced plasticity. To be more detailed, the maximum surface settlements are underestimated when not taking into consideration the elastic nucleus updated to

the last stress reversal, stress-strain hysteresis and elastoplastic transition, stiffness degradation and accumulation of plastic strain. Consequently, remarkable amount of plasticity is induced while moving inside the bounding surface and the soil behavior becomes more soft. Conditionally, destructuration, rotational hardening and stiffness degradation are activated in a certain manner since they are also governed by plastic straining. Moreover, the shape of the transverse settlement trough and the longitudinal settlement trough hurrying ahead of the shield machine are predicted slightly too flat independently of the drainage conditions. However, the necessity of accounting for non-monotonic or cyclic behavior might be decided from case to case in terms of risk assessment with respect to the importance of the aboveground edifices and urban infrastructure since the total magnitude of surface settlements is relatively small for mechanized tunneling in overconsolidated natural clay deposits.

As an outlook for further research on constitutive modeling of natural clay with application to mechanized tunneling the following issues could be addressed.

- Variations of the geometrical boundary conditions and initial conditions of the mechanized tunneling application case should be considered to numerically confirm the findings achieved in the present study. That is the diameter of the excavated tunnel area D, the overburden depth with respect to the excavated tunnel area H/D, the yield stress ratio YSR and the correlated coefficient of earth pressure at rest K_0 are varied, maybe even by employing GSA.

- Consideration of existing aboveground edifices as an extension of the investigated mechanized tunneling under greenfield conditions with special focus on safety issues, damage assessment and risk management will have practical relevance. However, results of a preliminary study showed that raft foundations on natural clay layers are not appropriate for the load transfer due to small stiffness and bearing capacity related to the small stress level of the shallow clay layers especially when it comes to destructuration. Anyhow, pile foundations have to be executed to transfer the loads to deeper natural clay layers by pile skin friction and pile toe resistance. In same manner, the construction of twin tunnels and the evaluation of the influence of their interaction could be also of practical interest.

- Spatial aspects with respect to the longitudinal and transverse tunnel direction such as inhomogeneous and layered ground profiles, aboveground geotechnical structures like damns and dikes and inclined or curved tunnels with varying overburden depth might be interesting to especially investigate the spatial bearing effects and settlement behavior and to activate the effects of anisotropy more pronounced.

- Further studies with an enhanced numerical 3D mechanized tunneling simulation model incorporating machine steering processes including re-meshing and jack thrust forces, pressure model to most appropriately represent the shield machine, lining segments with consideration of joints and tail void grouting with consideration of a thin grouting layer and time-dependent behavior of the grouting material are of minor importance.
- Evaluation of the influence of the mechanical properties of natural clay on the design of the precast concrete lining with respect to optimization of geometry, concrete strength and amount of reinforcement is of major practical importance.
- Performance and evaluation of field studies on mechanized tunneling in natural clay deposits are essential to confirm the numerical findings achieved in the present study by back calculation of the field case and subsequent comparison to the field measurements. Therefore, a convenient in situ measurement concept has to be elaborated regarding surface settlements, spatial distribution of ground movements, effective stress and excess pore-water pressure in the soil domain as well as internal forces, bending moments and radial displacements of the lining. The face support and grouting pressures have to be recorded during shield machine advance. Moreover, comprehensive field testing in the natural clay deposit and corresponding geotechnical laboratory testing are required in advance to experimentally determine the corresponding constitutive BSP model parameters and initial conditions.
- Analysis of the consolidation behavior of natural clay during mechanized tunneling in water-saturated deposits might be performed as a more precise enhancement of the investigated fully drained and fully undrained extreme cases. The incorporation of coupled hydro-mechanical computational phases will allow for time-dependent dissipation of the excess pore-water pressure and corresponding evolution of the effective stress path with ongoing excavation and construction process according to an appropriate consolidation theory (Terzaghi, 1923, 1925; Terzaghi and Fröhlich, 1936; Biot, 1941; Terzaghi, 1943).
- Analysis of the effects of viscoplasticity on the model response induced by mechanized tunneling in natural clay deposits is another option to be considered in further research. The viscous behavior originates from the complex structure of natural clay causing time-dependent effects which might be relevant when investigating the long-term behavior with respect to surface settlements and design of the lining. Therefore, the constitutive BSP model has to be enhanced by incorporating a convenient approach.

Bibliography

Adachi, T., Oka, F., Hirata, T., Hashimoto, T., Nagaya, J., Mimura, M. and Pradhan, T. B. S. (1995), 'Stress-strain behavior and yielding characteristics of Eastern Osaka clay', *Soils and Foundations* **35**(3), 1–13.

Addenbrooke, T. I., Potts, D. M. and Puzrin, A. M. (1997), 'The influence of pre-failure soil stiffness on the numerical analysis of tunnel construction', *Géotechnique* **47**(3), 693–712.

Al-Tabbaa, A. and Wood, D. M. (1989), An experimentally based bubble model for clay, *in* 'Proceedings of the 3rd International Symposium on Numerical Models in Geomechanics', pp. 91–99.

Alsahly, A., Stascheit, J. and Meschke, G. (2016), 'Advanced finite element modeling of excavation and advancement processes in mechanized tunneling', *Advances in Engineering Software* **100**, 198–214.

Amorosi, A., Boldini, D. and Germano, V. (2008), 'Implicit integration of a mixed isotropic-kinematic hardening plasticity model for structured clays', *International Journal for Numerical and Analytical Methods in Geomechanics* **32**(10), 1173–1203.

Amorosi, A. and Rampello, S. (2007), 'An experimental investigation into the mechanical behavior of a structured stiff clay', *Géotechnique* **57**(2), 153–166.

Anagnostou, G. and Kovari, K. (1994), 'The face-stability of slurry-shield-driven tunnels', *Tunnelling and Underground Space Technology* **9**(2), 165–174.

Anagnostou, G. and Kovari, K. (1996), 'Face stability conditions with earth-pressure-balanced shields', *Tunnelling and Underground Space Technology* **11**(2), 165–173.

Anandarajah, A. (2000), 'On influence of fabric anisotropy on the stress strain behavior of clays', *Computers and Geotechnics* **27**(1), 1–17.

Anandarajah, A. and Dafalias, Y. F. (1986), 'Bounding surface plasticity. iii: Application to anisotropic cohesive soils', *Journal of Engineering Mechanics* **112**(12), 1292–1318.

Anandarajah, A. and Kuganenthira, N. (1995), 'Some aspects of fabric anisotropy of soil', *Géotechnique* **45**(1), 69–81.

Anandarajah, A., Kuganenthira, N. and Zhao, D. (1996), 'Variation of fabric anisotropy of Kaolinite in triaxial loading', *Journal of Geotechnical Engineering* **122**(8), 633–640.

Andersen, K. H., Pool, J. H., Brown, S. F. and Rosenbrand, W. F. (1980), 'Cyclic and static laboratory tests on Drammen clay', *Journal of the Geotechnical Engineering Division* **106**(GT5), 499–513.

Asaoka, A., Nakano, M. and Noda, T. (2000), 'Superloading yield surface concept for highly structured soil behavior', *Soils and Foundations* **40**(2), 99–110.

Attewell, P. B. and Farmer, I. W. (1974), 'Ground deformations resulting from shield tunnelling in London clay', *Canadian Geotechnical Journal* **11**(3), 380–395.

Attewell, P. B. and Farmer, I. W. (1975), 'Ground settlement above shield driven tunnels in clay', *Tunnels and Tunnelling International* **7**(1), 58–62.

Avgerinos, V., Potts, D. M. and Standing, J. R. (2016), 'The use of kinematic hardening models for predicting tunnelling-induced ground movements in London Clay', *Géotechnique* **66**(2), 106–120.

Bakker, K. J. (2003), 'Structural design of linings for bored tunnels in soft ground', *Heron* **48**(1), 33–63.

Bamberg, L. R. (2009), The influence of oedometer cell diameter in testing of soft clays (in Norwegian), Diploma thesis, NTNU Trondheim, Norway.

Banerjee, P. K. and Yousif, N. B. (1986), 'A plasticity model for the mechanical behavior of anisotropically consolidated clay', *International Journal for Numerical and Analytical Methods in Geomechanics* **10**, 521–541.

Barciaga, T., Müthing, N., Datcheva, M. and Schanz, T. (2017), Cyclic response of natural Onsøy clay - part ii: Constitutive modeling, *in* 'Lecture Notes in Applied and Computational Mechanics. Holistic Simulation of Geotechnical Installation Processes: Theoretical Results and Applications', Vol. 82, pp. 275–296.

Barden, L. (1972), 'The influence of structure on deformation and failure in clay soil', *Géotechnique* **22**(1), 159–163.

BAST (2012), Zusätzliche technische Vertragsbedingungen und Richtlinien für Ingenieurbauten (ZTV-ING), Teil 5 - Tunnelbau, Abschnitt 3 - Maschinelle Schildvortriebsverfahren, German recommendation, Bundesanstalt für Straßenwesen.

Baudet, B. A. and Stallebrass, S. (2004), 'A constitutive model for structured clays', *Géotechnique* **54**(4), 269–278.

Belokas, G. and Kavvadas, M. (2010), 'An anisotropic model for structured soils. part i: theory', *Computers and Geotechnics* **37**, 737–747.

Benz, T. (2006), Small-strain stiffness of soils and its numerical consequences, PhD thesis, Universität Stuttgart, Germany.

Benz, T., Vermeer, P. A. and Schwab, R. (2009), 'A small-strain overlay model', *International Journal of Numerical and Analytical Methods in Geomechanics* **33**, 25–44.

Bergaya, F. and Lagaly, G. (2013), *Handbook of clay science - part A: fundamentals*, 2nd edn, Elsevier.

Bezuijen, A., Talmon, A. M., Kaalberg, F. J. and Plugge, R. (2004), 'Field measurements of grout pressures during tunelling of the Sophia rail tunnel', *Soils and Foundations* **1**, 39–48.

Bian, X., Hong, Z. S. and Ding, J. W. (2016), 'Evaluating the effect of soil structure on the ground response during shield tunnelling in Shanghai soft clay', *Tunnelling and Underground Space Technology* **58**, 120–132.

Biot, M. A. (1941), 'General theory of three dimensional consolidation', *Journal of Applied Physics* **12**(2), 155–165.

Bjerrum, L. (1954), 'Geotechnical properties of Norwegian marine clays', *Géotechnique* **4**(1), 49–69.

Bjerrum, L. (1963b), Allowable settlements of structures, *in* 'Proceedings of the 3rd European Conference on Soil Mechanics and Foundation Engineering', pp. 15–18.

Borja, R. I. and Amies, A. P. (1994), 'Multiaxial cyclic plasticity model for clays', *Journal of Geotechnical Engineering* **120**(6), 1051–1070.

Borja, R. I. and Lee, S. R. (1990), 'Cam-clay plasticity, part i: Implicit integration of elasto-plastic constitutive relations', *Computer Methods in Applied Mechanics and Engineering* **78**, 49–72.

Borja, R. I., Lin, C. H. and Montans, F. J. (2001), 'Cam-clay plasticity, part iv: Implicit integration of anisotropic bounding surface model with nonlinear hyperelasticity and ellipsoidal loading function', *Computer Methods in Applied Mechanics and Engineering* **190**(26-27), 3293–3323.

Brinkgreve, R. B. J., Kumarswamy, S. and Swolfs, W. M. (2016), PLAXIS 3D, Manuals, PLAXIS bv, The Netherlands.

Broere, W. (2001), Tunnel face stability and new CPT applications, PhD thesis, Delft University of Technology, The Netherlands.

Brown, S. F., Lashine, A. K. F. and Hyde, A. F. L. (1975), 'Repeated load triaxial testing of a silty clay', *Géotechnique* **25**(1), 95–114.

Burland, J. B. (1965), 'The yielding and dilation of clay', *Géotechnique* **15**(2), 211–214.

Burland, J. B. (1990), 'On the compressibility and shear strength of natural clays', *Géotechnique* **40**(3), 329–378.

Burland, J. B., Rampello, S., Georgiannou, V. N. and Calabresi, G. (1996), 'A laboratory study of the strength of four stiff clays', *Géotechnique* **46**(3), 491–514.

Burland, J. B. and Wroth, C. P. (1974), Settlement of buildings and associated damage, *in* 'Conference on the Settlement of Structures', pp. 611–654.

Burland, J. B. and Wroth, C. P. (1995), Assessment of risk of damage to building due to tunnelling and excavations, *in* '1st International Conference on Earthquake Geotechnical Engineering'.

Calabresi, G., Rampello, S. and Callisto, L. (1993), The leaning tower of Pisa - Geotechnical characterisation of the tower's subsoil within the framework of the critical state theory, Technical report, University of Rome La Sapienza, Italy.

Callisto, L. and Calabresi, G. (1998), 'Mechanical behaviour of a natural soft clay', *Géotechnique* **48**(4), 495–513.

Callisto, L. and Rampello, S. (2004), 'An interpretation of structural degradation for three natural clays', *Canadian Geotechnical Journal* **41**, 392–407.

Cattoni, E., Miriano, C., Boco, L. and Tamagnini, C. (2016), 'Time-dependent ground movements induced by shield tunneling in soft clay: a parametric study', *Acta Geotechnica* **11**(6), 1385–1399.

Chai, J., Miura, N., Zhu, H. H. and Yudhbir (2004), 'Compression and consolidation characteristics of structured natural clay', *Canadian Geotechnical Journal* **41**(6), 1250–1258.

Chambon, P. and Corte, J. F. (1994), 'Shallow tunnels in cohesionless soil: Stability of tunnel face', *Journal of Geotechnical Engineering* **120**(7), 1148–1165.

Chandler, R. J. (2010), 'Stiff sedimentary clays: geological origins and engineering properties', *Géotechnique* **60**(12), 891–902.

Cividini, A., Jurina, L. and Gioda, G. (1981), 'Some aspects of characterization problems in geomechanics', *International Journal of Rock Mechanics and Mining Sciences & Geomechanics Abstracts* **18**(6), 487–503.

Collins, K. and McGown, A. (1974), 'The form and function of microfabric features in a variety of natural soils', *Géotechnique* **24**(2), 223–254.

Cotecchia, F. (1996), The effects of structure on the properties of an Italian Pleistocene clay, PhD thesis, University of London, Imperial College of Science, Technology and Medicine, UK.

Cotecchia, F. and Chandler, R. J. (1997), 'The influence of structure on the pre-failure behaviour of a natural clay', *Géotechnique* **47**(3), 523–544.

Cotecchia, F. and Chandler, R. J. (2000), 'A general framework for the mechanical behavior of clays', *Géotechnique* **50**(4), 431–447.

Crouch, R. S. and Wolf, J. P. (1994a), 'Unified 3D critical state bounding-surface plasticity model for soils incorporating continuous plastic loading under cyclic paths. Part i: Constitutive relations', *International Journal for Numerical and Analytical Methods in Geomechanics* **18**, 735–758.

Crouch, R. S., Wolf, J. P. and Dafalias, Y. F. (1994b), 'Unified critical-state bounding-surface plasticity model for soil', *Journal of Engineering Mechanics* **120**(11), 2251–2270.

Cudny, M. and Vermeer, P. A. (2004), 'On the modelling of anisotropy and destructuration of soft clays within the multi-laminate framework', *Computers and Geotechnics* **31**(1), 1–22.

Dafalias, Y. F. (1986a), 'Bounding surface plasticity. i: Mathematical foundation and hypoplasticity', *Journal of Engineering Mechanics* **112**(EM9), 966–987.

Dafalias, Y. F. (1986c), 'An anisotropic critical state soil plasticity model', *Mechanics Research Communications* **13**(6), 341–347.

Dafalias, Y. F. and Herrmann, L. R. (1982), Bounding surface formulation of soil plasticity, *in* 'Soil Mechanics - Transient and Cyclic Loads', pp. 253–282.

Dafalias, Y. F. and Herrmann, L. R. (1986b), 'Bounding surface plasticity. ii: Application to isotropic cohesive soils', *Journal of Engineering Mechanics* **112**(12), 1263–1291.

Dafalias, Y. F., Herrmann, L. R. and Anandarajah, A. (1981), Cyclic loading response of cohesive soils using a bounding surface plasticity model, *in* 'International Conferences on Recent Advances in Geotechnical Earthquake Engineering and Soil Dynamics', pp. 253–282.

Dafalias, Y. F., Manzari, M. T. and Akaishi, M. (2002), 'A simple anisotropic clay plasticity model', *Mechanics Research Communications* **29**, 241–245.

Dafalias, Y. F., Manzari, M. T. and Papadimitriou, A. G. (2006), 'SANICLAY: simple anisotropic clay plasticity model', *International Journal for Numerical and Analytical Methods in Geomechanics* **30**, 1231–1257.

Dafalias, Y. F. and Popov, E. P. (1975), 'A model of nonlinearly hardening materials for complex loading', *Acta Mechanica* **21**, 173–192.

Dafalias, Y. F. and Taiebat, M. (2013), 'Anatomy of rotational hardening in clay plasticity', *Géotechnique* **63**(16), 1406–1418.

Dafalias, Y. F. and Taiebat, M. (2014), 'Rotational hardening with and without anisotropic fabric at critical state', *Géotechnique* **64**(6), 507–511. Technical Note.

Dang, H. and Meguid, M. (2008), 'Application of a multilaminate model to simulate the undrained response of structured clay to shield tunnelling', *Canadian Geotechnical Journal* **45**(1), 14–28.

DAUB (2010), Empfehlungen zur Auswahl von Tunnelvortriebsmaschinen, German recommendation, German Tunnelling Committee (ITA-AITES), Deutscher Ausschuss für unterirdisches Bauen e.V. (DAUB).

DAUB (2016), Recommendations for face support pressure calculations for shield tunnelling in soft ground, German recommendation, German Tunnelling Committee (ITA-AITES), Deutscher Ausschuss für unterirdisches Bauen e.V. (DAUB).

Davis, E. H., Gunn, M. J., Mair, R. J. and Seneviratne, H. N. (1980), 'The stability of shallow tunnels and underground openings in cohesive material', *Géotechnique* **30**(4), 397–416.

Delage, P. and Lefebvre, G. (1984), 'Study of the structure of a sensitive Champlain clay and of its evolution during consolidation', *Canadian Geotechnical Journal* **21**(1), 21–35.

DGGT (2014), *Empfehlungen des Arbeitskreises Numerik in der Geotechnik - EANG*, Deutsche Gesellschaft für Geotechnik e.V. (DGGT), Ernst und Sohn.

Dias, D. and Kastner, R. (2013), 'Movements caused by the excavation of tunnels using face pressurized shields - Analysis of monitoring and numerical modeling results', *Engineering Geology* **152**, 17–25.

Diaz-Rodriguez, J. A. (1989), 'Behavior of Mexico city clay subjected to undrained repeated loading', *Canadian Geotechnical Journal* **26**, 159–162.

Diaz-Rodriguez, J. A., Leroueil, S. and Aleman, J. D. (1992), 'Yielding of Mexico city clay and other natural clays', *Journal of Geotechnical Engineering* **118**(7), 981–995.

Do, N. A. and Dias, D. (2017), 'A comparison of 2D and 3D numerical simulations of tunnelling in soft soils', *Environmental Earth Sciences* **76**.

Do, N. A., Dias, D., Oreste, P. and Djeran-Maigre, I. (2014), 'Three-dimensional numerical simulation of a mechanized twin tunnels in soft ground', *Tunnelling and Underground Space Technology* **42**, 40–51.

Dowell, M. and Jarratt, P. (1972), 'The pegasus method for computing the root of an equation', *BIT Numerical Mathematics* **12**, 503–508.

Duncan, J. M. and Seed, H. B. (1966), 'Anisotropy and stress reorientation in clay', *Journal of the Soil Mechanics and Foundations Divison* **92**, 21–50.

Fargnoli, V., Gragnano, C. G., Boldini, D. and Amorosi, A. (2015), '3D numerical modelling of soil-structure interaction during EPB tunnelling', *Géotechnique* **65**(1), 23–37.

Fillibeck, J. (2012), Oberflächensetzungen beim Tunnelvortrieb im Lockergestein - Prognose, Messung und Beeinflussung, Habilitationsschrift, Technische Universität München, Germany.

Finno, R. J. and Clough, G. W. (1985), 'Evaluation of soil response to EPB shield tunneling', *Journal of Geotechnical Engineering* **111**(2), 155–173.

Franzius, J. N., Potts, D. M., Addenbrooke, T. I. and Burland, J. B. (2004), 'The influence of building weight on tunneling-induced ground and building deformation', *Soils and Foundations* **44**(1), 25–38.

Franzius, J. N., Potts, D. M. and Burland, J. B. (2005), 'The influence of soil anisotropy and K_0 on ground surface movements resulting from tunnel excavation', *Géotechnique* **55**(3), 189–199.

Fuentes, W., Tafili, M. and Triantafyllidis, T. (2017), 'An ISA-plasticity-based model for viscous and non-viscous clays', *Acta Geotechnica* .

Gajo, A. and Wood, D. M. (2001), 'A new approach to anisotropic, bounding surface plasticity: general formulation and simulations of natural and reconstituted clay behaviour', *International Journal for Numerical and Analytical Methods in Geomechanics* **25**, 207–241.

Galavi, V. and Schweiger, H. (2009), 'A multilaminate model with destructuration considering anisotropic strength and anisotropic bonding', *Soils and Foundations* **49**(3), 341–353.

Galli, M. (2016), Rheological characterisation of Earth-Pressure-Balance (EPB) support medium composed of non-cohesive soils and foam, PhD thesis, Ruhr-Universität Bochum, Germany.

Ganendra, D. and Potts, D. M. (1995), 'Discussion on evaluation of a constitutive model for overconsolidated clays by A. J. Whittle', *Géotechnique* **45**(1), 501–519.

Gasparre, A., Nishimura, S., Coop, M. R. and Jardine, R. J. (2007a), 'The influence of structure on the behaviour of London clay', *Géotechnique* **57**(1), 19–31.

Gens, A. and Nova, R. (1993), Conceptual bases for a constitutive model for bonded soils and weak rocks, *in* 'International Symposium on Geotechnical Engineering of Hard Soils-Soft Rocks', pp. 485–494.

Gens, A. and Potts, D. M. (1988), 'Critical state models in computational geomechanics', *Engineering Computations* **5**(3), 178–197.

Gonzalez, N. A., Rouainia, M., Arroyo, M. and Gens, A. (2012), 'Analysis of tunnel excavation in London clay incorporating soil structure', *Géotechnique* **62**(12), 1095–1109.

Graham, J., Crooks, J. H. A. and Lau, S. L. K. (1988), 'Yield envelopes: Identification and geometric properties', *Géotechnique* **38**(1), 125–134.

Graham, J. and Li, E. C. C. (1985), 'Comparison of natural and remolded plastic clay', *Journal of Geotechnical Engineering* **11**(7), 865–881.

Graham, J., Noonan, M. L. and Lew, K. V. (1983), 'Yield states and stress-strain relationships in a natural plastic clay', *Canadian Geotechnical Journal* **20**, 502–516.

Grammatikopoulou, A., Zdravkovic, L. and Potts, D. M. (2006), 'General formulation of two kinematic hardening constitutive models with a smooth elastoplastic transition', *International Journal of Geomechanics* **6**(5), 291–302.

Grammatikopoulou, A., Zdravkovic, L. and Potts, D. M. (2008a), 'The influence of previous stress history and stress path direction on the surface settlement trough induced by tunneling', *Géotechnique* **58**(4), 269–281.

Gras, J. P., Sivasithamparam, N., Karstunen, M. and Dijkstra, J. (2017a), 'Strategy for consistent model parameter calibration for soft soils using multi-objective optimisation', *Computers and Geotechnics* **90**, 164–175.

Gras, J. P., Sivasithamparam, N., Karstunen, M. and Dijkstra, J. (2017b), 'Permissible range of model parameters for natural fine-grained materials', *Acta Geotechnica* **90**, 164–175.

Gudehus, G. (1996), 'A comprehensive constitutive equation for granular materials', *Soils and Foundations* **36**(1), 1–12.

Guggenheim, S., Adams, J. M., Bain, D. C., Bergaya, F., Brigatti, M. F., Drits, V. A., Formoso, M. L. L., Galan, E., Kogure, T. and Stanjek, H. (2006), 'Summary of recommendations of nomenclature committees relevant to clay mineralogy: report of the Association Internationale pour l'Etude des Argiles (AIPEA) nomenclature committee for 2006', *Clays and Clay Minerals* **54**(6), 761–772.

Guggenheim, S. and Martin, R. T. (1995), 'Definition of clay and clay mineral: joint report of the AIPEA and CMS nomenclature committees', *Clays and Clay Minerals* **43**, 255–256.

Guggenheim, S. and Martin, R. T. (1996), 'Reply to the comment by D.M. Moore on "Definition of clay and clay mineral: joint report of the AIPEA and CMS nomenclature committees"', *Clays and Clay Minerals* **44**, 713–715.

Hanna, A. M. and Javed, K. (2014), 'Experimental investigation of foundations on sensitive clay subjected to cyclic loading', *Journal of Geotechnical and Geoenvironmental Engineering* **140**(11), 1–12.

Hashiguchi, K. (1977b), An expression of anisotropy in a plastic constitutive equation of soils, *in* 'Ninth International Conference on Soil Mechanics and Foundation Engineering', pp. 302–305.

Hashiguchi, K. (1979), Constitutive equations of granular media with an anisotropic hardening, *in* 'Third International Conference on Numerical Methods in Geomechanics', pp. 435–439.

Hashiguchi, K. (1980), 'Constitutive equations of elastoplastic materials with elastic-plastic transition', *Journal of Applied Mechanics* **47**, 266–272.

Hashiguchi, K. (1981), 'Constitutive equations of elastoplastic materials with anisotropic hardening and elastic-plastic transition', *Journal of Applied Mechanics* **48**, 297–301.

Hashiguchi, K. (1989), 'Subloading surface model in unconventional plasticity', *International Journal of Solids and Structures* **25**(8), 917–945.

Hashiguchi, K. and Chen, Z. P. (1998), 'Elastoplastic constitutive equation of soils with the subloading surface and the rotational hardening', *International Journal for Numerical and Analytical Methods in Geomechanics* **22**, 197–227.

Hashiguchi, K. and Ueno, M. (1977a), Elasto-plastic constitutive laws of granular materials, *in* 'International Conference on Soil Mechanics and Foundation Engineering', Vol. 9, pp. 73–82.

Hattab, M. and Fleureau, J. (2010), 'Experimental study of kaolin particle orientation mechanism', *Géotechnique* **60**(5), 323–331.

Hegemann, F., Galli, M., Schindler, S., Barciaga, T., Alsahly, A., Lehner, K. and Koch, C. (2014), Integrated data processing and simulation platform for mechanized tunneling - Showcase application on the Wehrhahn-Linie project in Düsseldorf, *in* 'Proceedings of World Tunnel Congress 2014 - 40th ITA-AITES General Assembly, Iguassu Falls, Brazil'.

Herrmann, L. R., Kaliakin, V. N., Shen, C. K., Mish, K. D. and Zhu, Z. Y. (1987), 'Numerical implementation of plasticity model for cohesive soils', *Journal of Engineering Mechanics* **113**(4), 500–519.

Hicher, P. Y., Wahyudi, H. and Tessier, D. (2000), 'Microstructural analysis of inherent and induced anisotropy in clay', *Mechanics of Cohesive-Frictional Materials* **5**, 341–371.

Hight, D. W., Böese, R., Butcher, A. P., Clayton, C. R. I. and Smith, P. R. (1992a), 'Disturbance of the Bothkennar clay prior to laboratory testing', *Géotechnique* **42**(2), 199–217.

Hight, D. W., Bond, A. J. and Legge, J. D. (1992b), 'Characterization of the Bothkennar clay: an overview', *Géotechnique* **42**(2), 303–347.

Hight, D. W., Paul, M. A., Barras, B. F., Powell, J. J. M., Nash, D. F. T., Smith, P. R., Jardine, R. J. and Edwards, D. H. (2003a), The characterisation of the Bothkennar clay, *in* 'Characterisation and Engineering Properties of Natural Soils', Vol. 1, pp. 543–597.

Homma, T. and Saltelli, A. (1996), 'Importance measures in global sensitivity analysis of nonlinear models', *Reliability Engineering & System Safety* **52**, 1–17.

Hong, Z., Zeng, L. L., Cui, Y. J., Cai, Y. Q., Lin, C. and Li, X. L. (2012), 'Compression behaviour of natural and reconstituted clays', *Géotechnique* **62**(4), 291–301.

Horn, N. (1961), Horizontaler Erddruck auf senkrechte Abschlussflächen von Tunnelröhren, *in* 'Landeskonferenz der ungarischen Tiefbauindustrie', pp. 7–16.

Hsu, C. C. and Vucetic, M. (2006), 'Threshold shear strain for cyclic pore-water pressure in cohesive soils', *Journal of Geotechnical and Geoenvironmental Engineering* **132**(10), 1325–1335.

Hu, C. and Liu, H. (2014), 'Implicit and explicit integration schemes in the anisotropic bounding surface plasticity model for cyclic behaviours of saturated clay', *Computers and Geotechnics* **55**, 27–41.

Hu, C., Liu, H. and Huang, W. (2012), 'Anisotropic bounding-surface plasticity model for the cyclic shakedown and degradation of saturated clay', *Computers and Geotechnics* **44**, 34–47.

Huang, M., Liu, Y. and Sheng, D. (2011), 'Simulation of yielding and stress-strain behavior of Shanghai soft clay', *Computers and Geotechnics* **38**, 341–353.

Hyodo, M., Hyde, A. F. L., Yamamoto, Y. and Fujii, T. (1999), 'Cyclic shear strength of undisturbed and remoulded marine clays', *Soils and Foundations* **39**(2), 45–58.

Hyodo, M., Yamamoto, Y. and Sugiyama, M. (1994), 'Undrained cyclic shear behaviour of normally consolidated clay subjected to initial static shear stress', *Soils and Foundations* **34**(4), 1–11.

Ieronymaki, E. S., Whittle, A. J. and Sureda, D. S. (2017), 'Interpretation of free-field ground movements caused by mechanized tunnel construction', *Journal of Geotechnical and Geoenvironmental Engineering* **143**(4), 04016114–1–13.

Jamiolkowski, M., Lancellotta, R. and Pepe, C. (1993), Leaning tower of Pisa - updated information, *in* 'Third international conference on case histories in geotechnical engineering', pp. 1319–1330.

Jansen, M. J. W. (1999), 'Analysis of variance designs for model output', *Computer Physics Communications* **117**, 35–43.

Jardine, R. J., Potts, D. M., Fourie, A. B. and Burland, J. B. (1986), 'Studies on the influence of non-linear stress-strain characteristics in soil-structure interaction', *Géotechnique* **36**(3), 377–396.

Jeremic, B. and Sture, S. (1997), 'Implicit integrations in elastoplastic geotechnics', *Mechanics of Cohesive-frictional Materials* **2**, 165–183.

Jiang, J. and Ling, H. I. (2010), 'A framework of an anisotropic elastoplastic model for clays', *Mechanics Research Communications* **37**, 394–398.

Jiang, J., Ling, H. I. and Kaliakin, V. N. (2012), 'An associative and non-associative anisotropic bounding surface model for clay', *Journal of Applied Mechanics* **79**(3), 031010.

Jung, Y. H. and Yune, C. Y. (2011), 'Reappraisal of the anisotropic bounding surface model of small-strain behavior for clays', *Journal of Civil Engineering* **15**(3), 463–472.

Kaliakin, V. N. (2005), Numerical implementation and integration of bounding surface models, *in* 'Poromechanics III - Biot Centennial (1905-2005)', pp. 371–376.

Kaliakin, V. N. and Dafalias, Y. F. (1989), 'Simplifications to the bounding surface', *International Journal for Numerical and Analytical Methods in Geomechanics* **13**, 91–100. Short communication.

Kämper, C., Putke, T., Zhao, C., Lavasan, A. A., Barciaga, T., Mark, P. and Schanz, T. (2016), 'Vergleichsrechnungen zu Modellierungsvarianten für Tunnel mit Tübbingauskleidung', *Bautechnik* **93**(7), 421–432.

Kan, M. E. and Taiebat, H. A. (2014a), 'On implementation of bounding surface plasticity models with no overshooting effect in solving boundary value problems', *Computers and Geotechnics* **55**, 103–116.

Kan, M. E., Taiebat, H. A. and Khalili, N. (2014b), 'Simplified mapping rule for bounding surface simulation of complex loading paths in granular materials', *International Journal of Geomechanics* **14**(2), 239–253.

Karstunen, M. and Koskinen, M. (2004), Anisotropy and destructuration of Murro clay, *in* 'A. W. Skempton Memorial Conference', Vol. 1, pp. 476–487.

Karstunen, M. and Koskinen, M. (2008), 'Plastic anisotropy of soft reconstituted clays', *Canadian Geotechnical Journal* **45**(3), 314–328.

Karstunen, M., Krenn, H., Wheeler, S. J., Koskinen, M. and Zentar, R. (2005), 'Effect of anisotropy and destructuration on the behavior of Murro test embankment', *International Journal of Geomechanics* **5**(2), 87–97.

Karstunen, M. and Yin, Z. Y. (2010), 'Modelling time-dependent behaviour of Murro test embankment', *Géotechnique* **60**(10), 735–749.

Kasper, T. and Meschke, G. (2004), 'A 3D finite element simulation model for TBM tunnelling in soft ground', *International Journal for Numerical and Analytical Methods in Geomechanics* **28**, 1441–1460.

Kasper, T. and Meschke, G. (2006a), 'On the influence of face pressure, grouting pressure and TBM design in soft ground tunnelling', *Tunnelling and Underground Space Technology* **21**, 160–171.

Kasper, T. and Meschke, G. (2006b), 'A numerical study of the effect of soil and grout material properties and cover depth in shield tunnelling', *Computers and Geotechnics* **33**, 234–247.

Kavvadas, M. (1982), Non-linear consolidation around driven piles in clays, PhD thesis, Massachusetts Institute of Technology, USA.

Kavvadas, M. (1983), A constitutive model for clays based on non-associated anisotropic elasto-plasticity, *in* 'Proceedings of the International Conference on Constitutive Laws for Engineering Materials - Theory and Application', pp. 263–270.

Kavvadas, M. and Amorosi, A. (2000), 'A constitutive model for structured soils', *Géotechnique* **50**(3), 263–273.

Kavvadas, M., Anagnostopoulos, A. and Kalteziotis, N. (1994), A framework for the mechanical behaviour of the cemented Corinth marl, *in* 'Geotechnical Engineering of Hard Soils - Soft Rocks', pp. 577–583.

Kavvadas, M., Litsas, D., Vazaios, I. and Fortsakis, P. (2017), 'Development of a 3D finite element model for shield EPB tunnelling', *Tunnelling and Underground Space Technology* **65**, 22–34.

Kennedy, J. and Eberhart, R. (1995), Particle swarm optimization, *in* 'Proceedings of the IEEE International Conference on Neural Networks IV', pp. 1942–1948.

Kirsch, A. (2009), On the face stability of shallow tunnels in sand, PhD thesis, University of Innsbruck, Austria.

Kolymbas, D. (1991), 'An outline of hypoplasticity', *Archive of Applied Mechanics* **61**, 143–151.

Komiya, K., Soga, K., Akagi, H., Hagiwara, T. and Bolton, M. D. (1999), 'Finite element modelling of excavation and advancement processes of a shield tunnelling machine', *Soils and Foundations* **39**(3), 37–52.

Koskinen, M. (2014), Plastic anisotropy and destructuration of soft Finnish clays, PhD thesis, Aalto University, School of Engineering, Finland.

Koskinen, M. and Karstunen, M. (2004), The effect of structure on the compressibility of finnish clays, *in* '14th Nordic Geotechnical Meeting (NGM 2004)', Vol. 1, pp. A11–A22.

Koskinen, M., Karstunen, M. and Wheeler, S. J. (2002), Modelling destructuration and anisotropy of a natural soft clay, *in* '5th European Conference on Numerical Methods in Geotechnical Engineering', pp. 11–20.

Krieg, R. D. (1975), 'A practical two surface plasticity theory', *Journal of Applied Mechanics* **42**(3), 641–646.

Kulhawy, F. H. and Mayne, P. W. (1990), Manual on estimating soil properties for foundation design, Technical Report Project 1493-6, EL-6800, Electric Power Research Institute, Palo Alto, USA.

Lacasse, S., Berre, T. and Lefebvre, G. (1985), Block sampling of sensitive clays, *in* '11th International Conference on Soil Mechanics and Foundation Engineering', Vol. 2, pp. 887–982.

Lagioia, R. and Nova, R. (1995), 'An experimental and theoretical study of the behaviour of a calcarenite in triaxial compression', *Géotechnique* **45**(4), 633–648.

Lambe, T. W. and Whitman, R. Y. (1969), *Soil mechanics*, Wiley.

Lambrughi, A., Rodriguez, L. M. and Castellanza, R. (2012), 'Development and validation of a 3d numerical model for TBM-EPB mechanised excavations', *Computers and Geotechnics* **40**, 97–113.

Lavasan, A. A. and Schanz, T. (2017b), Numerical investigation of hydromechanical interactions at the tail void of bored tunnels due to grouting, *in* '9th International Symposium on Geotechnical Aspects of Underground Construction in Soft Ground', pp. 131–147.

Lavasan, A. A., Zhao, C., Barciaga, T., Schaufler, A., Steeb, H. and Schanz, T. (2017a), 'Numerical investigation of tunneling in saturated soil: The role of construction and operation periods', *Acta Geotechnica* pp. 1–21.

Leca, E. and Dormieux, L. (1990), 'Upper and lower bound solutions for the face stability of shallow circular tunnels in frictional material', *Géotechnique* **40**(4), 581–606.

Leca, E. and New, B. (2007), 'ITA/AITES report 2006 on settlements induced by tunneling in soft ground', *Tunnelling and Underground Space Technology* **22**, 119–149.

Lee, C. J. and Sheo, S. F. (2007), 'The stiffness degradation and damping ratio evolution of Taipei silty clay under cyclic straining', *Soil Dynamics and Earthquake Engineering* **27**, 730–740.

Lee, K. M. and Rowe, R. K. (1990a), 'Finite element modelling of the three-dimensional ground deformations due to tunnelling in soft cohesive soils: Part I - Method of analysis', *Computers and Geotechnics* **10**(2), 87–109.

Lee, K. M. and Rowe, R. K. (1990b), 'Finite element modelling of the three-dimensional ground deformations due to tunnelling in soft cohesive soils: Part II - results', *Computers and Geotechnics* **10**(2), 111–138.

Lefebvre, G. and LeBoeuf, D. (1987), 'Rate effects and cyclic loading of sensitive clays', *Journal of the Geotechnical Engineering Division* **113**(5), 476–489.

Leroueil, S., Tavenas, F., Brucy, F., La Rochelle, P. and Roy, M. (1979), 'Behavior of destructured natural clays', *Journal of the Geotechnical Engineering Division, Proceedings of the American Society of Civil Engineers* **105**(GT6), 759–778.

Leroueil, S. and Vaughan, P. R. (1990), 'The general and congruent effects of structure in natural soils and weak rocks', *Géotechnique* **40**(3), 467–488.

Li, L. L., Dan, H. B. and Wang, L. Z. (2011), 'Undrained behavior of natural marine clay under cyclic loading', *Ocean Engineering* **38**, 1792–1805.

Li, T. and Meissner, H. (2002), 'Two-surface plasticity model for cyclic undrained behavior of clays', *Journal of Geotechnical and Geoenvironmental Engineering* **128**(7), 613–626.

Li, Y., Emeriault, F., Kastner, R. and Zhang, Z. X. (2009), 'Stability analysis of large slurry shield-driven tunnel in soft clay', *Tunnelling and Underground Space Technology* **24**, 472–481.

Liang, R. Y. and Ma, F. (1992), 'Anisotropic plasticity model for undrained cyclic behavior of clays. I: Theory', *Journal of Geotechnical Engineering* **118**(2), 229–245.

Lieske, W. (2015), Compression behaviour of a natural and remoulded clay, Master thesis, Ruhr-Universität Bochum, Germany.

Ling, H. I., Yue, D., Kaliakin, V. N. and Themelis, N. J. (2002), 'Anisotropic elastoplastic bounding surface model for cohesive soils', *Journal of Engineering Mechanics* **128**(7), 748–758.

Liu, M. D. and Carter, J. P. (1999), 'Virgin compression of structured soils', *Géotechnique* **49**(1), 43–57.

Liu, M. D. and Carter, J. P. (2000a), 'Modelling the destructuring of soils during virgin compression', *Géotechnique* **50**(4), 479–483.

Liu, M. D. and Carter, J. P. (2002), 'A structured Cam Clay model', *Canadian Geotechnical Journal* **39**, 1313–1332.

Liu, M. D. and Carter, J. P. (2003b), 'Volumetric deformation of natural clays', *International Journal of Geomechanics* **3**(2), 236–252.

Liu, W., Shi, M., Miao, L., Xu, L. and Zhang, D. (2013), 'Constitutive modeling of the destructuration and anisotropy of natural soft clay', *Computers and Geotechnics* **51**, 24–41.

Lo, K. Y. (1965), 'Stability of slopes in anisotropic soils', *Journal of the Soil Mechanics and Foundations Division* **91**(4), 85–106.

Low, H. E., Phoon, K. K., Tan, T. S. and Leroueil, S. (2008), 'Effect of soil microstructure on the compressibility of natural Singapore marine clay', *Canadian Geotechnical Journal* **45**, 161–176.

Lunne, T., Berre, T., Andersen, K. H., Strandvik, S. and Sjursen, M. (2006), 'Effects of sample disturbance and consolidation procedures on measured shear strength of soft marine norwegian clays', *Canadian Geotechnical Journal* **43**, 726–750.

Lunne, T., Long, M. and Forsberg, C. F. (2003), Characterisation and engineering properties of Onsøy clay, *in* 'Characterisation and Engineering Properties of Natural Soils', Vol. 1, pp. 395–427.

Mair, R. J., Gunn, M. J. and O'Reilly, M. P. (1982), 'Ground movement around shallow tunnels in soft clay', *Tunnels and Tunnelling International* **14**(5), 45–48.

Mair, R. J. and Taylor, R. N. (1997), Bored tunnelling in the urban environment, *in* '14th International Conference on Soil Mechanics and Foundation Engineering', pp. 2353–2385.

Mair, R. J., Taylor, R. N. and Bracegirdle, A. (1993), 'Subsurface settlement profiles above tunnels in clays', *Géotechnique* **43**(2), 315–320.

Manzari, M. T. and Nour, M. A. (1997), 'On implicit integration of bounding surface plasticity models', *Computers and Structures* **63**(3), 385–395.

Manzari, M. T. and Yonten, K. (2014), 'On implementation and performance of an anisotropic constitutive model for clays', *International Journal of Computational Methods* **11**(2), 1342009–1–31.

Mara, T. A. and Tarantola, S. (2012), 'Variance-based sensitivity indices for models with dependent inputs', *Reliability Engineering & System Safety* **107**, 115–121.

Martin, R. T. and Ladd, C. C. (1975), 'Fabric of consolidated Kaolinite', *Clays and Clay Minerals* **23**, 17–25.

Masin, D. (2005), 'A hypoplastic constitutive model for clays', *International Journal for Numerical and Analytical Methods in Geomechanics* **29**, 311–336.

Matsui, T., Bahr, M. A. and Abe, N. (1992), 'Estimation of shear characteristics degradation and stress-strain relationship of saturated clays after cyclic loading', *Soils and Foundations* **32**(1), 161–172.

Matsui, T., Ohara, H. and Ito, T. (1980), 'Cyclic stress strain history and shear characteristics of clay', *Journal of the Geotechnical Engineering Division* **106**(GT10), 1101–1120.

Mehli, M. (2015), Creep - creep of geomaterials, settlement analysis of onsoy test fill, Technical report, Norwegian Geotechnical Institute, Norway.

Mitchell, J. K. and Soga, K. (2005), *Fundamentals of soil behavior*, 3rd edn, Wiley.

Mitchell, R. J. (1970), 'On the yielding and mechanical strength of Leda clay', *Canadian Geotechnical Journal* **7**(3), 297–312.

Mitchell, R. J. (1972), 'Some deviations from isotropy in a lightly overconsolidated clay', *Géotechnique* **22**(3), 459–467.

Möller, S. (2006), Tunnel induced settlements and structural forces in linings, PhD thesis, Universität Stuttgart, Germany.

Möller, S. C. and Vermeer, P. A. (2008), 'On numerical simulation of tunnel installation', *Tunnelling and Underground Space Technology* **23**, 461–475.

Mollon, G., Dias, D. and Soubra, A. H. (2010), 'Face stability analysis of circular tunnels driven by a pressurized shield', *Journal of Geotechnical and Geoenvironmental Engineering* **136**(1), 215–229.

Moses, G. G., Rao, S. N. and Rao, P. N. (2003), 'Undrained strength behaviour of a cemented marine clay under monotonic and cyclic loading', *Ocean Engineering* **30**, 1765–1789.

Mroz, Z. (1967), 'On the description of anisotropic workhardening', *Journal of the Mechanics and Physics of Solids* **15**, 163–175.

Mroz, Z., Norris, V. A. and Zienkiewicz, O. C. (1978), 'An anisotropic hardening model for soils and its application to cyclic loading', *International Journal for Numerical and Analytical Methods in Geomechanics* **2**(3), 203–221.

Mroz, Z., Norris, V. A. and Zienkiewicz, O. C. (1979), 'Application of an anisotropic hardening model in the analysis of the elastoplastic deformation of soils', *Géotechnique* **29**(1), 1–34.

Müthing, N. (2017b), On the consolidation behaviour of fine-grained soils under cyclic loading, PhD thesis, Ruhr-Universität Bochum, Germany.

Müthing, N., Barciaga, T. and Schanz, T. (2017a), Cyclic response of natural Onsøy clay - part i: Experimental analysis, *in* 'Lecture Notes in Applied and Computational Mechanics. Holistic Simulation of Geotechnical Installation Processes: Theoretical Results and Applications', Vol. 82, pp. 257–274.

Nagel, F. and Meschke, G. (2011), 'Grout and bentonite flow around a TBM: Computational modeling and simulation-based assessment of influence on surface settlements', *Tunnelling and Underground Space Technology* **26**, 445–452.

Nash, D. F. T., Powell, J. J. M. and Lloyd, I. M. (1992a), 'Initial investigations of the soft clay test site at bothkennar', *Géotechnique* **42**(2), 163–181.

Nash, D. F. T., Sills, G. C. and Davison, L. R. (1992b), 'One-dimensional consolidation testing of soft clay from Bothkennar', *Géotechnique* **42**(2), 241–256.

Niemunis, A. and Herle, I. (1997), 'Hypoplastic model for cohesionless soils with elastic strain range', *Mechanics of Cohesive-Frictional Materials* **2**, 279–299.

Nieto-Leal, A., Kaliakin, V. N. and Mashayekhi, M. (2017), 'Improved rotational hardening rule for cohesive soils and definition of inherent anisotropy', *International Journal of Numerical and Analytical Methods in Geomechanics* **42**(3), 469–487.

Ohta, H., Yoshitani, S. and Hata, S. (1975), 'Anisotropic stress-strain relationship of clay and its application to finite element analysis', *Soils and Foundations* **15**(4), 61–79.

Okur, D. V. and Ansal, A. (2007), 'Stiffness degradation of natural fine grained soils during cyclic loading', *Soil Dynamics and Earthquake Engineering* **27**, 843–854.

O'Reilly, M. P. and New, B. M. (1982), 'Settlements above tunnels in the United Kingdom - their magnitude and prediction', *Tunnelling* **82**, 173–181.

Palmieri, F. and Taiebat, M. (2024), 'An activation mechanism for cyclic degradation of clays in bounding surface plasticity', *International Journal for Numerical and Analytical Methods in Geomechanics* **48**(9), 2303–2319.

Pande, G. N. and Sharma, K. G. (1983), 'Multi-laminate model of clays - a numerical evaluation of the influence of rotation of the principal stress axes', *International Journal for Numerical and Analytical Methods in Geomechanics* **7**, 397–418.

Papon, A., Riou, Y., Dano, C. and Hicher, P. Y. (2005), 'Single- and multi-objective genetic algorithm optimization for identifying soil parameters', *International Journal for Numerical and Analytical Methods in Geomechanics* **36**(5), 597–618.

Park, D. S. and Kutter, B. L. (2016), 'Sensitive bounding surface constitutive model for structured clay', *International Journal for Numerical and Analytical Methods in Geomechanics* **40**, 1968–1987.

Peck, R. B. (1969), Deep excavations and tunneling in soft ground, *in* 'Proceedings of the 7th International Conference on SMFE', pp. 225–290.

Perazzelli, P., Leone, T. and Anagnostou, G. (2014), 'Tunnel face stability under seepage flow conditions', *Tunnelling and Underground Space Technology* **43**, 459–469.

Pestana, J. M. and Whittle, A. J. (1999), 'Formulation of a unified constitutive model for clays and sands', *International Journal for Numerical and Analytical Methods in Geomechanics* **23**, 1215–1243.

Pietruszczak, S. and Mroz, Z. (1983), 'On hardening anisotropy of K0-consolidated clays', *International Journal for Numerical and Analytical Methods in Geomechanics* **7**, 19–38.

Pietruszczak, S. and Pande, G. N. (1988), 'Multi-laminate framework of soil models - plasticity formulation', *International Journal for Numerical and Analytical Methods in Geomechanics* **11**, 651–658.

Pietruszczak, S. and Pande, G. N. (2001), 'Description of soil anisotropy based on multi-laminate framework, Short Communication', *International Journal for Numerical and Analytical Methods in Geomechanics* **25**, 197–206.

Potts, D. M. and Addenbrooke, T. I. (1997), A structure's influence on tunnelling-induced ground movement, *in* 'Proceedings of the Institution of Civil Engineers - Geotechnical Engineering', Vol. 125, pp. 109–125.

Potts, D. M. and Gens, A. (1985), 'A critical assessment of methods of correcting for drift from the yield surface in elastoplastic finite element analysis', *International Journal for Numerical and Analytical Methods in Geomechanics* **9**, 149–159.

Potts, D. M. and Zdravkovic, L. (1999), *Finite element analysis in geotechnical engineering - Theory*, Telford.

Prager, W. (1956), 'A new method of analyzing stresses and strains in work-hardening plastic solids', *Journal of Applied Mechanics* **23**(EM5), 1177–1194.

Presti, D. C. F. L., Jamiolkowski, M. and Pepe, M. (2003), Geotechnical characterisation of the subsoil of Pisa Tower, *in* 'Characterisation and Engineering Properties of Natural Soils', Vol. 2, pp. 909–946.

Prevost, H. (1978), 'Plasticity theory for soil stress-strain behavior', *Journal of the Engineering Mechanics Division* **104**, 493–496.

Pusch, R. (1970), 'Microstructural changes in soft quick clay at failure', *Canadian Geotechnical Journal* **7**(1), 1–7.

Rampello, S. and Callisto, L. (1998), 'A study on the subsoil of the tower of pisa based on results from standard and high quality samples', *Canadian Geotechnical Journal* **35**, 1074–1092.

Rampello, S., Callisto, L., Viggiani, G. M. B. and Calabresi, G. (1996), The leaning tower of Pisa - Soil parameters for the numerical modelling of the tower resulting from the most recent investigations, Technical report, University of Rome La Sapienza, Italy.

Rankin, W. J. (1988), Ground movements resulting from urban tunnelling: predictions and effects, *in* 'Engineering Geology of Underground Movements, Geological Society Engineering Geology Special Publication', Vol. 5, pp. 79–92.

Rezania, M., Dejaloud, H. and Nezhad, M. M. (2014), SCLAY1S-BS: An anisotropic model for simulation of cyclic behaviour of clays, *in* 'Geomechanics from micro to macro'.

Rezania, M., Taiebat, M. and Poletti, E. (2016), 'A viscoplastic SANICLAY model for natural soft soils', *Computers and Geotechnics* **73**, 128–141.

Roscoe, K. H. and Burland, J. B. (1968), On the generalized stress strain behaviour of wet clay, *in* 'Engineering Plasticity', pp. 535–609.

Roscoe, K. H., Schofield, A. N. and Thurairajah, A. (1963), 'Yielding of clays in states wetter than critical', *Géotechnique* **13**(3), 211–240.

Roscoe, K. H., Schofield, A. N. and Wroth, C. P. (1958), 'On the yielding of soils', *Géotechnique* **8**(1), 22–53.

Rouainia, M. and Wood, D. M. (2000), 'A kinematic hardening constitutive model for natural clays with loss of structure', *Géotechnique* **50**(2), 153–164.

Rouainia, M. and Wood, D. M. (2001), 'Implicit numerical integration for a kinemtaic hardening soil plasticity model', *International Journal for Numerical and Analytical Methods in Geomechanics* **25**, 1305–1325.

Rowe, R. K., Lo, K. Y. and Kack, G. J. (1983), 'A method of estimating surface settlements above tunnels constructed in soft ground', *Canadian Geotechnical Journal* **20**(8), 11–22.

Saihi, F., Leroueil, S., La Rochelle, P. and French, I. (2002), 'Behaviour of the stiff and sensitive Saint-Jean-Vianney clay in intact, destructured, and remoulded conditions', *Canadian Geotechnical Journal* **39**, 1075–1087.

Saltelli, A. (2002), 'Making best use of model evaluations to compute sensitivity indices', *Computer Physics Communications* **145**, 280–297.

Saltelli, A., Ratto, M., Andres, T., Campolongo, F., Cariboni, J., Gatelli, D., Saisana, M. and Tarantola, S. (2008), *Global sensitivity analysis. The Primer*, John Wiley and Sons.

Sangrey, D. A. (1972), 'Naturally cemented sensitive soils', *Géotechnique* **22**(1), 139–152.

Sangrey, D., Henkel, D. and Esrig, M. (1969), 'The effective stress response of a saturated clay soil to repeated loading', *Canadian Geotechnical Journal* **6**(3), 241–252.

Schanz, T. (1998), Zur Modellierung des mechanischen Verhaltens von Reibungsmaterialien, Habilitationsschrift, Universität Stuttgart, Germany.

Schanz, T., Vermeer, P. A. and Bonnier, P. G. (1999), The hardening soil model: Formulation and verification, *in* 'Proceedings of the 1st International PLAXIS Symposium on Beyond 2000 in Computational Geotechnics', pp. 281–296.

Schanz, T., Zarev, V. and Barciaga, T. (2012), Adäquate Modellbildung für die numerische Analyse maschineller Tunnelvortriebe, *in* 'Beiträge zum 3. RuhrGeo Tag 2011: Innerstädtischer Tunnel- und Spezialtiefbau', pp. 131–146.

Schindler, S., Hegemann, F., Alsahly, A., Barciaga, T., Galli, M., Koch, C. and Lehner, K. (2014), 'Eine Interaktionsplattform für maschinelle Tunnelvortriebe - Anwendung am Beispiel der Wehrhahn-Linie in Düsseldorf; An interaction platform for mechanized tunnelling - applied to the Wehrhahn-Linie in Düsseldorf (Germany)', *Geomechanics and Tunnelling* **7**(1), 72–86.

Schofield, A. N. and Wroth, C. P. (1968), *Critical State Soil Mechanics*, McGraw-Hill.

Schweiger, H., Wiltafsky, C., Scharinger, F. and Galavi, V. (2009), 'A multilaminate framework for modelling induced and inherent anisotropy of soils', *Géotechnique* **59**(2), 87–101.

Seed, H. B. and Chan, C. K. (1966), 'Clay strength under earthquake loading conditions', *Journal of the Soil Mechanics and Foundations Division* **92**(SM2), 53–78.

Seidalinov, G. (2012), A simple anisotropic bounding surface plasticity model for cyclic response of clays, Master's thesis, The University of British Columbia, Vancouver, Canada.

Seidalinov, G. and Taiebat, M. (2014), 'Bounding surface SANICLAY plasticity model for cyclic clay behavior', *International Journal for Numerical and Analytical Methods in Geomechanics* **38**(7), 702–724.

Sekiguchi, H. and Ohta, K. (1977), Induced anisotropy and time dependence in clays, *in* '9th International Conference on Soil Mechanics and Foundation Engineering', pp. 229–238.

Sheng, D., Sloan, S. W. and Yu, H. S. (2000), 'Aspects of finite element implementation of critical state models', *Computational Mechanics* **26**, 185–196.

Skempton, A. W. (1970), 'The consolidation of clays by gravitational compaction', *Quarterly Journal of the Geological Society of London* **125**, 373–412.

Skempton, A. W. (1985), 'Residual strength of clays in landslides, folded strata and the laboratory', *Géotechnique* **35**(1), 3–18.

Skempton, A. W. and MacDonald, D. H. (1956), Allowable settlement of buildings, *in* 'Proceedings of the Institution of Civil Engineers', pp. 727–768.

Skempton, A. W. and Northey, R. D. (1952), 'The sensitivity of clays', *Géotechnique* **3**(1), 30–53.

Sloan, S. W. (1987), 'Substepping schemes for the numerical integration of elastoplastic stress-strain relations', *International Journal for Numerical Methods in Engineering* **24**, 893–911.

Sloan, S. W., Abbo, A. J. and Sheng, D. (2001), 'Refined explicit integration of elastoplastic models with automatic error control', *Engineering Computations* **18**(1-2), 121–194.

Smith, P. R. (1992a), The behavior of natural high compressibility clay with special reference to construction on soft ground, PhD thesis, University of London, Imperial College of Science, Technology and Medicine, UK.

Smith, P. R., Jardine, R. J. and Hight, D. W. (1992b), 'The yielding of Bothkennar clay', *Géotechnique* **42**(2), 257–274.

Sobol', I. M. (1993), 'Sensitivity estimates for nonlinear mathematical models', *Mathematical Modelling and Computational Experiment* **1**, 407–414.

Stallebrass, S. E. (1990), The effect of the recent stress history on the deformation of overcosolidated soils, PhD thesis, City University, London, UK.

Stallebrass, S. E. and Taylor, R. N. (1997), 'The development and evaluation of a constitutive model for the prediction of ground movements in overconsolidated clay', *Géotechnique* **47**(2), 235–253.

Stipho, A. S. (1978), Theoretical and experimental investigation of the anisotropically consolidated Kaolin, PhD thesis, University College, Cardiff, UK.

Suebsuk, J., Horpibulsuk, S. and Liu, M. D. (2011), 'A critical state model for overconsolidated structured clays', *Computers and Geotechnics* **38**, 648–658.

Taiebat, M., Dafalias, Y. F. and Peek, R. (2010), 'A destructuration theory and its application to SANICLAY model', *International Journal for Numerical and Analytical Methods in Geomechanics* **34**(10), 1009–1040.

Taiebat, M., Kaynia, A. M. and Dafalias, Y. F. (2011), 'Application of an anisotropic constitutive model for structured clay to seismic slope stability', *Journal of Geotechnical and Geoenvironmental Engineering* **137**(5), 492–504.

Takahashi, M. (1981), Transient and cyclic behaviour of a sandy clay, PhD thesis, Imperial College of Science and Technology, London, UK.

Talmon, A. M. and Bezuijen, A. (2009), 'Simulating the consolidation of TBM grout at Noordplaspolder', *Tunnelling and Underground Space Technology* **24**, 493–499.

Tamagnini, C., Castellanza, R. and Nova, R. (2002), 'Implicit integration of constitutive equations in computational plasticity', *Revue Francaise de Genie Civil* **6**(6), 1051–1067.

Tamagnini, C. and D'Elia, M. (1999), A simple bounding surface model for bonded clays, *in* 'Pre-failure Deformation Characteristics of Geomaterials', pp. 565–572.

Tarantola, A. (2005), *Inverse problem theory and methods for model parameter estimation*, SIAM.

Terzaghi, K. (1923), 'Die Berechnung der Durchlässigkeitsziffer des Tones aus dem Verlauf der hydrodynamischen Spannungserscheinungen', *Sitzungsberichte der Akademie der Wissenschaften in Wien, Mathematisch-Naturwissenschaftliche Klasse, Abteilung IIa* **132**, 125–138.

Terzaghi, K. (1925), *Erdbaumechanik auf bodenphysikalischer Grundlage*, Deuticke.

Terzaghi, K. (1943), *Theoretical Soil Mechanics*, Wiley.

Terzaghi, K. (1944), 'Ends and means in soil mechanics', *Engineering Journal* **27**(12), 608–615.

Terzaghi, K. and Fröhlich, O. K. (1936), *Theorie der Setzung von Tonschichten*, Deuticke.

van Langen, H. and Vermeer, P. A. (1991), 'Interface elements for singular plasticity points', *International Journal for Numerical and Analytical Methods in Geomechanics* **15**, 301–315.

van Olphen, H. (1977), *An introduction to clay colloid chemistry*, 2nd edn, Wiley.

Vermeer, P. A., Möller, S. and Ruse, N. (2003), 'On the application of numerical analysis in tunnelling', pp. 1–6.

Vermeer, P. A., Ruse, N. and Marcher, T. (2002), 'Tunnel heading stability in drained ground', *Felsbau* **20**(6), 8–18.

von Wolffersrdorf, P. A. (1996), 'A hypoplastic relation for granular materials with a predefined limit state surface', *Mechanics of Cohesive-Frictional-Materials* **1**, 251–271.

Vu, M. N., Broere, W. and Bosch, J. W. (2015), 'The impact of shallow cover on stability when tunnelling in soft soils', *Tunnelling and Underground Space Technology* **50**, 507–515.

Vu, M. N., Broere, W. and Bosch, J. W. (2017), 'Structural analysis for shallow tunnels in soft soils', *International Journal of Geomechanics* **17**(8), 04017038–1–12.

Vucetic, M. (1994), 'Cyclic threshold shear strains in soils', *Journal of Geotechnical Engineering* **120**(12), 2208–2228.

Vucetic, M. and Dobry, R. (1988a), 'Degradation of marine clays under cyclic loading', *Journal of Geotechnical Engineering* **114**(2), 133–149.

Vucetic, M. and Dobry, R. (1991), 'Effect of soil plasticity on cyclic response', *Journal of Geotechnical Engineering* **117**(1), 89–107.

Wang, W., Datcheva, M., Schanz, T. and Kolditz, O. (2006), 'A sub-stepping approach for elasto-plasticity with rotational hardening', *Computational Mechanics* **37**, 266–278.

Wathugala, G. W. and Desai, C. S. (1993), 'Constitutive model for cyclic behavior of clays. I: Theory', *Journal of Geotechnical Engineering* **119**(4), 714–729.

Wheeler, S., Näätänen, A., Karstunen, M. and Lojander, M. (2003), 'An anisotropic elasto-plastic model for soft clays', *Canadian Geotechnical Journal* **40**(2), 403–418.

Whittle, A. and Kavvadas, M. J. (1993), 'Evaluation of a constitutive model for overconsolidated clays', *Géotechnique* **43**(2), 289–313.

Whittle, A. and Kavvadas, M. J. (1994), 'Formulation of MIT-E3 constitutive model for overconsolidated clays', *Journal of Geotechnical Engineering* **120**(1), 173–198.

Wichtmann, T. (2016), Soil behaviour under cyclic loading - experimental observations, constitutive description and applications, Habilitationsschrift, Karlsruher Institut für Technologie, Germany.

Wichtmann, T., Andersen, K. H., Sjursen, M. A. and Berre, T. (2013), 'Cyclic tests on high-quality undisturbed block samples of soft marine Norwegian clay', *Canadian Geotechnical Journal* **50**(4), 400–412.

Wong, P. K. K. and Mitchell, R. J. (1975), 'Yielding and plastic flow of sensitive cemented clay', *Géotechnique* **25**(4), 763–782.

Wongsaroj, J., Soga, K. and Mair, R. (2007), 'Modelling of long-term ground response to tunnelling under St James's Park, London', *Géotechnique* **57**(1), 75–90.

Wongsaroj, J., Soga, K. and Mair, R. (2013), 'Tunnelling induced consolidation settlements in London clay', *Géotechnique* **63**(13), 1103–1115.

Wroth, C. P. and Wood, D. M. (1978), 'Theory of elasticity and consolidation for a porous anisotropic solid', *Canadian Geotechnical Journal* **15**(2), 137–145.

Xiao, H., Lee, F. H. and Liu, Y. (2017), 'Bounding surface Cam-Clay model with cohesion for cement-admixed clay', *International Journal of Geomechanics* **17**(1), 04016026–1–22.

Xu, Y., Sun, D., Sun, J., Fu, D. and Dong, P. (2003), 'Soil disturbance of Shanghai silty clay during EPB tunnelling', *Tunnelling and Underground Space Technology* **18**(5), 537–545.

Yang, C., Carter, J. P. and Sheng, D. (2014), 'Description of compression behaviour of structured soils and its application', *Canadian Geotechnical Journal* **51**(8), 921–933.

Yasuhara, K., Hirao, K. and Hyde, A. F. L. (1992), 'Effects of cyclic loading on undrained strength and compressibility of clay', *Soils and Foundations* **32**(1), 100–116.

Yasuhara, K., Yamanouchi, T. and Hirao, K. (1982), 'Cyclic strength and deformation of normally consolidated clay', *Soils and Foundations* **22**(3), 77–91.

Yin, Z. Y. and Chang, C. S. (2009a), 'Microstructural modelling of stress-dependent behaviour of clay', *International Journal of Solids and Structures* **46**, 1373–1388.

Yin, Z. Y., Xu, Q. and Hicher, P. Y. (2013), 'A simple critical-state-based double-yield-surface model for clay behavior under complex loading', *Acta Geotechnica* **8**, 509–523.

Yu, H. S., Khong, C. and Wang, J. (2007b), 'A unified plasticity model for cyclic behaviour of clay and sand', *Mechanics Research Communication* **34**, 97–114.

Zergoun, M. and Vaid, Y. P. (1994), 'Effective stress response of clay to undrained cyclic loading', *Canadian Geotechnical Journal* **31**, 714–727.

Zhao, C., Lavasan, A. A., Barciaga, T., Hölter, R., Datcheva, M. and Schanz, T. (2015b), Constitutive parameter adjustment for mechanized tunneling with reference to subsystem effects, *in* '8th International Conference on Numerical Methods and Applications', pp. 217–225.

Zhao, C., Lavasan, A. A., Barciaga, T., Kämper, C., Mark, P. and Schanz, T. (2017), 'Prediction of tunnel lining forces and deformations using analytical and numerical solutions', *Tunnelling and Underground Space Technology* **64**, 164–176.

Zhao, C., Lavasan, A. A., Barciaga, T. and Schanz, T. (2019a), 'Mechanized tunneling induced ground movements and its dependency on the tunnel volume loss and soil properties', *International Journal for Numerical and Analytical Methods in Geomechanics* **43**(4), 781–800.

Zhao, C., Lavasan, A. A., Barciaga, T., Zarev, V., Datcheva, M. and Schanz, T. (2015a), 'Model validation and calibration via back analysis for mechanized tunnel simulations - The Western Scheldt tunnel case', *Computers and Geotechnics* **69**, 601–614.

Zhao, C., Schmüdderich, C., Barciaga, T. and Röchter, L. (2019b), 'Response of building to shallow tunnel excavation in different types of soil', *Computers and Geotechnics* **115**, 103165.

Zhao, J., Sheng, D., Rouainia, M. and Sloan, S. W. (2005), 'Explicit stress integration of complex soil models', *International Journal for Numerical and Analytical Methods in Geomechanics* **29**, 1209–1229.

Zhou, J. and Gong, X. (2001), 'Strain degradation of saturated clay under cyclic loading', *Canadian Geotechnical Journal* **38**, 208–212.

Ziegler, H. (1959), 'A modification of Prager's hardening rule', *Quarterly of Applied Mathematics* **17**(1), 55–65.

Zienkiewicz, O. C., Leung, K. H. and Pastor, M. (1985), 'Simple model for transient soil loading in earthquake analysis. I. Basic model and its application', *International Journal for Numerical and Analytical Methods in Geomechanics* **9**, 453–476.

Zienkiewicz, O. C. and Pande, G. N. (1977), Some useful forms of isotropic yield surfaces for soil and rock mechanics, *in* 'Finite Elements in Geomechanics', pp. 179–198.

Schriftenreihe des Instituts für Grundbau, Wasserwesen und Verkehrswesen der Ruhr-Universität Bochum

Herausgeber: H.L. Jessberger

1 (1979) **Hans Ludwig Jessberger**
Grundbau und Bodenmechanik an der Ruhr-Universität Bochum

2 (1978) **Joachim Klein**
Nichtlineares Kriechen von künstlich gefrorenem Emschermergel

3 (1979) **Heinz-Joachim Gödecke**
Die Dynamische Intensivverdichtung wenig wasserdurchlässiger Böden

4 (1979) **Poul V. Lade**
Three Dimensional Stress-Strain Behaviour and Modeling of Soils

5 (1979) **Roland Pusch**
Creep of soils

6 (1979) **Norbert Diekmann**
Zeitabhängiges, nichtlineares Spannungs-Verformungsverhalten von gefrorenem Schluff unter triaxialer Belastung

7 (1979) **Rudolf Dörr**
Zeitabhängiges Setzungsverhalten von Gründungen in Schnee, Firn und Eis der Antarktis am Beispiel der deutschen Georg-von-Neumayer- und Filchner-Station

8 (1984) **Ulrich Güttler**
Beurteilung des Steifigkeits- und Nachverdichtungsverhaltens von ungebundenen Mineralstoffen

9 (1986) **Peter Jordan**
Einfluss der Belastungsfrequenz und der partiellen Entwässerungs-möglichkeiten auf die Verflüssigung von Feinsand

10 (1986) **Eugen Makowski**
Modellierung der künstlichen Bodenvereisung im grundwasserdurchströmten Untergrund mit der Methode der finiten Elemente

11 (1986) **Reinhard A. Beine**
Verdichtungswirkung der Fallmasse auf Lastausbreitung in nichtbindigem Boden bei der Dynamischen Intensivverdichtung

12 (1986) **Wolfgang Ebel**
Einfluss des Spannungspfades auf das Spannungs-Verformungsverhalten von gefrorenem Schluff im Hinblick auf die Berechnung von Gefrierschächten

13 (1987) **Uwe Stoffers**
Berechnungen und Zentrifugen-Modellversuche zur Verformungsabhängigkeit der Ausbaubeanspruchung von Tunnelausbauten in Lockergestein

14 (1988) **Gerhard Thiel**
Steifigkeit und Dämpfung von wassergesättigtem Feinsand unter Erdbebenbelastung

15 (1991) **Mahmud Thaher**
Tragverhalten von Pfahl-Platten-Gründungen im bindigen Baugrund,
Berechnungsmodelle und Zentrifugen-Modellversuche

Schriftenreihe des Instituts für Grundbau der Ruhr-Universität Bochum

Herausgeber: H.L. Jessberger

16 (1992) **Rainer Scherbeck**
Geotechnisches Verhalten mineralischer Deponieabdichtungsschichten
bei ungleichförmiger Verformungswirkung

17 (1992) **Martin M. Bizialiele**
Torsional Cyclic Loading Response of a Single Pile in Sand

18 (1993) **Michael Kotthaus**
Zum Tragverhalten von horizontal belasteten Pfahlreihen aus langen Pfählen in Sand

19 (1993) **Ulrich Mann**
Stofftransport durch mineralische Deponieabdichtungen:
Versuchsmethodik und Berechnungsverfahren

20 (1992) **Festschrift anlässlich des 60. Geburtstages von**
Prof. Dr.-Ing. H. L. Jessberger
20 Jahre Grundbau und Bodenmechanik an der Ruhr-Universität Bochum

21 (1993) **Stephan Demmert**
Analyse des Emissionsverhaltens einer Kombinationsabdichtung im Rahmen der
Risikobetrachtung von Abfalldeponien

22 (1994) **Diethard König**
Beanspruchung von Tunnel- und Schachtausbauten in kohäsionslosem Lockergestein
unter Berücksichtigung der Verformung im Boden

23 (1995) **Thomas Neteler**
Bewertungsmodell für die nutzungsbezogene Auswahl von Verfahren zur Altlastensanierung

24 (1995) **Ralph Kockel**
Scherfestigkeit von Mischabfall im Hinblick auf die Standsicherheit von Deponien

25 (1996) **Jan Laue**
Zur Setzung von Flachfundamenten auf Sand unter wiederholten Lastereignissen

26 (1996) **Gunnar Heibrock**
Zur Rissbildung durch Austrocknung in mineralischen Abdichtungsschichten
an der Basis von Deponien

27 (1996) **Thomas Siemer**
Zentrifugen-Modellversuche zur dynamischen Wechselwirkung zwischen Bauwerken
und Baugrund infolge stoßartiger Belastung

28 (1996) **Viswanadham V. S. Bhamidipati**
Geosynthetic Reinforced Mineral Sealing Layers of Landfills

29 (1997) **Frank Trappmann**
Abschätzung von technischem Risiko und Energiebedarf bei Sanierungsmaßnahmen für Altlasten

30 (1997) **André Schürmann**
Zum Erddruck auf unverankerte flexible Verbauwände

31 (1997) **Jessberger, H. L. (Herausgeber)**
Environment Geotechnics, Report of ISSMGE Technical Committee TC 5 on Environmental Geotechnics

Schriftenreihe des Instituts für Grundbau und Bodenmechanik der Ruhr-Universität Bochum

Herausgeber: Th. Triantafyllidis

32 (2000) **Triantafyllidis, Th. (Herausgeber)**
Boden unter fast zyklischer Belastung: Erfahrung und Forschungsergebnisse (Workshop)

33 (2002) **Christof Gehle**
Bruch- und Scherverhalten von Gesteinstrennflächen mit dazwischenliegenden Materialbrücken

34 (2003) **Andrzej Niemunis**
Extended hypoplastic models for soils

35 (2004) **Christiane Hof**
Über das Verpressankertragverhalten unter kalklösendem Kohlensäureangriff

36 (2004) **René Schäfer**
Einfluss der Herstellungsmethode auf das Verformungsverhalten von Schlitzwänden in weichen bindigen Böden

37 (2005) **Henning Wolf**
Zur Scherfugenbänderung granularer Materialien unter Extensionsbeanspruchung

38 (2005) **Torsten Wichtmann**
Explicit accumulation model for non-cohesive soils under cyclic loading

39 (2008) **Christoph M. Loreck**
Die Entwicklung des Frischbetondruckes bei der Herstellung von Schlitzwänden

40 (2008) **Igor Arsic**
Über die Bettung von Rohrleitungen in Flüssigböden

41 (2009) **Anna Arwanitaki**
Über das Kontaktverhalten zwischen einer Zweiphasenschlitzwand und nichtbindigen Böden

Schriftenreihe des Lehrstuhls für Grundbau, Boden- und Felsmechanik der Ruhr-Universität Bochum

Herausgeber: T. Schanz

42 (2009) **Yvonne Lins**
Hydro-Mechanical Properties of Partially Saturated Sand

43 (2010) **Tom Schanz (Herausgeber)**
Geotechnische Herausforderungen beim Umbau des Emscher-Systems
Beiträge zum RuhrGeo Tag 2010

44 (2010) **Jamal Alabdullah**
Testing Unsaturated Soil for Plane Strain Conditions: A New Double-Wall Biaxial Device

45 (2011) **Lars Röchter**
Systeme paralleler Scherbänder unter Extension im ebenen Verformungszustand

46 (2011) **Yasir Al-Badran**
Volumetric Yielding Behavior of Unsaturated Fine-Grained Soils

47 (2011) **Usque ad finem**
Selected research papers

48 (2012) **Muhammad Ibrar Khan**
Hydraulic Conductivity of Moderate and Highly Dense Expansive Clays

49 (2014) **Long Nguyen-Tuan**
Coupled Thermo-Hydro-Mechanical Analysis: Experimental and Back Analysis

50 (2014) **Tom Schanz (Herausgeber)**
Ende des Steinkohlenbergbaus im Ruhrrevier: Realität und Perspektiven für die Geotechnik
Beiträge zum RuhrGeo Tag 2014

51 (2014) **Usque ad finem**
Selected research papers

52 (2014) **Houman Soleimani Fard**
Study on the Hydro-Mechanical Behavior of Fiber Reinforced Fine Grained Soils,
with Application to the Preservation of Historical Monuments

53 (2014) **Wiebke Baille**
Hydro-Mechanical Behaviour of Clays - Significance of Mineralogy

54 (2014) **Qasim Abdulkarem Jassim Al-Obaidi**
Hydro-Mechanical Behavior of Collapsible Soils

55 (2015) **Veselin Zarev**
Model Identification for the Adaption of Numerical Simulation Models -
Application to Mechanized Shield Tunneling

56 (2015) **Meisam Goudarzy**
Micro and Macro Mechanical Assessment of Small and Intermediate Strain
Properties of Granular Material

57 (2016) **Oliver Detert**
Analyse einer selbstregulierenden interaktiven Membrangründung für Schüttkörper auf geringtragfähigen Böden

58 (2016) **Yang Yang**
Analyses of Heat Transfer and Temperature-induced Behaviour in Geotechnics

59 (2016) **Alborz Pourzargar**
Application of suction stress concept to partially saturated compacted soils

60 (2017) **Hanna Haase**
Multiscale Analysis of Clay-Polymer Composites for Geoenvironmental Applications

61 (2017) **Kavan Khaledi**
Constitutive modeling of rock salt with application to energy storage caverns

62 (2017) **Nina Silvia Müthing**
On the consolidation behaviour of fine-grained soils under cyclic loading

63 (2017) **Elham Mahmoudi**
Probabilistic analysis of a rock salt cavern with application to energy storage systems

64 (2017) **Negar Rahemi**
Evaluation of liquefaction behavior of sandy soils using critical state soil mechanics and instability concept

65 (2018) **Chenyang Zhao**
Numerical Modeling of Mechanized Tunnel Excavation:
Effects of Sub-systems and Advanced Process Simulation

66 (2018) **Tom Schanz (Herausgeber)**
Innovationen im Spezialtiefbau und in der Umweltgeotechnik
Beiträge zum RuhrGeo Tag 2018

67 (2019) **Linzhi Lang**
Hydro-Mechanical Behaviour of Bentonite-Based Materials Used for Disposal of Radioactive Wastes

68 (2019) **Usama Al-Anbaki**
Hydraulic Interaction of Soil and Nonwoven Geotextiles under Unsaturated Conditions

69 (2019) **Abhishek Rawat**
Coupled Hydro-mechanical Behavior of a Compacted Bentonite-Sand Mixture: Experimental and Numerical Investigations

Schriftenreihe des Lehrstuhls für Bodenmechanik, Grundbau und Umweltgeotechnik der Ruhr-Universität Bochum

Herausgeber: T. Wichtmann

70 (2019) **Mahmoud Qarmout**
Tunnel face stability using Kinematical Element Method (KEM)

71 (2021) **Raoul Hölter**
Optimal Experimental Design in Geotechnical Engineering

72 (2022) **Wolfgang Lieske**
Impact of polymer constitution on the hydro-mechanical behaviour of modified bentonite for the application in geotechnical and geoenvironmental engineering

73 (2022) **Patrick Staubach**
Contributions to the numerical modelling of pile installation processes and high-cyclic loading of soils

74 (2022) **Lingyun Li**
On the hydromechanical behaviour of loess and its effect on slope stability under rainfall infiltration

75 (2022) **Debdeep Sarkar**
Influence of particle characteristics on the behaviour of granular materials under static, cyclic and dynamic loading

76 (2023) **Torsten Wichtmann (Herausgeber)**
Umbau des Emscher-Systems – Geotechnische Erfahrungen
Beiträge zum RuhrGeo Tag 2023

77 (2023) **Abbas Farhat**
Fluidization and erosion of cemented granular materials. Experimental characterization and micromechanical simulation

78 (2023) **Andrea Geppetti**
Experimental and numerical investigations on the behaviour of tailing storage facilities under seismic loading

79 (2023) **Mohammad Hassan Sanayei**
Micromechanical modelling for the analysis of piping erosion in cemented soils for suction-assisted offshore foundations

80 (2024) **Christoph Schmüdderich**
Contributions to the stability assessment of slopes subjected to seismic loading

81 (2024) **Thomas Barciaga**
Constitutive modeling of natural clay with application to mechanized tunneling